Deformation and fluid processes in thrust sheets from the central Pyrenees

Submitted in accordance with the requirements for the degree of Doctor of Philosophy

by

Neil T. Grant

January 1989

Department of Earth Sciences, the University of Leeds

ABSTRACT

Deformation and fluid processes in thrust sheets are studied using a small thrust system in the footwall of the Gavarnie Thrust, central Pyrenees. This system comprises a set of blind thrusts that imbricate a thin Mesozoic cover succession (Triassic red beds and Upper Cretaceous limestone) in the Cirque de Barroude and produce a culmination in the Gavarnie Thrust. An intense cleavage developed within the culmination associated with the oblique tipping of thrusts as they climb from the basement into the cover strata. The distributed strain associated with the fault tips locally reactivated earlier folded thrusts by the development of upper strain detachments. The main detachment occurred along the Pic de Port Vieux thrust which forms the roof of the culmination. The reactivation occurred along the back-limbs of folds in the thrust and produced faults that cut across the fold crests. The movement on these upper strain detachments was intermittent and the faults were gently folded when inactive. The faults that formed within the zone of distributed strain are discontinuous and their development did not conform to foreland or hinterland propagation and more than one fault moved simultaneously. The overlying Gavarnie Thrust sheet extended sub-parallel to transport during the early stages of the culmination development. The concurrence of shortening in the footwall and extension in the hanging wall of the thrust implies that the it acted as mechanical boundary between two differently deforming plates. The extension of the upper plate (the Gavarnie Thrust sheet) is considered to have occurred during gravity spreading in response to an increased critical taper in the south Pyrenean thrust wedge. The increased taper possibly resulted from the shortening associated with the underplating of the lower thrust sheets in the central Pyrenees.

The composition and source of the ambient fluid in the thrusts and the fluid flow processes that operated during the fault activity have been studied using fluid inclusion microthermometry from cavity-fill quartz and from the chemistry of secondary phases in the cavities. The cavities formed by the hydraulic jacking of fault planes and they indicate the presence of syntectonic high fluid pressures. These pressures appear to have been generated in situ during the distributed deformation in the culmination and seismic pumping does not appear to have operated. The fluid is a high salinity Ca-Na-Cl brine. The presence of bitumen in the inclusions suggests the brine is a connate basinal brine and not of metamorphic origin. Heterogeneity of brine compositions between the different samples studied suggests that the fluid reservoir in the culmination was heterogeneous and produced by limited dilution of the connate brine with meteoric water. Fluid-rock ratios were low and the close correspondence between vein mineralogy and wall rock composition suggests that the fluids were equilibrated with the strata in the culmination. Local fluid flow pathways have been mapped using Mg-variations within chlorite. These show that limited fluid transfer occurred between the Cretaceous limestone and the adjacent basement or the Triassic red beds. This transfer appears to have been related to dilatancy pumping associated with the hydrofracture events. Large-scale fluid migration along the active faults did not occur even though local fracture permeabilities were high.

ACKNOWLEDGEMENTS

I take full responsibility for all the errors that occur within this thesis. The work could not have been accomplished however without the assistance of my family and many of my colleagues and friends. I would therefore like to thank my mum and dad and my grandmother for financial support and my brother Colin for motivation. I would also like to thank Dave, Mark, Sue, Alastair, Andy, Dave, Martin, and my other friends in Leeds for stimulating discussions regarding my work and other more interesting things. I would also like to thank Dr Bruce Yardley, Dr. Eric Condliffe, Dr. Geoff Lloyd and Mr. Tony Nicolls for guidance in using various bits of machinery and to Colin and Kieth for producing dozens of thin sections. I must also express gratitude to Dr. David Banks for his invaluable guidance and assistance during my fluid inclusion work and to my supervisors Dr. Rob Knipe and Dr. Andy McCaig for their guidance and encouragement during this work. I also want to especially thank Andy for his thorough review my the thesis and for greatly improving the text. Finally I wish to thank Mr Fred Faget and family and his donkey Benoit for support and friendship during my stays in the Pyrenees, the PNP occidental for permission to camp in the Cirque de Barroude , my field assistants Sue, Gary and John for company and to Sarah whose endless patience and support in the preparation of this work were invaluable.

TABLE OF CONTENTS.

LIST OF FIGURES

LIST OF TABLES

Abbreviations used in text.

BF= Bouneau formation
BIS= basement imbricate stack
BLS = back-limb splay
BSEM= back-scattered electron microscopy
BTFZ= basal Triassic fault zone
FDSF= Fourche de Sede formation
GT= Gavarnie Thrust
KBB=kink band boundary
LFS= lower fold structure
MFS= middle fold structure
NPF= North Pyrenean Fault
PAZ= Palaeozoic Axial Zone
P_f= fluid pressure
PPV= Pic de Port Vieux
PPVT= Pic de Port Vieux Thrust
SGP= Silurian graphitic phyllite
SMF= Sugar Marble formation
TEM= transmission electron microscopy
UFS= upper fold structure

CHAPTER 1

Introduction

1.1. Thrust systems.

Thrust systems are the linked arrays of low angle reverse faults that shorten continental crust in collision orogens. The geometry of these arrays is now reasonably well defined (Bally et al., 1966; Dahlstrom, 1970; Boyer and Elliott, 1982; Butler, 1982; Butler, 1987) and a number of geometric rules have been developed to aid interpretation of thrust structures (Dahlstrom, 1969; Ramsay and Hubert, 1987). The foremost rule employed is that sections should balance, that is they should be restorable to an original configuration via an admissable thrust sequence (Elliott, 1983). This rule is based on the assumption that the deformation is plane strain with conservation of area and line length and no movement across the plane containing the transport direction (Hossack, 1979). In recent years, the use of balanced sections in constructing palinspastic reconstructions has greatly improved the estimation of orogenic shortening.

While knowledge of thrust systems, their propagation sequences, the strain within thrust sheets and the displacements across orogens has advanced greatly, a number of features of thrust faulting have still to be considered. Some of these aspects are outlined below.

1.1.1. The role of linked faulting.

Restoration of deformed sections is facilitated by the assumption that all the thrusts link to a common floor detachment. This has been shown to be the case in a number of external thrust belts (eg. Elliott and Johnson, 1980; Boyer and Elliott, 1982; Price,1967). Where thrusting competes with distributed deformation the assumption of linked thrusting will not necessarily be valid and fault propagation sequences may cease to follow simple geometric rules. The internal deformation could occur by grain-scale processes viz pressure solution, crystal plasticity etc., or by the development of arrays of secondary faults (eg. Wojtal, 1986; Mitra and Wojtal, 1986). Fault sequences may be more difficult to define in distributed strain fields because the faults need not physically link to one another and may move independently and therefore simultaneously. The geometric rules developed in the external regions of belts have often been extrapolated ad hoc to the more internal regions without a full appreciation of how the faults actually develop and how they contribute to the overall deformation. The shortening estimates obtained using these techniques may be in err.

1.1.2. The propagation of thrusts.

The propagation of thrust faults has been a topic of some controversy. In most instances thrusts appear to propagate toward the foreland (piggy-back propagation) as a consequence of loading during linked thrust development (Dahlstrom, 1970; Boyer and Elliott, 1982). The reverse situation is known as break-back or hinterland propagation and the thrusts are designated out-of-sequence (Butler, 1987; Morley, 1988). The latter type of thrusts are becoming more frequently documented from thrust systems although little work has been done concerning their origins. One consequence of out-of-sequence thrusts is that older thrust sheets are buried by younger thrusts.

The discussion of foreland or hinterland propagation refers specifically to the development of the fault sequences and not to individual faults. The most common belief is that thrusts propagate as bedding-parallel flats that cut up section across competent units to form ramps (Rich, 1934). Gretner (1972) and more recently Eisenstadt and De Paor (1987) have forwarded an alternative mechanism: propagation by beam-failure. This mechanism considers that failure occurs first in the competent units which are initially stress supporting and only then in the incompetent units as a result of stress transfer. This mechanism predicts that linked faults only develop where fault capture occurs. Ellis and Dunlap (1988) have shown that thrusts on a range of scales have segmented displacement distributions that support formation by the linkage of previously discontinuous faults. The assumption that measured displacements along thrusts can be extrapolated across the whole fault surface is often employed in section balancing and restoration. This is another assumption that is not merited and it may lead to significant errors in shortening estimates.

1.1.3. The influence of stratigraphy.

The influence of lithological and stratigraphical variations on deformation style in thrust belts have only recently begun to be considered (Morley, 1986; Gillchrist et.al, 1987; Welbon, 1987). The sedimentary prisms that are invariably deformed in the thrust belts, are not composed of layer-cake sequences of strata but possess unconformities, growth faulting and facies variations that can all play a part in guiding thrust fault development. These heterogeneities may affect palinspastic reconstructions and therefore shortening estimates. Earlier episodes of deformation can also produces heterogeneities in the strata that have to be taken into account in constructing balanced cross sections. The use of simple layer-cake sections in orogenic restorations is another simplification that has often not been merited.

1.1.4. The role of fluids.

The role of fluids in thrust faulting is generally considered a mechanical one (Hubbert and Rubey, 1959; Gretner, 1972 and 1981; Mandl and Shippam, 1981; Cello and Nur, 1988) with the generation of high fluid pressures facilitating fault propagation by reducing frictional resistance on a detachment. The geochemistry and source of the fluids has received little attention as has the direction or mechanisms of fluid transport. Generalised fluid flow models for thrust belts have recently been proposed by Fyfe and Kerrich (1985) and Oliver (1986). Fyfe and Kerrich (op.cit) envisage that the flow regimes in thrust zones will follow a sequence from conditions of high P-T with locally derived fluid at low water/rock ratios during initiation of structures to high fluid fluxes of reduced metamorphic fluids as faults propagate and intersect hydrothermal reservoirs. Recent stable isotope work (Kerrich et.al, 1984, Kerrich, 1986a and 1986b, Buckhard and Kerrich, 1988) has shown that the final stages of faulting are often associated with influxes of downward circulating meteoric water. Oliver suggests that thrust belts act as 'squeegees' that expel formation waters towards the foreland or towards the interior of the orogen. These fluids carry with them hydrocarbons, dissolved metal cations etc and play an important role in most of phenomena associated with orogenies. The volumes of fluids involved are large, up to 30% of the volume of the strata involved in the deformation. The role of this fluid, its source reservoir and chemical composition, and the fluid flow processes that operate during the faulting have still to be properly evaluated.

1.2 Setting of this work.

This thesis will look at the deformation associated with, and the fluid processes that operated during, Alpine-aged thrusting in the central Pyrenees. The work will address some of the points outlined above. The Pyrenees represent an Alpine orogenic belt that formed largely by thrust- related processes (Choukroune and Seguret, 1973; Mattauer and Henry, 1974; Fischer, 1984; Parish, 1984; Williams and Fischer, 1985; Deramond et.al, 1985; Seguret and Daignieres, 1986; Fontbote, 1986). during convergence between Iberia and Europe (see chapter 2). The belt comprises both external and internal thrust sheets. The former are exposed in the south where a syntectonic foreland basin (the south Pyrenean Tertiary Basin) was imbricated by a thin-skinned foreland propagating thrust system (Labaume et al., 1985). The centre of the belt has a basement core that comprises two levels of thrust sheets (Munoz et al., 1986): (**Middle thrust sheets** that thrust basement over cover and **Lower Thrust Sheets** that imbricated mid-crustal basement. The exposure of basement in the central, topographically highest, part of orogenic belt provides an opportunity to study the deformation and fluid processes in the more internal thrust sheets and to see how this compares with the proposed models for thrust system evolution.

1.3 Aims of the thesis.

The main aims of the project are to document the style of mesoscopic deformation associated with thrusts that developed along a basement-cover interface and to assess the fluid processes in the fault system. The structures considered are located in an area extending from Cirque de Barroude to the Sierra Liena in the central Pyrenees (see figures 2.6 and 3.1 for location). They outcrop in the footwall of a major basement thrust sheet (the Gavarnie Thrust Sheet). Specific problems that will be covered in the work include:

1. Thrust fault geometries and sequences of development in regions dominated by distributed deformation.
2. Small scale structures associated with thrusts and their tectonic significance. In particular attention is focussed on arrays of secondary faults within thrust sheets.
3. The deformation mechanisms that operated during the thrusting, evaluated from the fault zone microstructures.
4. The physical and chemical affects of fluid in the fault zones and the role they play in determining the style and products of the deformation.

The data and results will be integrated into a tectonic synthesis that will hopefully show how an integrated approach to the detailed study of thrusts can help to formulate regional tectonic scenarios.

1.4. Methods of study

The basis of this study is detailed field work of selected areas within Cirque de Barroude. To place these studies in their regional context smaller-scale mapping has also been carried out extending from the Sierra Liena to the La Gela valley. Specimens for microstructural study were collected during the field work.

The microstructures of the field specimens were studied using both optical and transmission and back-scattered electron microscopy. The marriage of the field studies with the microstructural work enables a fuller assessment of the deformation processes to be made. In addition, fluid inclusions in vein quartz from fault-related cavities have been studied using microthermometric techniques. Together with a microchemical analysis of chlorite from the same veins this data enables some inferences to be drawn concerning fluid-rock reactions in the thrust system, the source of the fluids and the fluid flow processes.

1.5. Layout of the thesis.

The aims of the thesis have already been outlined, but more definitive aims will be given at the start of each chapter as a guide to the work that follows. The thesis is broken down into a further 6 chapters. Chapter 2 gives a brief review of the regional geology of the central Pyrenees and discusses current tectonic models. Chapter 3 describes the lithostratigraphy and regional structure of the study area. Chapter 4 presents a detailed description and interpretation of the structure of Pic de Port Vieux. This study is augmented by the results of the microstructural work (Chapter 5). Chapter 6 discusses the the fluid inclusion data and the chemistry of chlorite in the fault system. These are used to infer the fluid processes that operated in the fault system. Chapter 7 gives a summary of the main conclusions and outlines possible avenues for further research.

CHAPTER 2

An Introduction to the Pyrenees

This short chapter will outline current ideas on the structure and evolution of the central Pyrenees. It will serve to place the field work documented in Chapters 3 and 4 in its appropriate structural context.

2.1. The Age and Origin of the Pyrenees.

The Pyrenees is an Alpine orogenic belt separating the European craton from the Iberian microplate. It represents the active margin between the two plates and formed in the interval end- Cretaceous to Upper Eocene (Mattauer and Henry, 1974) during the northwest convergence of Iberia relative to Europe (Boillot, 1984) (figure 2.1). Constraints on the timing of the deformation are mainly stratigraphical and the onset of Pyrenean convergence can be witnessed in the late Cretaceous stratigraphic record with a facies change from marine to continental and a migration of basin margins away from the present day axis of the belt (Mattauer and Henry, op.cit; Curnelle et.al, 1982; Simo, 1986). Deformation related to this convergence is recorded first in the Upper Cretaceous in the east of the belt and migrated westward with time (Mattauer and Henry, op.cit; Curnelle et.al, op.cit). Accordingly uplift and erosion is greater in the east than in the west.

The Pyrenees are asymmetrical with predominantly southward displacements in the centre and east of the belt and mainly north directed displacements in the west (eg. on the Labourd Thrust (Seguret and Daignieres, 1985)). A southerly dipping active margin that developed in the Oligocene along the North Iberian margin represents the westward continuation of the orogen (Grimaud et.al, 1982) (figure 2.1). This along-strike diversity has been explained by Engeser and Schwentke (1986) in terms of a flip in the direction of subthrusting accommodated on a transform fault that was buried beneath later thrust sheets. Muller et al. (1988) consider this fault to be the Pamplona fault (see figure 2.5).

In the Cenozoic, active sedimentation continued in linear foreland basins to the north and south of the Pyrenees: the Aquitaine and South Pyrenean Tertiary basins respectively. The Palaeocene to Eocene history of the latter basin is well constrained by the observed contemporaneity of sedimentation and tectonics (Labaume et al., 1985; Farrel et.al, 1987). Undeformed Oligocene-Miocene sediments in the Ebro basin south of the orogenic belt represent a Pyrenean molasse sequence.

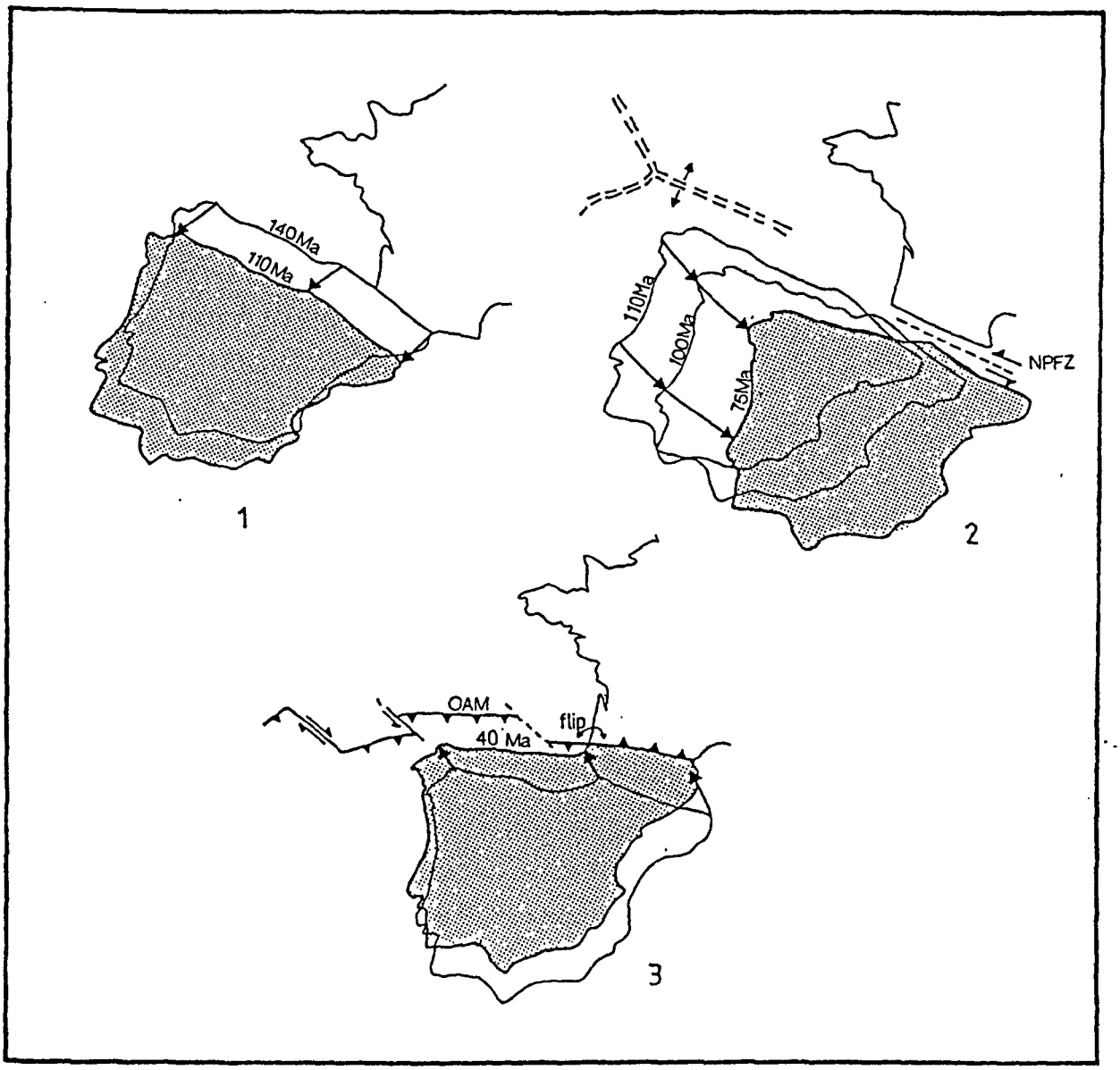

Figure 2.1. Mesozoic and Cainozoic movement of Iberia relative to a stable Europe (after Boillot (1984). 1. Pre late-Aptian distension. 2. Late-Aptian to Santonian. Sinistral strike slip occurred along the North Pyrenean Fault Zone (NPFZ) during sea floor spreading in the Bay of Biscay. 3. Palaeocene to Eocene Northwest plate convergence responsible for the Alpine Pyrenean orogenic belt. OAM: Oligocene Active Margin (after Grimaud et al., (1982). Note flip in the direction of subthrusting across the belt (cf. Engeser and Schwenke, 1986).

The Pyrenees is distinct from other Alpine orogenic belts in that its structural evolution was not associated with syntectonic regional metamorphism or regionally developed penetrative deformation (Banda and Wickham, 1986). The linear trace of the belt also contrasts markedly with the general arcuate nature of the Alps or the Himalaya. This lack of continuity with other Alpine belts is related to the relatively simple pre-Alpine evolution of the Pyrenean crustal segment. No oceanic crust was ever present in the segment and during the Mesozoic, opening of the Bay of Biscay was accommodated in the Pyrenees by the sinistral movement on the North Pyrenean Fault zone (figure 2.1). The linearity of this structural zone appears to have influenced the later Alpine evolution of the belt. For a review of the Mesozoic history of the belt see Puigdefabregas and Souquet (1986).

2.2. The Structure of the Pyrenees.

Traditionally the structure of the Pyrenees has been considered in terms of five structural zones (Mattauer and Henry, 1974) (figure 2.2). Both the North and South Pyrenean Zones display foreland fold-and-thrust belt geometries. These flank the Palaeozoic Axial Zone comprised mainly of Hercynian basement.

2.2.1. The North Pyrenean Zone (NPZ).

Recent models for the NPZ consider that it represents a series of basement blocks and their cover sediments thrust over the stable European Craton (Fischer, 1984; Peybernes and Souquet, 1984; Seguret and Daignieres, 1985 and 1986). The blocks are believed to have initially represented tilted fault blocks formed during Mesozoic rifting (Deramond et.al, 1985; Mattauer, 1985; Boillot, 1986). Shortening estimates across the zone vary between 18km (Fischer, op.cit) to 35-39km (Seguret and Daignieres, op.cit). The former is likely to be an underestimate because Fischer omitted the presence of tilted fault blocks and restored the thrusts using a southward thickening clastic prism. The NPZ is considered a backthrust zone to the more important south-directed thrusting in the belt (Fischer op. cit; Parish, 1984).

2.2.2. The Palaeozoic Axial Zone (PAZ).

The structure of the PAZ is still a subject of controversy. This is because the internal structure of the zone is not well known largely as a result of erosion of the Mesozoic and Cainozoic cover deposits and the superposition of Alpine and Hercynian structures. Collectively, proposed models for the PAZ fall into two groups:

1. thin-skinned interpretations, where the zone is considered allochthonous (Parish, 1984; Fischer, 1985; Williams and Fisher, 1984; Munoz et.al, 1986) and

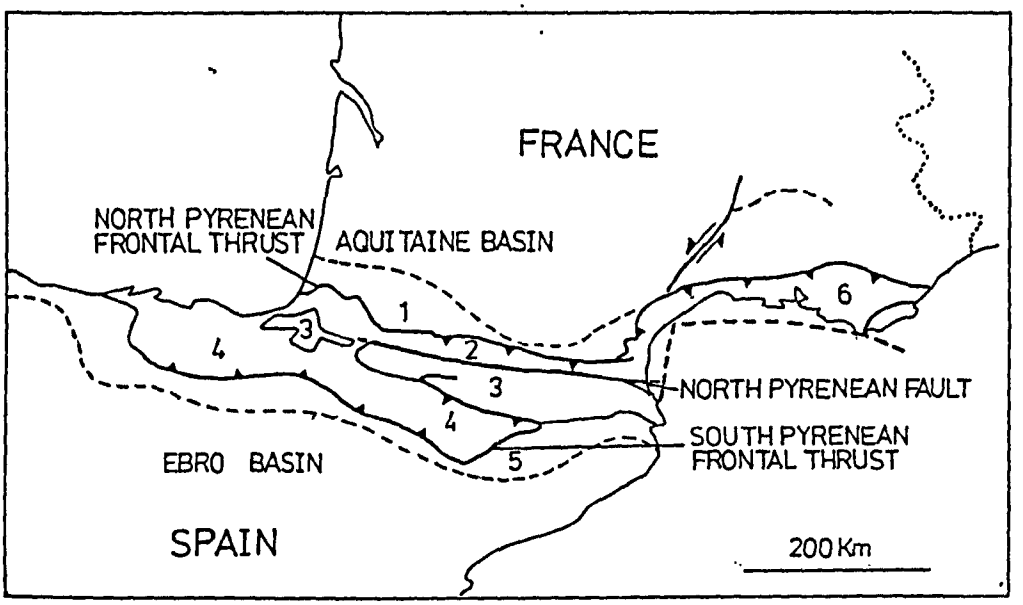

Figure 2.2. Structural zones of the Pyrenees (from Mattauer and Henry, 1974). 1. Northern Folded Foreland. 2. North Pyrenean Zone. 3. Palaeozoic Axial Zone. 4. South Pyrenean Zone. 5. Southern Folded Foreland. 6. Languedoc Province.

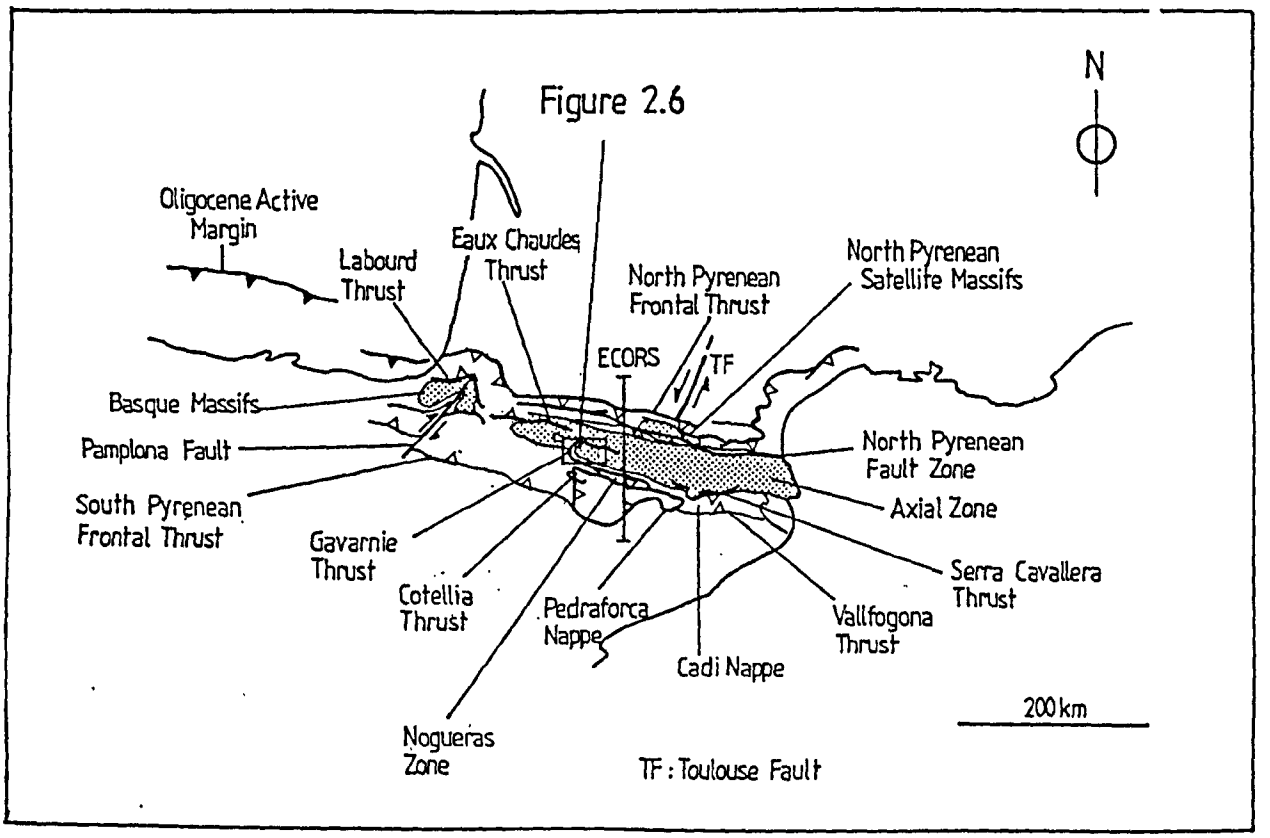

Figure 2.3. Main structural units of the Pyrenees showing location of the ECORS profile and structures named in text.

2. thick-skinned interpretations, in which which the zone is interpreted as a tectonically thickened autochthonous basement block (Choukroune and Seguret, 1973; Mattauer and Henry, 1974; Daignieres et al., 1982; Seguret and Daignieres, 1986).

2.2.2.1. Thick-skinned models.

The rationale behind the thick-skinned models is:
1. Most Alpine-aged structures in the PAZ (thrusts and shear zones) possess steep attitudes.
2. A 10km step in the Moho appears to occur across the northern margin of the Axial Zone approximately coincident with the surface trace North Pyrenean Fault Zone (NPFZ) (Daignieres et al., 1982). This fault is considered to represent the boundary between the European and Iberian plates (Mattauer and Henry, 1974).

The thick-skinned models consider that the North Pyrenean Fault Zone forms the axis of the belt and has not been deformed by later thrusting. The consequences of assuming an autochthonous (and therefore a pre-Alpine) origin for the PAZ are that it minimises shortening estimates and implies that the PAZ should have acted as a palaeogeographic high since the early Eocene (Munoz et.al. 1986). The overriding problem with thick-skinned models is that regional penetrative deformation of Alpine age has still to be convincingly shown for the Hercynian basement of the PAZ.

Seguret and Daignieres (1985 and 1986) have proposed an inhomogeneous strain model to explain how the thick-skinned deformation in the PAZ may link with the thin-skinned deformation of the foreland portions of the belt. This model (figure 2.4a) suggests that, when traced into the PAZ, thrusts root into a zone of distributed strain within the middle to lower crust and that the observed displacement on the major thrusts resulted partly from strain within the thrust sheets and partly from boundary displacements. The model is based on the consideration that shortening of the upper crust must be balanced somewhere by shortening of the lower crust. Vertical displacements produced by penetrative shortening in the PAZ are considered by Seguret and Daignieres (op. cit) to be transferred on natural curved fault surfaces into the horizontal displacements observed on major thrusts in the foreland. The model implies that the steep reverse faults observed in the PAZ were initiated as steep faults and have always possessed this attitude.

2.2.2.2. Thin-skinned models.

The thin-skinned interpretations of the PAZ consider the zone to represent a basement culmination developed above a northward dipping regional decollement. This model implies that steeply oriented reverse faults and shear zones within the zone were shallow

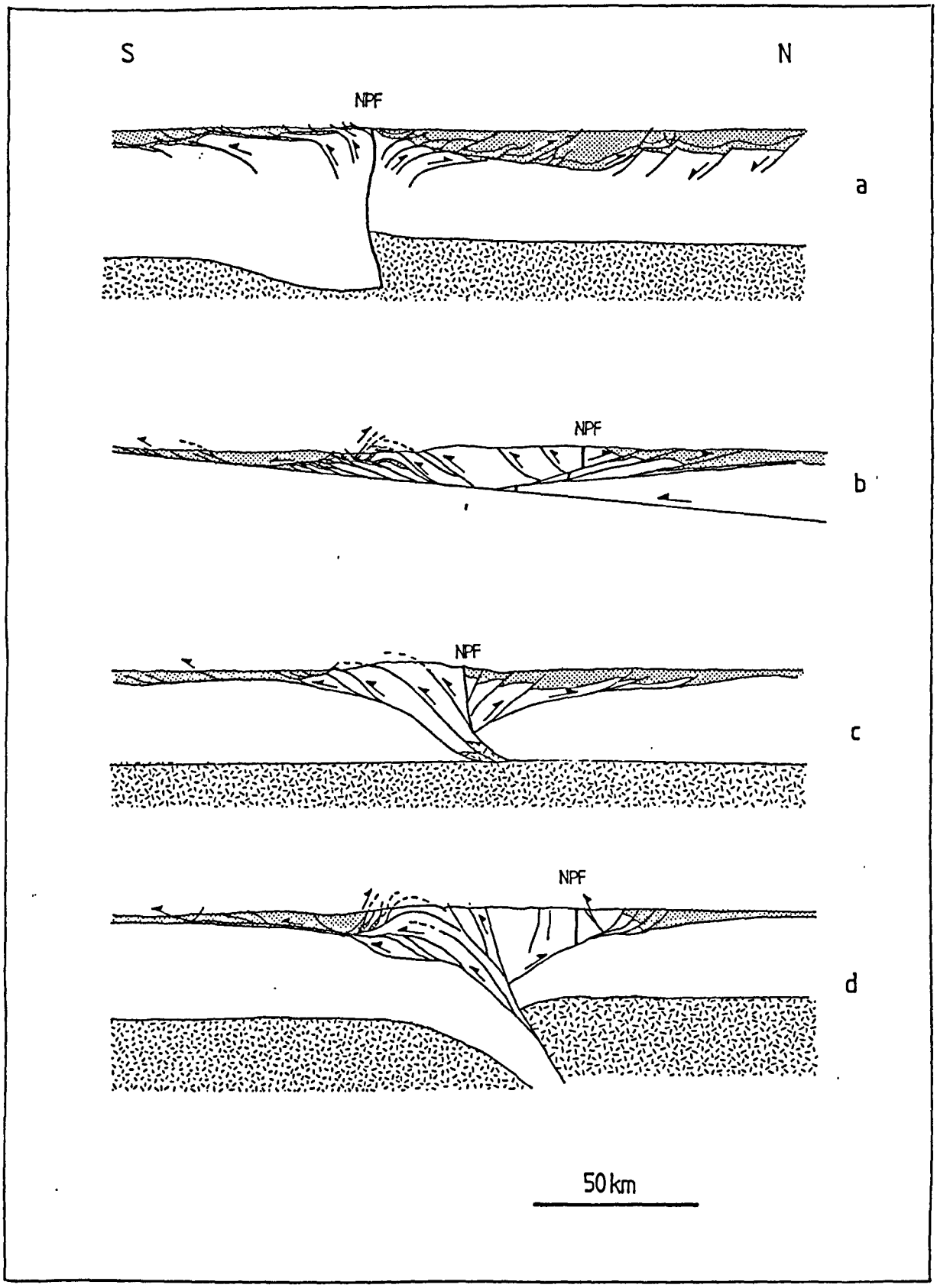

Figure 2.4. Recently published sections for the structure of the Pyrenees. a). Thick-skinned interpretation of Seguret and Dagnieres (1985). The North Pyrenean Fault (NPF) is considered the axis of the belt. b). Thin-skinned interpretation of Williams and Fischer (1984). c). Crustal duplex model of Deramond et al. (1985) d). Interpretation of the ECORS seismic section (Puigdefabregas et al., 1988).

structures back-rotated by piggy-back thrusting. The NPF is considered allochthonous and not the axis of the belt. A further implication of this model is that the PAZ cannot have had any palaeogeographic significance in the Mesozoic. Parish (1984) Williams and Fischer, (1984), Fischer (1984), Deramond et al., (1985), Williams (1985), Munoz et.al (1986) and Fontbote et.al (1986) all consider the structure of the PAZ best represented by an antiformal stack of basement thrust sheets.

The thin-skinned model is supported by a number of simple stratigraphic and structural observations. There is a lack of evidence in the stratigraphic record for a Pyrenean axis during Cretaceous sedimentation. Detailed work by Simo (1986) has shown that Upper Cretaceous sediments in the southern Pyrenees were deposited in a basin that deepened northwards to link with the north Pyrenean flysch trough. This trough developed in response to transtension along the NPF during the Upper Cretaceous transform motion between Iberia and Europe (Peybernes and Souquet, 1984). Palinspastic restorations of Cretaceous depositional sequences by Puigdefabregas and Souquet (1986) appear to show a similar picture across the length of the belt. The only palaeogeographic significance that can be conferred to the PAZ prior to Pyrenean deformation is that it occupied the shelf margin to the Iberian plate. This margin was faulted against the North Pyrenean trough along the NPF Zone. The palaeogeography of the north Iberian domain created in the Cretaceous did not appreciably change until the early Eocene when the South Pyrenean Tertiary Basin formed (Labaume et al., 1985).

Regional thin-skinned interpretations require continuity of displacement between the south Pyrenean foreland fold-and-thrust belt and the basement antiformal stack of the PAZ. This is achieved by postulating the existence of a regional north-dipping decollement and allows the NPZ to be interpreted as a back-thrust system (Fischer, 1984; Williams and Fischer, 1984). Williams and Fischer (op. cit.) consider the decollement to dip constantly northwards at an angle of approximately 6 degrees (figure 2.4b). Deramond et.al (1985) prefer to model the PAZ antiformal stack as occupying the whole crust with a decollement at crust-mantle interface (2.4c). In both models the NPF is truncated at depth by the northerly verging backthrusts of the NPZ.

Evidence in support of a regional decollement in the Pyrenees has come from the ECORS profile (ECORS, 1988). This seismic section yields new constraints on the geometry and continuity of structures in the Pyrenees and shows that the entire crust contains well-defined reflectors with a general fan-shaped geometry (figure 2.5). Although imaging of the middle crust is poor, it does seem to possess reflectors that, in its upper part, dip north and south to bound the PAZ. The age of these reflectors remains speculative, but they are believed to represent the expression of overthrusting and suggest a major decollement exists beneath the PAZ.

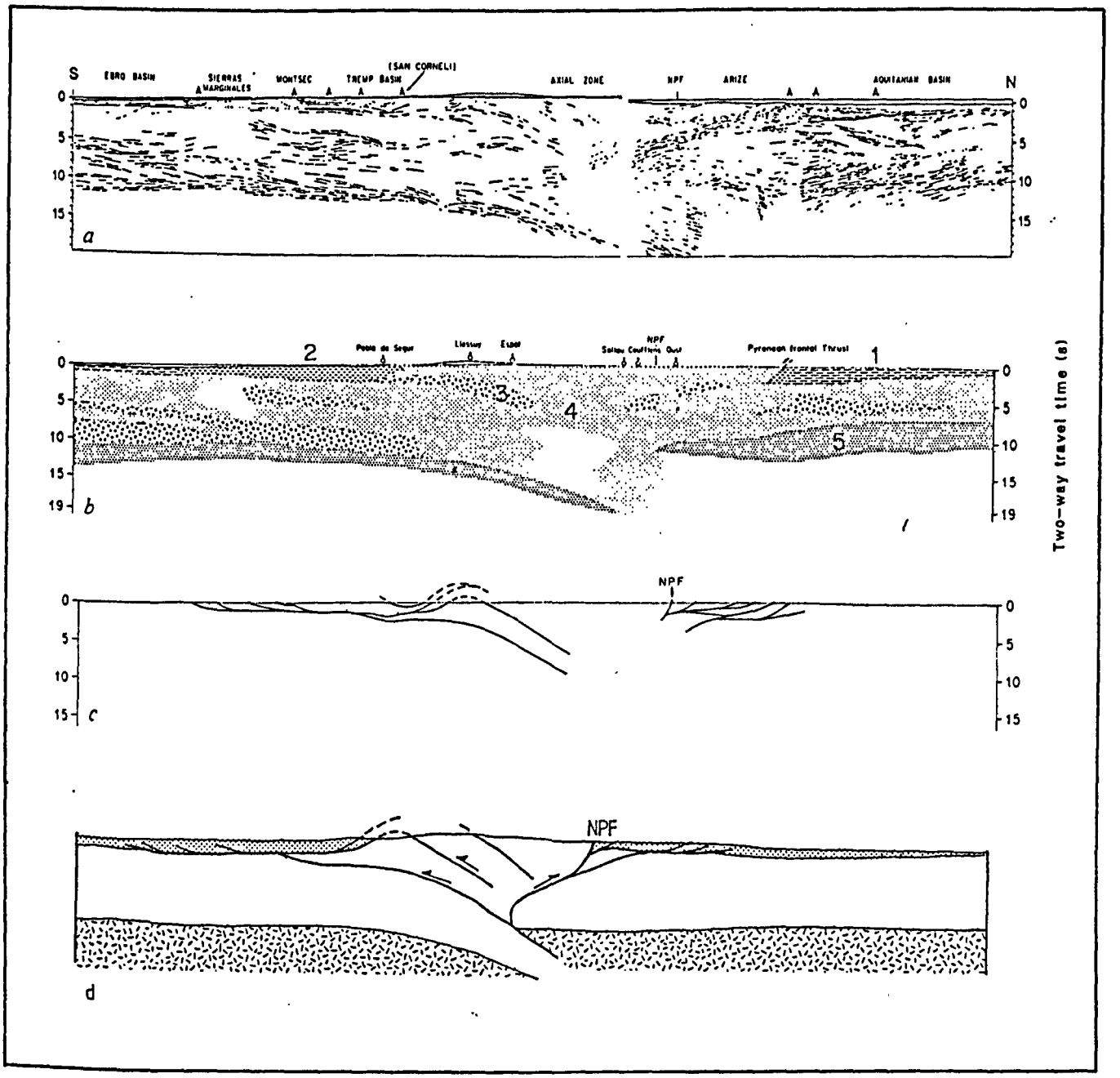

Figure 2.5. Interpretation of the ECORS reflection profile (ECORS Pyrenean team, 1988). a). Line drawing of entire profile. b). Main seismic facies along the profile: 1. undistrurbed reflectors. 2. same reflectors tectonically disturbed. 3. oblique reflectors of the middle crust. 4. domain of poorly defined reflectors. 5. layered deep crust. c). Geometry of major external thrusts from geological and seismic data. d). Possible solution consistent with ECORS data. The NPF is considered to be a Lower Cretaceous transform fault, active during the earlier stages of the evolution of the chain, and deformed later during the orogeny.

2.2.3. The South Pyrenean Zone.

The general evolution of thrusting in the South Pyrenees can be documented from the progressive deformation of the SPTB and movement of thrusts can often be accurately dated from the distribution of syntectonic deposits in the basin (Farrel et.al, 1987). Farrel et.al (op. cit.) recognise two main phases of thrusting. The first phase, dated from Palaeocene to mid-Eocene, involved thrusts that imbricated the Mesozoic cover sequences. In the central Pyrenees these thrusts detached at the level of the Keuper evaporite sequence. The thrusting was responsible for emplacement of high level nappes eg. the Cotiella and Pedraforca thrust sheets (figure 2.3). The second phase of thrusting occurred from mid-Eocene to Oligocene and involved the emplacement of basement thrust sheets onto the foreland: the Eaux Chaudes, Gavarnie, Nogueras and Cadi nappes. The emplacement of these lower structures breached the earlier thrusts and lead locally to the development of out-of-sequence thrusting (Farrel op.cit).

Munoz et al., (1986) have proposed a three-fold structural subdivision of south Pyrenean thrust sheets. Their work is based on mapping of the PAZ/SPZ boundary in the east of the belt, but continuity of structure across strike suggests it has universal application. The division recognises:

1. **Upper thrust sheets** comprising thrusts that detached within the cover and possess a complete Mesozoic sequence in their hangingwall. They include the Cotiella, Montsec and Pedraforca nappes. They appear to have originated north of the middle thrust sheets and nearer the axis of the Mesozoic North Pyrenean basin.
2. **Middle thrust sheets** comprising basement thrusts sheets that possess an incomplete cover sequence eg. the Gavarnie and Cadi nappes. This cover strata comprises basin margin deposits.
3. **Lower thrust sheets** formed solely of pre-Hercynian basement. These thrusts form the antiformal stack in the PAZ. They are only exposed in the east of the belt.

This classification redefines the structure of the Iberian margin of the Pyrenees and effectively makes the need for the distinction of separate structural zones obsolete. It will be adhered to in this thesis.

Shortening estimates across the south Pyrenees vary considerably depending on the regional models used. The main differences between the models reflect the different interpretations of the deformation in the PAZ. The thin-skinned model of Williams and Fischer (1984) and Williams (1985) (figure 2.4c) yield 75km of shortening across a section through the Nogueras Zone, an antiformal stack of Lower Thrust sheets. Bates (1987) has estimated between 60 and 70 km of shortening occurred within the Nogueras zone. The inhomogeneous strain model of Seguret and Daignieres (1985 and 1986) avoids linking thrusts in the PAZ to a regional decollement. The resultant balanced and restored sections emphasise the importance of shortening in the NPZ and significantly reduce

the estimated shortening across the PAZ and SPZ (figure 2.4a). Consequently they arrive at estimates of between 14 and 37 km for shortening across the SPZ and PAZ.

2.2.4 Displacement rates during thrusting.

Thrust displacement rates and the rate of migration of the thrust front in the southern Pyrenees have been estimated respectively by Williams and Fischer (1984) and Labaume et al., (1984). From their estimated total orogenic shortening of 106 km in the central Pyrenees achieved between the Palaeocene and Oligocene, Williams and Fischer (op.cit) calculated a time-averaged shortening rate of 0.62 cm/yr. Labaume et al., dated the migration of the deformation front in the SPTB from early Eocene to Miocene. Their estimated 35 km of shortening across a restored section 105 km in length translates into an advancement of the deformation front by approximately 0.35 cm/yr. Such figures are slightly lower than measured time-averaged plate velocities.

2.2.5. Uplift of the Pyrenees.

Maximum uplift in the Pyrenees has occurred across the PAZ. This zone however had no specific palaeogeographic significance in the Mesozoic (Fontbote et.al, 1986; Simo, 1986) and this uplift was presumably the product of Alpine deformation. The presence of Miocene and Pliocene erosion surfaces in the Pyrenees indicate that the present-day physiography is largely of Quaternary age (Mattauer and Henry, 1974). Uplift also occurred during active thrusting as witnessed by the southward migration and eventual closure of the SPTB (Labaume et al., 1985). This appears to have occurred in response to movement on the Middle and Lower thrust sheets during the Upper Eocene. In the lower Eocene the belt was not emergent as the presence of northerly sourced carbonate mass flow deposits in the SPTB points to the existence of a carbonate platform over the present day PAZ (Seguret et.al 1983).

2.3. The Structure and Lithostratigraphy of the Central Pyrenees

2.3.1. Lithostratigraphy.

The stratigraphy of the region has been described in detail by Van Lith (1965), Joseph (1972) and Deramond (1979). Only a brief description will be given here. The lithostratigraphy is summarised in figure 2.6.

The Hercynian basement comprises Cambro-Ordovician migmatitic psammites intruded by syn and post-kinematic granite and granodiorite bodies. The main intrusion is the Bielsa granite (Van Lith, 1965). Two main phases of deformation affected the

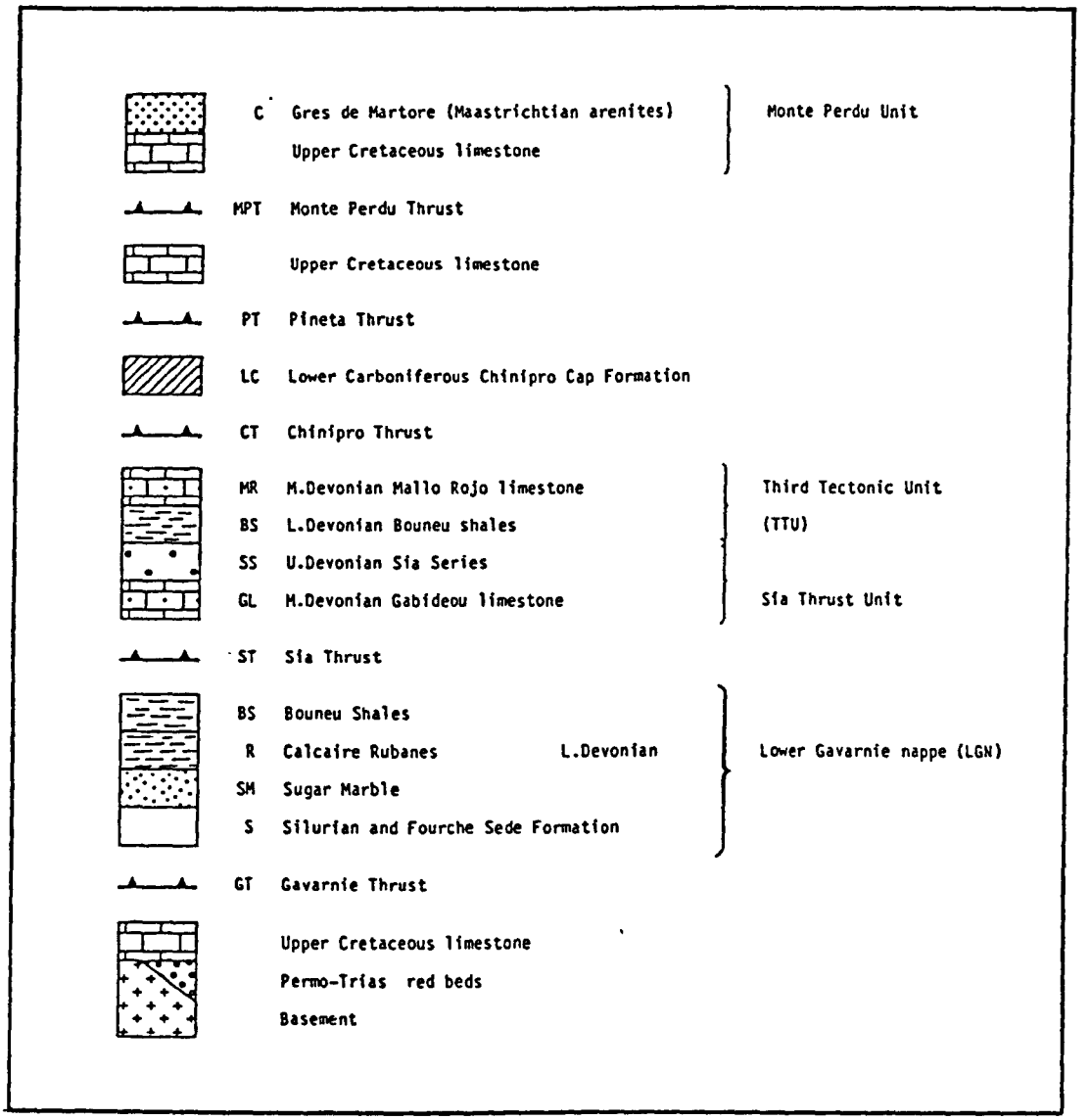

Figure 2.6. Summary diagram of the lithostratigraphy of the central Pyrenees (from Parish, 1984).

metasediments: D1 comprises N-S trending steeply plunging overturned folds that were refolded by the better developed E-W trending D2 structures (Deramond et.al, 1980).

The Mesozoic cover comprises a variably preserved Triassic red bed sequence that passes up into Keuper marls (the Pont de suert Fm. (Mey et.al, 1968)). These are overlain unconformably by Upper Cretaceous limestones. The red beds comprise a Bunter-aged mud- dominated fluvial sequence deposited in a widespread braided fluvial system (Zwart, 1979; Puigdefabregas and Souquet, 1986). The Upper Cretaceous strata comprise Cenomanian and Santonian biomicritic limestones (Martinez, 1968).

The Gavarnie thrust sheet comprises Upper Palaeozoic metasediments. These have been divided into four fault-bounded units (Van Lith, 1965, Parish, 1984) (figure 2.6).
1. The structurally lowest unit is referred to as the **Lower Gavarnie Nappe Unit (LGNU)**. It comprises five formations. The structurally lowest formation consists of 125 metres of black carbonaceous Silurian phyllite. This is overlain by the **Fourche de Sede Fm** (Joseph, 1972) that comprises 100-200 metres of interbedded limestones and shales. It is lower Devonian in age. The overlying **Calcaire Crystallin Fm.** (Sugar Marble) is a 200- 300 metre thick massive grey or white limestone unit. The **Rubanes Fm.** is a sequence of rhythmically interbedded limestones and calcareous shales. It is overlain by the **Bouneau Fm.** similar to the Rubanes Fm. but possessing sandstone beds.
2. The second unit is referred to as the **Sia Thrust Unit**. It comprises the Middle Devonian **Gabideous Limestone**, similar to the Sugar Marble, and the **Sia Series** a limestone-shale turbidite sequence of upper Devonian age (Joseph, 1972).
3. The **Third Tectonic Unit** consists of the **Mallo Rojo Limestone** and the Bouneau Fm. This is considered by Parish (1984) as a back-thrust slice of the LGNU.
4. The **Chinipro Cap unit** comprises the **Chinipro Cap Fm** a sequence of Carboniferous sandstones and shales (Van Lith, 1965).

The Mesozoic and Cenozoic strata in the hanging wall of the Gavarnie Thrust Sheet comprise limestones and sandstones of Cenomanian to Maastrichtian age (Deramond, 1979). These are overlain by Eocene flysch. This strata comprise the Pineta and Mont Perdu thrust sheets (Seguret, 1972).

2.3.2. Structure.

The area considered is shown in figure 2.7. It comprises, in the north, Hercynian basement of the PAZ and, in the south, the Upper thrust sheets of the SPZ. The main structure in the region is the Gavarnie Thrust which represents one of the Middle Thrust Sheets of Munoz et al. (1986). The present-day attitude of this thrust defines a regional-scale open culmination breached by erosion to form the Gavarnie and La Larri windows

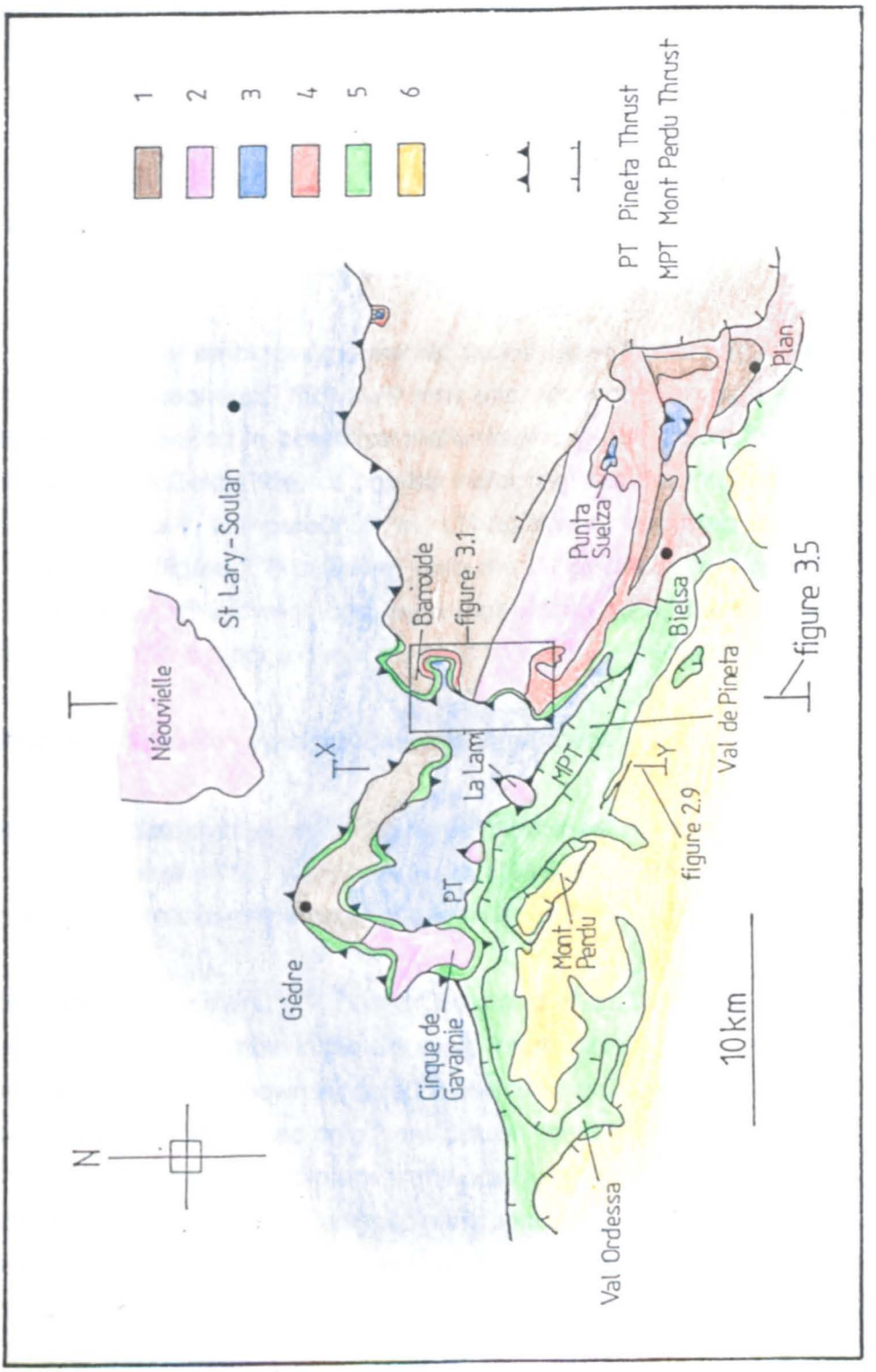

Figure 2.6. Surface geology of the Central Pyrenees. 1. Lower Palaeozoic Hercynian metasediments. 2. Hercynian Granite and granodiorite plutons. 3. Upper Palaeozoic strata of the Gavarnie Thrust sheet. 4. Triassic cover sediments. 5. Upper Cretaceous strata. 6. Eocene strata of the South Pyrenean Tertiary Basin. 7. Gavarnie Thrust. 8. Other main thrusts.

in the west, and the Bielsa window in the east. The thrust can be traced eastwards along strike until it disappears near Luchon.

The GT climbs elevation along strike from 1200 metres in the Cirque de Gavarnie to 2200 metres in Cirque de Troumouse to 2600 metres in Cirque de Barroude. Further east a klippe of Devonian limestone on Punta Suelza (2700m) is also believed to belong to the thrust sheet (Seguret, 1972). The minimum displacement on the thrust has been estimated from the footwall and hanging wall cut offs of the Upper Cretaceous strata as between 8 and possibly 15 km (Seguret, op.cit; Parish, 1984; McCaig, 1986). The displacement appears to increase eastwards from 8km in the Cirque de Gavarnie to 15 km for a section through the klippe of Punta Suelza.

The Gavarnie Thrust emplaces greenschist facies Upper Palaeozoic metasediments on a thin Mesozoic sequence that itself rests unconformably on high grade Hercynian basement. The contrast in basement metamorphic grade across the thrust has been interpreted by McCaig (1986) as possibly indicating that the thrust reactivated a pre-Triassic normal fault. Lamouroux et al., (1986) have interpreted shear zones in the Neovielle massif (figure 2.7) as linking onto the GT at depth and consider that these structures, initially of Hercynian age, were reactivated during the thrusting. Alpine-age movements on these shear zones have been shown by Losh (1985).

2.4. Structural Interpretations of the Gavarnie Thrust sheet.

Models for the deformation of the Gavarnie Thrust sheet have recently been published by Deramond et.al (1980, 1981) and Parish (1984). These models represent the end-member interpretations for the origin of the thrust.

1. The model of Deramond (1979) and Deramond et.al (1980 and 1981) is based on a quantitative analysis of strain in the Gavarnie Thrust sheet. A summary of the strain data of Deramond (op.cit.) is shown in figure 2.8 and the model proposed to explain the data is shown in figure 2.9. It is based on a Prantl cell, an apparatus in which a plastic material is deformed between two rigid platens. In the passive state, slip line theory predicts that for a horizontal compression with vertical platens shallowing upwards curved fault surfaces should develop in the deforming material (Deramond, op.cit.). In the model the metamorphic massifs in the Hercynian basement are considered to have acted as rigid blocks that deformed the intervening incompetent Palaeozoic sequence during Pyrenean N-S compression. The horizontal shortening of the Palaeozoic was accommodated by vertical uplift that produced a topographic slope and enabled gravity gliding of the upper Mont Perdu thrust sheet. The culmination in the thrust was not considered a product of the deformation but a vestige of the original attitude of the basement-cover interface. The Deramond model is a thick-skinned interpretation.

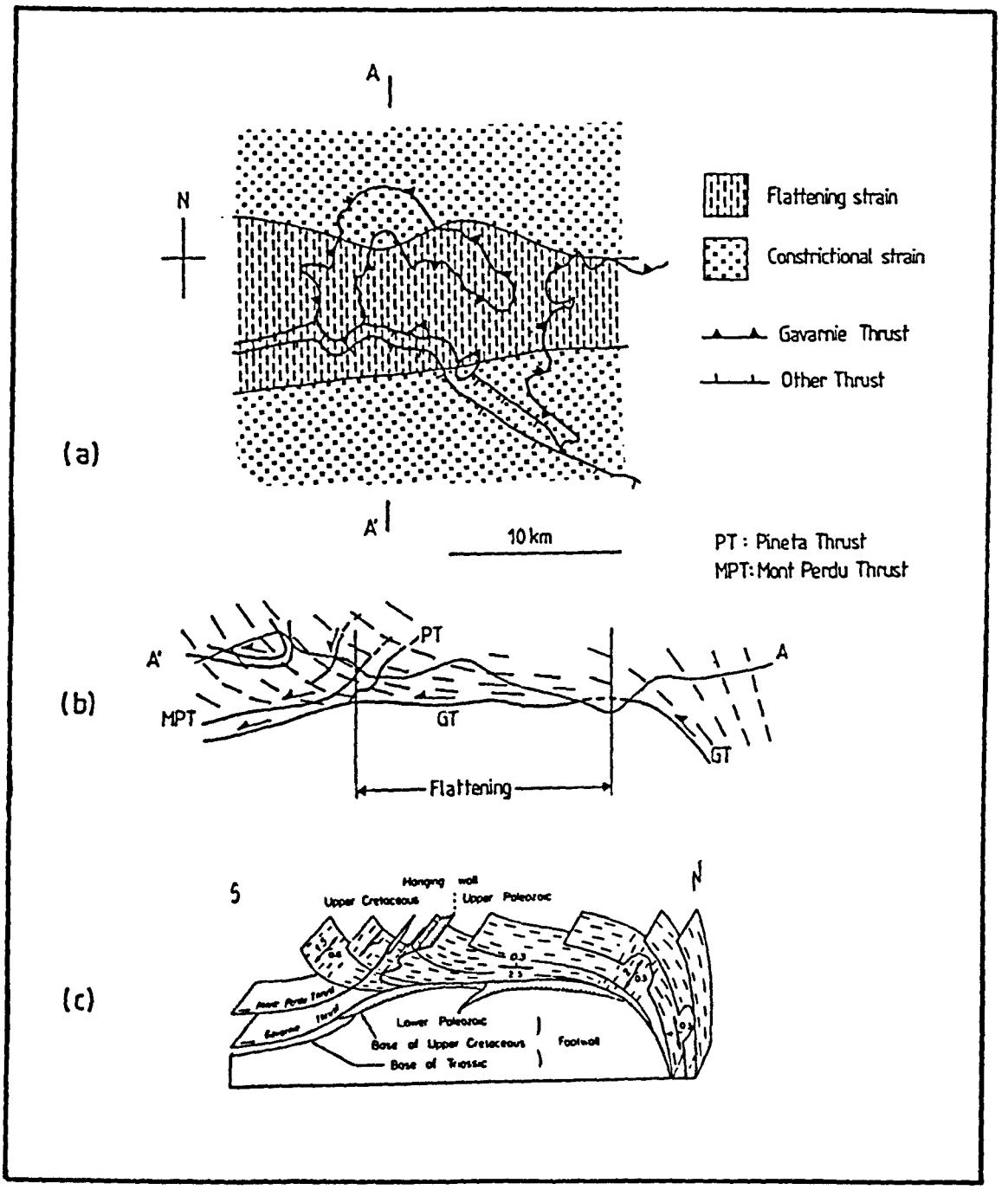

Figure 2.8. The strain within the Gavarnie Thrust sheet (after Deramond, 1979; Deramond et al., 1980 and Deramond et.al, 1981) a). Regional map showing the distribution of strain within the thrust sheet. b). Cross section AA' showing the attitude of the Alpine fabric in the thrust sheet. c). Summary diagram of strain data in the thrust sheet. From Seguret and Daignieres (1986, fig.5).

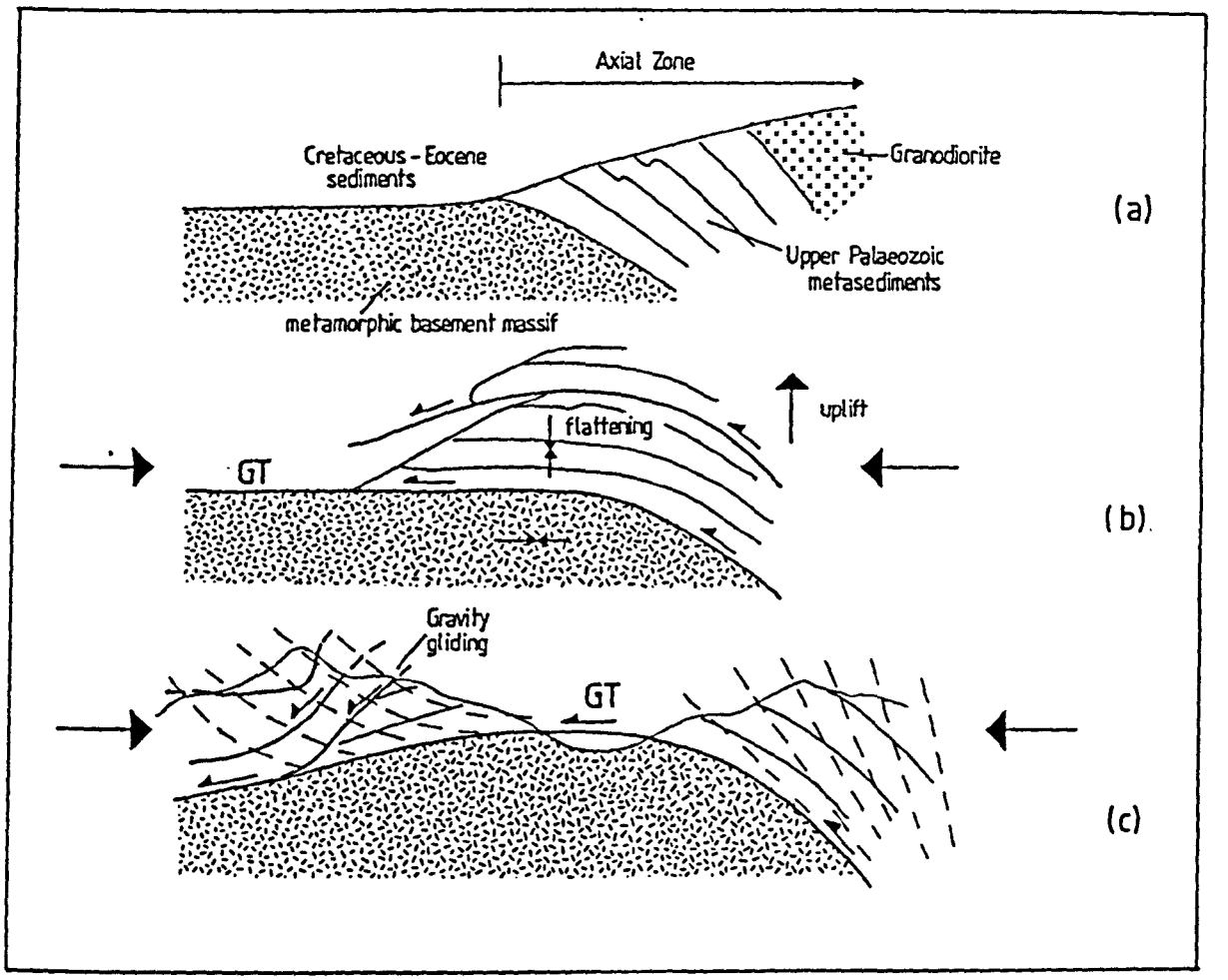

Figure 2.9. Model of Deramond (1979) to explain the formation of the Gavarnie Thrust. a). Initial configuration. Note inferred basement topography of the Axial zone.b). Shortening during Pyrenean convergence produces convex upwards thrusts in the bedded Upper Palaeozoic strata. The fault curvature is modeled by Deramond (op.cit.) as following slip lines within the plastically deforming Upper Palaeozoic sequence. The deformation is considered analagous to the deformation of a plastic material in a Prantl cell.The model predicts early uplift in the hinterland and the switch from shortening in thefootwall to flattening and extension in the hanging wall of the flat segment of the thrust. c). Final configuration showing gravity gliding off the front of the structure and Pyrenean cleavage.

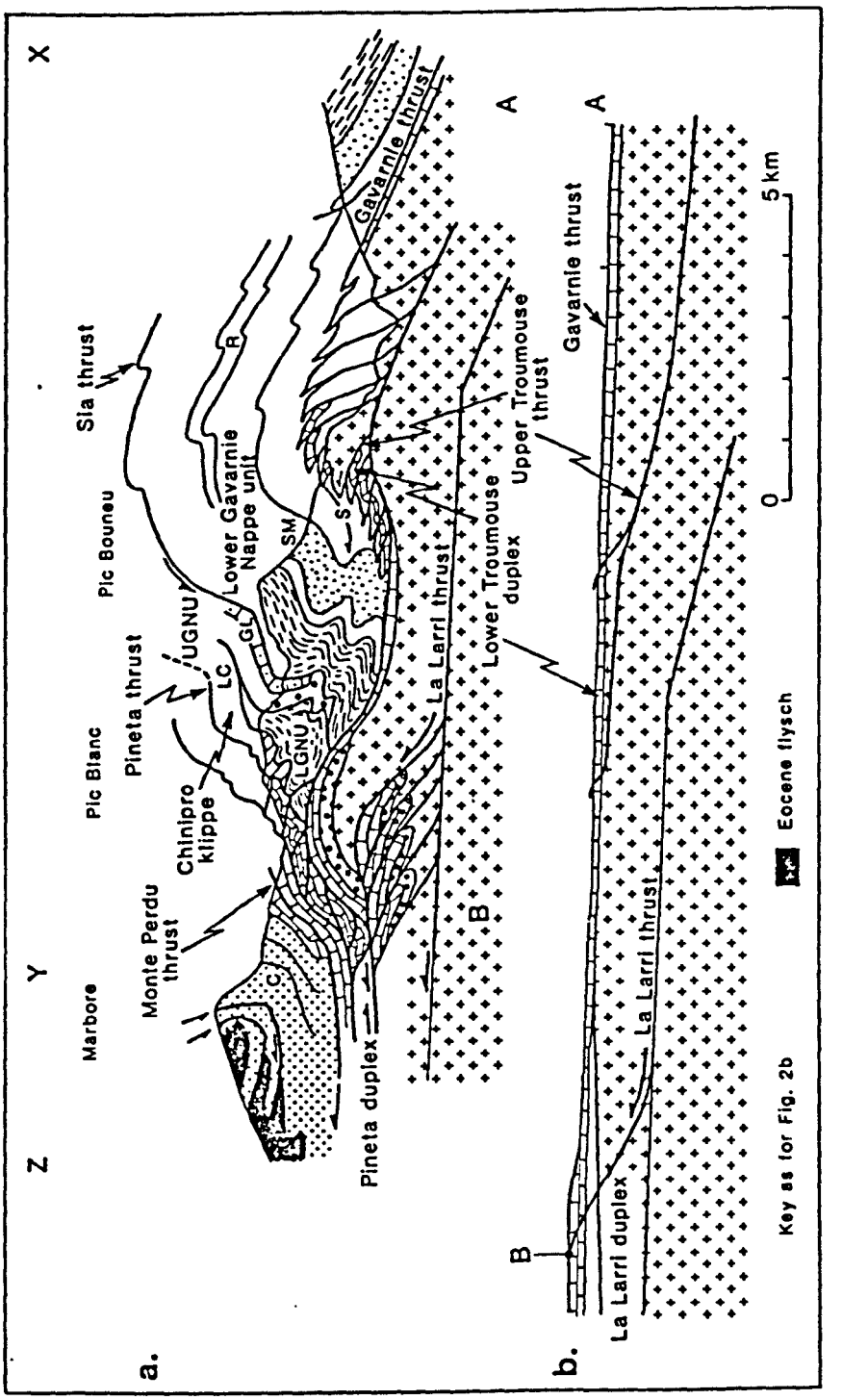

Figure 2.10. Thin-skinned interpretation of the structure of the Gavarnie Thrust sheet (from Parish, 1984). For key, see figure 2.7. The thrusts are shown by heavy lines. a) Cross section X-Y marked on figure 2.6. b) Restored section A-B for thrusts in the footwall of the GT. These thrusts record a minimum shortening of 25%.

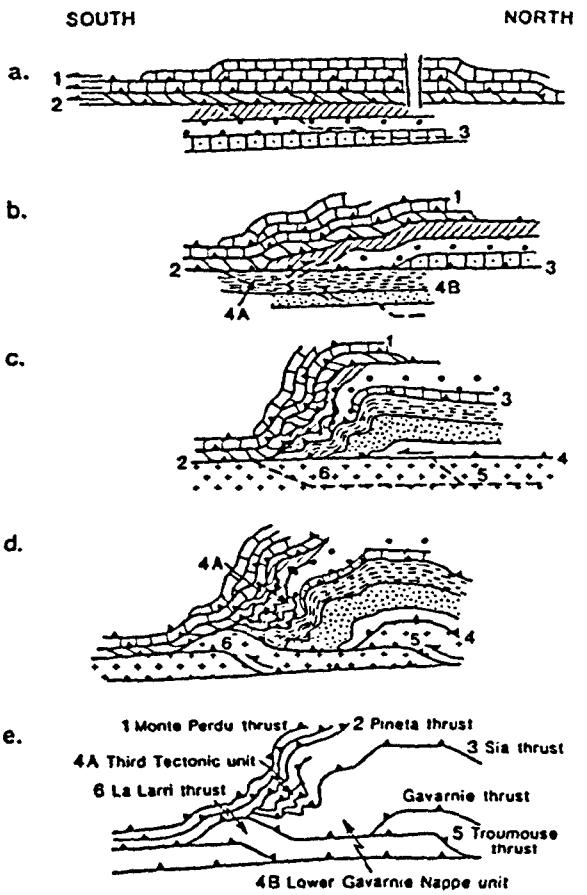

Fig. 5. Cross-section evolution diagrams for the evolution of the Gavarnie nappe. This diagram shows how the accretion of thrust-bounded horses on to the hangingwall of the overlying thrust, folds higher and earlier thrusts. This diagram depicts a piggy-back thrusting sequence where successively younger thrusts develop beneath higher and older thrusts, and as the younger thrusts climb ramps and join a higher décollement level the overlying thrusts are folded. Key as in Fig. 3. Heavy lines thrusts; broken lines incipient thrusts. Thrusting direction north to south. No exact scale is intended. (a) Formation of the Monte Perdu thrust (1); Pineta thrust (2). The Pineta floor thrust runs along a post-Hercynian unconformity, thus separating Mesozoic hangingwall rocks from previously deformed Palaeozoic rocks. Dashed line shows development of Upper Gavarnie nappe unit with Sia floor thrust (3) in footwall rocks. Note staircase trajectory of incipient thrust. (b) Accretion of upper Gavarnie nappe unit on to overriding Pineta thrust. Note folding of overlying thrusts by thrust (3) joining Pineta thrust (2). Incipient Gavarnie thrust (4) developing in footwall rocks. Horse 4A is back thrusted into the upper Gavarnie unit. Horse 4B is the Lower Gavarnie nappe unit. (c) Accretion of Lower Gavarnie nappe unit (4B), and back thrust (4A) onto the hangingwall of the overriding thrust sheet. Note the folding of all higher thrusts, and the development of a major frontal culmination wall. Thrust (4) is the Gavarnie thrust even though at point A the Gavarnie thrust joins with the Upper Gavarnie nappe floor thrust, and the Pineta thrust. The footwall rocks consist of basement and its Mesozoic cover. Dashed lines show the position of incipient thrusts (5), the Troumouse thrust, and (6) the Larri thrust. (d) Movement along the Troumouse thrust, and later movement along La Larri thrust has resulted in folding of the overlying older thrusts. This shows the present structure of the Garvarnie nappe. (e) Simplified sketch showing present relations of the major thrusts. Numbers denote sequence of thrust development with 1, Monte Perdu thrust; 2, Pineta floor thrust; 3, Upper Gavarnie nappe thrust (Sia thrust); 4, Gavarnie thrust; 4A, Third Tectonic unit backthrust; 5, Troumouse thrust; 6, La Larri thrust.

Figure 2.11. Model for the evolution of the cross section through/Gavarnie Thrust sheet shown in figure 2.10. (from Parish, 1984).

2. Parish (1982 and 1984) interpreted the structure of the Gavarnie Nappe as an antiformal stack of Palaeozoic and cover thrust sheets. The Palaeozoic thrust sheets in the hanging wall of the nappe comprise the four tectonic units discussed above: the Lower Gavarnie Nappe Unit (LGNU), the Sia Unit, the Third Tectonic Unit and the Chinipro Cap Unit. Because the relationship between the Sia and Chinipro Cap Units is unclear, Parish (op cit) considered they may represent portions of the same thrust sheet. He estimated that the minimum displacement of the LGNU was 10.5 km. Parish (op.cit) attributed the development of the culmination in the Gavarnie Thrust to folding on structurally lower thrusts represented in Cirque de Troumouse, by two small duplexes: the Lower and Upper Troumouse duplexes. He considered that movement over a frontal ramp on a major basement thrust, the La Larri thrust, was responsible for the regional culmination in the GT. The La Larri thrust represents a Lower Thrust in the classification of Munoz et al. (1986). The section constructed by Parish (op.cit) from Cirque de Troumouse to the Val de Pineta is shown in figure 2.10. The model proposed by Parish (op.cit.) for the evolution of the GT sheet is shown in figure 2.11.

While the inferred La Larri thrust is not exposed in the Gavarnie or La Larri windows, equivalent structurally lower thrusts are exposed further east in the Parzan Valley and the Valley of the Rio Cinca, north of the village of Plan (figure 2.7).

CHAPTER 3

Lithostratigraphy and Structure of the Barroude-Liena Area.

This chapter has two main sections: the first gives a brief description of the lithostratigraphy of the Barroude-Liena study area, the second will discuss some aspects of the structure of the area. The latter is discussed here rather than in chapter 4 to separate the more regional work from the detailed work done on Pic de Port Vieux.

3.1. Lithostratigraphy.

The general lithostratigraphy of the central Pyrenees has already been outlined in section 2.3. In the study area three main units can be distinguished:

1. Hercynian Basement,
2. Mesozoic cover strata.
3. Allochthonous Upper Palaeozoic strata of the Gavarnie Thrust Sheet.

3.1.1. The Hercynian Basement.

Throughout the Cirque de Barroude, the basement is composed of Hercynian migmatites and metasediments locally intruded by small granitic dykes, sills and granitic net vein complexes. Further south, in Cirque de Barrosa and on the Sierra Liena, the basement comprises the Bielsa granite; a large post-kinematic Hercynian granodiorite pluton (Van Lith, 1965).

The metasediments comprise a monotonous sequence of ochre coloured psammites and quartz-biotite schists possessing a strong bedding-parallel schistosity. Occasional white quartzite beds are present. The rocks are considered Ordovician in age (Van Lith, 1965). The psammites are folded by both N-S and E-W trending mesoscopic folds corresponding to the Hercynian D1 and D2 episodes (Deramond et al., 1980). The D2 phase occurred after the migmatisation. Numerous chlorite/quartz shear-fibre coated surfaces occur in the basement in zones adjacent to the Triassic unconformity and the Gavarnie Thrust. These cut across the Hercynian folds and are related to Alpine thrusting. A detailed structural study and synthesis of the basement lithologies will not form part of this thesis.

3.1.2. The Mesozoic.

In the study area, the Mesozoic strata comprised Permo-Triassic Red Beds and Upper Cretaceous limestone. They outcrop beneath the Gavarnie thrust and form a thin veneer between it and the Hercynian basement. The Triassic red beds are

unconformable on the basement and outcrop along the Pic de Port Vieux-Pic de Barrosa ridge and also along the flanks of Port de Barroude (figure 3.1). Extensive outcrops of Triassic also occur on the southern slopes of the Sierra Liena. The Upper Cretaceous limestone is unconformable on the Triassic strata and along the west side of the Cirques de Barrosa and Barroude and on parts of the Sierra Liena, it cuts out the Triassic and rests directly on the basement. The limestones are considered Cenomanian in age (Martinez, 1968). They outcrop adjacent to the Gavarnie Thrust along its entire outcrop length.

In Cirque de Barroude both the Triassic and Cretaceous strata dip westwards at 10-20 degrees although dips are modified on Pic de Port Vieux and Sierra Liena by thrust-related deformation. North of the cirque the strata dip north while on the Sierra Liena they have a southerly dip. The changes in dip across the study area reflect a large Alpine-age culmination that also folded the Gavarnie Thrust (see later).

The Triassic reaches a maximum of 45-50 metres thick on the 2763m summit south of Pic de Barrosa and on the Sierra Liena ridge. At two localities, Sierra Liena and Soum de Barroude (figure 3.1) the Triassic subcrop was controlled by NE-SW trending high-angle reverse faults. The Liena Fault (Van Lith 1965) is associated with Pb-Ag-Fe mineralisation that was mined during the last century. The Cretaceous limestone varied between 0.5 and 10 metres thick beneath the Gavarnie Thrust. In many areas the limestone had been internally thickened by thrusting (see later) and its original thickness below the GT is difficult to assess. On Sierra Liena the limestone thickens to 30 metres as a result off the GT cutting up-section.

The Triassic unconformity is irregular with the basal conglomerate filling an undulatory erosion surface. Some of the irregularities in the unconformity are the product of later faulting; others represent original palaeotopography (figure 3.2). In figure 3.2, cleavage in the Triassic mudstones is stacked against some of the faults suggesting they are pre-thrust structures. They may have been of similar age to the larger Liena and Soum de Barroude Faults as they possess similar orientations. The Cretaceous unconformity appears to be a planar erosion surface across the whole study area.

3.1.2.1. Sedimentology of the Triassic Red Beds.

Figures 3.3a and 3.3b show two structural/sedimentological logs of the Triassic that were taken 75 metres apart on Pic de Port Vieux. The logs were taken from (42186 4990 and 42205 4998). The Triassic red beds are composed of four main lithologies:

1. The base of the Triassic Red Beds is marked by a pebble-cobble orthoconglomerate unit. This contains subangular to subrounded clasts of basement lithologies, predominantly psammite and quartzite. It possesses a poorly sorted sand or red silt

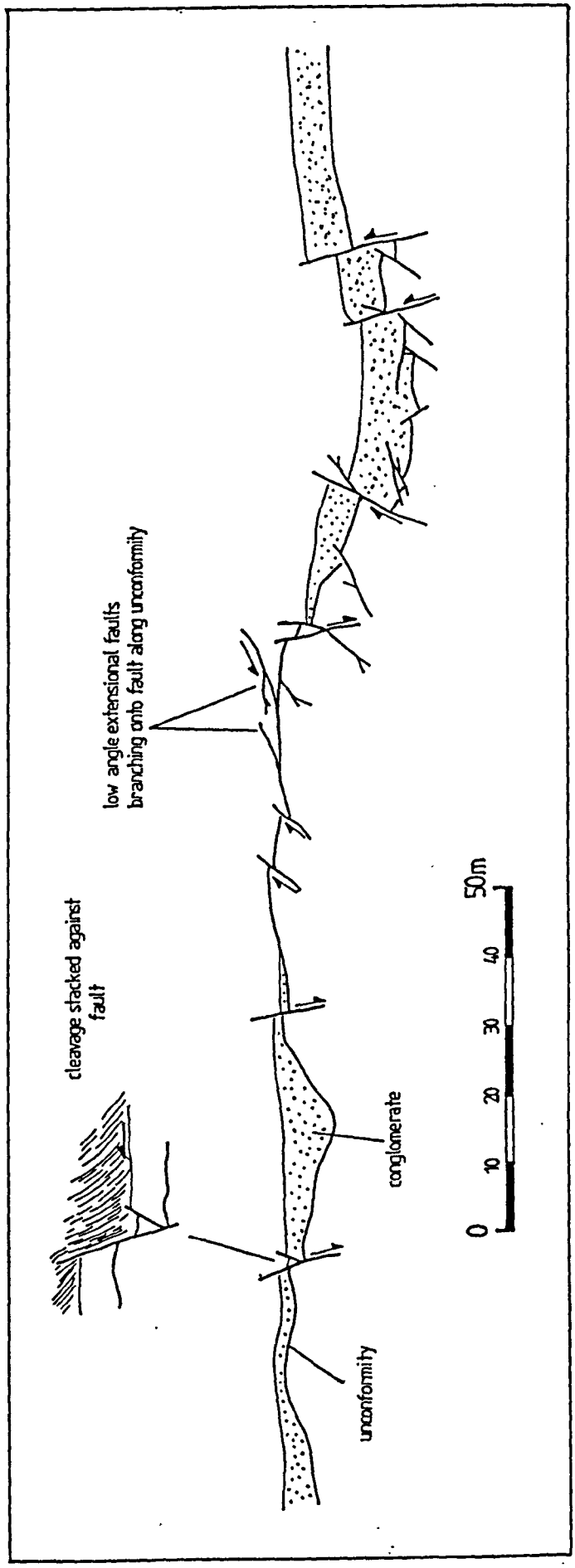

Figure 3.2. Cross section along Triassic unconformity on Pic de Port Vieux. From (4422400 49950) to (422810 50650) in figure 4.3. Note the variable thickness of the basal conglomerate unit and the pre-thrusting high angle faults. The inset shows buttressing of cleavage against one of the faults.

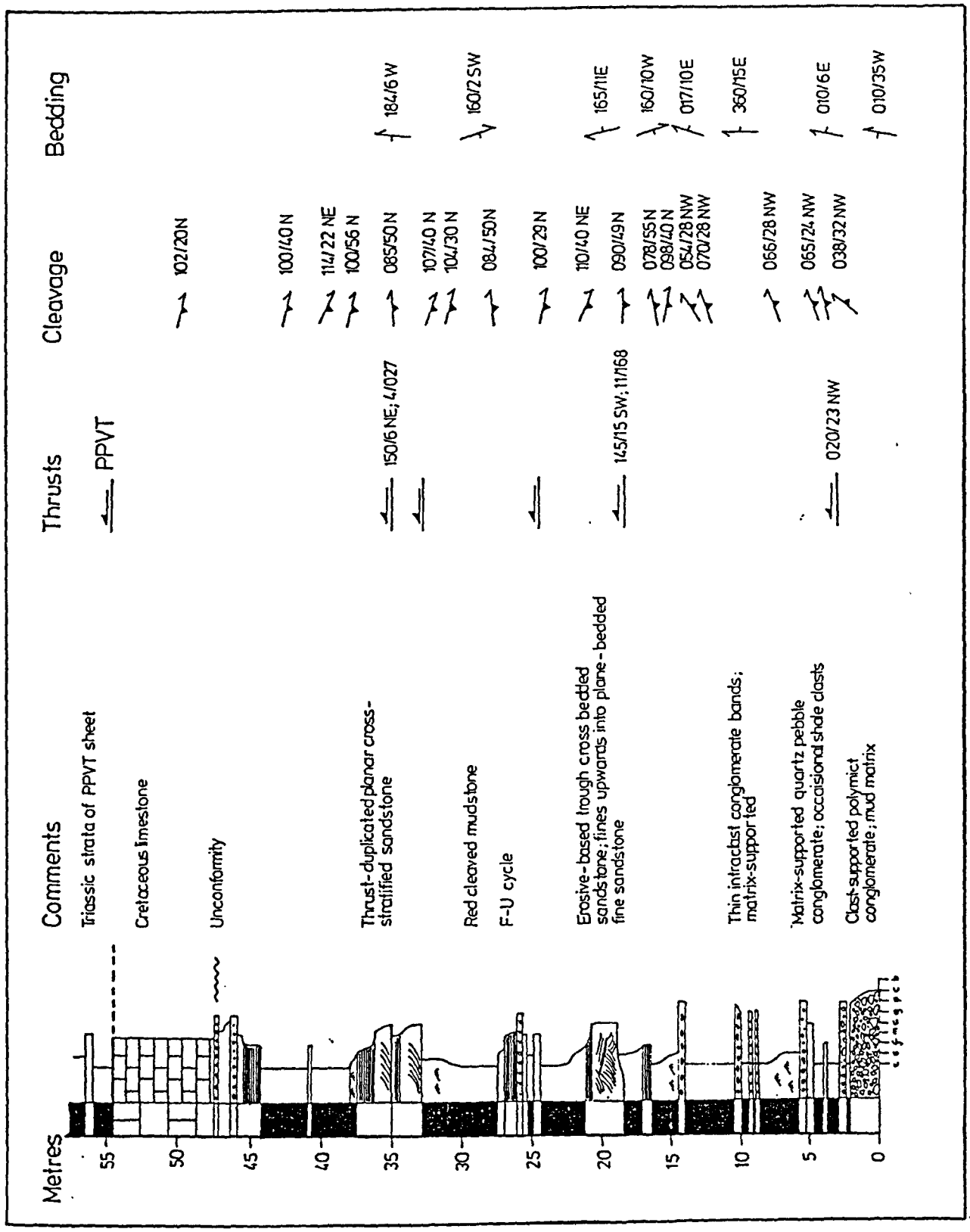

(a)

Figure 3.3. Two structural/sedimentological logs through the Triassic strata on Pic de Port Vieux. a). from (422400 49950) and b). from (421950 49899).

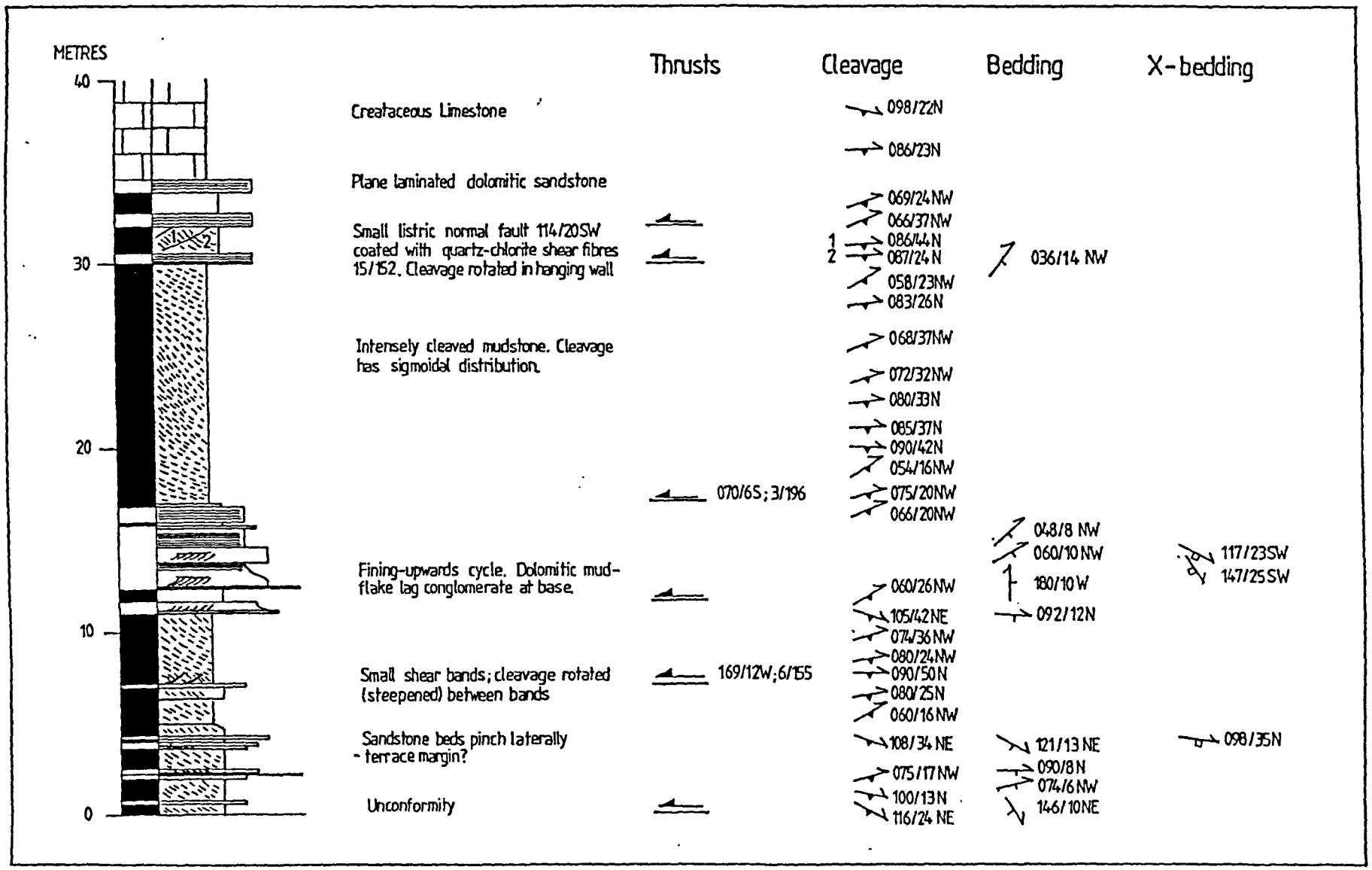
METRES
40
30
20
10
0
1
2
Thrusts
Cleavage
Bedding
X-bedding
Cretaceous Limestone
098/22N
086/23N
Plane laminated dolomitic sandstone
069/24NW
066/37NW
Small listric normal fault 114/20SW coated with quartz-chlorite shear fibres 15/152. Cleavage rotated in hanging wall
1 086/44N
2 087/24N
036/14 NW
058/23NW
083/26N
Intensely cleaved mudstone. Cleavage has sigmoidal distribution.
068/37NW
072/32NW
080/33N
085/37N
090/42N
054/16NW
070/65S; 3/196
075/20NW
066/20NW
048/8 NW
060/10 NW
117/23SW
147/25SW
Fining-upwards cycle. Dolomitic mud-flake lag conglomerate at base.
180/10 W
060/26NW
092/12N
105/42NE
074/36NW
080/24NW
Small shear bands; cleavage rotated (steepened) between bands
169/12W; 6/155
090/50N
080/25N
060/16NW
Sandstone beds pinch laterally - terrace margin?
108/34 NE
121/13 NE
098/35N
090/8N
075/17NW
074/6NW
100/13N
146/10NE
Unconformity
116/24 NE

(9)

matrix and often interdigitates with sandstone and siltstone lenses. The conglomerate varies between 1 and 10m thick.

2. Red cleaved shale often possessing dolomite nodules. This accounts for between 60 and 70% of the sequence. No dessication structures have been observed within the mudstone.

3. Red plane-bedded or cross-laminated siltstone and fine sandstone.

4. White or ochre coloured medium to coarse calcite/dolomite cemented crossbedded sandstone. A mudflake conglomerate lag deposit is often present at the base of some of the coarser units.

The strata are arranged in fining-upwards cycles. Occasionally thin (< 0.3m) matrix supported intraclast conglomerate beds occur separately from the coarse cross stratified sandstone beds. The matrix of these units is largely composed of ferroan dolomite. Correlation between the logs is noticeably difficult and points to the general lateral variability of the Triassic sequence.

The predominance of fine grained clastics in the Triassic sequence suggests deposition occurred in a relatively low energy environment. This environment was however punctuated by high energy events that deposited the sandstone-based fining upwards cycles. These cycles, comprising dune-bedded sands, upper phase plane bedded fine sands, ripple laminated silts and structureless muds, are probably the deposits of sheet-like floods or within shallow broad channels. The absence of water-escape and sole structures and the lack of lateral continuity in sandstone beds supports the latter interpretation. If a river channel interpretation is correct, then the absence of stacked sandstone units must imply channel abandonment occurred regularly and that the channels probably formed during flood events.

The dolomitic matrix-supported intraclast conglomerate occurs as thin isolated beds within the mudstone units. They probably represent thin mass flow deposits derived from a carbonate-dominated source area. The presence of carbonate deposition suggests local development of lagoonal conditions in the basin.

The depositional environment of the Triassic red beds was probably an extensive flood plain crossed by broad shallow flood- dominated channels. This agrees with the interpretations of Zwart (1979) and Lucas (1985) who consider the Bunter in the Central Pyrenees as the deposits of a braided alluvial system. It seems likely that the mudstone was deposited in a shallow lacustrine environment. The absence of dessication structures suggests the standing water may have been permanent. The red colouration of the mudstone and fine sandstone subfacies was the product of early diagenetic precipitation of hematite and amorphous Fe-oxides. This can be dated because occasional red shale clasts occur within the white crossbedded sandstone subfacies.

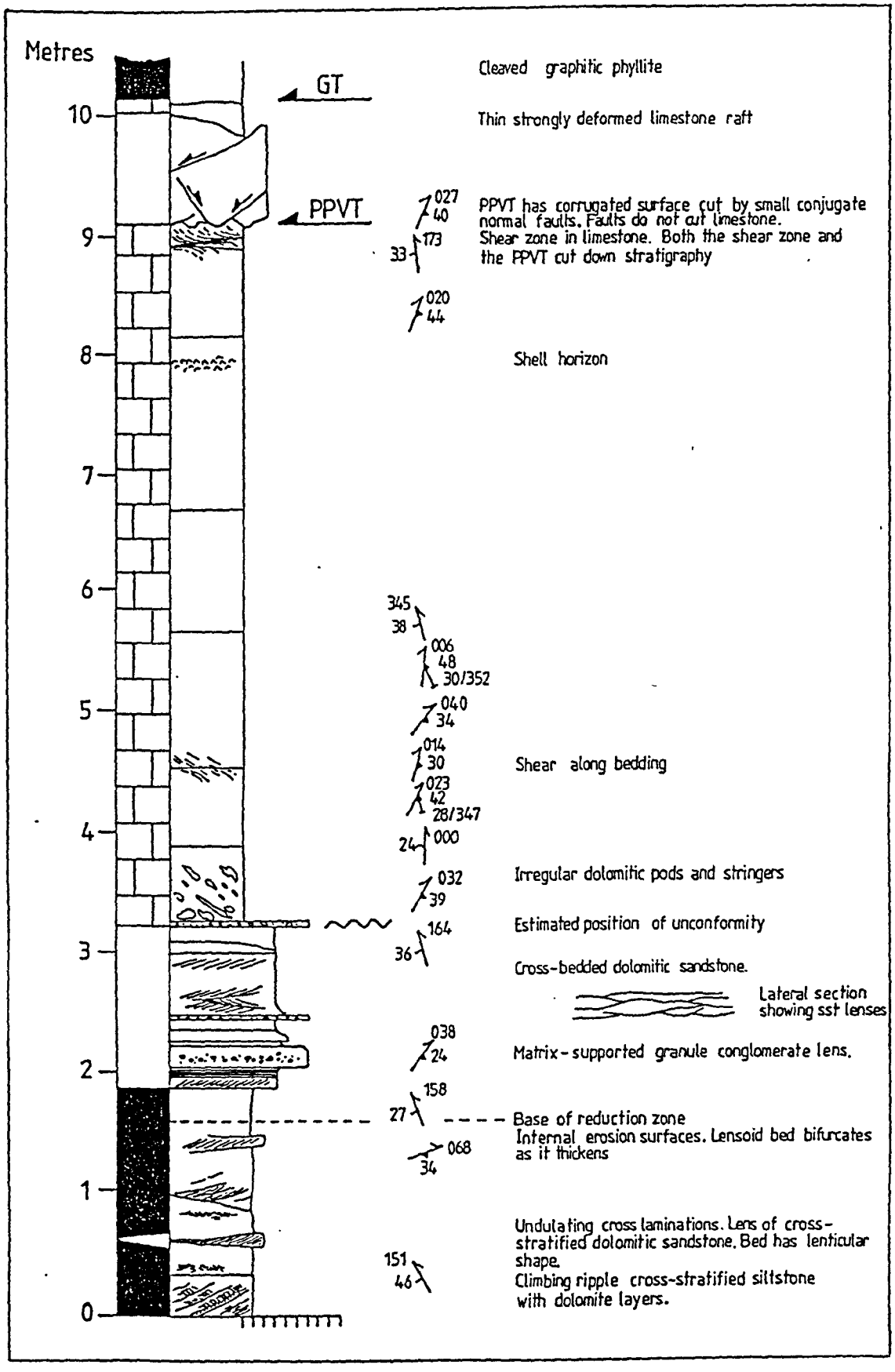

Figure 3.4. Structural/sedimentological log through the Upper Cretaceous limestone on Pic de Port Vieux. From (421928 49546).

Reddening must have occurred within the top few metres of the substrate during or shortly after deposition to allow reworking of the red mudstones during flood events.

3.1.2.3. Sedimentology of the Upper Cretaceous Limestone.

The Cretaceous limestone rests with planar unconformity on the Triassic Red Beds or directly on the basement. It was strongly deformed during movement on the Gavarnie thrust and locally possesses a strong mylonitic foliation. A sedimentological/structural log of the limestone is shown in figure 3.4. The unconformity is marked by either a poorly sorted conglomerate layer or by a series of ripple laminated dolomitic fine sandstone beds 1-2 metres thick. The conglomerate contains clasts of shale, limestone and vein quartz. The basal clastic units are succeeded by biomicritic limestone containing bivalves and rare nummulites. The development of the carbonate facies almost directly onto the unconformity surface points to a rapid transgression of the Cenomanian sea across a peneplain.

3.1.3. The Gavarnie Thrust Sheet.

An appraisal of the stratigraphy of the Gavarnie Thrust sheet (GTS) has already been given in section 2.5. This section will give a brief description of the main strata in the thrust sheet in the study area. These strata comprise the Lower Gavarnie Nappe Unit of Van Lith (1965) and Parish (1984).

At the base of the nappe is the Silurian Graphitic Phyllite Fm. (SGP), a black graphitic phyllite containing small 1-5 cm quartz augen. The augen appeared to represent folded and boudinaged veins. The phyllite possesses a strong slaty foliation that anastomoses around the augen. Exposed cleavage surfaces are often polished, especially near the base of the thrust sheet, and indicate that slip occurred on the cleavage during the shearing associated with nappe emplacement. Occasionally the phyllite has the appearance of a melange containing boulder sized clasts of folded sandstone and granite. A few thin dark grey dolomitic limestone beds are also interstratified with the graphitic phyllite. The lowest 20m of the graphitic phyllite contains abundant shear bands and thin slices of mylonitised Cretaceous limestone.

To the north and south of the Cirque de Barroude the SGP Fm. is overlain by the Sugar Marble Fm. In the cirque itself the phyllite is overlain by a 200m thick sequence of interbedded limestones and black shales that is itself overlain by the Sugar Marble (figure 3.5). The interbedded limestone and shales is possibly a wedge of Fourche de Sede Fm. (Van Lith, 1965). Description of these units has been given in section 2.5 and will not be elaborated on here. The Sugar Marble Fm. forms a distinctive thrust-parallel marker horizon in the thrust sheet. It is succeeded by the Calcaire Rubanes and the

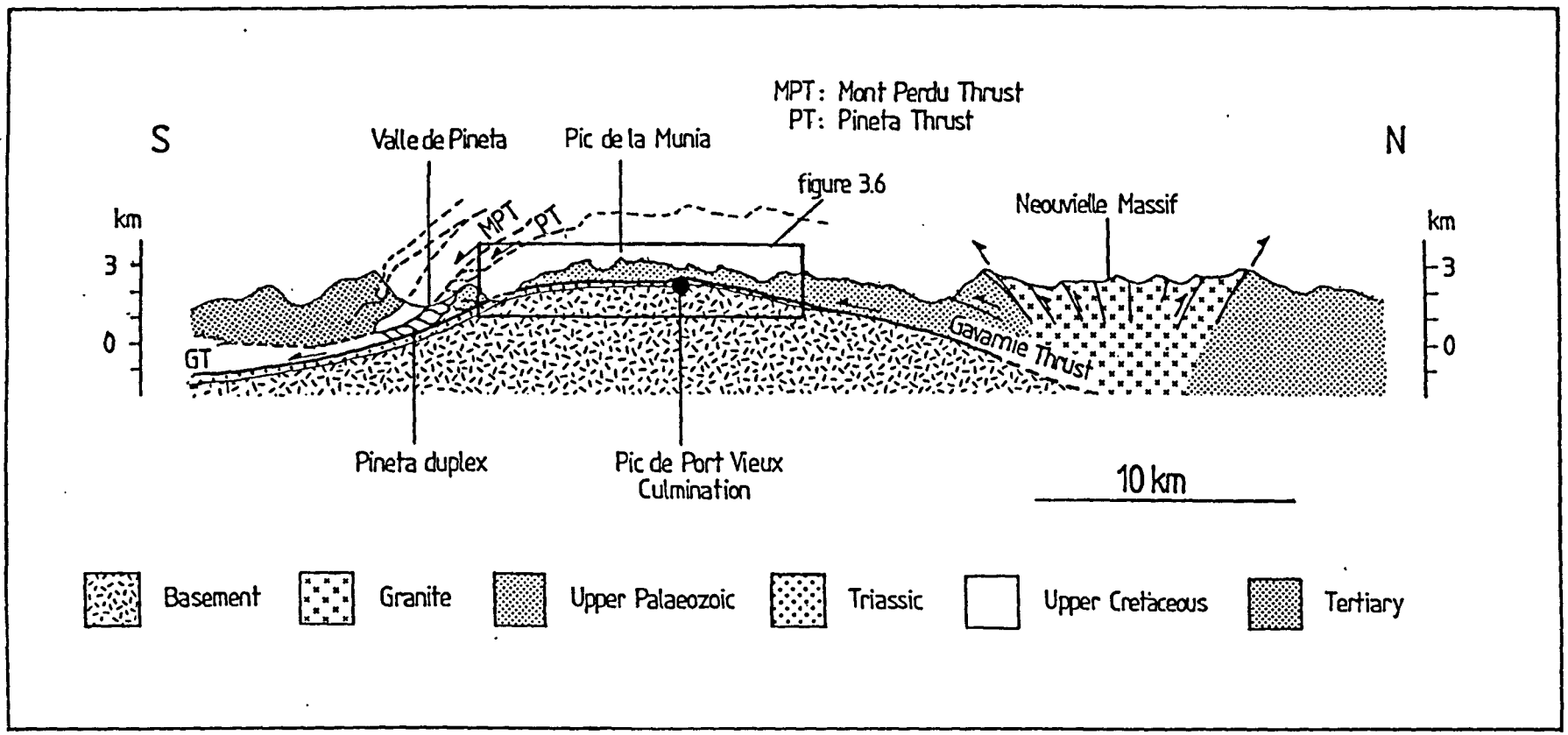

Figure 3.5. Small-scale cross section throgh the central Pyrennees and including the study area (See figure 2.6 for location). The section was constructed by across-strike interpolation of the published sections of Seguret (1972) and Parish (1984).

Bouneau Shales. These will be grouped together in the following discussion under the title of Bouneau Formation.

3.2 The Structure of the Barroude-Liena Area

A regional cross section through the Gavarnie Thrust sheet in the Central Pyrenees is shown in figure 3.5. The section portrays the large culmination in the thrust. A more detailed section from Cirque de Barroude to the Sierra Liena is shown in figure 3.6 Its approximate line of traverse is marked on figure 3.1. The section trends parallel to Barroude wall and was constructed by photogeological interpretation of the structures exposed on this cliff face.

3.2.1. The structure of the GT sheet.

3.2.1.1. Distribution of strata.

The SGP Fm. that outcrops along the base of the thrust sheet has a variable distribution. It reaches a maximum thickness of 100 metres south of Port de Barroude and along the flank of Pic de la Gela. The black phyllites are largely cut off in the hanging wall of the thrust just to the north of Robinera (figure 3.6) where a set of overturned folds detach onto the fault. These folds probably represent a sheared hangingwall ramp anticline. South of Robinera only a thin (1-10m) black shale unit is present along the fault plane.This thin layer comprises the three small klippen on the Sierra Liena.

In Cirque de Barroude the outcrop of the SGP is obscured by the scree apron along the foot of Muraille de Barroude. It appears however to thin below the large lens of Fourche de Sede Fm. (FDSF) that forms the core of a large south verging fold in the thrust sheet (figure 3.6). This fold will be referred to as the Troumouse anticline. The contact between the FDSF and the SMF is discordant with the overlying SMF truncating bedding in the FDSF. A number of normal faults in the FDSF also appear truncated by the contact with the marble. At (42044 4927) the contact is marked by an intensely sheared zone of interbedded dolomitic limestones and black shales. This probably represents a thin band of FDSF Fm. deformed by movement along the base of the unit. The contact may therefore be a fault although further analysis in other parts of the thrust sheet is necessary to confirm this origin. It is also possible however that the contact is a sheared unconformity.

The SMF outcrops as a thrust-parallel layer from Vallon de la Gela, north of the study area, to the Sierra de Espierba. The outcrop pattern is however disjointed with the metalimestone layer thickening and thinning along section. The thickness of the SMF is greatest in Cirque de Barroude where it reaches about 380 metres. The unit has the

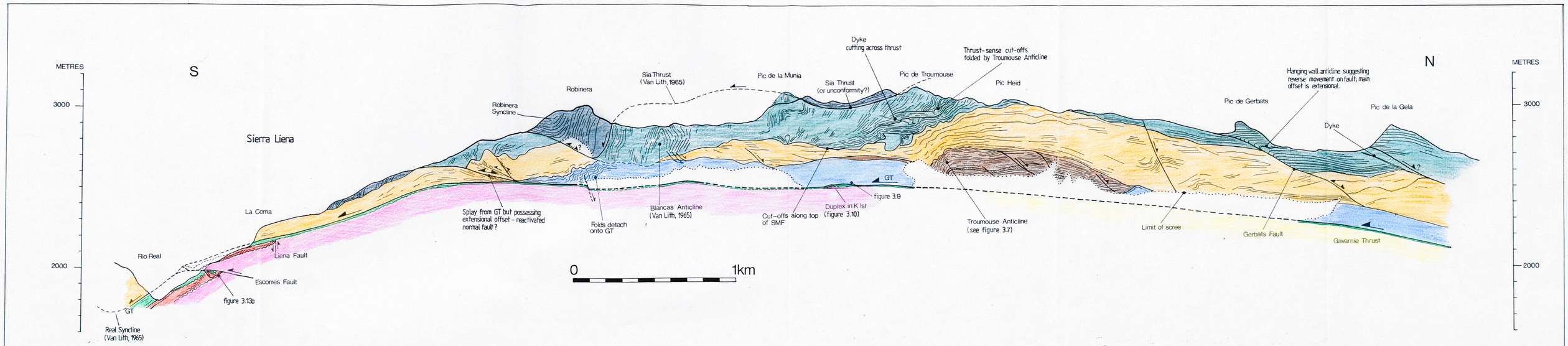

Figure 3.6 Cross section from Cirque de Barroude to Sierra Liena

Figure 3.6. 1:10000 cross section through the Gavarnie Thrust sheet and its footwall strata from Cirque de Barroude to the Sierra Liena. See figure 3.1 for key.

appearance of having been boudinaged on a large scale with a 500 metre long break in outcrop occurring between Robinera and Pic de la Munia (figure 3.6).

Numerous bedding cut-offs occur along the top of the SMF south of Pic de Troumouse with bedding in the overlying Bouneau Fm. abutting the SMF almost orthogonally. On Pic de Troumouse itself, a number of thrusts imbricate the BF and are folded by the Troumouse Anticline. A small dyke cuts across one of these faults (figure 3.6) suggesting that the thrust is pre-alpine in age. The thrusts branch from the top of the SMF. Their transport direction cannot be constrained from the two-dimensional exposure of the cliff-face and it is possible that some of the discordant contacts along the the top of the SMF are a result of a looking at a lateral section through the thrusts. This could explain why the fault marked L cuts first up and then back down section and perhaps reflects two lateral ramps.

Between Pic de Troumouse and Pic de la Munia the ridge crest comprises a sequence of shallowly dipping strata that truncate the steeply dipping strata of the underlying BF. This unit is considered by Van Lith (1965) and Parish (1984) as a klippe of the Sia Thrust Unit (STU). The Sia thrust cuts up section towards the south across the folded Bouneau shales. Van Lith (1965), Majeste-Menjoulas (1979) and Parish (op.cit.) also interpret the vertical dipping strata that comprise the summit of Robinera as part of the Sia Formation. The inferred trace of the Sia thrust is shown in figure 3.6. The thrust appears to branch onto the upper surface of the SMF on Robinera. It does not branch directly onto the GT.

3.2.1.2. Structural Interpretation.

Interpreting the distribution of strata in the Gavarnie Thrust sheet is complicated by the earlier Hercynian deformation that already affected the Upper Palaeozoic strata prior to thrusting. Consequently the timing of many structures is difficult to constrain and the original distribution of strata before the thrusting difficult to assess. The strata that comprise the LGNU do however possess an approximate layer-cake distribution subparallel with the thrust plane (figure 3.6) that suggests the thrust sheet has an approximate flat-on-flat geometry for much of its exposed length. It also suggests that the original structural configuration of the Hercynian basement was relatively simple prior to Alpine thrusting (McCaig, 1986). This geometry is however complicated by the irregular outcrop of the SMF, by the thick isolated lens of FDSF, and by the presence of the cut-off geometries along the upper boundary of SMF.

The tectonic nature of some of the formation boundaries eg. the top of the SMF, precludes a simple interpretation of the layer-cake distribution of strata. The isolated lens of FDS Fm. in the core of the Troumouse anticline is anomalous because any attempt to restore this structure meets with the problem of explaining where the rest of

the formation has gone and why the fold occurs. One possible model is shown in figure 3.7 with the lens interpreted as a remnant tilt block preserved beneath the unconformable SMF. Later reactivation of the bounding fault during emplacement of the GT produced the fold.

The Sia Thrust ramps sub-horizontally across the steeply dipping BF on the southern limb of the Troumouse anticline. Parish (1984) interpreted the Sia Thrust as part of an Alpine-age antiformal thrust stack within the Gavarnie Thrust Sheet, with the GT as floor fault (see figure 2.10). The trace of the Sia Thrust appears however to cut down section through the BF to link to the upper boundary of the SMF. The outcrop of the Sia Fm. on the summit of Pic de Munia could represent an outlier and the contact with the underlying strata an angular unconformity. This would allow the contact to cut up and down section without the unit possessing a tectonic origin. Another problem with the thrust interpretation is that the trace of the fault truncates the Blancas anticline (figure 3.6) yet this fold has been interpreted by Parish (1984) as post-dating movement on both the ST and emplacement of the third tectonic unit (see figure 2.10). The geometry exposed on the cliff face cannot be explained by simple layer-cake thrusting proposed by Parish (op.cit).

A number of normal faults occur within the thrust sheet and a number of faults appear to have had both normal and reverse displacements eg. the Gerbats fault (figure 3.6). These structures suggest that a phase of extension has occurred within the thrust sheet with the faults detaching within the SGP. It is difficult to constrain the timing of the extension from a photogeological interpretation because the sequence of movements on the large inaccessible faults is not known. It is possible that the apparent boudinage of the SMF formation is produced by normal faulting with the faults downthrowing to the W or NW. Further mapping is required to place the extension in the overall deformation sequence in the thrust sheet.

The above description and interpretation has been based largely on a photogeological interpretation of Muraille de Barroude. The section constructed indicates that many of the deformation features do not agree with proposed schemes for the thrust sheet. In particular, the presence of cut-off geometries along the SMF precludes the simple layer-cake model of thrusting that attributes all the observed large-scale deformation features to Alpine Thrusting. The presence of these cut-offs has not been incorporated into published models on the formation of the nappe (eg. Deramond et al. 1981; Parish 1984) and it must cast doubt on some of their interpretations. A phase of extension also occurred within the nappe and similarly does not appear in existing models. Further mapping is required to solve some of these problems.

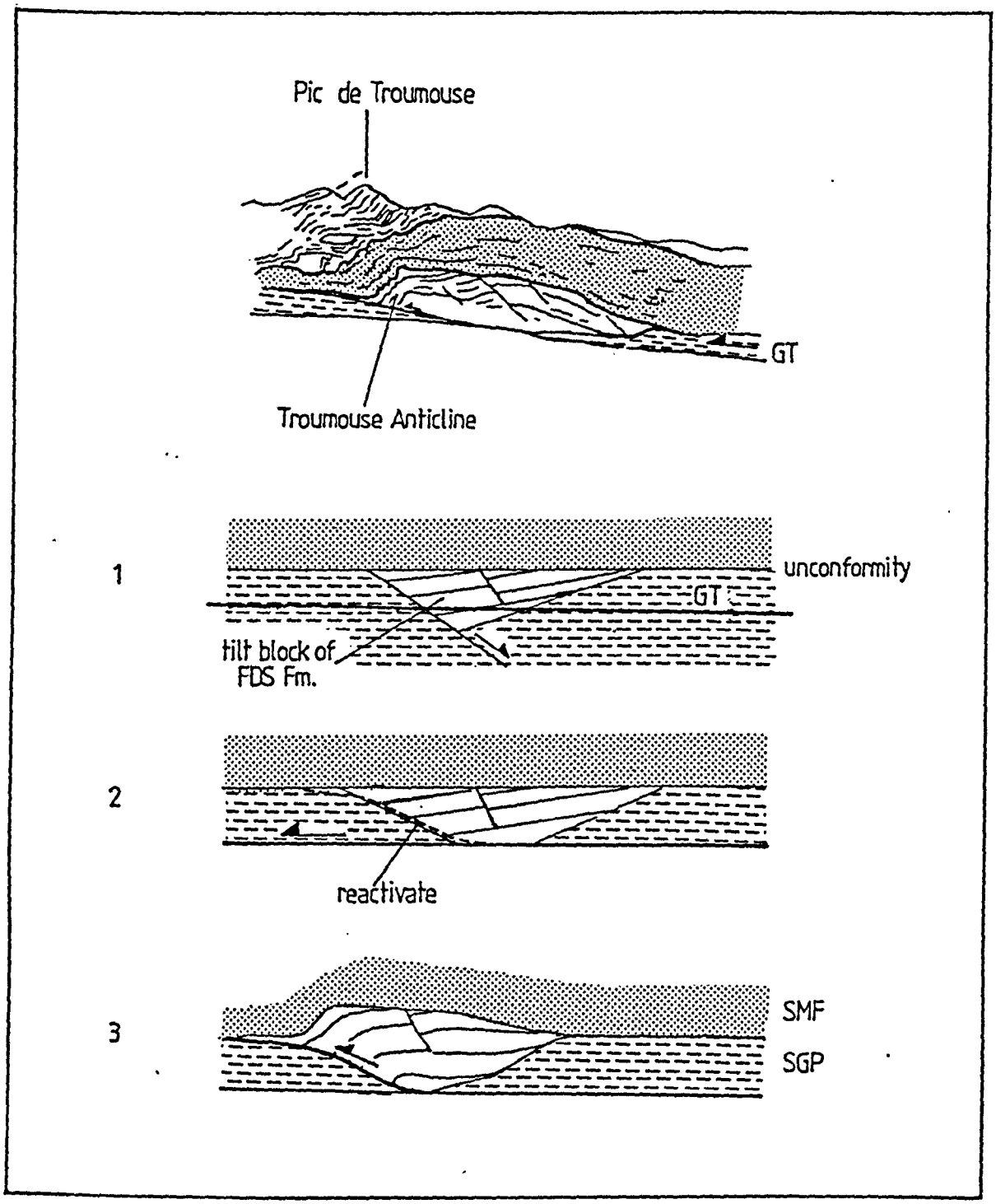

Figure 3.7. Possible model to explain the development of the Troumouse anticline. See text for discussion.

3.2.2. Mesoscopic structures in the SGP Formation.

The Silurian Graphitic Phyllite possesses an intense slaty cleavage. This is locally crenulated or folded by south-verging mesoscopic folds that are cut by later shear zones and shear bands. The sense of movement on these minor structures is consistent with southerly directed shearing during emplacement of the Gavarnie Thrust. The shear zones and shear bands are the most common thrust-related deformation feature within the phyllite (figure 3.8). Equal area plots of structural data collected from the SGP along the flank of Cirque de Barrosa are given in figure 3.9. Along this part of the section, the GT dips approximately 12 degrees west.

Cleavage in the SGP plots as a crude 'dog-legged' pattern (figure 3.9a) with a dominant NE strike and NW dip . This is oblique to the transport normal of the thrust sheet. The age of the cleavage is not known and it could be a Hercynian fabric reactivated during Alpine thrusting. The shear bands are Alpine in age as they cut slivers of mylonitised Cretaceous limestone interleaved with the phyllite.

The shear bands form arrays of discontinuous sub-parallel shear zones. While anastomosing bands do occur, the majority are discrete and sub-planar (figure 3.8). Evidence for different generations is lacking from the exposures studied and cross-cutting relationships are generally absent. The shear bands possess a range of sizes from a few decimetres long to greater than 5 metres in length. This distribution possibly represents bands at different stages in their evolution.

Poles to the shear bands (figure 3.9b) show a maximum at a high angle to the mineral fibre lineations that are developed on their surfaces (figure 3.9c). These lineations are parallel to the stretching lineations in the Cretaceous limestone mylonite in the footwall of the Gavarnie Thrust (figure 3.9d). The rotation of the cleavage in the phyllite into a shear band is plotted in figure 3.9e. The interpretation in figure 3.9f shows that the poles to the cleavage were rotated towards the pole of the shear band in the plane whose pole was the intersection between the original cleavage orientation and the shear band. This configuration suggests simple shear within the band (Skjernaa, 1980). The shear bands represent a late-stage pervasive fabric along the base of the thrust sheet. The cleavage and limestone slivers that are cut by the shear bands dip steeply (20-30 degrees) towards the thrust. This attitude is too steep to have been a product of the high shear strains along the base of the thrust and it appears to have been produced by clockwise rotation between the shear bands. This rotation appears similar to the rotation of fault blocks during domino faulting.

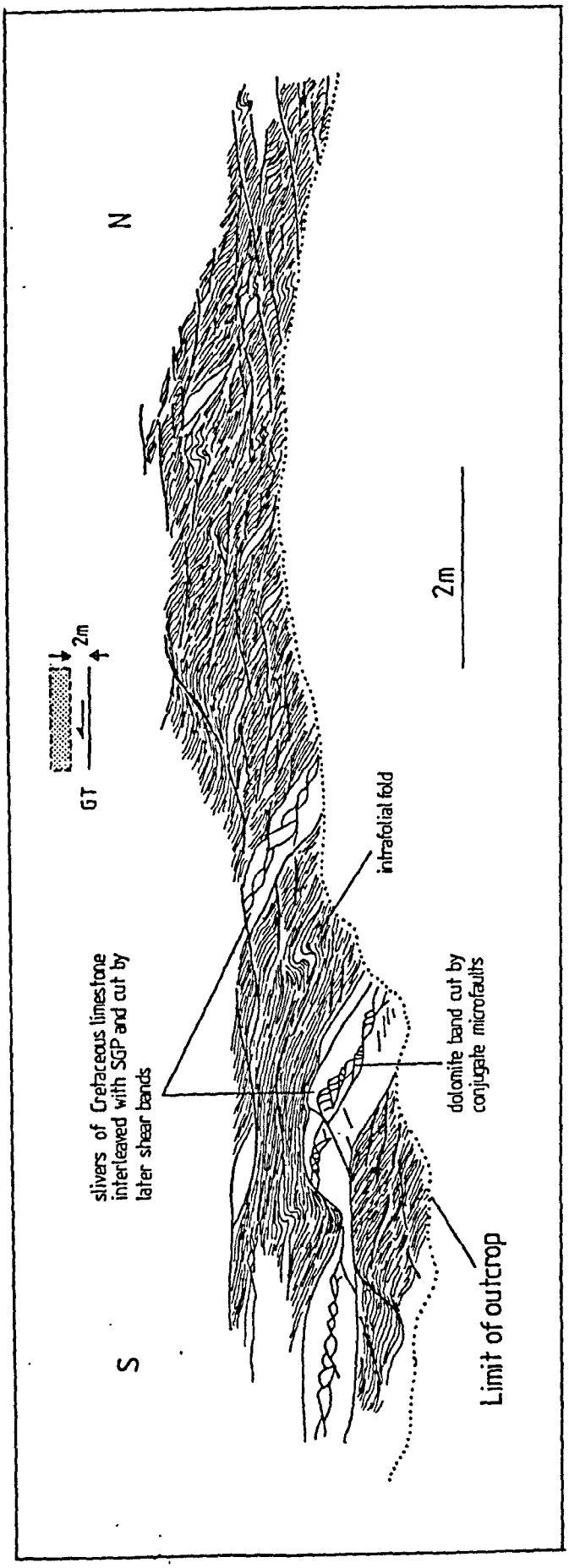

Figure 3.8. Sketch section showing shear band array in the SGP Fm. at base of the GT Sheet. From (42038 4898).

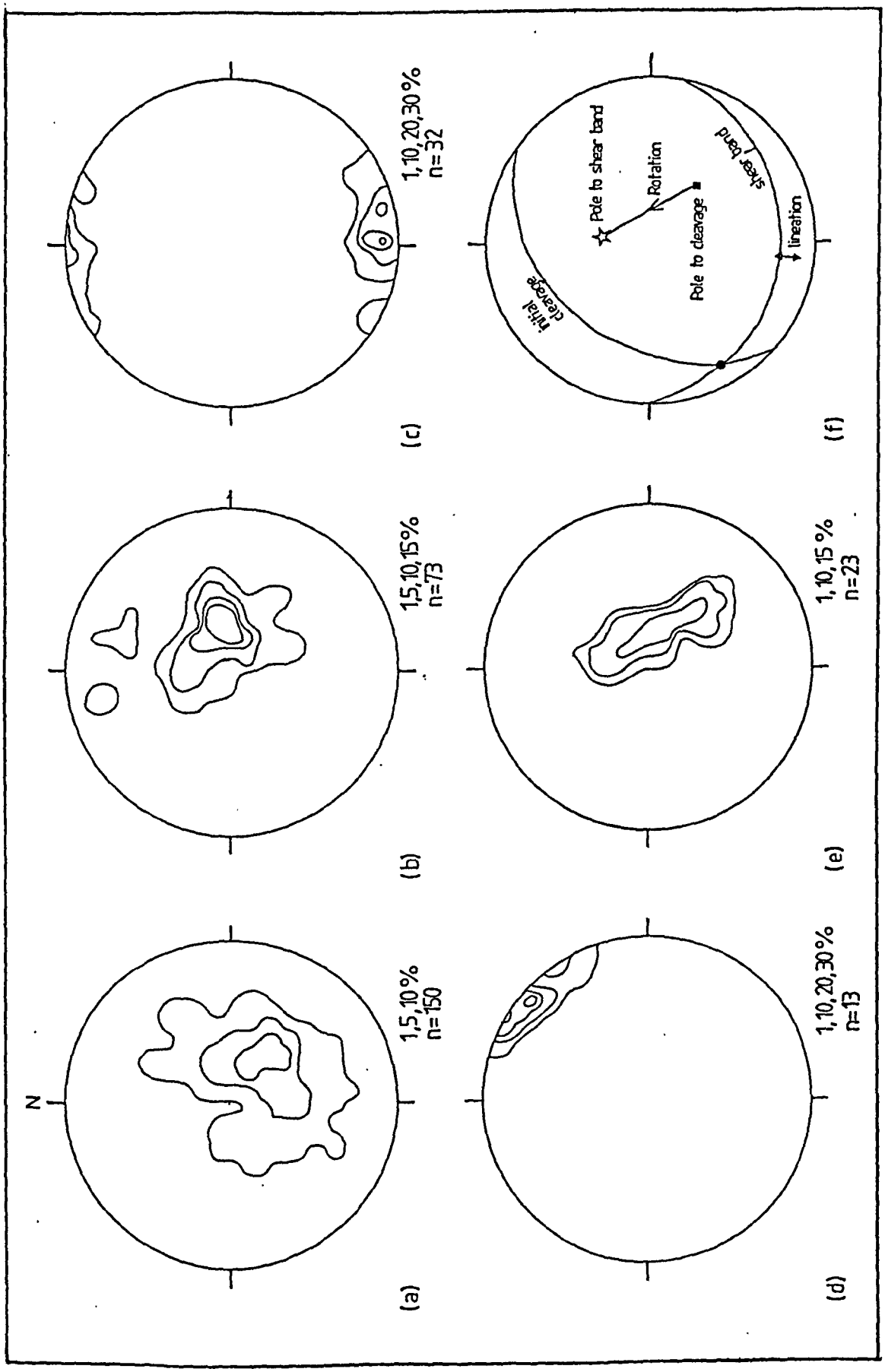

Figure 3.9. Structural data from the base of the SGP formation between (42060 4924) and (42038 4898). a) Poles to cleavage in the phyllite; b) poles to shear bands; c) lineations on shear bands; d) fold axes of intrafolial folds in the SGP. C is the profile plane. e) The reorientation of cleavage within one shear band; f) interpretation of reorientation of cleavage shown in e). All plots are hand-contoured.

3.2.3 Deformation in the footwall of the Gavarnie thrust.

3.2.3.1. The Mesozoic strata north of the Sierra Liena.

3.2.3.1.1. The Triassic strata

North of the Sierra Liena the Triassic red beds occur as discontinuous lenses beneath the Cretaceous unconformity. The strata within these lenses is deformed and possesses a slaty cleavage and bedding parallel thrusts (see figure 3.3) These features are Alpine in age because they pass without break into thrusts and cleavages in the overlying Cretaceous limestone. The thrusts are demarcated by the presence of centimetre thick layers of laminated quartz/chlorite shear fibres bordered by zones of small shear bands (see chapter 5). The thrusts appear to have localised along the contacts between different lithologies. In particular, there is a concentration of thrusts along the bases and occasionally the tops of the crossbedded sandstone beds. Small tip folds are locally developed where the faults have tried to cut up section across the sandstone beds. The thrust related deformation appears to detach along the Triassic unconformity.

Larger scale thrusting in the Triassic strata occurs on Pic de Port Vieux where a culmination is developed in the Gavarnie Thrust. The structures associated with these thrusts form the subject of chapter 4.

The cleavage in the Triassic strata refracts from the sandstone into the shale beds reflecting a greater component of bedding-parallel shear within the incompetent shales. However the local finite strain cannot correspond to bedding-parallel simple shear because discontinuities in strain occur along lithological contacts and the strike of the cleavage in the mudstones is variable. The presence of bedding-parallel thrusts reflect incompatibilities in strain between different beds and can only have formed if a component of pure shear was involved in the strain (Ramsay and Huber, 1987 p. 612). The pure shear component was probably a thrust tip effect. The changes in cleavage strike occurs both longitudinally and vertically through the Triassic sequence within the shale units e.g. figure 3.3b. These must reflect a component of layer parallel longitudinal strain (Coward and Kim, 1981) that may be associated with differential movement on individual thrusts (Sanderson, 1982; Coward and Potts, 1983).

3.2.3.1.2. The Upper Cretaceous limestone.

The Cretaceous limestone possesses a strong mylonitic foliation slightly oblique to bedding and a strong north-south stretching lineation. Elongate dolomite stringers are also extended parallel to the lineation. Where present, stylolites in the limestone parallel

the foliation. They suggest a component of vertical loading may have occurred after the Gavarnie Thrust sheet had been emplaced.

Where the limestone rests unconformably on the basement it is often imbricated by bedding-parallel thrusts and small duplexes. Similar structures appear absent where the limestone rests on the Triassic strata. An example of this style of deformation is shown if figure 3.10. The limestone is duplicated both internally and by thrusts that have breached the unconformity. A line-length restoration of the structure (figure 3.10b) gives a total of 213m of shortening. This is partitioned into 64m of shortening in the duplex while the earlier bedding parallel thrusts folded in the roof of the structure contribute a further 149m of shortening.The restoration shows that limestone in the duplex is anomalously thick. It was probably also internally thickened by bedding-parallel thrusts prior to the duplex forming. These would contribute a further 112 metres of shortening. The 325 metres of total shortening in this structure represents a strain of -73%.

While incomplete exposure prevented mapping of the distribution of thrusts in the Cretaceous limestone along the complete length of the Muraille de Barroude section it is likely that considerable internal duplication of the thin mylonite layer has taken place along much of the section. The granite beneath the the Cretaceous unconformity is intensely sheared and possesses a strong L-S fabric. Where this shearing occurs the limestone appears to have been effectively accreted to the base of the nappe.

According to regional geological maps (Seguret 1972), the Cretaceous limestone is present in the footwall of the thrust as far north as its present outcrop limit in the Vallon de la Gela. The corresponding hangingwall cut-off of the limestone occurs on the northern side of the Vallee de Pineta (figure 2.5). The distance between the cut-offs is approximately 11.5 km. This figure represents a minimum for the displacement in the nappe in the Muraille de Barroude section. The amount of internal shortening in the nappe is not known. The observed duplication within the Cretaceous limestone must significantly decrease the estimated displacement on the GT possibly by as much as a couple of kilometres if my local observations can be taken as representative for the complete outcrop length of the limestone.

3.2.3.2. Structure of the Sierra Liena.

On the southern flank of the Sierra Liena the Triassic and Cretaceous strata are folded together with the Bielsa Granite into a train of symmetrical, open to close mesoscopic folds cut by later thrusts (figure 3.6). The structural style therefore changes from thrusting in the Cirque de Barrosa and the Cirque de Barroude to folding further south. This change exactly corresponds with a change in regional sheet dip from gently west to steeply (35-45 degrees) south on the forelimb of the regional culmination.

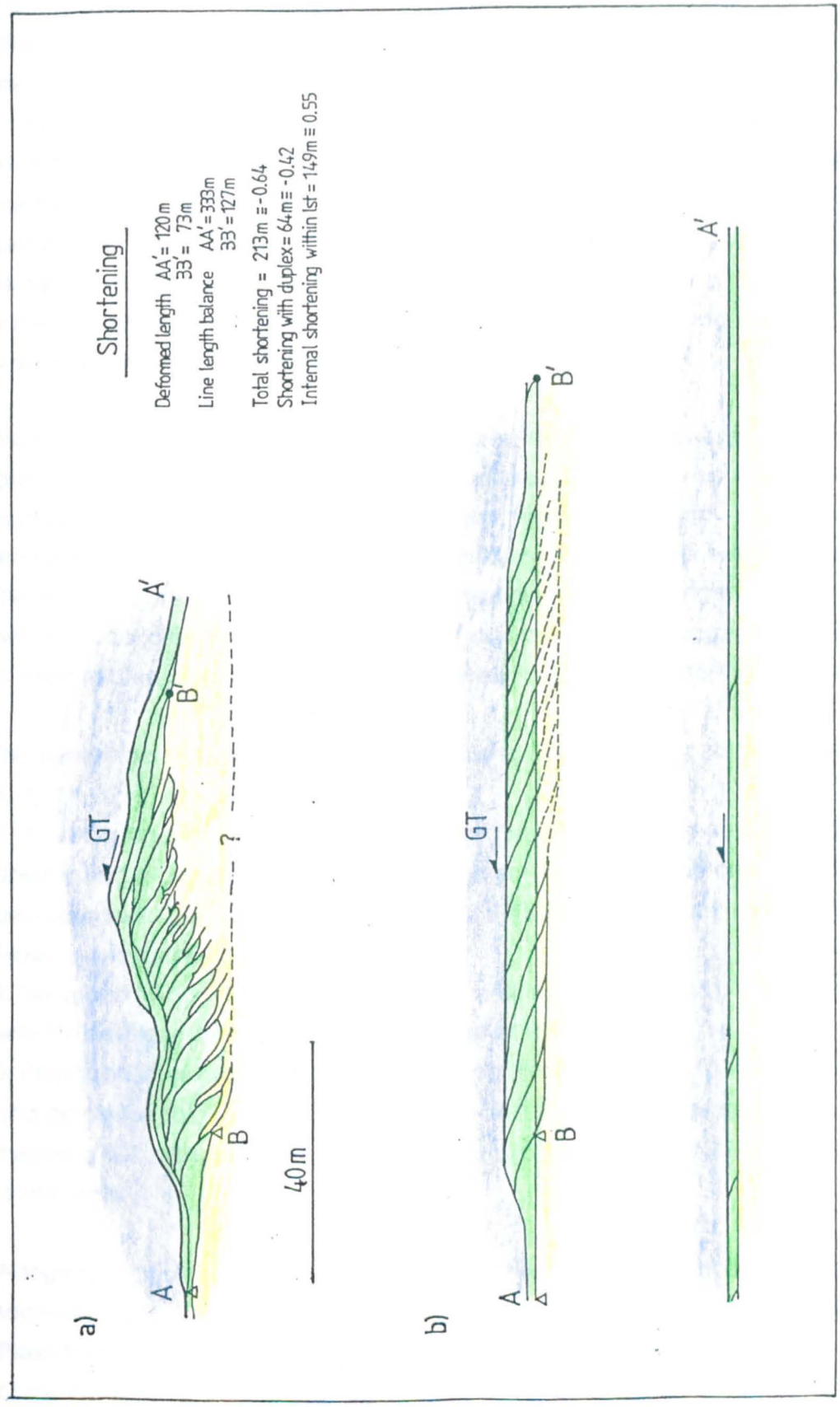

Figure 3.10 Deformation of the Upper cretaceous limestone unit in the footwall of the GT in Cirque de Barrosa. From (42034 4876). a). Sketch section of small duplex. b). Restored section with shortening estimate. See text for discussion.

The folds have wavelengths of 10-15 metres and amplitudes between 5 and 10 metres. Fold hinges can be traced as sublinear features along strike and suggests that the folds are buckles rather than folds associated with the tips of individual small thrusts. Figure 3.11 is a sketch section of part of the fold train profile and shows that the folds are predominantly symmetrical in profile. Structural data for the folds is shown in figure 3.12. The fold hinges possess four maxima that probably reflect local culminations and depressions along individual fold axes. The presence of slickenside lineations on bedding surfaces points to a flexural-slip mechanism for the folding. At (41968 4495) an earlier southerly verging fabric in the Triassic mudstone was found which is folded around one of the folds. This structure is sketched in figure 3.13a.

The folds are truncated by a number of thrusts. The largest of these placed the Bielsa granite directly on folded Triassic and Cretaceous strata and is known as the Escorres Fault (Van Lith, 1965). At (41978 4490) this thrust truncates a vertically dipping thrust that emplaces Triassic red beds on top of the folded Cretaceous limestone (figure 3.13b). The attitude of the earlier thrust suggests it was back rotated during the folding. Together with the local development of folded cleavage this structure suggests that an episode of thrust-related deformation affected the cover sequence prior to the folding.

The overall deformation sequence in the Sierra Liena appears to have been (figure 3.14):

1. Thrusting and cleavage development in the cover succession (figure 3.14b) This possibly had a decollement along the basement-cover interface and may have been associated with the emplacement of the GT. It is similar to the thrusting described in the Triassic strata further to the north.
2. Tilting and folding of the basement-cover interface (figure 3.14c). This was associated with the development of the regional culmination evident in figure 3.6.
3. Propagation of out-of-sequence thrusts (eg. the Escorres Fault) through the granite and across the folded cover strata (figure 3.14d). These thrusts probably breached the overlying GT although erosion and poor exposure prevent confirmation of this relationship.

Along the crest of the Sierra Liena ridge and further north on the unnamed 2763m summit southwest of Pic de Barrosa a set of north-south trending open folds are also present. These folds control the outcrop pattern of the outlier of Cretaceous limestone on summit of the Sierra Liena and the small klippen of SGP on the Sierra Liena occur in the synclinal fold closures. Folds with apparent longitudinal axes can also be seen in the Cretaceous limestone outcropping in the footwall of the GT on the Sierra de Espierba. The age relationship between this fold set and the culmination-related folds is unclear because of incomplete exposure across the Sierra Liena and because the expected dome-

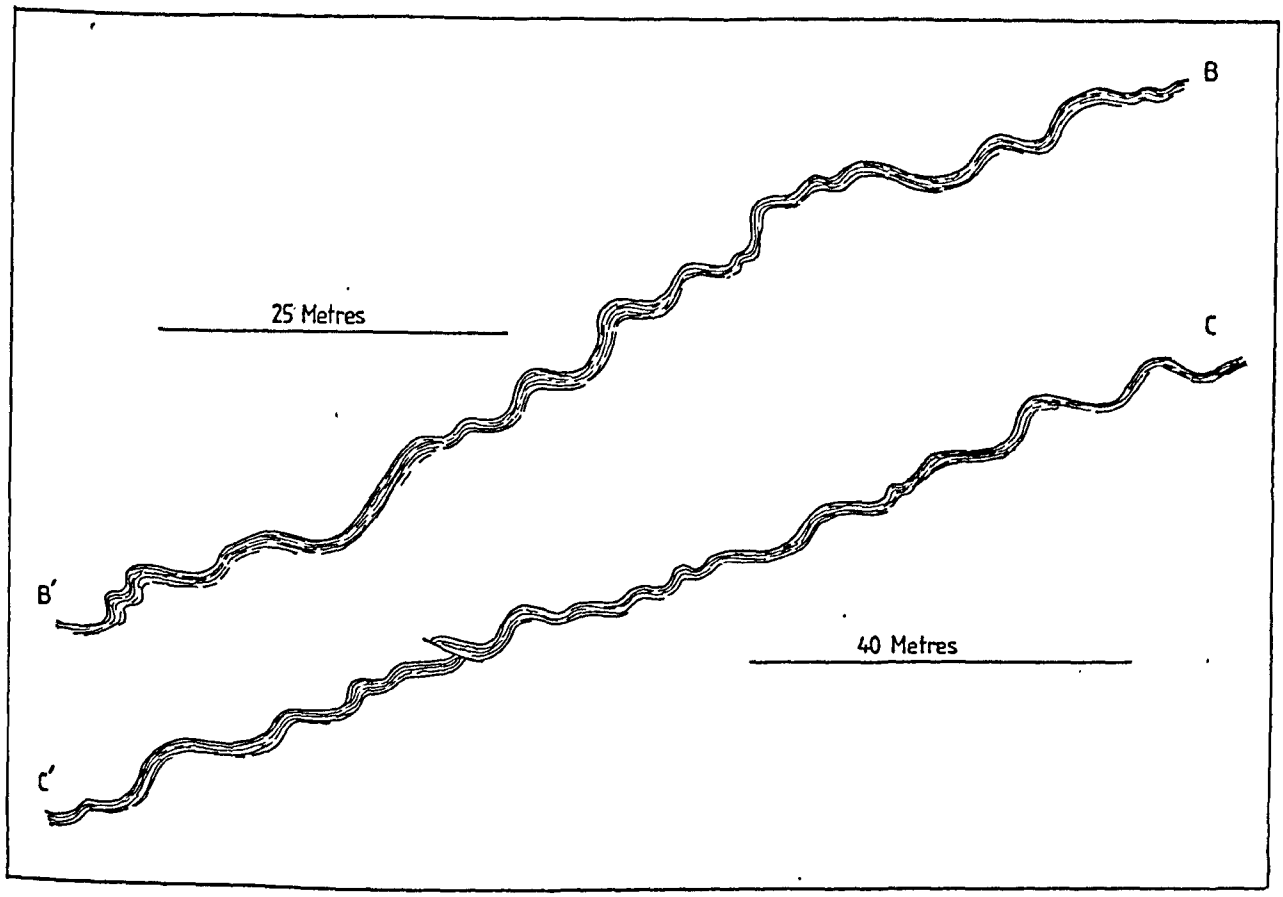

Figure 3.11 Sketch sections of the fold train in the Triassic strata of the Sierra Liena. See figure 3.1 for locations.

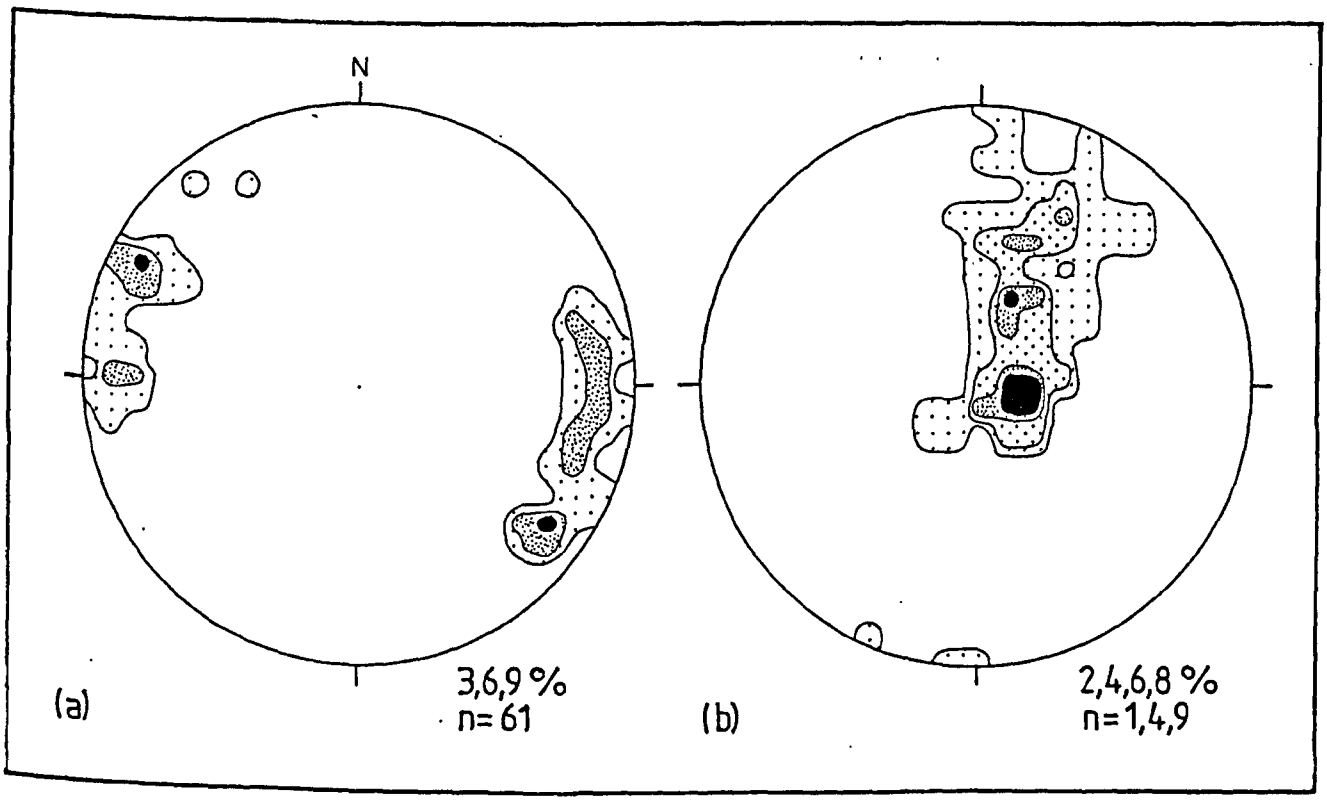

Figure 3.12. Structural data from the Sierra Liena folds. a) fold axes; b) poles to bedding. The four fold axis maxima are interpreted as the product of a dome-and-basin interference pattern between N-S and SSE-WNW trending folds.

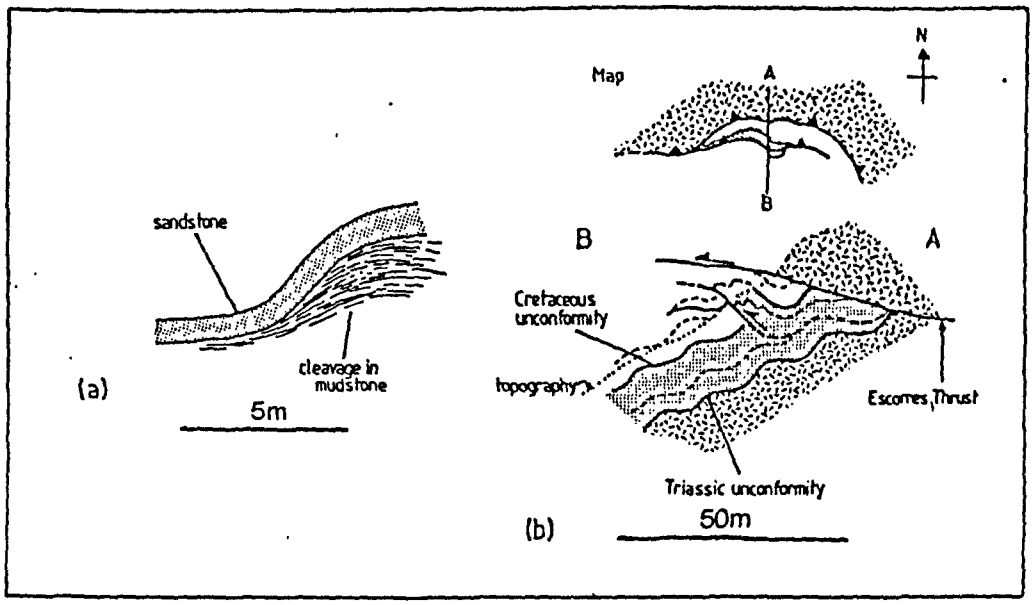

Figure 3.13. Mesoscopic fault-fold structures in the Sierra Liena. a) Folded early cleavage from (41968 4495). b) Sketch section through small thrust truncated by the Escorres Thrust. The small thrust is interpreted as an early structure back-steepened during the later folding. From (41978 4490).

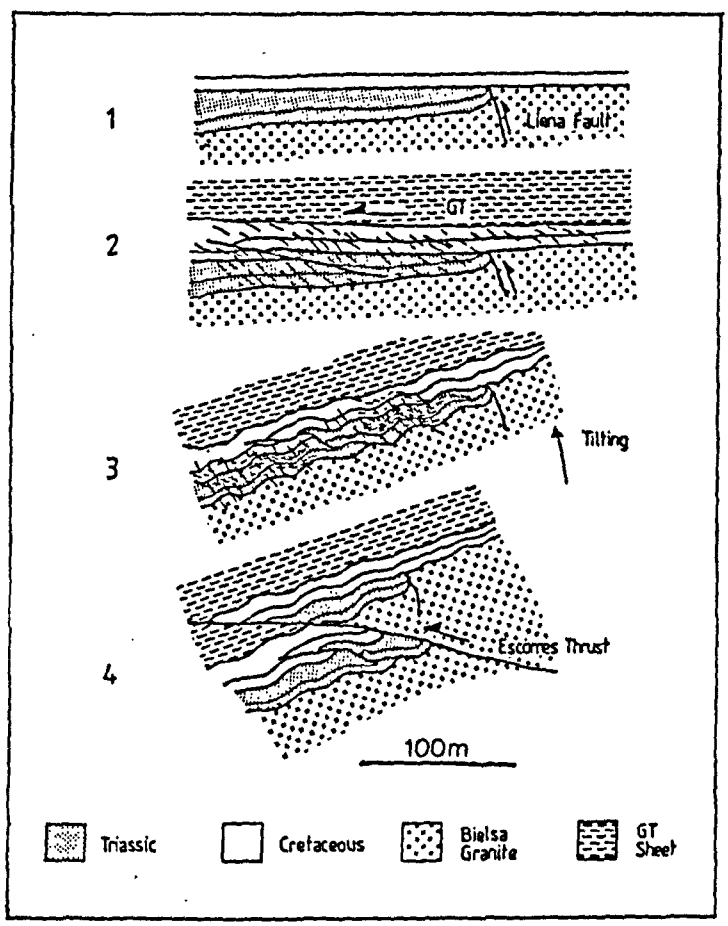

Figure 3.14. Deformation sequence in the Sierra Liena. 1. Initial configuration with pre-Cretaceous Liena fault. 2. Small thrusts and cleavage develop in the cover strata during the emplacement of the Gavarnie Thrust sheet. This deformation detaches along the basement-cover interface. 3. Folding and tilting of strata during development of regional culmination. 4. Out-of-sequence thrusts eg. the Escorres Thrust, cut across the fold train.

and-basin interference pattern between the orthogonal sets is obscured by the regional sheet dip and gentle nature of the folding. The four measured maxima of fold axes in (figure 3.12a) perhaps record this interference pattern.

3.3. Discussion

3.3.1. Regional framework.

The predominant structure affecting the Gavarnie Nappe in the section studied is the large regional culmination evident in figure 3.5. This culmination is also responsible for the the Gavarnie window further west (figure 2.7). Assuming the Upper Cretaceous unconformity was originally a sub-horizontal datum, then the culmination must be an Alpine structure. From the recognition of footwall thrusts that breach the GT in the Cirque de Troumouse, Parish (1984) concluded that the culmination was the product of duplex development on a blind thrust within the basement. He referred to this thrust as the La Larri Thrust and suggested that the thrusts outcropping in the Parzan Valley (the Sierra Liena) represent the continuation of the La Larri duplex towards the east. The interpretation of Parish is shown in figure 2.10.

Large thrusts outcrop in the Hercynian basement to the east of the study area near Punta Suelza (figure 2.7). These thrusts can be traced along strike toward the east and probably link with the structures in the Nogueras zone. The blind La Larri Thrust presumably represents the westerly continuation of these lower structures. The regional culmination can therefore be interpreted as the fold produced by the stacking of structurally lower thrusts in the Hercynian basement.

While the northerly outcrop of the GT strikes E-W, on the southern flank of the culmination the strike of the GT and the overlying Mont Perdu thrust is SE-NW. This convergence corresponds with the disappearance of outcropping large thrusts in the basement. The major folds in the basement of the Gavarnie Window are oblique to the transport direction (Parish, 1984) whereas the folds curve towards the east on the Sierra Liena and on Punta Suelza (Van Lith, 1965). The overall structural configuration strongly suggests that the thrusts responsible for the GT culmination lose displacement towards the west (figure 3.15) into a series of oblique tip-line folds. The sense of shear associated with these structures is dextral. This accords with the greater shortening estimates calculated for sections through the Nogueras Zone compared with sections further west (Seguret and Daignieres, 1986).

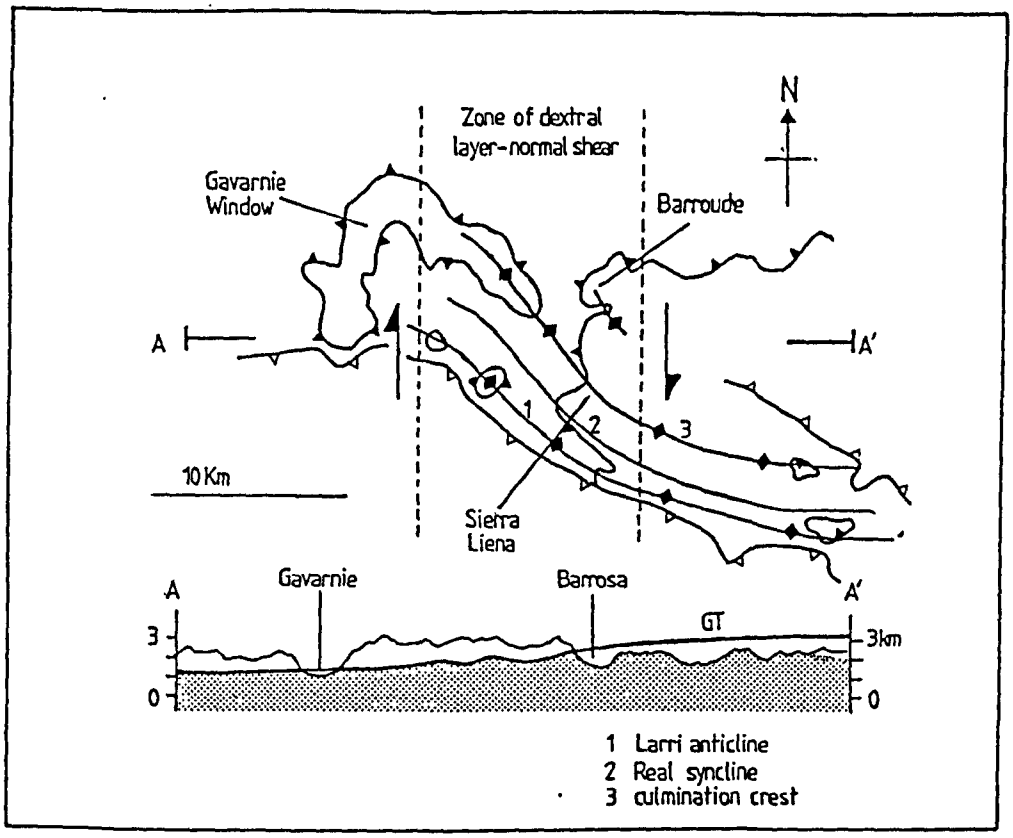

Figure 3.15. The trend of regional fold axes in the central Pyrenees. The curvature of the axes is interpreted as a zone of dextral layer normal shear above a set of blind oblique-tipping thrusts in the basement. The thrusts may have tipped because their propagation was obstructed by the Bielsa granite pluton. Section AA shows the lateral climbing of the GT towards the east produced by the blind structures.

3.3.2.The Barroude- Liena section.

The spatial association of N-S folding with the change in sheet dip across the Sierra Liena suggests a generic link between the folds and the culmination. Three possible scenarios exist (figure 3.16):

1. the folds formed prior to the development of the culmination and have since been tilted (figure 3.16a);
2. the folds formed during the arching of the culmination (figure 3.16b); or
3. the folds postdated the culmination (figure 3.16c).

In the first model (figure 3.16a) the folds could represent a phase of early layer parallel shortening that preceded movement of a large blind thrust over a ramp. This type of strain history has been documented by Kilsdonk and Wiltschko (1988). The layer-parallel shortening would be a frontal tip-strain and the culmination a large hangingwall anticline.

If the folds formed during the arching of the culmination (model 2) it possibly suggests the culmination developed above a leading imbricate stack on a major detachment. The forelimb of the culmination would shorten whereas the other limbs would have rotated passively. The out-of sequence thrusts were either break- back thrusts (Butler, 1987) that breached the tip zone or they were unrelated to the culmination and formed during a later phase of thrusting.

The third model could be explained by the distributed simple shearing of the already formed culmination. The south dipping limb would be in the shortening field of the incremental strain ellipse and so folds would form with southerly vergence (figure 3.16c). The thrusts that cut through the folds could then be Y shears and reflect strain hardening during progressive simple shear within the Bielsa Granite. The culmination would probably have owed its development to earlier thrust stacking.

The one-to-one correspondence between fold development and the southerly-dipping limb of the culmination suggests that the first scenario is unlikely to be correct. It would be fortuitous for this relationship to occur if shortening preceded tilting. The simple shear scenario is attractive because it would predict the observed fold distribution. It would be expected however that the folds that develop in simple shear possess asymmetric rather than the symmetric profiles. The symmetric buckle folds in the Sierra Liena may therefore suggest that simple shear was not involved in their development. This leaves the second scenario. It can explain both the distribution of folds and their symmetry and agrees with the inference from the regional framework that thrust tips should occur in the west of the region (Parish, 1984; Bates, 1987). This model seems the most plausible as an explanation for the Sierra Liena fold train.

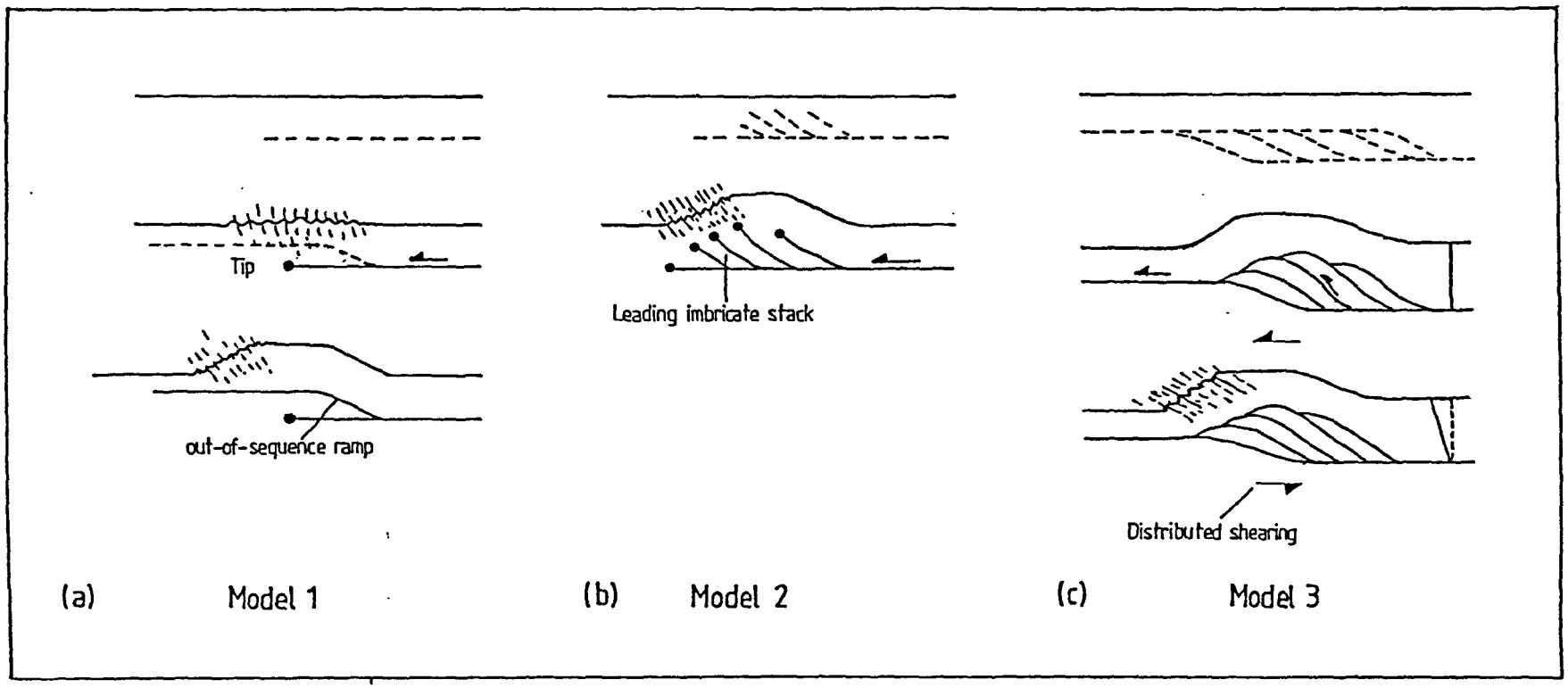

Figure 3.16. Models to explain the development of the regional culmination and the Sierra Liena fold train. a). Shortening succeeded by out-of-sequence ramping. Modified from Parish (1984). b). Folding above a set of blind thrusts in the basement. c). Folding of southerly dipping limb of a basement duplex culmination by superimposed simple shear.

The culmination in the Gavarnie thrust can probably be attributed to the presence of blind structurally lower thrusts. The east- west folds in the Sierra Liena suggest the blind thrust(s) possess frontal tips; further west, the clockwise rotation of the major folds responsible for the Gavarnie window (Parish, 1984) suggests oblique tips are developed (figure 3.15). This model differs from that of Parish (1984) who attributed the folds to ramp anticlines and linked the lower thrusts onto the Gavarnie Thrust.

3.3.3. Summary.

A study of structures in the Sierra Liena and Cirque de Barrosa reveals a progressive deformation sequence associated with Alpine thrusting. The earliest phase of thrusting involved minor thrusts and cleavage development in the cover strata. The deformation appears to have detached near the basement-cover interface and is relatively unmodified by later deformation north of the Sierra Liena. On the Sierra Liena these structures were folded into a train of symmetrical folds on the south limb of the regional culmination. This is interpreted as a result of a blind leading imbricate stack within the Hercynian basement. The curving of fold axes towards NW-SE suggests that the blind thrusts lost displacement obliquely in the west of the region. A late stage of thrusting is represented by out-of-sequence thrusts that cut through folds.

3.4. Conclusions.

1.The distribution of strata in the Gavarnie Thrust sheet and the presence of bedding cut-offs along the contacts suggests that the major formation boundaries are tectonic in origin. The deformation associated with these boundaries has not been incorporated into published tectonic models for the Gavarnie thrust sheet.

2. A phase of extension has occurred within the Gavarnie Thrust sheet. The age of the extension is not well constrained but some of the normal faults appear to post date the emplacement of the thrust sheet.

3. The Mesozoic strata were deformed during the emplacement of the Gavarnie Thrust sheet with the development of a strong slaty cleavage and bedding parallel thrusts. Localised shortening and layer normal shear strains in the strata appear to reflect differential displacements on the bedding parallel thrusts.

4. The thin layer of Upper Cretaceous limestone along the base of the Gavarnie thrust sheet has been extensively duplicated by minor thrusts that branch onto the Gavarnie thrust. The estimated 11.5km displacement on the thrust may be a significant overestimate when the displacement on the minor thrusts is taken into account.

5. The basement and Mesozoic strata on the southern limb of the regional culmination that folds the Gavarnie thrust are folded together into a train of symmetrical folds. The northwest curvature of the fold axes across the region suggests the folds are oblique tip-line folds associated with a blind imbricate stack of thrusts within the basement. It seems

that in this part of the Central Pyrenees the Lower Thrusts of Munoz et. al. (1986) do not branch onto the Gavarnie Thrust and that the displacement on these thrusts increases towards the east.

CHAPTER 4

The Structure of the Pic de Port Vieux Culmination

4.1. Introduction

The aims of this chapter are to document and interpret the thrust-related structures within the PPV culmination and to establish a model to explain the evolution of these structures. The chapter will be split into two main sections. The first will be mainly descriptive and will consider the structures developed in different parts of the culmination. The second part will interpret these structures, produce a general model for the culmination development and give some general conclusions regarding faulting and cleavage development.

Four locally developed phases of thrusting have been identified within the culmination and can be related to a progressive deformation sequence. These phases are:
P1. Early minor thrusts that duplicated the Mesozoic cover.
P2. Emplacement of the Gavarnie thrust.
P3. The development of the culmination.
P4. A late stage oblique reactivation on some of the earlier formed faults.

Before detailing the structures within the culmination an overview of the complete structure will be presented as a reference frame for the more specific work that follows. In addition a short precis of previous work will be given.

4.1.1 Previous Studies.

Comments on the geology of the Cirque de Barroude appear in the theses of Roddaz (1977), Majeste-Menjoulas (1979), Deramond (1979) and Lucas (1985). None of these authors however discuss the structure of Pic de Port Vieux in any detail. Lucas (p170-175) described the sedimentology of the Triassic red beds outcropping within the cirque and Deramond (1979, p16) concentrated on a regional strain analysis within the Gavarnie thrust sheet. Roddaz (p80-89) described an allocthonous sheet of Mesozoic strata resting on the Silurian strata of the Gavarnie Thrust sheet on the summit of Pic de Port Vieux and recognised three phases of Pyrenean deformation:
1. Mylonite development along the base of the Gavarnie thrust sheet.
2. A second cleavage overprinting the first fabric.
3. Late N-S trending fractures and folds.

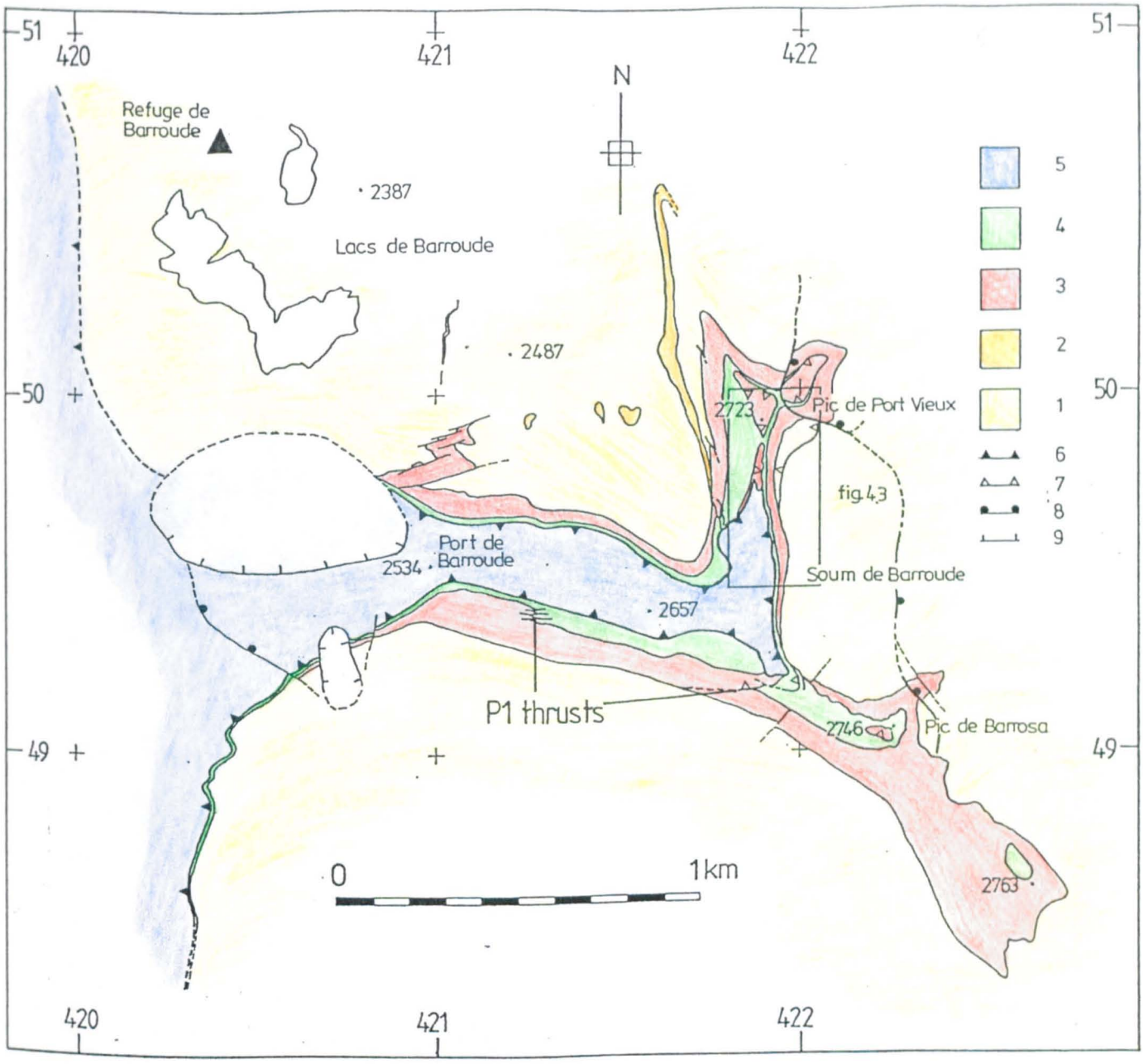

Figure 4.1. Map of Cirque de Barroude. 1. Migmatites (assumed Cambro-Ordovician metasediments); 2.Hercynian Granite/Granodiorite; 3.Triassic Red Beds; 4. Cretaceous limestone; 5. Gavarnie Thrust Sheet (Silurian/Devonian rocks); 6.Gavarnie Thrust; 7. minor thrust; 8. normal Fault; 9. boundary of landslide.

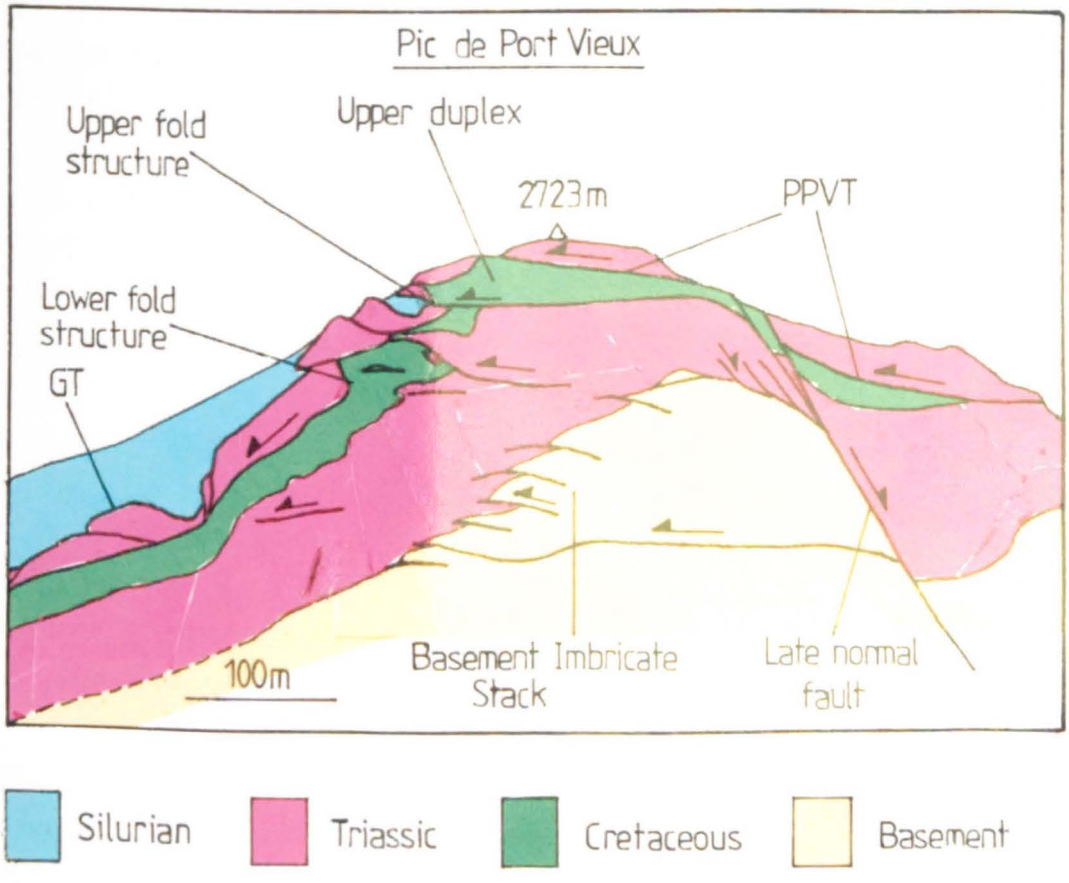

Figure 4.2.. Photograph of the east face of Pic de Port Vieux with important structures named. Looking NNW.

4.1.2. General Structure of Pic de Port Vieux.

The surface geology of Cirque de Barroude is shown in figure 4.1. The Gavarnie Thrust outcrops on the flanks of the cirque and is paralleled by the outcrop of Mesozoic strata. Pic de Port Vieux forms the eastern flank of the cirque and the east side of this mountain represents a 1km long transport-parallel cliff section (figure 4.2). Most of the work documented in this chapter has been completed on this cliff face.

The PPV culmination comprises the upper 100 metres of the mountain and is produced by a number of thrusts located both within the Hercynian basement and within the Mesozoic cover (figure 4.2). It occupies a similar structural position to the culminations produced by the Lower and Upper Troumouse duplexes exposed in the Gavarnie window (Parish, 1984) (figure 2.10) but is a separate structure (see later). A more detailed map of and section through the mountain is shown in figure 4.3.

The Silurian phyllite of the Gavarnie Thrust Sheet outcrops discontinuously on Pic de Port Vieux (figure 4.3a) and is locally breached and folded by structurally lower thrusts. These faults splay from a thrust that parallels the GT and which emplaced Triassic strata on the Upper Cretaceous limestone. This thrust will be referred to as the **Pic de Port Vieux Thrust (PPVT)**. It does not appear to have been named by previous workers.The PPVT sheet outcrops as a number of small klippen on PPV and can be traced as a 1-10 metre thick layer southwards along the ridge linking PPV to Pic de Barrosa (figure 4.3b). North of the summit of PPV the culmination is cut by a later NW-SE trending normal fault.

On the west side of the mountain, the Triassic strata in the hanging wall of the PPVT sheet has a discontinuous outcrop and has a hanging wall cut-off at (421812 49650) (figure 4.3a). Consequently, no Triassic strata outcrop adjacent to the GT contact on Port de Barroude. The inferred cut-off line trends oblique to the transport direction (figures 4.3a and 4.4). To the west of this line, the PPVT is intraformational within the Cretaceous limestone mylonite. The footwall ramp of the PPVT across the Cretaceous limestone is exposed on the northeastern ridge of the mountain (figure 4.4). The inferred trace of the cut-off line of the limestone is also oblique to the transport direction (figure 4.4) and agrees with the inferred hanging wall lateral cut-off of Triassic strata further south. The thrust ramp cuts gently across the Cretaceous limestone at an angle of 5-10 degrees to the Cretaceous unconformity.

A number of smaller thrusts are stacked structurally beneath the PPVT (figure 4.3b) and account for the development of the PPV culmination. Two main structures are present: **the Basement Imbricate Stack (BIS).** and the **Upper Duplex**. The former is a set of thrusts that imbricate the Hercynian basement and basal Triassic strata, the latter a small duplex that shortens the Cretaceous limestone beneath the summit of the mountain.

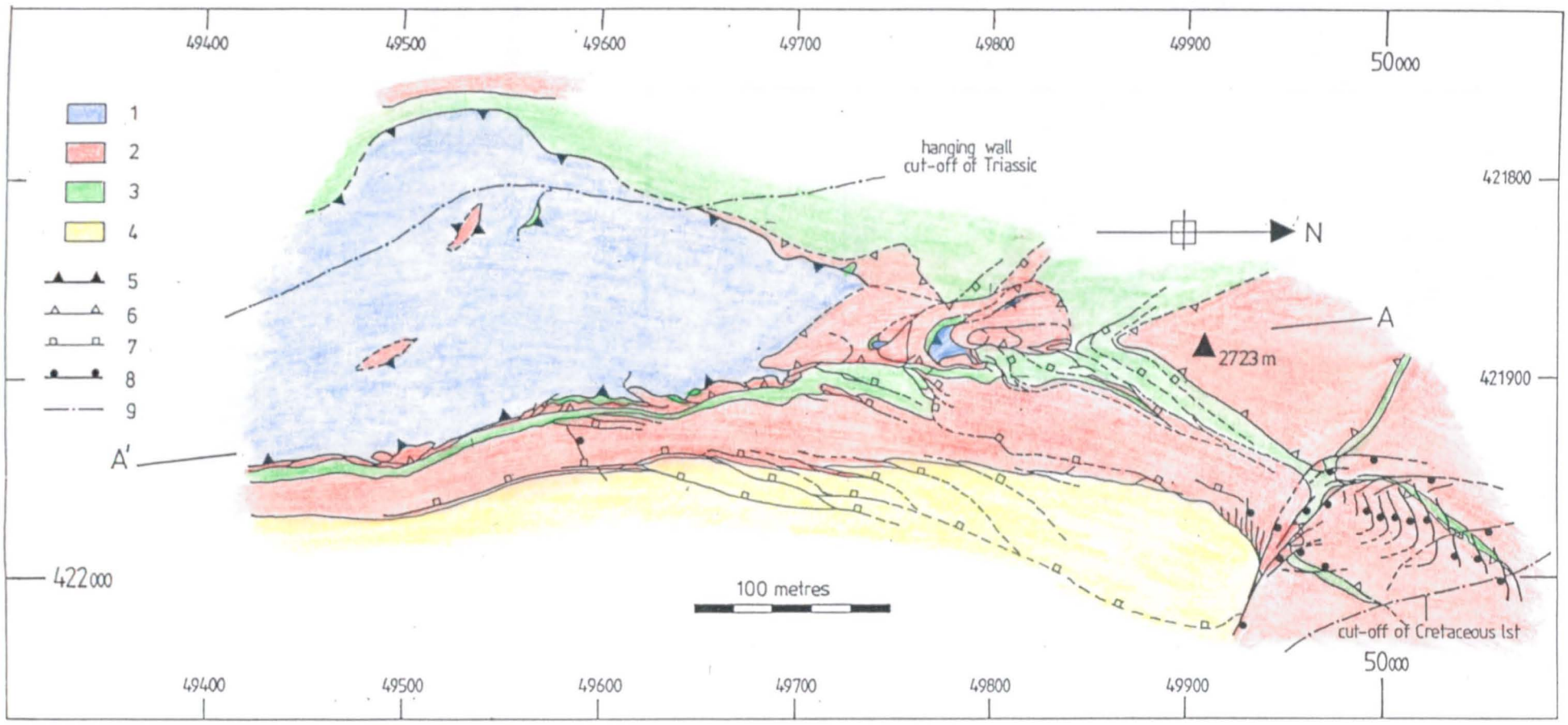

Figure 4.3. Map and N-S cross section A-A'of the Pic de Port Vieux culmination. The main structures discussed in text are named together with the relevant figures in which they occur. 1. Silurian Graphitic Phyllite (Gavarnie Thrust Sheet); 2. Triassic Red Beds; 3. Upper Cretaceous Limestone; 4. Hercynian Basement; 5. Gavarnie Thrust; 6. Pic de Port Vieux Thrust; 7.minor thrust; 8. normal fault; 9. cut-off lines of Triassic strata in hanging wall of the PPVT and of the Cretaceous limestone in the footwall of the thrust.

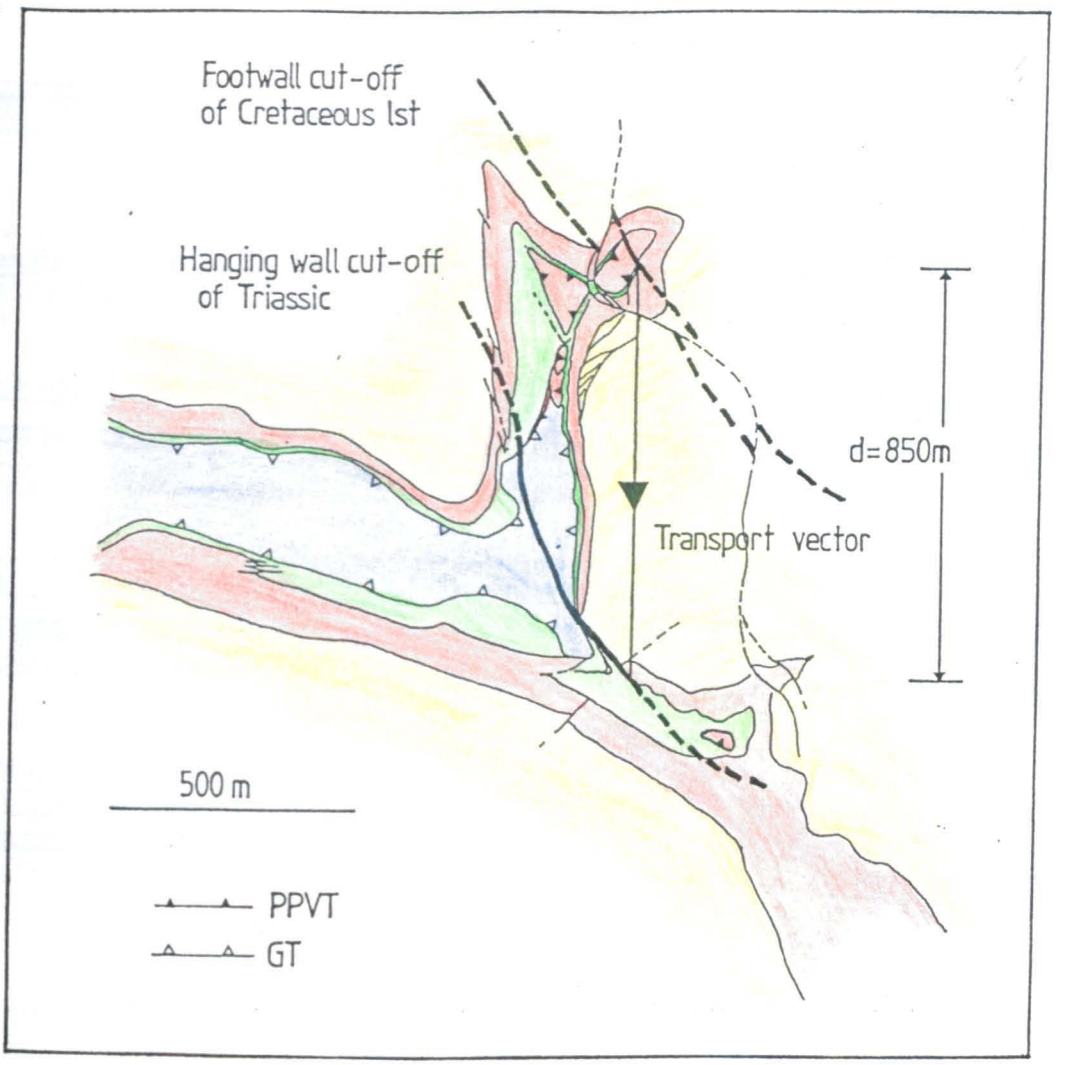

Figure 4.4. Topology of the Pic de Port Vieux Thrust showing the traces of the footwall cut off of the Cretaceous limestone and the hanging wall cut off of the Triassic strata. The lines are not strike lines. The estimated displacement on the thrust is 0.85km.

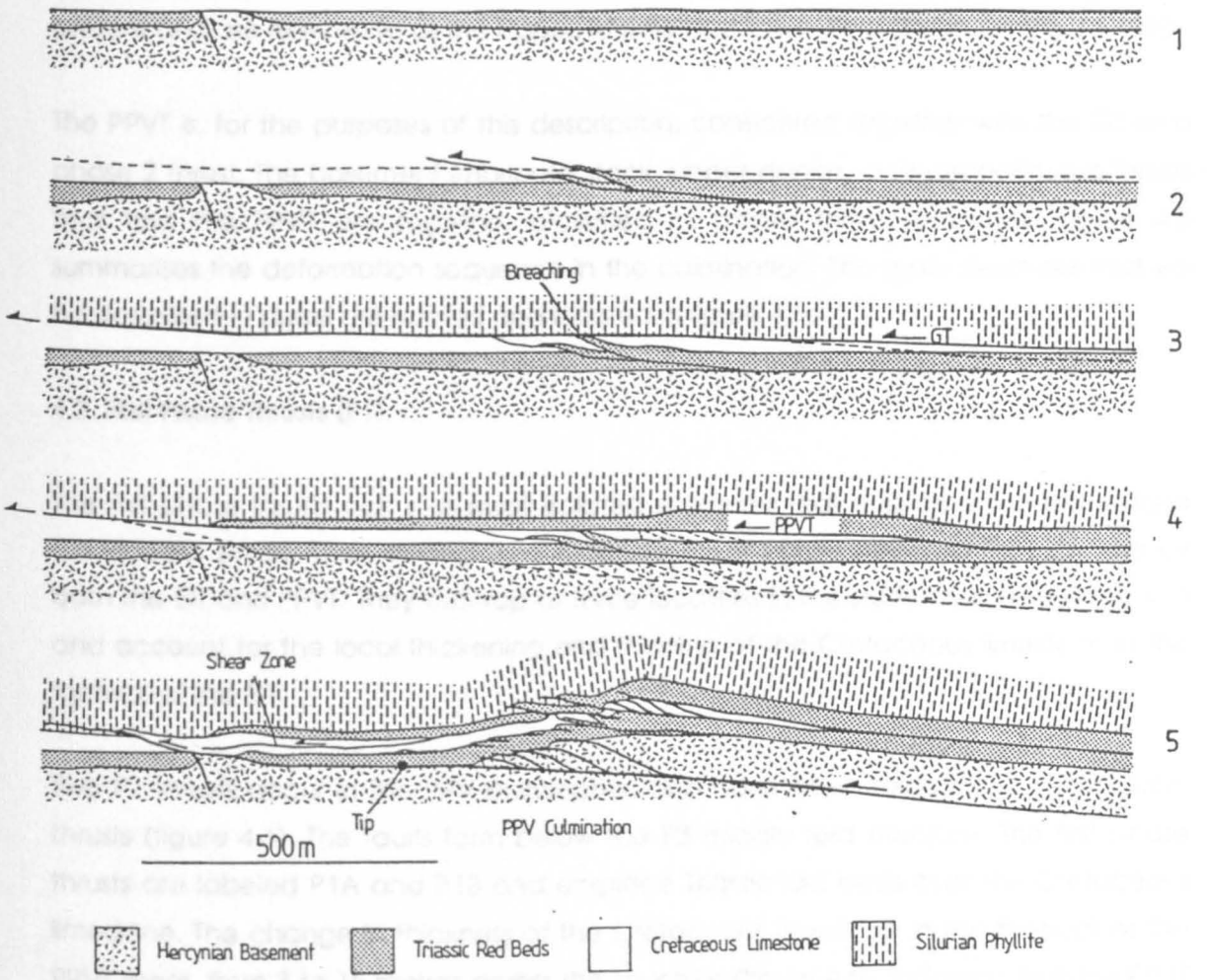

Figure 4.5. Summary model for the sequential evolution of the PPV culmination. 1. Initial configuration with planar Upper Cretaceous unconformity locally cutting out the Triassic red beds. 2. Phase 1 thrusts locally imbricating the Triassic and Cretaceous. The dotted line represents the future trace of the Gavarnie Thrust (GT). 3 and 4. Emplacement of the Gavarnie and Pic de Port Vieux Thrusts (phase 2 thrusts). The Gavarnie Thrust breaches the phase 1 thrusts. 5. Emplacement of phase 3 thrusts produce the culmination. The fourth phase of thrusting represents an oblique reactivation of some of the phase 3 thrust and is not shown.

These two structures are separated by 30-40 metres of cleaved and folded Triassic and Cretaceous strata cut by discontinuous thrusts. These thrusts tend to form tip folds within the Cretaceous limestone that fold the overlying PPVT sheet. Three main folds are present and are referred to as the Upper, Middle and Lower Fold Structures (figure 4.3b).

The PPVT is, for the purposes of this description, considered together with the GT as a phase 2 thrust. The basement imbricate stack, upper duplex, and discontinuous thrusts that fold the PPVT are together classified as phase three structures. Figure 4.5 summarises the deformation sequence in the culmination. The main structures that will be described in detail are named and located in figure 4.3b.

4.2. First Phase Thrusts (P1).

The first phase thrusts occur as small isolated structures that duplicate the Triassic and Cretaceous strata. They belong to a separate thrust phase because they are cut by both the GT and PPVT. They outcrop at three localities in the study area (see figure 4.1) and account for the local thickening and thinning of the Cretaceous limestone in the footwall of the GT.

Two P1 thrusts occur in the PPV culmination and have been folded and cut by later thrusts (figure 4.6). The faults form below the P3 middle fold structure. The first phase thrusts are labeled P1A and P1B and emplace Triassic red beds over the Cretaceous limestone. The change in thickness of the Cretaceous limestone in the footwall of the PPVT sheet, from 3 to 15 metres across the structure (figure 4.6), indicates that the PPVT must have post-dated thrusts P1A and P1B. The first three phases of thrusting are therefore clearly shown in this structure. On the west of the mountain (at 49809 421855 in figure 4.3a) the equivalent P1 thrust is also truncated by the PPVT although here the PPVT has cut at a deeper level across the earlier thrust.

The presence of the later phases of thrusting means that it is difficult to infer the original geometry, scale and displacement distributions on the P1 thrusts. They appear to represent localised structures that branched from a decollement within the Triassic strata possibly along the basal unconformity.

4.3. Second Phase Thrusts (P2).

The second phase of thrusting within the PPV culmination is represented by the emplacement of the GT and PPVT. These faults cut across the P1 thrusts but are not out-of- sequence as they emplace older strata on the earlier thrust sheets. As already mentioned in chapter 3, the displacement on the GT thrust is a minimum of 11.5km for a N-S section from the Val de la Gela to the Val de Pineta. The presence of a small klippe

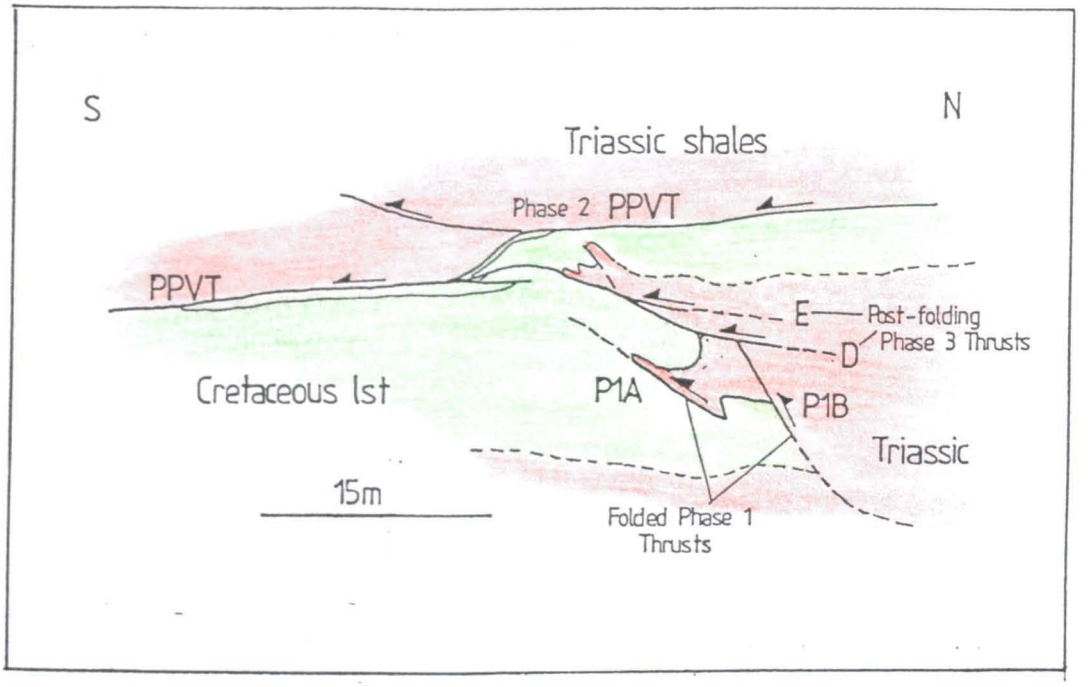

Figure 4.6. Sketch section of part of the Middle fold structure (see figure 4.3b for location) showing early phase 1 thrusts (P1A and P1B) cut by both the PPVT and later phase 3 thrusts D and E. The Cretaceous limestone in the footwall of the PPVT changes from 3 to 15 metres in thickness across the structure. Thrust P1A was folded by distributed strain and fault P1B back-rotated prior to the propagation of faults D and E.

of Triassic strata on the summit of Pic de Barrosa constrains the displacement on the PPVT to a minimum of 0.85km for north-south transport (figure 4.4).

The movement on the GT and PPVT produced a mylonitic foliation in the footwall Cretaceous limestone and a slaty cleavage in the Triassic red beds (see figure 3.4). The Triassic cleavage detaches on a fault along the basal unconformity or along a fault that follows the top of the basal conglomerate unit. It is possible that localised slip occurred along these faults during the emplacement of the GT or PPVT and contributed to the cleavage development. This seems likely because the Triassic strata possess a strong cleavage outside the zone of phase three thrusts in the PPV culmination and in strata not apparently duplicated by P1 thrusts.

4.3.1. Deformation in the Pic de Port Vieux Thrust sheet.

The PPVT sheet comprises a 1-20 metre thick layer of Triassic red beds and mylonitised Cretaceous limestone. The overall thickness of the thrust sheet increases towards the north although the hanging wall ramps that contribute to this thickening are difficult to observe within the sheet because of later deformation and intense reduction of the red beds. The overlying Cretaceous limestone in the thrust sheet outcrops as a series of discontinuous lenses or layers. Where it is missing from the GT contact, the limestone appears to have been plucked and incorporated into a tectonised zone coincident with the base of the GT sheet.

The PPVT is folded by the later P3 thrusts and many of the structures within the sheet especially in the ridge klippe (see figure 4.3a) relate to this later phase of deformation. It is instructive to consider the deformation in the thrust sheet in terms of two separate structural positions:

1. The summit klippe and Soum de Barroude sections (figure 4.3a) which are essentially unaffected by the later thrusting.
2. The ridge klippe which coincides with the forelimb of the culmination.

4.3.1.1. Deformation in the Summit Klippe and Soum de Barroude sections.

4.3.1.1.1. Geometry.

A sketch section through the summit klippe is shown in figure 4.7 and a sketch section through part of the Soum de Barroude section is shown in figure 4.8. The main mesoscopic deformation elements within both sections are arrays of extensional minor faults. These comprise:

1. high angle top-to-north faults, and
2. low angle top-to-south faults.

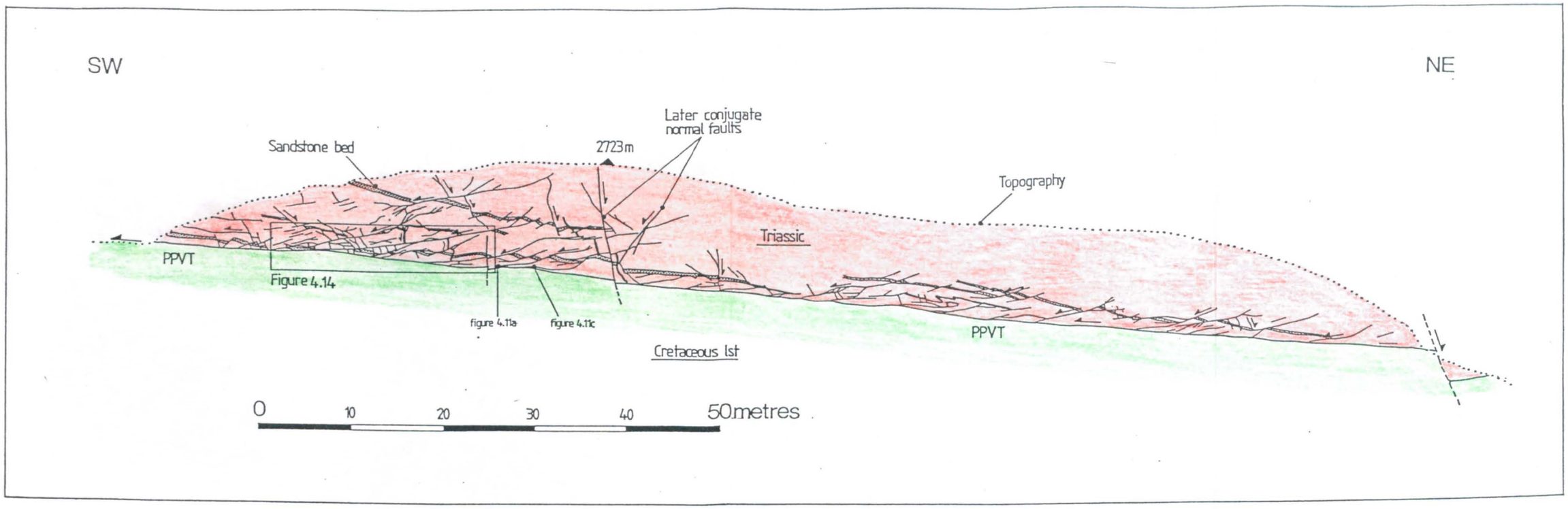

Figure 4.7. Sketch cross section through the summit klippe of the PPVT sheet. The thrust sheet is deformed by a complex array of low and high angle normal faults. The bedding in the fault blocks is rotated towards the thrust indicating that the low angle faults operated in a domino fashion.

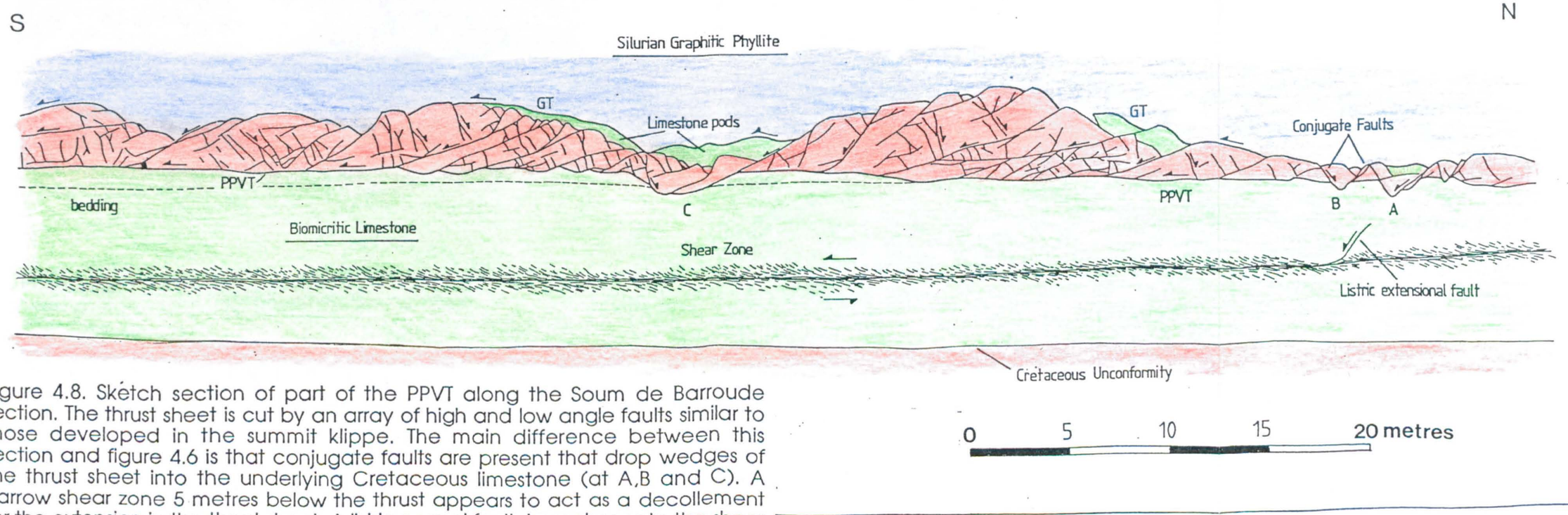

Figure 4.8. Sketch section of part of the PPVT along the Soum de Barroude section. The thrust sheet is cut by an array of high and low angle faults similar to those developed in the summit klippe. The main difference between this section and figure 4.6 is that conjugate faults are present that drop wedges of the thrust sheet into the underlying Cretaceous limestone (at A,B and C). A narrow shear zone 5 metres below the thrust appears to act as a decollement for the extension in the thrust sheet. A listric normal fault branches onto the shear zone below one of the conjugate fault blocks.

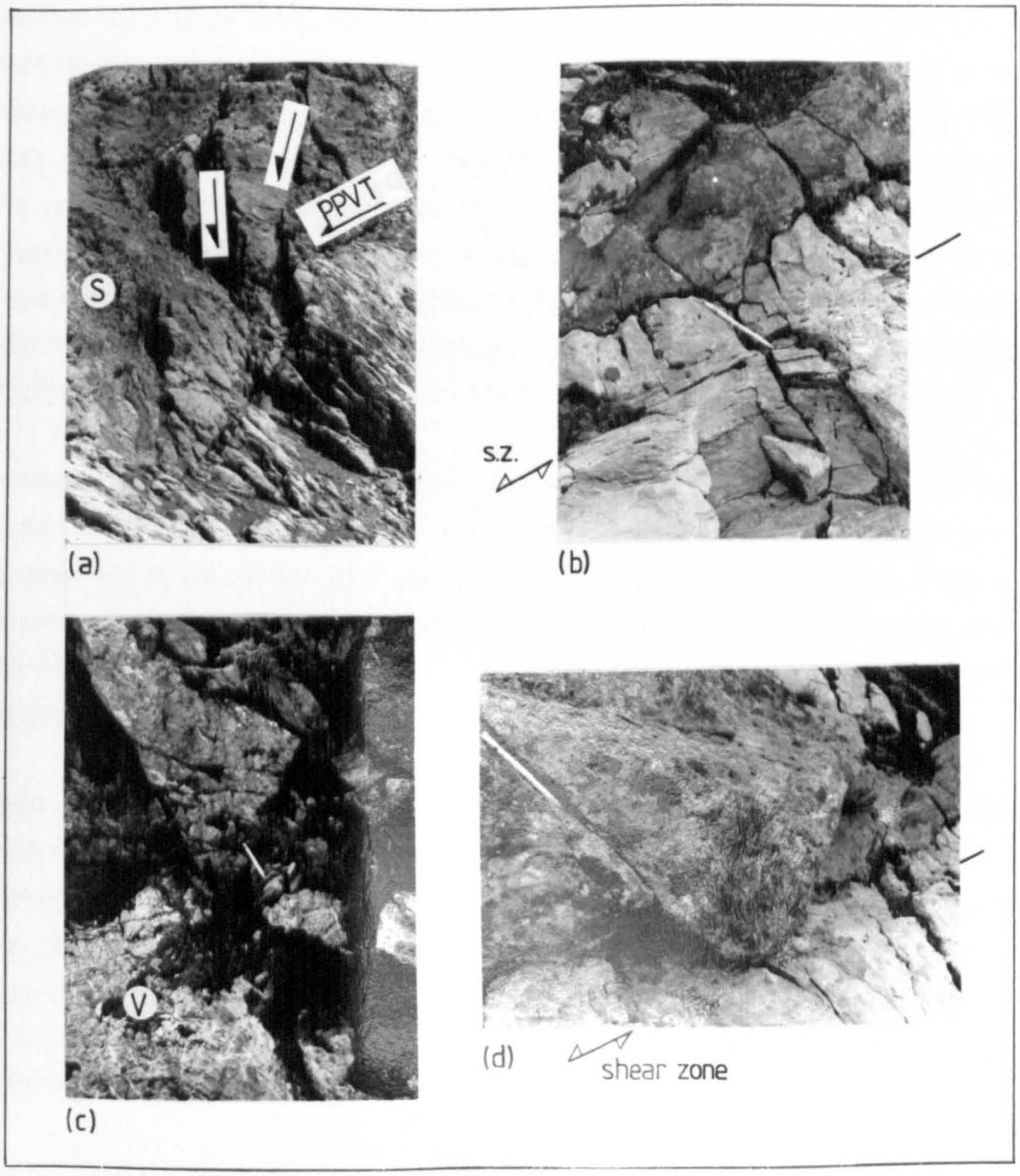

Figure 4.9. Photographs of extensional faults in the Soum de Barroude section of the PPVT sheet. a) Rotated low angle faults at the front of the PPV culmination (see figure 4.3b for location).
b) Small conjugate fault block within the PPVT sheet (see figure 4.12 for location). The faults cut across earlier corrugations in the thrust surface. The shear zone (s.z.) in the underlying Cretaceous limestone is not deformed by the faults.
c) Large conjugate fault block (block B in figure 4.7) dropping the PPVT into the footwall limestone. The extension in the limestone is accommodated by a swarm of high angle extension veins (V).
d) Another conjugate fault block in PPVT with the undeformed shear zone in footwall. The faults link together indicating simultaneous propagation and interaction. The faulting in the PPVT sheet suggests it behaved more competently than the footwall limestone during the extension.

Cross-cutting relations between the two fault sets consistently show that the low angle faults post-date the high angle faults although locally conjugate relations are developed.

The main difference in the geometry of the fault arrays in the two sections is that in the Soum de Barroude section the conjugate faults drop wedge-shaped blocks of the PPVT sheet up to 2 metres into the underlying limestone (eg at A, B and C in figure 4.8). These faults do not however continue through the limestone but link into one another (figure 4.9c and d) with the extension in the limestone accommodated on swarms of vertical extension veins. This geometry is summarised in figure 4.10. In the summit klippe the high angle faults tend to tip before meeting the PPVT and the low angle faults either branch onto the PPVT or also tip before meeting it. On some of the larger faults a reverse-drag roll-over was developed at the branch point with the thrust (figure 4.11a).

A narrow (5cm wide) shear zone outcrops below the PPVT along the Soum de Barroude section. In figure 4.8 this shear zone occurs 5 metres below the thrust. When traced north however it cuts up section to meet the thrust (figure 4.12). Occasionally conjugate en echelon sigmoidal vein arrays occur in the limestone above the shear zone and have orientations similar to the conjugate faults in the thrust sheet. The magnitude of displacement on the shear zone is unknown.

Figure 4.13 is a detailed section of the PPVT sheet north of pop- up structure shown in figure 4.12. The thrust sheet is is less than 0.2 metres in thickness and is cut by conjugate normal faults. It is also folded into a set of small corrugations between the faults with axes that plunge towards the NW. This part of the thrust sheet is tilted by the deformation associated with the culmination so that it now dips 45 degrees west. On rotating the thrust sheet back to the horizontal the fold axes adopt E-W attitudes. None of the folds or faults deform the shear zone in the limestone (figure 4.9b).

The low angle faults within the thrust sheet possess a continuum of sizes from discontinuous centimetre long fractures to large faults up to 25 metres in length. A detailed section through part of the summit klippe fault array is shown in figures 4.14 a,b and c. These can be found in the map pocket at the back of this thesis. The overall pattern of low angle faults is characterised by major faults (eg A,B, and C) that branch onto the PPVT, and smaller faults within the intravening fault blocks. These smaller faults are often cut by the the larger faults. High angle faults E,F and G appear to be conjugate to low angle fault D as they do not have counterparts in the footwall of of the fault. .

The low angle faults tip into either brittle-ductile shear zones (figure 4.15) or by splaying. In figure 4.14c, faults L-M possess horsetail splays at their terminations that appear to have

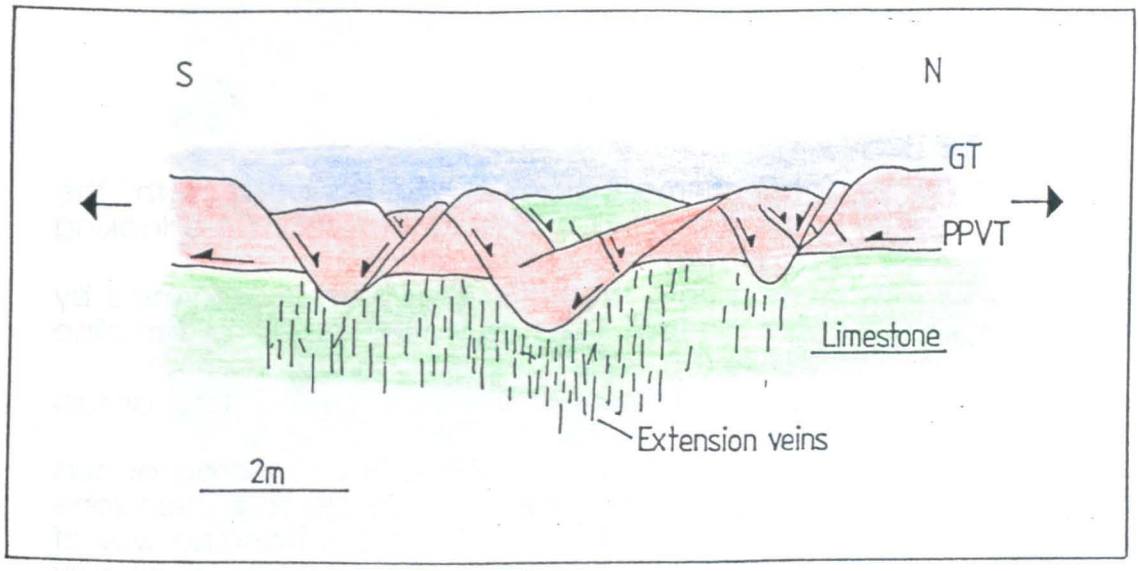

Figure 4.10. Detailed sketch section of linked conjugate faults (blocks B and C in figure 4.7) dropping wedge-shaped blocks of the PPVT into the footwall limestone and showing how the extension in the limestone is accommodated by vertical extension veins.

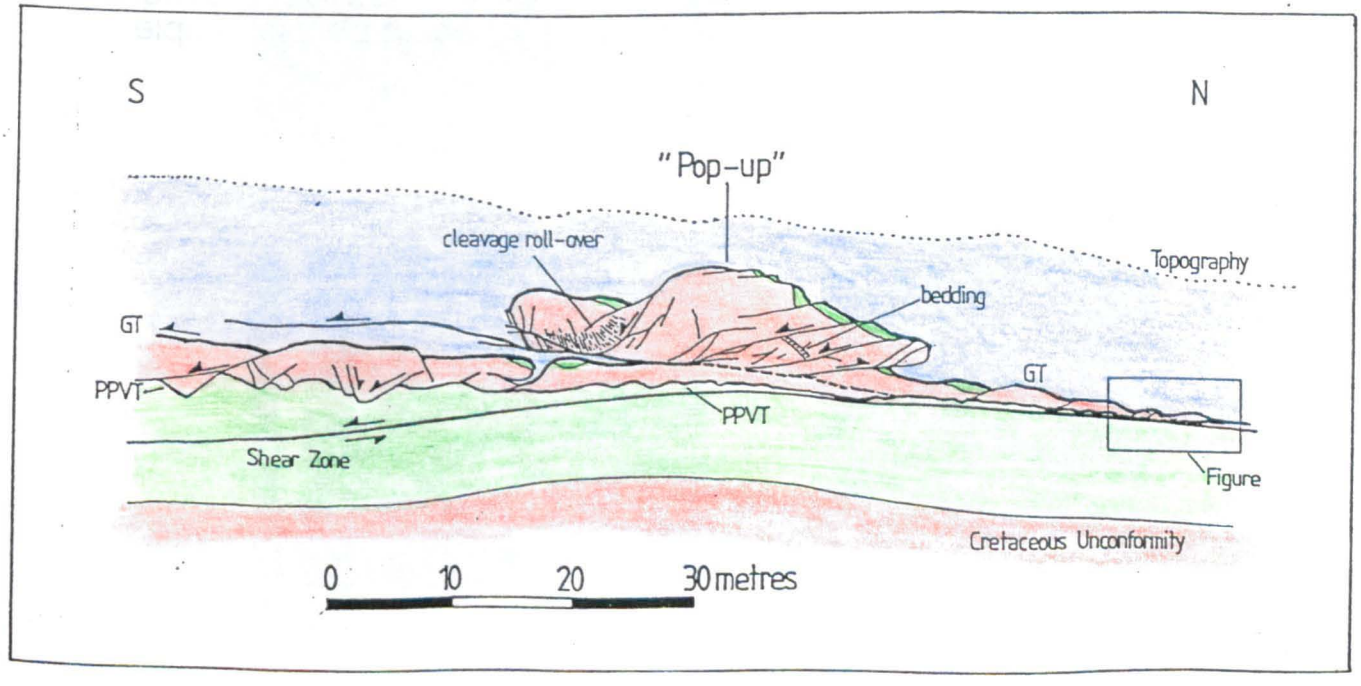

Figure 4.12. Sketch section across the 'pop-up' structure within the Soum de barroude section of the PPVT sheet. The low angle faults within the thrust sheet are deformed by the thrusts. The shear zone in the limestone beneath the thrust cuts down section south of the structure. Both the pop-up and the shear zone are folded by a gentle anticline interpreted as a tip-line fold associated the basal Triassic fault zone (see figure 4.3b).

Figure 4.11. Photographs of mesostructures associated with the extensional fault array in the summit klippe. All photographs are looking due west. See figures 4.6 and 4.14b and c for locations.
a) Low angle fault branching onto the PPVT. The thrust is deformed by reverse drag associated with the fault that has produced a small anticline within the footwall calcmylonite (M). Pencil is 14 cm in length.
b) Synthetic-sense extensional brittle-ductile shear zone cutting across bedding-parallel slip surface (SS) in cleaved shale.
c) Curved low angle fault approaching the PPVT. Reverse drag occurs where the fault branches onto the thrust. The thrust-parallel reduction zone (R) is displaced by the low angle fault. Cleavage in the hanging wall of the fault is steeper in attitude than in the footwall caused by a roll-over onto the curved fault. The note book is 22 cm in length.
d) Complex vein array within fault block bounded by high and low angle faults. The array comprises sheared north dipping veins (type 3 veins) and sub-parallel reverse and extensional shear zones (type 4 and type 5 veins respectively).
e) Roll-over of bedding onto low angle extensional fault. (fault C, figure 4.14b).
f) Bedding-parallel slip surfaces (SS) cutting earlier cleavage-normal extension veins. The veins have been folded by beding-parallel simple shear.
g) Folded type 1 veins in cleaved shale.

(a)

(b)

(c)

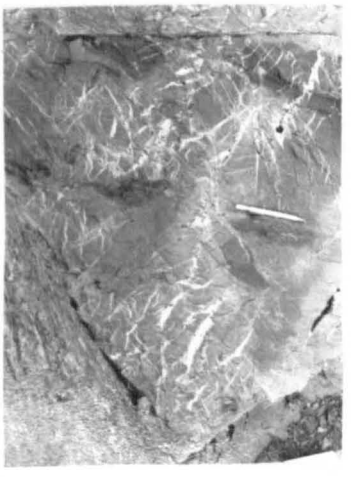

(d)

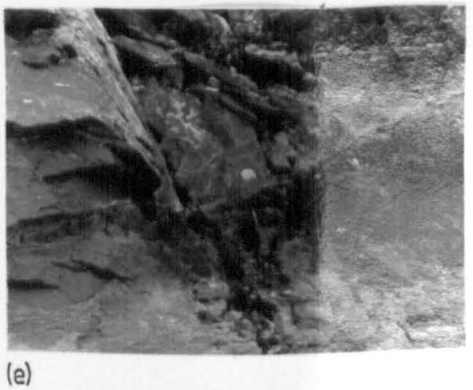

(e)

(f)

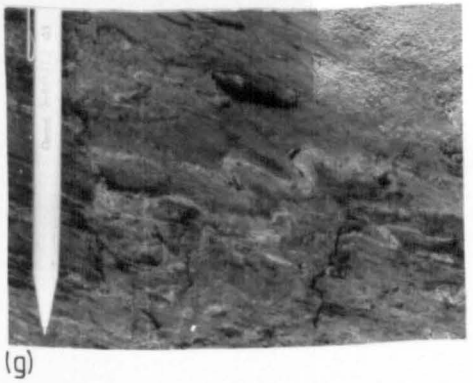

(g)

Figure 4.13 Detailed sketch section through the PPVT sheet (see figure 4.12 for location). The stereograms show cleavage and fault data from the thrust sheet. The thrust dips at 45 degrees into the plane of the paper.

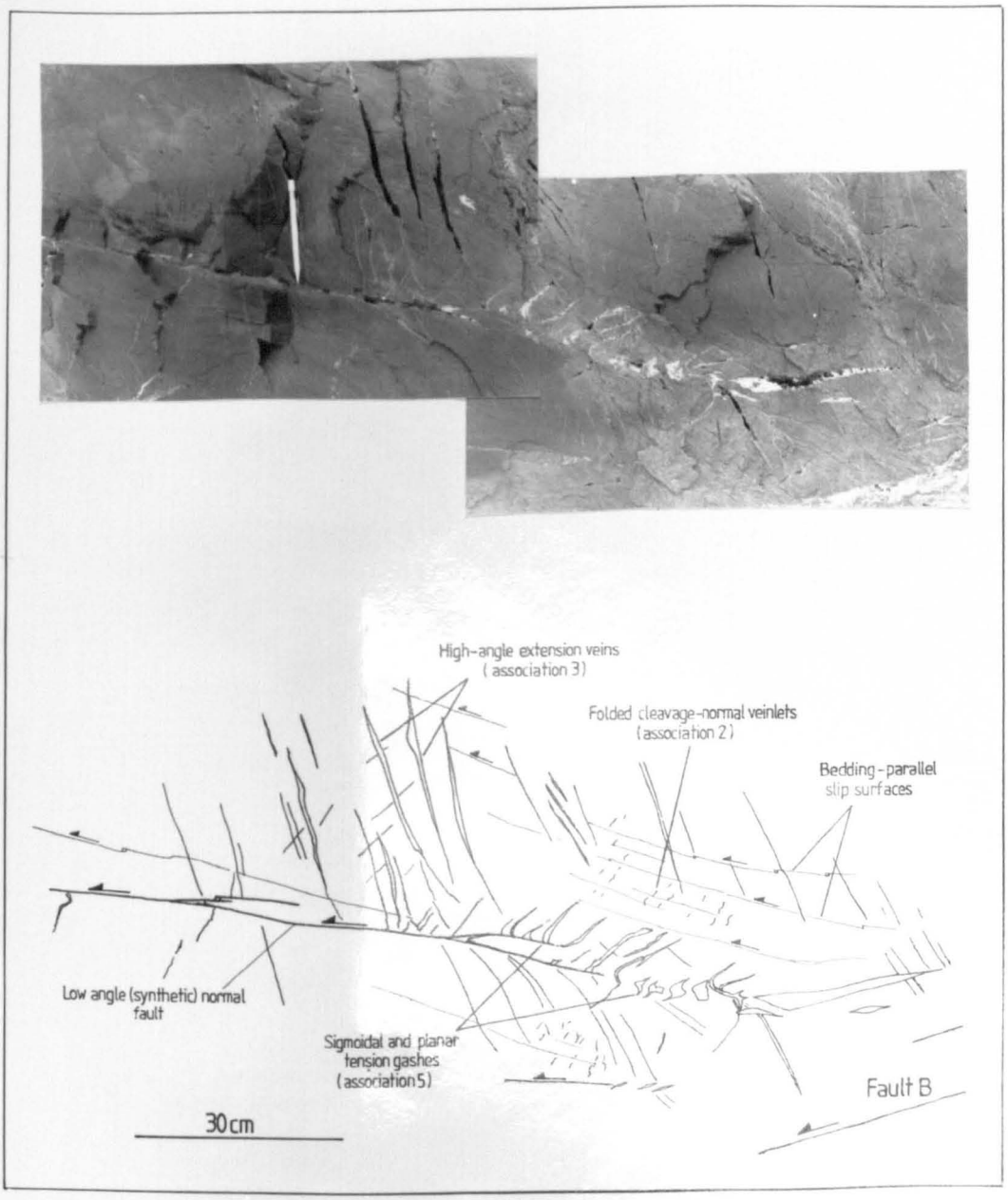

Figure 4.15. Montage of a low angle fault tipping into a brittle-ductile shear zone. The the different vein types in the wall-rocks are indicated in the line drawing. See figure 4.14c for location.

interacted in an attempt to link together. The high angle faults also tip into small shear zones or by splaying.

Apart from the high and low angle fault arrays one other type of slip surface is developed in the PPVT sheet: bedding-subparallel movement planes (surfaces marked SS in figure 4.14c and 4.15). These pre-date both the high and low angle faults and occur generally within siltstone and mudstone beds. They are folded into small isolated asymmetric folds that verge towards the south. Small pull-aparts on the surfaces indicate they moved top-to- south.

4.3.1.1.2 Orientation Analysis.

Structural data for the summit klippe and Soum de Barroude sections are plotted in figures 4.16 and 4.17. Along the summit klippe the PPVT has an orientation 045/15 NW. In the Soum de Barroude section the thrust dips north at approximately 10 degrees. In both portions of the thrust sheet the bedding dips north at a steeper angle than the thrust ie. it dips towards the thrust (figure 4.16a and figure 4.17a). This feature can also be seen in figure 4.7. Cleavage in the summit klippe has a point cluster distribution and possesses a northward dip slightly steeper than the bedding. The mean cleavage bedding angle is of the order of 5-10 degrees. In the Soum de Barroude section the cleavage has a more diffuse distribution that possibly suggests that it was gently folded about a NW-SE axis.

The secondary faults in the two sections have slightly different orientations with respect to the PPVT. In the summit klippe the high angle faults (figure 4.16d and 4.17d) strike approximately 50 degrees clockwise oblique to the thrust whereas they strike parallel with the thrust in the Soum de Barroude section. This difference can be explained largely by the tilting that affected summit klippe during development of the PPV culmination. The low angle faults in both sections are oblique to the thrusts. In the Soum de Barroude section two populations of low angle fault are present whereas only one is present in the summit klippe. The faults have listric geometries in the Soum de Barroude section and this feature can be seen from the orientation analysis (figure 4.17d).

In both sections the high angle faults show NE directed oblique slip (figures 4.14g and 4.15f). A small number of NW directed lineations on the high angle faults in the summit klippe represent a later cross cutting set (see below). The low angle faults in both sections have bimodal lineation patterns (figure 4.16h and 4.17e). In both cases cross-cutting relations between the shear fibres on the faults indicate that the SSE directed movement post-dated the SSW directed movement (summit klippe) and S directed movement (low angle faults in the Soum de Barroude section). The small set of NW directed lineations on the high angle faults appear to have formed during the second episode of movement on the low angle faults. As will be discussed later, this second

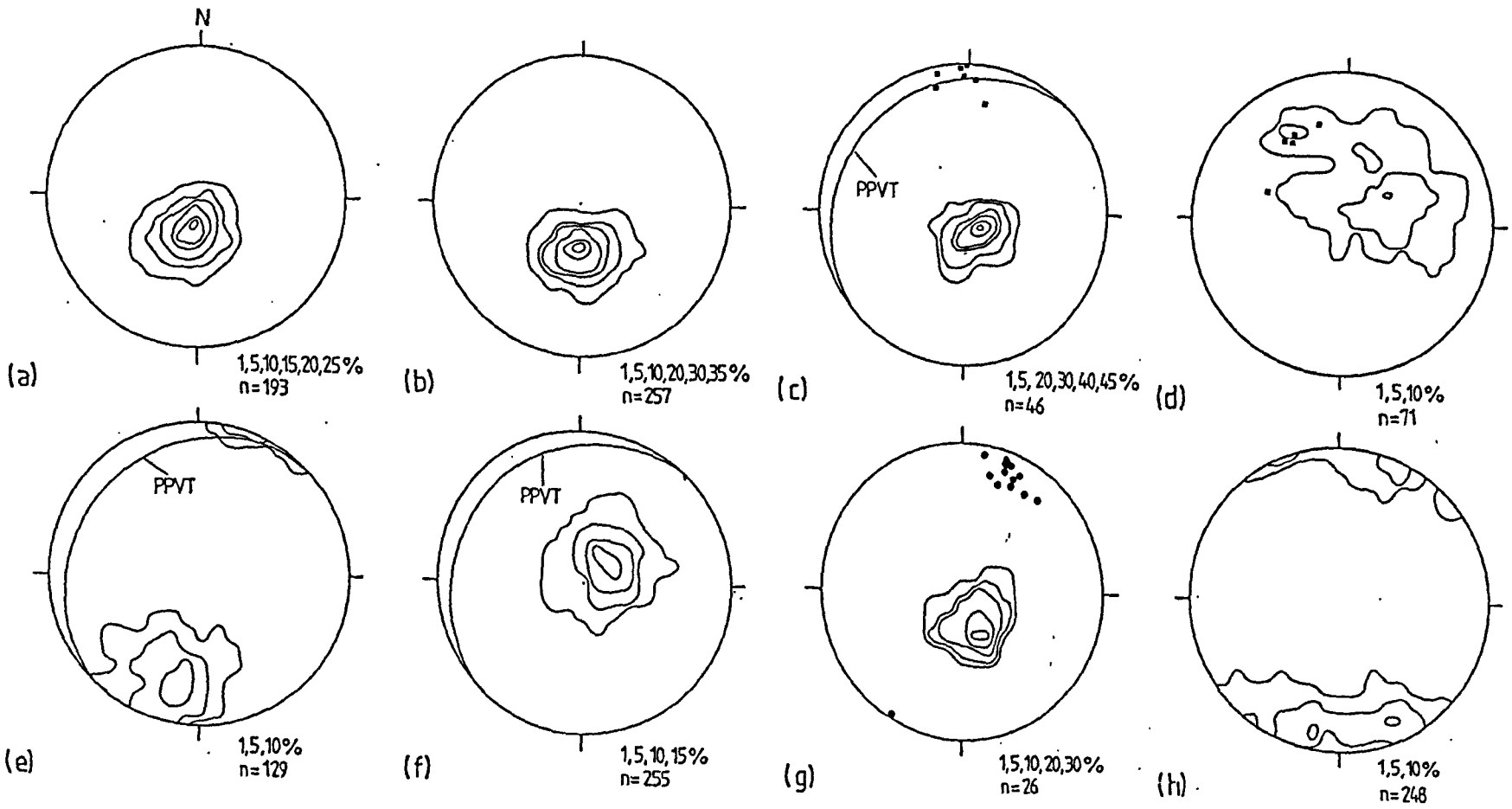

Figure 4.16. Structural data for the summit klippe. a) Poles to bedding; b) poles to cleavage; c) poles to the mylonitic foliation in the Cretaceous limestone. Stretching lineations (squares) and the inferred orientation of the PPVT are also shown. d) Shear fibre lineations on high angle antithetic normal faults. The squares are second lineations developed on five of the faults. e)Poles to high angle faults in the thrust sheet; f) poles to low angle faults in the thrust sheet; g) poles to bedding sub-parallel slip surfaces and shear fibre lineations on the surfaces (circles); h) shear fibre lineations on low angle extensional faults.

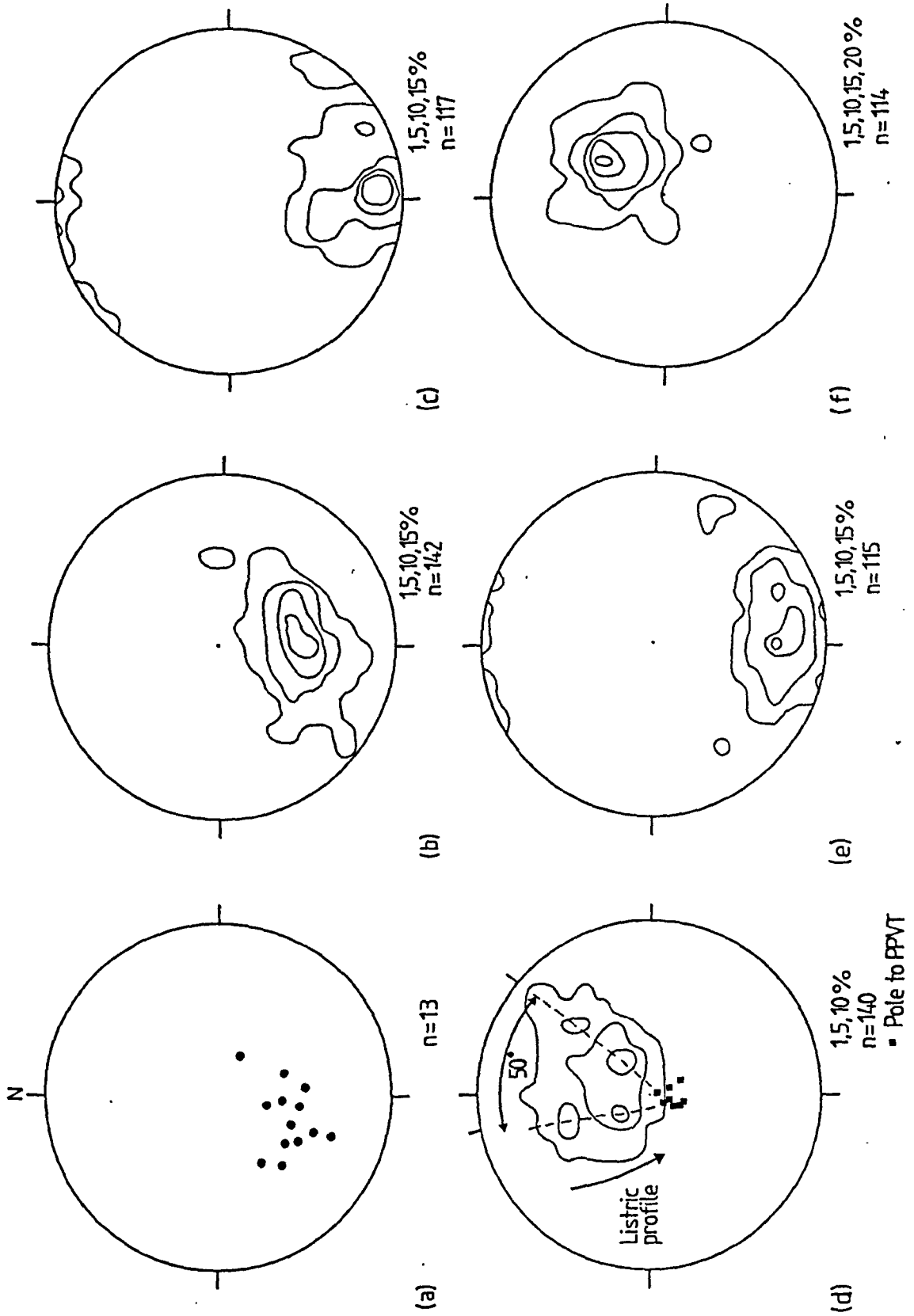

Figure 4.17. Structural data for the Soum de Barroude section of the PPVT sheet. a) Poles to bedding; b) poles to cleavage; c) lineations on low angle extensional faults; d) poles to low angle extensional faults; e) poles to high angle extensional faults; f) shear fibre lineations on high angle normal faults;

movement event on the low angle faults formed during the fourth phase of thrusting in the culmination.

4.3.1.1.3. Displacement distributions on faults.

The low angle faults displace bedding towards the PPVT although the enveloping surface of the bedding maintains an almost constant level above the thrust plane (see figure 4.7). This feature is accomplished by the complementary clockwise rotation of bedding between the low angle faults and accounts for the northward dip of bedding towards the thrust sheet.

The displacements on the low angle faults can be estimated by both offset bedding and offset high angle and occasionally low angle faults. The presence of two phases of movement on many of the faults (recorded by the bimodal lineation distribution) precludes accurate measurement of fault displacements however, because the individual displacements associated with each event are unknown. What is measured can be classified as the apparent total displacement in the plane of the section. This need not however, represent the finite displacement on the fault.

It was not possible to measure displacement profiles along the faults because:
1. Sandstone beds in the Triassic strata (the main marker horizons) are laterally variable and irregularly developed.
2. Correlating offset faults is subjective due to the high density of faults within the array.
In general the large low angle faults possess displacements of between 1 and 5 metres (eg faults A,B and C in figure 4.13). The smaller low angle faults possess displacements much less than 1 metre as do most of the high angle faults.

The displacement on some of the large low angle faults can also be estimated from the offset of the reduction zone along the PPVT. In figure 4.11c the displacement of the reduction zone is approximately 0.95 metres. The displacement on this fault can also estimated from offset bedding outwith the field of the photograph and was found to be 2 metres. The displacement on the fault therefore decreases towards the PPVT suggesting that the fault propagated towards and branched onto the thrust. The high angle faults possess similar displacement distributions and none actually cut or are cut by the PPVT. They also appear to have formed as discontinuities within the thrust sheet.

4.3.1.1.4. The vein record in the thrust sheet.

Apart from the presence of faults and cleavage in the PPVT sheet, the other important deformation product in the summit klippe is sets of veins. Five cross-cutting sets can be recognised:

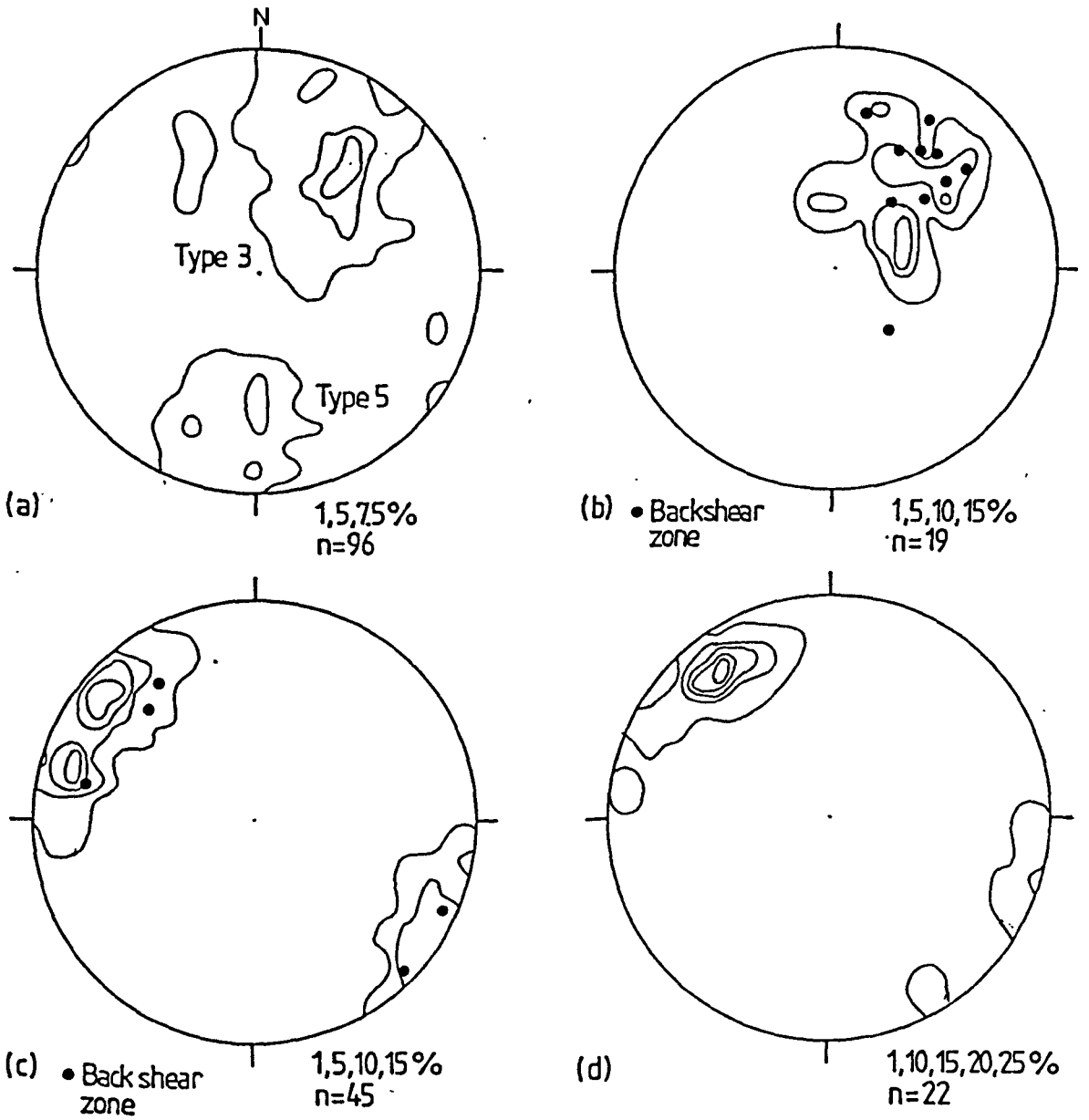

Figure 4.18. Structural data for the different vein sets in the summit klippe. a) Poles to planar extension veins. These represent the s_1 direction at the time of vein formation. Two sets are distinguished: type 3 and type 5 veins (see text). b) Poles to extensional shear zones within fault blocks. The back-shear zones (reverse displacements) are also shown. These possess similar orientations to the extensional zones. c) Fold axes of sigmoidal extension veins within the shear zones. d) Fold axes of type 1 veins and of the bedding sub-parallel slip surfaces.

1. Folded and boudinaged shear veins (figure 4.11g). The folds consistently verge in the direction of thrust transport.
2. Cleavage-normal veins (figure 4.11f). These occur only in the mudstone and siltstone beds and are folded by the simple shear deformation associated with the bedding parallel slip surfaces.
3. High angle north-dipping planar extension veins (figure 4.15). These veins are sheared by the near-field deformation associated with the low angle faults. The orientation of these veins is plotted in figure 4.18a.
4. Sub-horizontal extension veins (figure 4.11d). These occur in en echelon and sigmoidal arrays that record dextral top-to-north shear i.e. they formed in zones of back-shear. These zones cut across some of the high angle faults, but were deformed by others.
5. High angle planar and en echelon sigmoidal tension gashes (figures 4.14c and 4.11b). These cross cut vein associations 1-3 and appear related to movement on the low angle faults. Some type 5 veins are cut by type 4 veins while others post-date the back-shear zones. The en echelon sigmoidal vein arrays represent sinistral brittle-ductile shear zones that formed within the fault blocks. The planar members of this vein set are also plotted in figure 4.18a.

The general sequence of development of the five vein associations appears to have been 1-5 although types 4 and 5 often overlap. There is a progressive increase in the dilation associated with these vein sets and cavities are locally developed in the cores of type 4 and 5 veins.

The Type 4 and 5 shear zones that developed within the fault blocks (figure 4.14c) possess the same orientation and possess similar strikes to the low angle faults but steeper dips (figure 4.18b). The fold axes of the type 5 feather veins (veins that abutt the low angle faults) and shear zone tension gashes all possess similar orientations (figure 4.18c and d). The fold axes of the folded type 1 veins and of folded bedding-parallel slip surfaces are oblique to the normal to the inferred shear direction (the shear fibre lineation on the bedding-parallel slip surfaces). They have therefore been rotated clockwise. The fold axes of the later tension gashes are approximately perpendicular to the first movement vector on the low angle faults and appear unrotated.

4.3.1.2. Deformation in the Ridge Klippe.

4.3.1.2.1. Geometry.

The ridge klippe is arbitrarily defined as the portion of the PPVT sheet that occupies the folded limb of the PPV culmination. A sketch section through the thrust sheet is shown in

figure 4.19. The footwall structures have been omitted for clarity and will be discussed in the section 4.4.2.1.

The main mesostructures developed in the thrust sheet are again arrays of secondary faults. The distribution and intensity of the different fault types is however different from that of the the summit klippe and Soum de Barroude sections. Four types of minor fault are recognised:

1. High angle top-to-north extensional faults;
2. low angle contraction faults (these are labeled BLS in figure 4.19);
3. high angle extension faults; and
4. rotated low angle extensional faults.

The rotated low angle extensional faults are equivalent to the low angle extensional faults present in the two sections described above. They do not however have the same intensity of development and are more common south of the LFS (lower fold structure). The other main differences between the ridge klippe and the other sections are that a set of high angle synthetic normal faults is present (although relatively few in number) and that contractional faults are also present and cut across the other types of fault. Cross-cutting relationships between the extensional fault sets indicate that the high angle antithetic faults were the first to form.

The contraction faults form back-limb splays from the PPVT. These are splays that branch from the crest of a fold in the thrust surface and which therefore moved after the thrust sheet was folded. The significance of these faults will be discussed later.

A peculiar feature of the ridge klippe is its variable thickness. The thrust sheet is more than 10 metres thick above the lower fold structure yet is only 2-3 metres thick on the forelimb of the fold. A similar thickness distribution is evident on the deformed limb of the upper fold structure. Restoration of these structures indicates that the thickness variations predated the folding. One possible explanation is that the sheet was tectonically thinned by displacement on the low angle normal faults prior to the later deformation. Alternatively the variations could reflect the fact that the PPVT cut through strata that had already been heterogeneously deformed (folded or duplicated by thrusts) perhaps during the P1 thrusting. Thick portions of the thrust sheet may represent anticlines, thin portions synclines. The absence of bedding in the thrust sheet prevents elucidation of this problem.

4.3.1.2.2. Orientation Analysis.

Where discernible, bedding dipped NW (figure 4.20a) at a steeper angle than the dip of the thrust. This is similar to the bedding distribution in the other sections. Figure 4.21 is a

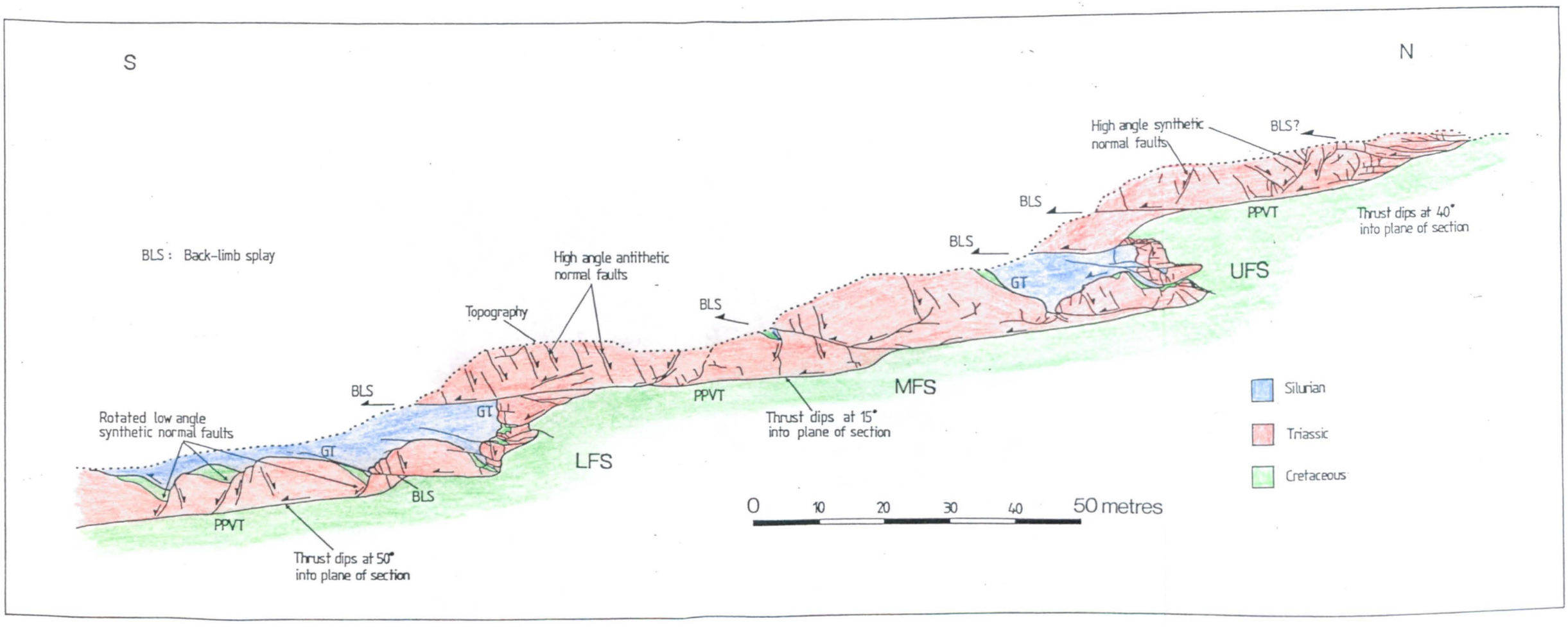

Figure 4.19. Sketch section through the Ridge klippe of the PPVT sheet. LFS: lower fold structure, MFS: middle fold structure; UFS: upper fold structure. Four types of mesoscopic fault are present in the thrust sheet: high angle antithetic normal faults, rotated low angle normal faults, high angle synthetic normal faults,.and contractional faults. The latter are labelled BLS which stands for **Back-limb splays**. These splays have formed by movement on the PPVT after it was folded and they post-date the other types of fault.

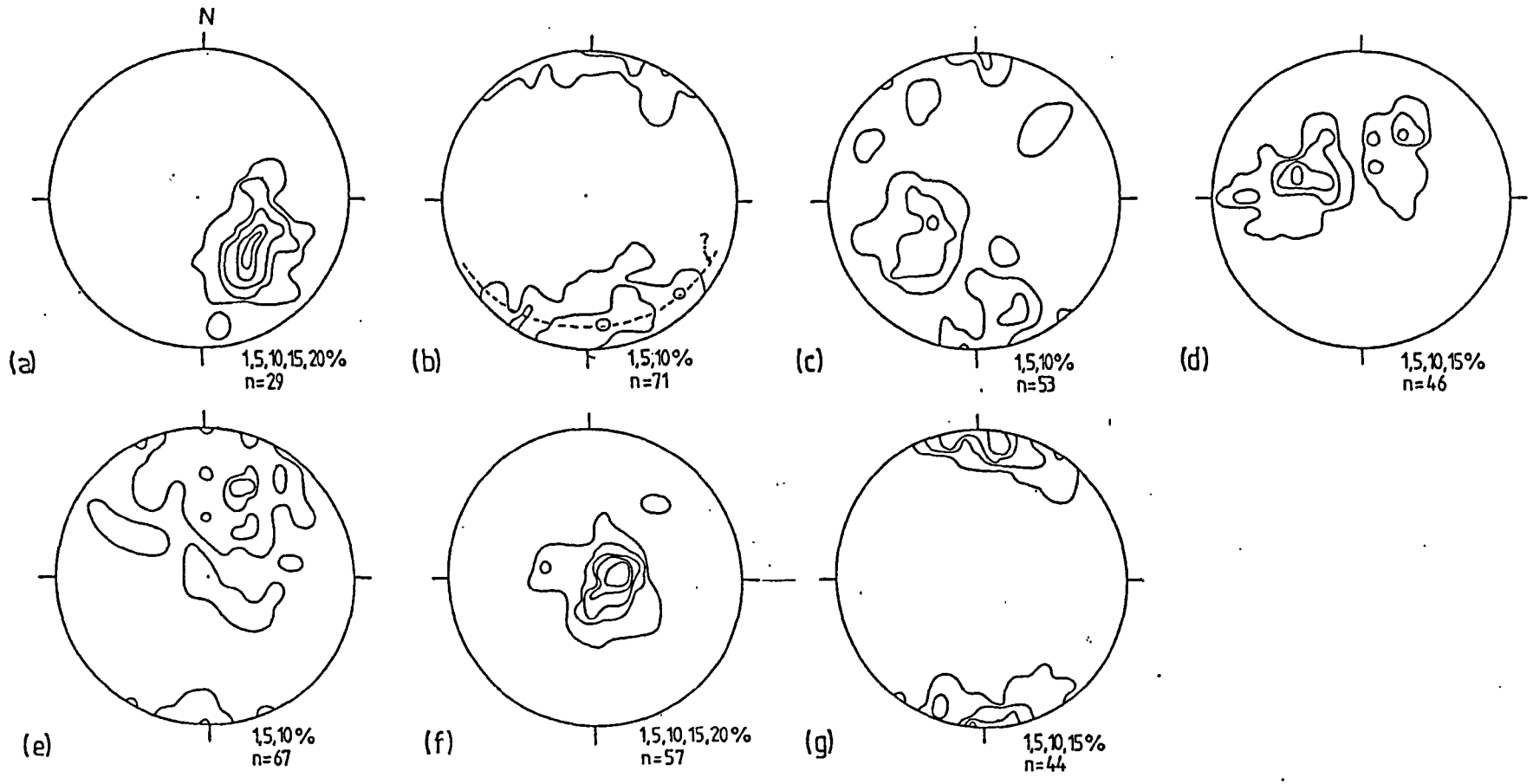

Figure 4.20. Structural data for the the ridge klippe. a) Poles to bedding; b) poles to high angle faults. These appear to lie on a partial great circle (dotted) and suggests that they have been folded; c) poles to high angle synthetic normal faults; d) Lineations on high angle antithetic normal faults. Two populations occur but not on the same faults. The faults with NE directed movements are probably conjugate to the high angle synthetic normal faults. The faults that moved NW are probably rotated earlier faults. e) Shear fibre lineations on high angle synthetic normal faults; f) poles to back-limb splays. g) shear fibre lineations on *back-limb splays.*

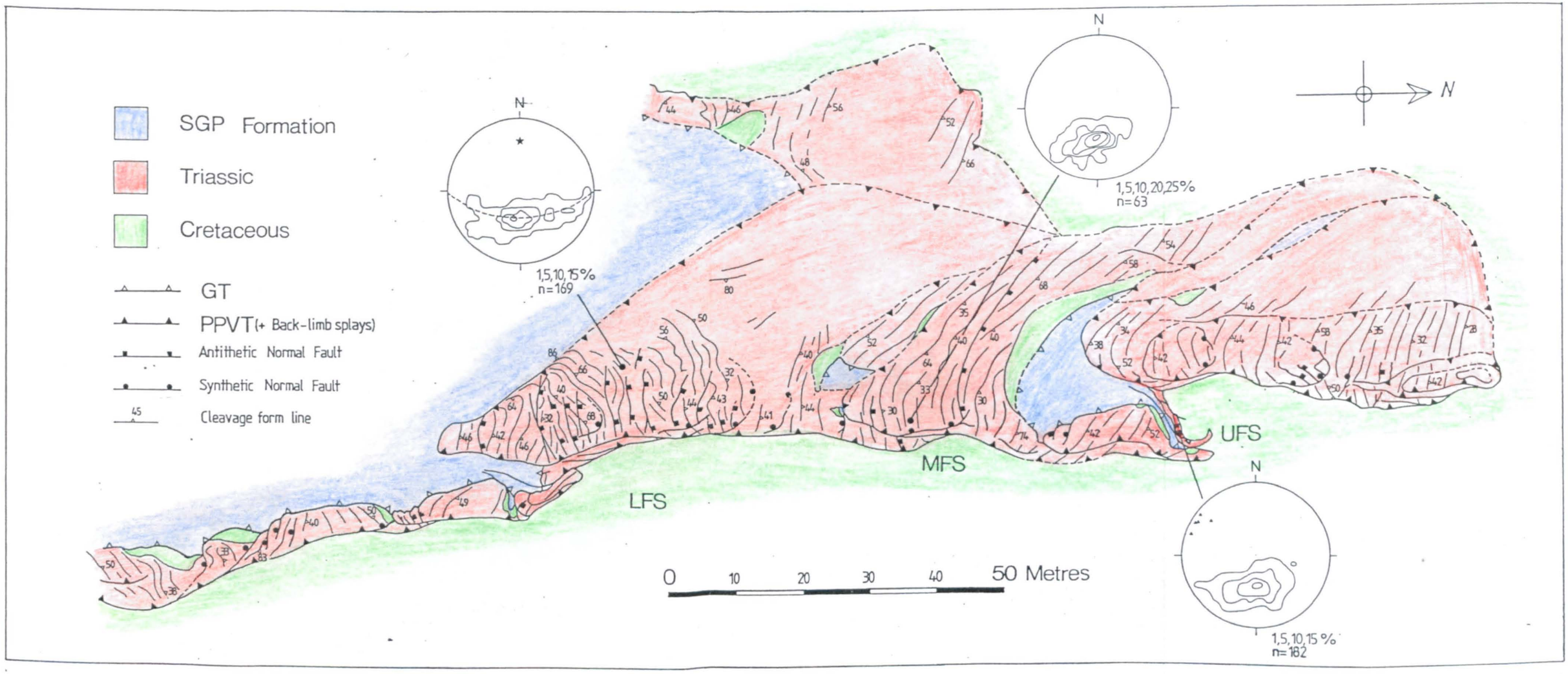

Figure 4.21 Cleavage form-line map for the ridge klippe. The cleavage has a general arcuate distribution except above the lower fold structure (LFS) where it is folded into N-plunging folds. The stereograms show poles to cleavage in hanging wall of the thrust above the lower, middle and upper fold structures.

cleavage form-line map of the ridge klippe. It shows that the cleavage is folded into a set of close symmetrical north plunging folds above the LFS and into a syncline above the upper fold structures (UFS). In between these structures the cleavage is less intensely deformed and possesses an arcuate distribution that approximately parallels the orientation of the cleavage in the footwall limestone (see section 4.4.2). In the northern part of the klippe, the cleavage fans back towards east-west and this is again similar to the fanning of cleavage in the footwall limestone (compare with figure 4.42).

In thin section the cleavage in the ridge klippe is more complex than is at first apparent on the mesoscale. Crenulation cleavages are developed on the overturned limbs of the fold structures while the main fabric in the sheet is a spaced pressure solution cleavage that appears to overprint an original more pervasive cleavage. The significance of these cleavages with regard to the structural sequence that has affected the ridge klippe is discussed in chapter 5.

The high angle antithetic normal faults possess a wide range of orientations (figure 4.20b) and possibly lie on a girdle reflecting folding about a steeply plunging N-S axis. This agrees with the folding of the cleavage in the thrust sheet. The lineations on these faults possess a bimodal distribution (figure 4.20d): a north east directed population and a west or west-north west directed population. Both record oblique-slip on the faults. The two lineations never occurred together on one fault: they represent distinct movement directions on different faults. Figure 4.22 is a histogram of measured fault strikes in which the faults have been separated into those having a component of easterly directed slip and those with a component of westerly directed slip. The graph shows that the sense of oblique-slip movement was not controlled by the orientation of the fault and therefore suggests that folding of the faults was not responsible for the lineation distribution.

The rare high angle synthetic normal faults occur north of the LFS as either isolated faults within the thrust sheet or as faults that branch onto the thrust (figure 4.19). Most of the faults moved WSW (figure 4.20e) and are probably conjugates to the high angle antithetic faults that moved NE.

4.3.2. Deformation in the Gavarnie Thrust sheet along the Soum de Barroude section.

Figure 4.23 shows the style of deformation that has affected the Silurian phyllite in the hanging wall of the PPVT sheet. It is also deformed by a complex array of contractional faults and conjugate normal faults. The pattern is similar to that developed in the PPVT sheet except for the presence of the contractional faults. These faults branch from a planar discontinuity that parallels the upper surface of the PPVT sheet and which cuts across the extensional faults within the sheet. Locally the contractional faults both

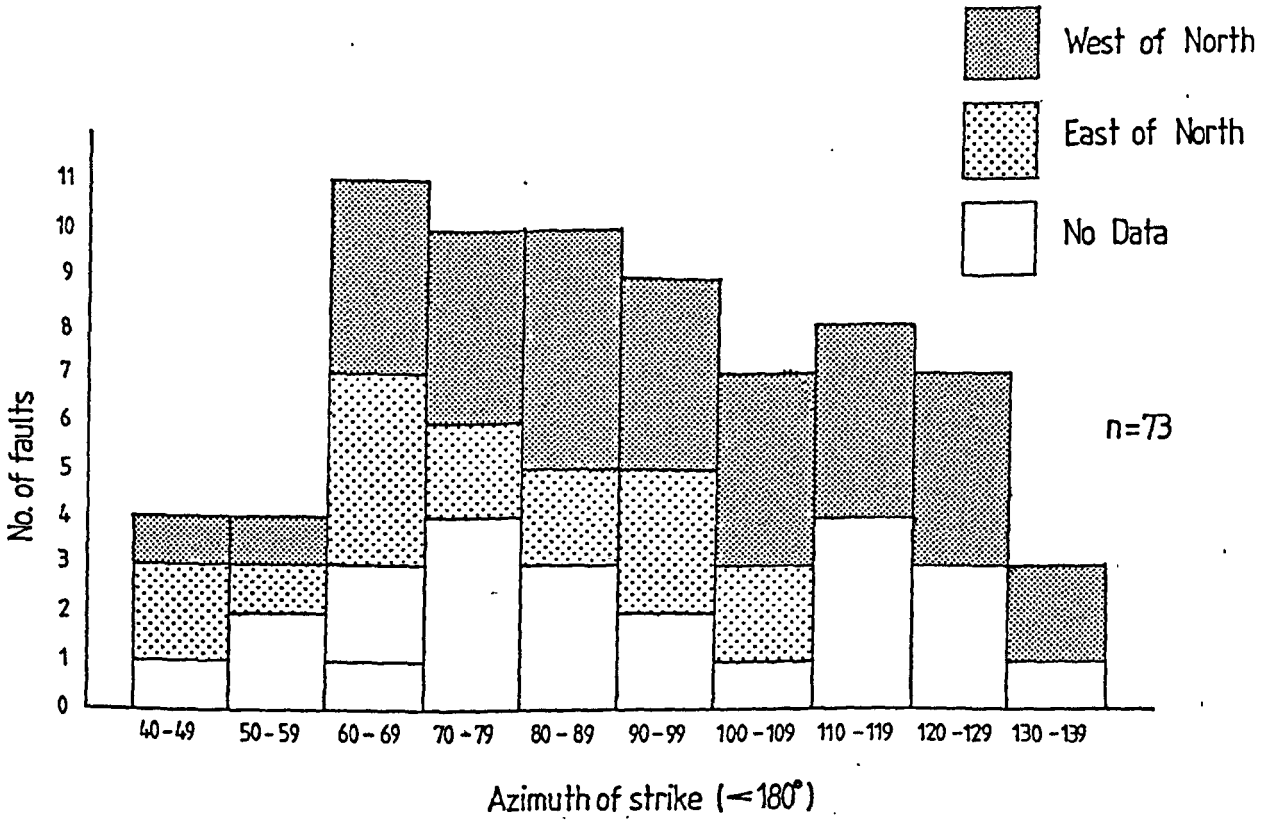

Figure 4.22 Histogram of strikes of high angle antithetic faults in ridge klippe. The faults are differentiated in terms of having moved obliquely west of north or east of north. The histogram shows that there is no apparent relationship between fault orientation and movement direction.

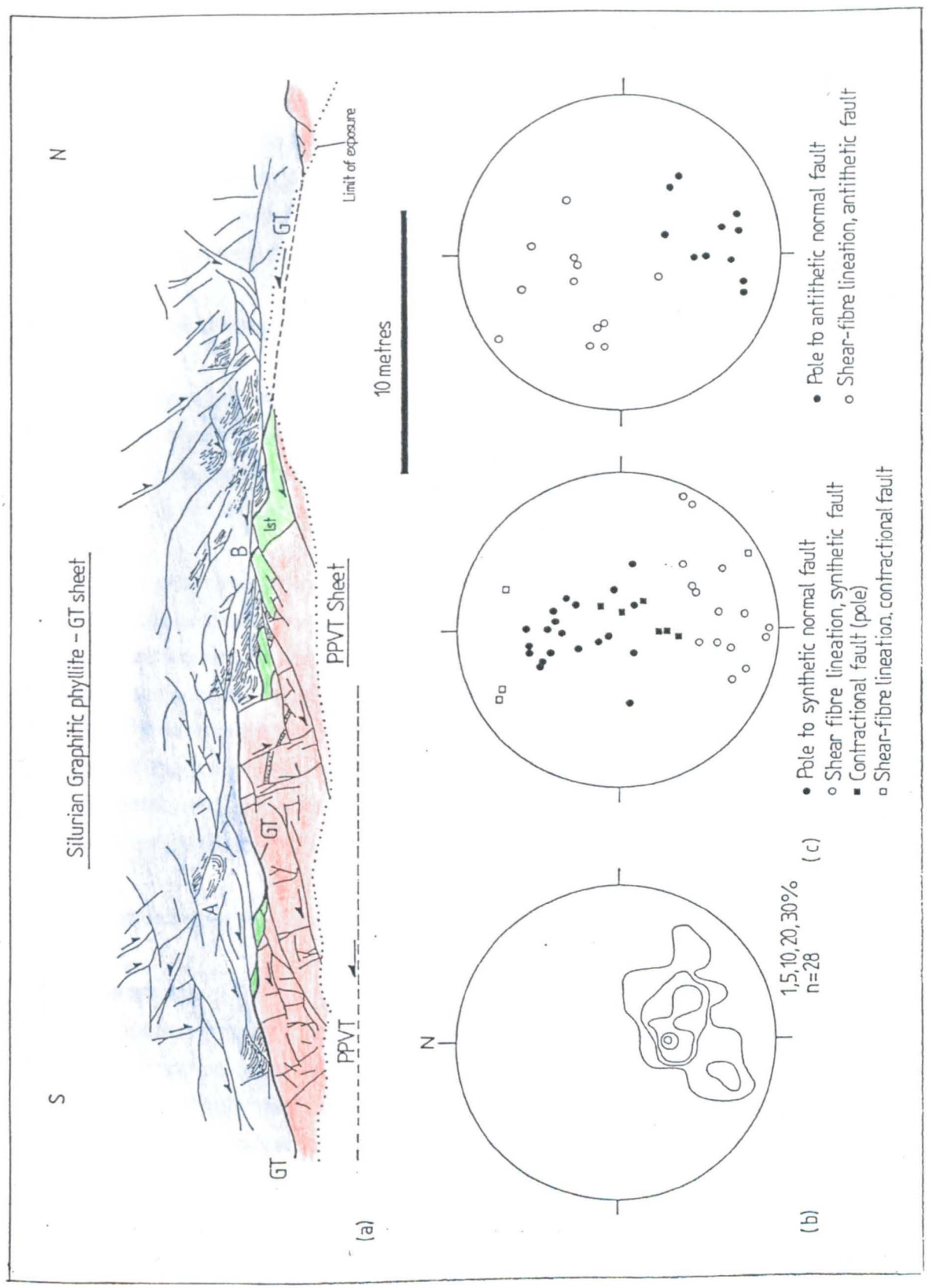

Figure 4.23. a) Sketch section of the deformation in the Silurian phyllite of the Gavarnie Thrust sheet along part of the Soum de Barroude section. b) and c): Structural plots of data from the phyllite; b) shows poles to cleavage, c) shows fault orientations and shear fibre lineations.

truncate and are truncated by the synthetic normal faults (eg. at A and B in figure 4.23) suggesting overall contemporaniety of formation.

The stereograms show that the faults in the phyllite are mainly dip-slip and possess similar orientations to the faults in the underlying PPVT sheet. The only difference in the faults is that the high angle faults in the exposure sketched show a component of NW slip whereas the equivalent faults in the PPVT sheet moved towards the NE. The significance of this feature is not known.

4.4. Phase Three Thrusts.

The phase three thrusts are classified as faults that folded the PPVT during their propagation and movement. In this sense all the faults that formed within the PPV culmination are considered P3 structures. They record a switch in the locus of deformation to the basement and Mesozoic cover in the footwall of the PPVT.

The main P3 structure is the basement imbricate stack. Above this structure the Triassic and Cretaceous strata are deformed by folds and discontinuous thrusts. These latter structures are responsible for the three main fold structures that deformed the PPVT (see figure 4.3b for location). It will be shown in this section that although not physically linked, the thrusts that formed within the Triassic and Cretaceous strata above the BIS are products of the same deformation and represent discontinuities that formed within a zone of distributed strain produced by the dramatic loss of displacement on the basement thrusts where they intersected the Triassic strata.

4.4.1. The structure of the Basement Imbricate stack and Basal Triassic Fault Zone.

4.4.1.1. Geometry.

A sketch section through the basement imbricate stack is shown in figure 4.24 The structure comprises a set of imbricate thrusts that appear to branch from a sub-horizontal discontinuity that outcrops at 2600 metres on the east face of the mountain (see figure 4.2). The basement strata comprises migmatised psammites cut by small granite and granodiorite intrusions. The main Hercynian fabric in this strata dips NE at between 50 and 60 degrees. It is difficult to trace the steeply dipping imbricate splays through this strata and the traces of the thrusts shown in figure 4.3b have had to be extrapolated away from where they cut the Triassic unconformity.

The complete structure appears to be composed of 6 imbricate splays (5 of which are shown in figure 4.25). The overall dimensions of the BIS are: length 250 metres and height 60 metres. The splays ramp steeply across the basal Triassic conglomerate and appear to flatten into the overlying mudstones (figure 4.24). The floor fault of the BIS is

breached by the thrust labeled 6 in figure 4.24. Whether the displacement on this fault links back onto the floor fault further north is difficult to tell due to the inacessibility of much of the structure.

Apart from the imbricate splays a set of secondary faults is also developed in the basement strata above the floor thrust of the BIS. These faults are restricted in developed to an irregular- shaped granodiorite intrusion and occur predominantly in a zone paralleling the Triassic unconformity. This zone appears to have been breached by fault 6 and also by the floor fault. The structure of this fault array and the nature of the faults will be described in more detail later.

Where the floor fault of the BIS ramps into the Triassic strata it splits into an anastomosing fault zone above the main basal conglomerate unit (figure 4.24). This fault zone will be referred to as the Basal Triassic Fault Zone (BTFZ). It comprises two closely spaced subparallel bounding thrusts, one along the upper surface of the basal conglomerate bed the other located 1 to 2 metres above this surface. These faults are linked by secondary faults that either splay upwards from the floor thrust (contractional faults) or downwards from the roof thrust (extensional faults).

4.4.1.2. Displacement distribution.

The displacement on the thrusts in the BIS is constrained largely from the offset of the Triassic unconformity. The measured or estimated displacements are shown in figure 4.24 The direction of these displacements is mainly towards the south (see figure 4.25d). No second movement direction was observed on any of the thrusts. The cumulative displacement on the linked splays (ie. excluding fault 6) is between 40 and 45 metres. The displacement in the BTFZ can be independently constrained by the offset of two pre-Cretaceous normal faults that are cut by the thrusts. The lower bounding thrust has a displacement of 2 metres, the upper of approximately 4 metres and it is apparent that displacement is not conserved across the structure. Mapping of the cliff face using binoculars has failed to trace the splays upwards to link with the thrusts developed in the Triassic adjacent to the Cretaceous unconformity. These structurally higher thrusts all appear to possess trailing tips. It appears therefore that the basement splays lose their displacement within the Triassic strata. Accordingly, the structure cannot be a duplex but is a leading imbricate stack (Boyer and Elliott, 1982).

4.4.1.3. Cleavage distribution in the Triassic strata of the BTFZ.

The Triassic mudstones possess a strong slaty cleavage that passes downwards into a spaced anastomosing coarse fabric in the matrix of the basal conglomerate. The fabric in the conglomerate detaches against a thrust along the plane of the

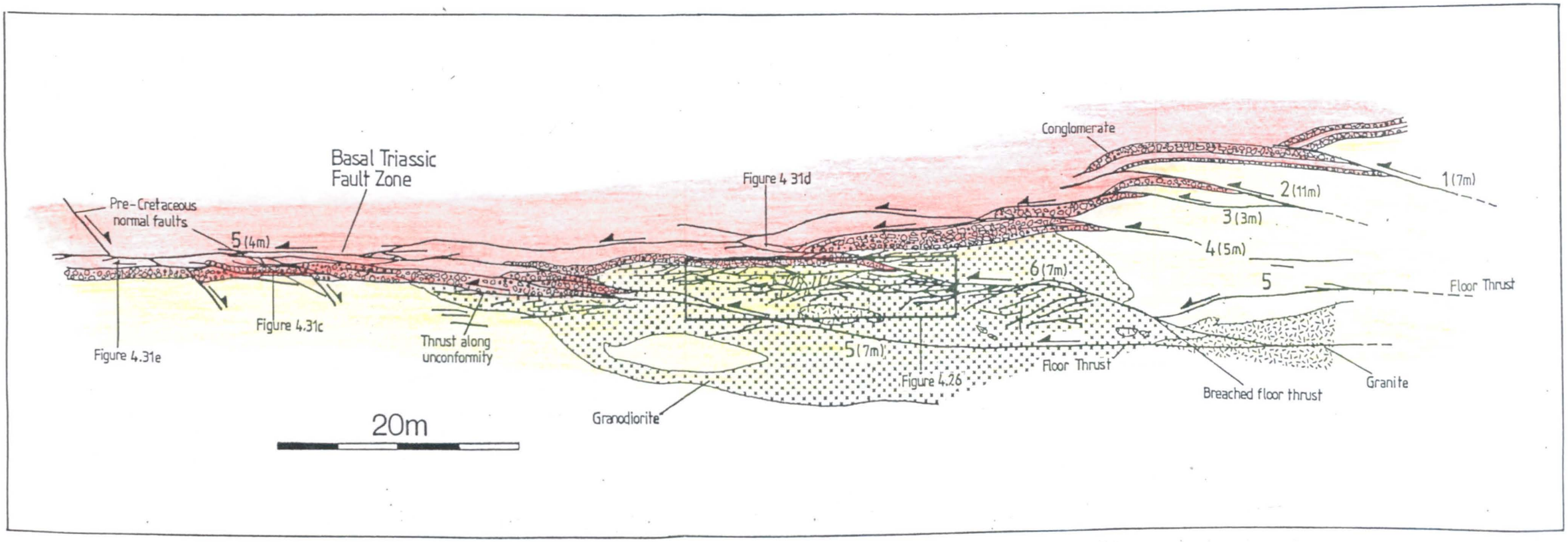

Figure 4.24. Cross section through Basement Imbricate Stack and Basal Triassic Fault Zone (BTFZ) showing location of structures described in text and displacements on thrusts.

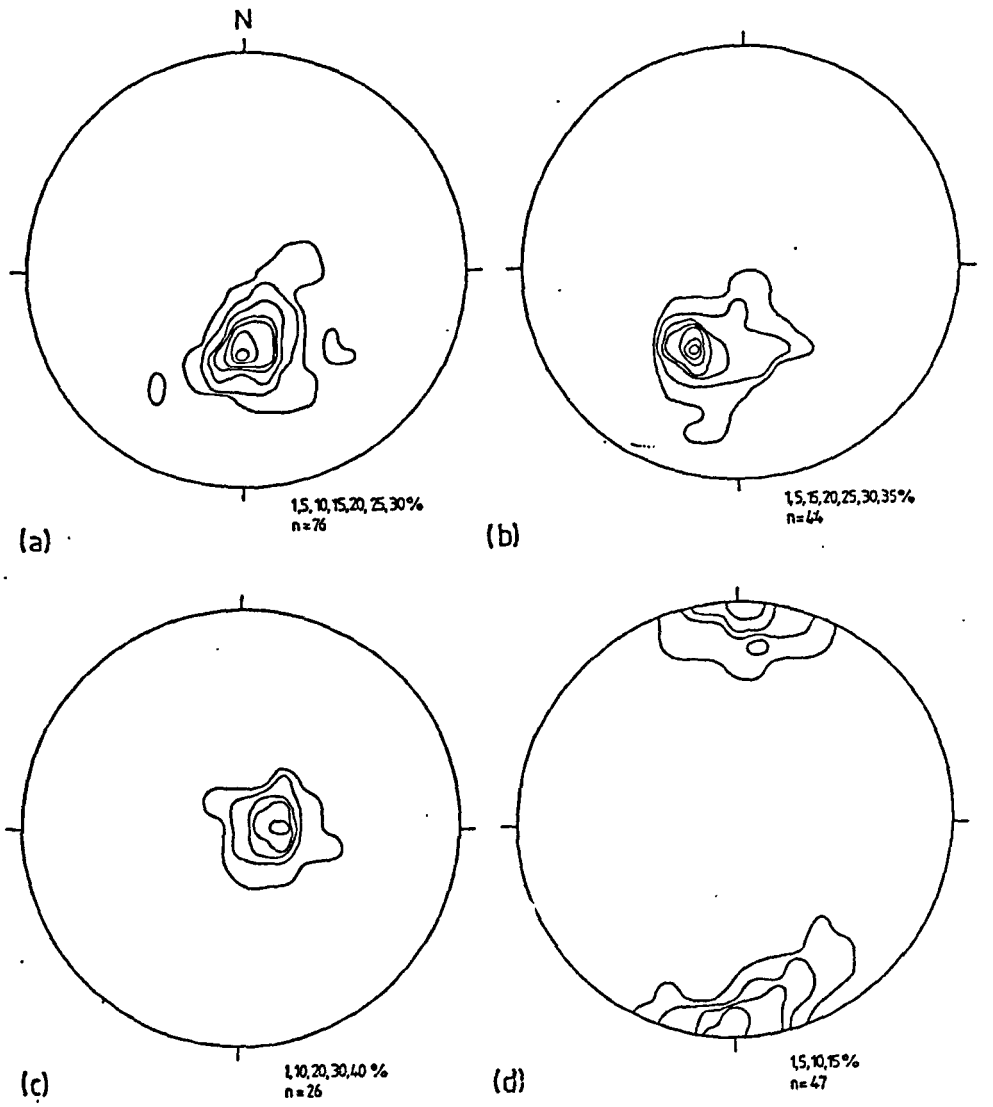

Figure 4.25. Structural data from the Basal Triassic Fault Zone (BTFZ). a) Poles to cleavage in Triassic strata within the BTFZ; b) poles to cleavage in the hanging wall of the BTFZ; c) poles to the main thrusts in the BTFZ; d) shear fibre lineations on main thrusts. The cleavage in the hanging wall is rotated clockwise and has a steeper dip than the cleavage within the fault zone itself.

unconformity (see figure 4.31c). The cleavage is deformed by the thrusts and no pre-cleavage thrusts occur in the BTFZ.

The cleavage within the BTFZ and directly in the hanging wall of the BTFZ is plotted in figures 4.25a and 4.25b respectively. It is apparent that the fabric in the fault zone has a different orientation from that in the hanging wall: the strike of the cleavage in the hangingwall appears to be rotated by approximately 26 degrees and has a 5 degree increase in dip.

4.4.1.4. Secondary Fault Arrays in the BIS and BTFZ.

As already mentioned, secondary faults occur both within the basement strata in the BIS and within the Triassic mudstones of the BTFZ. These faults all have the same characteristics and are quartz-chlorite shear-fibre coated slip surfaces. Some of the surfaces are also coated with hematite fibres.

4.4.1.4.1. The Basement Granodiorite Fault Array.

A detailed sketch section through part of the array is shown in figure 4.26. The location of this section is marked on figure 4.24. The fault array is a complex network comprising two principal types of fault:

1. Low angle faults. These possess top-to-south displacements and three orientations of fault can be distinguished: faults that are subparallel to the overlying Triassic unconformity, faults that dip shallowly south and faults that dip shallowly north. The latter two types appear to form splays from the former. The overall pattern of low angle faults appears therefore to comprise faults with the Y, R1 and P orientations (see figure 4.27 for terminology).
2. High angle faults. These all possess top-to-north senses of displacement and comprise faults whose traces dip steeply north and steeply south in the plane of the section. The latter have R2 orientations. The former are possibly rotated R2 faults or unrotated X shears (figure 4.27).

The distribution of these three fault types changes across the section and there appears, in particular, to be a concentration of the high angle faults in the centre of the section whereas the low angle faults are better developed away from this area.

A weak rough cleavage is developed within the granodiorite where it is cut by the secondary faults (figure 4.28d). Shear sense criteria on the faults include:

1. The deflection of the cleavage adjacent to the faults.
2. Stepped layers of shear fibres on fault surfaces and rhombohedral pull-aparts (figure 4.28a). These pull-aparts appear to be responsible for producing the fibre steps.
3. Offsets of leucocratic veins within the granodiorite (figure 4.28c).

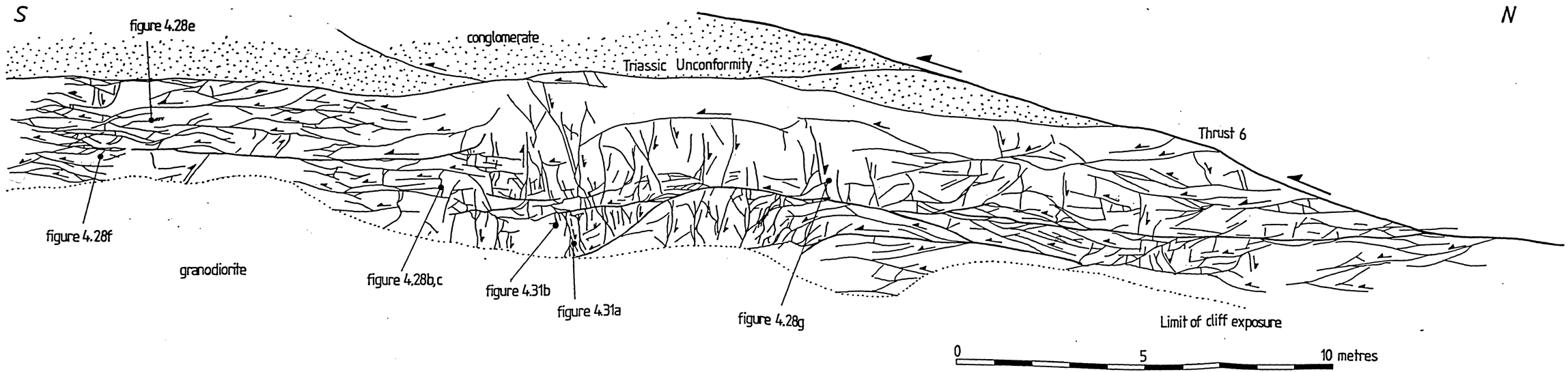

Figure 4.26 Basement Granodiorite fault array

Figure 4.26. Detailed sketch section across complex fault array within a basement granodiorite intrusion directly beneath the Triassic unconformity (see figure 4.24 for location). The array is cut by the out-of-sequence thrust, fault 6 (see figure 4.24). This thrust may have tried to use the earlier minor faults to propagate parallel to the unconformity before it cut across the unconformity. A less intense fault array is present in the hanging wall of fault 6. The sense of displacement on a number of the faults is shown. The low angle faults show top-to-south displacements; all the high angle faults have top-to-north displacements.

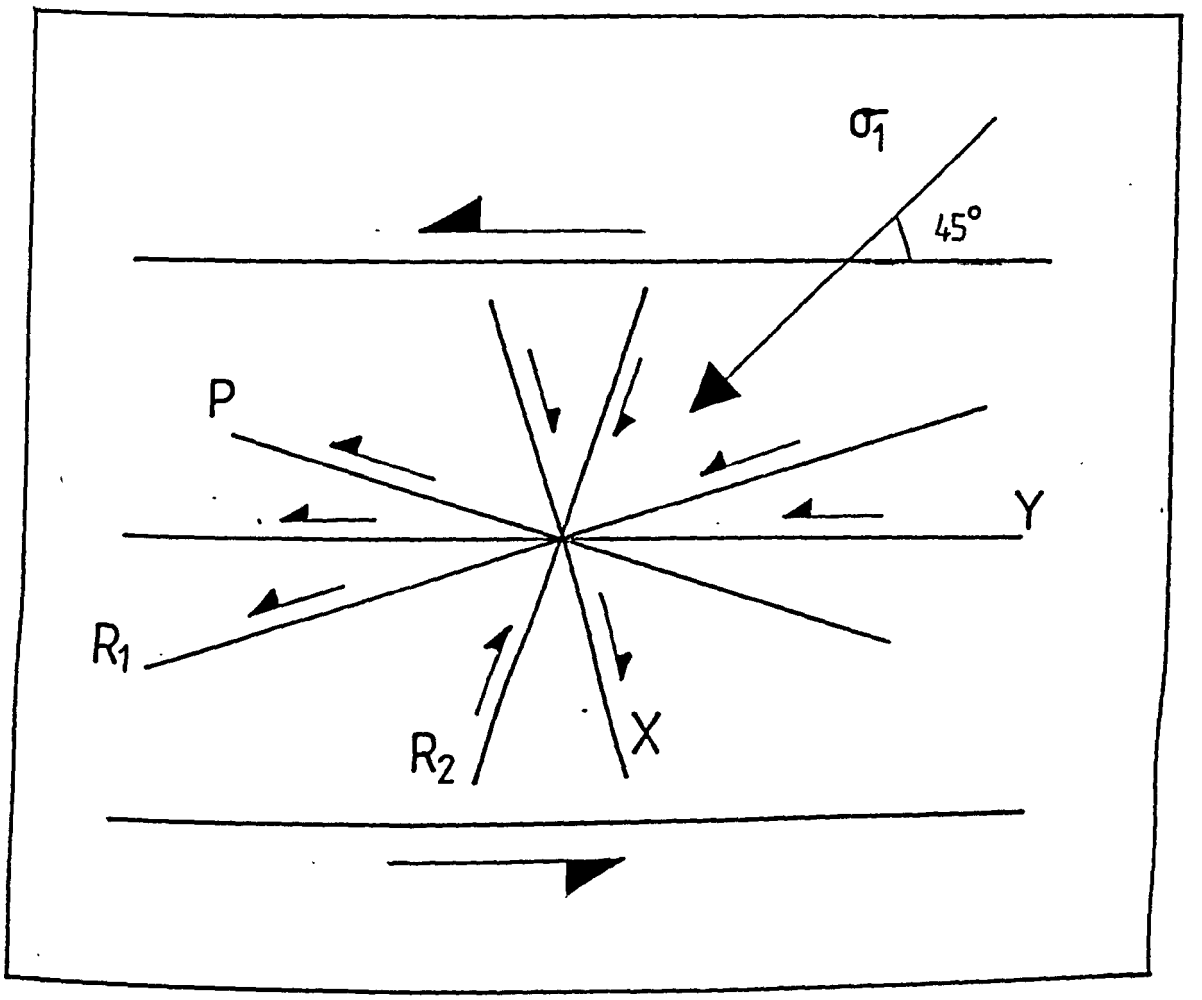

Figure 4.27. Orientations of secondary faults in shear zones.

Figure 4.28. Photographs of minor fault structures in the granodiorite fault array of the basal Triassic fault zone. All photographs looking west.
a) Rhombohedral pull-apart along a low angle fault. The fibres in the pull-apart contain chlorite crack-seal inclusion bands.
b) High angle fault folded but not cross cut by two low angle faults.
c) Conjugate faults off-setting a leucocratic vein within the granodiorite.
d) Conjugate faults linking together. The cleavage in the granodiorite bisects the obtuse angle between the faults. This fault geometry indicates simultaneous propagation and interaction of the faults.
e) Low angle fault tipping into a brittle-ductile shear zone.
f) Curved low angle fault terminating in a zone of extension (feather) veins.
g) Low angle fault terminating by splaying.

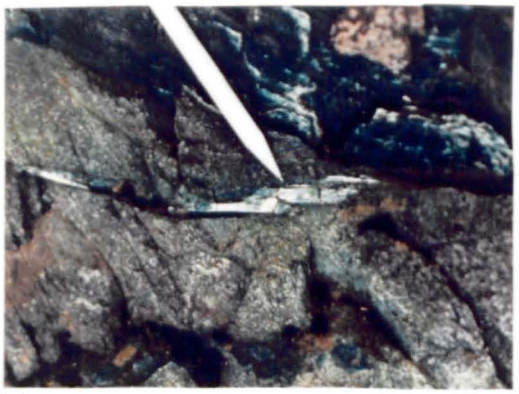

(a)

(b)

(c)

(d)

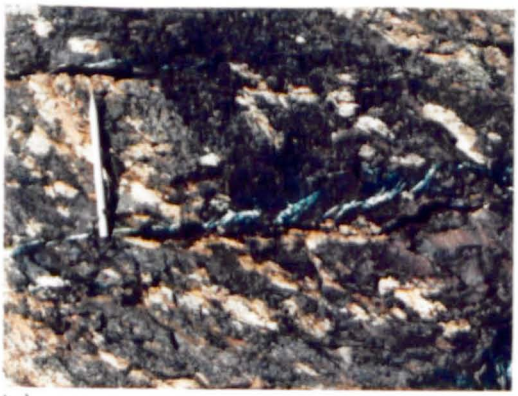

(e)

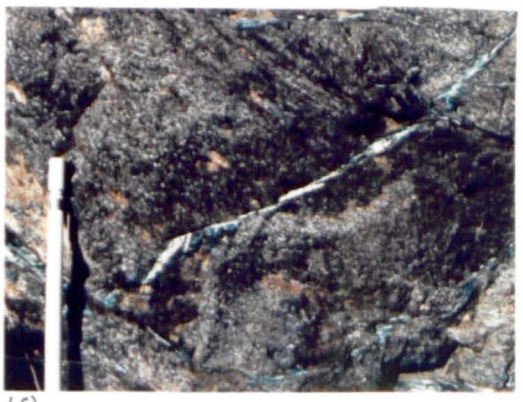

(f)

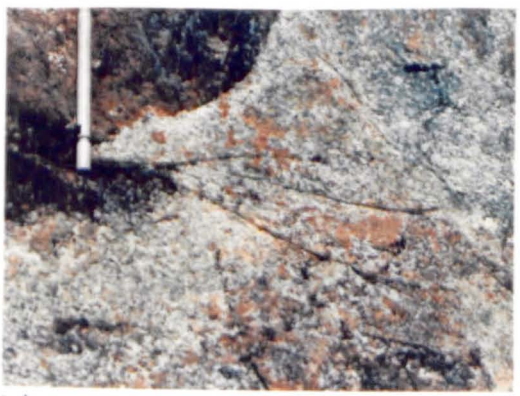

(g)

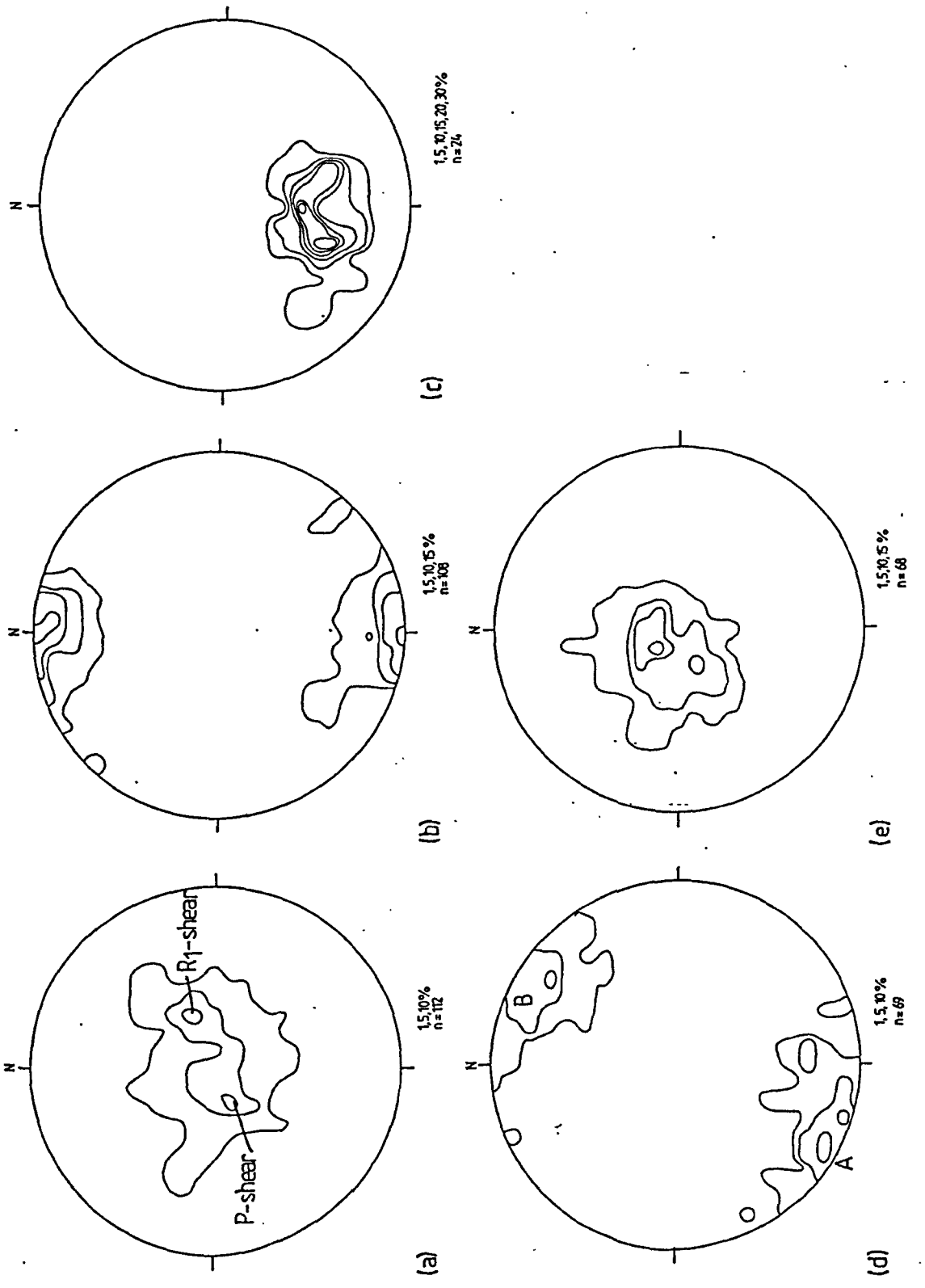

Figure 4.29. Structural data for the granodiorite fault array. a) Poles to low angle faults. Two main populations are present and are interpreted as R1 shears (A) and P shears (B). b) Shear fibre lineations on low angle faults; c) cleavage in granodiorite; d) poles to high angle faults. Two populations are present: a NE dipping set and a SW dipping set. The former are interpreted as R2 riedel shears, the latter as rotated R2 shears. e) Shear fibre lineations on the high angle faults. The two populations reflect the rotated and unrotated R2 riedel shears.

a) Orientation analysis.

Structural data for the fault array is plotted in figure 4.29. The high angle faults are, on average, sub-vertical and trend WNW (figure 4.29d). They dip steeply both NE and SW the former being contractional, the latter extensional in geometry. Shear fibre lineations on the faults have a bimodal distribution (figure 4.29e) with both NE and NW directed displacements. The NE directed displacements occur mainly on the faults possessing contractional orientations whereas the NW directed displacements occur on the faults possessing extensional orientations. The faults are mainly dip-slip.

The low angle faults possess a wider range of orientations than the high angle faults reflecting the three different types of fault recognised. Two maxima are present (figure 4.29a: a NE dipping set and a steeper SW dipping set. These reflect the P and R1 orientations which are prevalent in the overall array. Shear fibre lineations on these faults record predominantly southward displacement (figure 4.29b). The cleavage in the granodiorite dips NNW between 30 and 45 degrees. It bisects the the obtuse dihedral angle between the high and low angle faults (eg figure 4.28d).

b) Displacements on the faults.

The magnitude of displacement on the faults is generally difficult to measure due to the absence of markers in the granodiorite. Occasional vein offsets (eg figure 4.28c), the length of rhombohedral pull-aparts, and the offset of cross-cut faults can used to estimate displacement magnitudes. The displacement on the larger low angle faults is of the order of 0.1-0.5 metres. The high angle faults possess smaller offsets generally between 1 and 10 cm. This displacement distribution probably indicates that the low angle faults remained active longer than the high angle faults.

c) Patterns of Fault Interaction and Fault Tip Structures.

Fault interaction in the array is most clearly seen near the terminations of the small faults. In general the larger low angle faults appear to truncate the high angle faults and their mutual interaction is often more difficult to demonstrate. Two main types of interaction are observed in the fault array (figure 4.30):

1. **Truncation** (figure 4.30a). This pattern reflects the cutting of an early fault by a later fault without interference. It characterises the relationship between the larger low angle faults and the high angle faults.

2. **Fault Linking**. Five types of linking have been observed in the fault array and are shown in figure 4.30b.

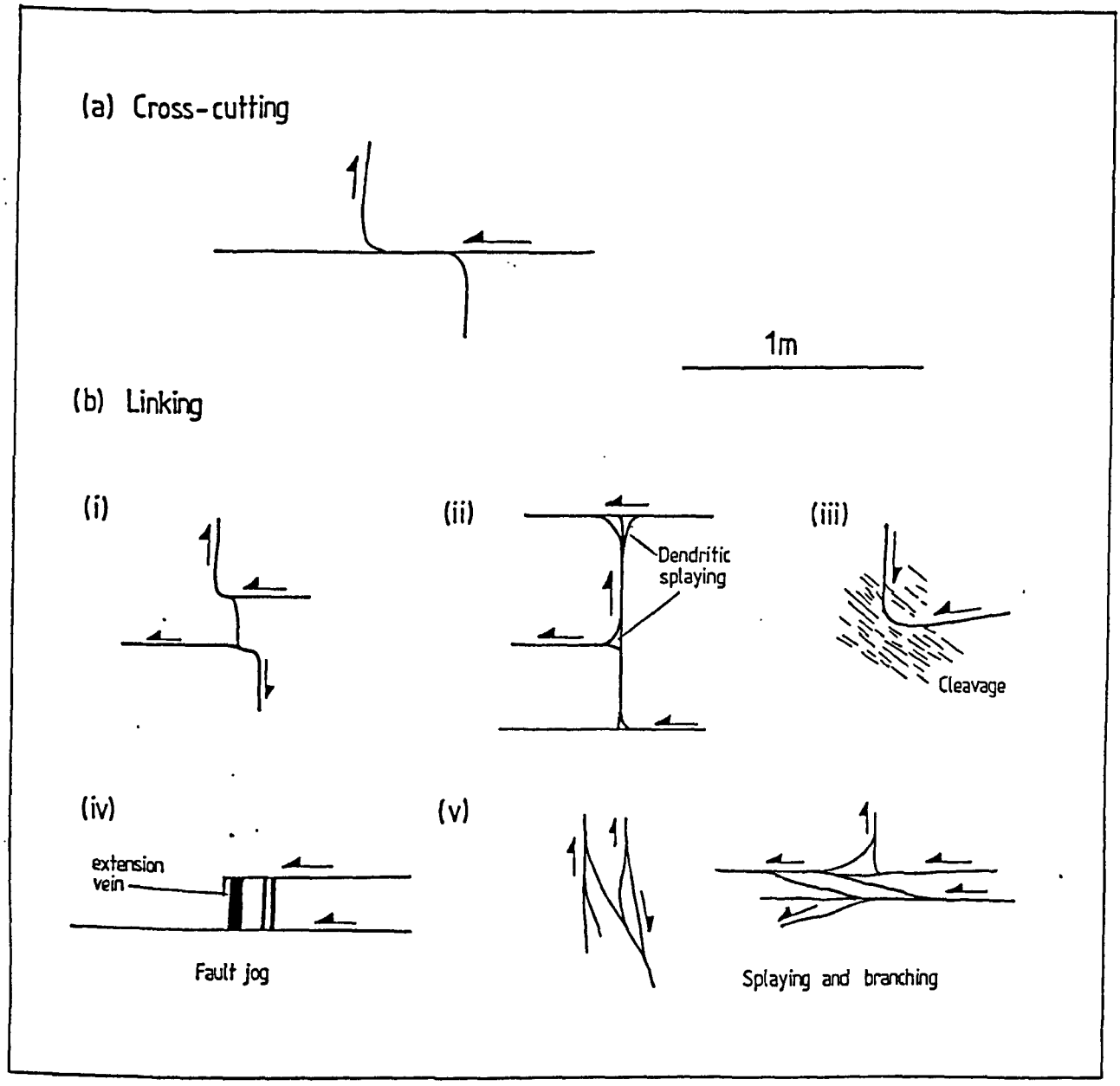

Figure 4.30. Patterns of interaction between high and low angle faults. The faults either cross cut without significant interaction (a) or they link together (b). The former indicates that one fault post-dated another, the latter often indicates simultaneous propagation and interaction. Five types of linking pattern have been identified: (i) Linking of high and low angle faults in which the low angle fault folds, but does not cut, the high angle fault. The high angle fault is probably an earlier fault that has interacted with, rather than been cross-cut by, the low angle fault. (ii) Linking of high and low angle faults by dendritic splaying of the faults. The faults that splay are later. (iii) Mutual linking of conjugate faults. (iv) Linking of two low angle faults by the formation of a dilational fault jog. (v) Linking by the splaying and branching of subparallel faults.

The patterns of fault linking suggest that overall the high and low angle faults propagated simultaneously. The complexities in linking patterns presumably reflect interference between the stress fields associated with the propagating fractures (Reches, 1988). This is especially the case for the dendritic splaying (figure 4.30b(ii)). Similar patterns of interaction have been observed in association with jointing (Dyer, 1988) and have been interpreted in terms of a younger joint set growing in a rotated stress field controlled by earlier through-going discontinuities. The presence of dendritic splaying suggests therefore that many of the high angle faults in the granodiorite fault array post-dated the large low angle faults. Other high angle that are folded and cut by the low angle faults are obviously earlier. The fault zone therefore developed progressively with earlier formed faults not necessarily reused to accommodate further strain after they had ceased activity. This latter observation explains the high density of faulting.

The branching and linking of faults in the array is similar to that documented by Reches (1988) from clay-cake experiments. He attributed these features to fault interaction produced by the non-uniform stresses generated at fault tips during differential motion on the discontinuous faults. The operation of a similar phenomenon in the granodiorite faults probably contributed to the complex fault pattern.

The fault array differs significantly from the strike-slip fault patterns documented by Segall and Pollard (1983) and Granier (1985). They found that the faults nucleated by shear along preexisting fractures or joints and that the tip zones were characterised by secondary extension fractures. Conjugate or branching faults were absent. This latter feature may have been the result of the use of pre-existing structures as fault planes during the strike-slip deformation. No pre-existing joints or fractures appear to have been utilised as fault surfaces in the granodiorite fault array and this has probably enabled a wider range of fault orientations to develop.

In addition to linking, some of the faults possess tips. Three styles of fault tip structure are preserved within the fault array:

1. A brittle/ductile shear zone containing an en echelon array of tension gashes (figure 4.28e). This type of tip was only observed on one low angle fault. It did not occur on the high angle faults.
2. A set of small tension gashes that abutt the fault (feather veins) (figure 4.28f). In discontinuous faults these are symmetrically located in the quadrants opposed to the relative displacement direction. This type of tip appears to have developed on faults whose propagation was not interfered with by neighbouring faults. It is similar to the ideal fault tip structure for an isolated fault in an elastic medium (cf. Pollard and Segall, 1988).
3. A set of dendritic splays (figure 4.28g and figure 4.31a). This type of tip is most commonly developed on high angle faults and has been discussed above. Its

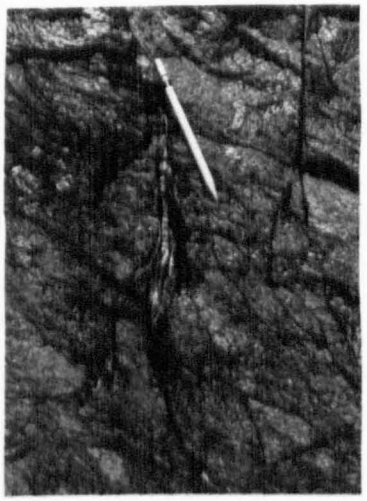

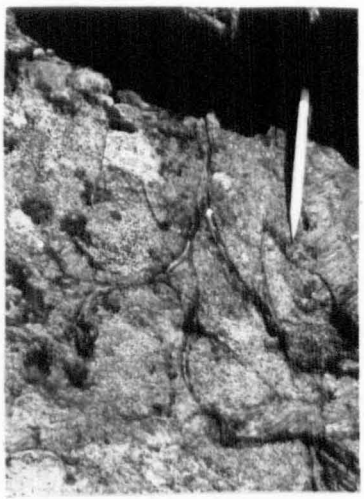

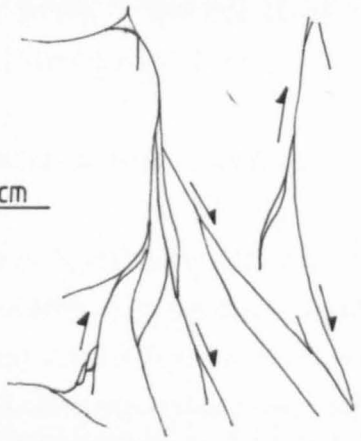

(a)

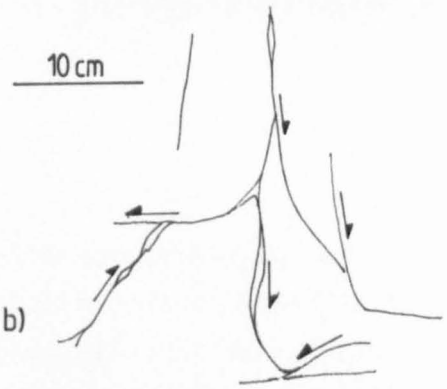

(b)

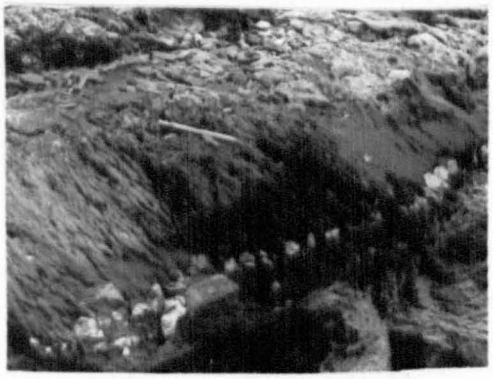

(c)

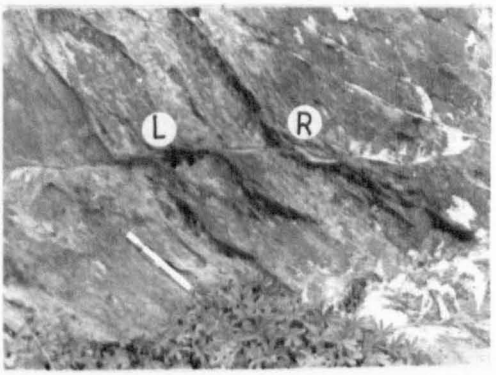

(d)

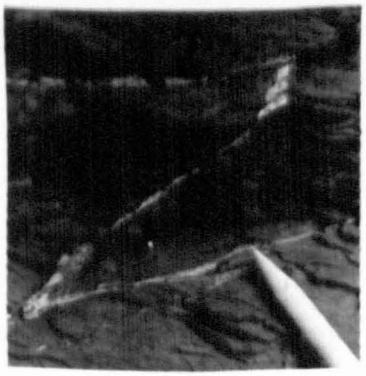

(e)

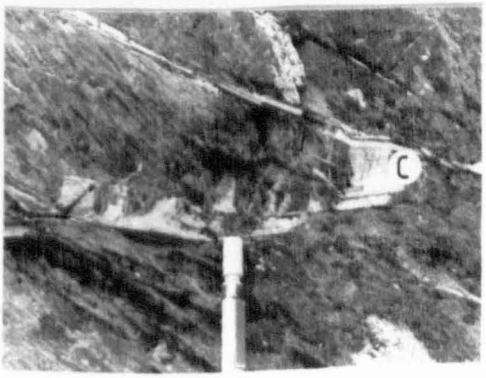

(f)

Figure 4.31 Photographs of fault patterns in the granodiorite and minor fault structures within the Triassic strata of the basal Triassic fault zone. See figure 4.23 and 4.25 for locations.
a) Splaying and branching of two subparallel closely-spaced high angle faults.
b) Splaying and linking of high and low angle faults.
c) Cleavage in the Triassic basal conglomerate. The fabric detaches on a thrust along the unconformity.
d) Small discontinuous fault cutting cleaved shale. The tips of the fault are marked by opposing zones of feather veining and rotation of the rock cleavage. The fault has a stepped profile. The left-facing step (L) is extensional and is marked by a fibre-filled pull-apart (dilational fault jog). The right-facing step is compressional (antidilational fault jog) and is linked by two curved fractures that enclose a small horse. The trailing tip has interacted with another slip surface which has blunted the feather veins.
e) Stepped cross fault linking two sub-parallel 'boundary' faults. The cross fault possesses two opposing zones of blunted feather veins where it has interacted with the two low angle faults. The geometry suggests that the cross fault initiated as a discontinuous fracture that when it linked to the boundary faults during propagation, transferred displacement across them. Cross faults possess unstable orientations and may be folded by fault-parallel shear associated with continued movement on the low angle faults.
f) Detail of the trailing tip of the fault shown in d). The blunting of the feather veins suggests that the steeper slip surface (possibly a P-shear) moved synchronous with the discontinuous fault.

predominance probably reflects the strong control of the interacting and interfering stress fields associated with the closely spaced faults on blunting fault propagation.

It seems likely that the granodiorite fault array is a failed attempt at the linking of a set of originally discontinuous enechelon faults in the granodiorite to form a through-going thrust parallel to the unconformity. The absence of the array in the neighbouring migmatised psammites presumably reflects the anisotropy and greater strength of this strata. It is possible that some of the faults in the array may have been reactivated or have formed in association with movement on the later out-of-sequence thrust labelled fault 6 (figure 4.24). Although later movement is difficult to demonstrate, the faults have an appropriate orientation to help accommodate footwall-collapse of the fault ramp. Ramp collapse on a set of low angle secondary faults in the footwall of a thrust with orientations similar to the low angle faults in the granodiorite fault array has recently been documented by Welbon (1988b).

4.4.1.4.2. The Basal Triassic Fault Zone.

The secondary faults in the BTFZ are all shear fibre coated fractures with predominantly P and R1 orientations. In contrast with the granodiorite fault array no high angle antithetic faults formed. Discontinuous faults are also present and often possess orientations subparallel to the main bounding thrusts. Small scale examples of fault interaction in the BTFZ are shown in figure 4.31d-f. The fault geometries indicate that minor faults within the zone often formed as isolated discontinuities that only linked to the larger faults during their propagation and interaction. In both figures 4.31d and 4.31e linking of faults has occurred by the development of dilational jogs at the fault tips.

4.4.2. Phase 3 related deformation in the strata above the BIS.

As already mentioned, the strata above the BIS possess a number of fault-fold structures (see figure 4.3a). This section will give a detailed description of two of these structures: 1. the lower and middle fold structures and 2. the upper fold structure and upper duplex. The understanding of how these structures formed is critical to determining the deformation sequence in the culmination. In addition the fault rocks that developed along the thrusts in the culmination will be described together with the fault rock assemblages present along the PPVT. The latter help to further constrain the deformation sequence.

4.4.2.1. The Lower and Middle Fold Structures.

A set of discontinuous thrusts occur within the cleaved Triassic mudstone above the BIS (figure 4.3b). These faults all have low angles of dip even though they truncate strata that

was tilted steeply westwards by the development of the culmination. The trailing tips of the faults are marked by anastomosing zones of slip surfaces that link to large tension gash arrays. When traced in the movement direction, the slip surfaces coalesce to become discrete fault planes that can be traced until they meet the contact with the overlying Cretaceous limestone where they tip into small folds. This section will describe the deformation associated with two of these tip structures: the Lower and Middle Fold Structures.

4.4.2.1.1. Geometry.

A sketch section through the structures is shown in figure 4.32. The LFS is a mesoscopic tip fold produced by one of the discontinuous faults (fault B). The tip fold deforms the overlying PPVT and GT and also an earlier thrust labeled fault A. The MFS is a formed by two phase 3 thrusts that cut across the P1 thrusts discussed in section 4.2 and branch onto and fold the PPVT.

A more detailed map and section across the tip of fault B is shown in figure 4.33 and is accompanied by a stratigraphic log of the folded strata. The Cretaceous unconformity is considered to occur at the base of the matrix supported dolomitic conglomerate. In figure 4.32 the unconformity was placed at the contact between the dolomitic sandstone and the overlying limestone solely to emphasise the form of the tip fold.

The strata in the footwall of fault B are folded by a set of symmetrical folds (figure 4.33b) that become more asymmetrical when traced downwards into the Triassic strata. The folds eventually die out into layer-parallel shortening within the Triassic mudstones. They are thus restricted in development to the bedded strata adjacent to and above the Cretaceous unconformity. The folds are cut by fault B which splays into a number of secondary faults towards its tip. The splay labeled 1 (figure 4.33b) branches downwards from the sub-horizontal portion of the thrust (labeled 2). This fault is not extensional however as it cuts upsection across the earlier folds. Restoration of this fold returns point V to point W. It appears therefore that splay 1 was folded, the fold then cut across by splay 2. This geometry suggests that the folding both pre- and postdated the initial development of fault B. A number of smaller splays also branch from fault 2 and tend to tip before meeting the overlying limestone. The overturned limb of the fold is also cut by numerous small, right-stepping, discontinuous, top-to-south shear zones (figure 4.34). A set of conjugate zones locally developed and are restricted to the core of a downward facing 's' fold.

On the forelimb of the tip fold the overlying PPVT sheet is cut be a complex array of secondary faults. The array differs from the more simple distribution of faults present in the less deformed limbs of the fold and is composed of fore thrusts which cut across

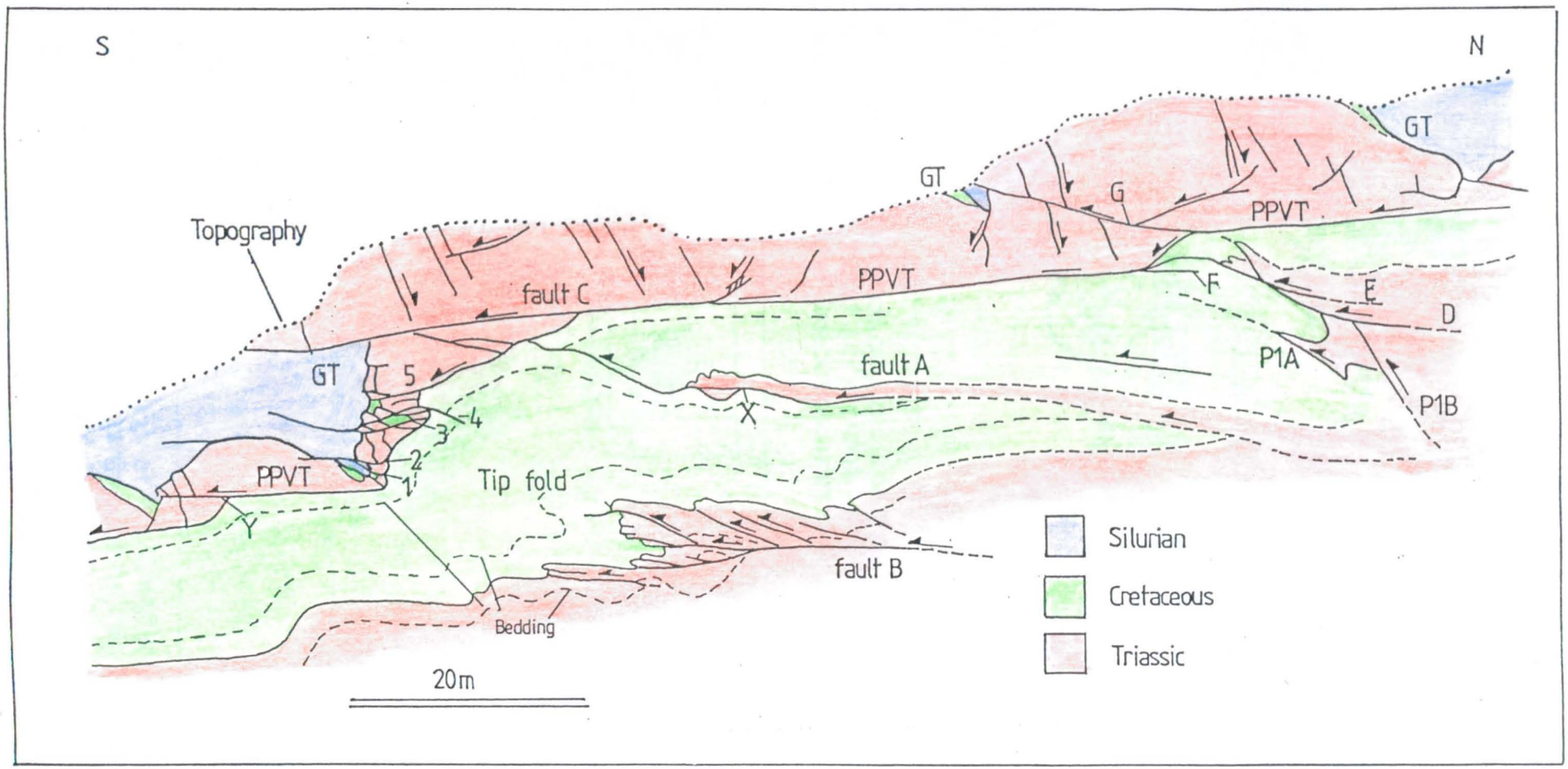

Figure 4.32. N-S sketch section across the lower and middle fold structures.

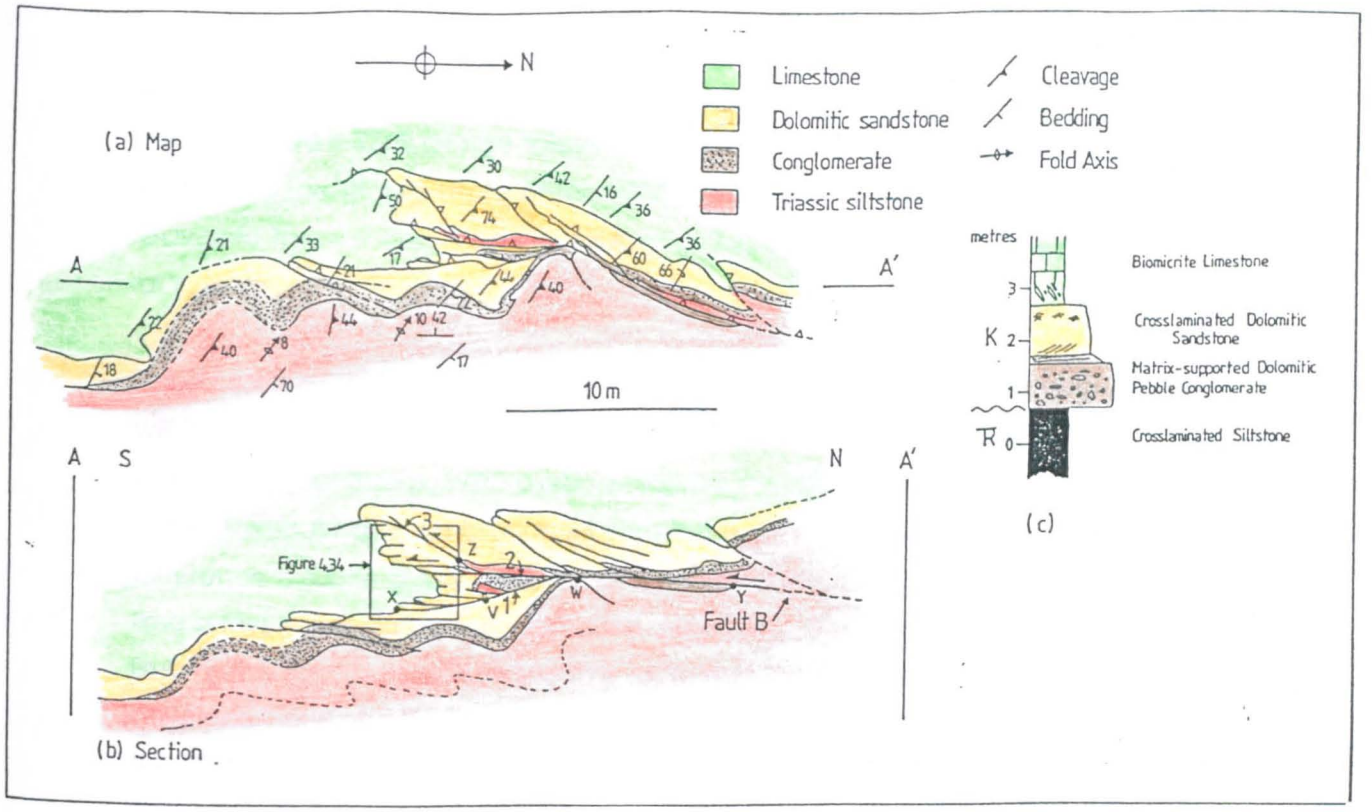

Figure 4.33. Detailed map (a) and cross section (b) of fault B in,figure 4.32. The significance of splays 1,2 and 3 and points V,W,X,Y and Z are discussed in text. c) Stratigraphic log across the Cretaceous unconformity.

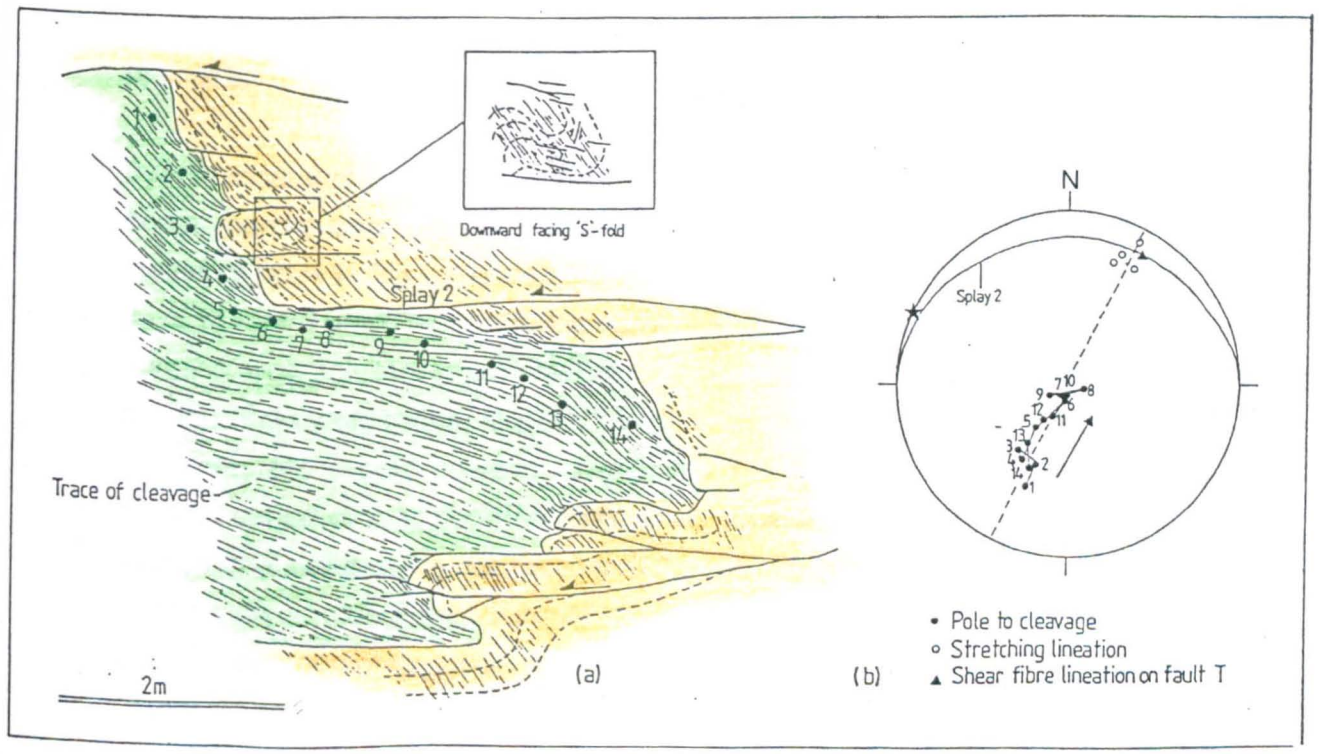

Figure 4.34. a) Detailed sketch section of the Cretaceous dolomitic sandstone-limestone contact in the overturned limb of the tip fold (see figure 4.33 for location). Splay 2 of fault B tips into a shear zone within the limestone. b) Stereogram of cleavage within the shear zone. The cleavage lies along a great circle whose intersection with the thrust is the transport direction. The configuration suggests simple shear. The fold appears to have formed first and then had its overturned limb sheared out by the later displacement on splay 2. The discontinuous faults above splay 2 appear to accommodate the stretching of the fold limb as it rotated into the incremental extension field for the shear (cf Ramsay et al., 1983, figure 6).

high angle faults downthrowing to the north. Five main thrusts can be identified (figure 4.32). Only thrust 4 breaches the PPVT and the others appear to branch from the thrust. Fault C (figure 4.32) is a large splay from the PPVT that cut across the crest of the fold and emplaced the Triassic strata of the PPVT sheet over the Silurian Graphitic Phyllite of the Gavarnie Thrust sheet. A smaller fault of similar geometry cuts across a fold in the PPVT at Y.

Thrusts such as fault C, which cut across the crestal points of folds in their own surfaces, will be referred to as **Back-limb Splays (BLS)** . These are to be distinguished from back-limb thrusts (Dahlstrom, 1970; p.341) which are thrusts that cut across the back-limb of an earlier fold but have not branched from a thrust that was folded by the earlier fold. The difference is subtle but important. A necessary constraint on the development of back-limb splays is that during the folding the orientation of the pre-existing thrust on the back-limb of the fold must remain suitable for further movement. Other back-limb splays are developed at X and Y in figure 4.32, while fault 2 in figure 4.33 and fault G that splays from the PPVT across the middle fold structure (figure 4.32) can be similarly classified. The presence of these back-limb splays points to the development of localised strain detachments along preexisting discontinuities during the shortening (see later).

4.4.2.1.2. Displacements on the Faults.

a) Fault B.

The displacement on fault B can be estimated using the cutoffs of the basal Cretaceous conglomerate bed. Fault 1 (figure 4.33) shows a displacement of approximately 4 metres at point V. This value decreases rapidly further south to accommodate the fault tip at X. Fault 2 has a lens of Triassic strata (probably a truncated anticlinal closure) in its hanging wall. This lens is overlain by dolomitic sandstone (the conglomerate bed is absent) and should restore to point Y to give the fault a displacement of 12 metres. The conglomerate should however overlie the Triassic mudstone as predicted by the footwall cut-off at Y. Its absence suggests that movement occurred out of the plane of section (the plane of the cliff face) and that the conglomerate cannot have formed a uniform layer along the unconformity. The displacement on fault 2 cannot be constrained accurately although it is probably of the order of 10-15 metres at point Z. The displacement on this fault represents the finite displacement on fault B.

b) Displacements in the MFS.

The displacements on P3 thrusts D and E can be estimated by matching the cut-offs of the P1 thrusts. This gives a combined displacement on the two thrusts of approximately 6 metres. Fault F has a displacement of 3 metres constrained by the imbrication of a layer

of limestone mylonite along the PPVT. These values are for the displacements in the plane of the section and assume the absence of displacement gradients on the faults.

c) Displacements on the back-limb splays of the PPVT.

Back-limb splay fault C has an estimated minimum displacement of 20 metres. This displacement is greater than can be explained even if the observed displacements on faults B, D and E were transferred in total onto the PPVT and the internal shortening associated with the fault-related folds neglected This discrepancy points to the existence of additional displacement on the PPVT. It will be argued later that this displacement is provided by a general upper strain detachment within the culmination. BLS fault G which formed across the MFS has a displacement of approximately 4 metres.

4.4.2.1.3. Orientation analysis.

Structural data for the LFS and MFS are shown in figure 4.35 The folds in the Triassic strata that are cut by fault B trend NW-SE and plunge shallowly towards the NW (figure 4.35a). Cleavage in the Triassic appears axial planar to these folds (figure 4.35b). The cleavage in the Cretaceous limestone (figure 4.35c) has a similar orientation. The orientation of the cleavage in both the Triassic and Cretaceous strata in the footwall of the PPVT therefore contrasts strongly with the folded cleavage that is present in the hanging wall of the thrust above the LFS (figure 4.21).

Poles to the folded PPVT and minor faults in the thrust sheet also possess a girdle distribution (figure 4.35d and e). In the LFS the folded PPVT has a similar orientation to the fold train in the Triassic strata but has a slightly more oblique axis. In the MFS the fold is E-W trending (figure 4.35d). Poles to fault B (figure 4.35f) also plot as a partial girdle with the same pi- axis as the folds in the Triassic strata.

Both fault B and the splays in the PPVT sheet possess bimodal lineation distributions (figure 4.35e and f). The means for the azimuths of these lineations are 210 and 172 for fault B and 197 and 164 for the faults within the PPVT sheet. In both cases cross-cutting and curved relationships between shear fibres on the fault surfaces consistently indicate that the 160-170 movement direction was the latter. This is identical to the relationship found on the low angle faults in the summit klippe of the PPVT sheet.

Rose diagrams of the lineation data for the LFS are shown in figure 4.36. The stretching lineations on the cleavage in the limestone record the same movement direction as the first movement azimuth on fault B. This direction is within 10 degrees of lying in the profile plane of the fold and is approximately perpendicular to the fold axis. Thus the first

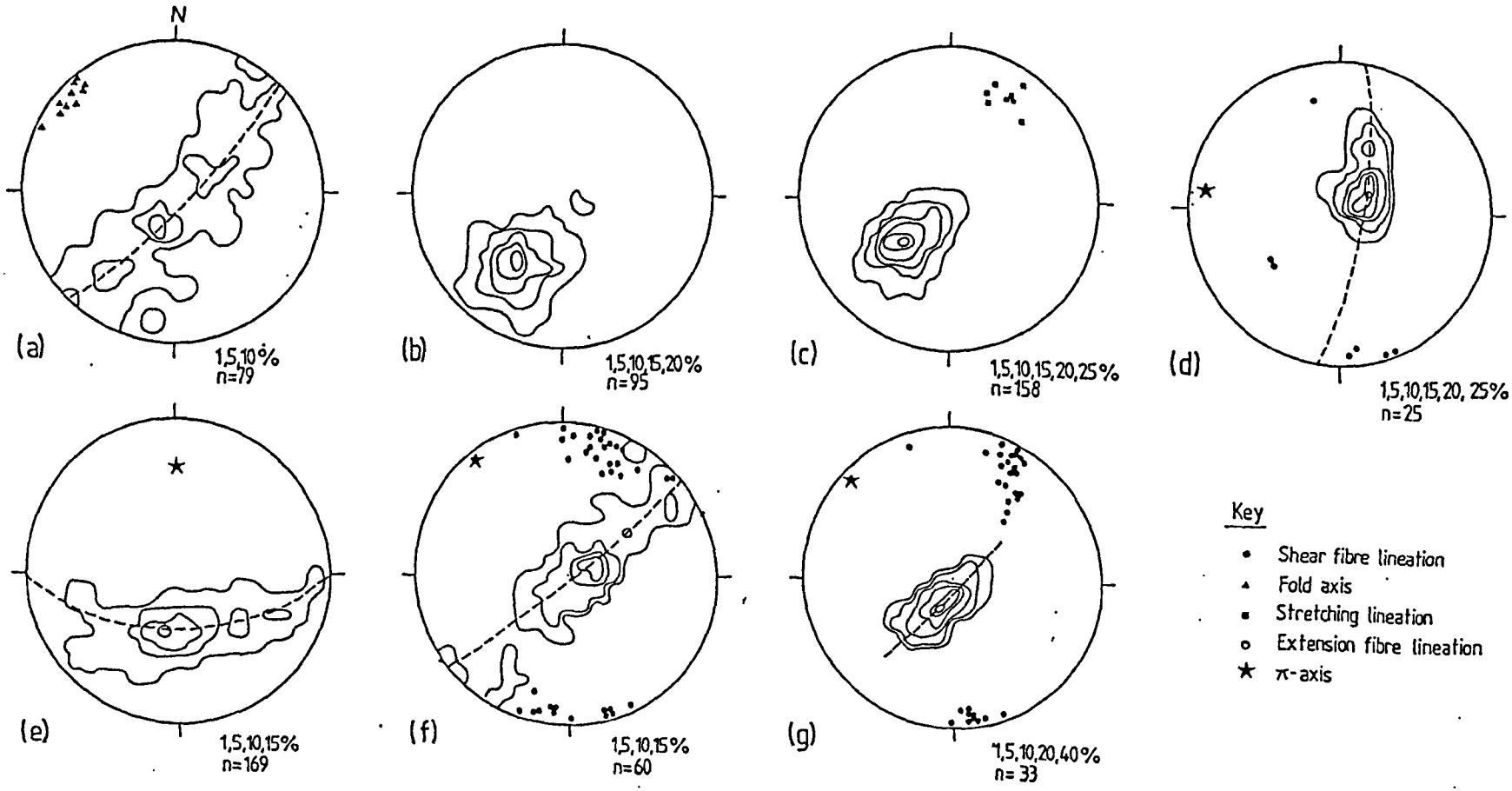

Figure 4.35. Structural data for the lower and middle fold structures. a) Poles to bedding in the Triassic red beds; b) poles to cleavage in the Triassic; c) poles to cleavage and stretching lineations in the Cretaceous limestone; d) poles to the PPVT in the middle fold structure and shear fibre lineations on the thrust; e) poles to cleavage in the PPVT sheet; f) poles to the PPVT and shear fibre lineations on the thrust in lower fold structure; g) poles to fault B and shear fibre lineations. Both fault B and the PPVT show bimodal lineation patterns.

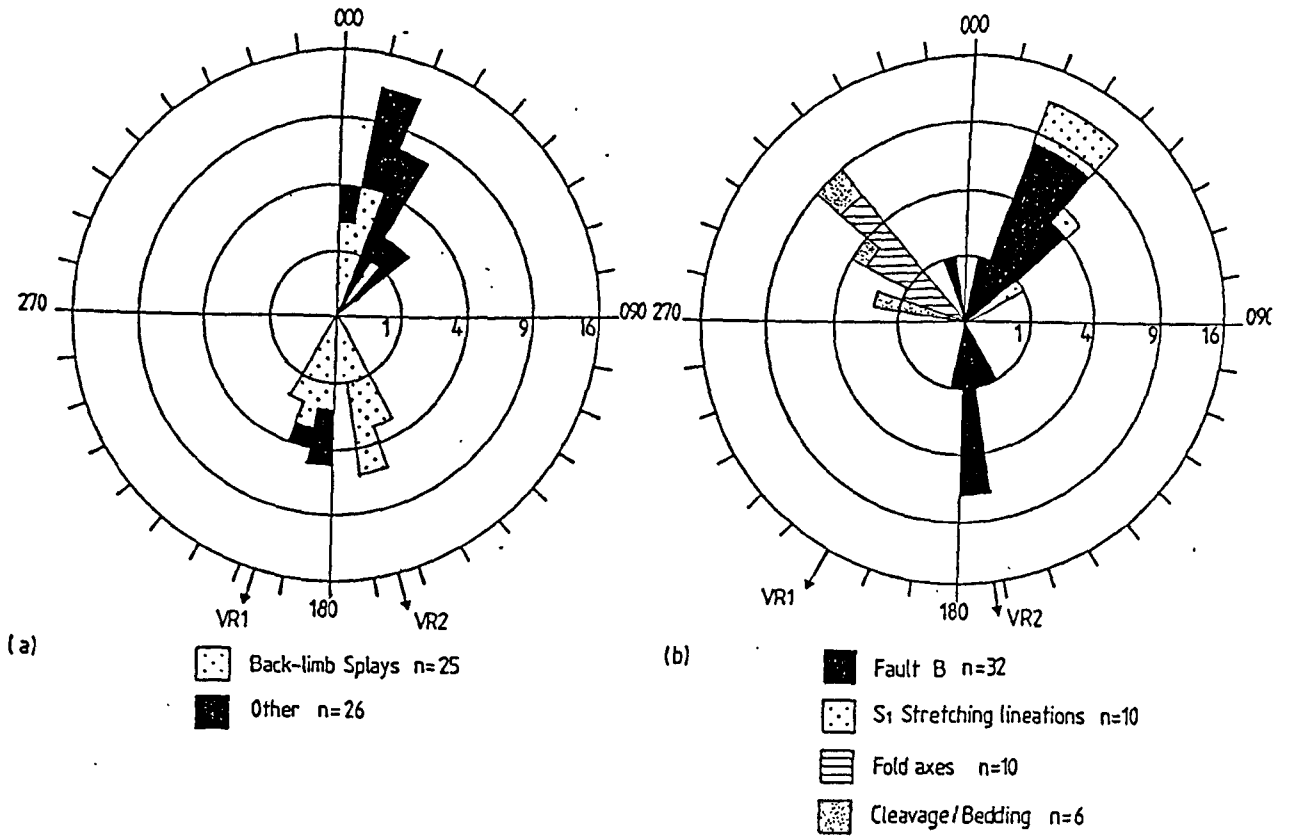

Figure 4.36. Rose diagrams of lineation data (azimuth of plunge) from the lower fold structure. a) Lineations on minor faults in the overturned PPVT sheet. These have been divided into back-limb splays and others (high angle faults). The data show that two phases of movement occurred on the back-limb splays but only one on the high angle faults. b) Linear data from other aspects of fold structure. Two phases of movement also occurred on fault B; the first phase parallels the direction of the stretching lineations on the cleavage, the second is counterclockwise oblique of the stretching lineation. Vector resultants (VR) of the fault lineations are also shown.

movement on the faults was clockwise oblique of the N-S regional movement direction. Cleavage/bedding intersection lineations in the Triassic strata are parallel to the fold axes and the folds do not appear to be transected.

4.4.2.2. The Upper Duplex and Upper Fold Structure.

These two structures occur 50 metres north of the middle fold structure (figure 4.3b). They will be considered together because, as will be shown, they are intricately related.

4.4.2.2.1. Geometry.

An approximate transport-parallel section through the two structures is shown in figure 4.37.

The upper duplex comprises a set of at least six thrusts within the Cretaceous strata beneath the summit klippe. These thrusts splay from a floor fault that approximately coincides with the Cretaceous unconformity. The positioning of these thrusts is partly inferred because they are difficult to trace due to the parallelism between the faults and the cleavage in the limestone.

The thrusts branch onto the PPVT apart from fault 2 which breaches the roof thrust at the crest of the structure and fault 6 which cuts across the crest of an earlier formed fold to breach the PPVT at the front of the structure. This earlier fold is a monocline that formed either as a buckle fold or as a hanging wall ramp anticline on a structurally lower thrust. Fault 6 is a back-limb thrust with respect to the monocline. It splits into a number of overlapping secondary thrusts above the fold crest. A more detailed sketch section of these secondary faults is shown in figure 4.38. The faults form a right-stepping en echelon array that deform the cleavage.

Three thrusts breach the PPVT in the UFS (figure 4.37) and are labeled J, K and L. Fault J occurs structurally below the floor thrust of the upper duplex and is probably an out-of-the-syncline thrust associated with the shortening that produced the monocline. Fault K represents the continuation of the floor thrust of the duplex. Fault L steps up from the level of the main floor thrust and is the upper fault of the right-stepping secondary faults. These faults together appear to represent a discontinuous ramp, movement on which folded the splay from the PPVT labeled fault M. Fault M emplaces the PPVT sheet over the Silurian phyllites of the GT sheet. It restores to a back-limb splay from the PPVT that formed across the initial monocline. Fault N (figure 4.37) is a later back-limb splay that cut across the crest of the folded fault M.

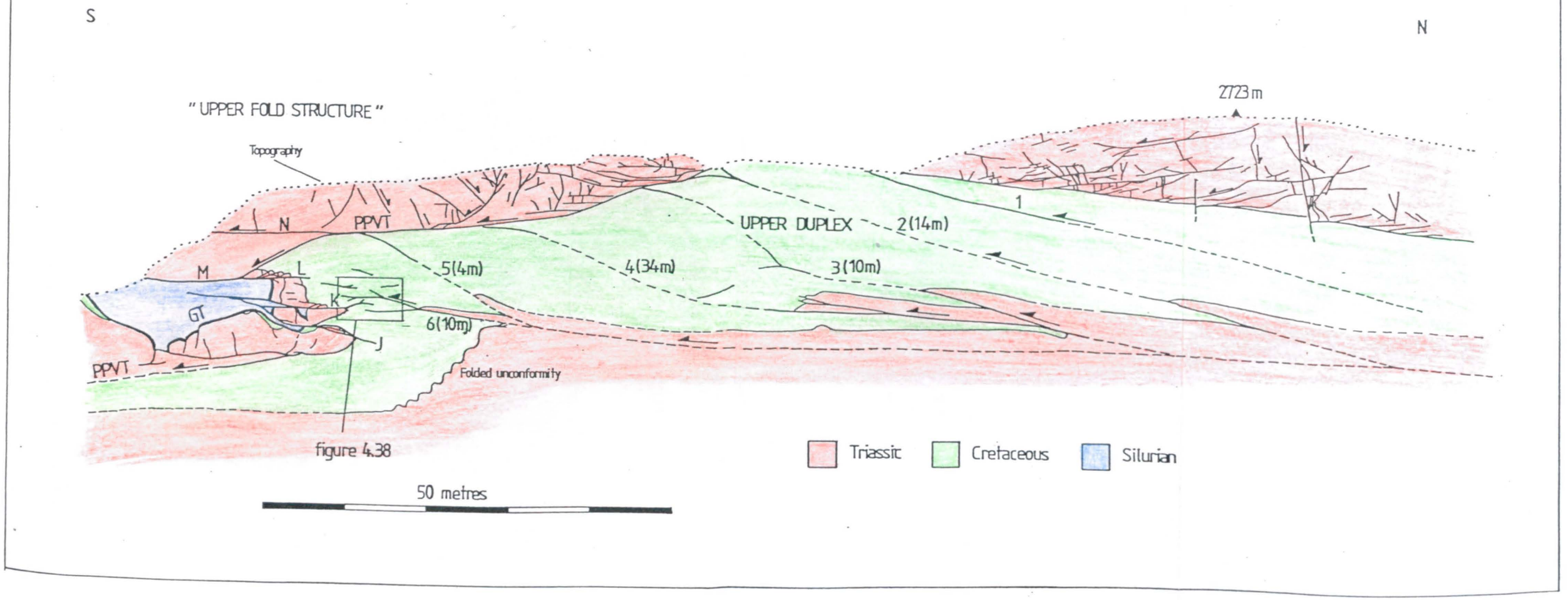

Figure 4.37. Cross section through the upper fold structure and upper duplex. The estimated displacements on the faults are shown.

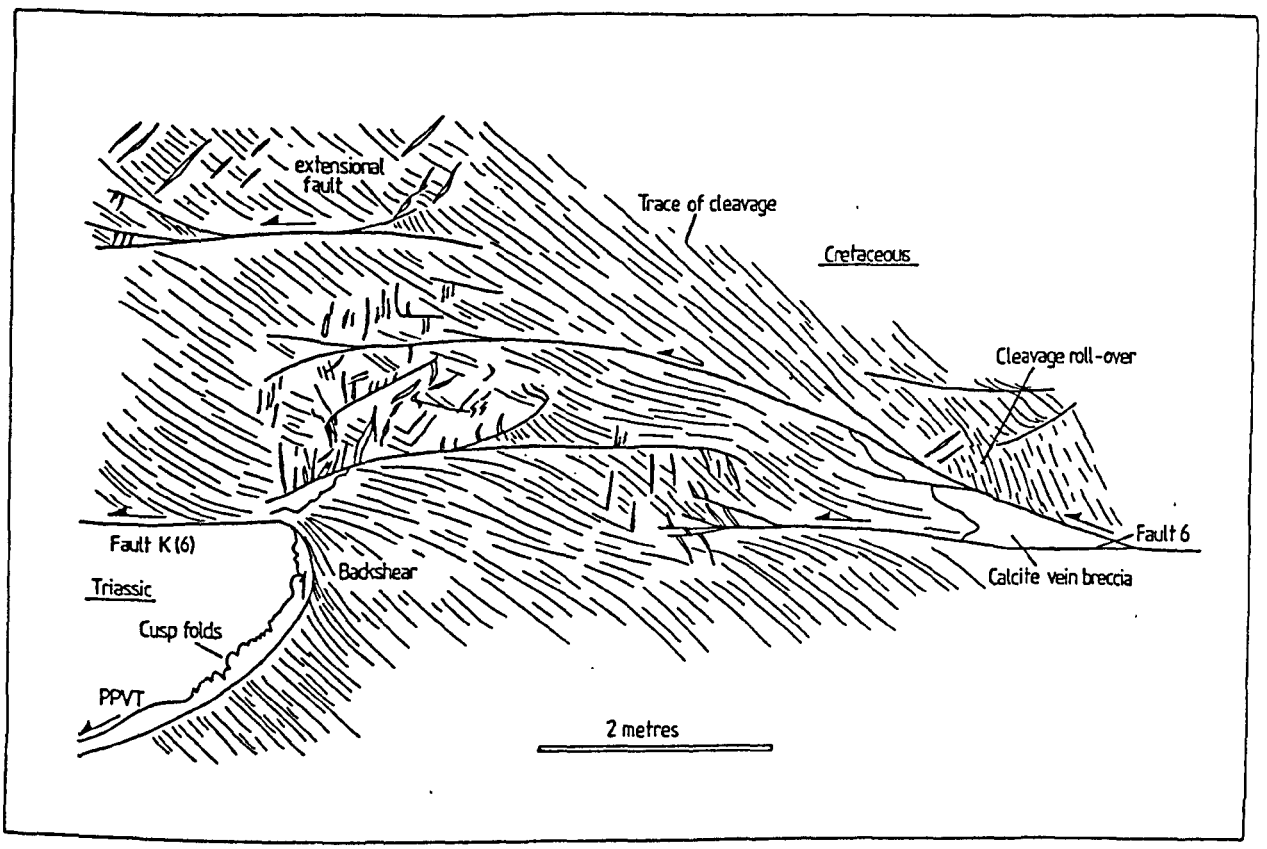

Figure 4.38. Detailed sketch section of secondary faults at the front of upper duplex. The en echelon faults deform the cleavage and are associated with swarms of extension veins. A cleavage- roll over is developed on one of the splays from the floor fault (fault 6) and probably formed as a result of movement on the inclined fault.

4.4.2.2.2. Fault displacements in the structure.

The displacements on the thrusts in the upper duplex are indicated in figure 4.37. These have been estimated from the footwall and hanging wall cut offs of the imbricated basal Cretaceous dolomitic sandstone unit directly above the floor of the structure. In the UFS the displacements on faults K and L can be constrained from the off set of the PPVT. Fault K has a displacement of approximately 4 metres and fault L a total displacement of approximately 3 metres. This distribution indicates that the displacement on fault 6 (10 metres where it cuts the crest of the monocline) decreases into the UFS.

4.4.2.2.3. Orientation analysis.

Structural data for the upper fold structure and upper duplex are shown in figures 4.39 and 4.41. Figure 4.39 shows the distribution of cleavage in individual horses from the upper duplex. The cleavage does not change orientation systematically across the individual thrusts although there is a general increase in cleavage dip towards the front of the structure accompanied by a clockwise rotation of cleavage strike. This feature is shown clearly by a cleavage strike line map (figure 4.40). The rotation of the cleavage strike mirrors that documented in the PPVT sheet above the upper duplex (figure 4.21) and suggests that the distributed shortening in the duplex also affected the overlying thrust sheet. This suggests that the roof thrust was not active during at least part of the cleavage development in the structure. Apart from fault 6 which clearly deforms the cleavage in the limestone the other thrusts are mainly cleavage-parallel and do not visibly deform or reorient cleavage. This suggests that the oblique cleavage development post-dated movement on some of the thrusts but predated movement on others. The duplex therefore appears to have had at least two phases of movement: one predating and one postdating the shortening responsible for the cleavage attitude in the structure.

Bedding in the dolomitic sandstone unit imbricated in the duplex plots as a pi-girdle (figure 4.41a) that defines the orientation of the hanging wall anticlines of the thrusts. These folds are clockwise oblique to regional N-S transport vector. Poles to the PPVT also have a girdle distribution defining the axis of the fold structure (figure 4.41b). This has a similar orientation to the axes of the hanging wall anticlines on the upper duplex thrusts.

The shear fibre lineations on the secondary faults associated with fault 6 possess a bimodal distribution that records both SSW and SSE directed movements (figure 4.41d). This distribution is also shown by the extension fibres from the tension gashes at the tips of the secondary faults in the limestone (figure 4.41e). These veins appear to have

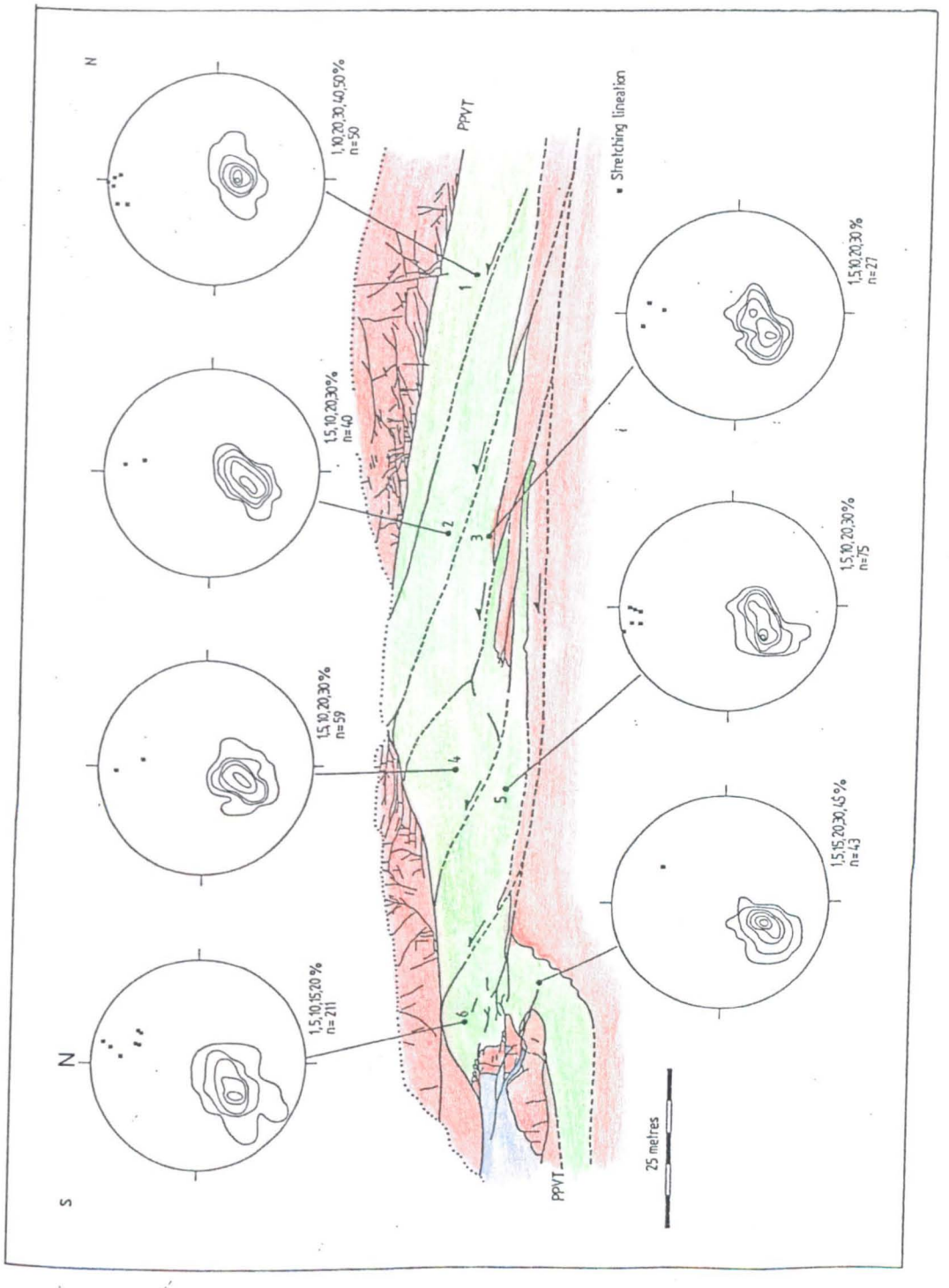

Figure 4.39. Cleavage within the upper duplex. The stereograms show the cleavage attitude for individual horses. There is a general rotation in cleavage strike from E-striking at the rear of the structure to NW-SE at the front of the structure accompanied by an increase in dip. The stretching lineations also rotate from N-S to NE-SW.

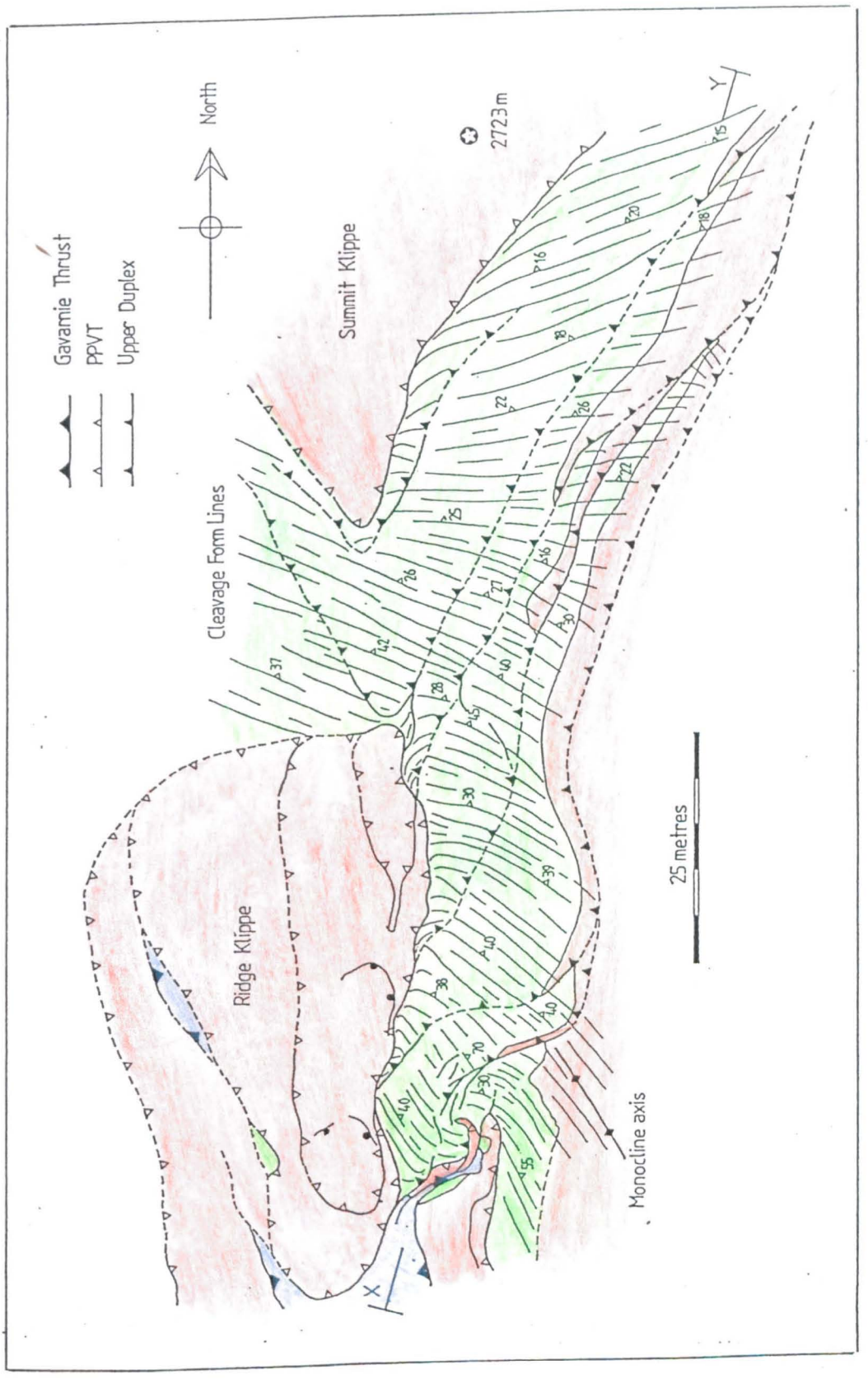

Figure 4.40. Cleavage form-line map for the upper duplex and upper fold structure. The cleavage fans across the structure but does not change orientation across individual faults. It is only deformed by the frontal thrust, fault 6. This distribution suggests that the duplex predated the development of the cleavage fan but that the frontal thrust was later reactivated. The rotation of the cleavage indicates an increasing dextral shear component in the deformation towards the front of the structure. This component is related to the oblique fault tips developed in the basement imbricate stack.

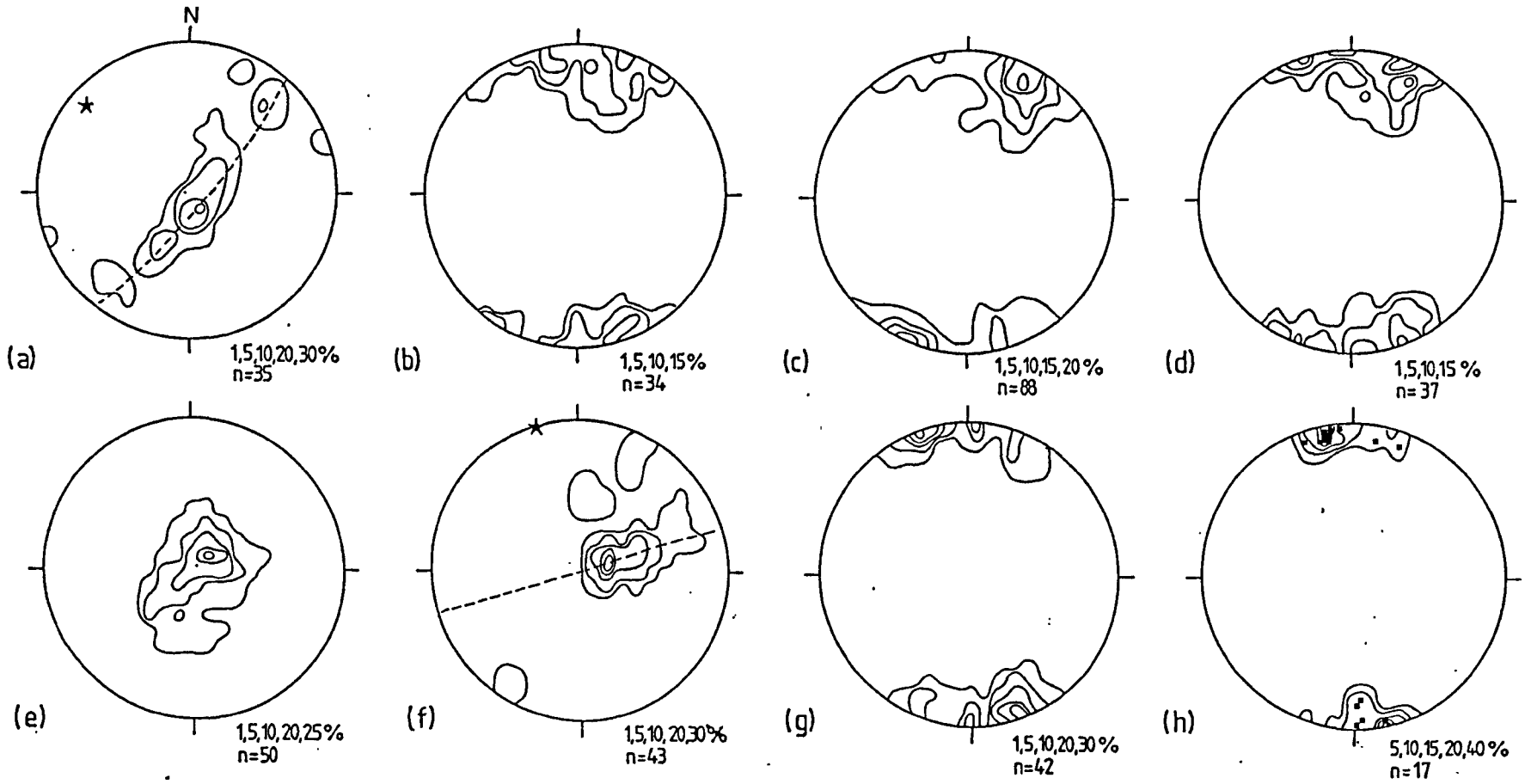

Figure 4.41. Structural data for the upper fold structure and upper duplex. a) Bedding in the Triassic. The girdle defines the hanging wall folds on the thrusts; b) shear fibres lineations on the PPVT; c) extension fibres from tension gashes associated with secondary faults in the limestone; d) shear fibre lineations on thrusts within the Cretaceous limestone; e) poles to the secondary faults in the Cretaceous limestone within the upper fold structure; f) poles to the PPVT within the upper fold structure; (g) shear fibre lineations on the faults that breach the PPVT and the back-limb splays M and N; h) stretching lineations in the mylonite along the PPVT on the back limb of the the UFS. The mylonite has only one lineation (approximately N-S) in contrast with the low angle faults in the PPVT sheet. and the secondary faults in the limestone

dilated parallel to the slip direction on the faults. Cross-cutting relationships between the sets of veins and between shear fibres on the faults indicate that the SSE movement vector again post dated the SSW movement vector. Lineations developed on the faults that breach the PPVT and on the BLS (faults M and N) also show the same distribution (figure 4.41f and g). The stretching lineations in the mylonite along the fault plane however only show one movement azimuth: towards the south (figure 4.41h).

4.4.2.2.4. Restoration.

Using the displacements observed on the thrusts, an area and line-length balanced and restored section of the upper duplex has been constructed figure (4.42). The restored section was constructed by area and line length balancing the deformed section. The template used was not assumed a priori, but was constructed during the area balance. The only constraints applied were that the observed displacement on the faults should restore and that the PPVT was planar and sub-parallel to the Cretaceous unconformity prior to formation of the duplex. The technique used was therefore not to construct a deformed section that balanced, but to construct a template and restored section that as near as possible balanced. This was feasible due to the excellent exposure of the duplex. The result suggests that the combined 70 metres of displacement on thrusts 2-7 represent c.42% shortening.

The shortening estimate must be considered schematic because the upper duplex cannot be properly restored for three reasons:

1. The intense cleavage in the limestone signifies that area and line-length change due to volume loss deformation has occurred.
2. The cleavage has an arcuate distribution (figure 4.40). While stretching lineations on the cleavage and the shear fibre lineations on the thrusts are approximately parallel (this implies no fault movement out of the plane containing the principal plane of strain occurred during cleavage development), no planar section can be constructed that always parallels the principal plane of the strain ellipse and the movement direction. This means that a component of lateral movement occurred across any planar section taken through the duplex. The deformed section through the upper duplex (figure 4.42a) was constructed parallel to the first shear fibre lineation as recorded on the faults near the front of the duplex. This direction is sub-parallel to the strike of the cliff face and problems with a lack of 3-D control on fault geometry are avoided. The problems associated with movement out-of-section mean that at the rear of the duplex the actual thrust transport directions and the cleavage stretching lineations are oblique to the plane of the cross section and area is gained due to movement of material into of the plane of section.
3. The presence of a second oblique displacement event on some of the thrusts in the duplex also violates the plane strain condition.

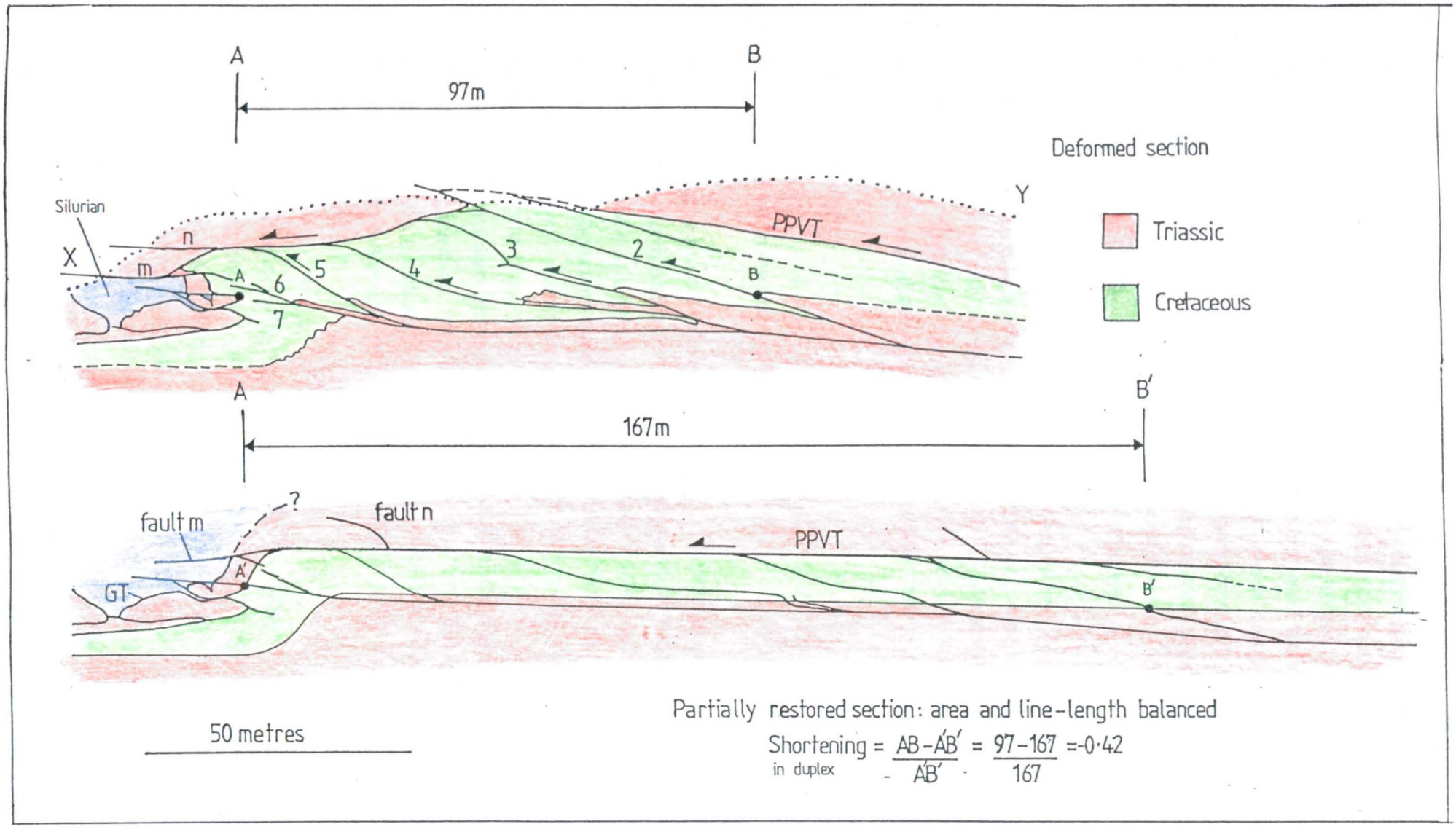

Figure 4.42. Balanced and partially restored sections across the upper duplex. Area balancing the upper duplex gives a minimum shortening of 0.42. The technique used to restore the section is discussed in the text.

As expected, problems with the area balancing were encountered and excess areas occur in horses 2 and 3 related to the area gains outlined above. The restoration technique used indicates that horse 2 has a minimum excess area of 12% in section XY (figure 4.42). One of the main results of the technique used is a necessary adjustment of the branch point spacing along the roof thrust (these are greatly increased in the restored section). The physical significance of a decreased branch point spacing in the deformed section is that it requires internal deformation of the horses and displacement gradients on the faults. While the restoration is only schematic the results are consistent with the inferred superposed cleavage within the duplex.

The 42% shortening estimate must be a minimum for the duplex. This is because no account has been taken of volume losses due to cleavage development or of area changes associated with the SSE directed second movement episode on some of the faults. Both will have had the effect of reducing area in the deformed section ie. reducing the calculated shortening in the restored section.

4.4.3. Fault Rocks.

4.4.3.1. Thrusts within the culmination.

All the Alpine-age faults within the basement and Triassic strata of the PPV culmination are discrete fractures coated with layers of quartz/chlorite shear fibres (eg. figures 4.28a and f, and figures 4.31 e and f). In addition, there does not appear to be any significant difference in the nature of these fault rocks between the small displacement (< 1m) and large displacement (>5m) faults. The pull-aparts within dilational jogs are also filled with fibrous quartz and they give an indication , at least on small faults, of the finite displacement. Inclusion bands within the quartz fibres (figures 4.28a and 4.31f) indicate that the fibres grew by a crack-seal mechanism (Ramsay, 1981). This is confirmed in thin section where, in addition to inclusion bands, the fibres are observed to possess a briquette-structure (Ramsay and Huber, 1983) characteristic of stretched fibres (Durney and Ramsay, 1973).

Inclusion bands also occur within the shear fibres that coat the planar portions of the faults and suggest that slip on the faults occurred by a crack-seal mechanism. This mechanism can be considered a stable sliding mechanism and involves the extensional microcracking of the mineral fibres along the fault plane accompanied by the sealing of the resultant fractures by material precipitated from solution, in this case quartz and chlorite. Once sealed, tectonic stresses are presumably transmitted across the fibres and another cracking event occurs when these stresses exceed the tensile strength of the fibre packet (Ramsay, 1980). For shear fibres, the movement on the fault

surface is therefore partitioned into frictional sliding on fibre surfaces and coaxial stretching (extension fracturing) of the intervening fibre packet.

Frictional slip occurs intermittently on the fibre surfaces during the fracturing of the fibres. The process of crack-sealing of shear fibres is therefore analagous to stick-slip behaviour (Gaviglio, 1986): a fracture opens during the slip phase which then heals or seals during the stick portion of the cycle. It would be expected that increasing the slip rate along the fault would be manifest by either a lengthening of individual crack events, an increase in the rate of cracking, or by a change to another slip mechanism. If the kinetics of mineral precipitation cannot keep pace with the dilatancy produced during cracking then fault-parallel cavities may form providing the rock is strong enough to support the overburden and/or the ambient fluid pressure is near lithostatic. The cavities should dilate parallel to the fibre axes.

During the stick-slip cycle, the fibre packet first suffers shear tractions before it fails in tension. At failure, the near-field principal stress must rotate towards the perpendicular to the fibre packet to account for the fibre stretching. This has been shown theoretically to be the case for an isolated shear fracture residing in an elastic medium and not subject to shear tractions at failure (Pollard and Segall, 1988). This reorientation of the stress field will favour crack-seal (tensile fracturing) in the shear-fibres that grow along the fault.

The presence of fibrous mineral growth along fault planes has been used to infer that a pressure solution slip sliding mechanism has operated (Elliott, 1976a). An integral part of this process is the removal of asperities along the fault surface by diffusional creep which is assumed to be rate determining for the sliding (Rutter and Mainprice, 1978). In the faults in the PPV culmination the removal of asperities by diffusional processes cannot be demonstrated even in thin sections of the fault rocks. The crack-seal slip mechanism that has operated on the faults can probably be considered an end member to the pressure-solution slip sliding mechanism in which fracturing and mineral precipitation in dilational jogs dominate.

4.4.3.2. Fault Parallel Cavities.

Fault-parallel cavities are a common feature along a number of thrusts within the PPV culmination. They are locally developed along the upper bounding thrust within the basal Triassic fault zone, along fault B in the lower fold structure, along a number of the back-limb splays in the PPVT sheet, and along the low-angle extensional faults in the summit klippe of the PPVT sheet. They all possess similar appearances and are elongate planar veins filled with randomly oriented euhedral quartz grains. Where developed these veins give the faults a layered appearance.

Brecciated shale clasts are present within the cavities and arrays of jigsaw extension fractures often develop in the adjacent wall rock. The observed mineral layering in the fault cavities appears to have been the product of different episodes of dilation ie. different fracture events within the cavity (see chapter 5). The layering implies that the dilation occurred across the fault and not along it and therefore suggests the cavities did not owe their origin to pull-aparts associated with large slip increments on the faults. The cavities appear to have formed by localised hydraulic jacking of the fault planes. The microstructures associated with these cavities are discussed in chapter 5.

4.4.3.3. Fault-rock Assemblages along the Pic de Port Vieux Thrust.

The fault rocks developed along the PPVT can be grouped into assemblages as any one part of the thrust displays more than one type of fault rock. Three different assemblages can be identified (figure 4.43):
Type 1. This assemblage comprises a layer of calcmylonite in planar contact with the hanging wall Triassic mudstones (figure 4.43c).
Type 2. This assemblage comprises a layer of cusp folds along the PPVT contact with the mylonite foliation in the limestone overprinted (crenulated) by cleavage in the limestone (figure 4.43b). Occasionally a chloritic fault surface separates the layer of cusp folds from the cleaved limestone. The cleavage is not sheared along this surface.
Type 3. This assemblage comprises a narrow calcmylonite shear zone that outcrops 5 to 30 centimetres below the thrust plane. It is separated from the the thrust by a layer of massive limestone containing dolomite bands and folded with the thrust contact. A shear-fibre coated fault surface cuts across the folds. The shear zone in the limestone deforms the cleavage in the footwall limestone but the line of intersection between the cleavage and the limestone is not perpendicular to the stretching lineation in the mylonite. Exotic slivers of Silurian Graphitic Phyllite are occasionally present along the PPVT contact.

The type 1 assemblage can be considered the simplest assemblage with the calcmylonite unmodified by later deformation events. Where extensional faults branch onto the thrust they often fold the mylonite (figure 4.11a). It is restricted in occurrence to along the summit klippe and parts of the Soum de Barroude section. The type 2 and type 3 assemblages occur on the deformed limb of the culmination: type 2 is developed on the forelimbs of the three fold structures while type 3 tends to form on the back-limbs of these structures.

The fault rock distribution reflects the different sequences of deformation experienced by the PPVT sheet in different parts of the mountain. The type 1 assemblage can be considered the 'protofabric' that evolved into either assemblages 2 or 3. The type 3

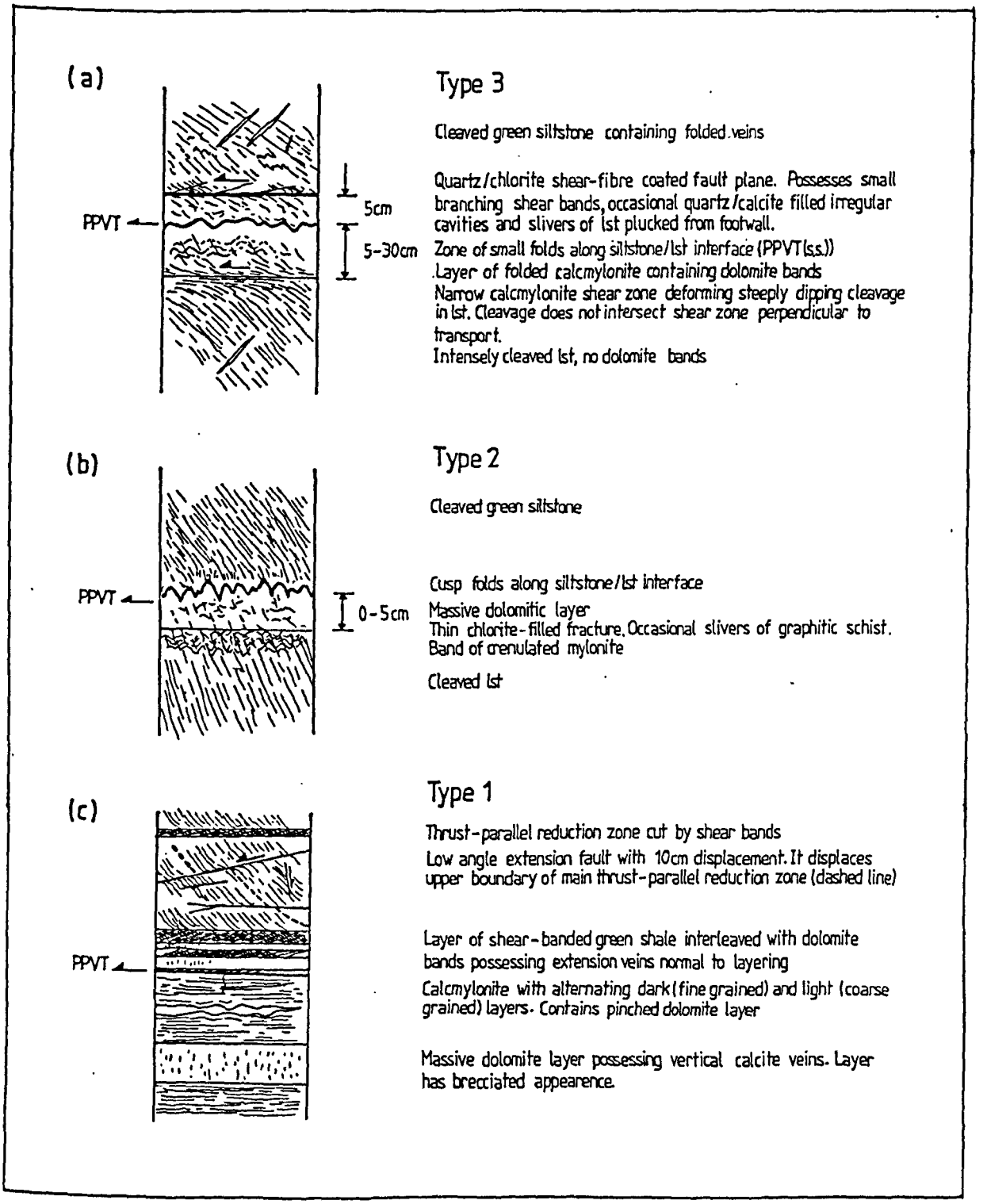

Figure 4.43. Fault-rock assemblages developed along the PPVT. The type 3 assemblage (a) occurs along the back-limbs of the fold structures. The type 2 assemblage (b) occurs along the forelimbs of the fold structures. The type 1 assemblage (c) occurs along the summit klippe and along parts of the Soum de Barroude section.

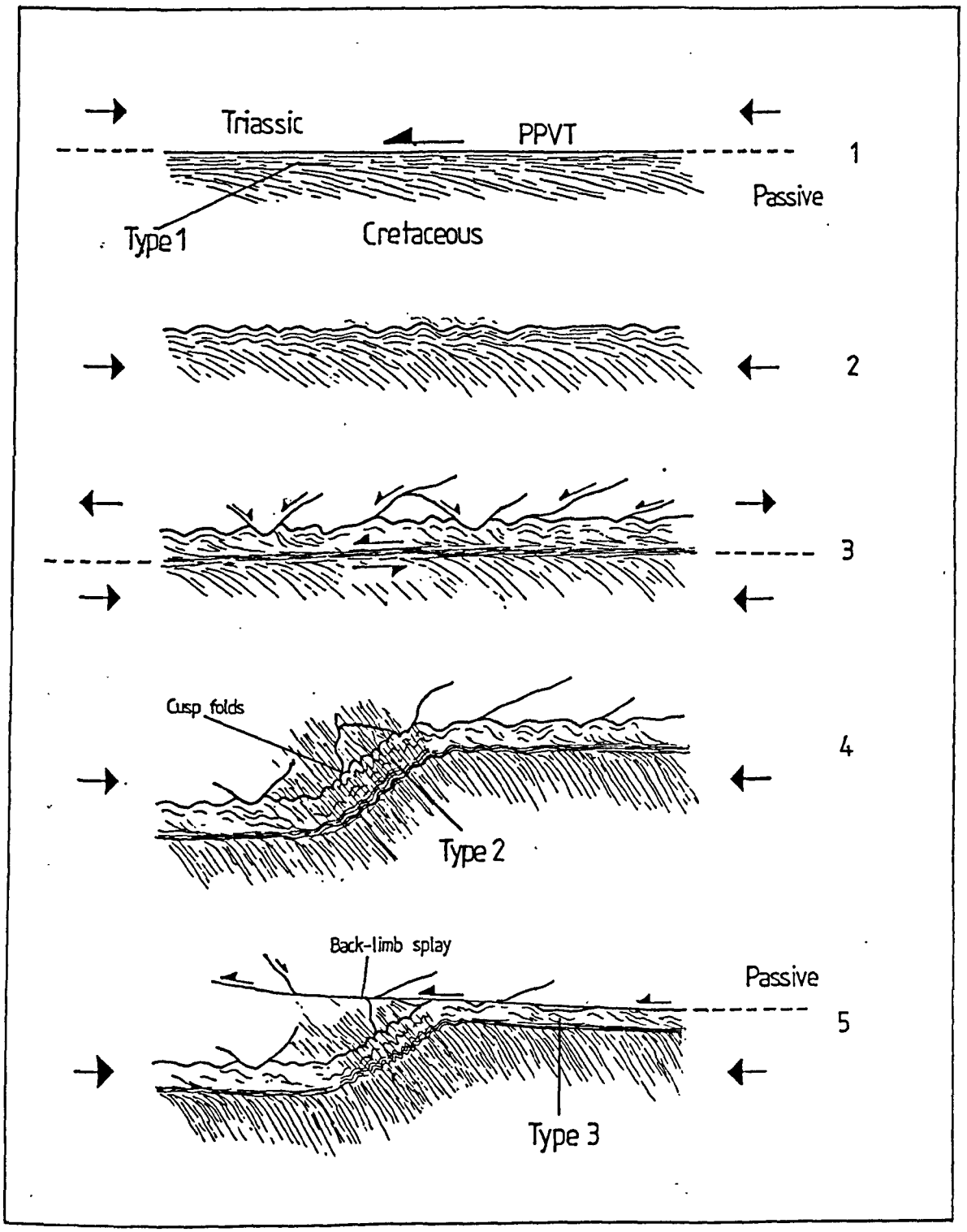

Figure 4.44. Sequential model to explain the evolution of the types 2 and 3 fault rock assemblages along the PPVT. 1. Emplacement of the PPVT produces a mylonitic foliation in the Cretaceous limestone (type 1 assemblage). 2. When thrusting switches to the footwall strata the overlying PPVT starts to fold. The thrust contact acts as an interface between two semi-infinite half-spaces and small corrugations develop. 3. A two-plate framework becomes established with extension in the PPVT occurring synchronously with the shortening in the footwall. The extension detaches along a mylonitic shear zone in the limestone that propagates adjacent to the folded thrust contact. 4. Major folding of the thrust then occurs associated with continued shortening on the footwall thrusts. The earlier shear zone is overprinted by cleavage formation on the forelimbs of the folds. This represents the type 2 assemblage. The original corrugations in the thrust contact tighten and become cusp folds. 5. The PPVT is reactivated by an upper strain detachment on the back-limbs of the folds. The brittle fault slices through the earlier corrugations and produces the type 3 assemblage.

assemblage records two phases of reactivation of the thrust, an early ductile phase that produced the calcmylonite shear zone, and a later brittle phase associated with the development of the back-limb splays. The inferred deformation sequence is summarised in (figure 4.44). The significance of this sequence is placed in the context of the development of the culmination in the section 4.6. 4.3.

4.5. Fourth Phase Thrusts.

It has been pointed out during the discussion of the P3 structures that many of the faults associated with the PPVT or which have formed directly in the footwall of the thrust possess a bimodal shear fibre lineation distribution. The first lineation is either south directed or it is directed SSW. The second lineation always cross cuts the first and is consistently oriented 30 to 40 degrees counterclockwise of the first movement azimuth. This SSE movement event occurs on a plethora of faults that are unlikely to have all formed and moved simultaneously eg. normal faults in the summit klippe, contractional faults in the ridge klippe, and discontinuous thrusts in the strata above the BIS. The fact that all these faults show the same second lineation suggests they were all reactivated together subsequent to their formation. This reactivation is tentatively ascribed to a fourth phase of thrusting. This deformation event appears to have been some form of distributed shearing possibly localised along the base of the PPVT/GT. It did not affect the structures in the BIS/BTFZ.

4.6. Discussion of the structure of Pic de Port Vieux.

4.6.1. *Fault sequence in the culmination.*

Two general models are forwarded for thrust propagation sequences (Boyer and Elliott, 1982; Butler, 1987): **foreland or piggy back propagation** where successive thrusts form in the footwall of the preceding thrusts, and **hinterland or break-back propagation** where the succeeding faults form in the hanging wall of the earlier thrusts. In addition **out-of-sequence thrusts** (Morley, 1988) are defined as thrusts whose movement is out-of-sequence with regard to the overall fault propagation sequence in the thrust system. Out-of- sequence thrusts can be either foreland or hinterland propagating. **Thrust breaching** (Butler,op.cit.) occurs where a later thrust cuts across and displaces earlier overlying thrusts. It can can lead to further complications especially where the later thrust is observed only in the hanging wall of the breached thrust. It then appears to be either a break-back thrust or an out-of-sequence thrust rather than a foreland propagating thrust.

The general thrust sequence within the PPV culmination (P1-P3) is overall foreland propagating although this is complicated by the breaching involved in the

emplacement of the GT and PPVT. Thus, locally within the culmination (eg. in the middle fold structure) the GT and PPVT appear to be out-of-sequence. However, because they emplace older strata (Hercynian basement and Triassic) over younger, they are still in-sequence. The folding of the PPVT and GT by the BIS related deformation (P3) again represents foreland propagation. The P4 thrusting is however out-of-sequence as it involves a late-stage reactivation of structurally higher thrusts.

Complications do however occur within this overall framework and can be clearly seen with regard to the fold structures.

As already shown, the lower fold structure is a tip fold associated with an inferred discontinuous thrust that propagated within the Triassic strata above the BIS (fault B, figure 4.32). This fault terminates within the Cretaceous limestone and cuts across an earlier fold train. The fold train can be related to a phase of initial distributed shortening associated with the development of the BIS. After fault B formed, it was gently folded (splay 1, figure 4.33) and then moved subsequent to this folding (splays 2 and 3). It therefore appears to have had two phases of movement or it appears to have moved continuously during the late-stages of the folding. This suggests that fault B formed and moved during only part of the movement history on the BIS.

A similar argument can be shown to apply to the back-limb splays on the PPVT that formed across the lower fold structure. Fault 5 (figure 4.32) represents an early BLS that was folded before movement on the larger splay fault C. The other secondary faults 1,2, and 3 within the forelimb portion of the PPVT may also have had origins as back-limb splays as they do not breach the PPVT but branch onto it. They possibly formed across the crests of the folds in the PPVT associated with the initial fold train. Fault Y represents one of these splays that was not deformed by the later tip fold of fault B. The presence of the back-limb splays indicates that the PPVT moved during and/or after the early fold train formed, and also during and/or after the larger tip fold formed. This movement is locally out-of-sequence with regard to the individual folds. It can be considered in-sequence with the development on the BIS however, because the movements are related to the overall distributed shortening above this structure via localised strain detachments (see below).

What is therefore being witnessed is a diachroneity in movement of faults that do not appear to physically link but whose displacements are linked through the medium of distributed straining above the BIS. In such a situation the concept of thrust propagation sequences break down. By changing the scale of observation an out-of-sequence thrust with respect to one structure can become an in-sequence thrust with respect to another structure that was ultimately responsible for producing the first structure. This

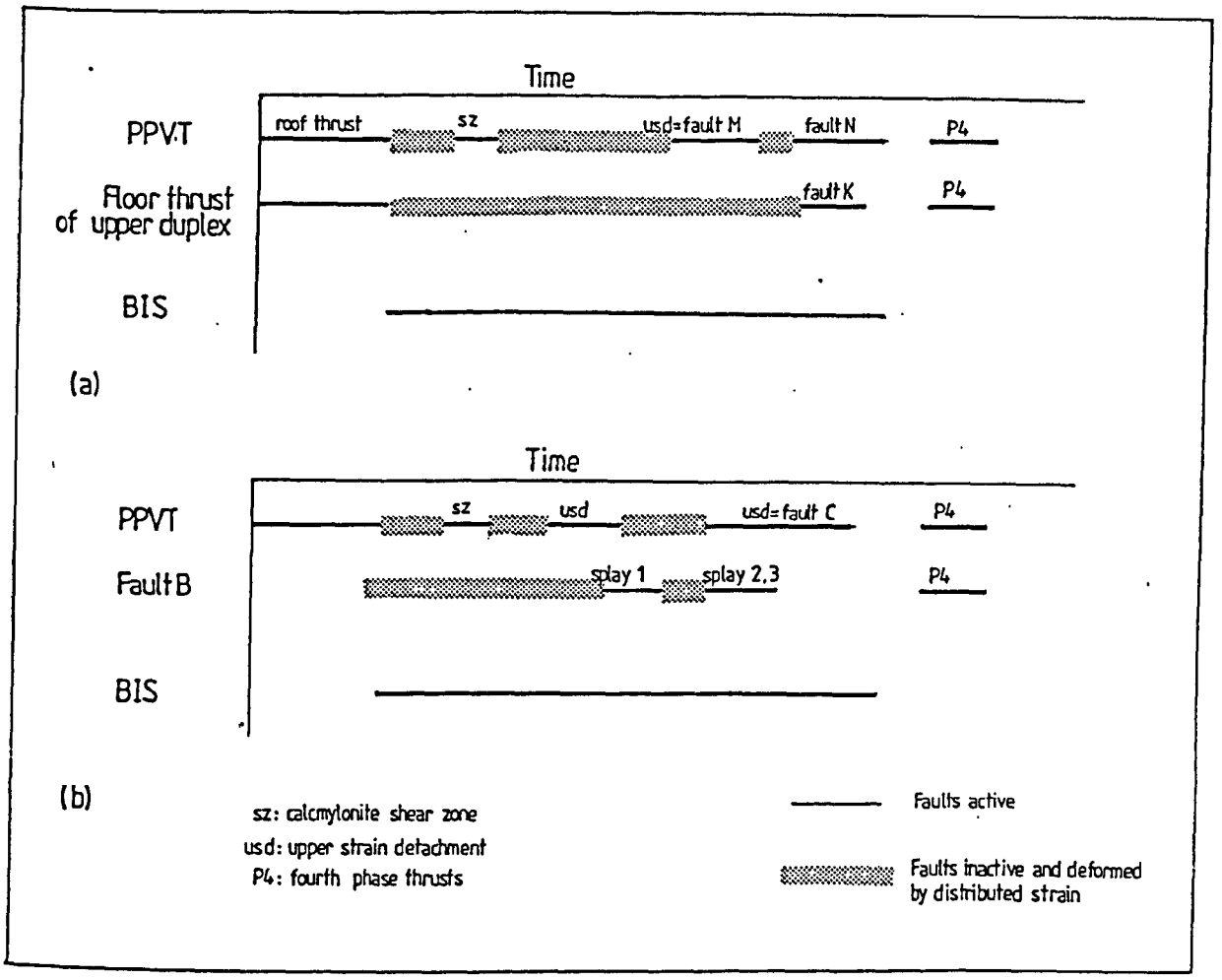

Figure 4.45. Fault-movement-time diagrams for the upper duplex (a) and the lower fold structure (b). In these diagrams time is plotted horizontally and the relative physical position of the thrusts plotted vertically. A line represents fault activity (localised deformation) the dotted bands represent periods when the faults are inactive or have not yet formed and the rock is deforming by cleavage development.(distributed deformation). The time-scale is only qualitative but is considered similar for each structure. The sequences of fault movement have been worked out from the superposition of structures. In both cases the PPVT has had a multiple movement history. It was initially active as the roof thrust to the upper duplex before the fault activity switched to the basement imbricate stack (BIS). During the movements on the BIS, the PPVT was reactivated first by formation of a shear zone in the footwall limestone and then as localised back-limb splays associated with the development of upper strain detachments. Fault B in the lower fold structure and fault K in the upper fold structure were also reactivated late in the movement history (they deform the cleavage) and cut across earlier formed folds. The diagrams portray the diachroniety of fault movements in the strata above the BIS.

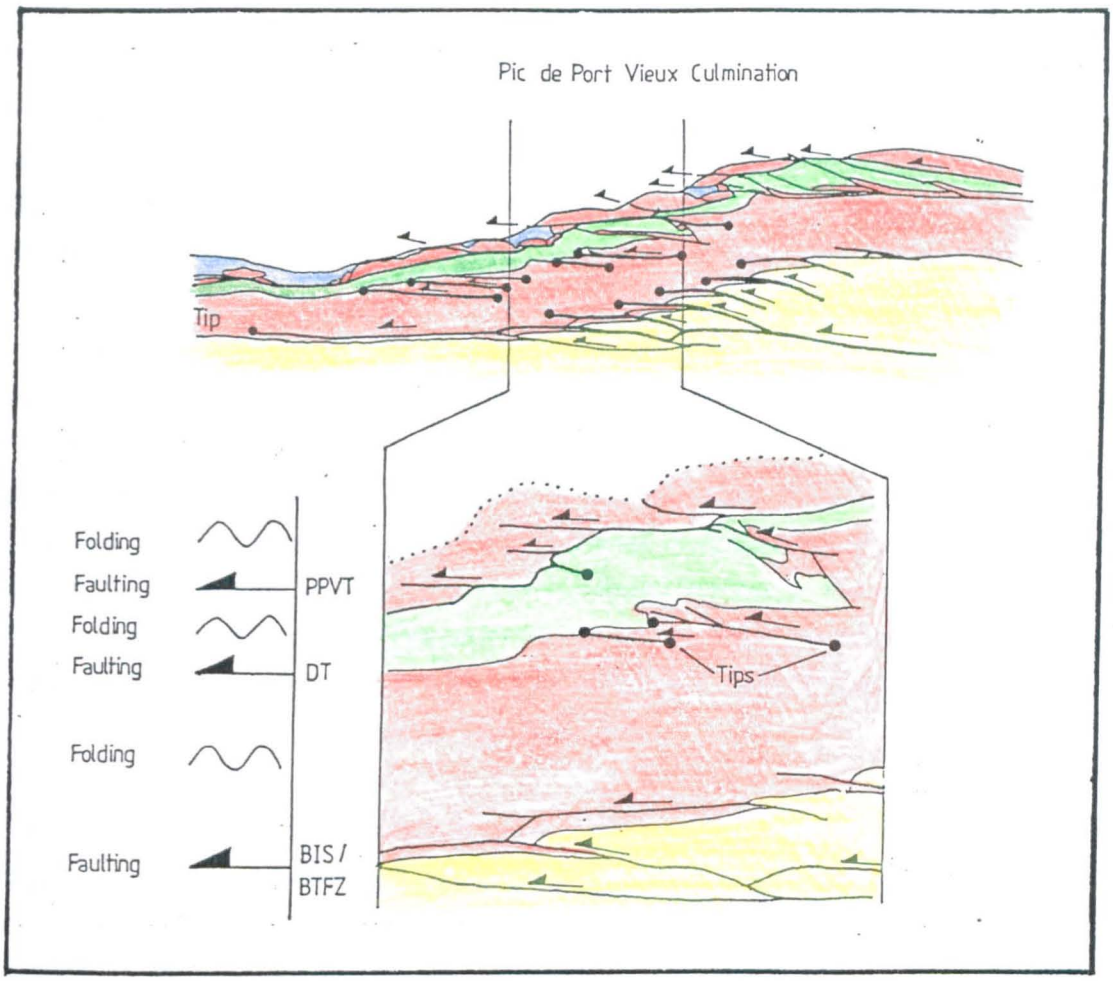

Figure 4.46. Definition of the two fault-fold-fault transitions in the PPV culmination. The transitions occur across both the Triassic cleaved shales and the Cretaceous limestone above the BIS. The strain detachments occur adjacent to the main lithological boundaries and suggest that these contacts played an important role in localising the thrusts. The contacts were however folded prior to the development of the strain detachments and thus changed from passive to active during the deformation. DT: discontinuous thrusts.

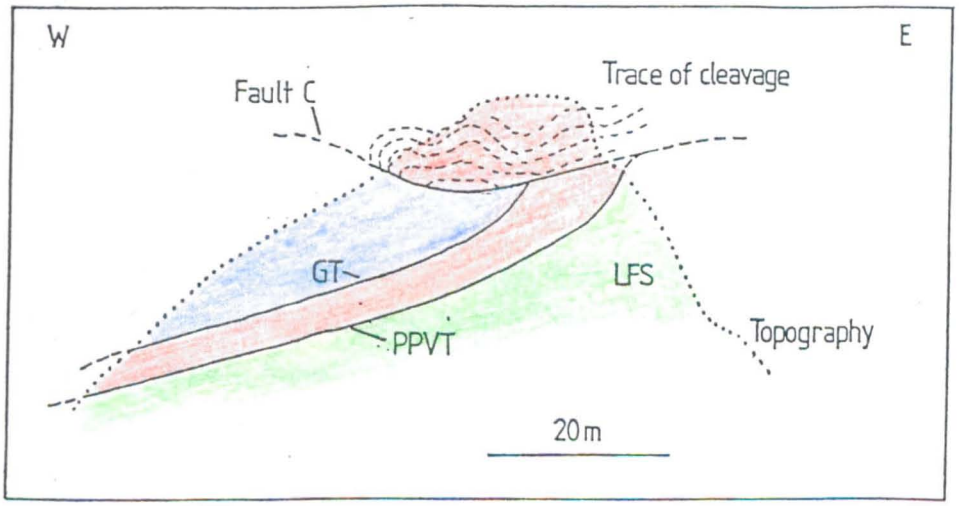

Figure 4.48 E-W cross section across the lower fold structure. The trace of the folded cleavage in the hanging wall of fault C is marked. The folds detach onto the thrust which has a concave-upwards profile. Movement over this fault surface is considered to have been responsible for the folding.

can be schematically portrayed in the form of a fault movement-time diagrams (figure 4.45).

In the upper fold structure/upper duplex an equally complicated movement sequence is developed with individual fault displacement episodes interspersed with periods dominated by more distributed strain. Prior to the formation of the large monocline, a first phase of movement developed within the upper duplex. More distributed shortening (including the development of the monocline) then deformed the thrusts and produced the present-day cleavage distribution in both the limestone and in the overlying PPVT sheet. The floor thrust at the front of the duplex (fault 6, figure 4.37) appears to have been reactivated during this shortening and breached the PPVT. This localised brittle deformation deformed the cleavage in the Cretaceous limestone within the upper fold structure. The earlier formed splays in the duplex remained however passive. At more-or-less the same time an upper strain detachment formed on the PPVT and is recorded by the movement on first fault M and then fault N (figure 4.39). A late stage break-back movement (Butler, 1987) appears to have occurred on fault 2 within the duplex and breached the PPVT at the crest of the culmination.

The fold structures do not interfere and it is therefore difficult to to determine their relative ages. The fact that both possess thrusts that deform cleavage and thrusts that were deformed by the more distributed shortening associated with the BIS suggests in all probability that they formed contemporaneously.

4.6.2. Cleavage-fault interaction.

The distribution of cleavage and faults in the PPV culmination suggests that two fault-fold-fault transitions occur within the structure (figure 4.46). The first represents the change from displacement on the BIS thrusts to shortening in the Triassic strata and back to discontinuous displacements on the thrusts that formed adjacent to the Cretaceous unconformity. The second transition occurs across the Cretaceous limestone with shortening transferred back onto slip on the PPVT to form the back-limb splays. Both these transitions represent localised upper strain detachments.

A simplified model explaining how an upper strain detachment works is shown in figure 4.47. The model requires the localisation of a fault within the zone of distributed strain that then propagates both forwards and backwards and transfers the zone of distributed strain further towards the foreland. The discontinuous thrust probably localises near a material inhomogeneity that was either pre-existing or which developed during the distributed deformation.

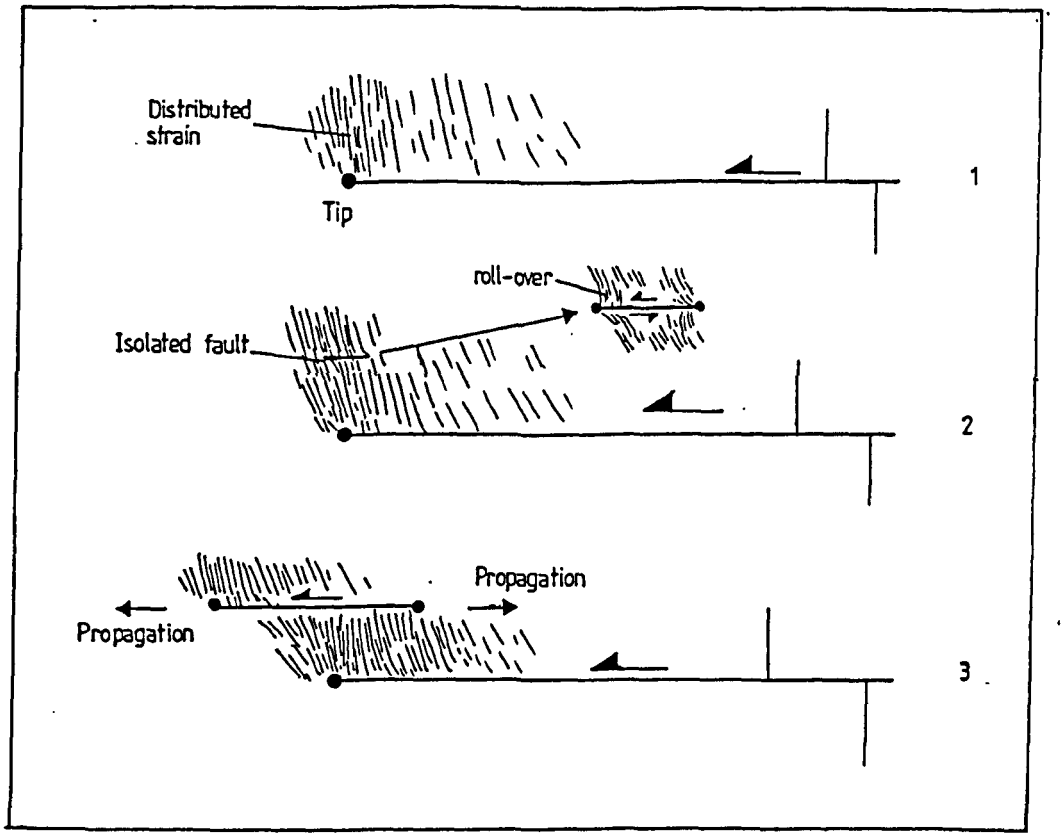

(a)

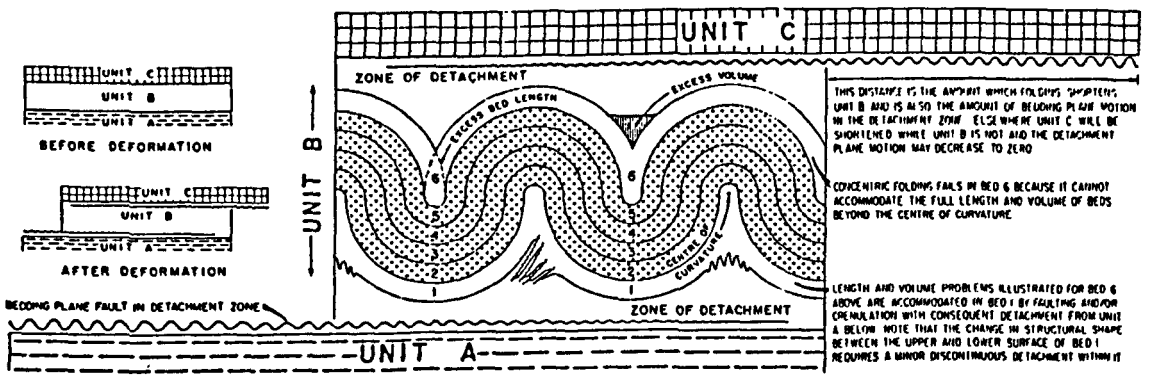

(b)

Figure 4.47. Models for upper strain detachments during thrusting. a) Model for the PPV culmination. 1. A zone of distributed strain develops at the tip of a fault. 2. At some stage during the deformation a small isolated fault localises within the tip zone. This fault deforms the earlier formed cleavage 3. The isolated fault propagates both forwards and backwards as the displacement on the lower fault continues. This has the effect of transferring the zone of shortening further toward the foreland. b) The detachment in concentric folding model of Dahlstrom (1969, figure 31).

The model is a modification of the 'upper detachment in concentric folding' model of Dahlstrom (1970) which is shown for comparison in figure 4.47b. Dahlstrom considered that the space problems associated with concentric folding in thrust belts could be accommodated by lower and upper detachments. The displacement on a lower detachment was transferred via the zone of folding into displacement on the upper detachment. In the PPV culmination, the upper detachment on the PPVT did not form as a means of accommodating concentric folds within the culmination. The folding that did developed was restricted to small buckle folds in the bedded strata adjacent to the Cretaceous unconformity. Shortening was primarily accommodated by cleavage development (distributed strain).

Morley (1987) used an upper detachment model to explain vertical strain variations in the Osen-Roa thrust sheet. He considered that detachment can occur where a competent unit is deformed independently above an incompetent unit; where the reverse situation occurs a detachment should not develop because the competent unit will exert a much stronger influence on the style of deformation. The detachment along the PPVT therefore appears anomalous because the cusp folds along the thrust contact indicate that the PPVT sheet was less competent than the underlying limestone during the distributed shortening.

From the discussion of the fault sequence in the culmination it appears that the upper strain detachment mechanism operated episodically on the PPVT and on a number of other thrusts (eg fault B and fault 6 within the upper duplex). In the intervening periods the faults were folded eg. cusp folds developed along the PPVT. This behaviour could reflect localised cycling of strain rates and/or fluid pressures in the fault system. Fast strain rates would favour faulting, slower rates folding and cleavage development. Alternatively an increase in fluid pressure could weaken the rock and allow it to fail. If this pressure were to decline then the rock would appear to harden. If the differential stress did not increase the deformation would switch back to being more distributed. Lithostatic fluid pressures are indicated by the presence of hydraulically fractured breccias and cavities along faults in the culmination. It is possible that fluid pressure cycling within the system contributed to episodic fault movements.

4.6.3. Cleavage attitude and tip strain within the culmination.

The cleavage in the Triassic and Cretaceous strata within the PPV culmination is approximately 45 degrees clockwise oblique of the cleavage that would be expected for the north-south thrust transport recorded by the shear fibre lineations in the BIS and BTFZ. The cleavage orientation also changes across the BTFZ and is more oblique in the hanging wall than in the footwall (figure 4.25). A fanning of cleavage also occurs from SE-NW to E-W towards the north of the upper duplex (figure 4.40) and a similar but reverse

fanning occurs south of the culmination along the Soum de Barroude section. These changes in cleavage strike are accompanied by an increase in dip and an increase in the intensity of the cleavage within the culmination.

The steepening and intensification of cleavage in the culmination reflects the distributed shortening in the structure associated with the loss of displacement on the imbricate splays in the BIS. This can be equated with leading tip strain. The rotation in cleavage strike indicates the presence of a dextral longitudinal shear component within the culmination and is indicative of a component of lateral tip strain (Sanderson, 1982; Coward and Potts, 1983). The combination of leading and lateral tip strains implies that the thrusts within the BIS tip obliquely within Pic de Port Vieux. This is supported by the absence of imbricate thrusts within the basement on the west side of the mountain. Accordingly, the basement thrusts responsible for the PPV culmination cannot link to the other thrusts that produced the Lower and Upper Troumouse duplexes in the Cirque de Troumouse.

4.6.3.1. Movement Directions on the Thrusts.

The first shear fibre lineations that developed on the discontinuous thrusts responsible for the fold structures and on the back-limb splays within the PPVT sheet consistently record movement towards the SW. This is clockwise of the regional movement direction and the movement direction of the thrusts in the BIS. Two possibilities exist: either these lineations were rotated passively during the oblique strain in the culmination, or they are unrotated and record a rotation in the movement direction of the faults due to the oblique strain. The latter situation is predicted by modelling by Gardener and Spang (1973) and from oblique fold axes in thrust belts by Coward (1984) and Ridley, (1986).

It has already been shown that the many of the faults that possess the oblique slip directions developed after the cleavage in the limestone ie. after a significant proportion of shortening had occurred in the culmination. The timing of the movements has also been shown to be synchronous with continued distributed shortening. It seems likely therefore that the movement directions on the faults record the oblique strain field in which the displacements took place ie. they are unrotated and record the rotational movements that must occur about a lateral fault tip (cf Coward, 1984). It is difficult however to categorically prove that the lineations have not been rotated.

4.6.3.2. Cleavage Discordance across the Pic de port Vieux thrust.

Apart from the fanning of cleavage within the upper duplex, the cleavage in the footwall of the PPVT has a relatively uniform attitude within the culmination. This contrasts markedly with the cleavage attitude in the ridge klippe of the PPVT sheet which is locally

folded about a N-S axis (figure 4.21). The deformation is most pronounced in in the hanging wall of fault C although a general discordance in cleavage attitude occurs across the PPVT through out the ridge klippe.

The N-S folding does not coincide with the NW-SE trending footwall structures. Mapping has shown that fault C (figure 4.32) has a concave-upward shape (figure 4.48). Movement over this fault surface could have generated the lateral shortening responsible for the folded cleavage. The fault surface would have been akin to two converging lateral ramps. An alternative interpretation is that fault C is folded by the lateral wall of a structure west of the mountain (cf. Butler, 1982b) and that this deformed the cleavage. This seems unlikely however because the underlying PPVT is not folded. The former interpretation is considered more feasible. The final attitude of cleavage in the PPVT sheet appears to been the result of the interplay between the distributed shortening and the later movement on the strain detachment that formed the back-limb splays.

4.6.4. The deformation sequence in the Pic de Port Vieux Thrust sheet.

4.6.4.1. The vein record.

The earliest veins in the PPVT are veins folded by the cleavage- related shortening (vein association 1). They are shear veins and presumably formed during early shear displacements in the strata. Whether these displacements were related to P1 or the P2 thrusting is not known. The veins must have formed oblique to the plane of bedding to have been deformed by bedding-parallel simple shear. The fact that these veins were boudinaged during cleavage development also suggests that they behaved passively during much of the shearing and probably rotated into their present orientations. They did not form by shear along the cleavage. The veins may originally have been shear bands or R1 shears that developed in the mudstone beds.

The cleavage normal veins (association 2) are extension veins that occur as swarms of thin veinlets in the mudstone beds. Some of these veins are deformed by the cleavage and in thin section can be observed to be truncated by pressure solution seams. This implies a dynamic relationship between the veins and cleavage. The veins probably formed parallel to the σ_1 principal stress direction (this would have been approximately parallel to the incremental shortening direction during cleavage development (Onash, 1983)). The veins probably developed in response to transient strain discontinuities and their presence solely in mudstone and siltstone beds may reflect higher strain rates in these lithologies (cf. Beach and Jack, 1982).

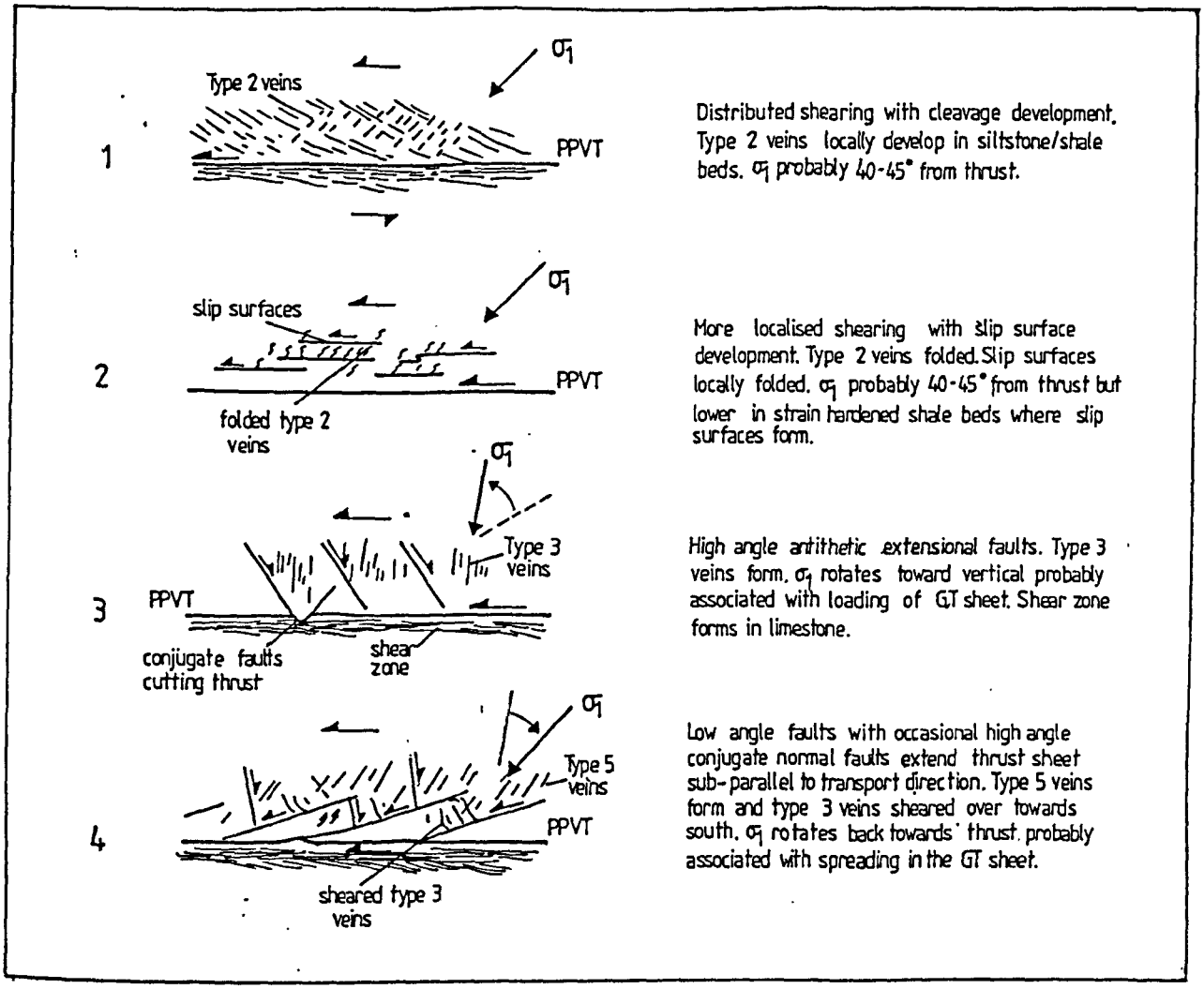

Figure 4.49. Sequential model to explain the relationship between vein orientations in the summit klippe of the PPVT and the inferred σ_1 direction. 1. The type 2 (cleavage normal veins) form during distributed shearing in the thrust sheet. The σ_1 direction was probably oriented 40-45 degrees to the thrust. 2. The deformation switches from cleavage development to shearing on bedding-subparallel slip surfaces. The σ_1 stress direction with respect to the thrust probably remained unchanged although it may have locally rotated to shallower angles in the mudstone beds where the slip surfaces formed. 3. Development of type 3 veins and high angle antithetic normal faults. The σ_1 stress direction rotated towards the perpendicular to the thrust and a shear zone decollement developed in the limestone in the footwall of the thrust. The rotation in σ_1 stress was probably associated with the loading of the GT sheet. 4. The development of the type 5 veins points to a rotation of σ_1 back towards the thrust. This rotation was σ_1 associated with the development of the low angle synthetic extension faults. The rotation in σ_1 stress is interpreted to reflect the switch from loading to spreading in the GT sheet.

The third vein association (steeply dipping planar extension veins) cuts across the discrete bedding-parallel slip surfaces. Although deformed by shearing associated with the low-angle normal faults, these veins always possess a steep attitude. They record a rotation in the σ_1 principal stress direction towards the perpendicular to the thrust.

The subhorizontal planar extension veins (association 4) formed in back-shear zones that possess identical orientations to the synthetic shear zones responsible for vein association 5. Two possible scenarios can be forwarded to explain the occurrence of these back-shear zones:

1. They could represent attempts to form back-thrusts. These faults may form above locked portions of active thrusts (Butler, 1982a). If the shear stress on the PPVT locally decreased but the the fault continued to move elsewhere, localised back-shear zones may have developed.
2. They could represent accommodation structures that preserve compatibility within the fault blocks during fault movement. The fact that some of the type 4 veins cut across type 5 veins but are themselves cut by the low angle faults suggests contemporaniety of formation with the low angle faults. This favours the second model.

The type 5 veins are oriented approximately 45 degrees to the synthetic shear zones and low angle faults (figure 4.18) . They were predominantly related to the tips of low angle faults (eg. figure 4.15) although some probably formed to accommodate local dilational strains associated with intrablock deformation. The change in orientation of the type 5 veins relative to the type 3 veins suggests that after originally rotating towards the vertical to produce the type 3 veins, the σ_1 principal stress then rotated back towards the thrust. The magnitude of this second rotation appears of the order of 30-40 degrees although the shearing of the type 3 veins during movement on the low angle faults prevents exact measurement. These rotations are summarised in figure 4.49.

The change from minor veining associated with cleavage development to large dilational veins later in the deformation sequence associated with mesoscopic fault arrays in the thrust sheet is similar to the deformation sequence documented in a thrust sheet from the external French Alps by Beach and Jack (1982). They used syntectonic vein arrays to interpret the deformation in the thrust sheet and found that the bulk of veins developed late in the deformation sequence when the thrust sheet behaved more competently. They infer that simple shear had ceased during the final stages of vein development when had rotated towards a steep orientation as a result of increased tectonic overburden. The change from early shear and cleavage related veins to large dilational veins associated with the progressive development of the different fault sets in the PPVT sheet is therefore very similar to that documented by Beach and Jack (op.cit).

Summary.

The deformation in the PPVT sheet appears to have changed from ductile (cleavage development and vein types 1 and 2) to more brittle deformation (faulting and vein types 3,4, and 5) with time. This was associated with first a rotation of σ_1 to near vertical (type 3 veins) and then a clockwise rotation of σ_1 back towards the thrust (type 5 veins). The development of the later vein sets may have occurred in response to changing environmental conditions or in response to strain hardening of the thrust sheet.

4.6.4.2. Fault arrays.

The first important discontinuities to form in the thrust sheet were the bedding-parallel slip surfaces. These possibly formed as C-planes within the shale beds and their presence suggests that the bedding anisotropy in the thrust sheet was inactive during their localisation. It is possible that higher strain rates in the mudstone beds were responsible for nucleating these discontinuities. A similar explanation was offered above to explain the cleavage normal vein swarms in the shale beds.

The slip surfaces were succeeded by the high angle extensional faults. Most of these faults tipped within the thrust sheet suggesting that they were active during the movement on the PPVT. Some however formed as conjugates to the low angle faults and cut the thrust plane eg. along the Soum de Barroude section. In addition high angle extensional faults are present in the ridge klippe even though in the same parts of the klippe low angle faults are absent. It is probable therefore that two generations of high angle faults developed in the thrust sheet:
1. an early set that formed during movement on the PPVT (sensu stricto); and
2. a later set that are conjugate to the low angle synthetic extensional faults. The fact that the low angle faults locally cut the PPVT (along Soum de Barroude) or fold it (along the summit klippe (figure 4.10a)) suggests that they formed when the PPVT plane (s.s) had ceased to be active. The calcmylonite shear zone in the limestone appears to have formed a decollement to this phase of faulting (see later).

4.6.4.2.1. Fault orientations.

a) High angle faults.

The majority of high angle faults in the PPVT sheet dip NNE and are extensional faults. These are unlikely to represent rotated R2 riedel shears because bedding in the thrust sheet was rotated clockwise during movement on the low angle extensional faults. This rotation would have prevented faults with an R2 orientation from attaining the observed orientation of the high angle faults. It is more likely that all the high angle faults formed as

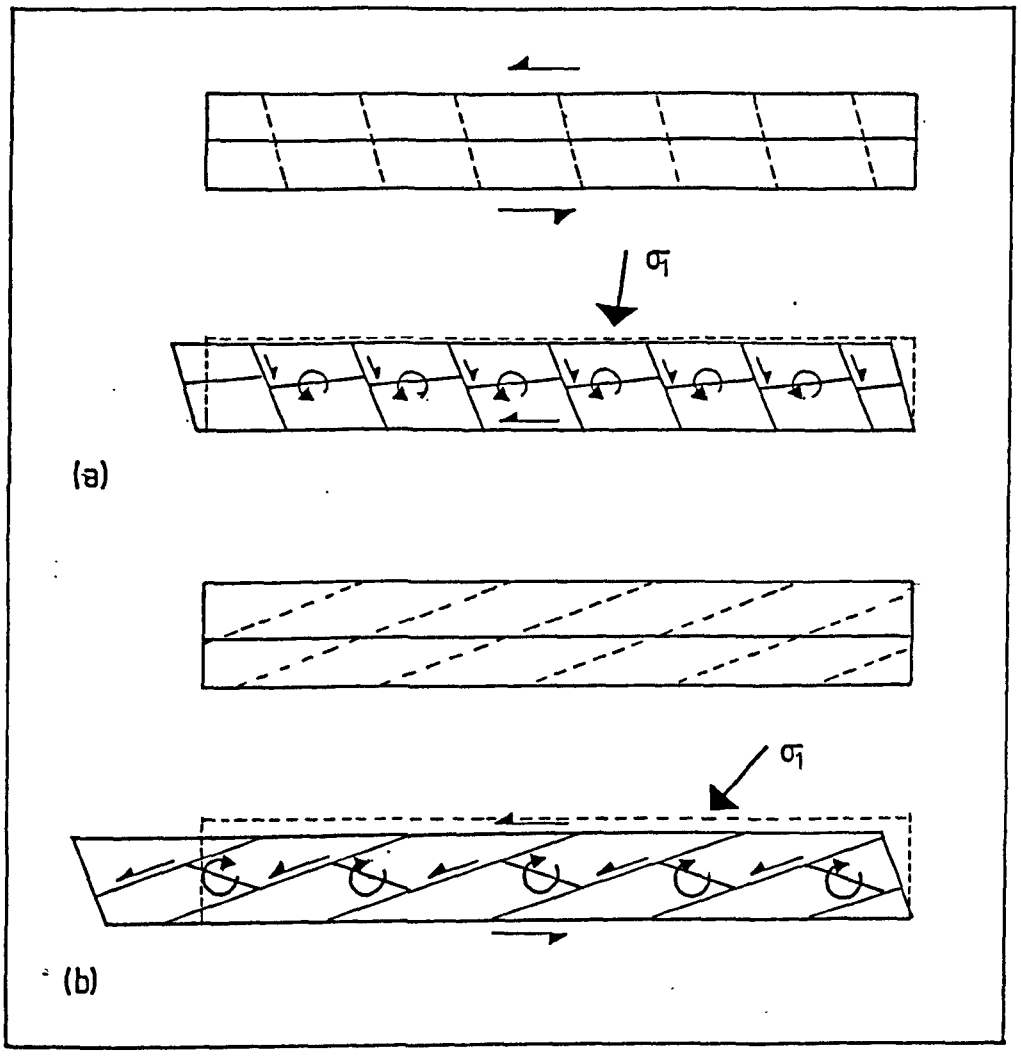

Figure 4.50. Domino model for the rotation of bedding between the high angle (a) and low angle (b) faults. In both cases the movement on the faults accommodates shearing and extension in the thrust sheet although the senses of rotation of the fault blocks are opposite. The inferred σ_1 direction is also shown. The greater extension occurs during movement on the low angle faults.

extensional faults within the thrust sheet. Where these are deformed it probably reflects heterogeneous intrablock deformation associated with movements on the low angle fault array.

The first generation of high angle faults that formed while the PPVT was active possess similar orientations to structures observed in sheared fault gouge by Logan et al., (1979) and referred to as X shears. These faults form conjugates to principal displacement shears (Y shears or C-planes). It is possible that the first generation of high angle faults formed to accommodate shearing and a component of flattening in the thrust sheet by a process of domino sliding (figure 4.50).

b) The low angle extensional faults.

Price (1977), Coward (1982) and Coward and Potts (1983) consider that low angle extensional faults in thrust sheets must have propagated backwards from the thrust and define fault enclosed units commonly referred to as a surge zones. The low angle faults in the PPVT sheet did not branch from the thrust but developed as discontinuous faults within the sheet that during propagation, branched onto the thrust. This is indicated by the displacement distribution on the faults and by the numerous minor faults that remained isolated.

The first lineations on the low angle faults indicate a movement directed approximately towards 200 ie. 20 degrees oblique of the original movement direction on the PPVT. Movement on the faults will therefore have extended the thrust sheet both parallel to and normal to the transport direction. The amount of extension is difficult to quantify due to the absence of suitable markers and uncertainties in the original thickness of the thrust sheet. This extension was accompanied by a rotation of bedding between the faults that suggests they also operated by domino sliding.

The faults possess orientations similar to R1 shears. These are the discontinuous Coulomb-Mohr faults that have been observed in the laboratory deformation of frictional-plastic materials (eg. Naylor, et al. 1986). In a frictional plastic material, faults form at $45 - \Phi/2$ to the σ_1 direction. During simple shear of such a material σ_1 is oriented at 45 degrees to the shear plane. Faults therefore subtend an angle of 17-20 degrees to the shear plane depending on the internal angle of friction Φ. An alternative origin for the faults is that they propagated parallel to slip lines in a layer of stratified plastic material sheared in the active state (Mandl and Shippam, 1981). It is unlikely that the PPVT sheet behaved plastically however because considerable dilatancy was associated with the deformation and the overall style of the faulting suggests that the thrust sheet behaved as a relatively competent unit. It is more likely that the faults represent R1 shears.

4.6.4.2.2. Fault distribution.

The distribution and intensity of the different types of mesoscopic extensional fault in the PPVT sheet changes across the culmination. The high angle faults appear to have a relatively even distribution in the thrust sheet. The low angle faults however have a much more heterogeneous distribution. They are more intensely developed in the summit klippe and Soum de Barroude sections than in the ridge klippe where only a few rotated low angle extensional faults occur. This fault distribution strongly suggests that the deformation responsible for the array of low angle faults occurred synchronous with the formation of the culmination.

The low density of low angle faults in the deformed forelimb of the culmination (the ridge klippe) probably reflects the early rotation of this portion of the thrust sheet out of an orientation suitable to accommodate the extensional strains that developed in the hanging wall of the thrust sheet. As the culmination continued to grow parts of the PVT sheet that were initially extended were then incorporated into the forelimb of the culmination and the extensional faults rotated. The distribution of these rotated extensional faults in the ridge klippe (figure 4.19) can therefore be used to suggest that the culmination propagated southwards with time.

The complete absence of low angle faults in the PPVT sheet above the upper duplex suggests that it pre-dated the extension and therefore also pre-dated the development of the BIS. This latter interpretation was also arrived at from a consideration of the cleavage-thrust relationships in the upper duplex.

Two end-member models can be forwarded to explain the extension in the PPVT sheet (figure 4.51):

1. Simple shear model. Simple shear along the base of the thrust sheet may be spatially partitioned into zones of coaxial stretching and zones of non coaxial flow (Lister and Williams, 1983; Platt, 1984). Sliding between and rotation of these domains preserves overall compatibility. Flow partitioning requires the presence of a material heterogeneity in the shear zone that in this case could have been represented by the competency contrast between the PPVT sheet and the Cretaceous limestone and Silurian phyllite. Partitioning of the flow field by slip along the thrust plane and along a discontinuity within the SGP formation could have allowed the thrust sheet to stretch coaxially while the limestone and overlying SGP formation deformed predominantly be distributed shearing (figure 4.51a).

2. Pure-shear model. This could involve extension within the thrust sheet (figure 4.51b) that is separated from the footwall strata by a decollement. In Pic de Port Vieux the decollement might be represented by the shear zone in the limestone. Oblate strains lead to extension in both the transport and transport normal directions while prolate

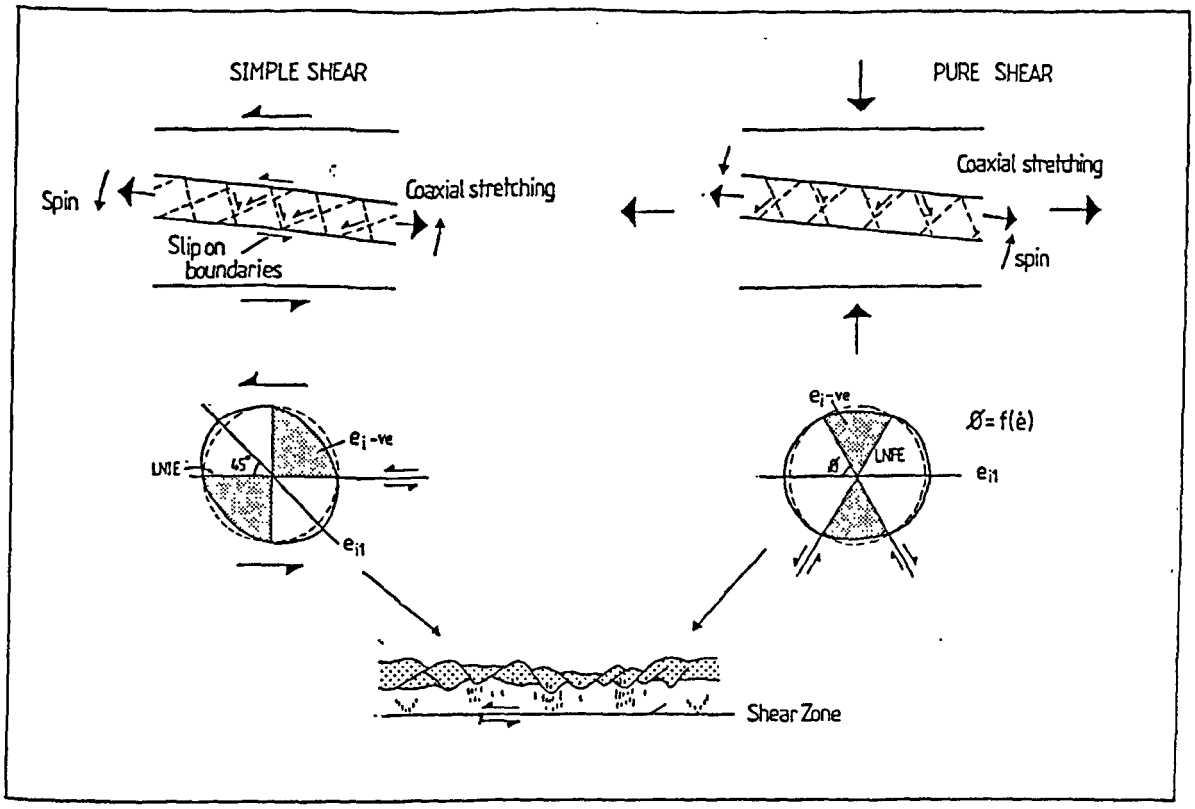

Figure 4.51. Possible end-member kinematic models to explain the development of the conjugate fault blocks in the PPVT sheet that extend the sheet parallel to transport. 1. Simple shear model. The PPVT sheet is considered an obliquely oriented competent unit deforming in a zone of distributed shear strain. Strain partitioning results in slip along the surfaces of the thrust sheet accompanied by extension of the sheet and spin (cf Lister and Williams, 1983; Platt, 1984). 2. Pure shear model. Flattening results in distributed coaxial extension in a zone along the base of the Gavarnie Thrust sheet. The competent PPVT sheet, originally oblique to the strain axes rotates and extends by conjugate faulting. The infinitesimal strain ellipses for both cases are shown. In the actual structure the extension detaches along a shear zone beneath the thrust. The presence of this shear zone cannot be explained by distributed simple shear along the base of the thrust sheet. Similarly the predominance of low angle extension faults in the thrust sheet disagrees with the pure shear model. It appears that a combination of both shearing and flattening best explains the actual structure.

strains favour stretching in the transport direction only. The extension would be most readily observed in a competent unit such as the PPVT sheet.

It seems that a combination of the pure and simple shear models may best explain the observed faulting in the PPVT sheet as the former does not explain the predominance of the low angle faults while the latter does not readily explain the presence of a decollement to the stretching. Kinematic models for this extension are discussed in section 4.6.6.

4.6.4.2.3. Comparisons with other thrusts.

Wojtal (1986) has studied the deformation associated with mesoscopic fault arrays from foreland thrust sheets in the southern Appalachians. He recognised three successive fault types:

1. Bedding-parallel faults;
2. low angle contraction faults;
3. high angle extension faults.

This classification refers to bedding in the thrust sheet and the high angle extension faults documented by Wojtal (op.cit.) have similar attitudes to the low angle faults documented in the PPVT sheet ie. they have synthetic movements with respect to the thrusting. The extension faults in the Appalachians are all oblique-slip faults.

The sequence of deformation documented by Wojtal (op.cit.) is first shortening and thickening followed by extension both parallel and normal to transport. He considers the deformation associated with the arrays of faults as a form of macroscopic grain boundary sliding and that the faulting acted as a grain size reducing mechanism. In an accompanying paper (Wojtal and Mitra, 1986), the displacement distributions on the mesoscopic faults together with the distributions of cataclastic fault rocks are explained in terms of strain hardening and softening within the thrust sheet. An increase in the width of the zone of mesoscopic secondary faulting with increasing displacement on the thrusts is considered by Wojtal and Mitra (op.cit.) to reflect strain hardening within the thrust sheet. They suggest that this might reflect a Hall-Petch relationship between fault block size and tectonic stress. Strain softening is considered to have operated in localising displacement onto the largest contraction faults in the mesoscopic arrays.

The fault arrays studied by Wojtal (1986) differ from those developed in the PPVT sheet in that high angle antithetic faults are absent from the Appalachian sheets whereas contractional faults are generally absent from the PPVT sheet. This difference can be explained by inferring an absence of initial internal shortening (associated with contraction faults) in the PPVT sheet: the strain history appears to have been dominated by thrust-parallel simple shear prior to formation of the extensional faults. Otherwise the

fault patterns in the thrust sheets are similar. The oblique slip on the low angle faults in the PPVT sheet is also similar to that documented by Wojtal on the high angle faults in Appalachian thrust sheets and probably records a similar component of flattening.

A significant difference between the faults in the PPVT sheet and the faults in the Appalachian thrust sheets is in the nature of the fault rocks. All the faults in the PPVT sheet, regardless of displacement, show the same fault rocks (see section 4.4.3). Breccias that are locally present on the larger faults are related to fault cavities and not to cataclasis during sliding on the faults. It is unlikely therefore that some form of grain-size sensitive strain softening mechanism, as envisaged by Wojtal and Mitra (1986), localised displacement on the larger low angle faults in the PPVT sheet. The larger faults are simply more likely to be the ones that had the longer displacement activity.

The final difference in the Appalachian and PPVT fault arrays is possibly one of timing with respect to thrust movement. The main extension that affected the PPVT sheet can be shown largely to have post-dated emplacement of the thrust sheet. Wojtal (1986) considers that the flattening observed in the Appalachian sheets occurred during the movement on the thrusts.

4.6.4.3. Fault rock assemblages.

The three assemblages recognised along the PPVT record the different deformation sequences that affected different parts of the PPVT within the culmination. The type 2 and 3 assemblages developed from the type 1 assemblage during the successive reactivation of the PPVT associated with the development of the upper strain detachment in the culmination. The general deformation sequence has already been outlined and summarised in figure 4.45.

The PPVT contact was gently folded prior to the development of the shear zone in the limestone directly beneath the fault. This early folding was presumably associated with the initiation of the upper duplex and BIS in the footwall of the thrust. The shear zone therefore represents a first strain detachment along the thrust. It also appears to represents a mechanical boundary between strata that was extending in the hanging wall and strata that continued to shorten in the footwall of the PPVT. This kinematic framework is indicated by the fact that none of the conjugate faults in the PPVT sheet cut the shear zone (eg. figure 4.12) and by the heterogeneous distribution of low angle extensional faults in the PPVT sheet.

The shear zone cuts down section in the limestone in the direction of transport (figure 4.12). This feature may have resulted from:

1. A thrust-sense shear zone cutting through strata that dipped more steeply north than the attitude of the zone; or
2. an extensional shear zone cutting sub-horizontal strata.

The former interpretation requires that southward tilting has occurred after the shear zone formed. This tilting did occur further north associated with the PPV culmination and it also affected the Soum de Barroude section but is later than movement on the shear zone. It is not possible therefore to show that the shear zone was contractional in origin. Platt and Leggett (1986) have documented thrusts cutting down section into their footwall by a mechanism that they refer to as footwall plucking. It is more likely, considering the development of extensional structures in the hangingwall strata, that the shear zone was extensional in origin rather than cut into its footwall by footwall plucking.

The shear zone was folded and overprinted by cleavage on the forelimbs of the fold structures within the ridge klippe. This attests to the continued shortening in the footwall strata after the extension in the overlying strata had ceased. As already mentioned the rotation of the ridge klippe above the lower structures was probably responsible for the absence of any extension in this part of the thrust sheet. The second upper strain detachment then formed on the back-limbs of the fold structures within the ridge klippe. This is represented by the brittle fault that cuts across the earlier formed folds along the PPVT contact in the type 3 assemblages. As already mentioned movement on this second detachment appears to have been episodic.

4.6.5. Summary.

The detailed mapping of the PPV culmination has revealed a complex deformation sequence that resulted in different structural styles developing in different parts of the culmination. The major division appears to have occurred along the PPVT with the PPVT sheet recording a different deformation history from the footwall strata. In particular the thrust sheet appears to have been extended in the transport direction synchronous with P3 shortening in the culmination. The extension was not a result of the thrust sheet stretching over the culmination (cf. Butler, 1982b) but appears to have occurred on a more regional scale, affecting, in particular, the thrust sheet outside the culmination.

The concurrence of the different deformation regimes (shortening and cleavage development in the basement and Triassic strata, and extensional faulting in the overlying PPVT sheet) implies that the PPVT and thus the GT represented a mechanical boundary between strata effectively belonging to the basement and being actively shortened, and strata that was deforming under different influences in the overlying nappe and being actively extended in the transport direction. The shortening in the culmination was largely the product of oblique tip strain associated with the loss of displacement in the BIS.

4.6.6. Comparisons with the Sierra Liena.

The deformation sequence in the PPV culmination of folding, localised to the forelimb of the structure, and later thrusting is similar to that developed on the Sierra Liena where the fold train is cut by the Esccores thrust. This may suggest a similarity between the overall structural framework of the PPV culmination and the framework for the larger regional culmination. It is therefore possible that the regional culmination is a product of folding above a blind imbricate stack of basement thrusts (see chapter 3). Faults such as the Escorres thrust are possibly discontinuities that formed within the tip zone similar to the discontinuous thrust that formed in the PPV culmination.

4.6.7. Tectonic models for the extension along the base of the Gavarnie Thrust sheet.

The extensional strains observed within the PPVT sheet are developed throughout its 1km long outcrop length. Where the thrust sheet is absent from the base of the Gavarnie thrust sheet a lack of other markers means that extensional strains are more difficult to observe. It is possible however that the large shear bands in the Silurian phyllite (figure 3.8) and some of the large extensional faults present in the Muraille de Barroude section (figure 3.6) may represent the same phenomenon. This section will address the question of how and why the extension occurred.

Extensional strains along the bases of other large thrust sheets have generally been inferred from the symmetry of mylonite fabrics in the fault zones (Law et al., 1984). The cross-girdle c-axis fabrics in these mylonites are taken to infer coaxial strains. Law et al., (op.cit) consider the observed flattening strains to be an example of natural deformation partitioning that could have been the product of:

1. Movement of a competent unit over a ramp (model A(i), figure 4.52a). A variation of this model is that the competent unit resists folding and results in thinning of the underlying weaker strata (model A(ii)).
2. Loading beneath a frontal culmination (figure 4.52b).
3. Extensional flow during gravity spreading (figure 4.52c).

The first model of Law et al., (op.cit.) is not directly applicable because the GT and PPVT sheets were already emplaced prior to the observed extension. The later folding of the GT sheet that produced the regional culmination (figure 3.5) could however have generated extension along the base of the GT sheet in response to the resistance to folding of the thrust sheet. This situation is similar to that shown in figure 4.52 (model A (ii)). The second and the third models can be treated together because in both it is the lithostatic load of the thrust sheet that produces the extension. In the second model the relaxation of the driving stresses for thrust emplacement allows the principal stress to

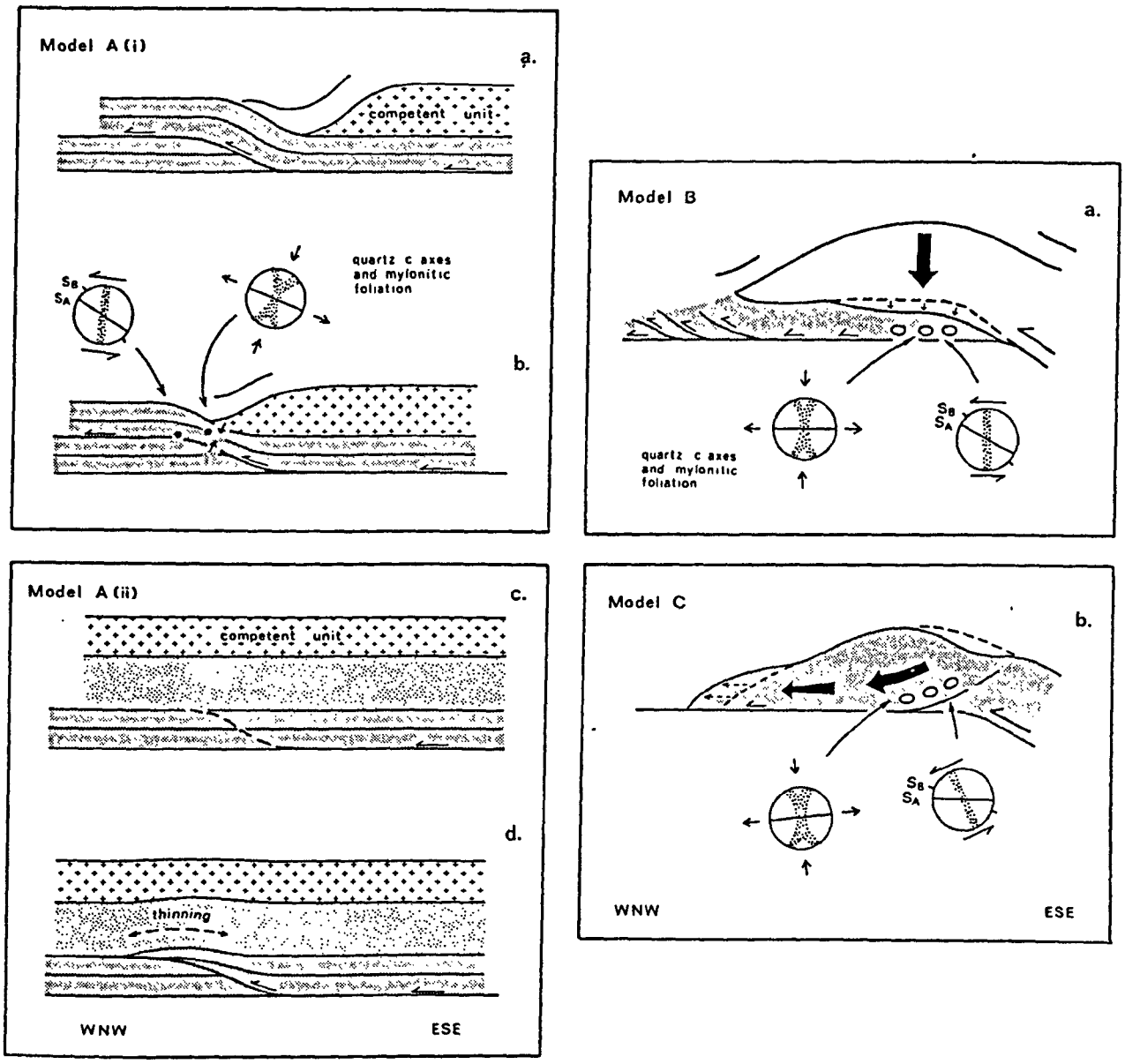

Figure 4.52. Tectonic models proposed by Law et al., (1984) to explain the development of coaxial deformation in a thrust sheet. Model A. (i) Thinning of incompetent material when a competent unit is transported over ramp. The thinning is envisaged to occur by strain partitioning in layers that are slipping with respect to one another. (ii) Thinning of a weaker unit in response to the resistance to bending of an overlying competent unit as the weak unit is transported over a ramp. Model B. Loading associated with the emplacement of a frontal culmination produces coaxial thinning of weaker footwall units. Model C. The coaxial thinning results from extensional flow associated with gravity spreading. Quartz c-axes and strain ellipses which may be associated with the deformation are indicated. Sa and Sb refer to the C- and S-foliations in an S-C mylonite (see Lister and Snoke, 1984). The thinning observed along the base of the Gavarnie Thrust sheet post-dates nappe emplacement. The most likely models that correspond to this deformation are either model A(ii) with the extension associated with the folding of the nappe during the development of the regional culmination (see figure 3.5), or model C in which the extension results from the action of gravity.

rotate towards the vertical in response to the load of the overlying thrust stack. In the third model the spreading of the thrust belt again occurs in response to the load but this model is less specific in terms of the tectonic framework.

In the PPVT the extension occurred while the strata beneath the nappe were actively shortening ie. the driving stress for thrust emplacement was still active. This suggests that model 2 of Law et al., may not be directly applicable. This leaves gravity spreading (model C). As discussed below the dynamics of thrust belts are compatible with the concurrent shortening and extension that is observed in Pic de Port Vieux and gravity spreading may ultimately have been the driving mechanism responsible for the extension.

A number of papers have recently been published that model the mechanical behaviour and properties of orogenic belts (eg. Elliott, 1976b; Chapple, 1978; Davis et al., 1983, Platt, 1986). They all start with the same assumption that orogenic belts can be treated as wedge shaped continua that show negligible yield strength. The main differences between the models concern the assumptions made with respect to the macroscopic properties of the belts. A comprehensive review of the different concepts involved can be found in Platt (1986).

Although orogenic wedges are expected to show complex nonlinear viscosity, Platt (1986 and 1987) has considered the simplifying assumption that the wedge shows macroscopic linear viscosity as this describes pressure solution (Rutter, 1976) which is probably the most volumetrically important deformation mechanisms in the upper crust. Using equilibrium theory Platt (op.cit) derived a stability criterion for wedges:

$$\tau_b = \rho g h \alpha - 2\tau_{xx}\theta - 2\frac{\partial \tau_{xx}}{\partial x}.h$$

This equation states that the downward traction exerted on the wedge by the crustal slab sliding beneath it is balanced by three terms:

1. A gravitational term produced by the surface slope α of the wedge. This is identical to the driving force for the flow of glaciers (eg. Elliott, 1976b).
2. The longitudinal shear stress τ_{xx} acting within the tapered wedge. It depends on the angle of taper θ (the sum of the angle of dip of the basal decollement and the surface slope).
3. The gradient $\partial\tau_{xx}/\partial x$ in the longitudinal deviatoric stress.

Internal deformation of the wedge results from processes such as accretion which change the shape of the wedge and produce instability. The particular case of interest here is the processes that can lead to thinning (extension) of the wedge. Extension will

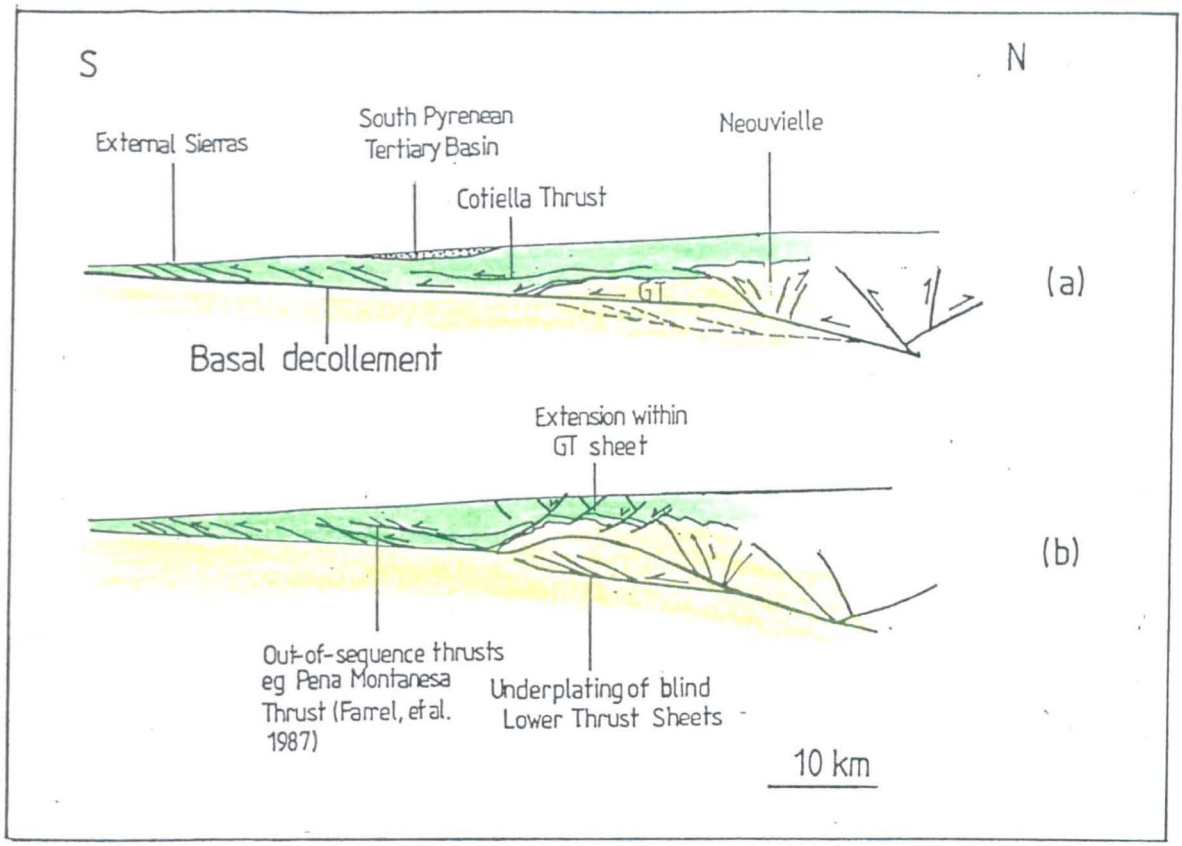

Figure 4.53. Possible dynamic orogenic wedge model for the south Pyrenees. Geometry of thrust belt adapted from Williams and Fischer (1984), Seguret (1972) and Ecors (1988). a) Configuration of the thrust belt prior to the movement of the lower thrust sheets. b) Configuration of the wedge after movement of the lower thrust sheets produces a blind imbricate stack. The Gavarnie Thrust sheet is folded into a large culmination. Extension is envisaged to occur within the GT sheet to preserve stability of the wedge during the formation of the culmination. The spreading in the Gavarnie Thrust sheet occurs either due to an increase in topographic slope or an increase in the dip of the basal detachment. Further towards the foreland the extensional flow produces out-of-sequence thrusts. Farrel et al. (1987) have shown that out-of-sequence movement occurred on the Pena Montanesa thrust and suggest that this was related to movement of the lower thrust sheets. Because the lower thrusts are blind (see chapter 3), the displacement on the Pena Montanesa thrust cannot link to the deformation further north. One possibility is that the movement on the thrust occurred in response to the extension in the GT sheet. Evidence for a dynamic wedge scenario comes from the observed simultaneity of extension in the GT sheet and shortening in the PPV culmination. On a larger scale, synchronously developing regimes of extension and shortening are predicted from stability analyses in accretionary prisms (eg. Platt, 1986a and 1986b).

occur when the gravitational term outweighs the sum of the longitudinal stress and deviatoric stress gradient terms in the above equation or if τb decreases. The former will occur if the topographic slope α is too large. One way of increasing both α and θ is to underplate at the rear of the wedge allowing the longitudinal stress to become become tensional (Platt, op.cit). A decrease in τ_b could occur during ductile yield (softening) along the base of the wedge. Softening could occur by a change to grain-size sensitive creep during dynamic recrystallisation (Schmid, 1983) or by the production of transient fine grained reaction products within the fault zone (White and Knipe, 1978; Rutter and Brodie, 1988).

One prediction from the Platt model is that gravity spreading in the higher portions of the wedge may occur concurrently with active shortening in the lower portions of the wedge. This agrees with the deformation observed in the PPV culmination which might represent an example of the transition zone between the two different tectonic regimes. An increase in topographic slope in the central Pyrenees associated with the movement on the lower thrusts that produced the regional culmination may have ultimately been responsible for the observed extension. A possible scenario is shown in figure 4.53.

Further work is necessary to constrain more clearly:
1. the regional extent of the extension within the Gavarnie Thrust sheet;
2. the time relationships between the extension and the development of the regional culmination.

4.7. General implications for other thrust belts.

4.7.1. The interaction between faults and distributed strain.

The study of structures in the PPV culmination has shown that in regions of distributed strain (in Pic de Port Vieux this strain is associated with a blind imbricate stack) fault sequences break down and more than one fault can move simultaneously. This results because localised upper strain detachments develop along pre-existing specific interfaces eg. earlier thrusts. The behaviour of these is however time-dependent and may change during the deformation due to either changes in strain rate, fluid pressure or as a result of strain softening or hardening (cf. Wojtal and Mitra, 1986). This may lead to episodic and diachronous fault movements. In the periods between fault slip episodes the faults may be folded by more distributed strain and the later movements that occur on the faults could lead to the production of back-limb splays as occurs along the PPVT.

It might be expected therefore that in other thrust structures or systems where significant distributed deformation (cleavage) accompanies the thrusting, that the specific

sequences of displacements on the faults will not necessarily conform to simple propagation models. In addition the faults may not all necessarily link to a basal decollement. Both these features have important implications for section balancing especially in the more internal regions of orogenic belts where distributed strain competes with thrusts and shear zones to shorten the crust. The ad hoc linking of all thrust to basal décollements may be an oversimplification of the actual fault distributions and could significantly overestimate the true shortening involved in mountain belts.

4.7.2. Fault propagation and interaction.

The process of fault interaction can be understood more readily on the scale of individual small faults. On the scale of the fault arrays as a whole it becomes much more difficult due to the complexity of the fault patterns. The main feature that is apparent from the different fault arrays studied in the PPV culmination is that a number of faults propagate simultaneously and it is the interaction of these faults that produces much of the complexities in the fault patterns.

The fact that the faults can often be demonstrated to have linked together during propagation eg. within the summit klippe and basement granodiorite fault arrays, suggests that many possess segmented displacement distributions. This agrees with the fault propagation model of Ellis and Dunlap (1988). Before they link together however complex patterns of linking and branching splays develop at the fault tips. Once a through going fault forms these splays may be transported along the faults as either horses or inherited fractures arrays. It is therefore not necessary that all the secondary faults associated with larger faults form as a consequence of displacement on the larger faults.

4.8. Summary and conclusions.

4.8.1. Deformation sequence in the Pic de Port Vieux culmination.

Four local phases of trusting can be identified in the PPV culmination:
P1. Minor imbrication of the Mesozoic strata.
P2. Emplacement of the Gavarnie and Pi de Port Vieux Thrust sheets.
P3. Development of the culmination.
P4. Oblique reactivation of some of the earlier thrusts.
The sequence P1-P3 is foreland propagating. P4 is an out-of- sequence event related to SE directed distributed shearing along the base of the Gavarnie Thrust sheet. The Gavarnie Thrust locally breaches the P1 thrusts.

4.8.2. Deformation in the Pic de port Vieux thrust sheet.

1. The overall sequence of deformation in the PPVT sheet changed from distributed shearing (cleavage development) to deformation that involved mesoscopic arrays of extensional faults.
2. Three different fault arrays are present in the PPVT sheet and are related to a progressive deformation sequence. This involved localised shear on bedding-parallel slip surfaces followed by transport-parallel and transport-normal extension. The extension was accommodated first on a set of high angle top-to-north faults and then on a set of low angle top-to-south faults.
3. The high angle faults formed during emplacement of the thrust sheet, the low angle faults record a later extension of the the sheet after the PPVT (*sensu stricto*) had ceased movement and displacement switched to a shear zone in the footwall limestone.
4. Both fault arrays developed as isolated discontinuities within the thrust sheet rather than branched from the fault.
5. The extension in the footwall Cretaceous limestone was accommodated by swarms of extension veins and detached along the shear zone in the limestone.
6. The change in the type of extensional fault appears related to a 30 degree clockwise rotation in the σ_1 stress from approximately perpendicular to the thrust during or after movement on the high angle faults to oblique to the thrust during movement on the low angle faults. This rotation is recorded by successive high angle vein arrays in the thrust sheet. Most of the extension was accommodated on the low angle faults.
7. The intrablock deformation in the fault array was accommodated by the development of extension veins and reverse and extensional shear zones. The back-shear zone possess similar orientations to, and both cut and are cross cut by, the extensional shear zones. They record localised shortening strains that developed within the rotating fault blocks.
8. Bedding is rotated between the low angle faults which appear to have operated in a domino-slip fashion.
9. The rotation of the σ_1 stress was not related to movement of the thrust sheet over a ramp and is interpreted as a change in the dynamics of the overlying thrust wedge as initial loading was superceded by spreading and extensional shearing.
10. The extension in the thrust sheet is modeled in terms of the stability of an orogenic wedge (Platt, 1986) and it may have occurred in response to active underplating within the south Pyrenees thrust belt.

4.8.3. Secondary fault arrays.

1. Secondary fault arrays developed within the PPVT sheet and within a fault zone along the Triassic unconformity. All the the faults are shear-fibre coated movement planes.
2.The mechanism of slip on the faults was by a crack-seal stick- slip mechanism.

3. The complexity of the fault patterns appears to have resulted from the simultaneous propagation and interaction of a large number of faults. Interaction is represented by the linking of different generations of fault or faults of the same generation. The linking occurs by the formation of fault jogs, by development of dendritic patterns of splays, or by mutual linkage between conjugate faults.
4. The larger faults appear to have developed by the linking together of smaller originally discontinuous faults and show the greatest displacements. Localisation of displacement did not occur by a change in slip mechanism.
5. The faults tip by splaying, by the development of feather vein arrays or into shear zones (en echelon sigmoidal vein arrays). High angle faults tend to tip by splaying whereas low angle faults tend to tip into shear zones or feather vein arrays. Where splaying occurs it is often a result of the interaction of the propagating fault with a pre-existing discontinuity.

4.8.4. Deformation in the Pic de Port Vieux culmination.

1. The culmination formed as a result of two structures: a duplex within the Cretaceous limestone and a leading imbricate stack of thrusts in the Hercynian basement.
2. Cleavage-fault relations suggest that the duplex formed before the basement imbricate stack but was reactivated during movement on the lower structure.
3. The basement imbricate stack is an oblique tip structure and the cleavage, folds axes and fault movement directions are rotated up to 45 degrees clockwise in the overlying strata.
4. Distributed shortening in the Triassic strata above the BIS intensified cleavage. The main effect of this deformation was a localised reactivation of earlier thrusts within the tip zone. This occurred by the development of upper strain detachments.
5. The main upper strain detachment in the culmination occurred along the PPVT. The reactivation was restricted to the back-limbs of folds in the thrust and produced new faults that cut across the fold crests. This type of fault is called a back-limb splay.
6. The upper strain detachment on some of the faults operated intermittently and when they were inactive the faults were folded. The later movements on the folded faults occurred on back-limb splays.
7. The development of an upper strain detachment produces diachronous faulting in which a later fault moves while the earlier fault is still moving. As a result the sequence of movement of secondary thrusts in the culmination does not agree with simple foreland or hinterland propagation models. The faults are locally out-of-sequence but on the scale of the whole structure are in-sequence.
8. In restoring structures where upper strain detachments it is probably best to area balance and ignore all but the boundary displacements. This can only be done however where the minor faults can be shown to be discontinuous. By making the

assumption that the these faults must all link to a basal decollement will greatly overestimate shortening in the thrust system.

9. Upper strain detachments in thrust systems may be expected to occur where distributed strain (tip strain) affects a rheologically layered sequence of strata. The layering controls the location of the detachments.

CHAPTER 5

Cleavage and Fault Zone Microstructures

5.1 Introduction

This chapter is divided into two main parts. The first part will describe the fabrics and microstructures within the Mesozoic strata of the PPV culmination. The aims will be to identify the main microstructural processes that operated and to try and link these to the observed mesostructures. In particular the control of deformation mechanisms on the observed competency variations between the Triassic shales and Cretaceous limestone will be assessed. The second part of the chapter will describe in detail the microstructures developed in a 20 metre wide deformation zone adjacent to the Gavarnie Thrust at (420120 51630) (figure 3.1). The basement strata within and outside this zone were extensively altered prior to Alpine thrusting. It will be shown that this alteration has strongly influenced the style of the deformation in the zone and also allows some comments to be made regarding the scale and mechanisms of fluid infiltration into the fault zone. A comparison between the shortening-dominated deformation of PPV and the shear-dominated deformation within the GT fault zone also helps to assess the importance, if any, of kinematics in determining the deformation mechanisms that operate. Appendix 1 summarises the techniques employed in this study.

5.2. Microstructure of fabrics and faults in the Pic de Port Vieux Culmination.

5.2.1. Cleavages in the Triassic and Cretaceous strata.

5.2.1.1. Types of cleavage.

Both spaced and continuous cleavages (Borradaille et.al., 1982) occur within the Mesozoic strata of Pic de Port Vieux. In the Triassic red beds a slaty cleavage is developed in mudstone and siltstone beds and a spaced pressure solution cleavage is present in the sandstone and conglomerate units. The latter fabric either refracts into the slaty cleavage or is cut by faults along the bedding contacts (see figure 3.3). A spaced pressure solution cleavage is also developed in the fine grained strata of the ridge klippe of the PPV culmination (see figure 4.3 for location). This fabric is much less intense and often absent from equivalent lithologies in the summit klippe of the thrust sheet. In addition to these cleavages a crenulation cleavage is also present in the Triassic strata and is restricted in development to the forelimbs of the fold structures in the PPVT and to the hanging wall of the folded P1 thrust shown in figure 4.6.

Figure 5.1. Photomicrographs of slaty cleavage microstructures in the Triassic strata of Pic de Port Vieux.
a) Composite spaced pressure solution seam (S3/S2) cutting crenulated fabric (S1) in microlithon. PPL. Sample B8533.
b) Spaced pressure solution seam (S3) cutting across an oblique fabric designated (S2) in the microlithon. S2 is a rough pressure solution cleavage that crenulates S1. PPL. Sample B8533.
c) Low magnification of bedding-subparallel slaty cleavage. XPL. Sample NFS4.2.
d) Boudinaged quartz vein subparallel to the slaty cleavage. XPL. Sample NFS4.1.
e) Folded clastic mica flake. This grain has split along cleavage fractures with the different packets deforming disharmonically. A quartz-filled microextension site (Q) has opened up between the folded layers. Note that the orientation of the kink-band boundaries in the folded grain do not parallel the cleavage (Cl). This relationship is shown graphically in figure 5.3a. (A) denotes annealed kink band boundaries. XPL. Sample B8580.
f) Deformed clastic mica aggregate with recrystallised grain (N) growing along one of the fold limbs. The orientation of this grain is oblique to the bulk cleavage orientation. XPL. Sample NFS4.1.
g) Deformed clastic mica aggregate showing development of internal cleavage lamellae. These have formed by the annealing of original kinks and folds within the grain. The cleavage domains possess an oblique grain fabric that represents the original fold limb attitude. XPL. Sample NFS4.1.
h) Deformed clastic mica grain with new cleavage lamellae defined by recrystallised grains (N) that have grown original kink-band boundaries. XPL. Sample NFS4.1.

The fine grained Cretaceous limestone also possesses both a slaty and a spaced cleavage. This former is defined by a grain-shape fabric which is developed in the microlithons of the latter. Both these fabrics are coplanar. A locally developed crenulation cleavage in the limestone is restricted to the forelimbs of the fold structures where the earlier fabric that was folded is the mylonite foliation that formed during the emplacement of the PPVT (see figure 4.44). The other fabric type present in the limestone is a mylonite foliation that developed within the shear zone that parallels the overlying PPVT (see chapter 4 for a discussion of this structure).

The distribution of the cleavage types is strongly controlled by the deformation sequence that affected different parts of the culmination. As already shown in chapter 4 the cleavage initially formed during the first and second phases of thrusting and was intensified within the culmination during the third phase of thrusting. This latter phase of deformation was also responsible for the development of the crenulation cleavages in both the Triassic Cretaceous strata. The mylonite foliation in the limestone is also interpreted to have formed during the P3 thrusting (see section 4.4.3.3).

5.2.1.2. Cleavages in the Triassic strata.

This study will concentrate on the the slaty and spaced cleavages that formed within parts of the PPVT sheet. These fabrics are representative of the range of cleavages developed in the finer grained Triassic strata.

5.2.1.2.1. Slaty cleavage.

At high magnifications the slaty cleavage has a domainal character comprising thin cleavage lamellae that anastomose around lenticular microlithons (figure 5.1c and figure 5.2a and 5.2b). The microlithons are aligned parallel to the cleavage lamellae and help to define the slaty cleavage.

The cleavage lamellae are composed of dimensionally oriented phyllosilicate grains possessing large aspect ratios (generally greater than 10:1). These grains appear to have had two origins: as large clastic grains that rotated into the cleavage orientation and as new grains that grew along the cleavage lamellae. The large elongate phyllosilicate grains (figure 5.1c and 5.2c) are probably clastic in origin because the form of these grains is similar to folded bedding-parallel clastic grains in the same samples. The very narrow elongate mica grains do not appear to have a clastic equivalent and are probably recrystallised matrix grains.

The microlithons are composed of clastic mica grains, very fine grained matrix mica aggregates and lenticular-shaped quartz grains. These three grain types have

Figure 5.2. BSEM micrographs of slaty cleavage microstructures. In these micrographs low contrast denotes low atomic weight. Quartz is black, pyrophyllite dark grey, illite grey, chlorite off-white and opaque minerals brilliant white.
a) Slaty cleavage in siltstone showing well-developed domainal fabric. The thin cleavage lamellae anastomse around lenticular microlithons composed of lenticular quartz grains and clastic mica aggregates. Sample NFS4.2.
b) Split-field micrograph showing a deformed interlayered chlorite/mica grain. The layering in the grain is truncated against the cleavage lamella suggesting that DMT processes have removed part of the grain. Sample NFS4.2.
c) Split-field micrograph showing folded interlayered muscovite/pyrophyllite grain. Sample NFS4.2.
d) Heterogeneous bedding sub-parallel cleavage. The fabric is defined by the preferred dimensional orientation of clastic mica aggregates (C), large clastic mica grains (pyrophyllite grain (P)), mud pellets (M), and fine grained matrix aggregates (A). The zoned grain (T) is probably tourmaline. Sample NFS4.2.
e) Split-field micrograph showing a new cleavage-parallel grain (N) growing along kink band boundary in a folded clastic mica grain.
f) Intense slaty cleavage showing a more general alignment of constituents. The elongate quartz grains are a product of DMT deformation. Note that grain (F) appears to have deformed by fibre-loading.
g) and h) Thin stepped cleavage lamella (C) developed within clastic mica aggregate. This cleavage domain changes from having a discrete margin (S) to a more zonal margin (B) (see Borradaille et al., 1982 for definition of these terms) where the pyllosilicates bend into the cleavage orientation. At (S) the lamella is defined by a new grain that has grown along a KBB.

deformed differently during cleavage development and each is considered individually below.

1. The clastic mica grains.

Two types of clastic grain can be recognised, the large mica flakes and coarse (greater than 10 microns) grain aggregates. The latter probably represent small lithic clasts. The large mica flakes are generally single grains composed of interlayered chlorite-muscovite (figure 5.2b), muscovite-pyrophyllite (figure 5.2c) or chlorite-pyrophyllite (figure 5.2b). They deformed predominantly by folding and kinking (figure 5.3), the folding accommodated by a combination of buckling and slip along 001 cleavage fractures. Quartz-filled microextensional sites are often developed in the saddles of the folds and also between different fracture-bound layers within the grains (figure 5.1e).

The microfolds and kinks within the mica flakes possess a range of interlimb angles with a slightly skewed distribution (figure 5.3a). The mean of 54 measured angles was 124 degrees. The axial planes of the folds and kink-band boundaries (KBB) are rarely oriented parallel to the cleavage (figure 5.3b) whereas one limb of the kink or fold was often subparallel to the cleavage (figure 5.3c). This data agrees with the experimental results of Hobbs et.al, (1982) who showed that kinks form normal to the local direction of shortening (which is not necessarily parallel to the bulk shortening direction due to grain-scale heterogeneities) and then rotate away from this direction during a noncoaxial strain history. In the deformed micas studied here, it appears that the kinking favoured rotation of one limb into the cleavage orientation.

The lithic clasts comprise slightly mismatched packets of mica layers (figure 5.1f,g and h and figure 5.2e and g). Compositional variations within these grains (figure 5.2e and g) probably reflect muscovite-pyrophyllite interlayering or muscovite- phengite interlayering. These grains deformed predominantly by microfolding and kinking with the axial planes of the folds forming sub-parallel to the cleavage. Recrystallised grains often occur along the microfold axial planes (figures 5.1f,g,h and figure 5.2e).

Recrystallisation of the microfolds has produced a cleavage lamellae-microlithon texture within individual lithoclasts. The cleavage lamellae are defined by the new recrystallised grains along the folds (figure 5.1h) or by the fold limbs themselves (figure 5.1g). Where the latter define the cleavage lamellae they appear to have formed by the migration of kink-band boundaries. This process will be discussed in more detail later. The production of these two types of cleavage domain structure is shown schematically in figure 5.4. The microlithons comprise mica grains oriented at a high angles to the cleavage domains (figure 5.1g and h and figure 5.2e and g) and represent relict fold limbs or fold hinges. Removal of the high angle grains by pressure solution

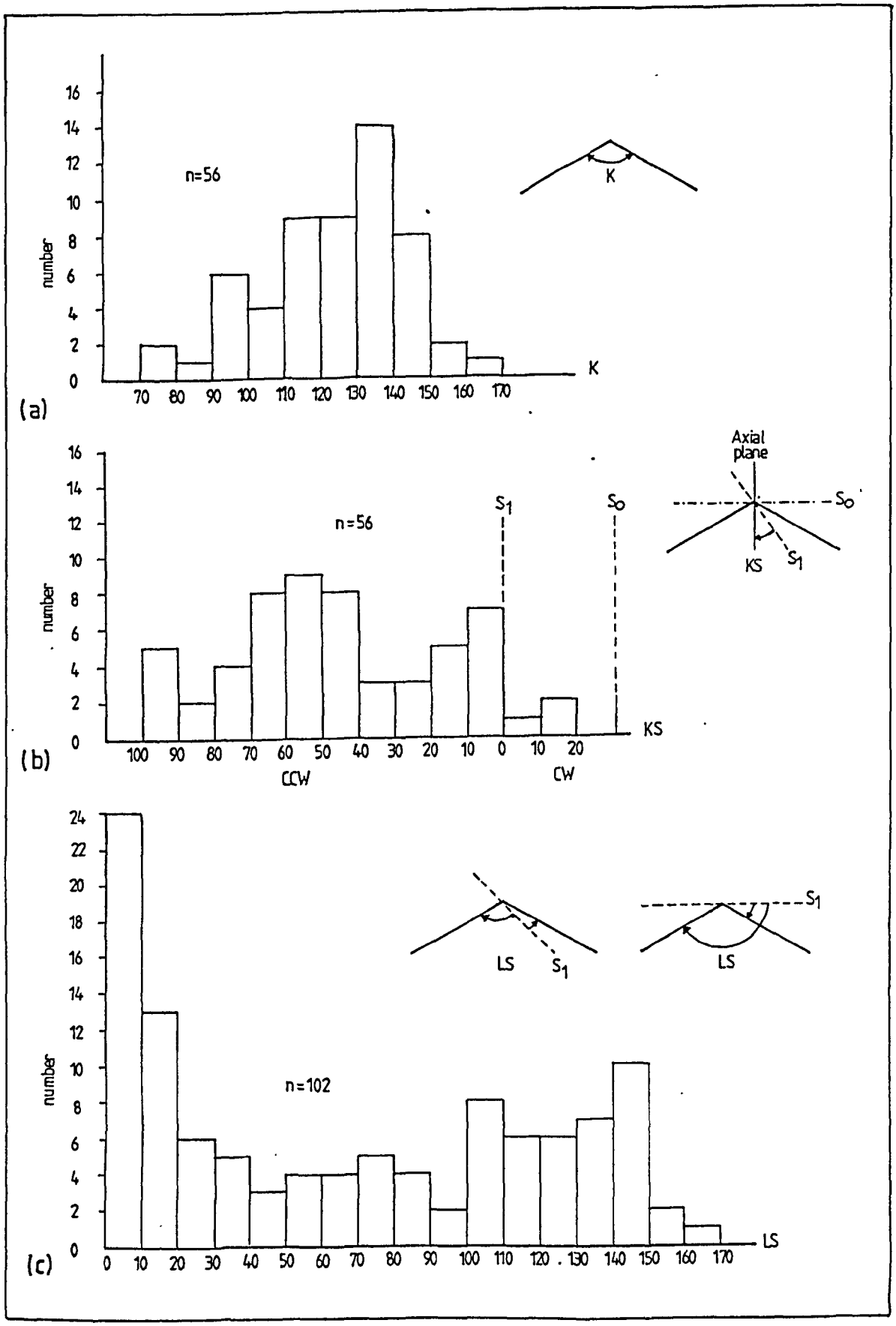

Figure 5.3. Angular relations in deformed clastic mica flakes from sample B8580. a) Histogram of kink angles. b) Histogram of angles between kink band boundaries and the cleavage orientation (angle KS). Most of the kinks are at high angles to the cleavage. CW denotes clockwise from cleavage, CCW denote counterclockwise. c) Histogram of limb-cleavage angles (LS). Both limb-cleavage angles are plotted in this diagram. One limb tends to lie close to the cleavage orientation.

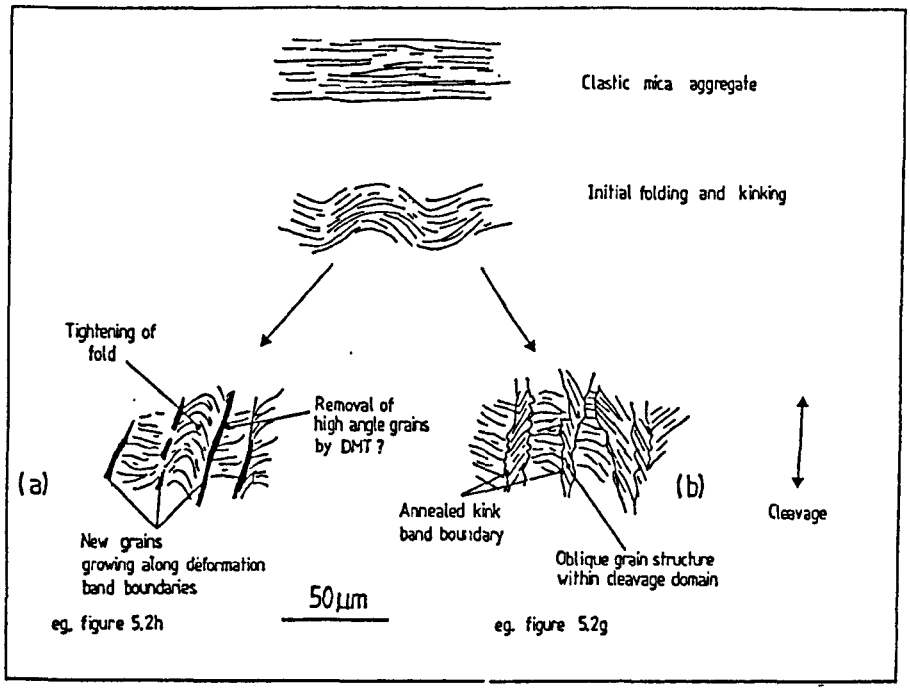

Figure 5.4. Model showing how the different types of cleavage lamellae microstructure observed within the deformed clastic mica aggregates evolve from original folded grains. The cleavage lamellae can form either by the growth of new recrystallised grains along kink band boundaries (a) or these boundaries can anneal by grain boundary migration recrystallisation (b) to form an oblique grain structure.

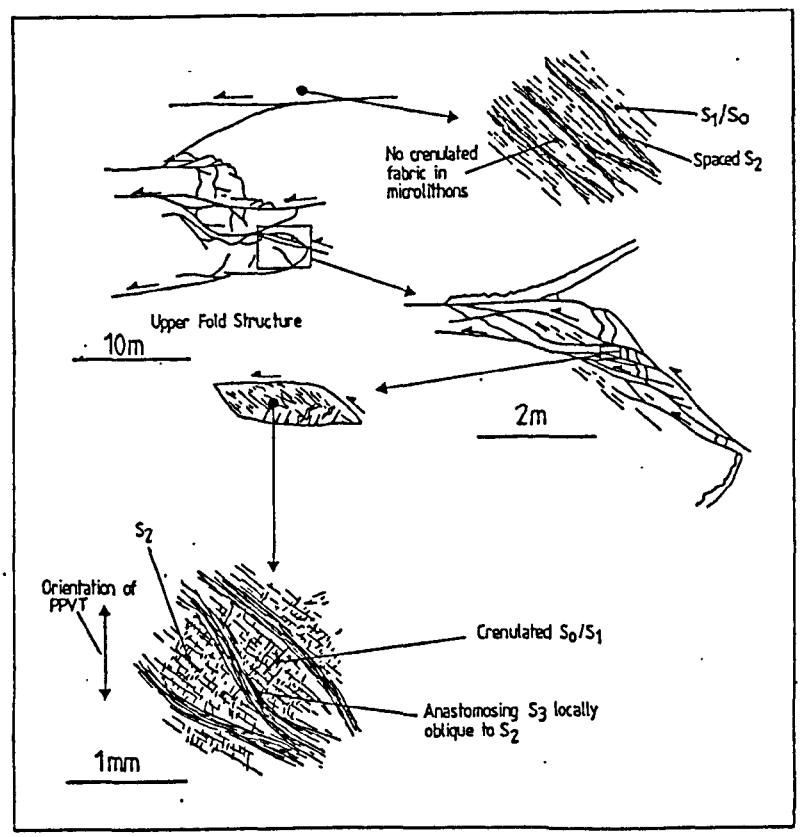

Figure 5.5. Sketch of the cleavage relations in the PPVT sheet in the fore- and back-limbs of the upper fold structure. In the forelimb of the structure the microlithons possess two fabrics: a crenulated fabric denoted S1/S0, and S2, a rough pressure solution cleavage (see figure 5.2a and b). S3 is the later anastomosing spaced pressure solution cleavage sub-parallel to S2. In the back-limbs of the fold the crenulation cleavage is absent from the microlithons and the fabric in the microlithons is a composite S0/S1 fabric. The spaced pressure solution seams S2 are the equivalent of S3 in the forelimb of the fold. The cleavage distribution shows that the initial fabric in the PPVT sheet S1/S0 was overprinted by deformation related to movement on footwall thrusts.

may have contributed to the development of the new fabric in the lithoclasts fabric but is difficult to prove.

2. Matrix phyllosilicates.
These comprise aggregates of very fine grained phyllosilicates which are generally too fine grained to be resolved optically or by using BSEM (eg see figure 5.2d). However, they probably deformed by similar mechanisms to those which affected the larger clastic grain aggregates.

3. Quartz grains.
The quartz grains show a grain-shape fabric parallel to the slaty cleavage. The grains are generally lenticular in shape with planar boundaries against the cleavage-parallel phyllosilicate grains (figure 5.2a and 5.2f). Pressure shadows developed on these grains are composed of delicately intergrown mica and quartz. The grain shapes suggest that the quartz grains were partially removed by dissolution along the interface between the grains and the cleavage lamellae with local precipitation along with neoformed mica in the pressure shadows. Most grains show no evidence for crystal plasticity and undulose extinction and deformation lamellae are only observed in mutually impinging quartz grains.

The optical and BSEM examination of the slaty cleavage therefore reveals that the fabric formed by a combination of three main processes:
1. Kinking and microfolding. This strongly affected the clastic mica grains and probably also the mica grains of the matrix.
2. Recrystallisation. This occurred predominantly in the cleavage lamellae and in the deformed lithic clasts. It is distinguished by the presence of thin elongate grains within the cleavage lamellae with aspect ratios different from the clastic micas.
3. Pressure solution (DMT). This process strongly affected the quartz grains. Its contribution to the deformation of the micas is more difficult to assess but it helped to strengthen the fabric by forming mica beards on the deformed quartz grains.

5.2.1.2.2. Spaced pressure solution cleavage.

This discussion will restrict itself to the fabrics that developed in siltstone beds of PPVT sheet since these can be closely related to the deformation sequence in the culmination.

The cleavages are defined by zones of intense pressure solution (P domains, Knipe, 1981) that comprise dimensionally oriented quartz grains and elongate dimensionally and crystallographically oriented mica grains. Both grain types are bordered by thin anastomosing films of opaque material. In the intervening microlithons (Q domains) the

quartz grains have lower aspect ratios and the crystallographic orientation of the micas is less well defined. A rough disjunctive cleavage within the microlithons is defined by discontinuous pressure solution seams. This fabric is generally parallel to the P domain fabric but locally it is oblique (figure 5.1b). This latter situation occurs where the P domains anastomose and it suggests that the P domains post-date the fabric in the microlithons ie. the deformation changed from distributed to banded pressure solution with time (cf Cobbold, 1977).

In the ridge klippe the forelimbs of the folds in the PPVT sheet possess a crenulation cleavage. This cleavage is the rough fabric in the microlithons. The earlier fabric is either bedding or a bedding-subparallel cleavage and is defined by the dimensional orientation of quartz and clastic mica grains (figure 5.1a). These samples can therefore be considered to possess three fabrics:

1. Crenulated S1.
2. The rough S2 pressure solution fabric in the microlithons.
3. The anastomosing spaced S3 that is locally oblique to S2.

Figure 5.5 is a sketch of the apparent cleavage relationships in the PPVT sheet around the upper fold structure. The overall cleavage distribution suggests that the spaced anastomosing pressure solution fabric and the rough pressure solution fabric formed during or after the folding ie. they represent an overprinting cleavage related to the development of the culmination. This agrees with the mesoscopic cleavage attitude and explains the virtual absence of similar spaced pressure solution fabrics in the summit klippe. It also appears that DMT processes were more important during the formation of the overprinting fabric than during the initial fabric development related to thrust sheet emplacement.

5.2.1.3. Foliations in the Cretaceous limestone.

5.2.1.3.1. Mylonitic foliation.

The mylonitic foliation is developed in the fine-grained calcite- rich layers. These layers have a grain size of the order of 5-10 microns. The fabric is defined by the dimensional preferred orientation of the calcite grains and by thin pressure solution seams. The grains tent to possess slightly serrated grain boundaries. Occasionally an S-C relationship (Lister and Snoke, 1984) is developed in the mylonite (figure 5.6h). The C-planes comprise narrow shear zones that deformed the oblique 'S' fabric. The pressure solution seams and thin stylolites are parallel to the C-planes. The only optical deformation features present are weak undulose extinction and occasional twinning in the fine grained calcite.

Figure 5.6. Microstructures in Cretaceous limestone.
a) Calcite-filled extension fractures cutting dolomite band within calcmylonite layer. Small blebby calcite grains are possibly replacing the dolomite which itself has locally replaced quartz grains (white). The calcite is stained red. PPL. Sample BL6.
b) Small cataclastic shear zone cutting calcite veins in the dolomite band. PPL. Sample BL6.
c) Slightly deformed conjugate e-twins deforming coarse grained vein calcite at the margin of a calcmylonite shear zone. The sense of shear is top-to-right. XPL. Sample B85170.
d) Healed microfractures (cleavage 1 fractures (Ghandi and Ashby, 1979) in neighbouring grain to that shown in (c). XPL. Sample B85170.
e) Core-and-mantle structure in same vein calcite as (c) and (d) but from within shear zone. PPL. Sample B85170.
f) Close up of core-and-mantle structure showing recrystallisation along twin planes in the deformed calcite grain. XPL.
g) Grain structure in cleaved limestone. The cleavage is defined by a strong shape fabric of flattened calcite grains. The opaque grain is a pyrite porphyroblast overgrown by hematite. PPL. Sample B8530.
h) S-C texture in calcmylonite. XPL. Sample B85170.

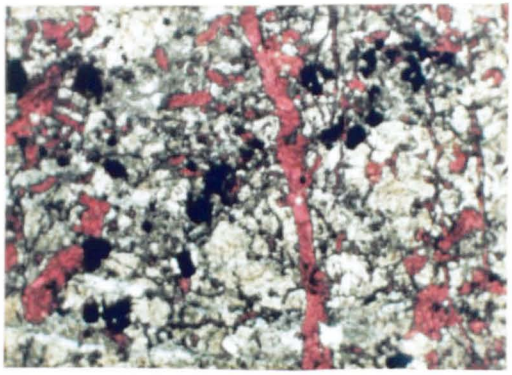

(a) 300 µm

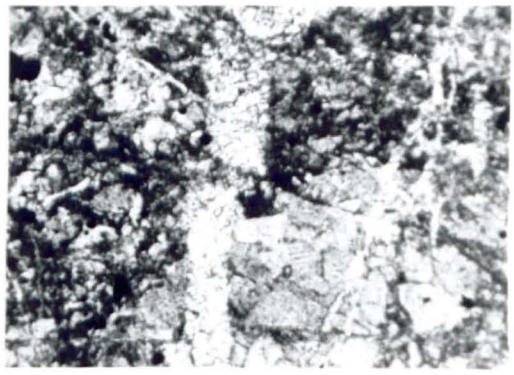

(b) 300 µm

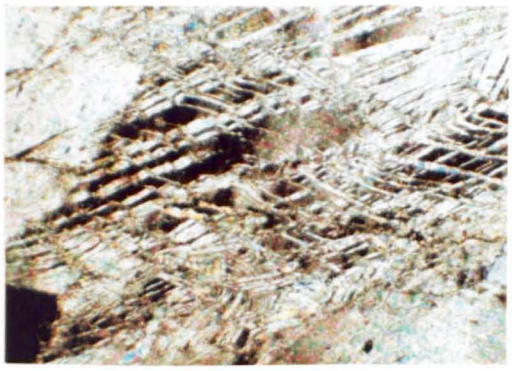

(c) 300 µm

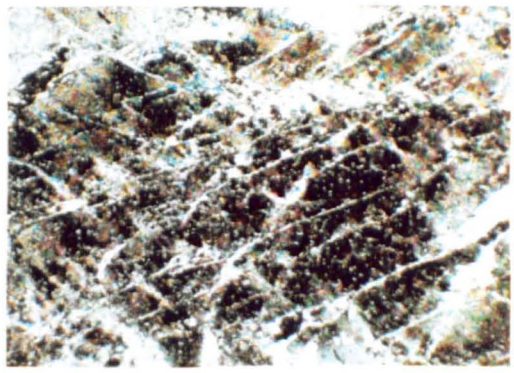

(d) 300 µm

(e) 200 µm

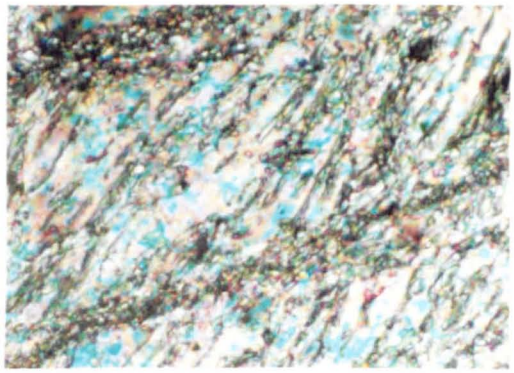

(f) 50 µm

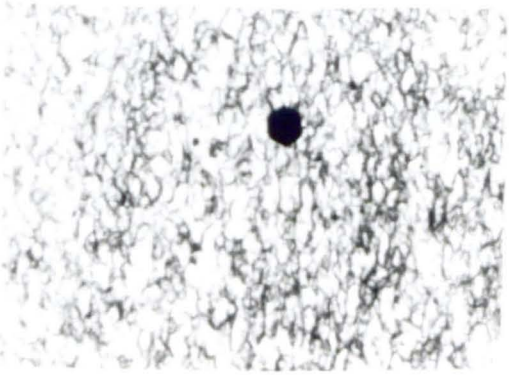

(g) 50 um

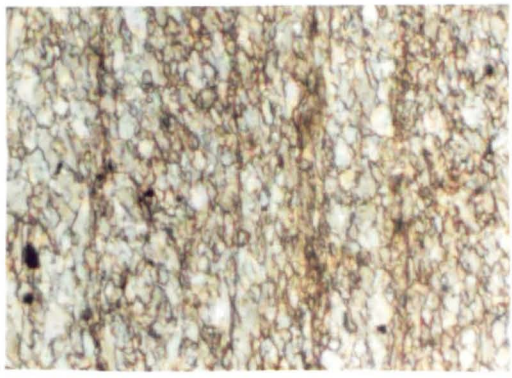

(h) 50 µm

Deformed blocky calcite extension veins are sometimes present in the calcmylonite layers and some are sheared into near- parallelism with the mylonitic foliation. These veins appear to have formed initially at high angles to the foliation and can often be traced into high angle veins in adjacent dolomite bands. Where present quartz fibres within the sheared veins do not show optical strain features and appear relatively undeformed.

At the margins of the mylonite layers the initially coarse grained calcite in the extension veins deformed by a combination of conjugate e-twinning (figure 5.6c) and fracturing (figure 5.6d). When traced further into the shear zone the coarse calcite grains in the vein develop a core and mantle structure (White, 1976) as subgrains form along the grain boundaries and along the earlier formed twin planes (figure 5.6e and f). The size of the subgrains is visibly smaller than the grain size in the sheared limestone. When sub-parallel with the foliation the vein is reduced to a thin layer of relict calcite grains mantled by small recrystallised grains. The grain size of the latter grains is comparable with matrix calcite. Pinch and swell structures are locally developed within the vein and suggest that the vein the still represents a relatively competent band within the mylonite.

The dolomite layers within the mylonite deformed primarily by cataclasis and are often cut by thin cataclastic shear zones (figure 5.6b) and numerous thin calcite-filled extension veins. Some of the dolomite layers appear to have formed by the replacement of quartz and appear themselves to have been partially replaced by blebby calcite grains (figure 5.6a). The quartz possibly represents original extraclasts in the micritic limestone or deformed vein material.

Other constituents in the mylonite include:
1. Syntectonic pyrite porphyroblasts: these possess asymmetric fibrous calcite pressure shadows. the calcite fibres were faced-controlled (Durney and Ramsay, 1973). The pyrite was often mantled by a thin layer of hematite or intergrown hematite and magnetite. This appears to have been a late stage replacement product.
2. Chlorite: this occurs as both small (10-20 micron) lath-like grains that often grow across the foliation in the dolomite layers, and as 'fish' (Lister and Snoke, 1984) oriented parallel to the S-foliation in the calcmylonite layers. It therefore exhibits both syn- and post-tectonic relationships with respect to the mylonitisation. These grains can be classified as chlorite 'fish' (Lister and Snoke, 1984).

5.2.1.3.2. Cleavage.

The main difference between the cleavage and mylonitic foliation in the Cretaceous limestone is one of orientation with respect to the overlying PPVT. The cleavage in the

limestone is defined primarily by a shape fabric in the fine grained calcite grains whose size is identical to those in the mylonite (figure 5.6g). The main textural differences compared with the mylonite are that C-planes are absent and the grains do not have serrated boundaries. At low magnifications, the fabric often shows a spaced appearance defined by bands of light (coarser grained) and dark (finer grained) calcite. Narrow spaced pressure solution seams parallel the grain shape fabric.

Dolomite occurs either as ptygmatically folded layers or small isolated subhedral grains. The folded dolomite layers are developed where the mylonitic foliation (with its dolomite layers) is overprinted by the cleavage. Pyrite porphyroblasts possess symmetrical pressure shadows in the cleaved limestone and are indicative of coaxial deformation (figure 5.6g) during cleavage development.

5.2.1.4. Discussion of Fabric development.

5.2.1.4.1. Deformation mechanisms.

The deformation mechanisms that operated during fabric development in the Triassic shales and the Cretaceous limestone are markedly different. The cleavage (ie shortening) in the shales developed primarily by micro-scale folding of grain aggregates and pressure solution. Recrystallisation played a significant role in generating the cleavage but how this contributed to the deformation is difficult to assess. In the PPVT sheet the partitioning of these deformation mechanisms appears to have changed with time increasingly favouring pressure solution. This may reflect strain hardening of the cleaved rock during progressive deformation as the grains that possess orientations suitable for folding and rotation are consumed. Alternatively it may simply reflect the kinematics of the deformation with pressure solution favoured during P3 shortening rather than during the initial P1/P2 shearing of the strata.

The flattened grain structure and serrated grain boundaries in the mylonitic foliation suggest that it formed by intercrystalline slip (Schmid, 1983; Schmid et al., 1986). However the present-day grain structure is unlikely to represent the total strain within the sheared limestone. This suggests that although intercrystalline slip may have contributed to the fabric development another mechanism is required to produce the intense foliation and high shear strains. The small grain size of the limestone suggests that grain boundary sliding may also have operated. This deformation mechanism is indicated by the absence of a stretching lineation on many of the foliation surfaces. Petrofabric analysis is ideally required to assess whether GBS did contribute to fabric development as it should not result in a crystallographic preferred orientation within the mylonite.

The grain shape fabric in the cleavage limestone could have developed from grain-scale pressure solution or as a result of intercrystalline slip. The absence of serrated grain boundaries suggest that GBS cannot be ruled out as a contributing process. Petrofabric analysis is again ideally required to assess these mechanisms. The fabric intensity was augmented by more localised pressure solution that generated the spaced pressure solution seams and fine grained pressure solution stripes. These features possibly developed later than the grain shape fabric because they are locally oblique to this fabric. The pressure solution seams may reflect a similar time sequence of development as shown in the Triassic shales with DMT favoured late in the overall deformation history.

5.2.1.4.2. Competency variations.

The refraction of cleavage within the PPV culmination together with the development of cusp folds between the Cretaceous limestone and the Triassic shales indicate that the limestone was the more competent lithology during shortening. This does not however appear to have been the case during the shearing associated with emplacement of the GT and PPVT sheets when the limestone was used preferentially as a slip horizon. Outside the PPV culmination the cleavage refracts from the Triassic shales into the Cretaceous limestone opposite to the relationship developed within the culmination. It appears therefore that competency switching occurred during the distributed shortening in the culmination. This suggests that the limestone was stronger than the shales when shortened but weaker when sheared. A similar conclusion was reached by Schmid (1975) when trying to explain cusp folds between the Lochseiten mylonite and the Flysch along the base of the Glarus Thrust sheet in the central Alps.

The main difference in the deformation mechanisms between the shearing and the shortening of both the shale and the limestone in PPV is that DMT appears to have been more active during shortening. The main difference in deformation mechanisms between the lithologies is that crystal plasticity and possibly grain boundary sliding dominated in the limestone but were probably subordinate to grain folding, rotation and DMT in the shale.

The preferential development of shear zones in the limestone can be explained by softening of the limestone during shearing. The softening mechanism may have been geometrical (the alignment of slip planes during intercrystalline slip (Schmid et.al, 1986)) and/or it may have involved grain boundary sliding. Equivalent bulk softening in the shale is unlikely because of its compositional heterogeneity and because the temperature of deformation (around 300 °C (see chapter 6)) is below the quartz brittle-ductile transition. When sheared the shale was therefore likely to have been the stronger.

The partitioning of deformation mechanisms in the two rock types when they were shortened was probably initially similar to those when they were sheared, although as suggested above, this appears to have changed to more DMT dominated with time. The limestone did not however soften relative to the shale. This may have been in part a product of geometrical hardening in the limestone and may in part have reflected the operation of a Hall-Petch stress relationship in the limestone. The former can be explained by the progressive alignment of slip planes in the calcite normal to the principal stress during a coaxial strain history (Law, 1987). The latter reflects the grain size dependence of the yield stress in deformations at low homologous temperature (Mitra, 1978). This effect has been shown to hold in limestone within the temperature range 20-300 °C (Olsson, 1974). The fine grained limestone would therefore have appeared very strong when shortened and would have remained very strong. In contrast the shales are unlikely to have exhibited this behaviour and may even have softened as pressure solution became more important. The latter statement is suggested by the observation that the cleavage is more differentiated in the flames of the cusp folds than in the cusps themselves.

5.2.2. Fault-related microstructures

This section will describe the microstructures associated with thrust faults in the Triassic strata. Two main types of microstructure are developed:

1. arrays of shear bands and slip surfaces adjacent to fault surfaces;
2. fault-parallel cavities.

Both these structures deformed cleavage associated with the thrusting. The mechanisms of slip on the faults has already been discussed in section 4.4.3.

5.2.2.1. Shear bands and slip surfaces.

5.2.2.1.1. Hanging wall.

Shear bands are the most common fault-related microstructures in the hanging wall of the thrusts. They also observed in the footwall of low angle extensional faults. They are coated with layers of either white mica or fibrous quartz and chlorite. Conjugate arrays are often present and possess a 40-50 degree apical angle that is bisected by the cleavage (figure 5.7a).

The conjugate shear bands are often spatially related to stretched cleavage-parallel veins that deformed by a combination of necking (figure 5.1d) and movement on conjugate shear bands (figure 5.7). The latter microstructures often helped to accommodate the flow of material into the necked portions of the veins (figure 5.7). The

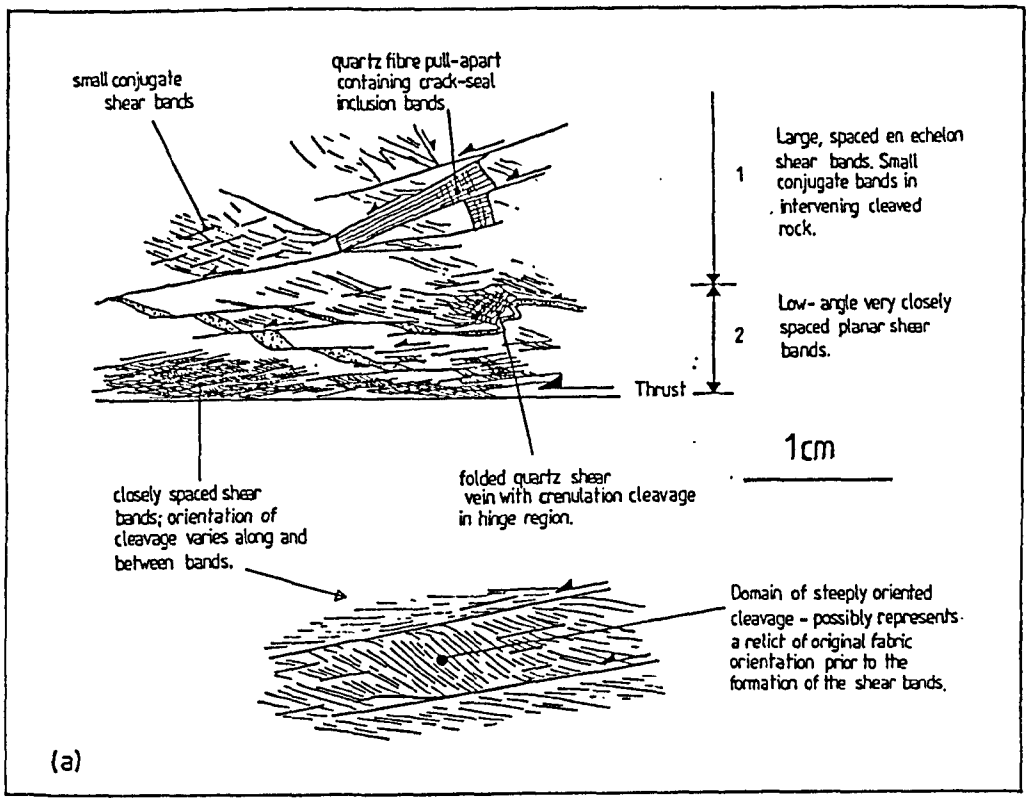

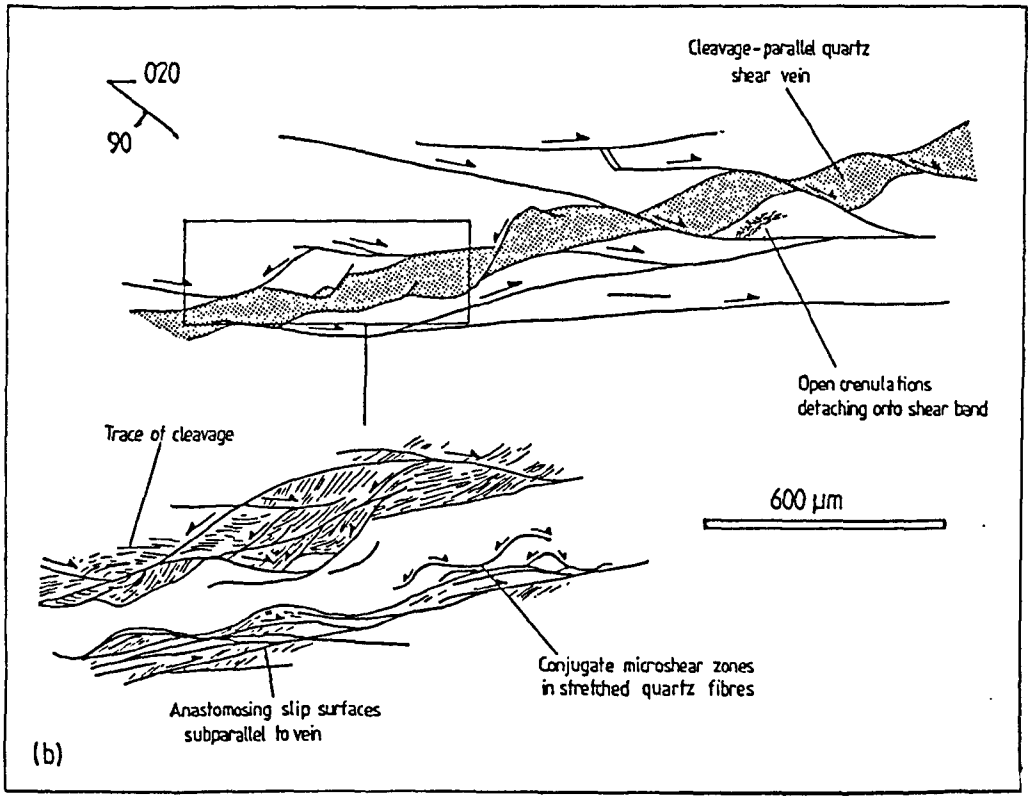

Figure 5.7. Shear band microstructures in the hanging wall of thrusts in the PPV culmination. a) Sketch summarising the distribution of shear bands in relation to the thrust. Two zones are distinguished: 1. A zone of large widely spaced shear bands making angle of about 20 degrees to the thrust. 2. Within 1cm of the thrust a zone of intense low angle shear bands (approximately 10 degrees) is present. Much of the cleavage in this zone has been sheared towards the shear band orientation although domains possessing a steeper orientation exist. These domains are probably relicts of the original cleavage attitude. Sample B8567. b) Sketch showing the spatial relationship between conjugate shear bands and and a deformed quartz shear vein in zone 1. The detailed sketch shows how the conjugate shear bands link to accommodate the flow of material into the boudin necks. This vein has suffered an almost coaxial stretch even though it resides in a zone of simple shear strain. Sample B8569.

deformation of these veins probably represents an example of strain partitioning (Lister and Williams, 1983). The fault-related simple shear in the directly hanging wall of a thrust is, in the vicinity of the veins, accommodated by slip on discrete surfaces, coaxial stretching of the system parallel to the plane of anisotropy and spin (Platt, 1984). In figure 5.7, the discrete surfaces are clearly present and represented by the vein-parallel slip surfaces. The strain partitioning model of Platt (op.cit.) for the development of conjugate shear bands in shear zones is shown in figure 5.8 and appears to agree with the observed microstructures. Recent work by Goldstein (1988) has suggested that shear bands in competent layers deformed in simple shear zones may originate as mode 1 (extension) fractures that are then used as shear fractures to extend the unit (figure 5.8b). This model cannot however explain the conjugate shear bands in the competent layers.

A feature of the shear bands is that they 'refract' across deformed veins (figure 5.7). This leads to listric geometries and the production of cleavage roll-overs. In figure 5.7b a set of open crenulations of the cleavage occur within the hanging wall of one such shear band. This feature probably reflects localised shortening associated with the rotation on the listric shear band.

5.2.2.1.2. Footwall microstructures.

The footwall of the thrusts are often marked by narrow zones of slip surfaces that possess both shear band and thrust sense orientations. An example of these microstructures is shown in figure 5.9a. The two sets of movement planes branch onto or off of the main thrust plane. Cross cutting relationships are rare and it appears that both types of slip surface moved synchronously. Similar sets of structures were developed adjacent to the low angle extensional faults in the summit klippe (figure 5.9b) although on a meso- rather than microscale. They appear to represent linked arrays of R1 and P fractures that probably accommodate the stretch of cleavage sheared into the fault zone in a similar way to the conjugate shear bands and slip surfaces that partition strain in the hangingwall of the faults.

5.2.2.2. Fault-parallel cavities.

As already described in section 4.4.3. many of the larger faults that cut the Triassic strata in PPV culmination often possess a layered distribution of vein quartz comprising:
1. a planar slip surface coated with layers of quartz/chlorite shear fibres.
2. a narrow band of randomly oriented euhedral quartz grains that appeared to have grown into a fault parallel cavity.
This section will focus on the microstructures associated with these layered fault rocks. The cavities formed along thrust faults within the culmination and along low-angle

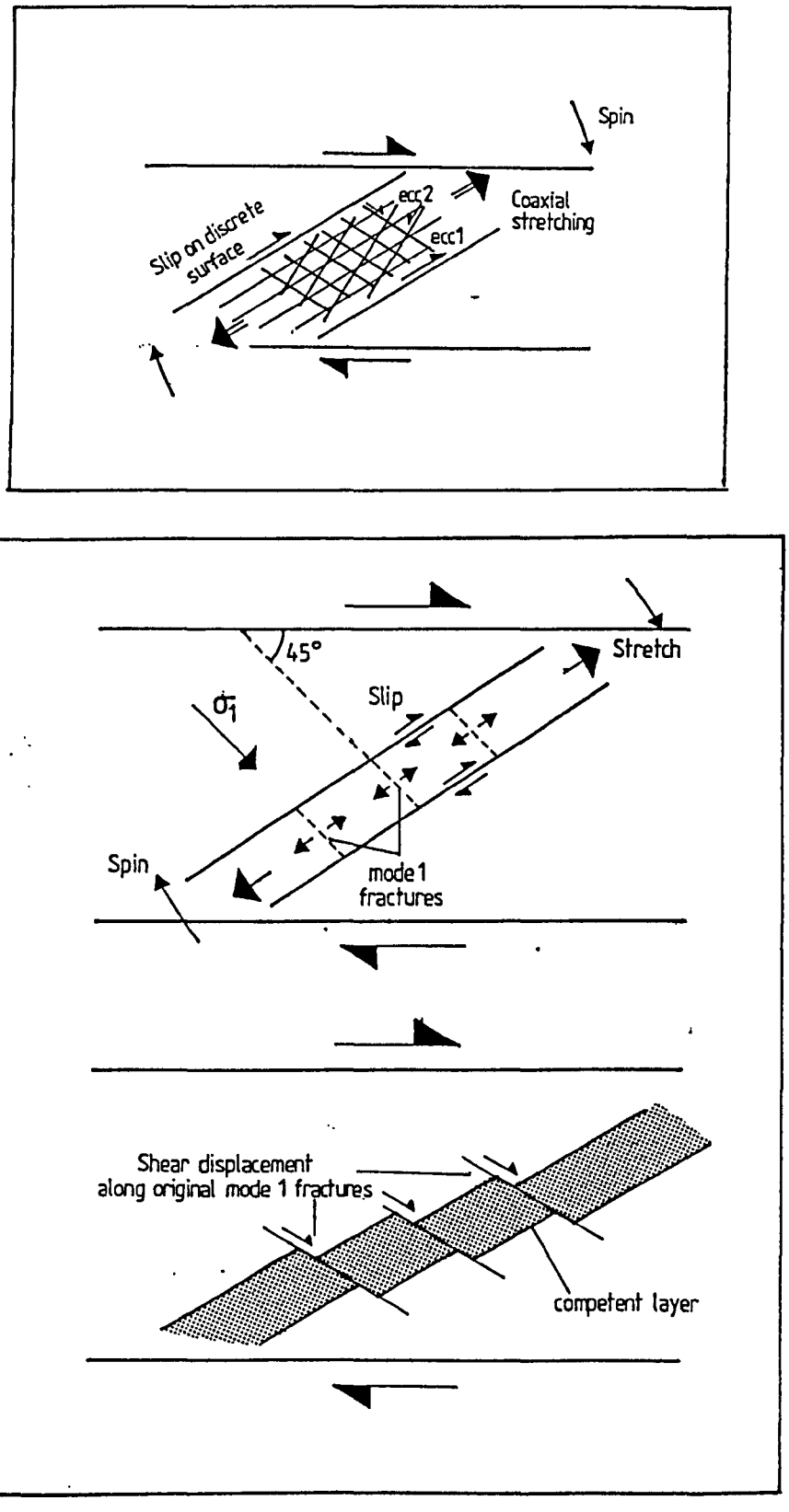

Figure 5.8. a) Strain partitioning model for the development of conjugate shear bands in a shear zone. The simple shear is partitioned into slip on discrete surfaces (parallel to the cleavage), coaxial stretching of the intervening lithons and spin of the lithons. From Platt (1984). ecc1 and ecc2 refer to the two extensional crenulation cleavages (shear bands) observed in the shear zone. b) Model of Goldstein (1988) for the development of shear bands cutting a competent layer within a shear zone. The shear bands nucleate on original extension fractures (mode 1 fractures) within the competent layer. This model cannot explain the development of conjugate shear bands which must originate as mode 2 fractures.

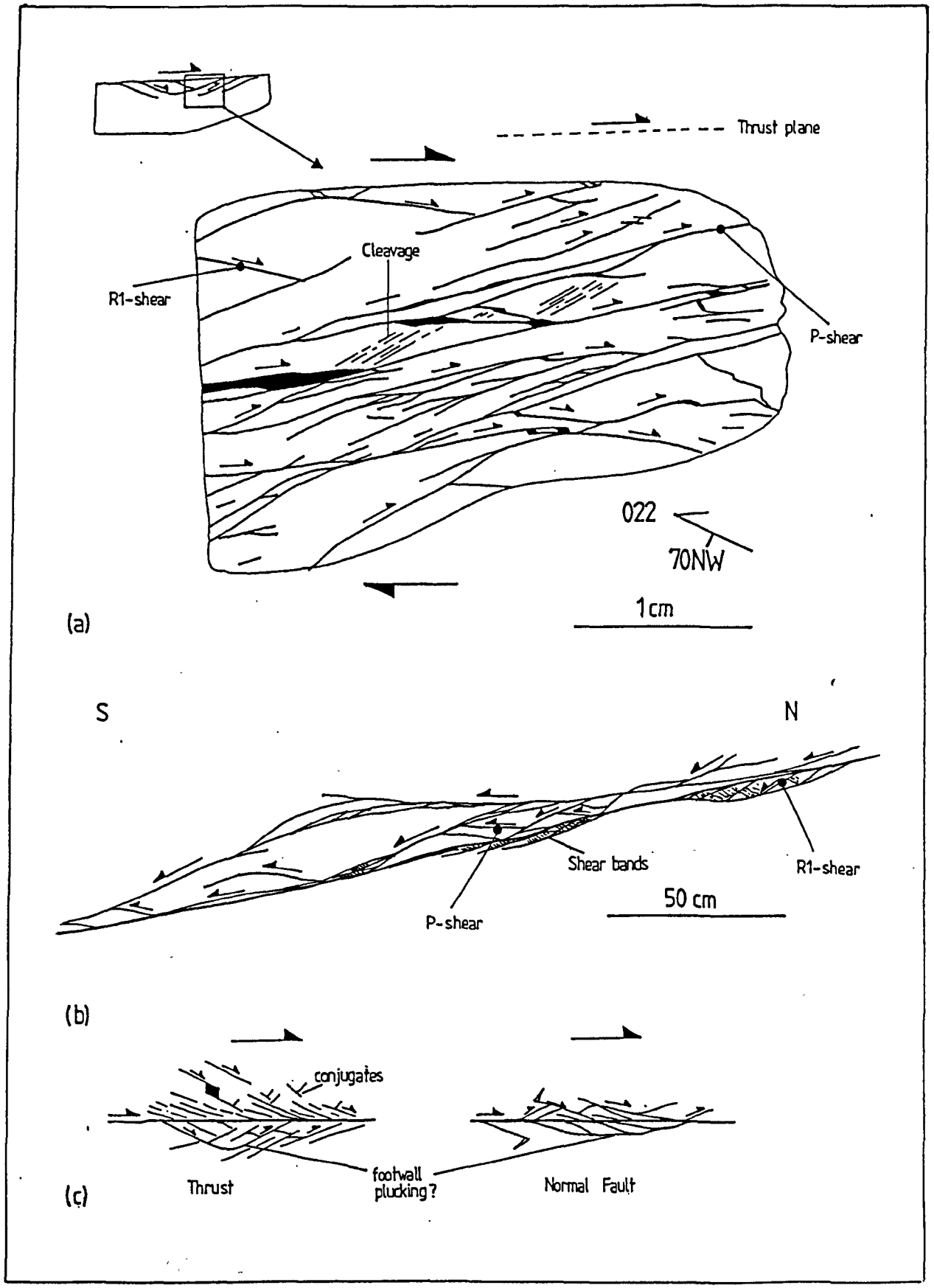

Figure 5.9. Slip surface structures in the footwall of faults in the Triassic strata. a) Array of slip surfaces in a xz thin section the footwall of a thrust along the top of a fine sandstone bed. The pattern comprises fractures with R1 (shear band) and P (thrust) orientations. Sample B8568. b) Mesoscale secondary fractures developed adjacent to a low angle extensional fault in the PPVT sheet (fault B, figure 4.14). This array also contains both R1 and P fractures. c) Summary sketches showing the fracture distributions around thrust and normal faults. Note that linking of R1 and P fractures in the footwall of the faults could lead to footwall plucking (cf Platt and Leggat, 1986).

Figure 5.10. Microstructures associated with the fault-parallel cavities in the PPV culmination.
a) Summary of main features present in the cavities.
b) Photomicrograph of fine grained quartz growing from fracture surface within cavity. The grain size increases away from the fracture surface (F-F').
c) Chlorite pendants and small euhedral quartz grains growing into void along roof of cavity.
d) and e) Optical strain features within cavity fill. (d) Twinning in calcite and deformation bands in quartz. (e) Healed microfractures (cleavage 3 type fractures (cf. Ghandi and Ashby, 1979)) perpendicular to Böehm lamellae (see Mitra (1976) for a discussion of the origin of Boehm lamellae).

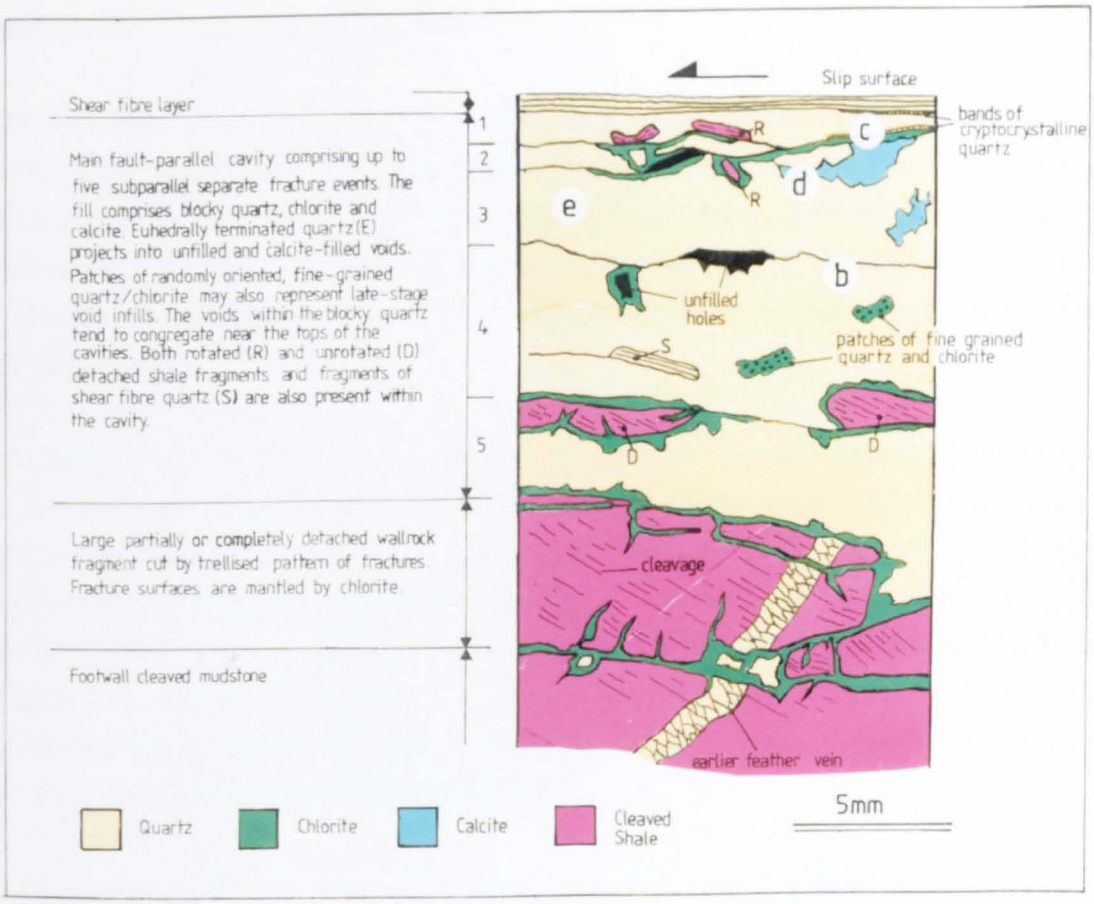

(a)

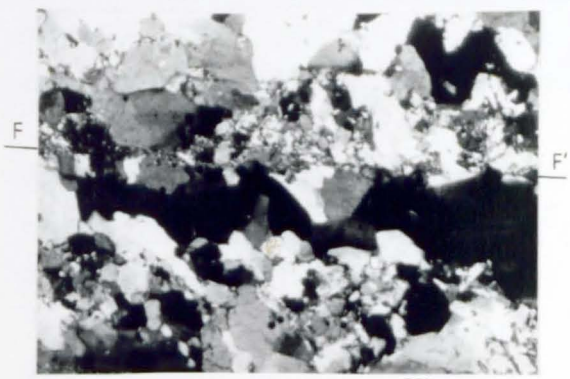

(b) 200 µm

(c) 50 µm

(d) 200 µm

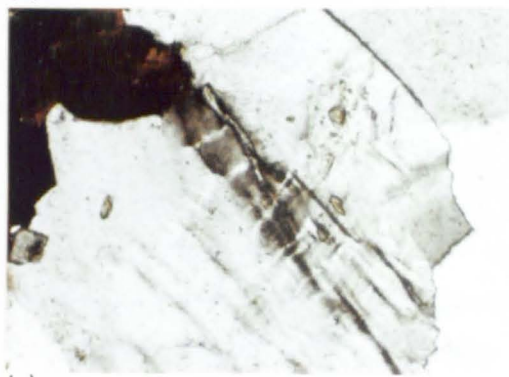

(e) 50 µm

extensional faults within the PPVT sheet. Both had similar microstructures and the salient features are summarised in figure 5.10a.

The slip surface is marked by a layer of quartz shear fibres possessing a blocky grain texture. The grain size in the fibres increases away from the margins of the layer. The quartz shows undulose extinction and occasionally deformation bands and deformation lamellae are present (figure 5.10e). Thin bands of microcrystalline quartz are often developed along the bounding fracture that forms the wall of the main fault-parallel cavity.

The main cavity is filled predominantly with anhedral blocky quartz. Euhedral quartz grains project into voids within this layer that are filled with late-stage calcite or fine grained quartz and chlorite. The voids tend to form towards the tops of the cavities and this feature may reflect a geopetal texture. A number of irregular fracture surfaces sometimes cut through the main cavity and are coated with either fine grained quartz (figure 5.10b) or chlorite (figure 5.10c). These fractures record different opening events within the cavity. Both rotated and unrotated lithic fragments occur within the cavities and are predominantly mantled with chlorite.

The cleaved shale in the footwall or hanging wall of the fault is dissected by a jig-saw like vein pattern. The veins walls are generally coated with rosettes of chlorite in a similar way to the detached fragments in the cavity. These fracture patterns suggest that cavity opened in response to hydrofracturing and not to the opening of a pull-apart during movement over an uneven fault surface.

Apart from the quartz, the calcite fill also shows signs of later deformation and is often twinned (figure 5.10d). These features suggest that the faults moved subsequent to the sealing of the cavities.

5.2.3. Summary

A range of microstructures are associated with the thrust-related deformation in the PPV culmination. Distributed deformation involved the production of cleavages in both the Triassic and Cretaceous strata. The cleavage in Triassic strata developed by a combination of rotation (kinking) and recrystallisation of deformed phyllosilicate grains and DMT. The latter appears to have become increasingly more important through time, especially within the PPVT sheet. In the Cretaceous limestone, the fabric probably formed by a combination of crystal plasticity and DMT. The latter process appears to have also become more important later in the fabric evolution.

Where the deformation was more localised eg. along the fault zones, the cleavage is cut by zones of shear bands and secondary fractures. The fracturing post-dated cleavage development. The shear band arrays accommodated stretching within the fault zones during continued fault-parallel shear. During the movement on the phase three thrusts hydraulic fracturing produced fault-parallel cavities and localised jigsaw brecciation. Away from the fault zones cleavage probably continued to develop to accommodate the strains produced by displacement gradients on the thrusts. Thus different deformation histories developed and different deformation mechanisms operated in different parts of the thrust system at the same time, related to both the host lithology and the proximity to faults.

5.3. Fault zone microstructures in the basement.

5.3.1. Introduction

The main aims of this section have already been outlined. The outcrop of the fault zone that is used for this study is located at (420120 51630) (figure 3.1). At this locality, the Hercynian structures in the basement strata are overprinted by a 20 metre wide deformation zone parallel to the thrust. A structural log across the zone is shown in figure 5.11. This log will be referred to as the **Basement Log (BL)**. Before describing the microstructures that developed in the fault zone, a brief description of the mesostructures will be given as these were not covered in either chapter 3 or chapter 4.

5.3.2. Mesoscopic deformation.

5.3.2.1. Description.

The basement strata comprise folded migmatitic psammites intruded by concordant and discordant granite lenses. The folds, which are more-or-less unmodified by the Alpine deformation more than 20 metres below the thrust, have E-W trends and verge north, typical of D2 Hercynian folds (Deramond et.al, 1980). The folding was accommodated mainly by flexural slip perpendicular to the fold hinges and only a weak axial planar fabric is present. This is best developed in the concordant granite layers.

In the deformation zone the Hercynian folds are overprinted by closely spaced Alpine-age slip planes. These increased in intensity towards the thrust. Relict fold axes in this zone have north-south trends (figure 5.12b) and appear to have been rotated towards the transport direction during shearing. The slip planes form a closely spaced anastomosing array. A continuum of movement plane sizes are present but for the purposes of this discussion, two orders of movement plane are distinguished:

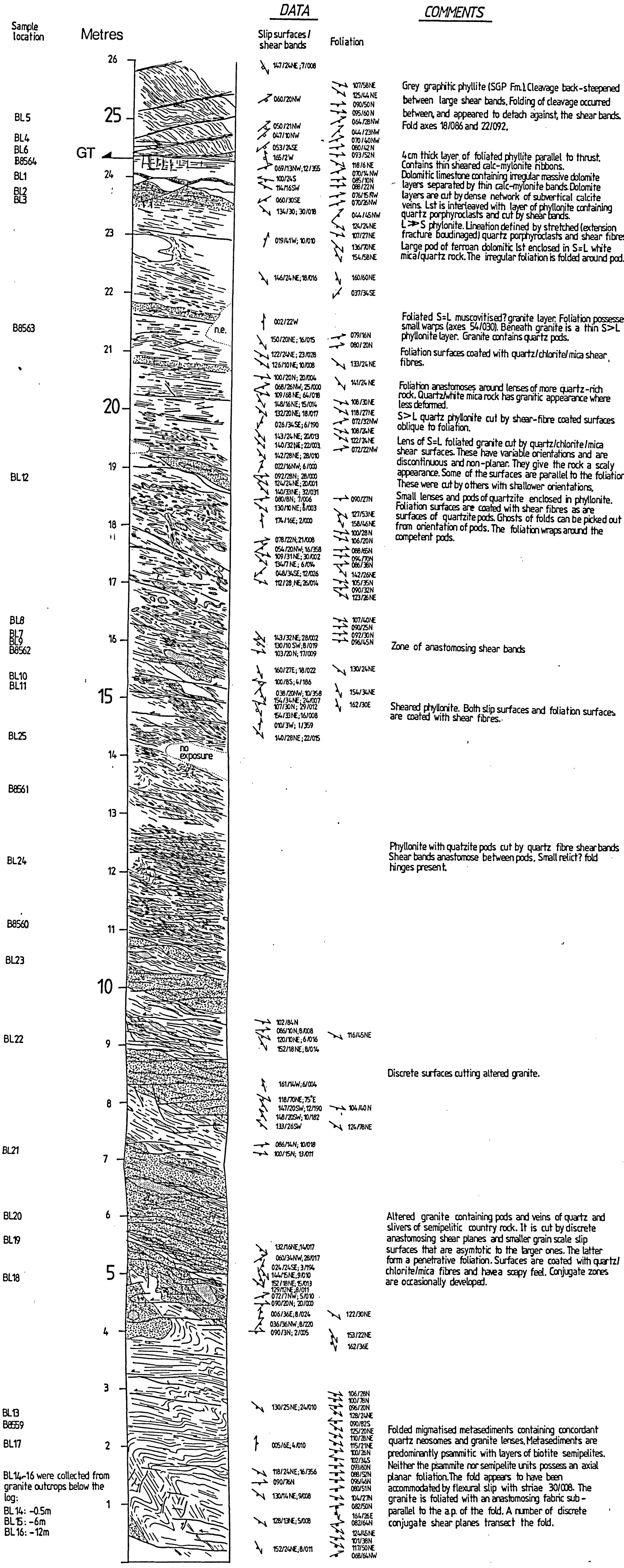

Figure 5.11. Structural log of the deformation zone in the footwall of the Gavarnie thrust.

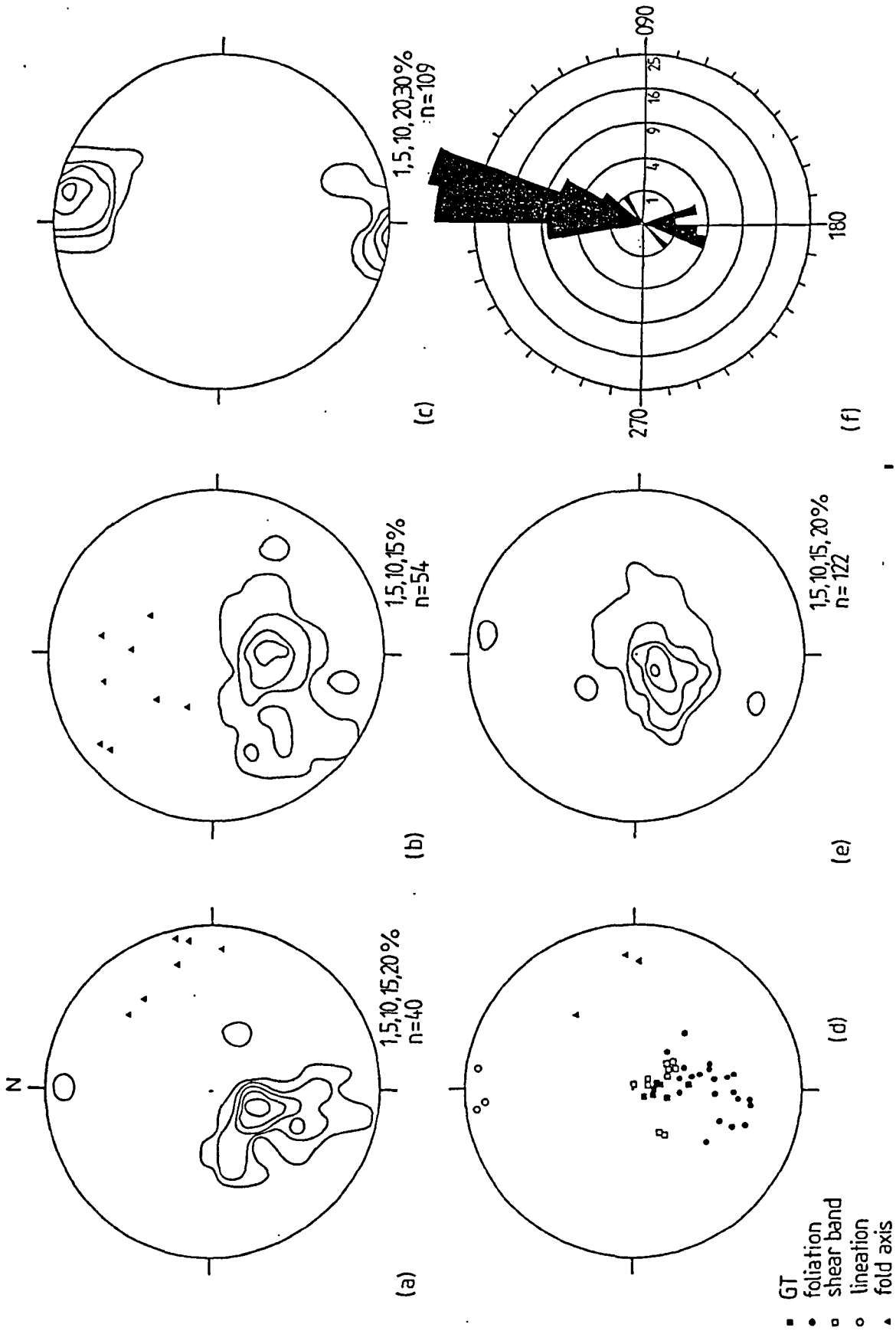

Figure 5.12. Stereograms of structural data from the deformation zone. a) Poles to folded Hercynian fabric. b) Poles to the phyllonite foliation in the deformation zone. c) Shear fibre lineations developed on slip surfaces. d) Structural data for the SGP Fm of the GT sheet. e) Poles to slip surfaces in the deformation zone. f) Rose diagram of azimuths of plunge of lineations on slip surfaces.

1. mesoscopic surfaces coated with quartz, chlorite and white mica shear fibres. These are more prevalent in the granitic than in the metasedimentary layers.
2. grain-scale shear surfaces that form within the rock bounded by the larger zones.

The majority of mesoscopic slip surfaces dip north east (figure 5.12e) slightly oblique to the north-dipping GT thrust. The shear fibre lineations on the surfaces record north-to-south transport (figure 5.12c and f).

A foliation is also developed in the sheared basement strata. This fabric is deformed by the slip surfaces and anastomoses around the quartz grains in the migmatite and in the granite. The foliation has a lustrous phyllonitic appearance and overlaps in orientation with the original Hercynian fabric (compare figure 5.12b and c).

The slip surfaces decrease in intensity within the upper 8 metres of the log and the basement strata is more strongly foliated than further from the thrust. Adjacent to the overlying Cretaceous unconformity the sheared basement possesses a strong linear fabric defined by stretched quartz porphyroclasts and shear fibre coated movement surfaces. This zone is cut by large shear bands and vertical quartz-calcite extension veins that branch from the tips of the shear bands. In the logged section a large pod of Cretaceous ferroan dolomitic limestone outcropped within this zone 1 metre below the Cretaceous unconformity.

The GT (*sensu stricto*) is separated from the sheared basement strata by a 0.5m thick layer of Cretaceous calcmylonite (at 24 metres in figure 5.11). It comprises a lower lenticular layer cut by shear bands and a more planar upper unit. These are separated by a thin layer of foliated granite indicating the limestone was duplicated during the thrusting. Similar interleaving of limestone and granite was noted along the Muraille de Barroude section in Cirque de Barrosa (chapter 3).

The contact between the limestone and the overlying SGP formation of the GT sheet is coated with quartz shear fibres. Above this layer, the SGP formation is cut by megashear bands that branch obliquely onto the thrust. The foliation between the shear bands dips steeply north and possesses small disharmonic upright folds that appear to detach on the shear band surfaces.

5.3.2.2. Interpretation.

The deformation in the fault zone is mainly accommodated on discrete anastomosing slip surfaces. These form a penetrative fabric on the scale of the whole zone. The development of both the slip surfaces and phyllonitic foliation appear to have been facilitated by the alteration of the basement strata. The absence of feldspar in granite outcropping below the fault zone suggests that the alteration is not restricted to the zone

and implies that the alteration is not itself controlled by the deformation. It is probably an earlier phenomenon that may have been related to late stage metasomatism during the Hercynian orogenesis.

The formation of the slip surfaces could reflect a change to more brittle deformation with time accompanied by a broadening of the overall fault zone. This change could have resulted from a change in the deformation. The shear bands present in the upper 2 metres of the deformation zone are demonstrably late-stage features as they are not deformed by later movements. The shear bands record late strain localisation within the upper part of the fault zone.

5.3.3. Microstructures

The deformation in the fault zone involved both phyllonite development and the development of shear fracture arrays. Both formed within and were presumably facilitated by the earlier alteration of the basement strata. A description of the alteration is therefore necessary if the microstructural evolution of the deformation zone is to be understood.

5.3.3.1. Alteration of the basement strata.

5.3.3.1.1. Composition.

The main constituents of both the granitic and metasedimentary protoliths in the altered basement were quartz, fine-grained white mica and interlayered chlorite-mica stacks (retrogressed biotites). Feldspar was not observed in any of the specimens studied including those collected from granite outwith the deformation zone. Pyrite and tourmaline and relict andalusite represent minor constituents in the rock. The proportions of the various mineral phases have been estimated by point counting and are shown graphically in figure 5.13.

The proportions of main constituents, quartz, white mica and retrogressed biotite do not vary systematically across the deformation zone (figure 5.13a) and the variations that exist are probably inherited from the protolith. Important trends exist however in the composition of fracture- fill phases:

1. The proportion of fracture fills in thin section increases upwards in the deformation zone and agrees with the mesoscopic intensity distribution of the slip surfaces.
2. The relative proportions of the phases changes systematically across the deformation zone (figure 5.13a). In particular quartz and chlorite vary antipathetically white mica and are important in a narrow zone 10 metres below the thrust.

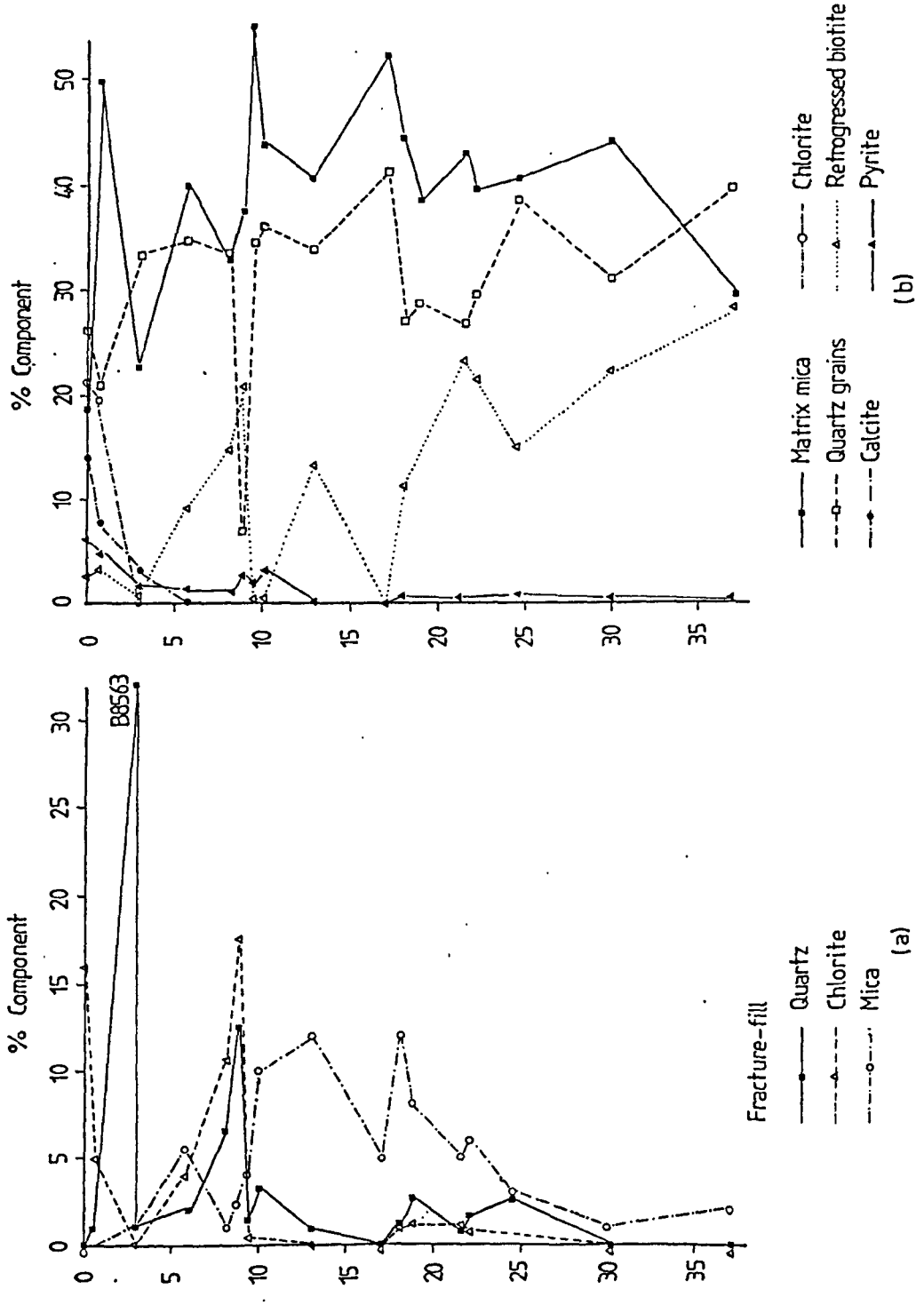

Figure 5.13. Graphs showing the mineral proportions in samples from the deformation zone plotted against depth below the Gavarnie Thrust. The mineral proportions are based on point counting using 300 data points. a) Fracture-fill phases as a proportion of the total rock. b) Constituent minerals as a proportion of the total rock.

3. Calcite and chlorite are important phases in a narrow zone adjacent to the Cretaceous limestone (figure 5.13b). The calcite occurs as fibrous pressure shadow and fracture fills and also partially replaces the quartz. The chlorite also occurs as a fracture fill and partially replaces the white mica matrix.

5.3.3.1.2. Chemistry.

In most of the samples studied white mica occurs as a fine grained felted mosaic of rosette-shaped aggregates surrounding the other minerals. The largest grains, up to 200 microns in diameter, probably represent relict muscovites from the original granite or psammite. Smaller matrix grains (less than 50 and sometimes less than 10 microns in size) probably represent alteration products of feldspar.

The XRD and microprobe analyses from samples BL13, 17, 22 and 25 show that the matrix is a variable proportions of pyrophyllite and muscovite. In figure 5.14a, the mica analyses plot as a dog-legged field in the AKF space. The upper leg trends towards pyrophyllite, the lower towards celadonite. The elbow in the distribution occurs near the composition of ideal muscovite. A cluster of analyses falling close to ideal pyrophyllite represent analyses from fibrous micas that grew along the slip surfaces. (Appendix 2 gives representative microprobe results).

In figure 5.14b, the probe analyses have been recalculated in terms of mole % of three components: celadonite, muscovite and pyrophyllite, using the technique outlined by Stephens et.al, (1979). The majority of analyses fall on a linear trend between pyrophyllite and a muscovite composition containing 20% celadonite (ie. phengite). However, a number of analyses have a negative calculated pyrophyllite component and appear to fall on a second linear trend below the triangle. The significance of these analyses is shown in figure 5.15 and they appear to represent analyses of interlayered chlorite/ mica grains.

The mineral assemblage in the altered strata is characteristic of advanced argillic alteration (Hemley et al., 1980) where the original strata has suffered extreme acid leaching. The most likely reactions that were involved in the alteration are:

1. K-feldspar + $2H^+$ = pyrophyllite + 2quartz + $2K^+$.
2. Andalusite + 3quartz + H_2O = pyrophyllite.

The absence of kaolinite and the alteration of andalusite in the rock suggests that the alteration occurred within the temperature range 270-360 °C (Hemley, et al., op.cit.).

3. Calcite and chlorite are important phases in a narrow zone adjacent to the Cretaceous limestone (figure 5.13b). The calcite occurs as fibrous pressure shadow and fracture fills and also partially replaces the quartz. The chlorite also occurs as a fracture fill and partially replaces the white mica matrix.

5.3.3.1.2. Chemistry.

In most of the samples studied white mica occurs as a fine grained felted mosaic of rosette-shaped aggregates surrounding the other minerals. The largest grains, up to 200 microns in diameter, probably represent relict muscovites from the original granite or psammite. Smaller matrix grains (less than 50 and sometimes less than 10 microns in size) probably represent alteration products of feldspar.

The XRD and microprobe analyses from samples BL13, 17, 22 and 25 show that the matrix is a variable proportions of pyrophyllite and muscovite. In figure 5.14a, the mica analyses plot as a dog-legged field in the AKF space. The upper leg trends towards pyrophyllite, the lower towards celadonite. The elbow in the distribution occurs near the composition of ideal muscovite. A cluster of analyses falling close to ideal pyrophyllite represent analyses from fibrous micas that grew along the slip surfaces. (Appendix 2 gives representative microprobe results).

In figure 5.14b, the probe analyses have been recalculated in terms of mole % of three components: celadonite, muscovite and pyrophyllite, using the technique outlined by Stephens et.al, (1979). The majority of analyses fall on a linear trend between pyrophyllite and a muscovite composition containing 20% celadonite (ie. phengite). However, a number of analyses have a negative calculated pyrophyllite component and appear to fall on a second linear trend below the triangle. The significance of these analyses is shown in figure 5.15 and they appear to represent analyses of interlayered chlorite/ mica grains.

The mineral assemblage in the altered strata is characteristic of advanced argillic alteration (Hemley et al., 1980) where the original strata has suffered extreme acid leaching. The most likely reactions that were involved in the alteration are:

1. K-feldspar + $2H^+$ = pyrophyllite + 2quartz + $2K^+$.
2. Andalusite + 3quartz + H_2O = pyrophyllite.

The absence of kaolinite and the alteration of andalusite in the rock suggests that the alteration occurred within the temperature range 270-360 °C (Hemley, et al., op.cit.).

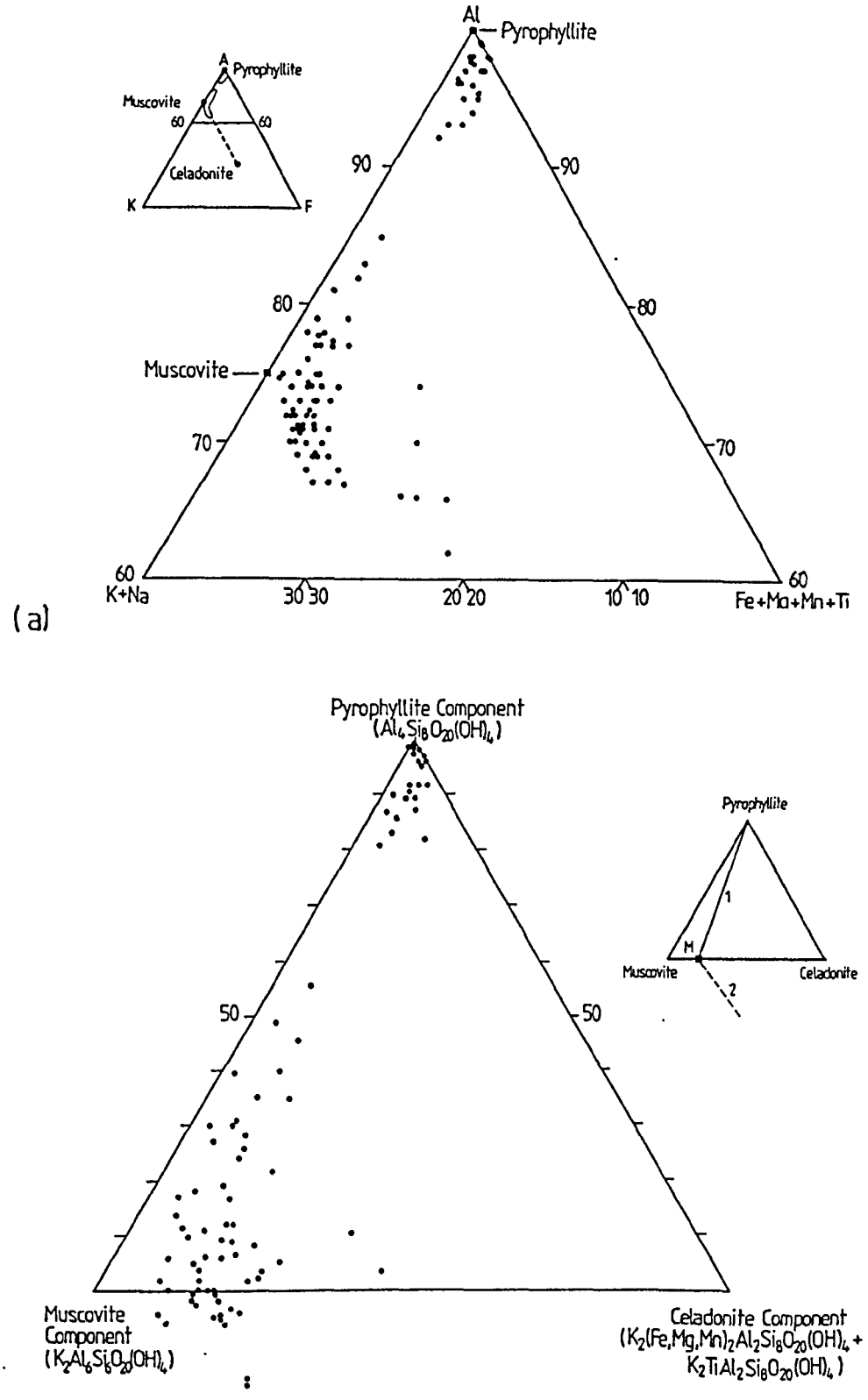

Figure 5.14. Microprobe analyses of matrix mica grains and fibrous mica grains growing along the slip surfaces in the deformed basement strata. a) AFM plot of all analyses. The data plot on a dog-legged field representing mixtures of muscovite and pyrophyllite and muscovite and phengite. b) The data shown in (a) recast in terms of three mineral components: pyrophyllite, celadonite and muscovite (after Stephens et al., (1979) (see appedix 2). Two trends are apparent: a series between pyrophyllite and muscovite containing 20% celadonite and a series with negative calculated pyrophyllite components (see inset).

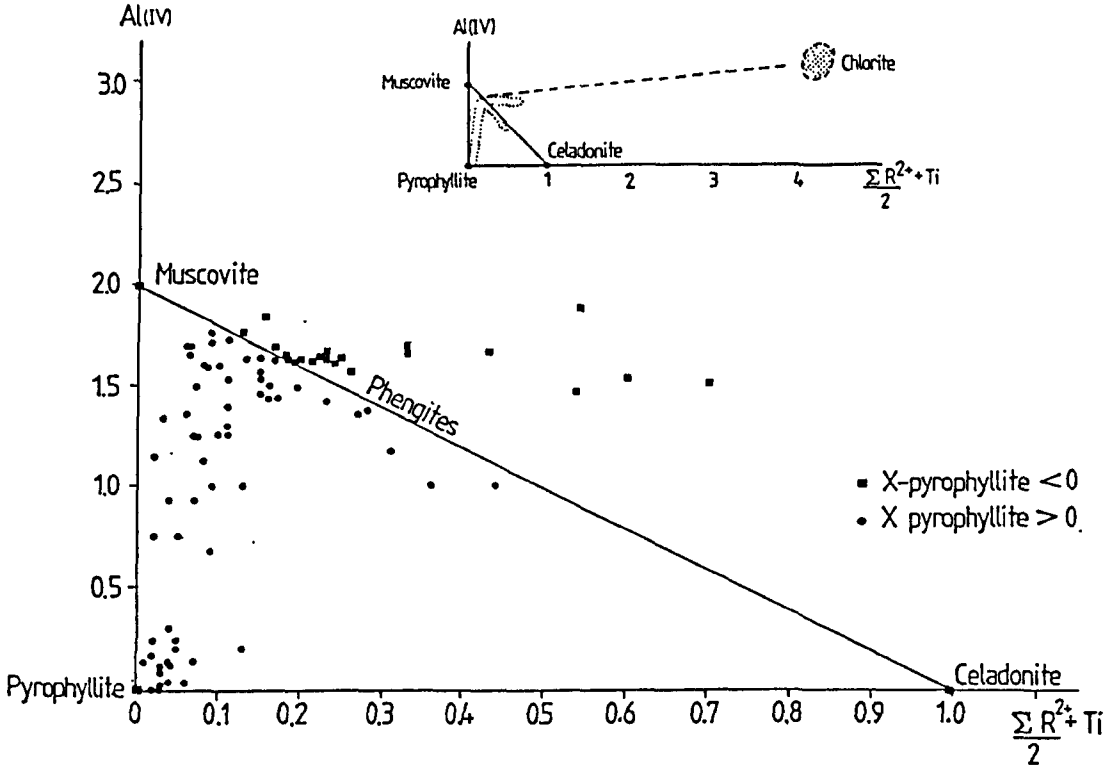

Figure 5.15. Plot of tetrahedral aluminium vs total octahedrally coordinated cations for the analyses shown in figure 5.15. Compositions with negative and positive pyrophyllite components have been separated. The analyses possessing negative calculated pyrophyllite plot in a subhorizontal field above the celadonite-muscovite join. The inset shows that these compositions possibly reflect analyses of grains composed of interlayered phengite and chlorite.

5.3.3.2. Thrust-related microstructures in the mica matrix.

5.3.3.2.1. Introduction.

Cleavage development and shear fracturing is largely confined to the fine grained mica matrix of the altered basement. The relative intensity of these deformation features changes across the fault zone with fracturing more persistent below 10 metres of the thrust and cleavage (phyllonitic foliation) development more intense nearer the thrust. A BSEM and TEM study of both the cleavage development and fracturing in the strata indicates the deformation mechanisms involved and how these change across the fault zone. The description of these microstructures is therefore separated into distal and proximal relationships with respect to the Gavarnie thrust.

5.3.3.2.2. Foliation below 3 metres from the thrust.

The matrix foliation does not vary significantly in morphology below approximately 3 metres of the thrust. It has a heterogeneous distribution even on the grain scale and is most strongly developed adjacent to the large quartz grains. The fabric has an asymmetrical development around these grains and suggests that it formed partly in response to the rotation of the quartz grains during shearing (figure 5.16a). It is also deflected towards the grain scale slip surfaces that anastomose through the rock. The small grain size of the matrix prevented optical examination of the fabric even in ultrathin thin sections and most of the following description will be based on results of a BSEM and TEM study of the fabric.

The foliation is defined by a shape fabric in muscovite-pyrophyllite grains and by the preferred orientation of aggregates of grains (figure 5.17b). Individual grains often have fan-like morphologies that presumably are products of their original growth. At the grain scale the foliation is domainal comprising short sub-planar cleavage lamellae and broader intercleavage domains.

1. Microstructures in the intercleavage domains.

The domains comprise interlayered muscovite-pyrophyllite grains generally oriented at high angles to the foliation trace. Most are either folded or kinked with a wide range of axial plane orientations. This presumably reflects the original random orientation of the mica grains and it appears to have contributed to the discontinuous nature of the cleavage lamellae.

Apart from folding, two other deformation-related microstructures have been observed within the domains: annealed microkinks and recrystallised grains that grow along kink-

Figure 5.16. Optical micrographs of microstructures in the altered basement strata within the deformation zone.
a) Heterogeneous fabric development in the matrix mica. The fabric intensity has an asymmetric distribution around the quartz similar to that developed around incipient d-type porphyroclasts (Passchier and Simpson, 1986). This suggests the rigid quartz grains have started to rotate during shearing. XPL. Sample BL20.
b) Annealed grain texture in quartz grains. This texture probably formed during the Hercynian aged deformation and metamorphism that affected the basement prior to Pyrenean thrusting. XPL. Sample BL20.
c) Folded retrogressed biotite grain cut by branching slip surfaces. The retrogressed grains occur both within and outside the deformation zone and appear to have formed during Hercynian retrograde metamorphism. The original biotite has been converted into an interlayered phengite-chlorite grain. The folding of these grains occurs again both within and outside the deformation zone and may have initially occurred during the Hercynian D2 folding that produced the mesoscopic folds seen in the basement strata at outcrop. The slip surfaces are related to the shearing associated with movement on the GT. XPL. Sample B8560.
d) Deformation features in quartz grains related to the Pyrenean thrusting. The photograph shows deformation bands and deformation lamellae concentrated at a point contact between two grains. In general the quartz grains behaved as resistant inclusions within the mica matrix . XPL. Sample B8560.
e) Intensely sheared basement granite collected from 1 metre below GT. The original matrix mica has almost totally recrystallised into a strong phyllonitic fabric. The original quartz grains have deformed primarily by extension fracturing, the fractures filled with calcite. XPL. Sample BL3.
f) Intensely sheared basement granite from 0.25 metres below the thrust. The rock has been extensively metasomatised with the original muscovitic phyllonite fabric syntectonically replaced by clinochlore. The fractured quartz grains have also been partially or totally replaced by calcite and clinochlore. XPL. Sample BL1.

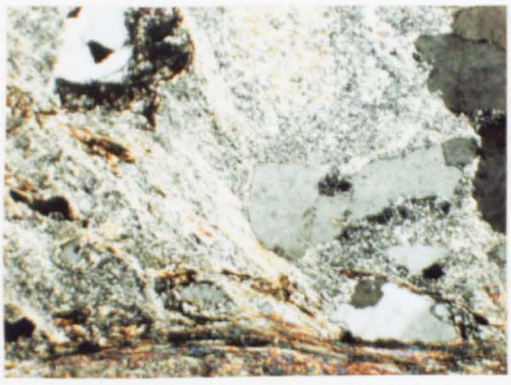

(a) 300 µm

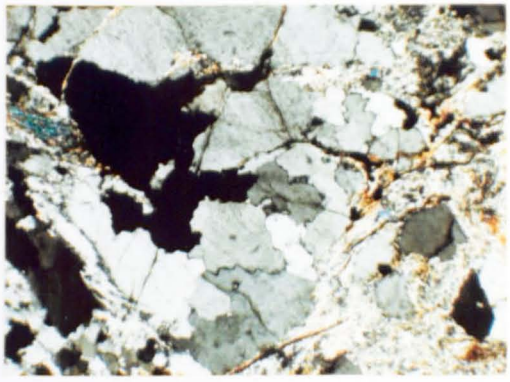

(b) 300 µm

(c) 200 µm

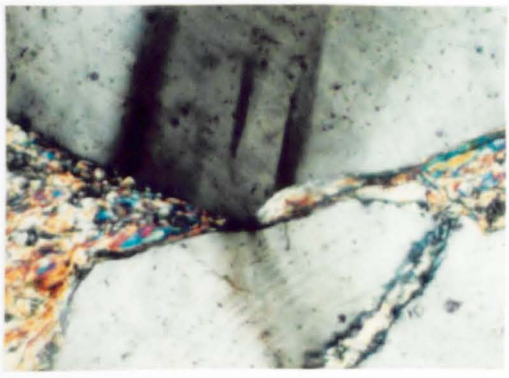

(d) 100 µm

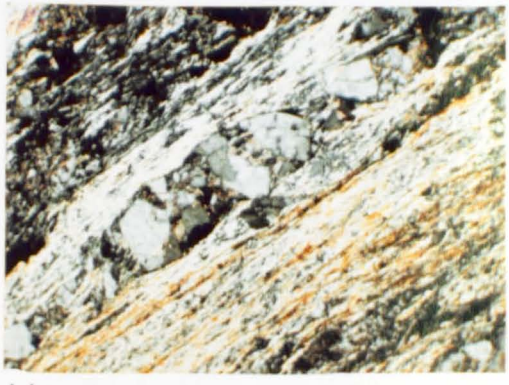

(e) 300 um

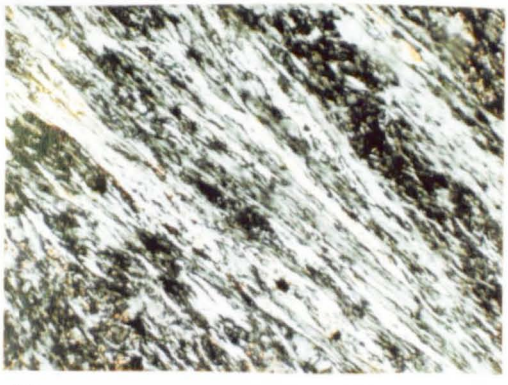

(f) 200 µm

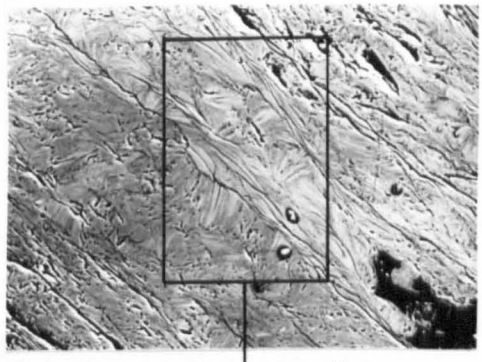

(a) 60 µm

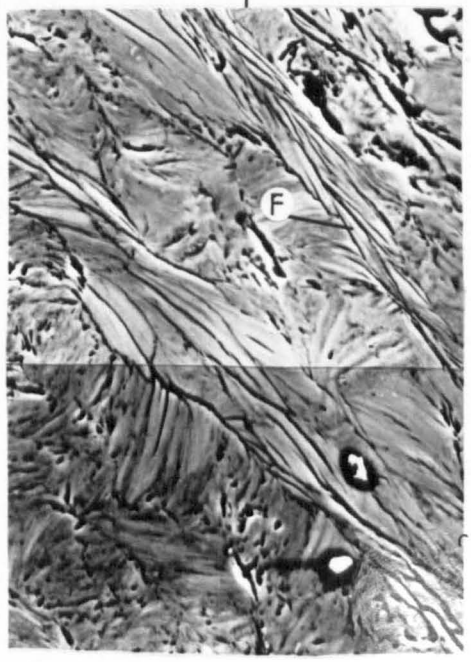

(c) 20 µm

(f) 30 µm

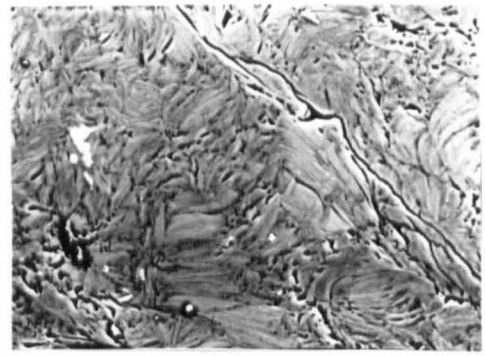

(b) 30 µm

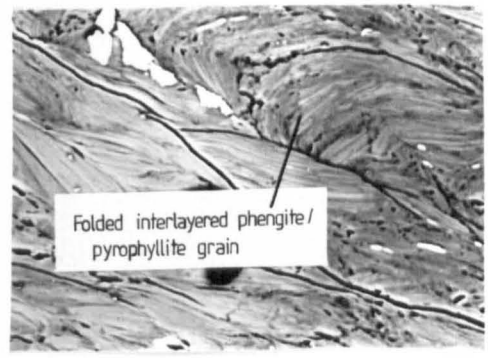

(d) 30 µm

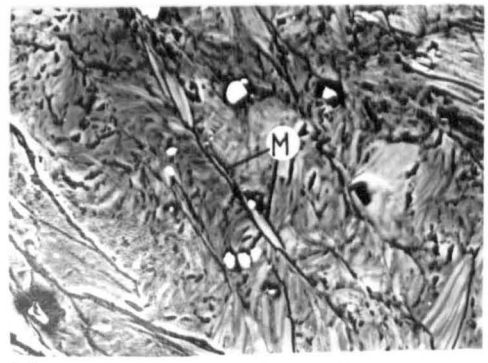

(e) 30 µm

(g) 20 µm

Figure 5.17. BSEM micrographs of microstructures in cleaved mica matrix. All micrographs come from sample B8563.
a) Micrograph showing the domainal nature of the cleavage. The cleavage domains are smooth zones of oriented phyllosilicates separated from one another by microlithons comprising grains at high angles to the cleavage.
b) Grain structure in microlithon. Deformation of small interlocking mica grains has occurred by a combination of folding and kinking.
c) Detail of cleavage domain. The domain possesses a feather-like grain structure comprising overlapping small grains that show stepped boundaries with the microlithon grains. Exact parallelism between the cleavage and the cleavage domain grains is rarely achieved.
d) Folded and locally fractured grain showing stepped axial plane that indicates that slip has occurred along the interlayer boundaries during folding.
e) Small recrystallised grains growing along cleavage lamella.(M)
f) Cleavage domain possessing well-developed feather structure. This appears to have developed by annealing of the kink-band boundary (K). The kink-band boundary has a lower back-scattered contrast than the kinked grain.
g) Deformed muscovite-pyrophyllite grains showing compositional variations along grain boundaries and kink band boundaries. (P) denotes possible overgrowth structures on some phyllosilicate grains.

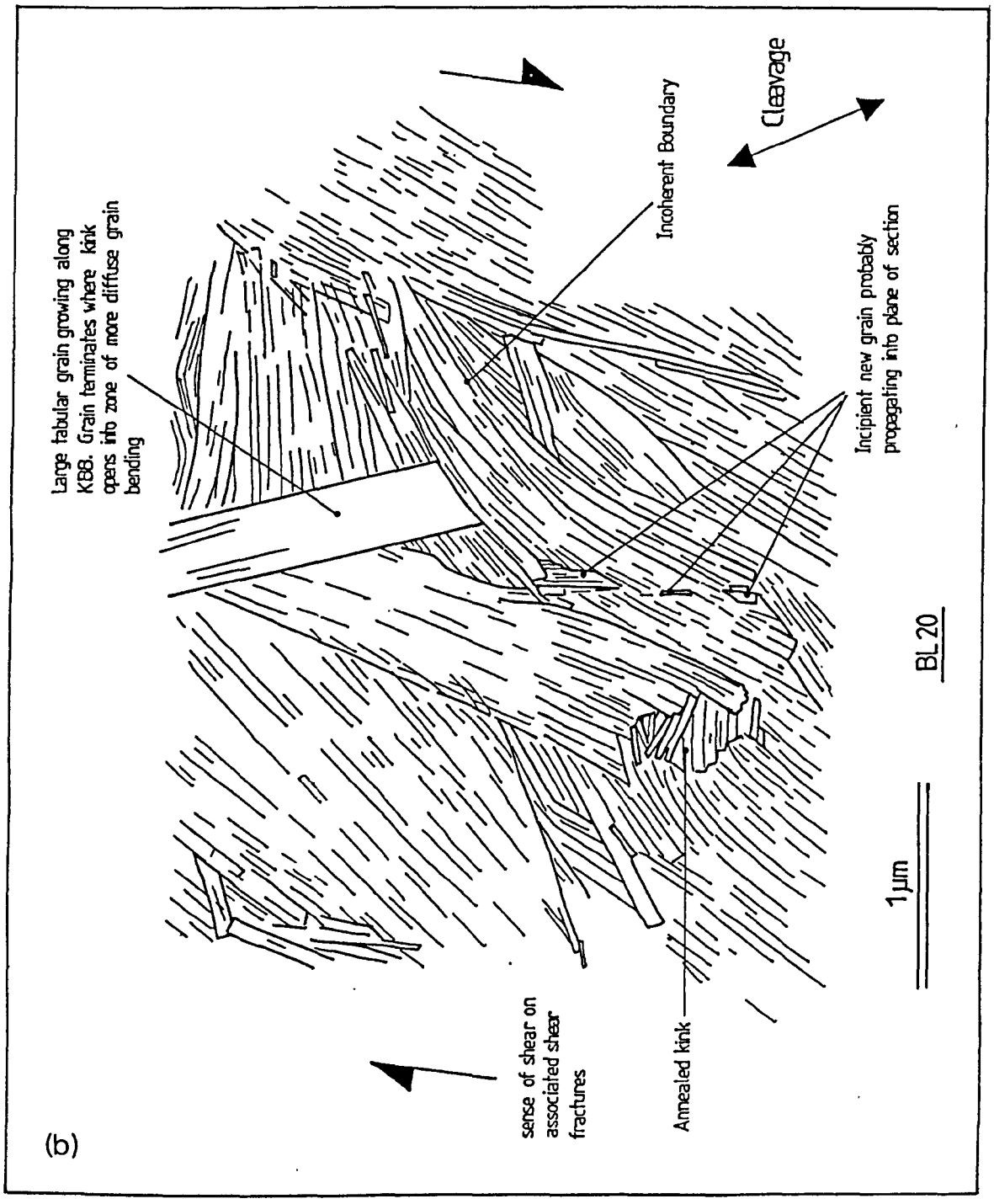

Figure 5.18. a) TEM montage showing mica grain structure within an intercleavage domain. These structures are interpreted as the product of partial annealing of folds and kinks within the initially high angle phyllosilicate grains. b) Interpreted line tracing of montage.

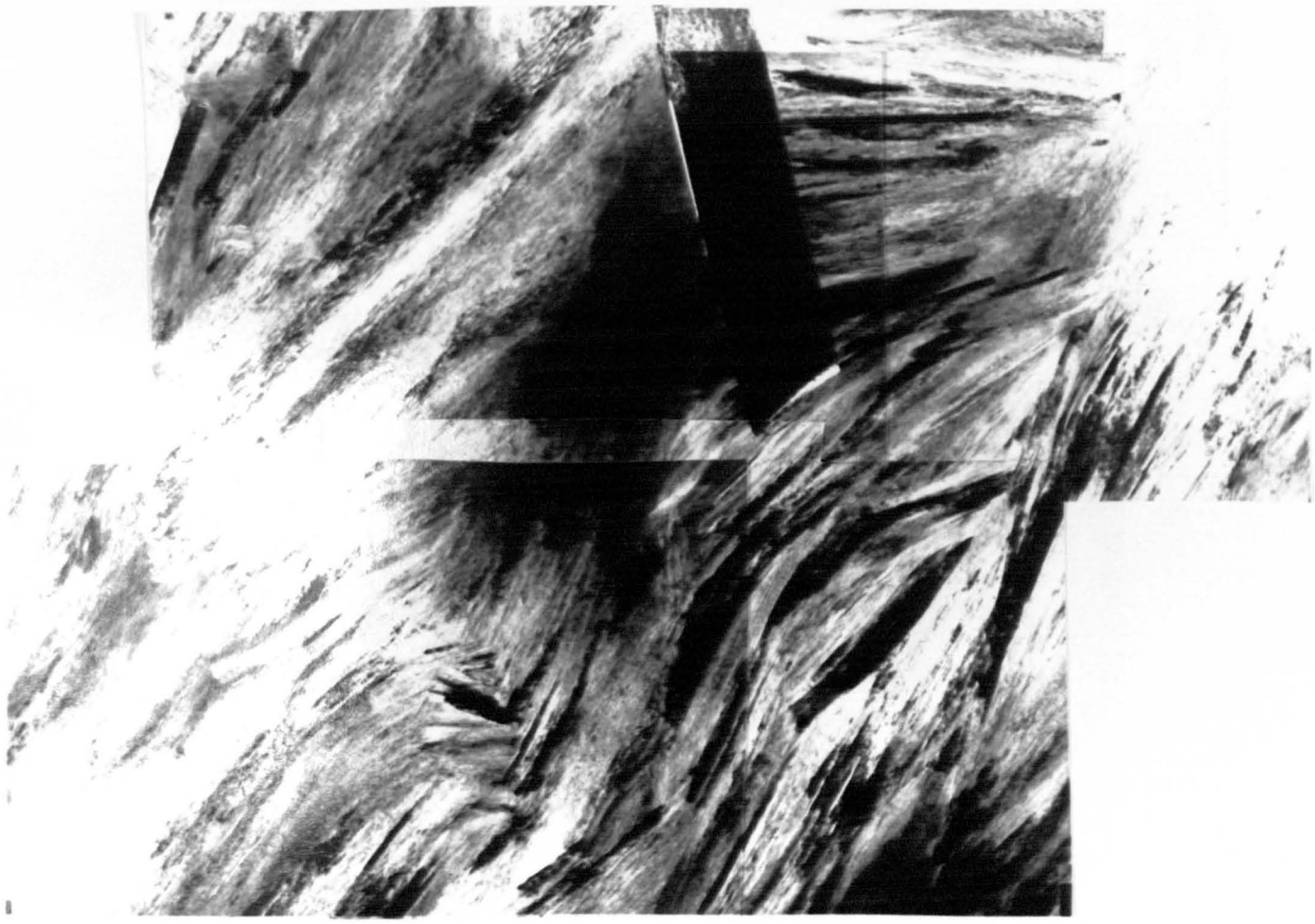

(a)

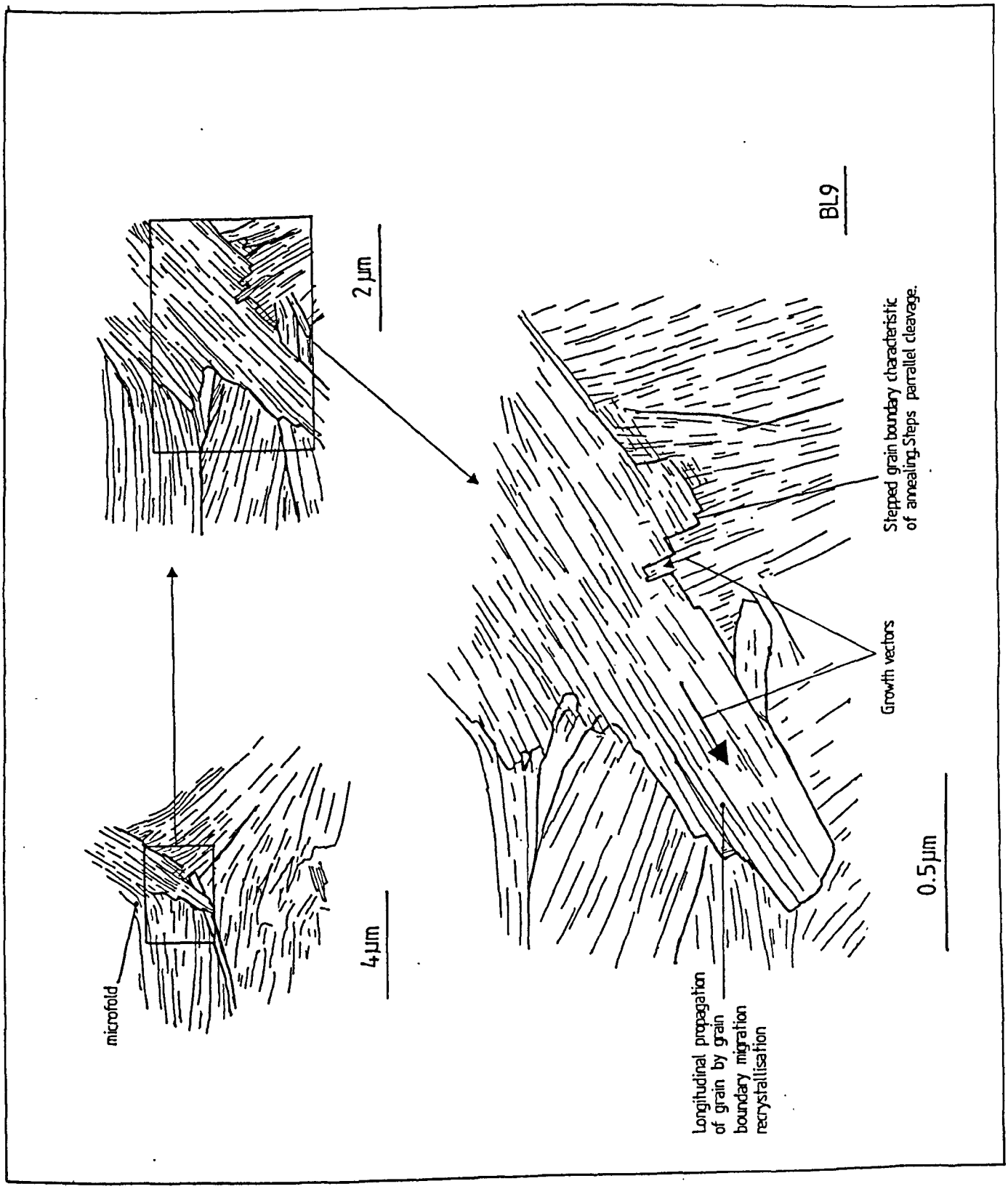

Figure 5.19. Interpreted line tracing of a TEM montage of an annealed kink band boundary. Interpenetration of the grains has occurred by grain boundary migration recrystallisation. The migration occurs primarily parallel to the 001 cleavage.

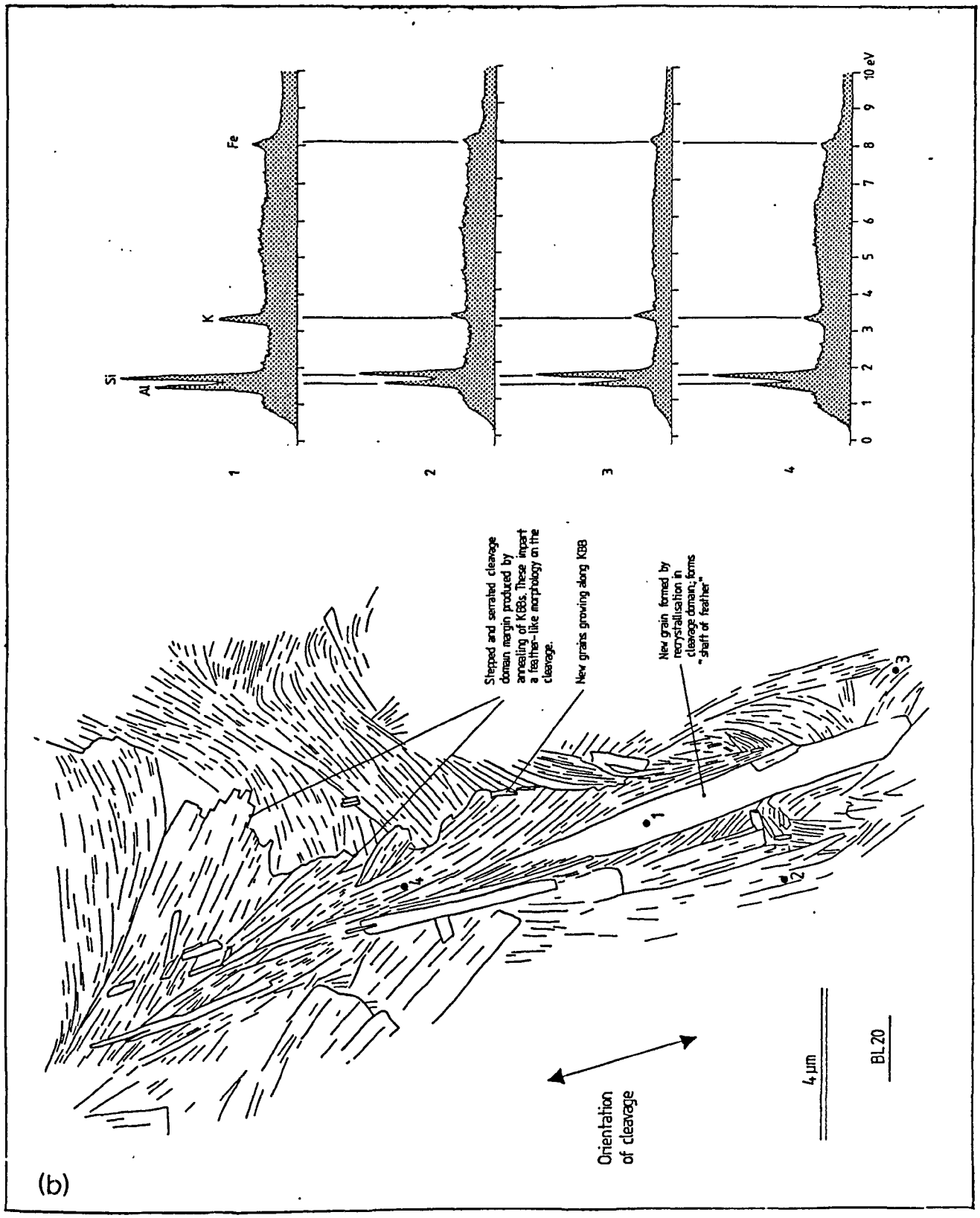

Figure 5.20. a) TEM montage showing feather structure of cleavage domain. b) Interpreted line tracing of montage. The oblique grain structure in the cleavage domain appears to have formed by the annealing of KBBs at the margin of the domain. The cleavage microstructure is similar to that developed in the clastic mica aggregates in the Triassic shales (figure 5.1g). The EDS waveforms of four spot analyses are shown and indicate that the new grain is more muscovitic in composition than the material that it replaces.

a

band boundaries (figure 5.18). In the former, the kink band boundary has been removed by grain boundary migration recrystallisation with the formation of two interlocking grains. Figure 5.19 shows another example of an annealed kink band boundary. The interpenetration and stepped nature of grain boundaries is characteristic of this process (Vernon, 1977). In the latter, nucleation and growth of a new, presumably strain free grain, has removed the kink band boundary and produced three grains. Internal strain energy presumably provides the driving force for the nucleation (Etheridge and Hobbs, 1974). Similar textures have been documented in fine grained slates by Knipe and White (1977) and White and Knipe (1978).

2. Cleavage domain microstructures.

The cleavage domains have short sub-planar traces defined by narrow zones of oriented micas. The micas are often oblique to the margins of the domains and impart a feather-like morphology on the cleavage lamellae (figures 5.17c, 5.17f and 5.20). The oblique grains subtend angles between 5 and 40 degrees. In figure 5.20 the feather-like structure is enhanced by the growth of a large new muscovite grain along the centre of the cleavage domain, replacing the original oblique grain structure. Qualitative EDS analysis of the old and new grains indicate that the latter possess higher K and lower Fe and Si than the former. This points to localised metamorphic reactions within the cleavage lamellae with mica of more muscovitic composition replacing the original pyrophyllite-phengite mixture.

Recrystallisation is not restricted to within the cleavage lamellae. Figure 5.21 shows a large grain boundary bulge consuming high angle intercleavage domain grains along the margin of a cleavage lamella. This structure leads to a transition from a diffuse zone of grain bending into a sharp truncated margin to the cleavage domain. Thus, three types of cleavage lamellae border microstructure can be recognised (figure 5.22):

1. A serrated margin formed by the overlapping terminations of elongate mica grains oriented obliquely to the cleavage lamellae (figure 5.22(3)). These grains form the barbs of the feather structure documented above. The serrated cleavage margins probably from the annealing of kink or deformation bands. This suggests that the feather-like structure of the cleavage lamellae is primarily a product of kinking and implies that grain rotation played an important role in initiating the cleavage domains.
2. A diffuse margin formed by the progressive gentle curving of phyllosilicate grains into the cleavage lamella orientation (figure 5.22(2)). Diffuse cleavage margins reflect the initial microstructure that is modified to produce the feather structure.
3. A discrete, planar boundary (figure 5.22(1)). This develops where the elongate cleavage grains are exactly parallel to the lamellae borders and the grains in the the intercleavage domains abutt this border at high angles. This microstructure may have

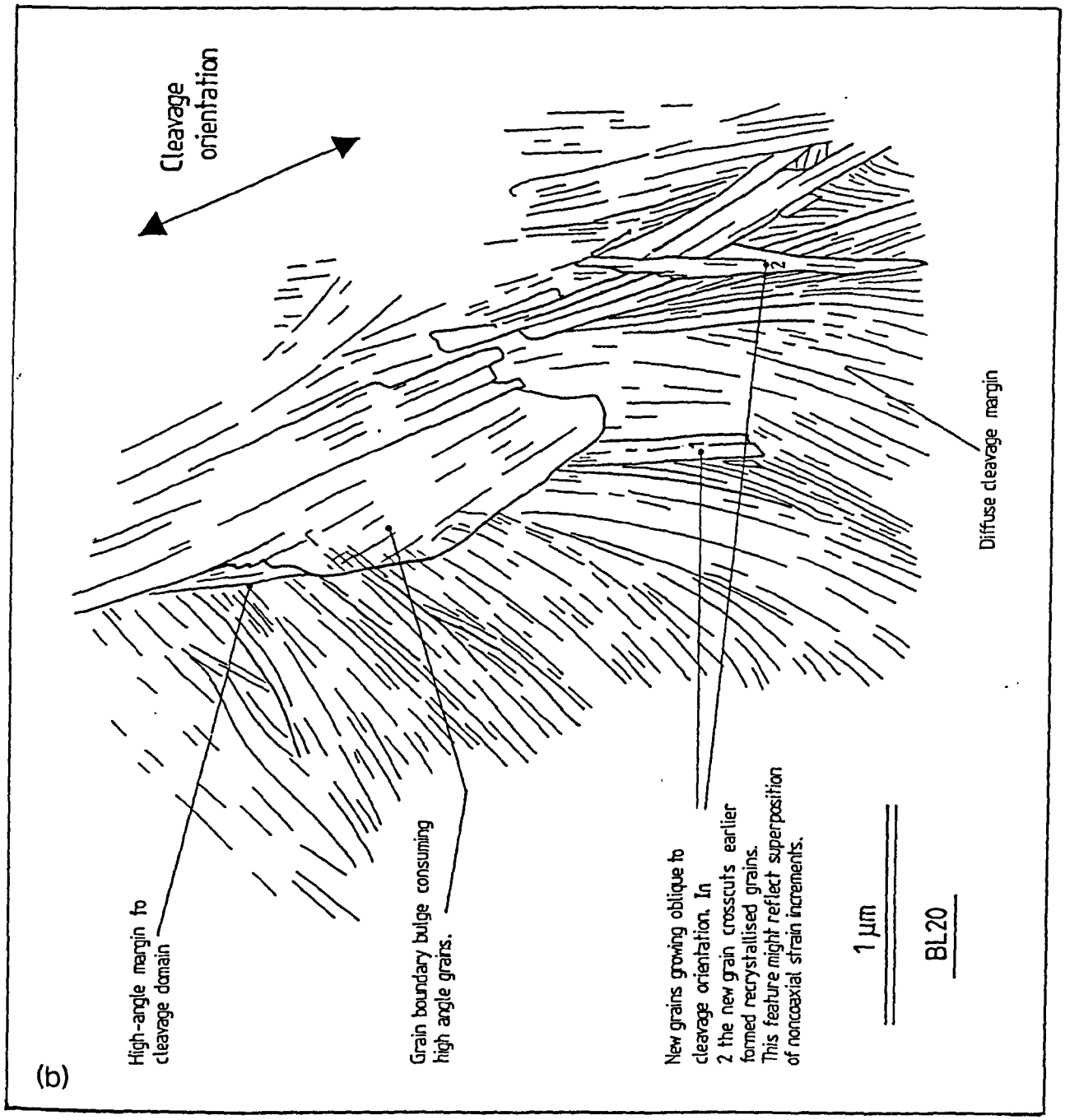

Figure 5.21. a) TEM montage showing a grain boundary bulge from a cleavage domain grain consuming high angle grains in the adjacent microlithon. b) Interpreted line tracing of montage.

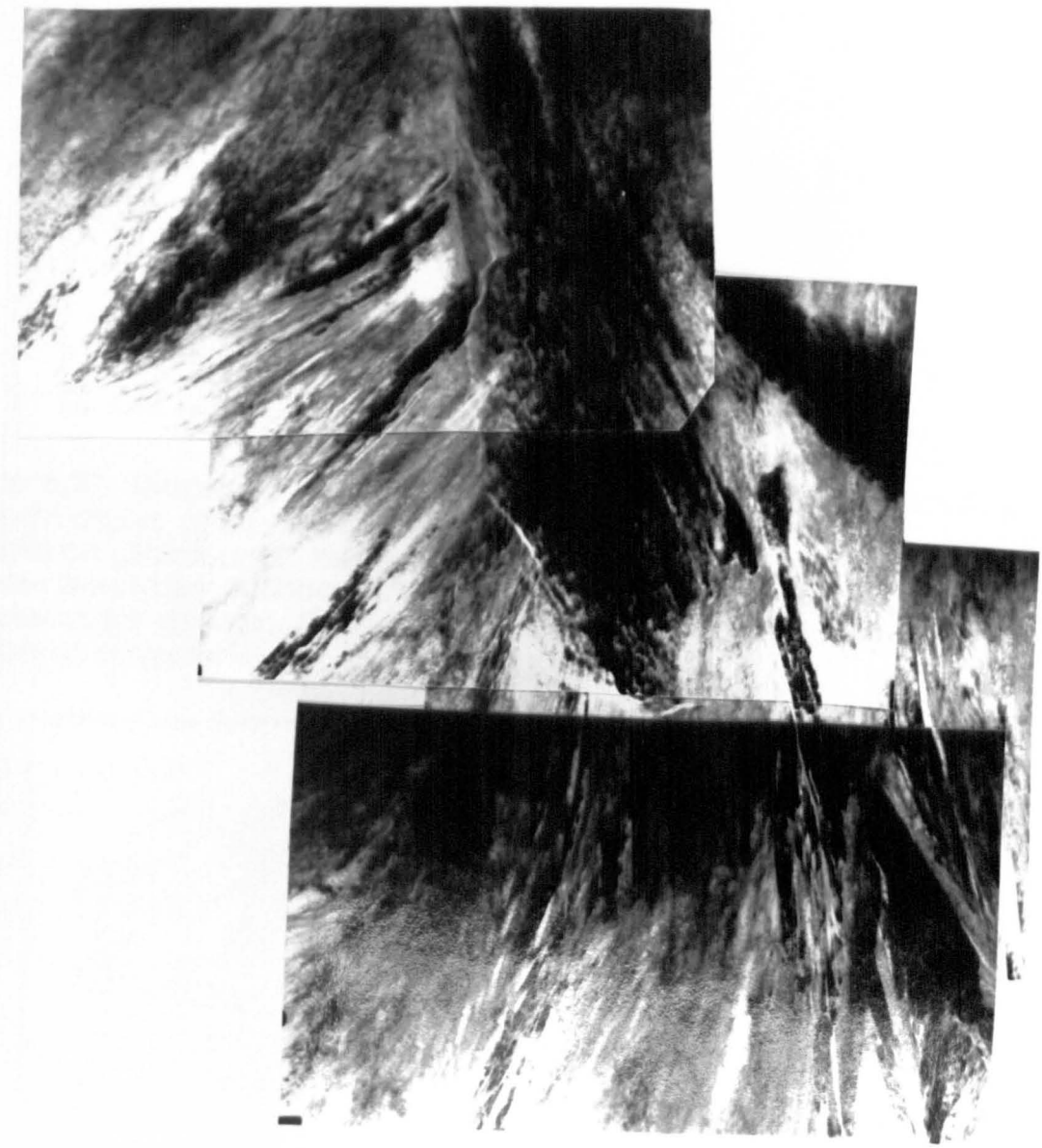

1μm

a

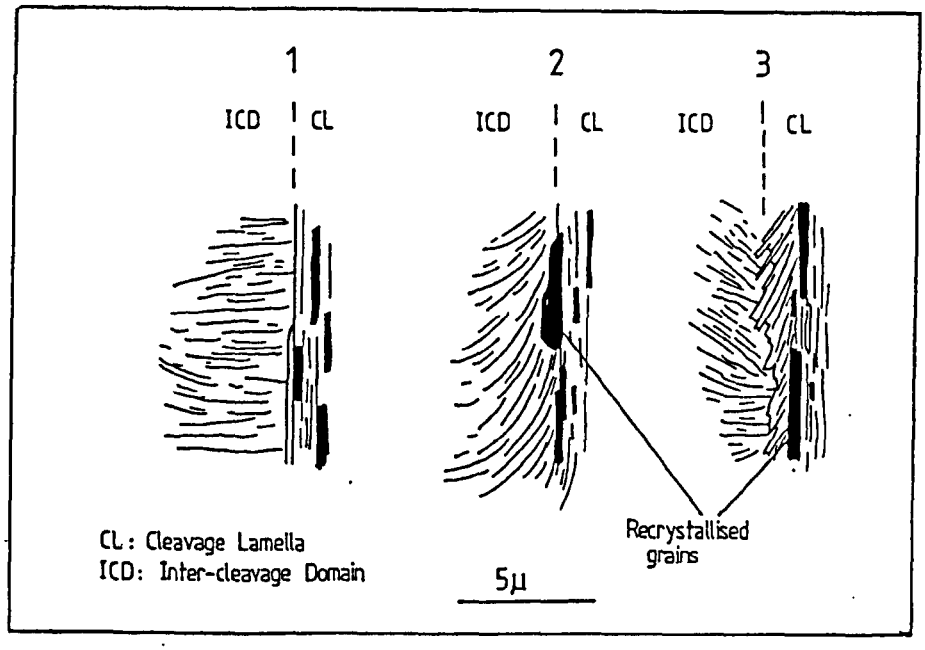

Figure 5.22. Diagram summarising the types of cleavage domain boundary microstructures observed in the matrix mica. 1. Discrete boundary where the microlithon grains abutt the cleavage grains at high angles. 2. Diffuse or zonal domain boundary defined by the progressive bending of microlithon grains into the cleavage domain. 3. Feather structure produced by migration of original kink-band boundaries.

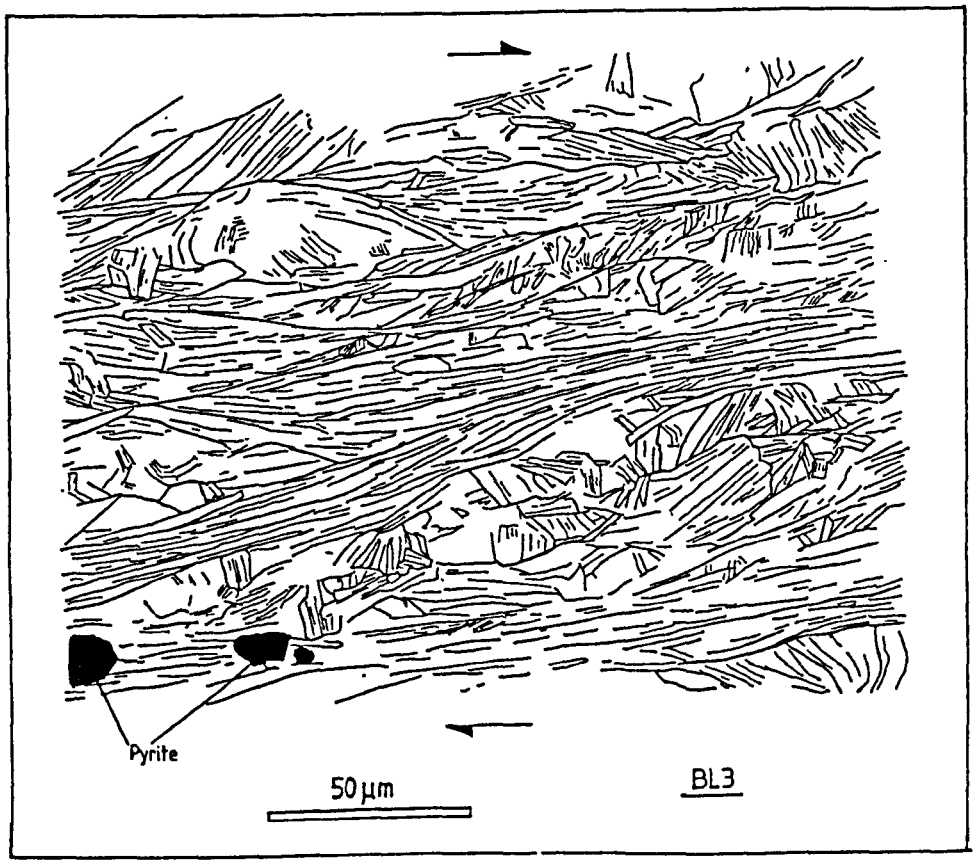

Figure 5.23. Line tracing from a BSEM montage of the phyllonite fabric developed in sample BL3. The intense fabric domains anastomose around lenticular phyllosilicate aggregates containing grains at high angle to the main foliation.

formed by either recrystallisation or by pressure solution ,that has removed a previously formed diffuse or serrated lamella margin microstructure.
No fine grained break down zones comprising kinked and folded phyllosilicate grains as described by White and Knipe (1978) and Knipe (1981) are observed along the cleavage lamellae borders. The growth of new grains within the lamellae did however give them a laminated appearance.

Apart from the elongate grains within the discrete, narrow cleavage lamellae, other large grains are also dimensionally oriented parallel or subparallel to the cleavage. These grains are composed of discordantly interlayered muscovite and pyrophyllite. The discordance in the interlayering takes the form of incoherent boundaries (Lee et.al, 1984 and 1985) that are probably an original growth feature of the grains. Incoherent boundaries are small-angle planar boundaries separating misoriented packets of mica layers. Similar incoherent boundaries in the cleavage lamellae grains account for their feather-like structure. The large cleavage-parallel grains represent grains whose original (pre-deformation) attitude was sub-parallel to the extension direction.

Pyrophyllite has a lower back-scattered contrast than the phengitic muscovite. If syndeformational metamorphic reaction promoted growth of muscovite in the cleavage lamellae then this should be reflected in BSEM micrographs of the cleavage by an absence of pyrophyllite in the cleavage lamellae and the presence of new muscovite grains in the lamellae that grow across the original interlayered pyrophyllite/ muscovite grains. The BSEM micrographs shown in figure 5.17 do not however reveal marked compositional differences between the phyllosilicates in the cleavage and intercleavage domains.

Some of muscovite grains sub-parallel to the cleavage often appeared however to possess pyrophyllite overgrowths (figure 5.17g) while pyrophyllite also appears to concentrate along annealed KBBs. These features provide the only clear evidence for the operation of diffusional processes during the cleavage development as pressure-solved quartz grains were not involved in the fabric development. The presence of the pyrophyllite overgrowths on some of the grains suggests that the local grain boundary fluid had a low K^+/H^+ activity ratio. This is supported by the predominance of pyrophyllite in the associated shear fractures. Where new muscovite grains have grown within the cleavage lamellae they probably record a domain with a higher K^+/H^+ activity ratio. The presence of both neoformed or recrystallised muscovite and pyrophyllite in the cleavage different lamellae suggest therefore that the fluid ambient composition was heterogeneous on the grain scale and probably controlled by local grain-grain reactions. This suggests that the lamellae did not provide channelways for advecting fluid.

Small stubby phyllosilicate grains, often oriented at high angles to the elongate cleavage grains, occupy the spaces between mismatched larger grains in the cleavage lamellae. These small grains formed either as infills of microextension sites (Knipe, 1981) produced during grain boundary sliding or they represent relicts of deformed grains that have been largely removed by recrystallisation. The latter interpretation is supported by the presence of diffusely intergrown grains (figure 5.19) in which two cross-cutting cleavages are developed. This phenomenon does not appear to be a product of the imaging of overlapping grains because interference fringes are absent. It is more likely a product of the growth of a new grain across an old grain during recrystallisation. Knipe (1981) has used similar 'diffuse grain terminations' to infer grain growth by recrystallisation.

The general irregular nature of cleavage margins, the rough nature of the lamellae and the serrated grain boundary textures strongly suggest that no shear displacements occurred along the cleavage lamellae in the samples studied.

5.3.3.2.3. The phyllonitic foliation adjacent to the thrust.

The mesoscopic deformation pattern indicates that the sheared granite evolved from an S=L to an L>>S tectonite as the shear strain increased. The most intense linear fabric occurs in samples BL1, 2 and 3 collected between 23 and 24 metres in the log (figure 5.11). The fabric in these samples comprises phyllosilicate layers possessing a strong preferred orientation (phyllonite layers) and sub-parallel layers of fractured quartz porphyroclasts. Fractures in the quartz are filled with calcite and chlorite. A number of chlorite filled fractures sub-parallel to the foliation are also present (see later).

Figure 5.23 shows a line tracing of a BSEM montage of the phyllonite fabric in sample BL3. The foliation is defined by broad zones of sub-parallel phyllosilicate grains that anastomose around lenticular domains or augen of coarser grained micas. These domains represent relict aggregates in which the grain boundaries and cleavage within the grains are oriented predominantly at high angles to the main fabric. Shear displacements occurred along the fabric and are indicated by the presence of offset phyllosilicate porphyroclasts (figure 5.24). In this example, slip occurred along 001 cleavage fractures in the grain. The most intensely cleavage domains therefore appear to represent narrow shear zones.

A considerable proportion of the matrix in sample BL1 comprises chlorite that replaced the original muscovite. This chlorite proved difficult to ion beam thin with the result that only the mica component of the foliation is able to be studied using the TEM. The fabric comprises elongate phyllosilicate grains with a strong preferred orientation that separate narrow bands of high angle grains (figure 5.24). The overall grain boundary

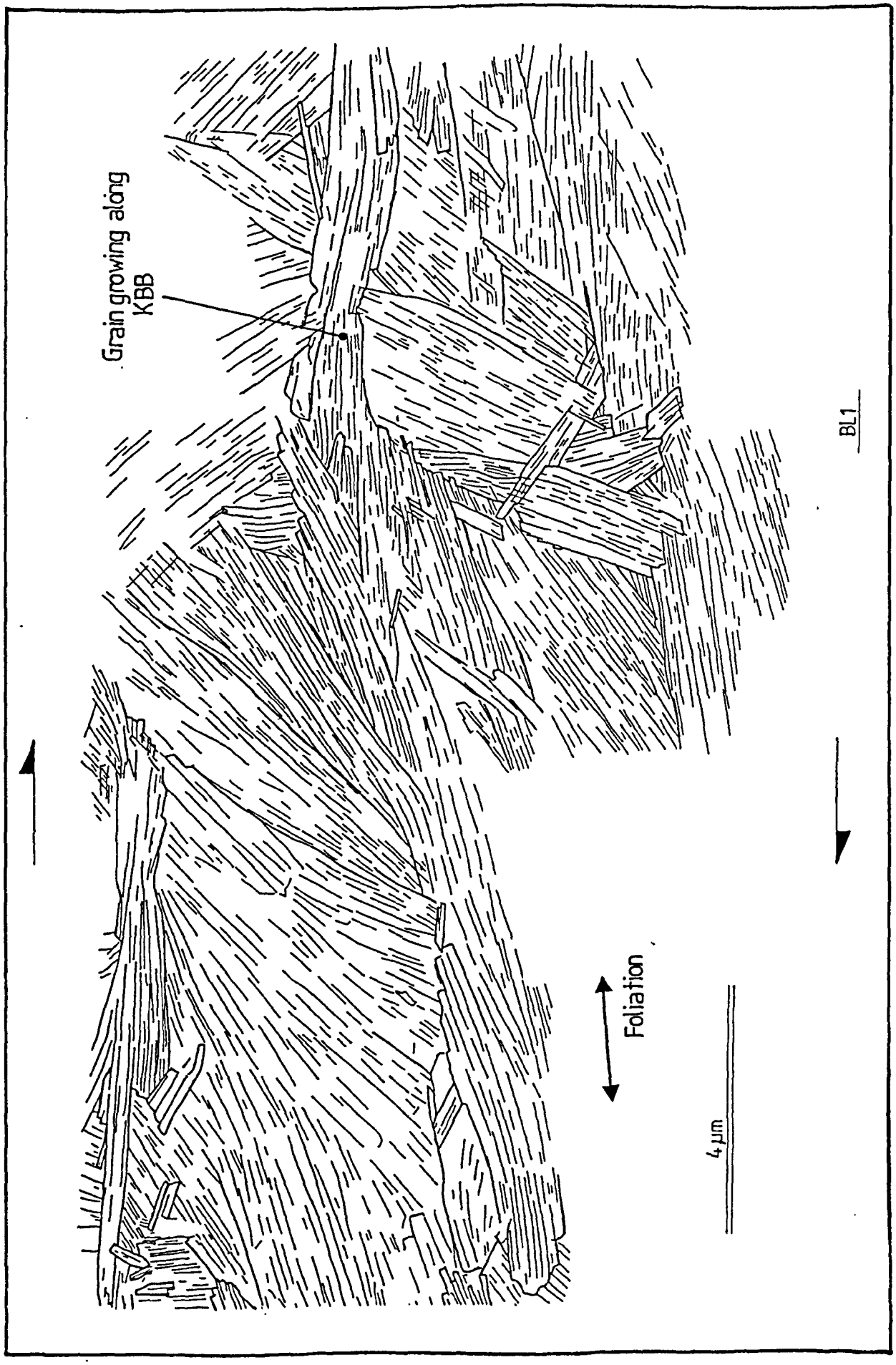

Figure 5.24. Line tracing of TEM montage of phyllonitic fabric in sample BL1. The grain structure is similar to that in cleaved sample further from the thrust. New grains have grown along original kink-band boundaries.

structure is similar to that documented in samples BL20 and BL9 and the cleavage domains have a feather-like structure. This suggests that similar deformation processes operated in the matrix during the fabric development although it was subject to greater shear strains.

In sample BL1 the cleavage domain spacing is about 5 microns and is considerably narrower than in samples BL9 or BL20. High angle lamellae boundaries are also more common. Individual cleavage domains do not appear significantly broader than in the less deformed samples from further from the thrust. This possibly suggests that the fabric intensified by the formation of more cleavage domains rather than by the widening of already existing domains.

5.3.3.2.4. Fractures.

a) Slip surfaces.

1. Slip surface geometries.

In thin section the slip surface patterns reflect the geometries of the grain-scale shear fractures. Slip surface patterns were constructed by mapping the arrays of fractures onto A4 size photographs of individual thin sections using a petrological microscope. Ten samples were mapped and results are shown in figure 5.25.

There is a general increase in the density of fracturing towards the thrust accompanied by an increase in the dilation associated with the fractures. Furthest from the thrust (samples BL14 and BL16) the fractures are short and discontinuous. Although these samples come from outside the 20 metre wide deformation zone shown in figure 5.11, they indicate a weak shear overprint in the rock. With decreasing distance from the thrust the fracture intensity and fracture lengths increase and conjugate arrays develop eg. sample BL19. The fracture distribution is however inhomogeneous and sample BL21 possesses a poorly developed conjugate fracture array although it was collected from closer to the thrust than, for example, sample BL19.

In sample BL19 the lower part of the thin section contains only a few spaced fractures whereas the upper part contains a close- spaced conjugate array. The lower domain also possesses a smaller quartz grain size than the upper domain and consequently a closer quartz grain spacing. This suggests that there is perhaps a relationship between grain size and the degree of fracturing with the finer-grained layers behaving more competently than the coarser-grained layers. A similar relationship is implied between samples BL9 and BL12 with the finer grained BL12 containing a wider fracture spacing.

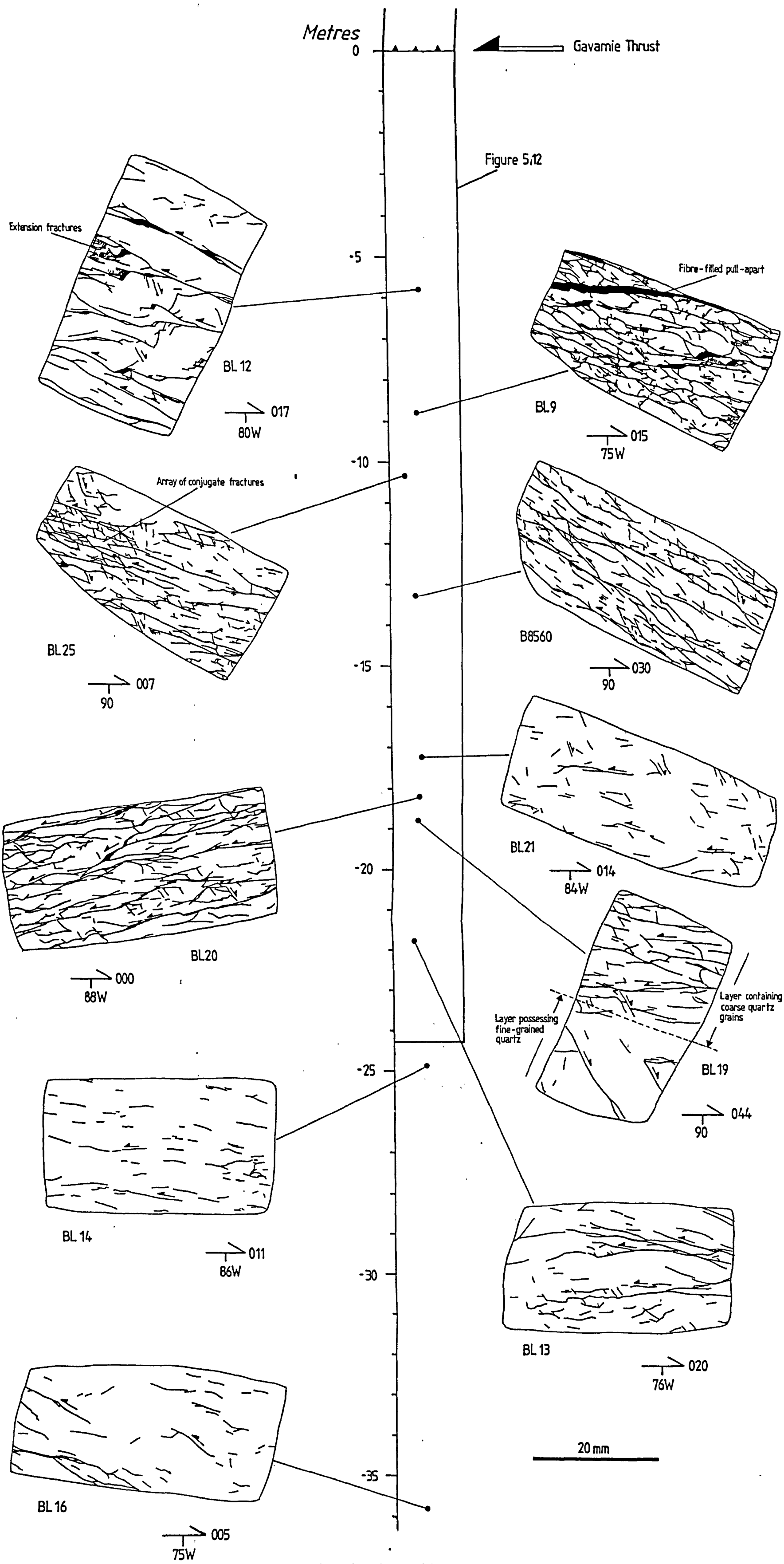

Figure 5.25 Line tracings of fracture patterns in xz thin sections from basement log positioned in terms of depth collected below the Gavarnie Thrust. There is a general increase in fracture intensity towards the thrust. The trapezoidal fracture arrays comprise conjugate fractures that link around the rigid quartz grains.

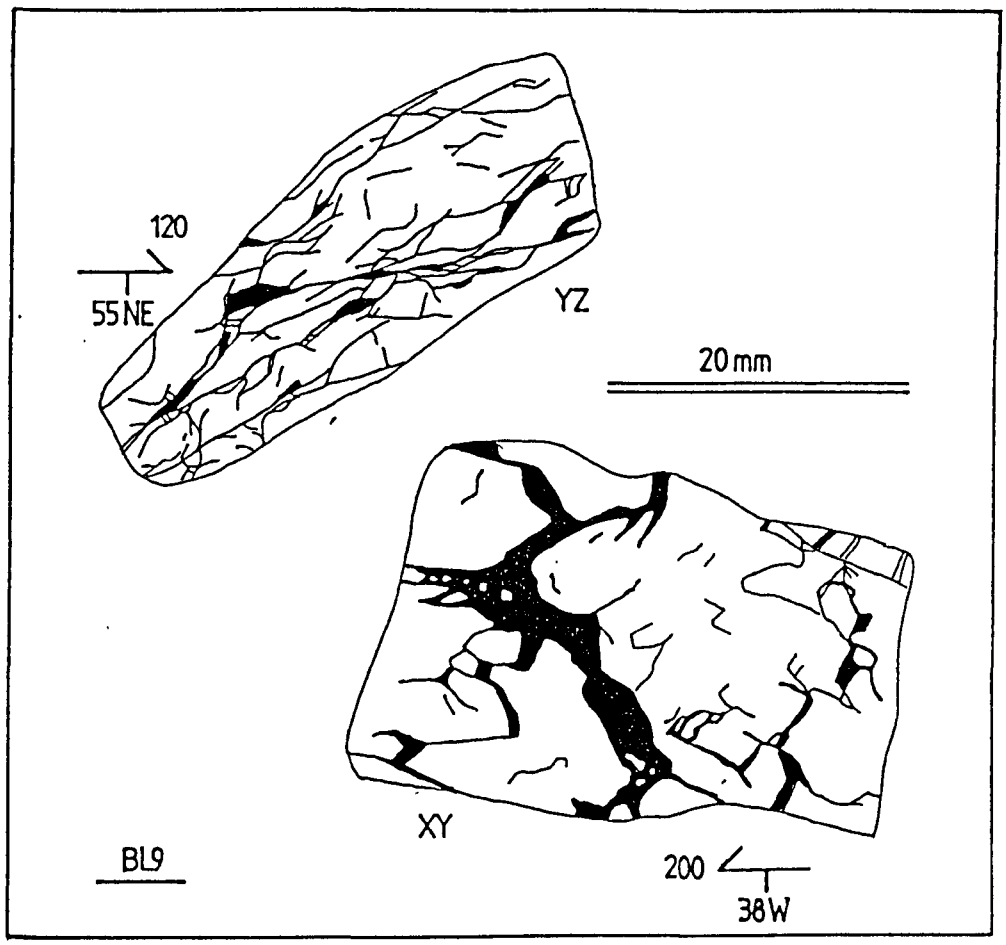

Figure 5.26 Fracture maps for xy and yz sections of sample BL9. The shaded areas represent fibrous quartz-chlorite fracture-fills.

This possibly suggests that the altered basement strata obeyed a Hall-Petch type failure relationship (Wojtal and Mitra, 1986).

In sample BL9 the fracturing differs slightly from the other samples with the additional development of irregular extension fractures that link around the resistant quartz grains. Conjugate fractures are less well-developed in this sample and this possibly reflects the greater ease with which extension rather than shear fractures linked around the quartz grains.

The xy and yz fracture patterns for sample BL9 are shown in figure 5.26. In both thin sections the pattern is trapezoidal. This suggests that the in three dimensions the fractures link to form irregular shaped polyhedra around the quartz grains (figure 5.27). The idealised shapes of these polyhedra can be constructed by considering the different types of fracture pattern seen in the different coordinate planes (figure 5.27a). They link together to form octahedral, truncated octahedral or rhombohedral forms. The number of slip surfaces appears to vary between three and five.

The complete slip surface network is segmented by the large mesoscopic slip surfaces with the intervening blocks deforming by grain-scale shears fractures. In the more deformed samples eg. BL9, the grain-scale slip surfaces can be considered penetrative on the scale of the fault zone. In a sense, the rock deformed by a form of cataclastic flow with sliding occurring on fracture- bound polyhedra. The effective minimum grain size produced during this process was limited by the grain size of the resistant quartz grains.

b) Slip surface microstructures.

The slip surfaces are narrow shear fractures filled with fibrous pyrophyllite, chlorite and quartz. These secondary minerals infill extension sites produced by slip on fractures that were oriented oblique to the movement direction. The fibres track the movement direction. Quartz and chlorite tend to form along the larger more dilatant slip surfaces with the smaller fractures filled solely with pyrophyllite or zoned pyrophyllite-muscovite (figure 5.28).

1. Quartz fibres.

Quartz fibres usually link displaced quartz grains (figure 5.29b) and contain crack-seal chlorite or mica inclusion bands or planar bubble trails perpendicular to the fibre margins. The healed fractures often have zig-zag profiles (figure 5.29d) which appear to have been the product of tensile fracturing along weak cleavage planes within the chlorite and grain boundaries within the mica matrix. The width of individual microcrack

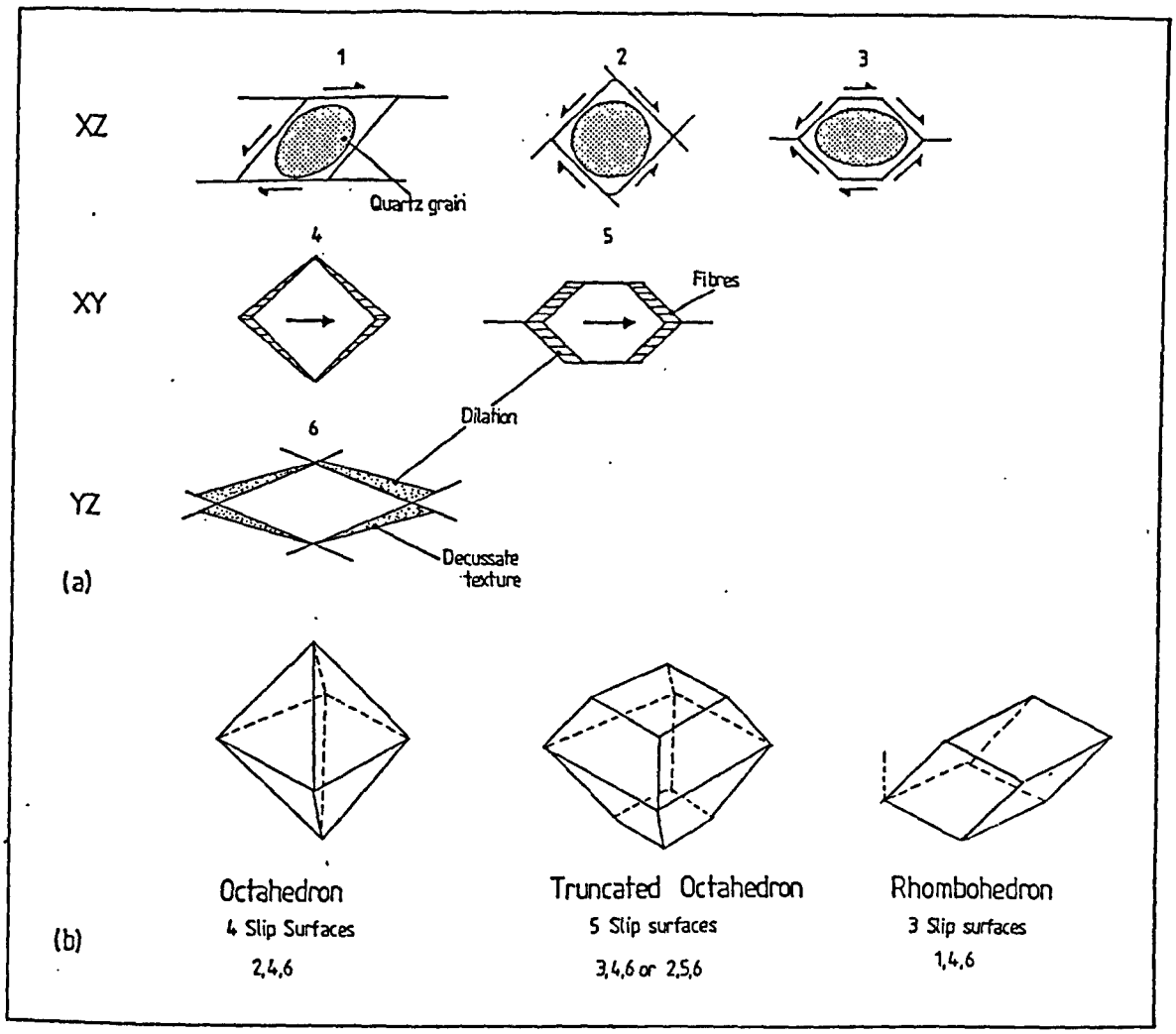

Figure 5.27. Schematic diagram showing the orientation of the slip surfaces observed in thin section and the possible idealised shapes formed by combining these patterns in 3 dimensions. a) Different types of pattern for xz, xy and yz sections. b) In three dimensions the trapezoidal array of slip surfaces link to form either octahedra (4 surfaces), truncated octahedra (5 surfaces) or rhombohedra (3 surfaces) that enclose the resistant quartz grains. In reality the shapes are more irregular than those envisaged here.

Figure 5.28 BSEM micrographs of slip surface microstructures. All micrographs are from sample BL12.
a) and b) Conjugate slip surfaces cutting fine grained muscovite/pyrophyllite matrix. The surfaces link around the quartz grains to give a trapezoidal pattern. Pull-aparts along the stepped fractures are filled with pyrophyllite (shaded).
c) Detail of (a) showing step in slip surface around large interlayered pyrophyllite-muscovite grain. The step is filled with fibrous muscovite and pyrophyllite.
d) Small pyrophyllite-filled stepped slip surface cutting matrix mica. The matrix is composed of very fine grained intergrown pyrophyllite and muscovite and slightly larger interlayered muscovite-pyrophyllite grains.
e) Montage of stepped shear fractures showing zoned pyrophyllite-muscovite fill in pull-aparts.

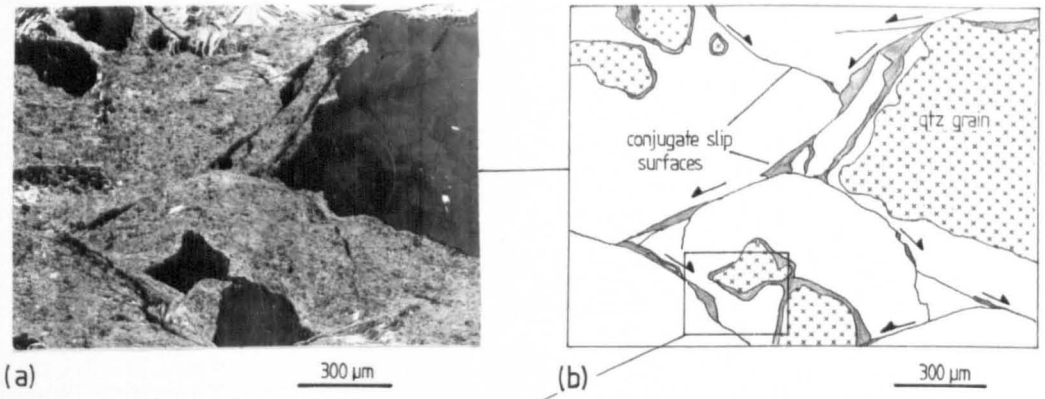
conjugate slip surfaces
qtz grain
(a)
300 µm
(b)
300 µm

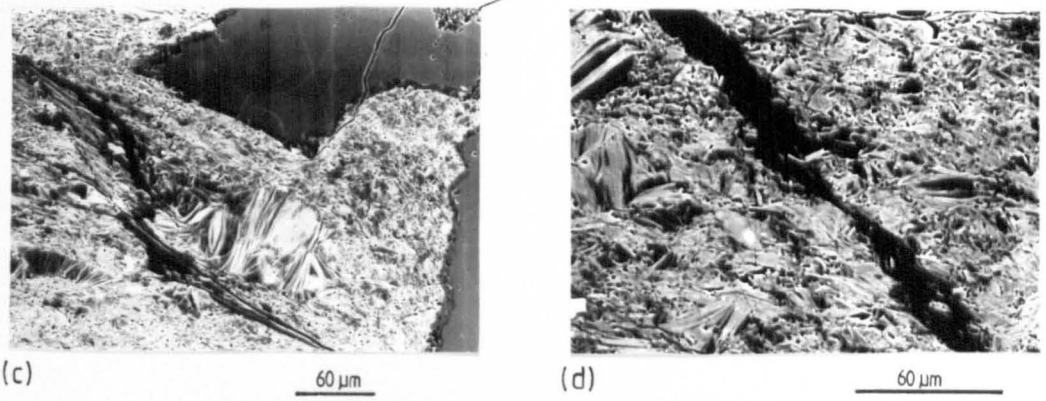
(c)
60 µm
(d)
60 µm

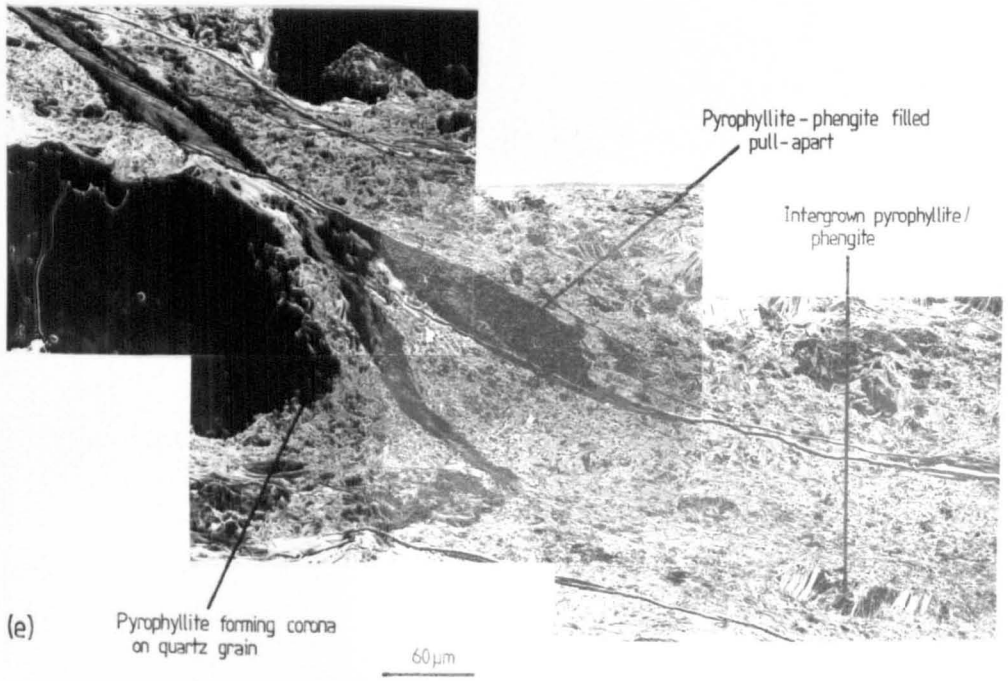
Pyrophyllite - phengite filled pull-apart
Intergrown pyrophyllite / phengite
(e)
Pyrophyllite forming corona on quartz grain
60 µm

(a) 300 µm

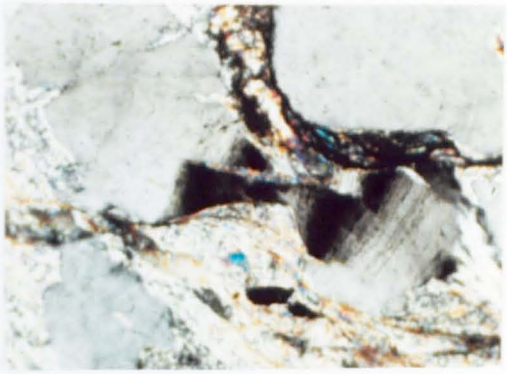

(b) 200 µm

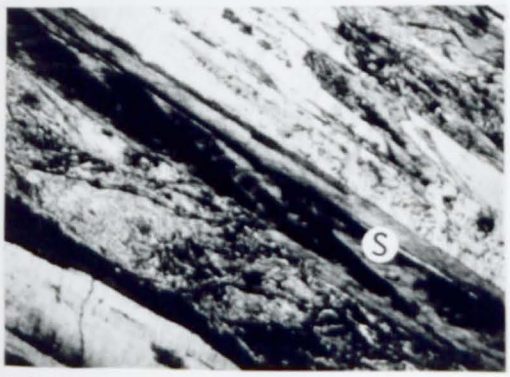

(c) 300 µm

(d) 200 µm

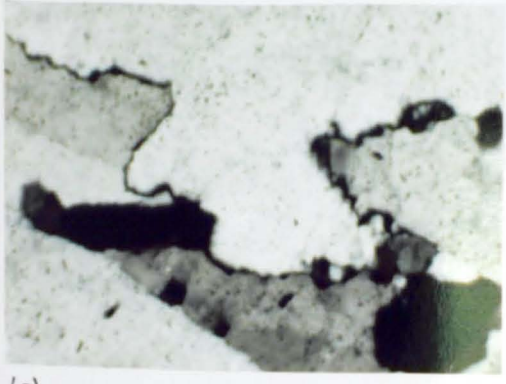

(e) 200 µm

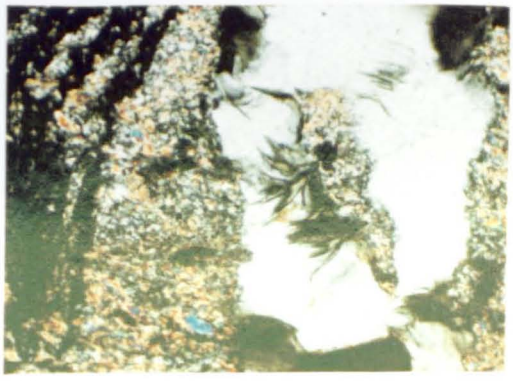

(f) 200 µm

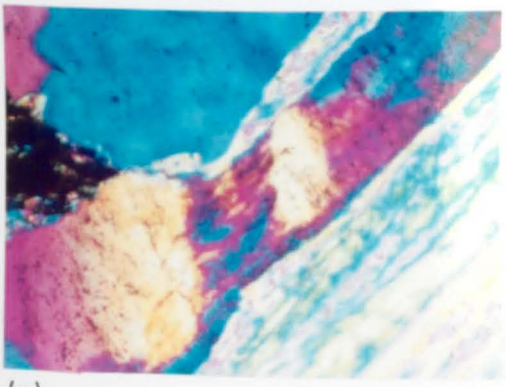

(g) 50 µm

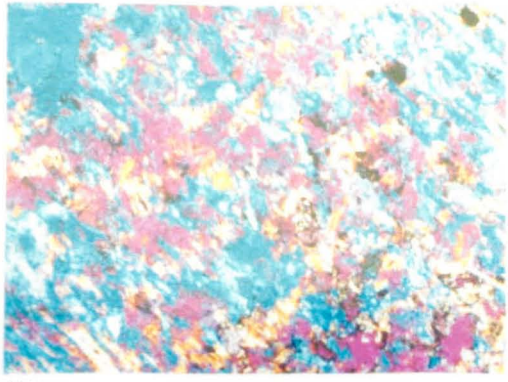

(h) 200 µm

Figure 5.29. Optical micrographs of slip surface microstructures.
a) Pyrophyllite-quartz filled stepped shear fracture cutting cleaved mica matrix. XPL. Sample BL20.
b) Quartz grain cut by a shear fracture and linked by quartz fibres. Crack-seal fluid inclusion bands within the quartz grain change orientation into the shear fibre. The fractures do not appear to have been rotated but indicate changing fracture orientations within the quartz grain as the displacement on the shear fracture increased. The fractures furthest from the slip surface are probably the oldest. They suggest that the grain was extended prior to slip on the shear fracture. This may suggest the shear fracture nucleated on an extension fracture. XPL. Sample B8560.
c) Intrafibre shear bands cutting oblique mineral cleavage in chlorite fibre. XPL. Sample B8562.
d) Zig-zag chlorite crack-seal inclusion bands in quartz shear fibre. XPL. Sample B8562.
e) Grain boundary bulge at margin of quartz fibre. XPL. Sample B8562.
f) Delicate fibrous chlorite growing into crack-seal vein (xy section). This morphology suggests that a dilatant fluid-filled void formed when the vein initially opened. XPL. Sample B8562.
g) Necking of a quartz fibre at margin of pull-apart. The stretching of this fibre in the pull apart must have occurred at a slower strain rate than required to cause crack-seal fracturing of the fibre. XPL with quartz sensitive tint. Sample B8560.
h) Chlorite-filled microfractures in phyllonite fabric. XPL with quartz sensitive tint. Sample BL1.

increments is between 10 and 20 microns. The margins of the fibres are either planar or dentate. In the former the margins are defined by chlorite inclusion trails that represent the transform fractures along which shear displacements were localised (Ramsay and Huber, 1983). The dentate fibre boundaries occur between fibres not separated by inclusion trails. Occasionally lobate grain-boundary bulges occur between neighbouring fibres (figure 5.29e). Both microstructures probably represent the first stages of fibre annealing.

2. Chlorite fibres.

Large chlorite fibres possess sigmoidal or oblique cleavage traces (figure 5.29c) that are always aligned in the direction of slip. The cleavage traces tend to curve asymptotically into the fibre margins and can be used as a shear criterion. Intrafibre shear bands often transect the chlorite shear fibres (figure 5.29c) and occasionally the fibres possess S-C like microstructures (fibre-parallel shear zones cutting the oblique cleavage). Crack-seal inclusion bands are rare in the chlorite fibres and only occur adjacent to the wallrock-fibre contact. Smaller shear fractures possess chlorite fibres with the 001 cleavage parallel to the fibre boundaries.

b) Fracturing in the phyllonite .

In the samples BL1, 2, and 3 brittle deformation occurs predominantly in the form of extension veins and fractured quartz grains. Slip surfaces comparable with those developed in the more distal parts of the deformation zone are absent and localised shear displacements occur along either foliation-parallel shear zones (figure 5.30a) or shear fractures, and on cross-cutting the shear bands.

The original quartz grains are deformed predominantly by stable mode 1 fractures (extension fractures that do not cut the matrix) (figure 5.30d).The fractures appear to have formed by a combination of fibre loading (White et al., 1980; Lloyd and Fergusson, 1982) and by replacement along fluid inclusion trails. The fractures are filled by fibrous calcite while chlorite is often seen adjacent to the matrix (figure 5.30d). The shearing within the matrix rotated the inequant quartz fragments and produced rolling structures (figure 5.30c) and passive folds in the matrix fabric similar to those modeled by Van der Dreissche and Bruhn (1987). The rotation of the quartz porphyroclasts also reoriented the original extension fractures into orientations favouring shear displacements (figure 5.31). Shear displacements also occur on fractures parallel to the shear plane (figure 6.31c).

Small chlorite-filled fractures are occasionally developed within the mica matrix in the pressure shadows of the quartz grains (figure 5.29h). The oriented growth of the chlorite helps to augment the phyllonite foliation (cf. Cox and Etheridge, 1983). Some of these

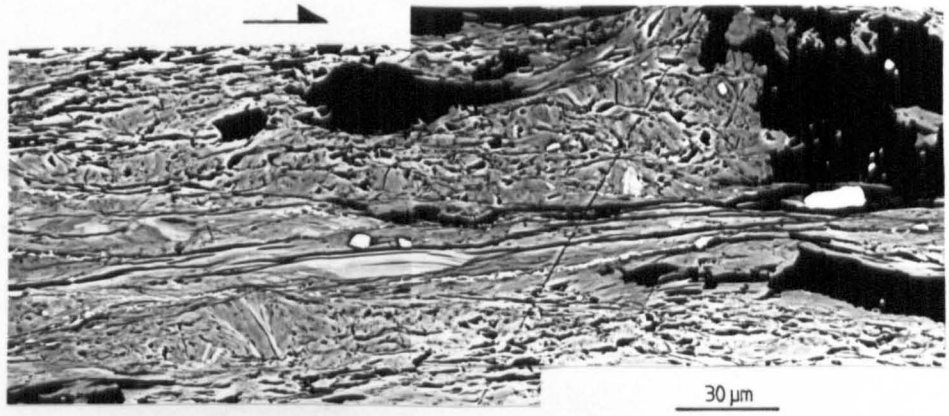

(a)

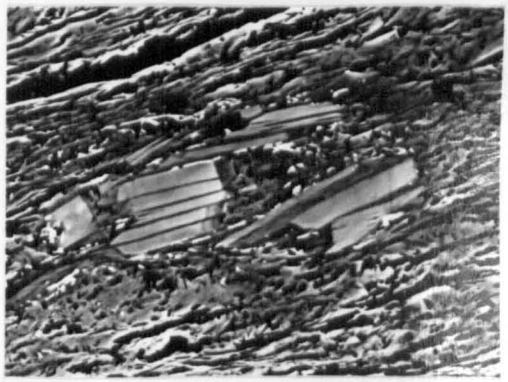

(b)

(c)

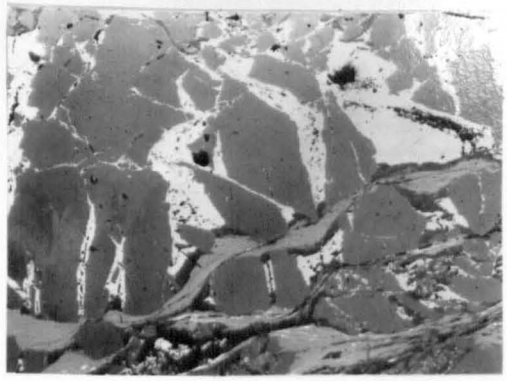

(d)

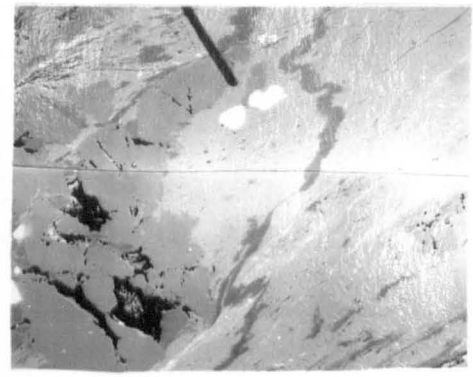

(e)

Figure 5.30. BSEM micrographs of microstructures in the phyllonite adjacent to the thrust.
a) Montage of thin shear zone. The zone is defined by a strong orientation of elongate phyllosilicate grains. These contrast with the finer grained phyllosilicates in the matrix. Sample BL3.
b) Shear displacements along mineral cleavage in porphyroclast. Sample BL3.
c) Rolling-structures in detached quartz fragments linked by clinochlore tails. Sample BL1.
d) Calcite-filled stable extension fractures in quartz grain. These fractures appear to have formed by a combination of replacement of the quartz by calcite and by fibre-loading. Clinochlore tends to form along the margins of the calcite veins. Sample BL1.
e) Folded clinochlore-filled extension vein in mica matrix Sample BL1.

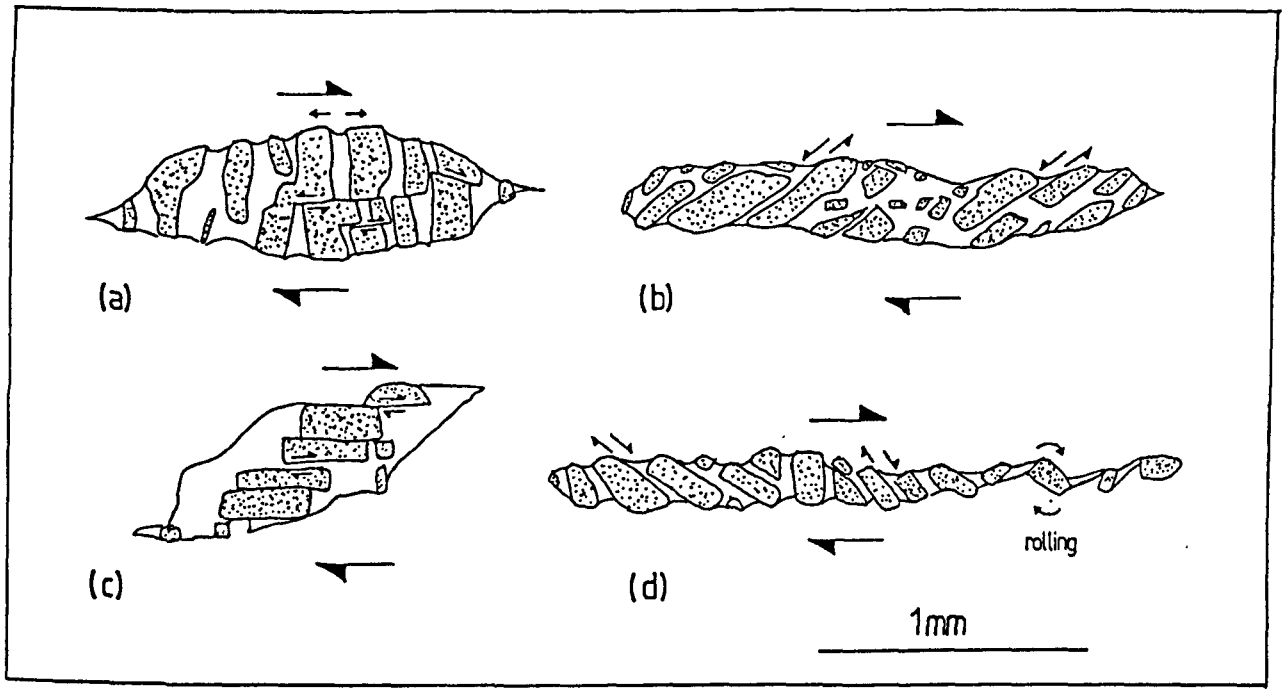

Figure 5.31. Different types of fracture pattern observed in quartz porphyroclasts in sample BL1. a) Extension fracturing. The movement of individual fragments is facilitated by shear fractures within the grain. b) Rotated extension fractures showing antithetic shear displacements. c) Grain deformed by shear fractures parallel to shear plane. d) Rotated extension fractures showing synthetic shear displacements. Detached grain fragments develop rolling structures.

fractures are folded by continued shearing (figure 5.30e) and point to cyclicity between ductile shearing and fracturing during the deformation. Large transgranular fractures are related to the displacement on the late-stage shear bands that cut across the foliation-parallel shear zones and shear fractures.

5.3.4. Discussion

5.3.4.1. Synthesis of cleavage development.

The main deformation mechanism involved in the cleavage development appears to have been folding and kinking of grains. This affected grains at high angles to the shortening direction and was responsible for the rotation of grains towards the cleavage orientation. Once formed, the folds and kinks were then annealed by a recovery-recrystallisation process that involved:

1. Grain boundary migration recrystallisation responsible for migration of kink band boundaries; and
2. the nucleation and growth of strain free grains parallel to the kink band boundaries and parallel to the cleavage domains.

These processes produced characteristic stepped and interdigitating grain boundaries. The steps are bounded by the mineral cleavage in neighbouring grains. Similar observations concerning the deformation of phyllosilicates have been made by Etheridge and Hobbs (1974), Vernon (1977) and Wilson and Bell (1979) but from much coarser-grained rocks. The role of DMT in producing the fabric is difficult to quantify due to the absence of marker grains although its presence is attested by local grain overgrowths.

A diagram summarising the cleavage formation processes is shown in figure 5.32 for three different initial grain structures. The development of the cleavage can be considered a three stage process (steps 2-4 in figure 5.32):

1. Initial kinking and folding of grains. The grain rotation is probably facilitated by grain boundary sliding.
2. Annealing of grain and kink-band boundaries. This produces the feather-like cleavage structure.
3. Recrystallisation of the cleavage-lamellae grains. This is a recovery process that produced large probably strain-free cleavage-parallel grains. It appears to be accompanied by local metamorphic reaction.

5.3.4.2. Fracture development.

The slip surface arrays represent the shear failure of the mica matrix following the plastic flow that produced the foliation. This time sequence possibly suggests that the fractures

represent some form of ductile fracture linked to the creep in the mica matrix. This is also suggested by the observation that many of the fractures tend to form within the more cleaved domains. The equivalent fracture mechanism in ceramics is transgranular creep fracture (Ghandi and Ashby, 1979) where the fractures form by the nucleation, plastic growth and coalescence of voids. It is difficult to show conclusively whether the fractures propagated as mode 1 (extension) fractures or mode 2 (shear) fractures. The presence of stepped fracture profiles (the steps represent small tensile fractures) and oblique slip on many of the fractures possibly imply that the fractures initially propagated as mode 1 fractures that were then used for shear displacements.

The shear displacements on the linked fracture arrays can be envisaged as akin to fracture assisted grain boundary sliding ie. cataclastic flow. As pointed out by Schmid (1983) this is a ductile deformation mechanism although it is fracture assisted. The overall fracture arrays probably formed by the propagation and linking of individual fractures that appear to have nucleated in the zones of increased deformation bordering the resistant quartz grains. The large fractures localised the greatest displacements and eventually developed into the mesoscopic slip surfaces. The smaller fractures linked together to form a pervasive fabric in the intervening rock. The linking of fractures occurred primarily by the formation of the stepped tensile fractures and by fracture splaying. Conjugate sets developed although most of the displacement is concentrated on the the top-to-south fractures. It was the movement over the stepped fractures that produced the observed dilation in the fault zone.

The overall geometry of the fracture arrays is similar to that documented from the footwall of some of the small thrusts from within the PPV culmination (see figure 5.8a). The fault zone probably represents a larger scale example of this style of footwall deformation and it is feasible that the mesoscopic fracture pattern (figure 5.11) can similarly be interpreted as an interaction of synchronously developing P and R1 shears. This would explain why most of the fractures do not form parallel to the thrust.

5.3.4.3. Finite strain state within the fault zone.

Few of the mesoscopic or microscopic slip surfaces within the deformation zone are coplanar with the overlying Gavarnie Thrust. The question that must be asked is: can the overall movement of these fracture sets have approximated heterogeneous fault-parallel simple shear within the deformation zone?

The fibres developed on the slip surfaces all record the same north-south directed slip. This indicates that no movement occurred out of the plane containing the movement direction and suggests that the bulk strain within the zone is plane strain. Two other factors must be considered: the orientation of the slip surfaces and the dilation within the

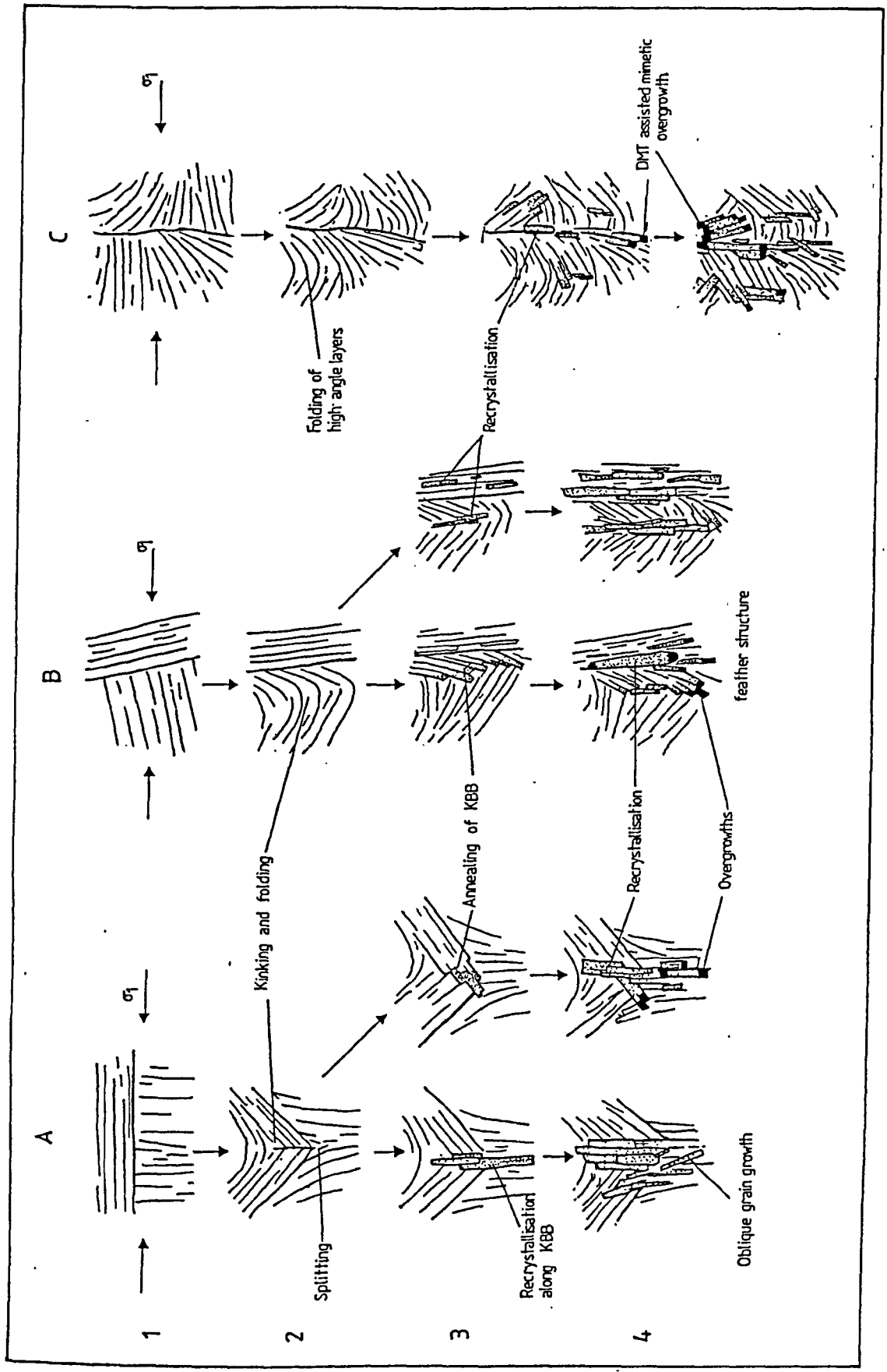

Figure 5.32. Diagram summarising the evolution of cleavage in the mica matrix for three different initial grain arrangements (A,B and C). Stage 2 involves initial folding and kinking of the high angle grains. Stages 3 and 4 represent progressive annealing of the deformation band boundaries formed during the folding and recrystallisation within the cleavage domains to produce large strain free grains. These processes are augmented by DMT that produces overgrowths on some of the grains.

fault zone. McCaig (1987) has discussed the compatibility of fracture generated dilatancy in shear zones with boundary-parallel simple shear. He recognises four possible types of extensional fracture (figure 5.33a). Only types C fractures violate simple shear within the fault zone because they must result in deformation of the shear zone boundaries. The other fracture orientations result in shear zone dilation but are compatible with simple shear as the shear zone boundaries are not required to deform. The reason for generating dilation in the shear zones could be to accommodate a superposed irrotational strain on the shear zone/wallrock system during shearing.

Comparison with the rhombohedral pull aparts along the slip surfaces suggest they correspond to type C fractures for thrust parallel simple shear. It is unlikely therefore that the local strain state responsible for the formation of the grain-scale slip surfaces in the deformation zone coincided with thrust- parallel simple shear.

The conjugate slip surfaces must have accommodated stretching in the blocks bounded by the mesoscopic shear surfaces (figure 5.33b). The resultant pattern is therefore similar to that modeled by Platt (1984) and shown in figure 5.8a. It is possible that the overall simple shear in the deformation zone was partitioned into pure shear in the units bound by the mesoscopic slip surfaces coupled with sliding on these surfaces and spin of the whole system (see figure 5.8a). The pure shear stretch is recorded by the development of the conjugate grain-scale fractures. The absence of strain markers within the granite prevents further qualification of this model. It does explain why the grain-scale shear zones are incompatible with simple shear.

The development of shear bands and vertical extension veins suggest that a component of flattening affected at least the upper parts of the deformation zone. It would be difficult to differentiate the effects of this flattening from the extension produced in the above model for the conjugate grain scale slip surfaces. However, the overall 3-D pattern of the slip surfaces, in which the polyhedra are more lenticular shaped in the yz plane than in the xy or xz planes (compare sample BL9 in figure 5.25 and 5.26), is similar to that predicted by Gapais et al., (1986) for plane strain zones that have suffered a component of flattening. The possible strain state for the fault zone is shown in figure 5.33c. The overall strain ellipses for the zone have to be prolate in the direction of thrust transport to agree with the inferred plane strain state.

As already mentioned, the grain scale shear fractures form the surfaces of polyhedra that enclose the resistant quartz grains. The xy,yz and zx fracture patterns can be combined to form rhombohedral, octahedral and truncated octahedral polyhedra (figure 5.27) and suggest that the deformation was accommodated on between 3 and 5 fracture surfaces. Reches (1978) has shown that 5 (for a irrotational general deformation) and 6 (for a rotational deformation) slip surface orientations are required to produce a

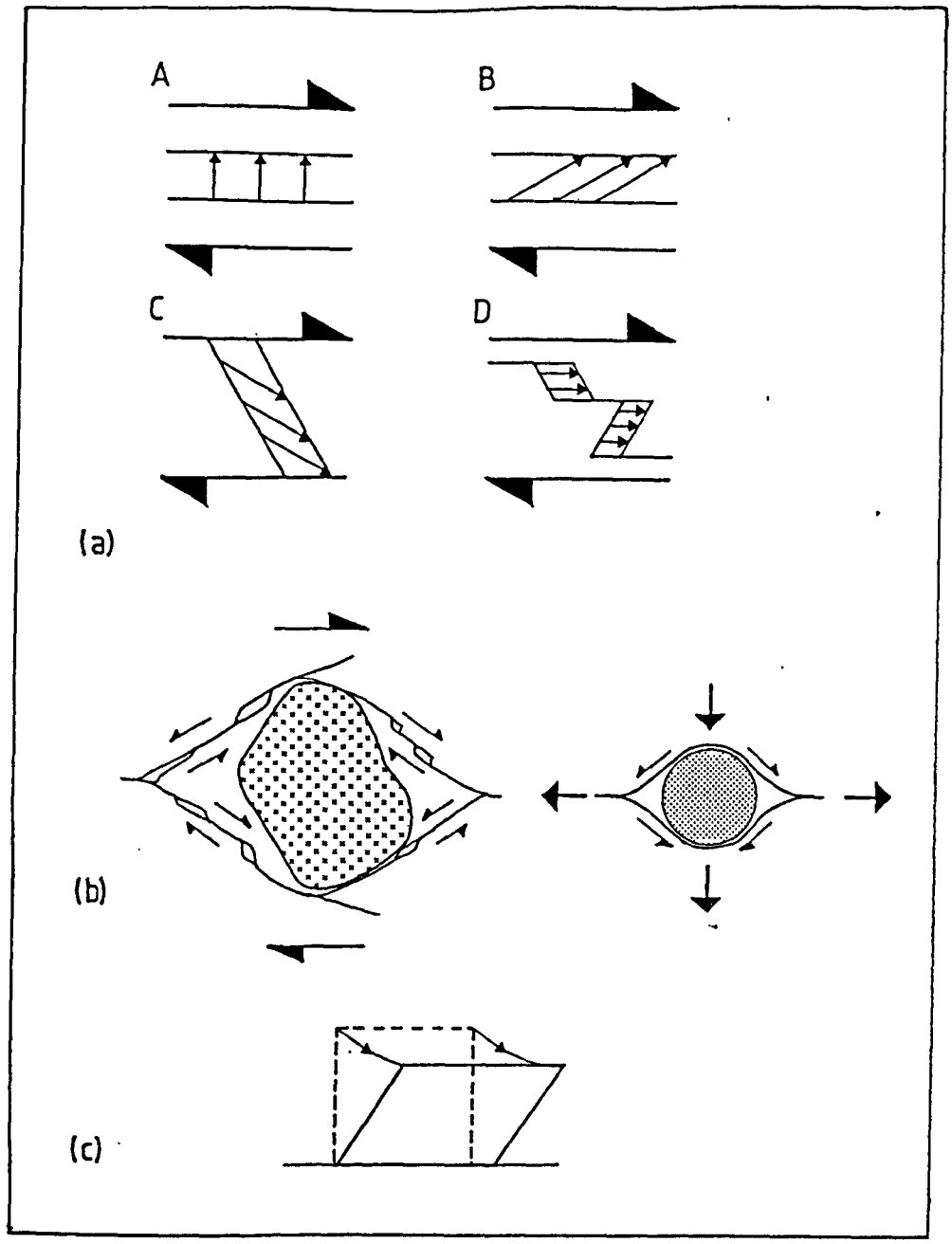

Figure 5.33. a) Types of fracture dilatancy possible in simple shear zones. A: Boundary-parallel extension vein dilating normal to shear zone displacement direction. B: Boundary-parallel vein dilating oblique to shear zone displacement field. C: Oblique vein dilating oblique to shear zone displacement field. D: Oblique extensional veins dilating parallel to shear zone displacement field. Only type C veins lead to heterogeneous wall deformation. (After McCaig, 1987). b) Orientation of displacements on conjugate slip surfaces enclosing quartz grain. The displacements on these surfaces cannot correspond to simple shear on the grain scale. The displacements are more like those expected for pure shear. c) Possible deformation model for the strain in the fault zone. It is envisaged as shear plus flattening across the shear plane.

homogeneous deformation without the generation of voids. This is equivalent of the Von Mises criterion for plastic deformation in crystalline materials. It is possible that the dilatancy generated within the fault zone was a necessary product of the deformation simply because the observed polyhedra generated during the shearing possessed fewer surfaces than required to satisfy the Von Mises criterion.

5.3.4.4. Fracture fill compositions and fluid sources.

The composition and chemistry of the fracture-fill phases changes spatially across the deformation zone. Both quartz and chlorite are more important as fracture filling phases in the more intensely fractured (and therefore more dilatant) samples and appear preferentially developed in a zone located 10 metres below the thrust. Pyrophyllite shows a concomitant decrease in this zone. In some fractures it also changes to a muscovitic composition in the pull aparts (eg. figure 5.28). Calcite fracture fill only occurs in the intensely sheared phyllonite adjacent to the thin layer of Cretaceous limestone mylonite at 24 metres in the log. The presence of this calcite is accompanied by replacement of the matrix mica by chlorite (figure 5.16f).

The composition of chlorite in the fractures is studied in detail in chapter 6. The results of this study show that the chlorite composition changes systematically across the deformation zone, and becomes very Mg rich adjacent to the thrust. A blip however occurs in a narrow zone 10 metres below the thrust where the chlorites are more Mg rich than expected (see figure 6.18). This zone correlates precisely with the zone in which the fracturing is most intense and in which the fractures are preferentially sealed by quartz and chlorite. It also coincides with the zone where extension rather than shear fractures in the mica matrix link around the quartz grains. Together these features suggest that:
1. The zone was a locus for increased fluid flow due to its greater fracture permeability.
2. The fluid that was present in the zone was not derived from the immediate wall rock and precipitated an exotic mineral assemblage.
3. The fluid had a higher Mg^{2+}/Fe^{2+} activity ratio and higher Si^{4+} activity than the fluid in the adjacent altered rock. The former feature correlates with the fluid associated with the limestone which was responsible for the localised Mg-metasomatism of the basement adjacent to the Cretaceous unconformity.
4. The fluid pressure in the zone may have been higher than in the surrounding rock to explain the predominance of tensile rather than shear fracturing around quartz grains.

The main implications of the fracture-fill composition and fracture-fill distribution in the fault zone are:
1. Fluid was preferentially channelled along two zones, one parallel to the Cretaceous unconformity, the other some 10 metres below the PPVT thrust. The latter zone appears to have tapped fluid from the former.

2. Although extensively fractured, the rock outside these two narrow zones does not appear to have provided a pathway for externally derived fluid. Instead, the predominance of pyrophyllite-filled fractures suggests that the fluid was equilibrated with the altered basement. It was probably derived locally within the deformation zone. This suggests that overall major fluid advection did not occur within the zone and that the fluid-rock ratios were low.

5.3.4.5. Possible environmental controls on the fracturing in the fault zone.

The deformation in the fault zone switched from phyllonitisation to predominantly shear fracturing with time and was accompanied by significant dilation. This general change in the mode of deformation could have occurred in response to reducing the ambient pressure or temperature or by an increase in the ambient fluid pressure during continued movement on the Gavarnie Thrust.

A reduction in the pressure and/or the temperature are most likely to have occurred if uplift and erosion accompanied the movement on the GT. The tectonic thinning of the thrust sheet inferred in chapter 4 would also have had a similar effect. Uplift can be demonstrated to have occurred during thrusting in the central Pyrenees and is recorded in the stratigraphic record by the closure of the South Pyrenean Tertiary basin (Labaume et al., 1985; Farrel et al., 1987). Whether this uplift coincided with the movement of the middle or the lower thrusts sheets is however unclear and this may or may not have been responsible for the change in deformation within the GT fault zone.

An increase in fluid pressure would have reduced the effective confining pressure and possibly enabled dilatancy to occur. While high fluid pressures can be shown to have existed late in the phase 3 thrust episode (chapter 4) the the shearing documented in the basement log was associated with the emplacement of the GT and is therefore probably a phase 2 event. Fluid inclusion studies (chapter 6) show however that the same fluid existed in the basement log fault zone and in the fault-parallel cavities in the PPV culmination. This feature could reflect contemporaniety of deformation or the fact that because fluid: rock ratios were low the same fluids existed in the fault system over a considerable period of the deformation. The latter interpretation may be the more likely and agrees with the inference, based on the chemistry of the fracture fills, that the fluids were locally equilibrated and probably locally derived.

5.3.4.5. Comparisons between the deformation mechanisms that operated in the basement and Mesozoic strata during thrusting.

Comparison can be made between the processes inferred to have operated to produce the cleavage in the Triassic strata of the PPV culmination and the processes

that produced the foliation in the GT fault zone. In both strata the cleavage appears to have formed by a combination of the three main processes outlined above in section 5.3.4.1. The partitioning of the deformation mechanisms is however different and only the small lithic clasts in the Triassic shales appear to have deformed identically to the mica matrix of the basement. This latter feature presumably reflects the similar composition of the the lithic clasts and the mica matrix.

Pressure solution was more active in the Triassic shales where it primarily affected the fine quartz grains and produced anastomosing pressure solution striping. In the basement strata the quartz grains are much larger in comparison to the matrix phyllosilicate grains and generally acted as rigid inclusions. This disparity in deformation styles probably reflects the difference in relative grain size between the quartz and the matrix phyllosilicates in the different lithologies and the different strain histories of the strata. The basement strata were deformed predominantly in simple shear, the Triassic shales in shortening in the tip zones of thrusts. These differences appear to have affected the partitioning of deformation mechanisms with DMT more active in the coaxial rather than noncoaxial strain history. This may also help to explain the change from slaty to spaced cleavage in the ridge klippe of the PPVT where the original slaty fabric developed during emplacement of the thrust and the spaced fabric during the later shortening. The matrix phyllosilicates appear however to deform by similar processes in both strain histories to generate the cleavage.

5.4. Conclusions.

5.4.1. Deformation in the PPV culmination.

1. The cleavage in the Triassic strata formed by a combination of kinking and localised pressure solution of phyllosilicate grains, and pressure solution of quartz grains. Recrystallisation of the matrix phyllosilicate grains occurred within the cleavage lamellae and along the KKBs.
2. DMT processes were more active during the P3 shortening than during the P1/P2 shearing in both the Triassic shales and the Cretaceous biomicritic limestone.
3. The fine grained limestone appears to have deformed by a combination of crystal plastic and grain boundary sliding mechanisms. Crystal plastic processes are more readily apparent in coarse-grained calcite veins deformed within the calcmylonite. Similar mechanisms may have operated during the later cleavage development in the limestone which, in addition, were augmented by pressure solution.
4. Deformation kinematics viz. coaxial or noncoaxial strain histories, appear to have combined with the fine grain size of the limestone to control its competency relative to the Triassic shales.

5.3.2. Deformation in the GT fault zone.

1. The basement strata appear to have suffered advanced argillic alteration prior to thrust related deformation.
2. A phyllonitic fabric developed in the altered strata adjacent to the thrust. This fabric appears to have developed by a combination of kinking, migration of kink band boundaries and recrystallisation of strained phyllosilicate grains within the resultant cleavage lamellae. Relict quartz grains in the altered strata deformed by fracturing and grain rotation. They were not involved in the ductile shearing.
3. The ductile fabric in the fault zone is overprinted by an array of shear fractures that cut through the mica matrix of the altered strata leaving the quartz grains relatively undeformed. The fractures possess a continuum of scales and anastomose to produce a penetrative shear fabric in the strata.
4. In three dimensions the slip surfaces define polyhedra that enclose the resistant quartz grains. The dilation associated with movement of these fractures may have been related to the fact that the number of slip surface orientations did not satisfy the Von Mises Criterion.
5. The finite strain state within the fault zone appears best approximated by a combination of simple shear and flattening. This agrees with the extension inferred in the GT sheet from mesostructures (chapter 4).
6. The fracture system in the altered basement was fed by two fluids: one in equilibrium with the altered basement strata, the other of external origin. This latter fluid produced Mg metasomatism in the basement adjacent to the thrust and accounts for the observed changes in fracture fill chemistry within the fault zone. The fluid appears to have been sourced from the layer of Cretaceous mylonitic limestone that occurs adjacent to the Gavarnie Thrust . The strong hostrock control on fluid compositions suggests that fluid:rock ratios within the fault zone were small and that major fluid flow was not channelled along the fault zone.

CHAPTER 6

Fluid and Mineral Geochemistry in thrust-related cavities

The aims of this chapter are to characterise the fluid that was present during the thrusting in Cirque de Barroude and to come to some conclusions regarding the fluid processes in the PPV culmination. The chapter is divided into 3 sections. The first section will study the composition of the fluids using a microthermometric analysis of fluid inclusions hosted in vein quartz. The second section will consider the chemistry of the chlorite in the thrust-related veins. The third section will discuss the results of the first two sections in the context of fluid flow processes and fluid-rock reactions in the thrust system. It will be shown that the composition of vein chlorite in particular provides a powerful tool in determining fluid flow pathways and the degree of control exercised by the host rock on the fluid composition.

6.1. Fluid inclusion studies.

6.1.1. Introduction.

The deformation within the PPV culmination and associated with the emplacement of the GT occurred in the presence of aqueous fluids. These fluids were trapped in the form of small inclusions within the minerals that precipitated in veins and cavities in the deforming rock. In this section, the results of the microthermometric analysis of primary and secondary fluid inclusions from quartz veins within the PPV culmination are reported. These provide information on the physical conditions of deformation and on the compositions of the fluids that were present at the time of deformation.

After trapping, each fluid inclusion can be considered a closed system of constant density (Roedder 1984). An inclusion must therefore lie on an isochore in P-T space. When trapped as a single phase, a vapour bubble will form within the inclusion when it cools and intersects the vapour-pressure curve for the fluid (figure 6.1). The P-T path followed on cooling must lie along the particular isochore for the inclusion composition. Note that the trapping conditions refer to the fluid phase in the vein or cavity: only if this fluid is lithostatically pressured and in thermal equilibrium with the host rock will the trapping conditions exactly correspond with the ambient conditions of deformation.

Three measurements are made during the thermometric analysis of an inclusion using a heating-cooling stage:

1. The homogenisation temperature, T(h). This corresponds with the temperature at which the vapour bubble disappears on heating i.e. it corresponds with the temperature where the isochore for the inclusion composition meets the vapour-pressure curve

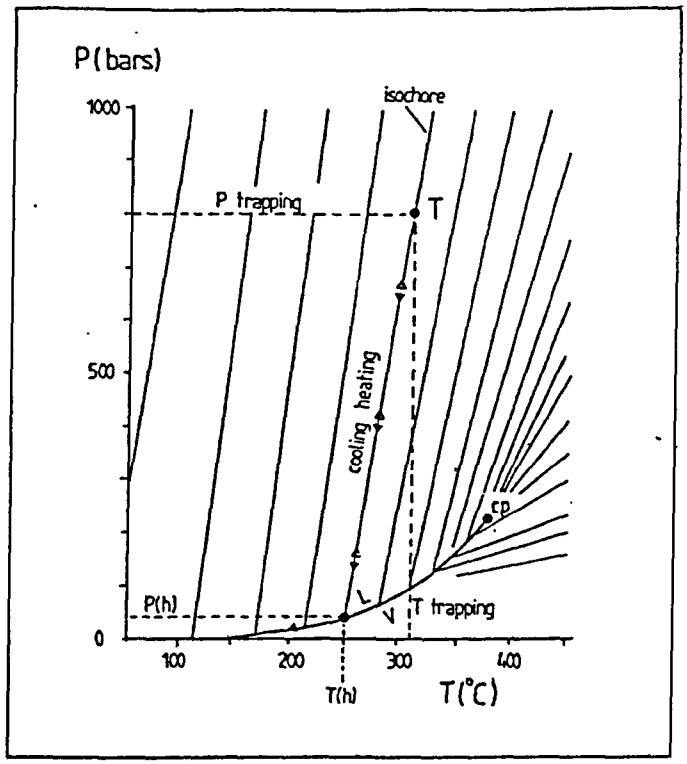

Figure 6.1. Isochores for a fluid showing the relationship between the trapping conditions (T) and the homogenisation temperature T(h). CP is the critical point.

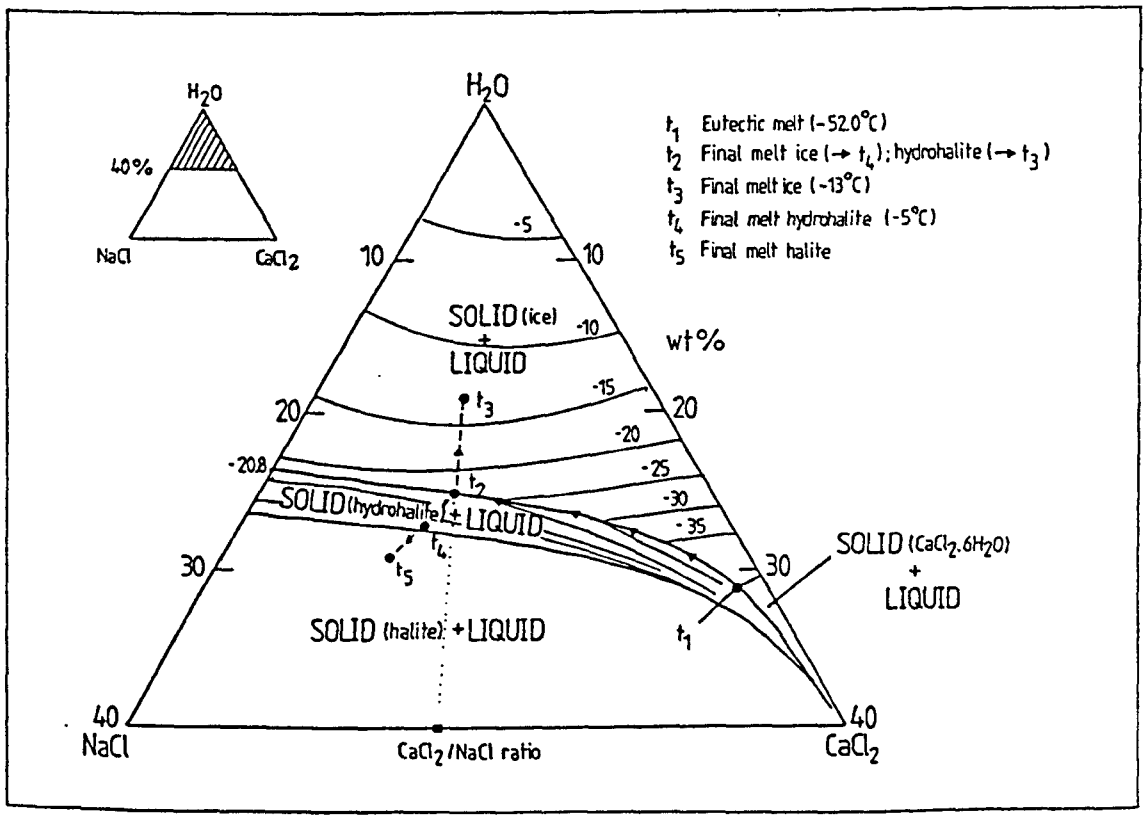

Figure 6.2. Phase relations in the system NaCl-$CaCl_2$-H_2O with isotherms also plotted (from Shepherd et al., (1985, fig. 6.7)). Two melting paths, t1-t2-t3 and t1-t2-t4-t5 are shown. See text for discussion.

Dissolved species	Eutectic temperature (°C)	Eutectic composition (wt. %)	Solid phases			Solid melting relations
			H_2O	ice	hexagonal colorless RI ε 1.313 ω 1.309	0°,congruent
NaCl	-20.8	23.3% NaCl	$NaCl \cdot 2H_2O$	hydrohalite	monoclinic colorless RI 1.416	+0.1°, incongruent
			NaCl	halite	cubic colorless RI 1.544	
KCl	-10.6	19.7% KCl	KCl	sylvite	cubic colorless yellowish RI 1.490	
$CaCl_2$	-49.8	30.2% $CaCl_2$	$CaCl_2 \cdot 6H_2O$	antarcticite	hexagonal colorless RI ε 1.393 ω 1.417	+30.08°,incongruent
$MgCl_2$	-33.6	21.0% $MgCl_2$	$MgCl_2 \cdot 12H_2O$			-16.4°, congruent
NaCl-KCl	-22.9	20.17% NaCl 5.81% KCl				
$NaCl-CaCl_2$	-52.0	1.8% NaCl 29.4% $CaCl_2$				
$NaCl-MgCl_2$	-35	1.56%NaCl 22.75%$MgCl_2$				

Table 6.1. Melt data for solid species in solution. From Crawford (1981).

Sample	Host Rocks	Mineralogy	Description
49454	Triassic red beds (reduced)	Quartz, calcite	Cavity in splay off PPVT thrust plane
49453	Triassic red beds	Quartz, hematite	Cavity in tension gash at fault termination
49448	Triassic red beds	Quartz, chlorite, ankerite	Cavity along thrust
49443	Altered granite	Quartz, chlorite	Cavity along minor thrust
7433	Triassic red beds (reduced)	Quartz, chlorite, calcite	Cavity in PPVT thrust plane
49209	Granodiorite with advanced argillic alteration	Quartz, chlorite, pyrophyllite	Shear vein (i.e. fibres parallel to wall)

Table 6.2. Summary of samples analysed.

(figure 6.1). T(h) does not coincide with the trapping T unless the fluid was boiling at the time of entrapment.

2. The eutectic melt temperature, T(e). When frozen, the fluid will start to melt at a temperature that depends critically on the composition of the fluid. For NaCl brines, eutectic melting occurs at T= -20.8 °C. For brines with additional components T(e) is depressed by characteristic amounts (table 6.1).

3. The final melt temperature, T(m). This temperature depends on the fluid salinity. In low salinity fluids ice is the solid phase that melts; in higher salinity brines other components (hydrates) may be present. The final melting temperatures of these phases can be used to estimate the fluid composition (Crawford et al., 1979; Crawford 1984; Shepherd and Rankin, 1985). The most common hydrate is hydrohalite ($NaCl.6H_2O$).

The phase behaviour of saline solutions on freezing and heating is shown in figure 6.2. The system portrayed in this diagram is $NaCl\text{-}CaCl_2\text{-}H_2O$. As will be shown later this system accords with the fluid compositions encountered in PPV culmination. First melting occurs at the ternary eutectic T_1 where one of the solid phases melts (this is usually $CaCl_2$). The eutectic temperature of -52.0 is characteristic for brines containing $CaCl_2$. Once all the $CaCl_2$ has been consumed, the melt composition evolves along the cotectic curve separating the Hydrohalite + L field from the Ice + L field as both solids melt. When one of the solids is consumed the fluid composition moves into the opposing field and moves along a line towards the H_2O apex (in the Ice + L field, path $T_2\text{-}T_3$) or towards the NaCl apex (in the NaCl + L field, path $T_2\text{-}T_4\text{-}T_5$). The final melt temperature T_3 or T_5 defines the composition of the fluid. The final melt temperature of the first solid phase to melt defines the Ca:Na ratio of the fluid.

Microthermometry therefore allows a minimum estimate of the trapping temperature, T(h), and an estimate of the fluid composition (from T(m)) in terms of fluid salinity and Ca:Na ratio. The true trapping conditions can only be estimated from the microthermometric results with the use of additional information eg. if either the temperature or pressure can be estimated independently.

6.1.3 Location of samples and description of inclusions.

The six samples chosen for this study come from fault-parallel cavities in the PPV culmination. Only fluid inclusions from quartz crystals in these cavities have been studied. The location of the samples is shown in figure 6.3 and more details are given in table 6.2.

Both primary and secondary inclusions in the quartz grains have been analysed. The primary inclusions occur as either randomly oriented groups of small inclusions (figure 6.4a), as groups of inclusions with long axes arranged parallel to the faceted

Figure 6.4. Micrographs of fluid inclusions.
a) Irregular group of oval shaped inclusions. These inclusions are tentatively interpreted as primary. From sample 49453.
b) Plane of large two-phase liquid-vapour secondary inclusions. From sample 49453.
c) Large irregular inclusions containing lumps of a green amorphous substance (H) that is interpreted as a bitumen. A small rhombic calcite daughter crystal (C) is present in one of the inclusions. From sample 49454.
d) Large irregular primary inclusion possessing 3 lumps of hydrocarbon (H). From sample 49454.

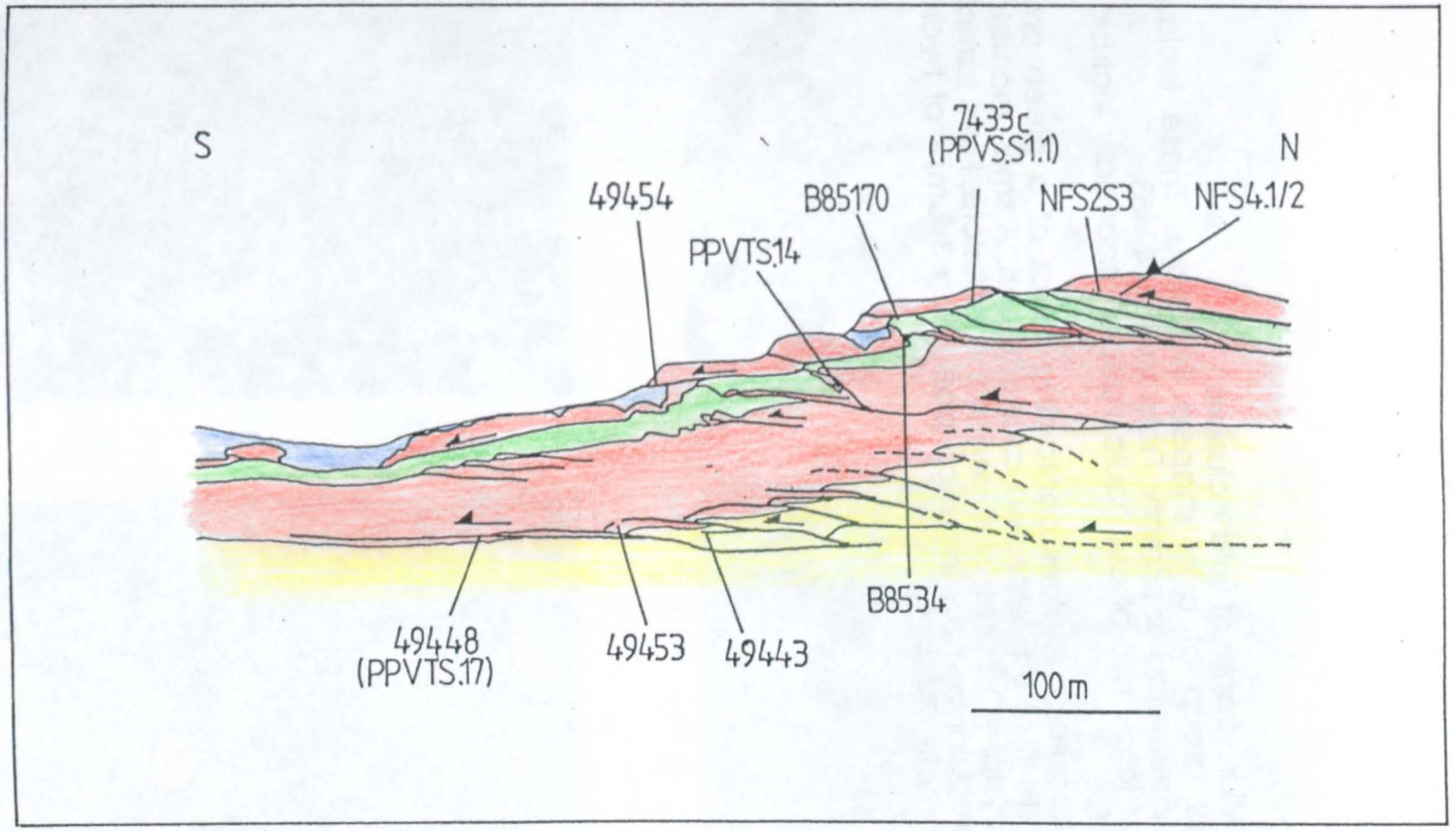

Figure 6.3. Locations of samples studied.

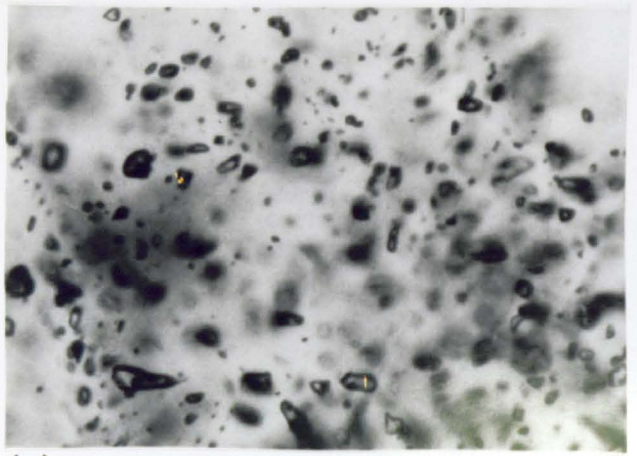

(a) 200 µm

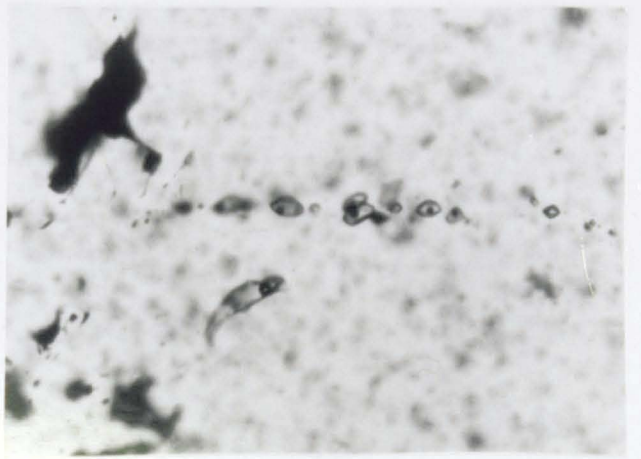

(b) 200 µm

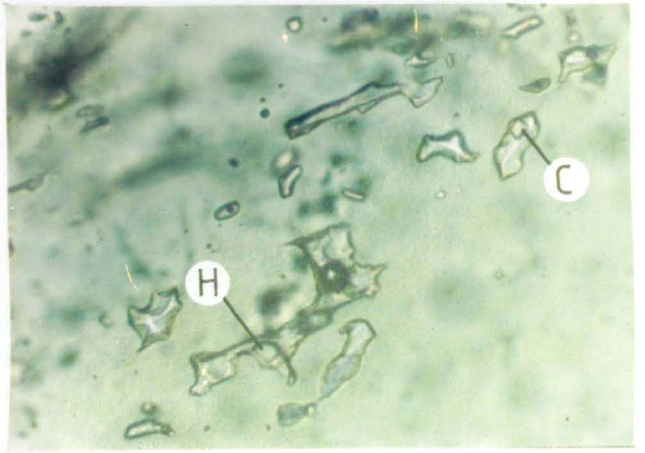

(c) 40 µm

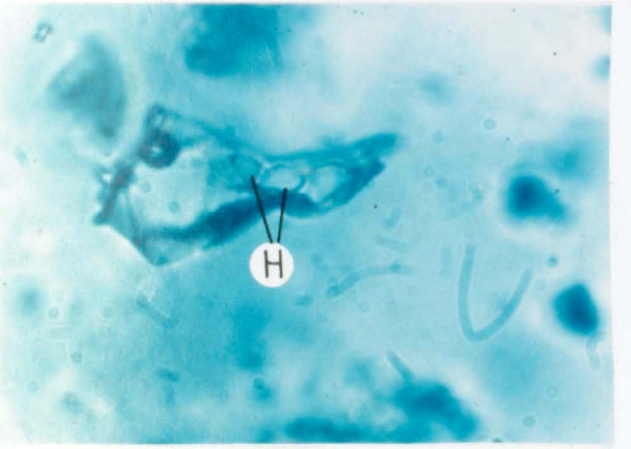

(d) 20 µm

terminations of the quartz grains (these probably represent growth zones in the quartz crystal (Bodnar et al., 1984)) or as planes of inclusions parallel to the boundary between two crystals. The secondary inclusions form along healed fractures in the quartz (figure 6.4b). The distinction between these two types of inclusion is often subjective (Roedder, 1984) especially in dense inclusion arrays such as shown in figure 6.4a. A sampling bias is also introduced in the measurements because only the larger inclusions are studied due to ease of optical examination.

Two types of primary inclusions have been recognised in the quartz: irregular elongate inclusions up to 50 microns in length (figure 6.4c and d) that are partially necked-down, and smaller more oval inclusions 5-20 microns in size (figure 6.4a). The secondary inclusions are usually large oval-shaped inclusions 20- 40 microns in diameter (figure 6.4c). Most of the inclusions studied are two phase liquid-vapour systems. A few inclusions however contained small phyllosilicate flakes and rare daughter crystals (figure 6.4c) possibly of calcite. In addition, a proportion of the inclusions also contained lumps of a high relief, pale green, amorphous solid (figure 6.4d). This material occurred predominantly in the large irregular primary inclusions. It did not freeze on cooling and did not dissolve on heating of the inclusions up to T=350 °C. In one inclusion it interfingered with the ice crystals on freezing suggesting that the substance was a viscous liquid. It is tentatively identified as a bitumen (Banks, pers.comm., 1988). The bitumen did not fluoresce in UV light.

6.1.4. Microthermometry results.

Melting point and homogenisation data were obtained from the inclusions in the quartz veins with a Linkham TH heating-freezing stage attached to a Leitz microscope.

All the inclusions show eutectic melting temperatures in the range -40 to -52 °C. This wide range is accounted for primarily by the difficulty in detecting the initially small amount of eutectic melt often produced in the inclusions.

The final melt temperatures of ice and homogenisation temperatures are shown in figure 6.5. Here, T(h) has been plotted against T(m) and the data also plotted in the form of histograms. The six samples analysed all possess similar data distributions. Two main populations of fluid can be recognised:
1. a fluid with a final melt in the range -22 to -27 °C (Fluid A); 2. a fluid with a higher T(m) in the range -14 to -17 °C (Fluid B).
In sample 49454, a third subordinate population of inclusions is observed (fluid C) and show final melts for ice in the range -9 to -10 °C. Fluid A corresponds with the more concentrated brine and occurs in samples 7433, 49448, and 49453. Fluid B occurs in 49454,

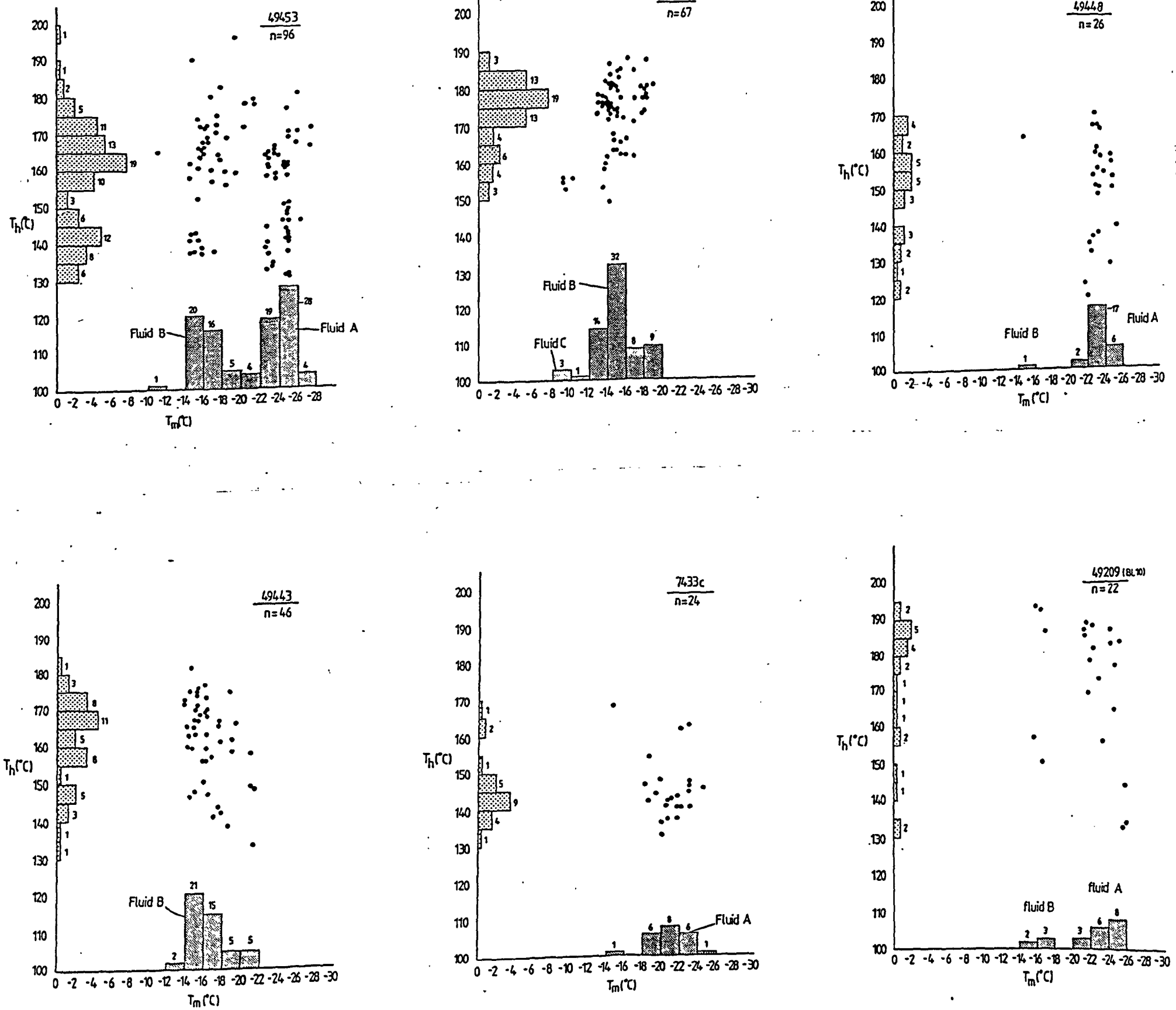

Figure 6.5. Microthermometry data from the six samples analysed. T(h) is plotted against Tm(ice). Histograms of the data are also shown.

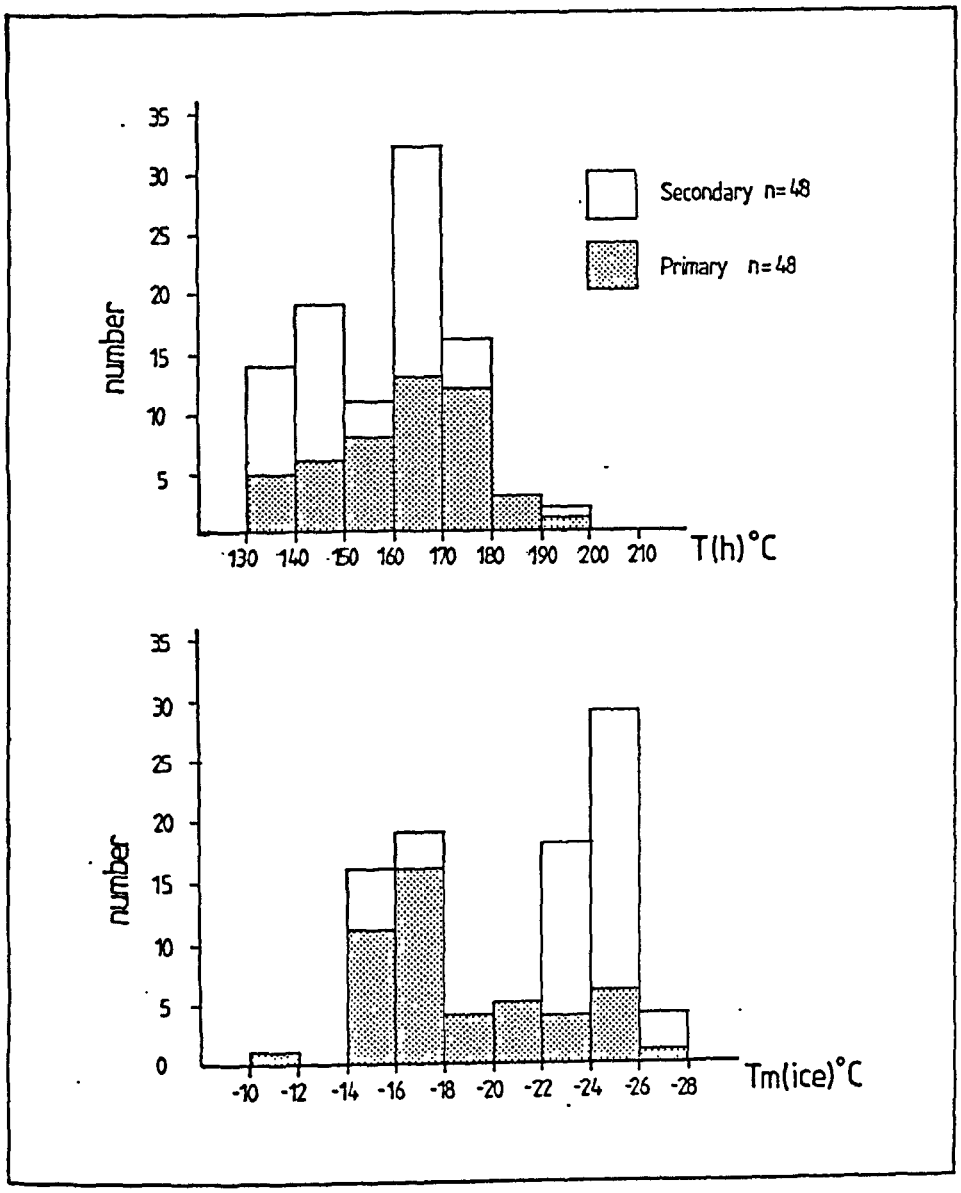

Figure 6.6. Histograms of T(h) and Tm(ice) for sample 49453 with primary and secondary inclusions differentiated. Fluid A occurs mainly in the secondary inclusions, fluid B in the primary inclusions.

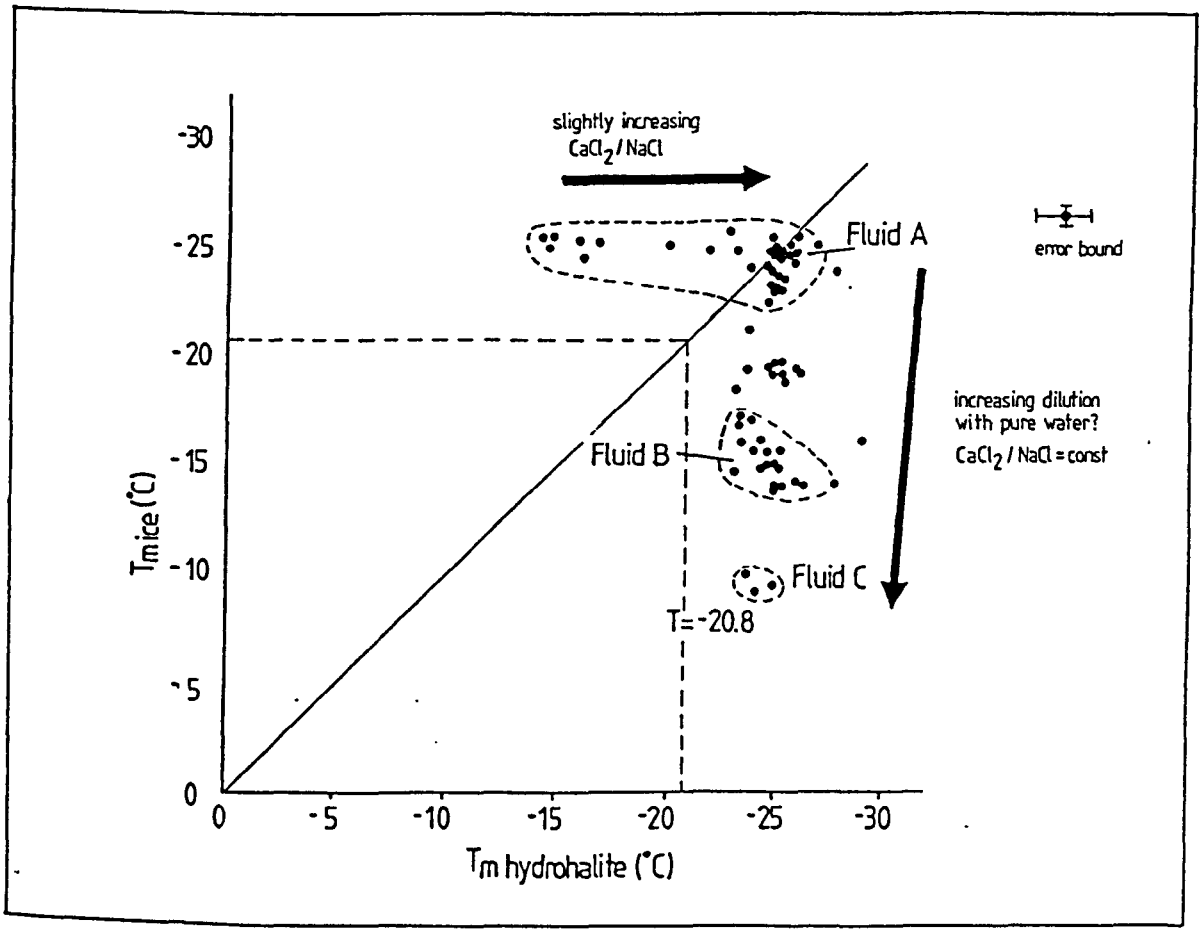

Figure 6.7. Plot of Tm(ice) against Tm(hydrohalite)for samples 49453 and 49454. Two trends are apparent: 1. A decrease in Tm(ice) at constant Tm(hydrohalite).which indicates that fluids A,B and C have almost constant Ca/Na ratios. This suggests that the three fluids have formed by the variable dilution of fluid A with pure water. 2. An increase in Tm(hydrohalite) at constant Tm(ice). This subsidiary trend reflects a slight increase in the Ca/Na ratio with decreasing salinity and may reflect a secondary mixing line between fluid A and a more sodic brine not recorded in any of the inclusions studied.

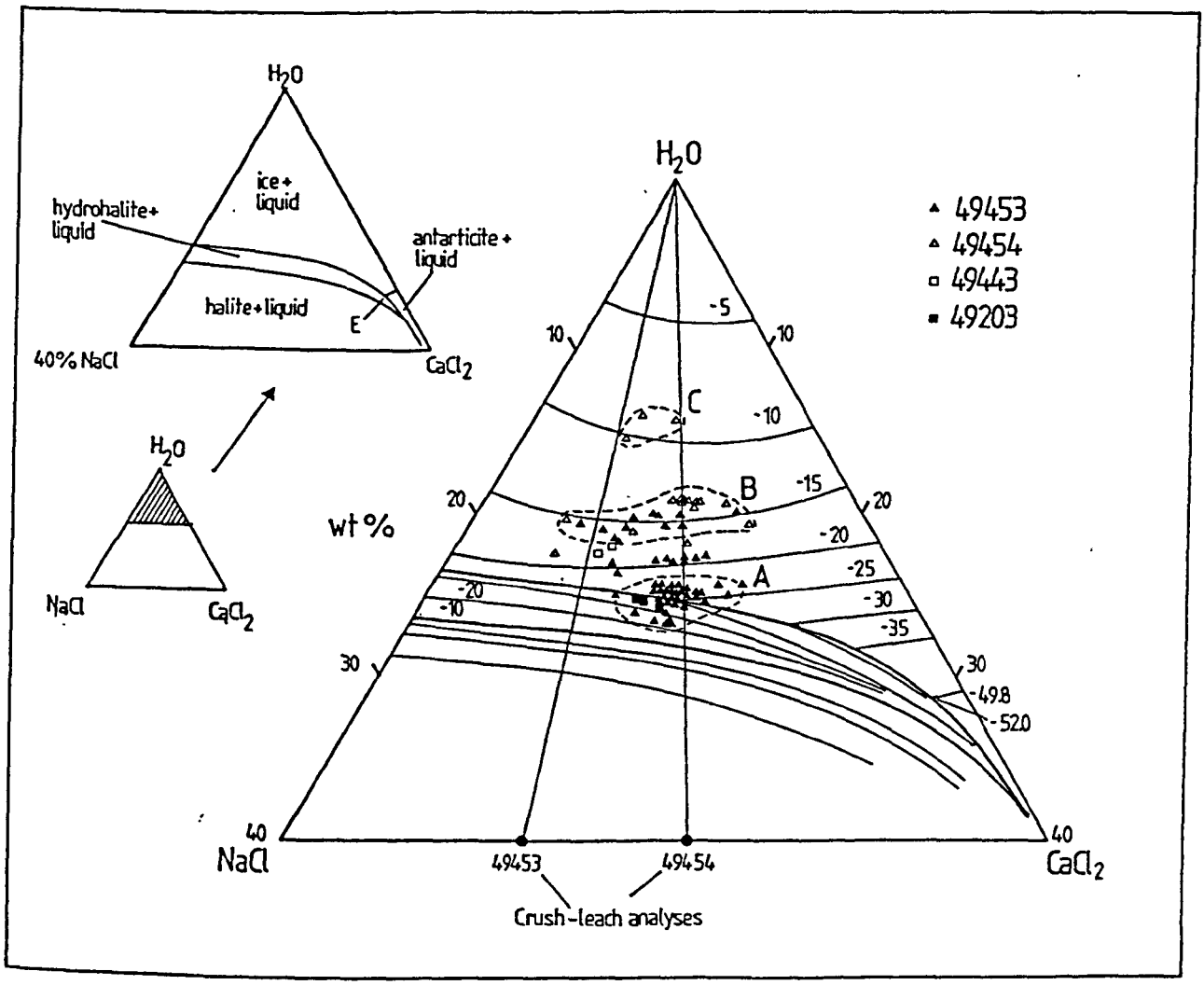

Figure 6.8. Final melt data plotted on the phase diagram for a NaCl-$CaCl_2$-H_2O fluid. The fields for fluids A,B and C have been differentiated. See text for discussion.

49443, 49203 and 49453 and may also be present in small proportions in the other samples. The bitumen solids have been identified in inclusions of both fluids A and B.

All the samples have similar distributions of homogenisation temperatures, the majority falling in the range 135-185 °C with a general concentration of the data towards the higher end of this range. A bimodal T(h) distribution is present in sample 49453 and occurs in both the primary and secondary inclusions (figure 6.6a). There is however no apparent differences in the homogenisation temperatures of fluids A and B. In sample 49453 fluid A occurs predominantly in the secondary inclusions (figure 6.6) although it also occurs in a few inclusions identified as primary in origin. The fact that both fluids have the same T(h) range and occur as primary inclusions in the samples suggests that they must have coexisted in the fault system at the time of formation of the cavities.

Hydrate final melt temperatures have been obtained from the larger primary and secondary inclusions in samples 49454 and 49453. In most of the inclusions studied the hydrates (hydrohalite) melted before the ice. In a few very saline inclusions, the ice melted first (figure 6.7). The melting range for the hydrohalites is -24 to -27°C for fluid A and -23 to -26°C for fluid B. These interpretation of these ranges together with the other microthermometric measurements is discussed in detail below.

6.1.5. Interpretation of microthermometry results.

6.1.5.1. Brine compositions.

The low first melt temperatures of the fluids indicates that both fluids A and B are calcic brines. The final melt data has been plotted in a portion of the phase diagram for the system NaCl- $CaCl_2$-H_2O in figure 6.8. The data for the different fluids plot as elongate fields within the diagram. The width of the fields can be explained largely in terms of experimental error due to the difficulty in observing the final melting of the minute hydrohalite grains. The imprecision in the data is magnified by the fact that the cotectic curve is almost parallel to the isotherms in the range of fluid compositions of interest. This means that a variation in final melt temperature of as little as 1 degree (the probable accuracy of the heating stage) is translated into a large variation in fluid composition on the phase diagram. Some of the variability might additionally be explained in terms of internal variations in the Ca/Na ratios of the fluid in different inclusions. This possibility cannot however be qualified due to the scale of the previous effect.

The Ca/Na ratios of the fluids in samples 49453 and 49454 have been measured by Dr. David Banks at Leeds University using a modified crush-leach technique and are also shown in figure 6.8. For details of this technique see Bottrell et al. (1988). Neglecting the experimental errors of the hydrate melt data, the crush-leach analyses agree

reasonably well with the phase data for sample 49454, but not for sample 49453. Sample 49454 represents fluid B (see figure 6.5); sample 49453 represents a mixture of fluids A and B. The crush-leach result for sample 49453 appears to have too much Na in the analysis. Errors associated with crush-leach analyses are considered small as the technique should suppress the adsorption of polyvalent cations on the quartz surfaces created during crushing an should also minimise contamination (Bottrell et al. (op.cit.). The analyses of samples 49453 and 49454 are therefore considered accurate and have been reproduced in a number separate runs. One explanation for the discrepancy between the microthermometric and crush-leach results for sample 49453 is that the quartz possesses sub-micron size disseminated halite inclusions not visible in using the optical microscope (Banks, pers.comm. 1988).

The compositions of fluids A, B and C are almost colinear in figure 6.8 ie. the fluids possess similar Ca/Na ratios. This linearity is also shown in figure 6.7 where the hydrate final melt temperature has been plotted against the final melt temperature of ice. It can be seen that inclusions of intermediate composition between fluids A and B plot along the same trend. This trend probably represents a mixing line. The fact that the Ca/Na ratio of the fluids is virtually constant suggests that one of the fluids involved in the mixing probably possessed a very low salinity (Banks pers.comm. 1988).

A subsidiary trend is also apparent within fluid A in figure 6.7. This represents a slight increase in the $CaCl_2$/NaCl ratio of the fluid with decreasing salinity. It must be emphasised that the variations in composition along this trend are very slight compared with those between fluids A,B and C (see figure 6.8). This subordinate trend could represent a mixing line between fluid A and a fluid with a slightly higher salinity and higher NaCl/$CaCl_2$ ratio that has so far not been found in any of the inclusions studied.

6.1.5.2. Fluid sources.

The microthermometry results suggest that fluid mixing probably generated the range of fluid salinities found in this study. As already mentioned one end member fluid appears to have been a low salinity fluid and was possibly of meteoric origin ie. pure water in composition. The amount of water that entered the system must however have been low because the amount of dilution required to produce fluid B from fluid A (a change of only 5 wt% NaCl equivalent) only requires a water/fluid A ratio of 0.2. To generate fluid C (12 wt% NaCl equivalent) requires a water/fluid A ratio of 1.17. The other end-member fluid will be assumed to be fluid A as no other candidates have been found. It has a salinity of approximately 25 wt% NaCl equivalent.

Fluid A can be categorised as a Na-Ca-Cl brine. Brines of similar composition have been reported from studies of metamorphic rocks (Crawford et.al, 1979a and 1979b), from ore

deposits (Kerrich et.al, 1987), from geothermal systems (Burruss and Hollister, 1979) from saline basement ground waters (Frape et.al, 1984) from ground water in sedimentary cover rocks (Mullis, 1987) and from oil field brines (Collins, 1975).

High salinity in brines is generally interpreted in terms of either dissolution of evaporite beds (Carpenter et al., 1974) or due to removal of H_2O by hydrolysis reactions. The high Ca- chloride content of brines is generally considered to be generated at higher temperatures by retrograde mineral reactions (Crawford et al., 1979) or at low temperatures by equilibria with secondary minerals (Frape et al., 1984). Frape et.al (op.cit.) consider that the Ca concentration in brines reflects a geochemical trend that is largely independent of rock type. They found however that minor elements in the fluid, such as Mg and Fe, are apparently controlled by local host-rock geochemistry.

The range of brine compositions documented by Mullis (1987) from the Swiss Molasse basin is broadly similar to those documented here although they were trapped at lower temperatures (30-140 °C). He suggests that the compositional range of the brines reflects dilution by migrating fluids during major Alpine tectonic events. A similar scenario might possibly explain the mixing inferred in the PPV fault system and is discussed later.

The presence of the bitumen in both fluids A and B suggests that they are mature formation brines and that they are unlikely to have been of metamorphic origin. The host rocks (the Triassic red beds) are unlikely themselves to have been hydrocarbon source rocks and the fluids must therefore have migrated into this strata either before thrusting commenced or during the thrusting. The brines could have been derived from the overlying Mesozoic strata or they could have migrated into the fault system from the Eocene strata of the south Pyrenean Tertiary basin during Alpine deformation.

6.1.5.3. Possible explanations for the observed T(h) range.

The distribution of inclusion homogenisation temperatures indicates that both fluids A and B possess a range of densities. Isochores for fluids A and B have been interpolated from the data of Potter and Brown (1977) and are shown in figure 6.9. The observed density ranges could have resulted from:

1. If all the inclusions were trapped at the same temperature then the range may reflect variations in the fluid pressure in the veins and cavities at the time of trapping. Such fluid pressure fluctuations will occur where the rate of dilation exceeds the ability of the system to maintain fluid pressure equilibration in the newly created fractures and is likely to occur in strata with low hydraulic conductivity (Walder and Nur, 1984). Fluid pressure fluctuations have a strong influence on quartz solubility (Helgeson and Lichtner, 1987) and a pressure drop will cause quartz to precipitate.

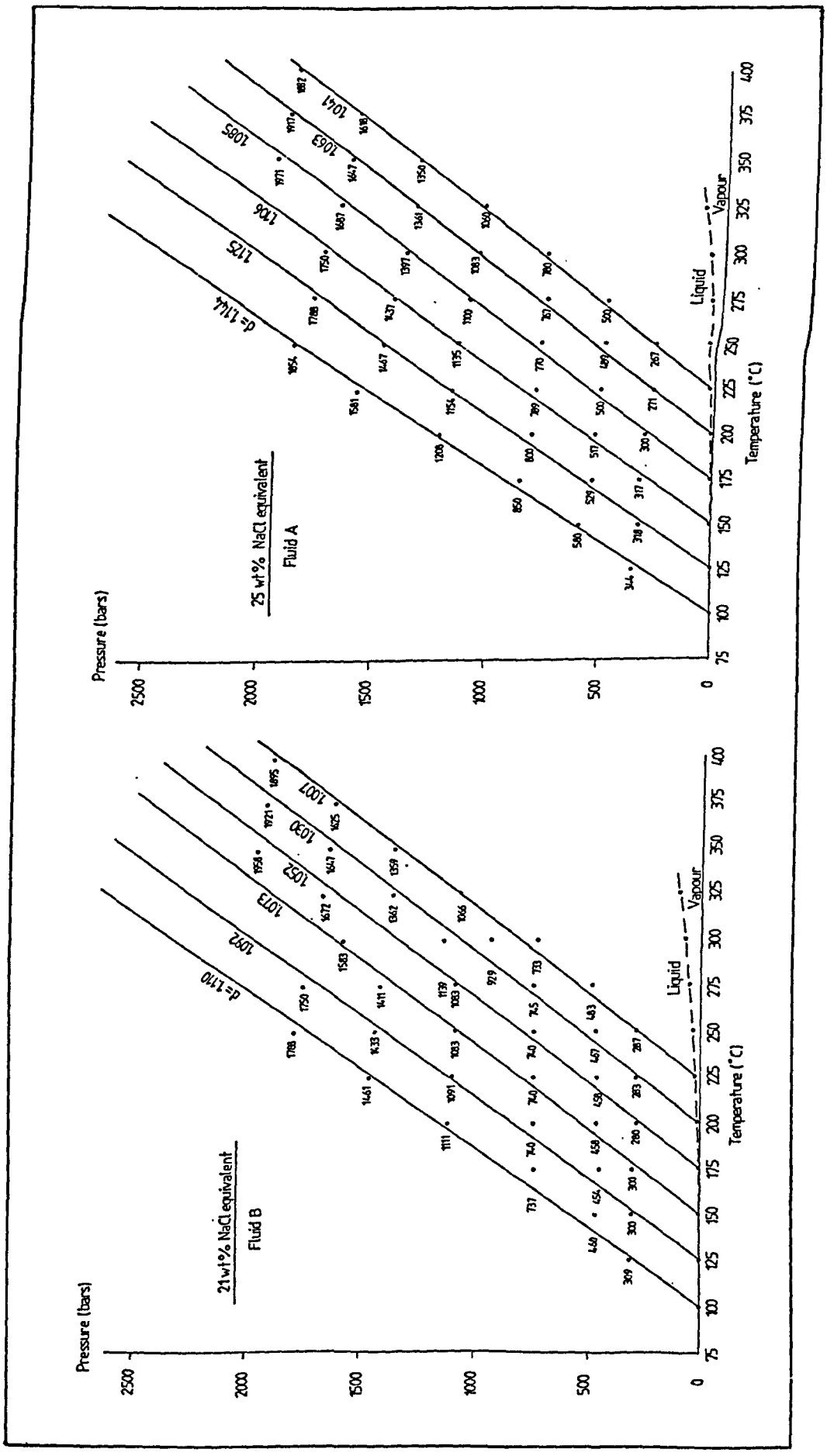

Figure 6.9. Isochores for NaCl fluids with salinities equivalent to fluids A and B. The numbers adjacent to the data points refer to the pressure linearly interpolated from the data of Potter and Brown (1977). The isochores were drawn by linear regression of the data points.

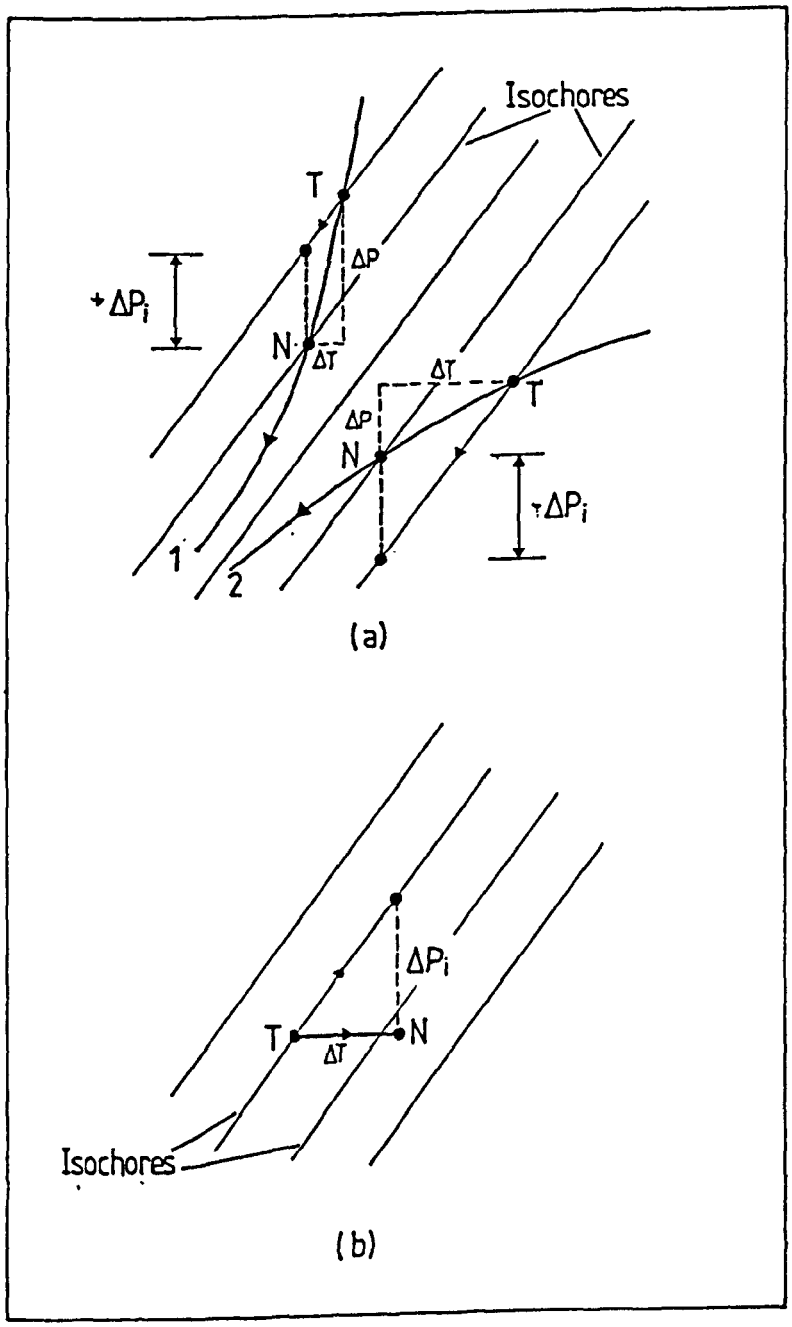

Figure 6.10. Schematic diagram showing the effect of uplift path on the fluid pressure within an inclusion. Modified from Crawford et al. (1979a). a). Uplift along path 1 (high dP/dT) produces overpressuring of magnitude +ΔPi between the fluid in the inclusion and the ambient conditions, N. If this pressure differential is great enough, microhydrofracturing of the inclusion will occur and it will leak to the pressure of N. Point T represents the original trapping conditions. For uplift along path 2 (low dP/dT) the resultant pressure differential, -ΔPi, will not produce hydrofracturing. b). Effect of isobaric heating on the fluid pressure in an inclusion. This will also produce a positive pressure differential and could also generate microhydrofracturing.

2. If all the inclusions were trapped at constant pressure then the T(h) range implies variations in fluid temperature. Geothermal anomalies can be associated with flowing fluid (eg Vrolijk et al., 1988). It seems unlikely that such anomalies existed during thrusting since both fluid populations show the same T(h) distribution. An alternative is that the cavities remained open during and after the deformation with quartz being continually precipitated as the temperature dropped during uplift and cooling. The presence of deformation microstructures in the cavity phases suggests however, that this did not occur and that the cavities opened and sealed during the fault activity.
3. The inclusions could have leaked. This could be due to:
a) Later deformation may have ruptured the inclusions allowing them to reequilibrate with the ambient conditions.
b) Microhydrofracturing may have occurred associated with uplift or an increase in the ambient temperature (Crawford et.al, 1979; Burruss and Hollister, 1979). The effect of uplift path is schematically shown in figure 6.10a. If uplift occurs without significant cooling (ie. a large $\partial P/\partial T$ gradient (path 1)) then the inclusion pressure will exceed the ambient pressure. The tensile strength of regular, oval quartz inclusions is approximately 1 kbar (Burruss and Hollister, op.cit). The strength of irregular shaped inclusions is likely to be less due to the development of stress concentrations at vertices in the inclusion surface. Microfracturing and leakage will occur if a suitable pressure differential is generated (perhaps of the order of a few hundred bars for irregular inclusions). Uplift accompanied by rapid cooling ($\partial P/\partial T$ low (path 2) would produce underpressuring of the inclusion and it would be unlikely to leak.

An alternative means of overpressuring inclusions is by isobaric heating (figure 6.10b). This might be expected during the thermal equilibration of the footwall of a large thrust sheet (Oxburgh and Turcotte, 1974) and could apply to the strata in the footwall of the GT. This has a similar effect to uplift along a path with a large $\partial P/\partial T$ gradient.

A corollary on leakage is that it decreases fluid density leads to the inclusions possessing higher T(h) than they would if no leakage had occurred. The estimate of trapping pressure for a given trapping temperature is then lower than the true trapping pressure. If leakage was responsible for the observed range of T(h) it implies that the the true trapping conditions are better approximated by the higher density isochores.

The 50 degree°C range of homogenisation temperatures corresponds with a pressure difference of approximately 700 bars (figure 6.11). This pressure difference could either correspond with the tensile strength of the quartz inclusions (if microhydrofracturing was the process responsible for the inclusion distributions) or it could represent the maximum magnitude of fluid pressure fluctuations associated with vein dilation. Differentiating between these alternatives is not possible on the basis of the data collected here.

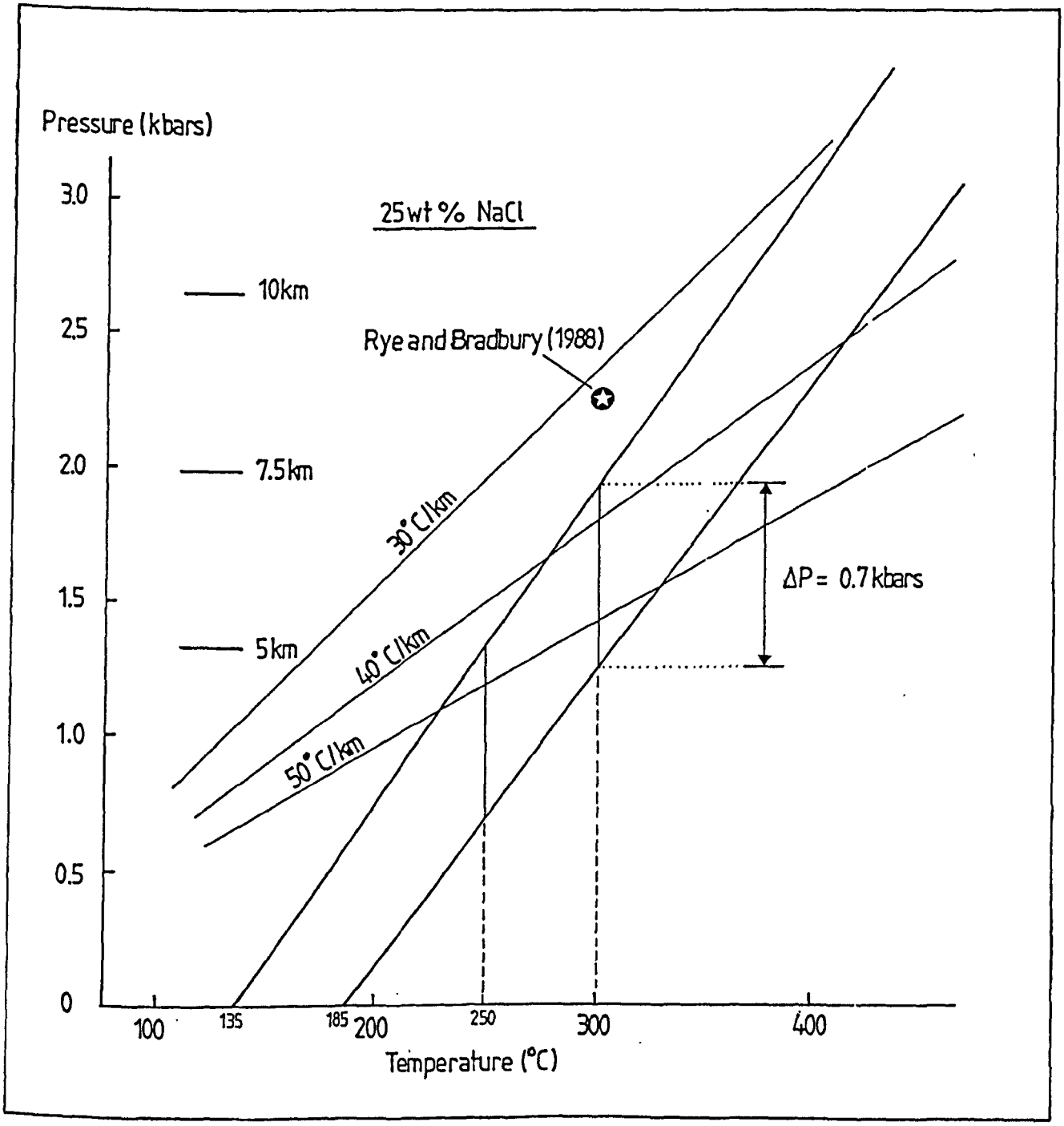

Figure 6.11. Estimation of the trapping conditions of the cavity quartz using isochores for fluid A and trapping temperatures between 250 and 300°C. The predicted range of trapping conditions lies between linear geotherms of 40 and 50 °C/km. The pressure difference of 700 bars refers to the maximum difference in trapping pressure calculated for the observed range of homogenisation temperatures of the inclusions.

6.1.5.4. The conditions of trapping and deformation.

The conditions of entrapment can be estimated from figure 6.11 only if an independent estimate of either T or P can be made. Rye and Bradbury (1988) have estimated a deformation temperature of approximately 300 °C from calcite-dolomite and stable isotope geothermometry of syntectonic veins in the Pineta thrust complex. This complex comprises the Upper Cretaceous and Tertiary strata of Mont Perdu Nappe and outcrops in the Val de Pineta some 10km south of Cirque de Barroude (figure 2.6).

The lack of significant new metamorphic mineralogy in the Triassic red beds and the stability of pyrophyllite in some of the cleavages suggests that the trapping temperatures were probably around 250-300 °C (Hemley et al., 1980) and agree with the Rye and Bradbury estimate. Using the inclusion isochores and this temperature range gives an upper bound of trapping pressures around 1.5-2Kbars (figure 6.11). This is in agreement with the likely 5-8km cover thickness that existed in this part of the Pyrenees during thrusting. The estimated geothermal gradient of around 40 °C/km is higher than that assumed by Rye and Bradbury (1988).

6.2. Vein chlorites and Mg-metasomatism.

This section will consider the chemistries of chlorites from fault-related veins in the Cirque de Barroude. It will be shown that the chlorite acted as a sensitive register of changing fluid chemistries in the veins and that these changes can be related to localised fluid advection between the Cretaceous limestone and the Triassic strata or between the Cretaceous limestone and the basement (where the Triassic strata is absent).

6.2.1. The location of the chlorites studied.

Chlorite forms an abundant component in thrust-related veins in the PPV culmination. It also occurs in similar veins within the basement strata deformed by the Gavarnie Thrust. Chlorite from two particular vein associations will be studied:

1. fault-parallel cavities from the PPVT sheet of the summit and ridge klippes, and
2. veins within the GT fault zone described in chapter 5.

The occurrence of the fault-parallel cavities in the PPV culmination is given in chapter 4 and their microstructures are discussed in chapter 5. The distribution and mode of occurrence of chlorite in the GT fault zone has also been described and interpreted in chapter 5.

Figure 6.12. Secondary and Back-scattered EM micrographs of chlorite growth features in fault-related veins and cavities.
a). SEM micrograph of pseudo-uniaxial chlorite plates in cavity fill. From sample 49453. Scale bar is 300 microns.
b). Microkinking and folding of chlorite platelets adjacent to euhedral quartz grain. This feature is thought to reflect deformation synchronous with the growth of the quartz. Scale bar is 100 microns.
c). Branching of chlorite platelets. Scale bar is 60 microns.
d). BSEM image of microkink in chlorite platelet adjacent to grain boundary. This is probably another growth-related deformation phenomenon. Scale bar is 10 microns.
e). Compositionally zoned chlorite grains within a cavity (BSEM image). From sample NFS4.1. Scale bar is 200 microns.
f). Concentrically zoned chlorite laths replacing dolomite (dark) in wall rock of sample NFS4.1 (BSEM image). Scale bar is 20 microns.
g). Micron scale growth zones in cavity-fill chlorite from sample NFS4.2 (BSEM image). The line marked B-B' represents microprobe traverse. The Mg number profile along this traverse is shown in figure 6.16c. Scale bar 60 microns.
h). Growth zones in cavity-fill chlorite from sample NFS2.S3 (BSEM image). The scale bar is 30 microns.

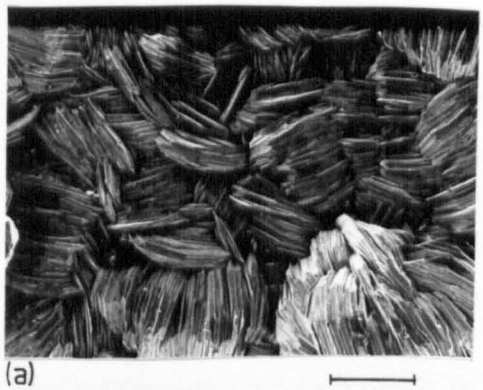

(a)

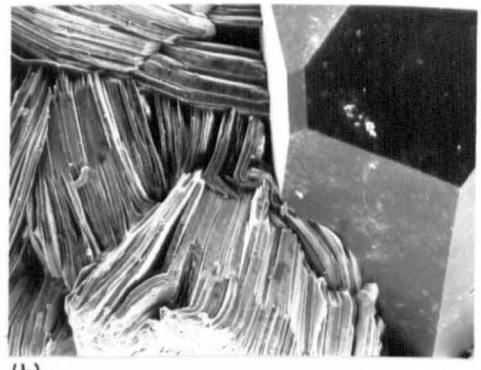

(b)

(c)

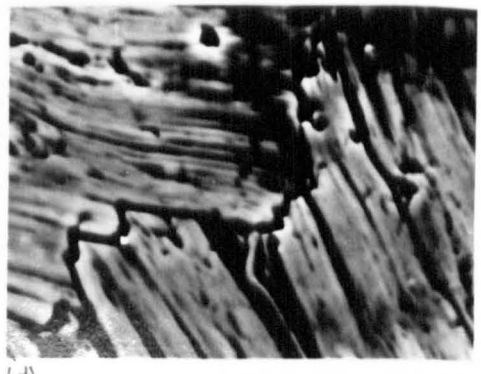

(d)

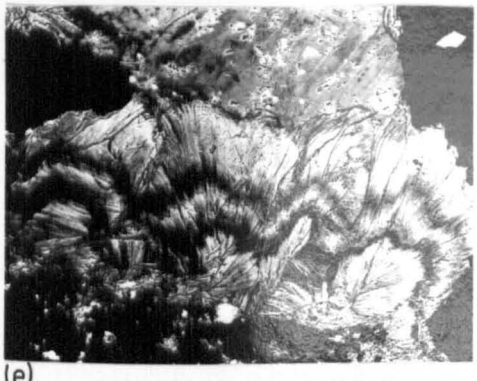

(e)

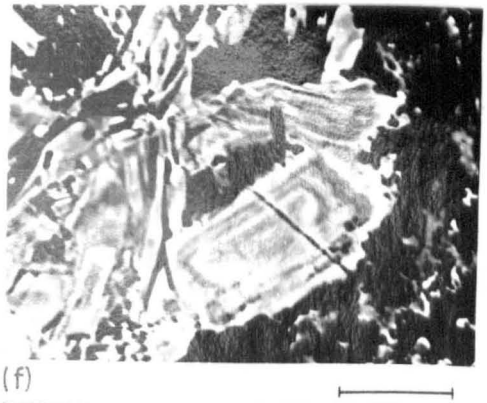

(f)

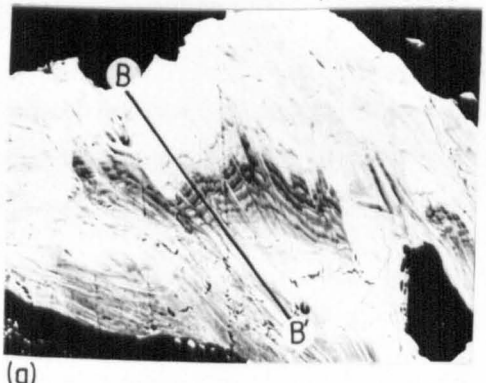

(g)

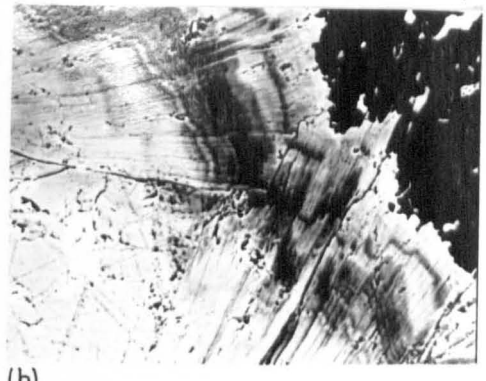

(h)

6.2.2. Morphology of the chlorites.

6.2.2.1. Vein Chlorite.

The morphology of the fracture-fill chlorites depends on whether they precipitated in extension veins, crack-seal shear veins or in open cavities. In extension veins the chlorite possesses a linear decussate texture similar to that documented by Cox and Etheridge (1983) and McCaig (1987). The cavity fill chlorites occur as pseudo-uniaxial plates arranged in rosette-shaped aggregates (figure 6.12a). These aggregates appear to have developed as a result of radial growth of the chlorite platelets. Due to interference from neighbouring grains the final sectional form of the chlorite grains is commonly fan-shaped (see figure 5.10e).

Other growth-related features that can be seen in the cavity-fill chlorites include the branching of individual platelets (figure 6.12c) and the presence of small grain margin kinks and microfolds (figure 6.12b and d). The former microstructure is responsible for the divergent growth form of the platelets, the latter is possibly a result of interfering grain growth. In figure 6.12b the growth of the euhedral quartz grain appears to have deformed the surrounding chlorite.

6.2.2.2. Alteration Chlorite.

The chlorite that replaces the dolomite in the PPVT sheet shows an ordered pattern of interlocking grains (figure 6.13). The two dominant orientations present do not parallel the cleavage in the rock but appear to parallel crystallographic planes within the dolomite. It is possible that twin or mineral cleavage planes were utilised as reaction sites within the dolomite during the replacement. The alteration post-dated the formation of cleavage in the rock.

The chlorite grains that replace muscovite and pyrophyllite in samples BL1 and BL3 from the basement log have a strong preferred orientation parallel to the phyllonitic foliation (see figure 5.16). It was syntectonic in age.

6.2.3. Chlorite chemistry.

6.2.3.1. Chlorite in the PPVT sheet.

6.2.3.1.1. Sample NFS2.S3.

This specimen comes from directly adjacent to the footwall of normal fault A in figure 4.14a. A sketch of the cavity studied is shown in figure 6.14. The cavity is rimmed by

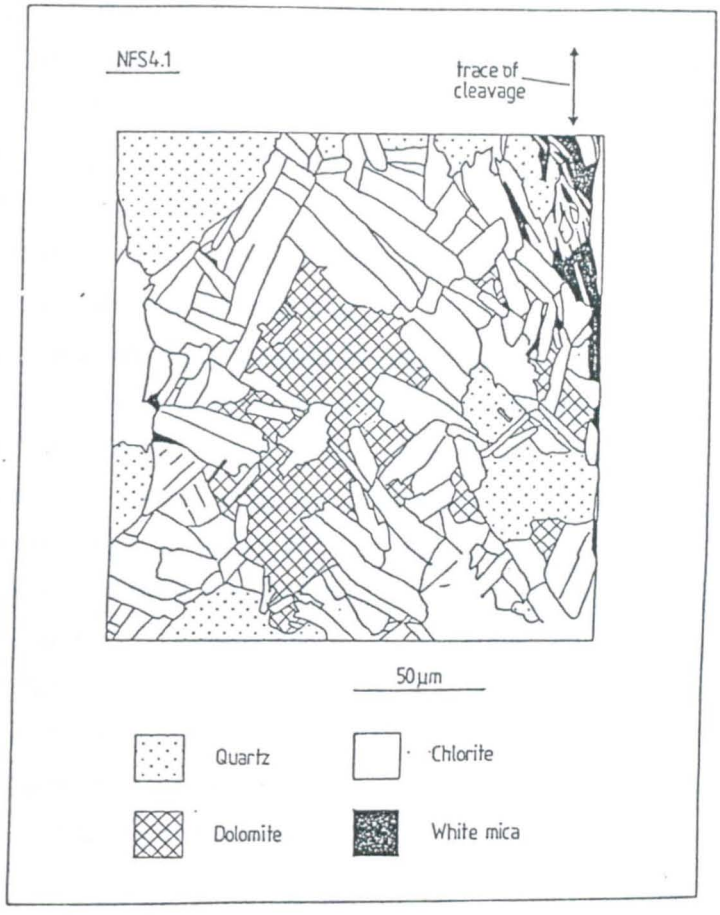

Figure 6.13. Sketch of chlorite replacing dolomite in sample NFS4.1 (from BSEM montage). The chlorite has an ordered growth pattern that suggests crystallographic control within the dolomite on the chlorite grain growth. The chlorite grows across the cleavage in the rock and the alteration and by inference, the faulting, postdates cleavage formation in the thrust sheet.

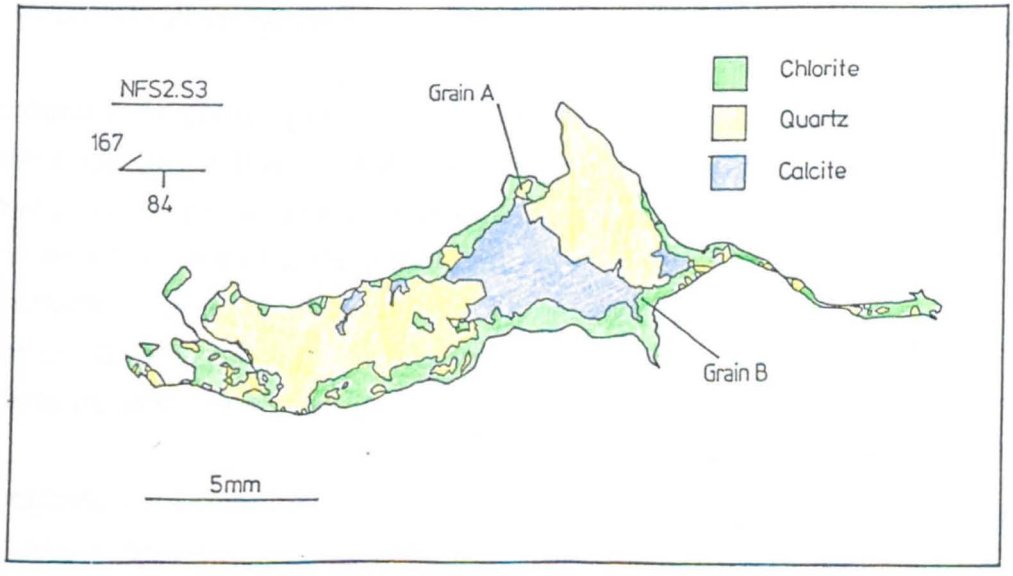

Figure 6.14. Sketch of cavity in sample NFS2.S3. BSEM micrographs of grains A and B are shown in figure 6.15.

rosettes of chlorite possessing discrete growth zones. These can be traced around the cavity and identical zones occur in chlorites from another cavity in the same specimen. Four features of the zones are worth noting (figure 6.15):

1. the zones step across individual cleavage traces;
2. unconformities are present;
3. thin stripes of variable composition chlorite occur between the growth zones and parallel to the cleavage traces; and
4. some of the zones have ragged boundaries.

The first feature is either a primary growth feature or is the result of small displacements between the chlorite plates in the rosette. The former interpretation seems more feasible because some of the some of the steps die out when traced parallel to the cleavage (eg. at X in figure 6.15a). The near constancy of individual zone widths suggests that individual platelets had constant growth rates. Unconformities between zones represent dissolution surfaces and point to disequilibrium between the chlorite deposited during one phase of growth and the fluid responsible for the next growth zone. The wedges of different composition that follow cleavage traces are probably cracks that are filled by later chlorite. The cracks may have formed either as a result of dissolution or as a result of the physical parting of cleavage planes.

Ragged zone boundaries have only been observed in two adjacent grains (figure 6.15b and c). The boundaries separate chlorite of greatly differing composition. In these grains, small inclusions or islands of the chlorite showing lower back-scattered contrast (more Mg rich) occur above the ragged compositional boundary. These islands can only be explained by solid-state replacement. It appears that the ragged boundary was a product of the substitution of Fe for Mg within the chlorite rather than dissolution and reprecipitation. The boundary appears therefore to be a 'frozen in' exchange front.

Microprobe analyses were made at 2 micron steps across the growth zones shown figure 6.15a (along traverse A-A'). Representative analyses are given in Appendix 2a. The Mg number profile across the zones (figure 6.16a) confirms that the atomic number contrast recorded by the BSEM micrographs reflects variations in the Mg-Fe content of the chlorites. The size of the probe spot is of the order of 3-4 microns and scales with the width of individual zones. Only the broader growth zones can therefore be resolved with confidence in these profiles.

The chlorite compositions plot as a sloping linear trend in an AFM diagram (figure 6.16b). This trend records the solid solution field for the chlorite. It indicates that the substitution of Mg for Fe in the chlorite octahedral layer is accompanied by the substitution of Si for Al. This agrees with the results of Foster (1962), Curtis et.al (1985) and Kranidiotis and MacLean (1987) which are based on the analyses of a number of different grains rather than one zoned grain. All the chlorites are ripidolites (see figure 6.20).

Figure 6.15. Growth zoning in cavity-fill chlorite of sample NFS2.S3.
a). Montage of growth zoning in grain A of figure 6.14. Note the development of a major unconformity near the grain margin and the presence of cleavage-parallel stripes. The line A-A' marks a microprobe traverse using a 2 micron step distance between successive analyses. The results of this traverse are shown in figure 6.16a. See text for further discussion.
b). Ragged zone boundary truncating the original growth zones in another grain from the cavity (grain B in figure 6.14).
c). Small islands of different composition chlorite (caries texture) lying above the ragged boundary of (b). This feature suggests the ragged boundary is a solid-state replacement feature.

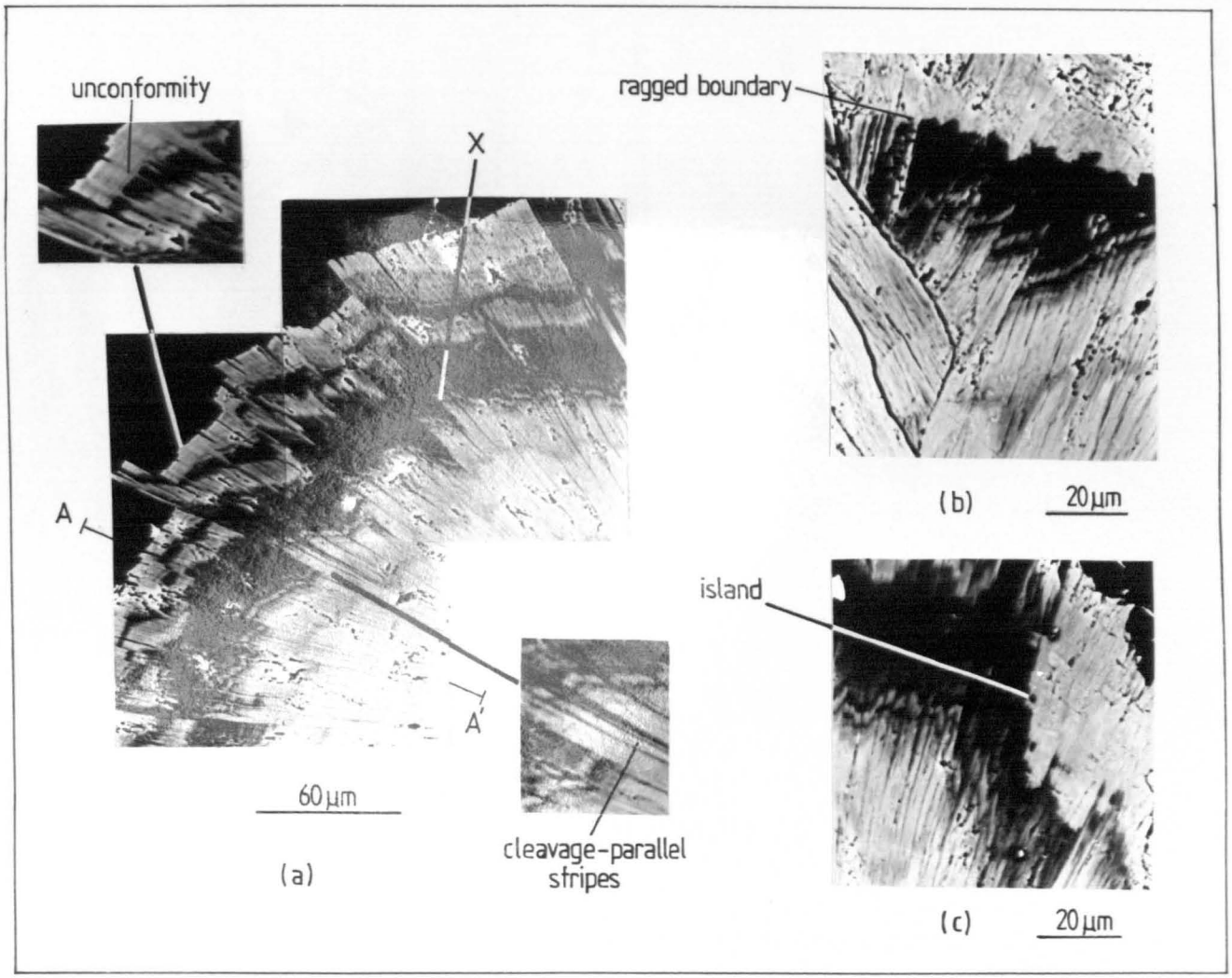
unconformity
X
A
A'
60 μm
(a)
cleavage-parallel stripes
ragged boundary
(b)
20 μm
island
(c)
20 μm

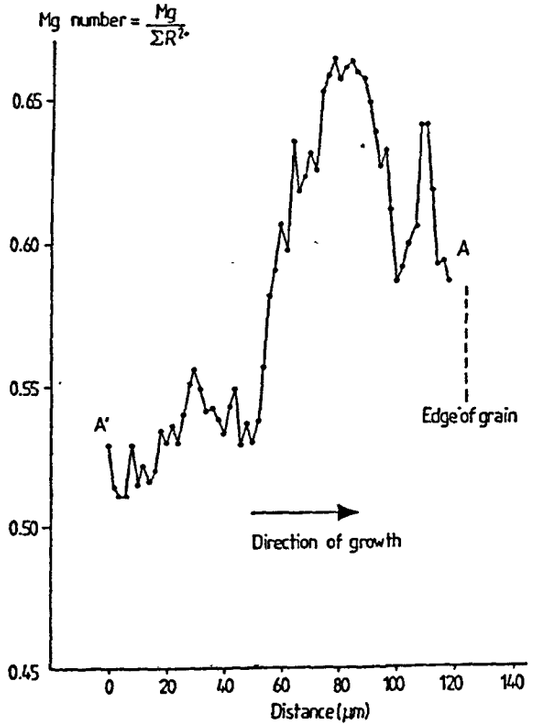

(a)

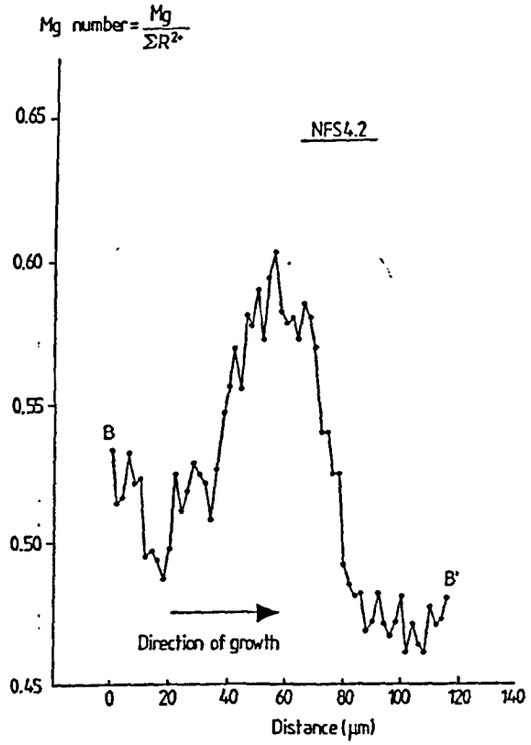

(c)

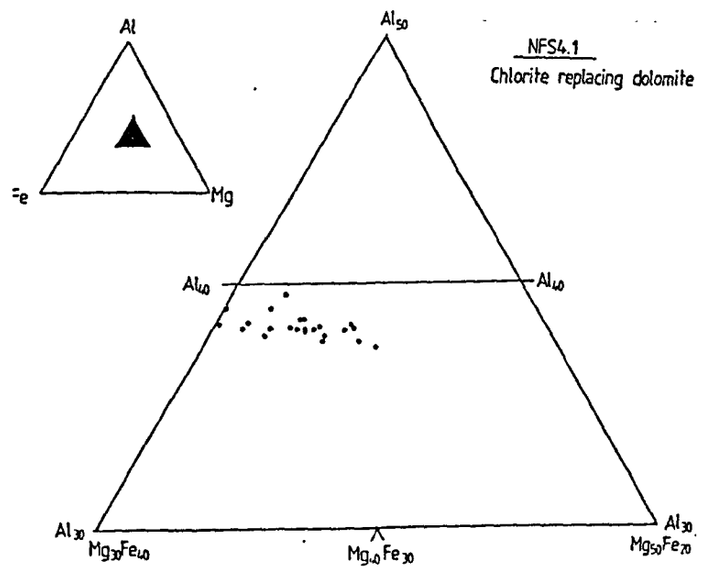

(e)

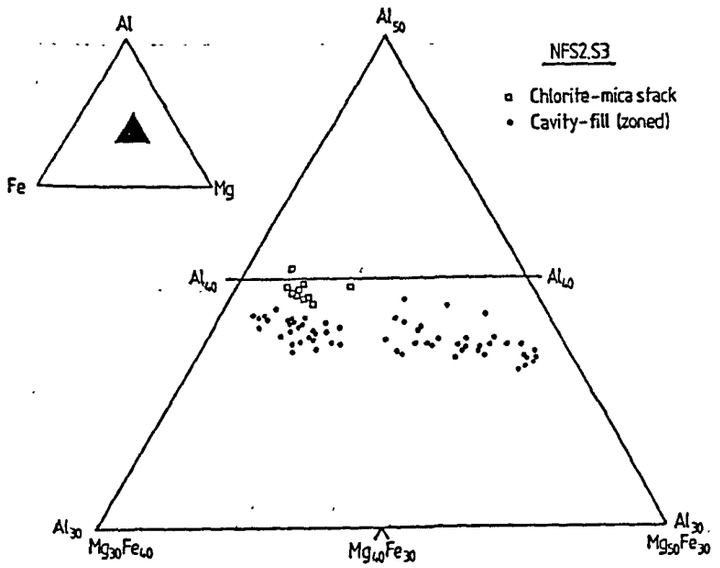

(b)

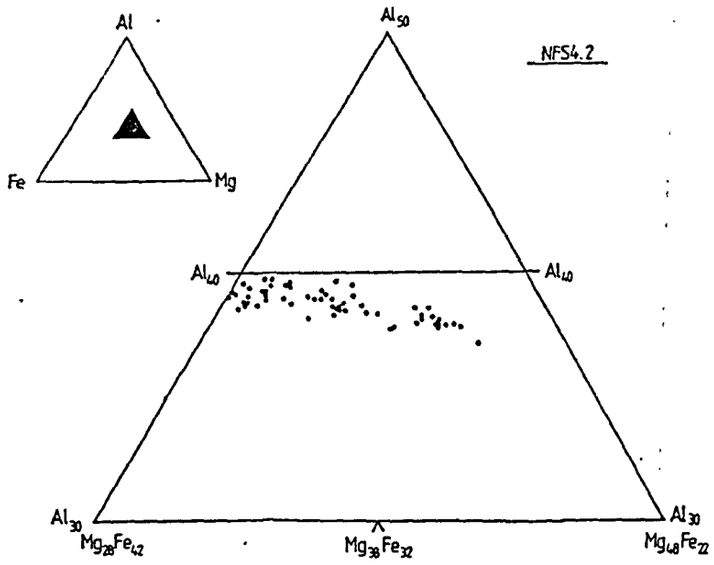

(d)

Figure 6.16. Mg number profiles and AFM plots of chlorite microprobe analyses. a). Mg number profile of traverse A-A' (figure 6.15a). Sample NFS2.S3 b). AFM plot of chlorite compositions, NFS2.S3. c). Mg-number profile of traverse B-B' (figure 6.12g). Sample NFS4.2. d). AFM plot of chlorite compositions, NFS4.2. e). AFM plot of chlorite replacing dolomite in sample NFS4.1.

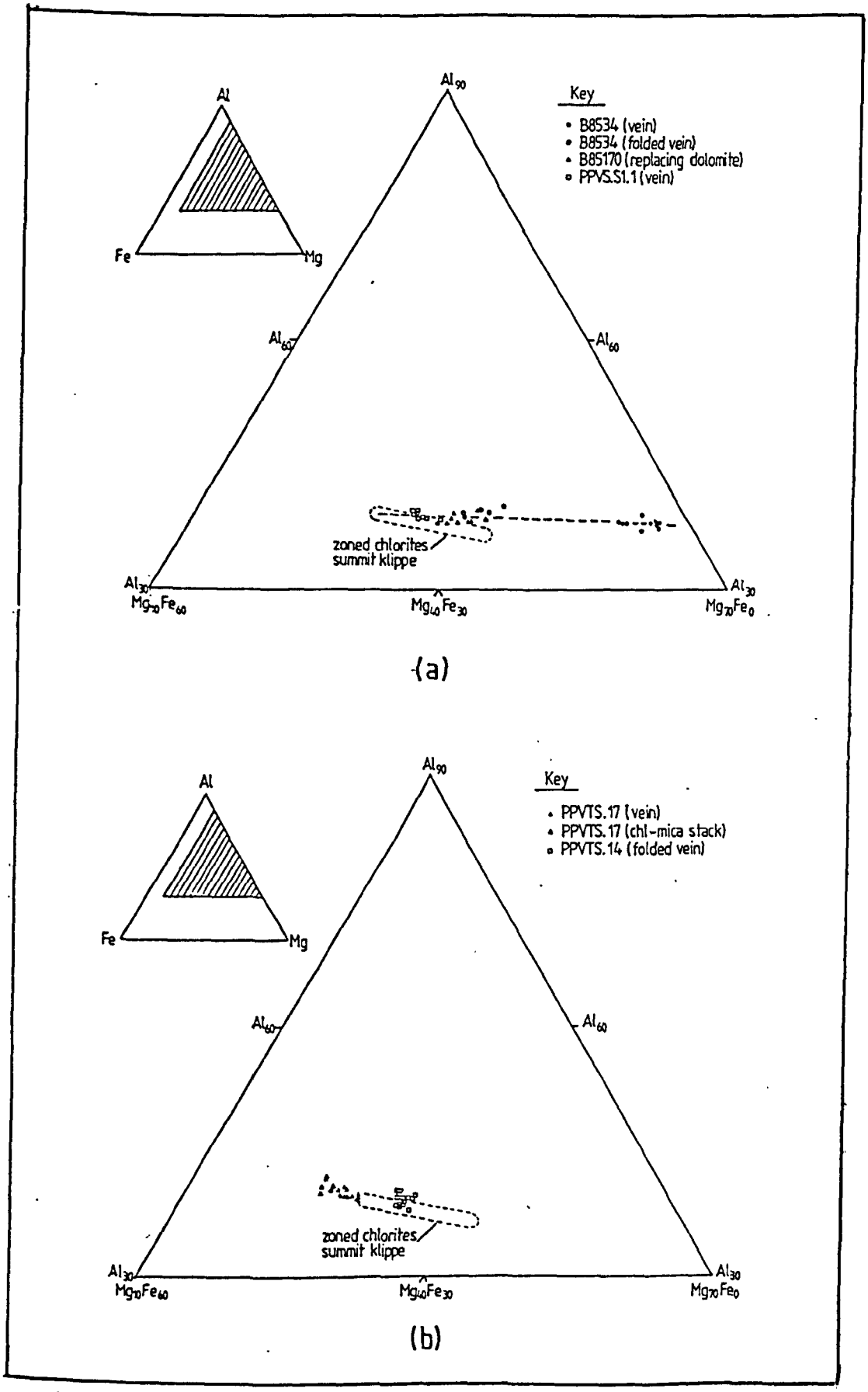

Figure 6.17. a) AFM plot of chlorite analyses from cavity and vein chlorites in the PPVT sheet of the Ridge Klippe. The analyses appear to plot along a constant Al trend. b) AFM plot of vein and wall rock chlorite compositions in the Triassic strata in the footwall of the PPVT. Both the cavity-fill chlorite and wall rock chlorite-mica stacks in the footwall strata have slightly higher Al contents than the zoned chlorites from the PPVT sheet.

The compositions of chlorite mica stacks within the wallrock of the cavity were also analysed. They have a Mg-number similar to the minimum observed in the zoned cavity chlorites but have slightly higher Al contents.

6.2.3.1.2. Samples NFS4.1 and NFS4.2.

Both these samples come from cavities along normal fault B in figure 4.13c. The samples were collected 1.5 metres apart. The chlorite in both samples is zoned but they possess different zonal patterns (figure 6.12e and g). Both patterns also differ from the pattern developed in NFS2.S3. The Mg number profile and the AFM plot for sample NFS4.2 is shown in figure 6.16c and d. The solid solution field is identical to that of sample NFS2.S3 although slightly extended.

A thin ferroan dolomite bed is present in the hanging wall of the cavity in NFS4.1. The dolomite adjacent to the fault contact is partially replaced by small tabular chlorite grains (see figure 6.13). BSEM reveals that these grains are concentrically zoned (figure 6.12f). Microprobe analyses of the zones (figure 6.16e) indicates that they have an identical solid-solution field to the vein chlorites in the same sample. They presumably precipitated from the same fluid.

6.2.3.1.3. Chlorites in the Ridge Klippe.

Chlorite veins and associated Mg-metasomatism occur in a zone bordering the PPVT thrust plane. Microprobe analyses of the are plotted in figure 6.17a. The chlorites have a wide range in compositions with the most Mg rich (clinochlore) filling veins and cavities in sample B8534. Overall the chlorite compositions appear to define a horizontal (constant Al) linear substitution field. This contrasts with the sloping field of the zoned chlorites in the summit klippe.

6.2.3.1.4. Chlorites in the Triassic strata in the footwall of the PPVT.

Chlorites from two samples (PPVTS.14 and PPVTS.17) were analysed. Sample PPVTS.14 was collected from the hanging wall of fault P1A in the middle fold structure (figure 4.6). Sample PPVTS.17 was collected from the basal Triassic fault zone and corresponds to sample 49448 of the fluid inclusion analyses. In sample PPVTS.14, the chlorites analysed occur in folded shear veins; in sample PPVTS.17 the chlorites occur in cavities and in chlorite- mica stacks from the cleaved Triassic shale wall rock. The microprobe results are plotted in figure 6.17b. The chlorites in sample PPVTS.14 have similar compositions to the wall rock mica stacks in sample NFS2.S3. Those in sample PPVTS.17 are more Fe rich and plot within a field that coincides with an extension of the zoned-chlorite field of

sample NFS2.S3. The cavity-fill chlorites in this PPVTS.17 have a higher Mg content than the chlorites in the adjacent wall rock.

6.2.3.2. Chlorites in the basement log section.

Chlorite was analysed from a suite of samples (for locations of the samples see figure 5.12. The chlorite occurs as interlayered chlorite-muscovite grains (these represent retrogressed biotites), as a fracture-fill, and as a replacement of the muscovite and pyrophyllite matrix (figure 5.17).

The chlorite Mg-number profile for the deformation zone is shown in figure 6.18 together with the location of the samples studied. The graph shows that the Mg/Fe ratio of the chlorites increases towards the thrust. The dotted line represents a schematic interpolation of the data. Three features are worth noting:

1. The most Mg rich chlorites analysed come from within the thin layer of Cretaceous limestone parallel to the thrust plane. These chlorites occur along subhorizontal stylolites in the limestone. Chlorite grains possessing lower Mg contents are also present in the limestone and account for the bifurcation in trends shown in figure 6.18. These chlorites occur as small fish (Lister and Snoke, 1984) within the mylonite.
2. A secondary Mg number maximum occurs between 8 and 9 metres below the Gavarnie Thrust. The position of this maximum corresponds precisely with the most dilatant fracture zone within the sheared basement.
3. Below about 10 metres from the thrust the chlorites have a uniform composition. This composition is however slightly more Fe rich than the retrogressed biotite grains in the wallrock.

The chlorites within any one sample tend to be compositionally homogeneous. This is reflected by the short length of the Mg number bars in figure 6.18. Discrete compositional growth zones similar to those observed in the chlorite of the PPVT sheet have only been observed in a vein-fill in sample BL3. The extreme compositions of these zones have Mg numbers of 89 and 97. The vein chlorites from the basement strata plot along a linear substitution field in an AFM ternary diagram (figure 6.19) that records the sympathetic substitution of Si for Al as Mg substitutes for Fe. The chlorites in Sample BL6 i.e. within the Cretaceous limestone plot below this field ie. they have lower Al contents. They appear to fall within an extension of the zoned chlorite field of the summit klippe chlorites. The retrogressed biotites appear to plot along different trends (2 and 3) reflecting mixing with mica.

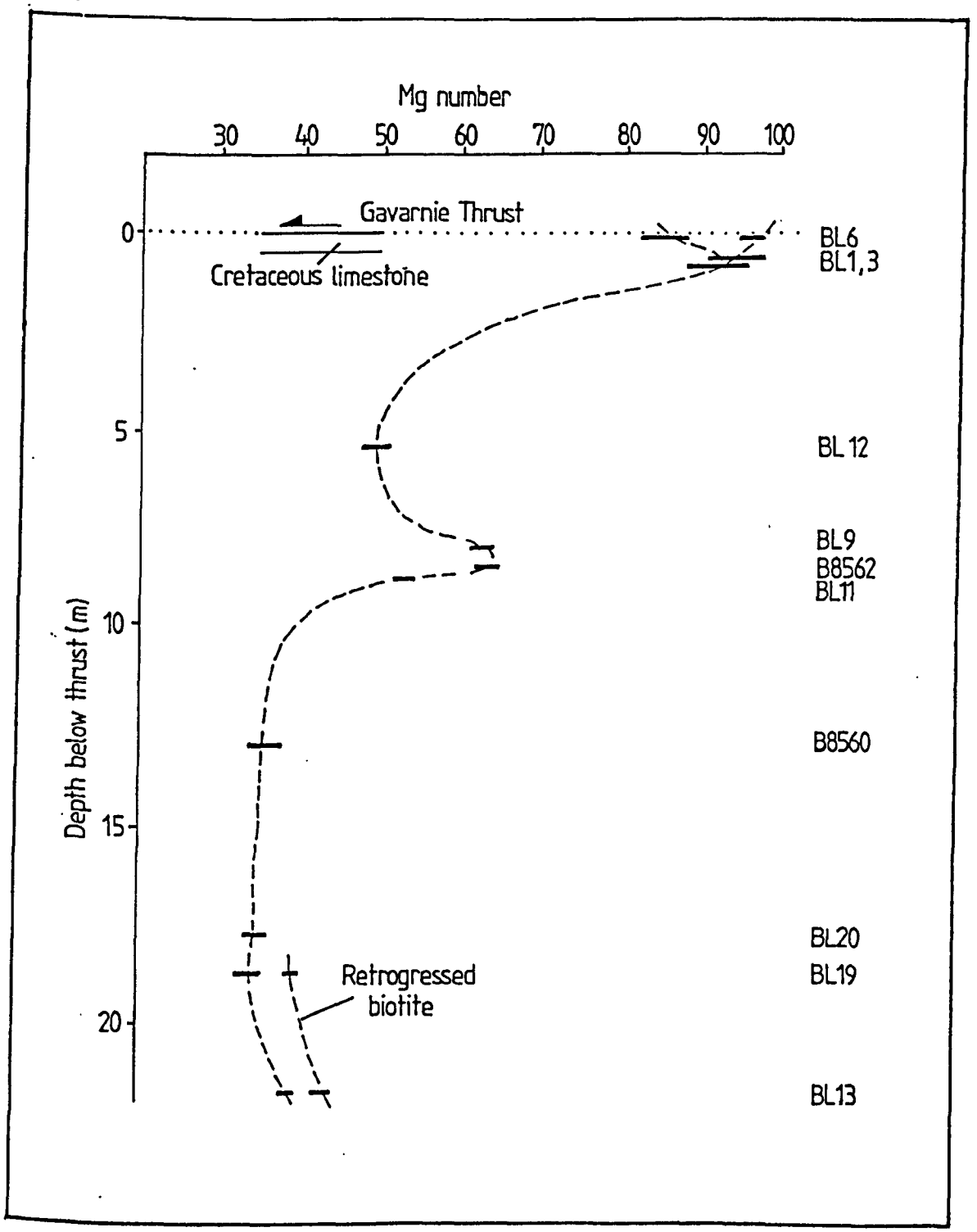

Figure 6.18. Mg-number profile of fracture-fill chlorites in the basement log. The profile shows that the chlorites become increasingly Mg-rich towards the thrust and that a secondary peak occurs 9 metres below the thrust. The general increase in Mg number can be equated with the proximity of the thin Cretaceous calcmylonite layer along the thrust. The secondary maximum coincides with an intense fracture zone that appears to have acted as a high permeability channelway for the flow of Mg-rich fluid sourced from the overlying limestone unit.

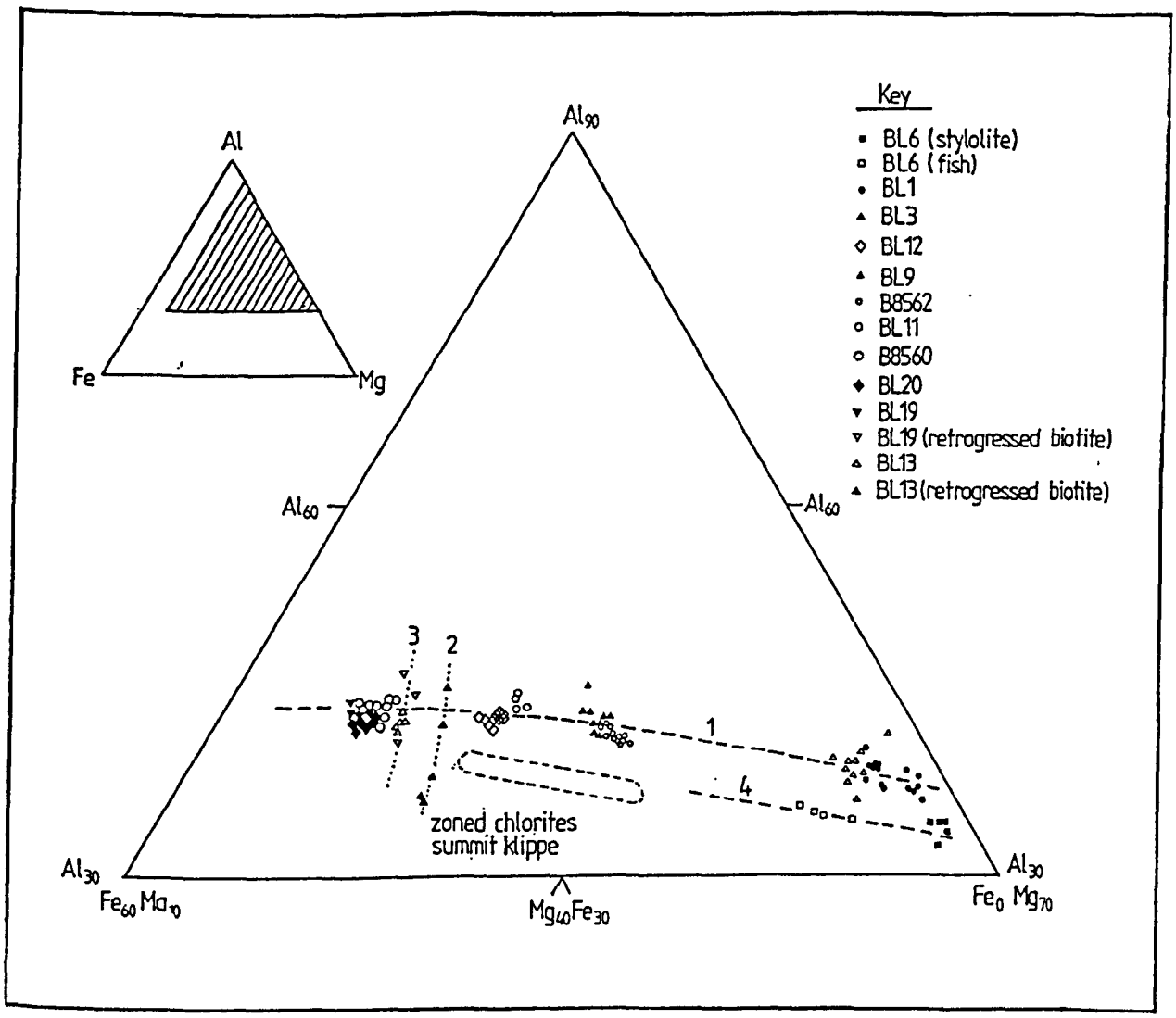

Figure 6.19. AFM plot of chlorite analyses in basement log. The chlorites in the altered basement strata define a linear substitution trend. For comparison, the field of zoned chlorites in the Summit Klippe of PPVT sheet is also plotted. Note that these chlorites fall on a the same substitution trend as the chlorites in the thin layer of Cretaceous limestone separating the sheared basement from the GT Sheet. This trend is relatively Al-poor compared to the chlorites within the altered basement.

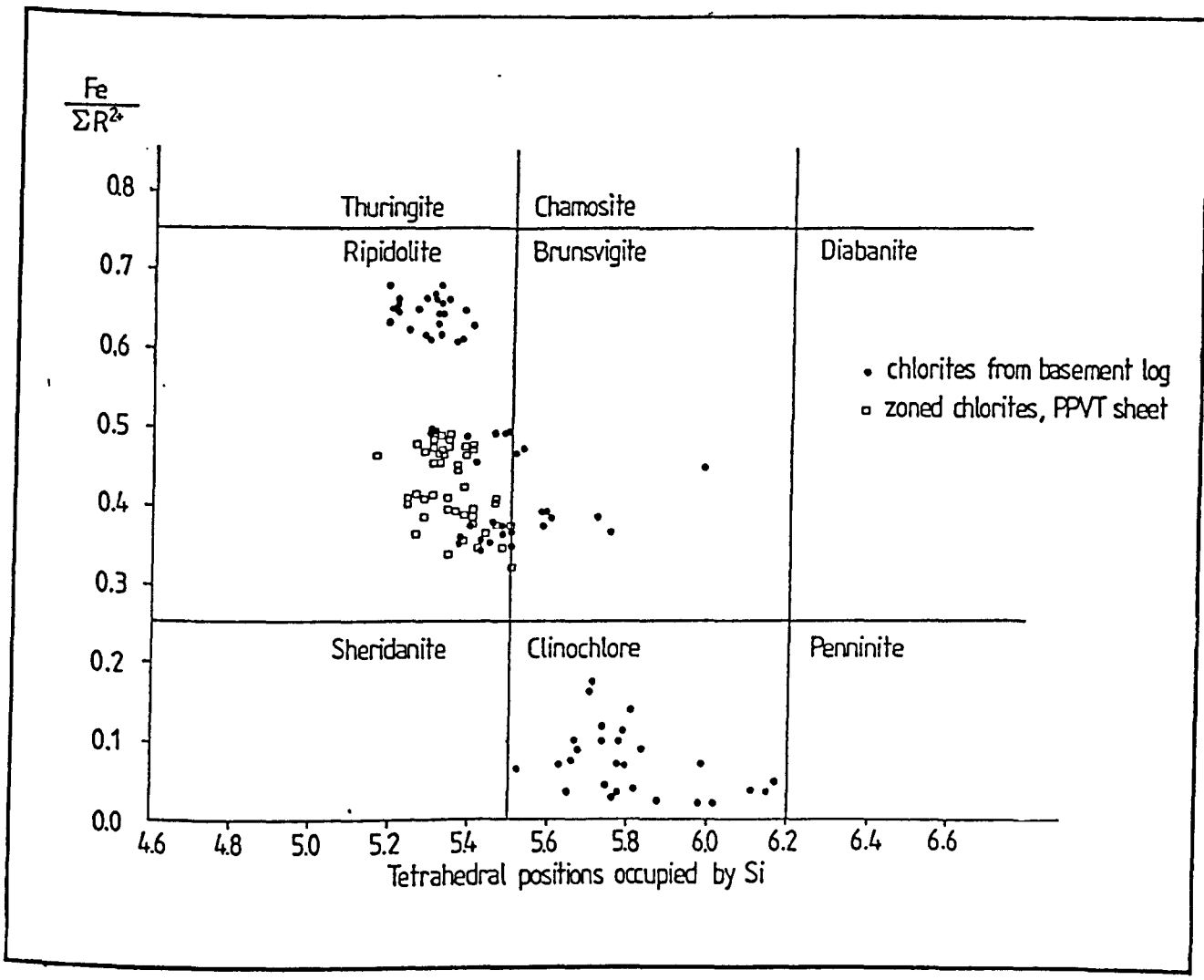

Figure 6.20. Foster diagram showing the compositions of all the chlorites analysed. The more Fe-rich chlorites are ripidolites, the Mg-rich chlorites are clinochlore.

6.2.4.3. Chlorite Compositional Trends.

The wide range of chlorite compositions within single chlorite grains and within the fault system as a whole allows a study of the chlorite compositional trends to be made. The chlorites plot in the ripidolite and clinochlore fields of Foster (1962) (figure 6.20).

As already noted, there is an appreciable decrease in Al content of the chlorites with an increase in the Mg/Mg+Fe ratio. This can be explored further by plotting the tetrahedrally and octahedrally coordinated Al against one another and against the Mg number (figure 6.21 and 6.22). Both Al(iv) and Al(vi) decrease sympathetically as Mg substitutes for Fe in the chlorites of both the basement log and of the PPVT sheet (figure 6.21). This relationship agrees with the results of Foster (1962) and implies that the substitution is of the form:

$$Si^{4+} + R^{2+} = Al^{3+}(iv) + Al^{3+}(vi)$$

Comparison of the different trends shows that the Al(iv) contents tend to be identical for both the basement chlorites and the chlorites in the PPVT sheet (both summit and ridge klippes). The main variation in Al occurs in the Al(vi) which is significantly higher in the basement chlorites. This trend can also be seen in figure 6.22 which also shows that the zoned chlorites from the summit klippe have slightly lower Al(vi) than corresponding chlorites in the ridge klippe or in the footwall Triassic strata.

6.2.4. Interpretation of chlorite chemistry.

6.2.4.1. Interpretation of compositional trends.

It appears from figures 6.17 and figure 6.19 that the chlorites from the basement log and those from the PPVT sheet form four distinct solid solution series. These are summarised in figure 6.23. Series 1 represents Al enriched chlorites that precipitated in the aluminous muscovite-pyrophyllite-quartz rock of the basement (see chapter 5). Series 2-4 can, in comparison, be considered to represent Al poor chlorites. These formed within the Cretaceous limestone adjacent to the GT and within the Triassic red beds. Series 2 represents the trend recorded in the chlorites from the strata in the ridge klippe. Series 3 comprises all the wall rock chlorites analysed from the Triassic red beds. Series 4 represents the most Al-poor chlorites and comprise the zoned chlorites in the summit klippe of the PPVT sheet, and the chlorites in the Cretaceous limestone from the basement log (sample BL6). Note that series 2 is anomalous because it does not show the expected Al substitution with increasing Fe/Fe+Mg ratio.

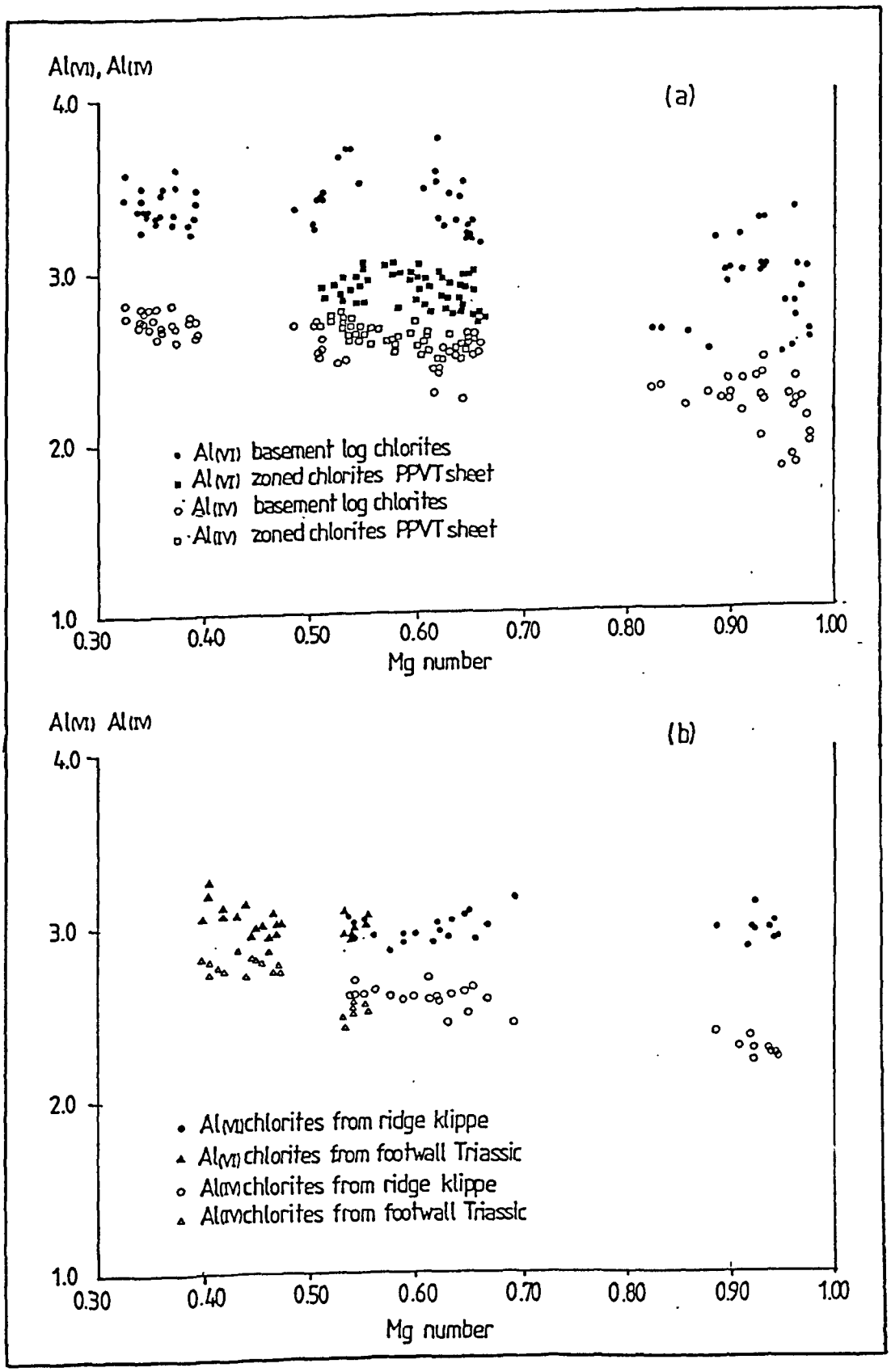

Figure 6.21. Compositional plots of Al(iv) and Al(vi) against Mg- number. a). Basement Log and zoned chlorites from PPVT sheet. b). Chlorites from Ridge Klippe and footwall Triassic strata. Both plots show a linear substitution trend of decreasing Al(iv) and Al(vi) with increasing Mg-number. For a given Mg-number the chlorites from the different rock types possess the same Al(iv) but different Al (vi). The variations in chlorite Al content shown in the AFM diagrams solely reflects variations in the octahedrally coordinated Al (Al(vi)).

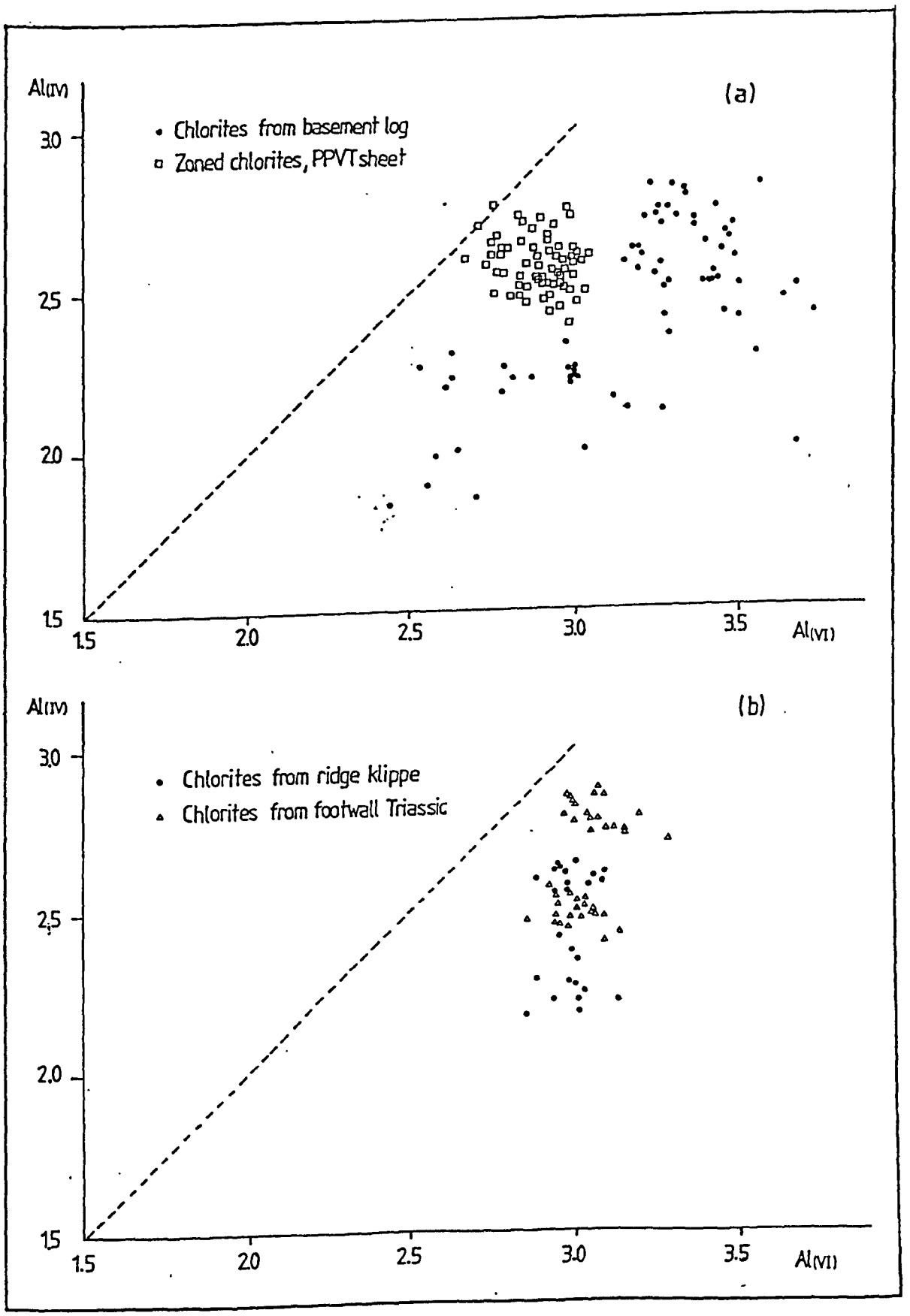

Figure 6.22. Plots of Al(iv) against Al(vi). All the chlorites plot below the line Al(iv)=Al(vi) although chlorites from different rocks plot in different fields within the diagram. Both plots again show that the chlorites in the basement log have high Al(vi) compared with the other chlorites.

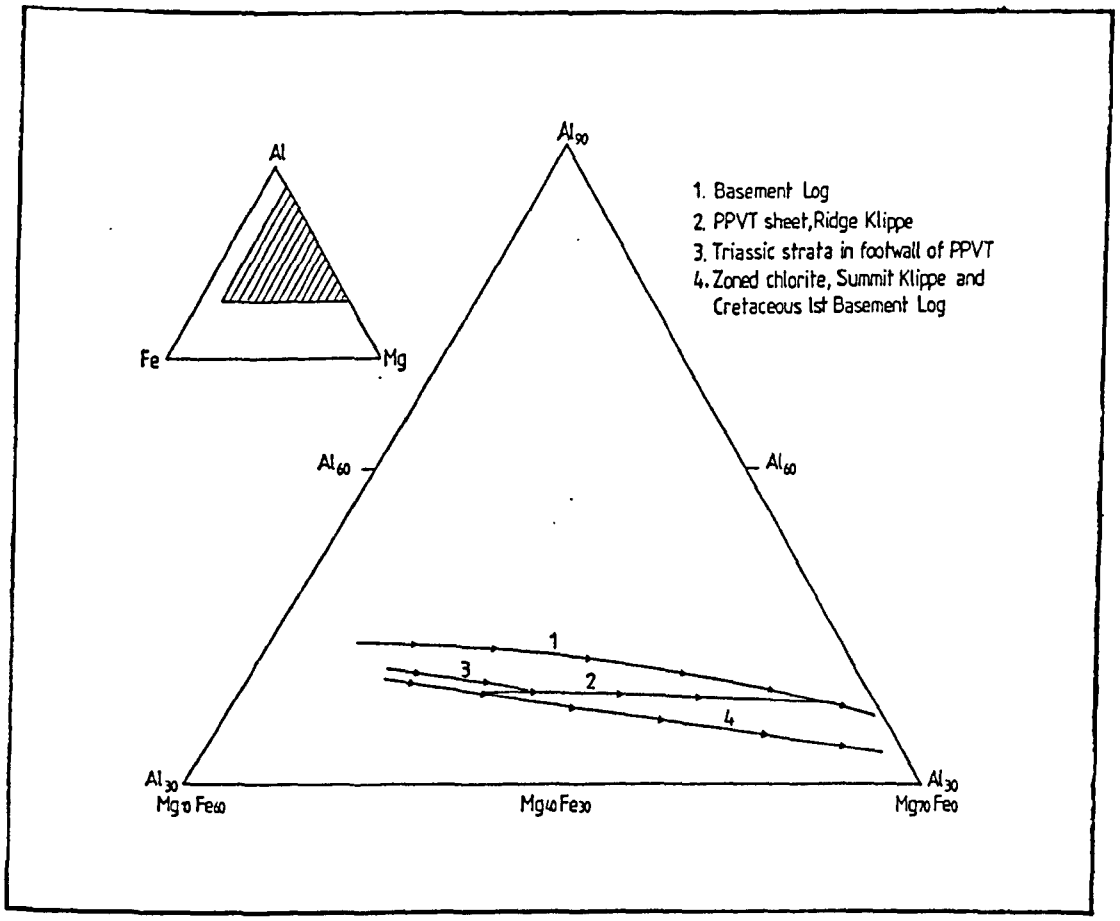

Figure 6.23. Summary AFM diagram showing the chlorite compositional trends for the different sample areas.

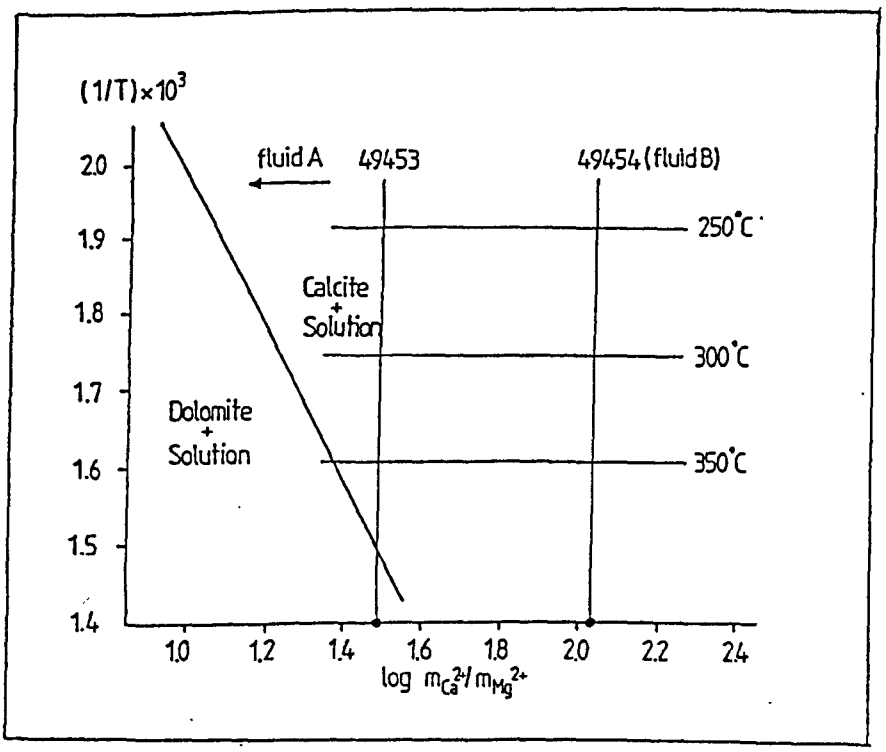

Figure 6.24. Plot of the stability fields for dolomite and calcite (after Rosenberg and Holland (1964)) showing the calculated Ca/Mg ratios from the crush leach analyses of samples 49453 and 49454. For the inferred trapping conditions, fluid B plots well within the calcite field. Fluid A should lie to the left of sample 49453 which represents a mixture of fluids A+B. It may or may not lie within the calcite stability field.

Similar compositional trends to series 1 and 4 have been noted by Kranidiotis and MacLean (1987). From a study of chlorite compositions in an altered rhyodacite stock, they differentiated Al-saturated and Al-undersaturated species related to the presence or absence of another aluminous phase in the rock and concluded that the composition of the chlorite can be related to the bulk composition and mineralogy of the host rock.

The results of Kranidiotis and MacLean (1987) agree in part with the data presented here. Chlorites in the aluminous basement strata have high Al in the form of Al(vi) whereas those from the adjacent Cretaceous limestone have considerably lower Al(vi). The chlorites from the PPVT sheet have a more complicated relationship with their host rock. The cleaved Triassic red beds are aluminous in terms of possessing other Al rich phases (micas) yet the chlorites, especially those in the fault-parallel cavities within the summit klippe, have relatively low Al(vi). Moreover, the zoned cavity chlorites possess lower Al contents than the chlorite-mica stacks in the adjacent wall rock. In the ridge klippe however the cavity chlorites have similar Al contents to the wall rock chlorites (folded veins).

In terms of fluid chemistry, the Al(iv) in chlorite precipitating from a fluid should be related to the Al/Si activity ratio of the fluid while the Al(vi) should be related to the $Al^{3+}/Fe^{2+}+Mg^{2+}$ activity ratio. The similarity of the Al(iv) contents for chlorites with the same Mg-number but from different host strata (figure 6.21) suggests that the fluid Al^{3+}/Si^{4+}activity ratio was virtually independent of the rock type. The trends for Al(vi) indicate that the $Al^{3+}/Fe^{2+}+Mg^{2+}$ activity ratio of the fluid was however strongly controlled by rock type. This difference may reflect the high silica activity in the fluid compared with the other species.

A relationship also appears to exist between Mg number and host- rock composition. This is shown most clearly in the basement log. The Mg number profile from chlorites in the log (figure 6.18) appears to record a gradient in Mg^{2+}/Fe^{2+} activity in the fluid related directly to the Cretaceous limestone bed adjacent to the thrust. The reversal in the Mg-number trend for the chlorite fish in the calcmylonite bands (figure 6.18) is therefore anomalous. However, this trend might reflect a higher Fe^{2+}/Mg^{2+}activity ratio in the fluid within the calcmylonite bands than within the dolomite bands. This could be related to focussed fluid flow and enhanced element mobility in the mylonite layers (cf. Sinha et al., 1986).

6.2.4.2. A possible source for high Mg-chlorite.

The stability of calcite and dolomite in chloride solutions has been experimentally determined by Rosenberg and Holland (1964). Plotting the Ca/Mg ratio obtained from

the crush-leach analyses of the fluids onto their figure 2 (figure 6.24), shows that fluid B was in equilibrium with calcite for the assumed range of trapping temperatures. Fluid A may or may not have been in equilibrium with dolomite because its Mg/Ca ratio has not been determined from the crush leach analysis of sample 49453 (the analysis represents fluids A+B). This analysis suggests that if fluid B was to come into contact with dolomite it would produce dedolomitisation.

The fluid inclusions in quartz from sample 49203 (sample BL10) indicate that fluid A and probably fluid B were both present in the GT fault zone during deformation (see figure 5.6). It seems logical to postulate that the high Mg-chlorites present in the fault zone were precipitated from fluid B after it had acquired a high Mg^{2+}/Fe^{2+} activity ratio by reaction with the limestone. Dedolomitisation is indicated texturally in the limestone (sample BL6) by the presence of small blebby calcite grains that replace the dolomite (figure 5.11a). The Mg-metasomatism of the adjacent basement phyllonite can therefore be understood in terms of syntectonic fluid-rock reaction between the phyllonite and a fluid equilibrated with the limestone. A similar conclusion probably applies to the Mg-metasomatism that occurs along the PPVT.

6.2.4.3. Interpretation of chlorite zoning.

The zoned chlorites probably record fluctuating Mg/Fe activity ratios in the fluid. Where the chlorites in the veins and the chlorites in the chlorite-mica stacks in the wall rock have similar Mg numbers, it probably indicates that the Mg^{2+}/Fe^{2+} activity ratio of the fluid was equilibrated with the wall rock. Where a difference exists the fluid was probably externally derived (probably from the Cretaceous limestone). The zoned chlorites in the fault-parallel cavities appear therefore to record the pulsing of flow of limestone-equilibrated fluid through the fault-cavity system in the PPVT sheet.

The pattern of zoning is different in the chlorites precipitated in different cavities, even in cavities along the same fault. This indicates that each cavity must have had a distinct fluid flow history possibly because they did not all form simultaneously or were not all linked to exactly the same fluid reservoir.

6.3. Fluid flow processes in the thrust system.

6.3.1. Introduction

This section will try and answer some of the questions concerning the fluid processes in the thrust system that have still to be addressed. These include:

1. How do fluids A and B coexist in the fault system?
2. How are the inferred lithostatic fluid pressures generated in the system?

3. What is the scale of the fluid flow and what pathways are used?
4. What might be the driving forces for fluid flow?
5. How is meteoric water introduced into the fault system?

It must be emphasised that analysis of the fluid inclusions in quartz and chlorite compositions from the fault-parallel cavities means that only the fluids present during third phase of thrusting have been studied. Whether the earlier thrust phases occurred in the presence of fluid of different compositions to that found in the cavity-fill quartz is not known.

6.3.2. The generation of high fluid pressures in the fault system.

Brace (1980) has shown that for crystalline rocks in the upper crust, permeabilities are sufficiently large that pore fluid pressures greater than hydrostatic cannot be maintained over geological periods of time. Accordingly high fluid pressures must represent transient phenomena. High P_f existed within the PPV culmination and was responsible for the observed fault-parallel cavities. Similar cavities are absent from along faults outside the culmination and suggest that a relationship may have existed between the deformation in the culmination and the generation of the high P_f. Within the Gavarnie Thrust fault zone the observed transition from ductile to brittle shearing accommodated by grain-scale fracturing is also inferred to have occurred under high P_f (chapter 5). This suggests that a relationship may also have existed between emplacement of the GT sheet and the generation of high P_f. These two possibilities will be explored below.

6.3.2.1. The generation of high P_f during faulting.

High P_f in fault zones can arise from either seismic pumping (Sibson et al., 1975, 1987; Sibson,1981) or from elastic and inelastic porosity reduction (Walder and Nur, 1984; Cello and Nur, 1988).

6.3.2.1.1. Seismic pumping.

The mechanism of seismic pumping envisages that the build up of elastic strain prior to an earthquake opens up swarms of microcracks that close when the stress is relaxed during slip on the fault. The closure of the cracks expels the pore water and generates overpressures. These then lead to episodic hydrofracturing in the vicinity of the fault zone. Evidence for seismic faulting in the PPV culmination (cataclasis) is lacking and the movement on the thrusts appears to have occurred by an aseismic crack-seal stick-slip mechanism. It seems likely that seismic pumping is not applicable to the faults under study.

Simulated stick-slip faulting experiments by Teufel (1980 and 1981) have shown however that pore pressures drop during slip events due to increased fracturing, but build up as a result of compaction prior to failure. This behaviour is the opposite of that responsible seismic pumping and has more in common with the dilatancy pumping model of Etheridge et al., (1984). It suggests that stick-slip faulting and dilatancy are coupled and result in an ingress of fluid into the fault zone during slip events. The mechanical effect of this fluid has been modeled by Rice and Simmons (1976) who show that it is likely to stabilise fault slip due to the increased stiffness of the medium in the draw down region. This type of dilatancy-diffusion response is probably reflected in the crack-seal slip mechanism observed for the faults in the PPV culmination.

6.3.2.1.2. Inelastic porosity reduction.

Pore compressibility, pore sealing by mineral precipitation and deformation by crystal plasticity or DMT can combine to reduce the porosity of the rock mass. Walder and Nur (1984) have shown that these inelastic processes are rapid under crustal conditions. If the porosity reduction rate is large relative to the permeability then lithostatic fluid pressures may develop. Quantitative modelling by Cello and Nur (1988) have shown that lithostatic fluid pressures can develop in 2×10^4- 2×10^5 years for geologically realistic strain rates of 10^{-14} and that this only requires 1-3% porosity reduction.

Tectonic strain can therefore result in the generation of high pore pressures and is likely to be an important mechanism in low permeability rocks deforming at high strain rates. High permeability and fluid pressure dissipation will occur during fracture episodes and the overall process is likely to be cyclical (Cello and Nur, 1988). This mechanism predicts that high P_f should be generated in zones of distributed deformation eg. at the tips of faults and it seems directly applicable to the deformation in the PPV culmination.

6.3.2.2. The generation of high P_f during thrust sheet loading.

Gretener (1981) concluded that it is not possible to generate lithostatic fluid pressures below a thrust plane by loading alone and considers that aquathermal pressuring may be important. There is however a time lag of up to 1-2 My between the loading and the development of overpressuring as the footwall rocks heat up. It is therefore difficult to account for the syntectonic generation of high P_f. Onepossibility is that loading results in compaction by pore compressibility and it this generates the high P_f (Shi and Wang, 1986). Shi and Wang (1988) consider that loading is the most important mechanism in generating high P_f in accretionary prisms. Loading during emplacement of the GT sheet is indicated by the presence of vertically oriented veins (vein association 3) within the

PPVT sheet (see section 4.6.4.1). It is therefore feasible that loading could have contributed to the inferred high fluid pressures.

6.3.2.3. High P_f and hydrofracture in the PPV culmination.

From the above discussion it seems likely that the generation of overpressures during distributed shortening can best account for the observed high P_f in the PPV culmination. The generation of these fluid pressures would have been favoured by the low intrinsic permeability of the stratigraphic sequence. The multiple fracture episodes in some of the cavities (chapter 5) suggests that cycling of high fluid pressures occurred within the system.

Cavity formation appears to have been restricted to faults in the culmination. This presumably reflects the low tensile strength of these discontinuities and the presence of a sub-vertically oriented least principal stress. Episodes of hydrofracture occur when the stress conditions are represented by:

$$\sigma_3 - P_f \geq T$$
$$\sigma_1 - \sigma_3 \leq 4T$$

(Kerrich, 1986). T is the tensile strength of the sealed fault plane. The first inequality represents the condition where the fluid pressure exceeds the confining pressure by an amount equal to or greater than the tensile strength of the rock. The second inequality is the condition for the suppression of shear failure (Secor, 1965).

6.3.3. Fluid flow in the fault system

6.3.3.1. The scale of fluid flow.

Fluid flow (advection) can be demonstrated to have occurred within the fault system. The presence of zoned chlorites in the PPVT sheet suggest fluid flowed upwards from the footwall limestone into the overlying thrust sheet. In the basement log a secondary maximum of Mg-rich chlorites 10 metres below the Gavarnie Thrust suggest that fluid originally in equilibrium with the limestone was channelled into a dilatant fracture zone. The direction of the fluid flow in the latter case is unconstrained but may have been lateral.

The fluid flow system in GT fault zone appears to have been wallrock-dominated even though the zone is extensively fractured (see discussion in chapter 5). Similar conclusions can be reached from the observed heterogeneity in fluid inclusion compositions in the fault-parallel cavities in the PPV culmination. The observed chlorite compositional variations appear only to record the relatively small-scale fluid transfer

Figure 6.25. Examples of fluid flow pathways in the thrusts studied. The pathways have been mapped by analysing chlorite compositions. Fluids equilbrated with the Cretaceous limestone have a high Mg/Fe activity ratio whereas fluids equilibrated with the Triassic red beds and Hercynian basement have a low Mg/Fe activity ratios. When fluid flows from the limestone into the surrounding strata it precipitates chlorites with a higher Mg number than chlorites in the host rock. The chlorite composition can therefore be used as a tracer of fluid flow. a) Fluid flow in the PPV culmination. Zoned cavity-fill chlorites in the PPVT sheet record the flow of fluid from the limestone into the overlying red beds. The association of the Mg/Fe zoned chlorites with the fault-parallel cavities indicates that hydrofracture of the faults provided the high permeability channelways that focussed fluid flow. The dilatancy associated with the hydrofracture may have been responsible for the pumping of the fluid along the fracture network. b) Fluid flow within the Gavarnie Thrust fault zone. The chlorite Mg number profile for the fault zone indicates that fluid, originally equilbrated with the limestone, was channelled along a high permeability fracture zone 10 metres below the thrust. The adjacent rock, although also extensively cut by slip surfaces, appears to have remained relatively impermeable. The slip surfaces were filled by pyrophyllite and muscovite from a fluid equilibrated with the altered basement strata. Fluid flow in both examples was strongly controlled by fault-related permeability and was associated with hydrofracture within the fault zones. The scale of fluid flow was however local (between adjacent lithological units) and no evidence exists for major fluid advection associated with the thrusting.

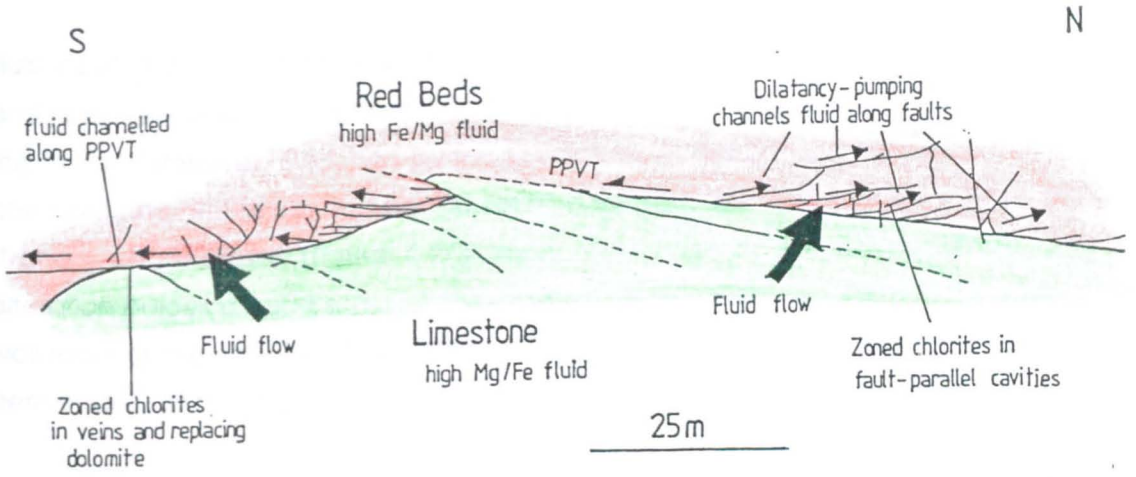

(a) PPVT sheet

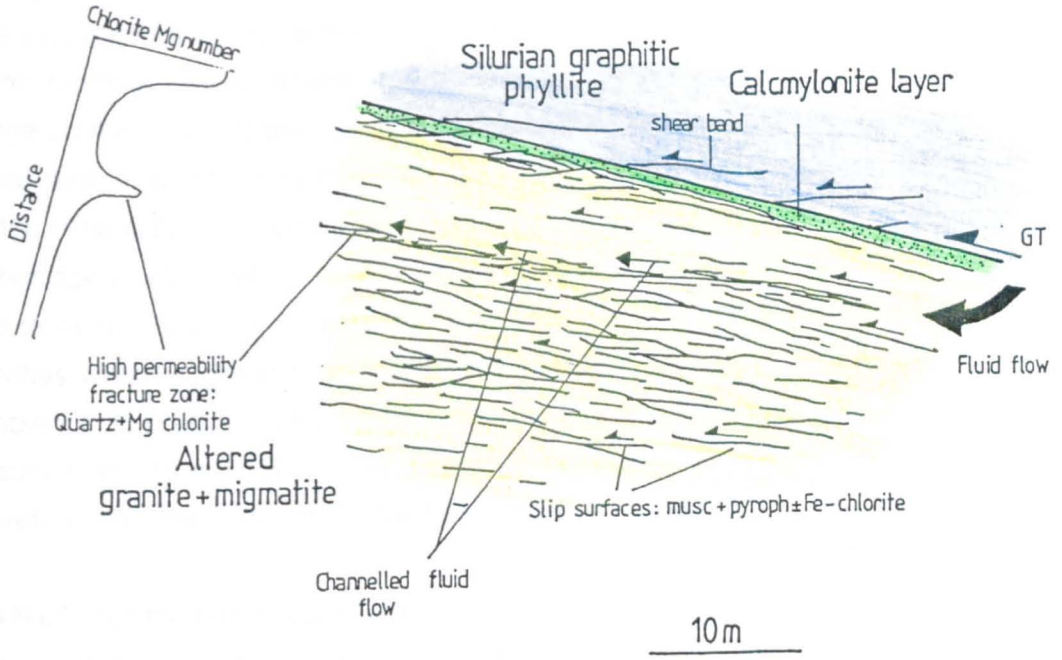

(b) GT fault zone

between different rock units which possessed internally buffered fluid. There is little evidence to suggest that large-scale fluid fluxes occurred within the fault system.

6.3.3.2. Fluid flow pathways.

Fluid input into the system must have occurred to explain the inferred dilution of fluid A and its presence in the Triassic strata in the first place. The most likely pathways used are the faults themselves. Evidence for this flow is seen in the general localisation of chlorite compositional variations to specific faults and fractures and suggests that flow was strongly channellised (figure 6.25). More pervasive flow is indicated by chloritic alteration haloes around some of the cavities but these are localised to the immediate wall rocks of the fractures. The absence of widespread porous flow reflects the very low permeability of the strata.

6.3.3.3. Driving forces for fluid flow.

The presence of compositionally zoned chlorites suggests that fluid pulsing occurred within the fault-cavity network. The presence of both fluids A and B in primary inclusions in the cavity-fill quartz also suggest that fluid pulsing operated and served to introduce these fluids into the cavity from different reservoirs that must have coexisted in the fault system. The pulsing probably occurred in response to some form of dilatancy pumping (Etheridge et al., 1984; Lister et al., 1986) related to fracture or hydrofracture episodes. This does not however explain the presence of alteration haloes around some of the cavities which suggest that the fluid pressure in the cavities was greater than the ambient fluid pressure in the wall rock (cf Yardley, 1983). Dilatancy pumping is expected to suck fluid into the newly formed fracture porosity and not the reverse. It cannot have therefore operated throughout the flow history in a cavity.

It is likely that the fluid pressure will equilibrate quicker in a cavity than in the draw-down region in the surrounding wall rock. This may be aided by the fact that fluid flowing from a narrow feeding fracture into a cavity must increase in pressure in accordance with Poseilles' Law. It is possible that this effect will result in fluid flow into the wall rock at the end of a fluid pulsing event and this could cause localised alteration if the bulk of the fluid in the cavity was externally derived via the fracture network (figure 6.26).

6.3.3.4. The coexistence of fluids A and B in the fault system.

As already pointed out the fact that primary inclusions of fluids A and B occur within quartz grains in the same cavities suggests that these fluids coexisted in the system. It seems logical to suggest that they resided in different reservoirs that were periodically tapped during fracturing. The origin and location of these reservoirs is not known. The

Figure 6.26. Model for the fluid flow history in a fault parallel-cavity. a) The stages involved in the cavity development. 1. Development of planar fault. 2. Hydraulic fracturing produces cavity along fault. The rapid dilatancy sucks local fluid into the cavity from the wall rock and external fluid into the cavity from high permeability fractures along the fault plane. The graph models the fluid pressure draw down in the wall rock adjacent to the cavity. 3. The fluid pressure equilibrates in the cavity due to fluid flow along the fault-parallel feeding fractures before the pressure equilibrates in the low permeability wall rock. This results in the infiltration of external fluid into the wall rock and the development of an alteration halo around the cavity. The alteration involves the replacement of dolomite by chlorite or the replacement of white mica by chlorite. The graph shows that the magnitude of draw down in the wall rock has decreased but that its width has increased as the pressure pulse associated with the initial dilatancy travels through the wall rock. 4. The fractures that feed the cavity seal and the fluid pressure in the system equilibrates. The cavity remains open however due to its large size. 5. Dilatancy in another part of the system and opening of the feeding fractures result in a pressure pulse that pumps fluid rapidly through the open cavity. This pulsing of fluid is recorded by zoned chlorites and different fluid inclusion populations in the quartz. b) Schematic fluid pressure chart for cavity and adjacent wall rock. Hydrofracturing occurs when the ambient fluid pressure exceeds the confining pressure plus the tensile strength of the fault plane (T). Pf (amb) is the ambient fluid pressure; Pc the fluid pressure in the cavity on dilation. The various stages are outlined. Pf-Pc is the pressure drop associated with dilation. From the fluid inclusion populations (see figure 6.5 and 6.11) it may be as large as 700 bars.

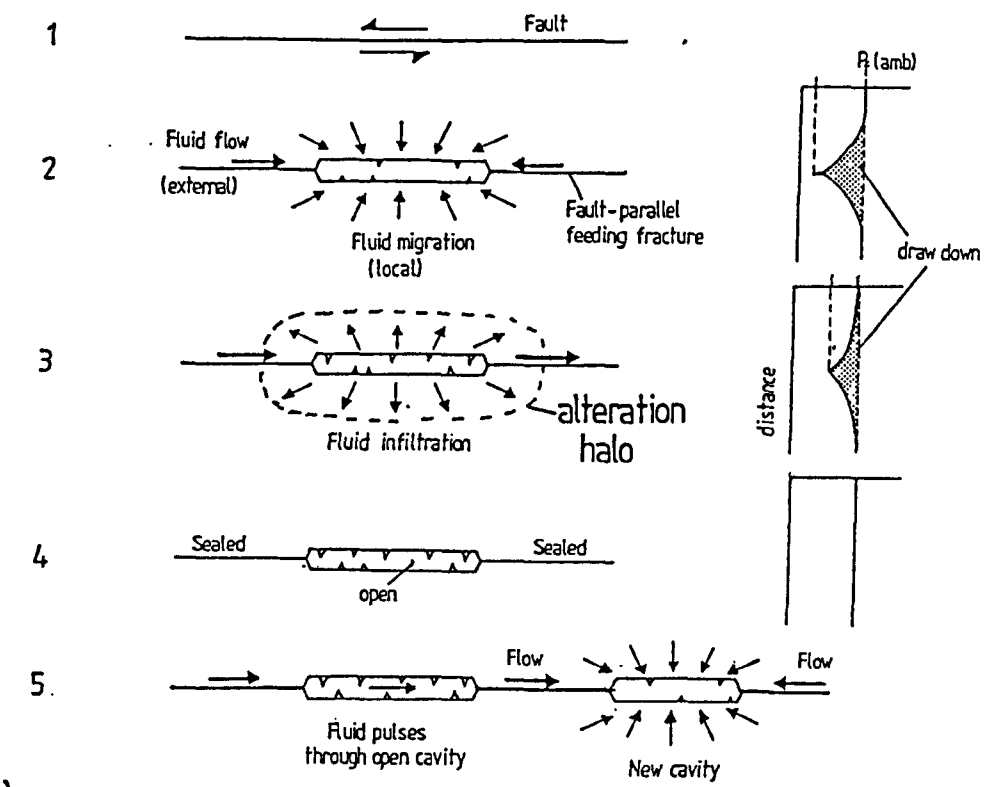

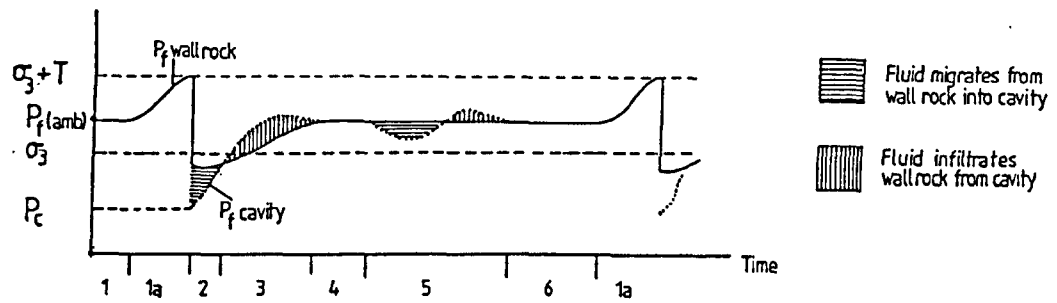

Stage 1 Fault active or passive
Stage 1a Fluid pressure increases
Stage 2 Hydrofracture jacks open fault. Fluid migrates into cavity and flows along feeding fractures.
Stage 3 Fluid flow along feeding fractures equilibrates Pf in cavity. Draw down in wall rock takes longer to equilibrate due to low intrinsic permeability. Fluid infiltrates wall rock.
Stage 4 Feeding fractures seal, cavity remains open.
Stage 5 Fluid pulses through cavity due to dilatancy pumping associated with new cavity elsewhere in system.
Stage 6 Feeding fractures seals, cavity remains open or seals.

(b)

pressure pulse associated with rapid fracture dilatancy would have flushed fluid rapidly from either or both these reservoirs into the fault-cavity system (figure 6.26).

It is feasible that complete fluid exchange in a cavity would have been promoted by the rapidity of the pulsing and it is this feature that is considered to have prevented mixing of fluids A and B. During and after the pulsing the fractures that link the cavity network would start to heal as quartz and chlorite were precipitated from the solution. At the ambient temperatures in the fault system (250-300°C) these narrow cracks would seal very quickly (Smith and Evans, 1984). Rapid sealing would also have prevented the mixing of fluids A and B after the initial dilatancy driven pulsing had ceased. This suggests that it may have been difficult to to homogenise fluid compositions by localised and repeated fracturing in the fault system.

The cavities themselves probably remained as fluid filled voids between fracture episodes. This can explain the inferred numerous episodes of fluid pulsing that produced the zoned chlorites. The low intrinsic permeability of the wall rocks probably helped maintain high fluid pressures in the cavities once the linking fractures had sealed. Once sealed the fluid pressures would have built up in preparation for another episode of dilatancy-induced pulsing (Etheridge et.al, 1984; Parry and Bruhn, 1986).

6.3.4. Fracture sealing.

The veins and cavities are sealed by quartz, calcite and chlorite. Chlorite can be demonstrated texturally to have been precipitated first and generally coated fracture walls. Quartz coprecipitated with the chlorite where the wall rocks were quartzose. The precipitation of quartz is favoured by a decrease in either temperature or pressure or by a decrease in pH of the solution (Fournier, 1986).

The most likely causes of quartz precipitation in the veins and cavities are either fluid pressure fluctuations as a result of dilatancy or a decrease in temperature along the flow path. Parry and Bruhn (1986) have calculated that at a temperature of 300°C a pressure reduction of 1kb would result in a 14% reduction in quartz solubility. Because the fluid sources and regional fluid flow directions are not constrained it is difficult to assess whether fluid flow down a temperature gradient contributed to quartz deposition in the PPV culmination.

Calcite can be precipitated by a decrease in total pressure at constant m_{CO2}, by a decrease in m_{CO2} due to boiling, by an increase in temperature, by a decrease in fluid salinity or an increase in solution pH (Holland and Malinin, 1979). The large size of the calcite crystals suggests low nucleation rates and therefore low degrees of supersaturation. The switch from quartz to calcite deposition was accompanied by

dissolution of the quartz. This could be explained by a temperature increase. The inferred dilution of the saline Na-Ca-Cl brine with pure water could also have produced calcite deposition. Unfortunately no fluid inclusions suitable for analysis were found in the calcite so the this latter hypothesis could not be tested. CO_2 effervescence due to decompression seems unlikely because the fluids trapped in the quartz are only two phase liquid-vapour systems and appear to have low m_{CO2}

6.3.5. Introduction of meteoric water into the system.

A problem that remains to be explained is how downward percolating meteoric water (presumably at hydrostatic pressures) entered into and mixed with the lithostatically pressured fluid regime at the base of the GT sheet. Downward percolation of meteoric waters has been shown to contribute to large scale volume loss deformation in thrust sheets but only in the upper 1km of the crust (Engelder, 1984). Stable isotope studies (eg.Kerrich et al., 1984) however, reveal that incursion of meteoric waters into deeper levels of high angle faults and shear zones is a common phenomenon. Mixing of meteoric and metamorphic fluids has also been shown to have occurred near the brittle-ductile (B-D) transition in detachment zones of metamorphic core complexes (Kerrich and Hyndman, 1986; Reynolds and Lister, 1987).

Losh (1985) and more recently McCaig (1988) have proposed models to explain the downward flow of meteoric fluid into the ductile regime. Both models use the coupling between earthquakes and fluid overpressuring ie. the seismic pumping mechanism of Sibson et al.(1975). Losh (op.cit) considers that fluid is drawn down into the shear zones from a zone of high fluid pressure and reduced permeability coincident with the quartz brittle-ductile (B-D) transition. The zone of high fluid pressure resulted from self-sealing of the shear zone conduit by quartz precipitated from ascending and therefore cooling fluids. Because earthquakes nucleate within this zone of the crust then associated hydrofracturing will propagate into the ductile regime and seismically generated high P_f will be pumped downwards. McCaig (op.cit) considers that the phase difference between stress and dilatancy cycles across the B-D transition will cause fluid flow to be driven into the ductile regime. This arises because brittle deformation may 'overshoot' into the ductile regime where, because of lower permeabilities, rapid fracture propagation and dilatancy produce a fluid pressure differential between the overpressured fluid in the B-D zone and the fluid in the in the ductile regime. This pressure differential is considered to draw fluid down across the B-D transition.

Mixing of meteoric and formation of metamorphic waters near the brittle-ductile transition via some form of mass pumping associated directly with active faulting seems the most plausible means of explaining the presence of meteoric water incursion into lithostatically pressured domains. It is possible that faulting associated with the

observed extension in the GT sheet allowed small quantities of water to bleed into the thrust system. A similar model has been proposed by Burkhard and Kerrich (1988) to explain the incursion of fluids with meteoric oxygen isotopic signatures into the crystalline basement of the Helvetic nappes.

6.3.6. Summary.

The late stages of thrusting in the PPV culmination were associated with the presence of high fluid pressures. These were probably generated during distributed shortening within the structure coupled with the loading of the overlying thrust sheets. Slow fluid pressurization led to the development of fault-parallel cavities that were only slowly sealed. Pulsing of fluids occurred within the cavities possibly due to time- dependent fracturing in neighbouring parts of the fracture system. The resultant dilatancy acted as a pump that flushed fluids through the open cavities resulting in complete exchange and only limited mixing. This mechanism is a modification of the dilatancy pumping models of Etheridge et al. (1984) and Lister et al. (1986). The cavities remain open throughout successive cycles of the process. The model can explain the presence of primary inclusions of different fluid compositions in vein quartz, the presence of zoned chlorites in the cavities, and alteration haloes surrounding the cavities.

The mixing of a formation brine with pure water appears to have been responsible for variations in fluid compositions. This may have occurred outwith the confines of the system analysed (the PPV culmination) but the products were chanellised through the fault system. The pure water component possibly represents descending meteoric water introduced at depth into the regional thrust system during extension in the overlying Gavarnie Thrust sheet. The amount of dilution observed suggests however that this draw-down was small. Large scale fluid flow within the thrust system cannot be demonstrated to have operated from the results of this study.

6.3.7. Comparisons with other studies of fluid flow in thrust belts.

Studies of fluid flow in thrust belts have primarily focussed attention on the stable isotopic signatures of syntectonic vein material (Losh, 1985; Rye and Bradbury, 1988, Bradbury and Woodell, 1988 and Burkhard and Kerrich, 1988). These studies tend to show a change from closed to open system behaviour as deformation shifted from ductile to brittle and as fluid pressures diminished due to increased hydraulic conductivities. The scale of fluid transport is considered to have been of the order of kilometres and to have been channelled along fault zones. Bradbury and Woodell consider that individual thrust sheets behave as entirely separate hydrodynamic units. The isotope studies suggest that the fluid sources are primarily:

1. Low $\delta^{18}O$ formation brines expelled from sediments and basement by tectonic compaction.
2. High $\delta^{18}O$ metamorphic fluid derived from devolatilisation reactions beneath the thrust pile. In the case of the central Pyrenees, Losh (op.cit.) and Bradbury and Woodell (op.cit.) consider that metamorphic fluids were discharged via basement shear zones into fault systems in the overlying cover strata.
3. Low $\delta^{18}O$ meteoric surface water.

These studies have not considered the compositions of the fluid and have inferred fluid geochemistry from the observed isotopic exchange paths.

The present study has shown the fluids present during the faulting were high Ca-Na-Cl formation brines. Preliminary $\delta^{18}O$ data on quartz veins from the PPV (B.Spiro, written comm. 1988) give values of around +18 per mil. At 250-300 °C the fluid from which these veins precipitated must have had a composition of between +9 and +11 per mil (Matsuhisa et al., 1979). This figure compares favourably with that obtained by Bradbury and Rye (1988) (from the Pineta thrust complex) and by Losh (1985) (from shear zones in the the Neovielle massif). They suggest however that the fluid was derived from metamorphic dehydration of the basement or Triassic strata. The results of this study suggest that in the Cirque de Barroude the ambient fluid was not of metamorphic origin (Grant et al., in prep) but was mature formation water.

This highlights one major problem with stable isotope results, that fluids of greatly differing origin and geochemical histories can have similar isotopic signatures. In studying fluids in thrust systems the importance of fluid inclusion work must be emphasised when considering fluid origins.

6.4. Conclusions.

6.4.1. Fluid inclusion analysis.

1. Two fluids (referred to as fluids A and B) coexisted at the time of deformation. They appear to have been generated by slight mixing between a Na-Ca-Cl brine and meteoric water.
2. The inclusions of both fluids contain bitumen solids that suggest they were mature formation brines and not metamorphic fluids.
3. The trapping conditions were in the range 250-300°C and 1.5- 2Kbars pressure.
4. If microhydrofracturing was responsible for leakage of the inclusions, then the tensile strength of the inclusions may have had an upper bound of approximately 700 bars. Alternatively this figure could represent the maximum fluid pressure fluctuations that occurred during formation of the fault-parallel cavities.

6.4.2. Chlorite analyses.

A combined BSEM-microprobe study of chlorites from fault-related veins and cavities in the PPV culmination and from shear veins in the Hercynian basement within the GT fault zone has shown:

1. The chlorites in the PPVT sheet are compositionally zoned in terms of Fe and Mg. The zones occur as discrete micron-scale growth bands in the cavity-fill chlorites.
2. A gradient in Mg/Mg+Fe content of chlorites occurs in the sheared Hercynian basement adjacent to the GT. These chlorites also fall on an Al(vi) enriched trend when compared with the zoned chlorites in the Triassic shales and the Cretaceous limestone.
3. Syntectonic fluid-rock reaction with the limestone appears to have stripped Mg from the dolomite (dedolomitisation) and precipitated Al-poor, Mg-rich chlorites. In the Triassic red beds and Hercynian basement the chlorites that formed were Fe-rich. These differences suggest that host rock composition was the major control on the minor element chemistries of fluids A and B. 4. The host-rock control on the fluid chemistry suggests fluid- rock ratios were low (see chapter 5 for a further discussion).
5. The presence of Fe-Mg zoned chlorites appears to reflect the localised pulsing (advection) of fluid equilibrated with the limestone along high permeability fracture zones in the Triassic and basement strata.

6.4.3. Fluid processes.

1. Fluid flow appears to have been channelled along fault zones while the surrounding rocks remained generally impermeable.
2. The inferred pulsing of fluid within these zones probably occurred by dilatancy pumping associated with hydrofracture episodes.
3. Seismic pumping is unlikely to have operated because the faults slipped by an aseismic crack-seal process. It is more likely that high fluid pressures in the fault system resulted from inelastic porosity reduction (distributed strain) associated with the movement on the thrusts.
4. Cavities along faults probably remained open between fracture events with the fluids probably 'sealed in' at lithostatic pressure. This was facilitated by the low permeability of the wall rocks and rapid sealing of the feeding fractures.
5. The presence of a range of fluid compositions in the fault- related veins suggests that the reservoir that fed the fault system was heterogeneous. It may have comprised different fluid pockets isolated from each other and tapped during fracture episodes.
6. Rapid sealing of the fault zones after fracture episodes is considered to have prevented homogenisation of the fluid compositions in the fault system.

Chapter 7

Conclusions and Future work.

7.1. Introduction

This thesis studies the meso- and micro-scale deformation in thrust sheets from the Central Pyrenees. In addition the fluids involved in the thrusting and some of the fluid flow processes that operated have been assessed. The approach adopted has been to integrate detailed structural mapping with a microstructural and microchemical analysis of cleavage, fault rocks and vein phases. The results suggest that this type of integrated approach can be successful in understanding how faults interact with their host strata and how they influence fluid processes during deformation.

The study of fluid processes has used fluid inclusions to characterise the fluid compositions and provide an estimate of the deformation conditions, and has used the chemistry of vein phases to infer fluid flow pathways , characterise fluid-rock interactions, and assess the scale of fluid migration in the fault system. Structural mapping has enabled a sequence of deformation to be deduced in which the timing of fault movement and fluid flow can be placed and a microstructural study of cleavage development enables the attendant deformation mechanisms to be identified. The main conclusions associated with each of these lines of research are outlined below.

7.2. Regional structure of the Central Pyrenees (chapter 3).

1. The distribution of strata in the Gavarnie Thrust (GT) sheet and the presence of bedding cut-offs suggest that the major formation boundaries in the GT sheet are tectonic in origin. The deformation associated with these boundaries does not appear to have been incorporated into published models for the Gavarnie Thrust sheet and this brings into questions some of the conclusions reached by these models.
2. A phase of extension has occurred within the Gavarnie thrust sheet. The age of the extension is not well constrained but some of the normal faults appear to post date the emplacement of the thrust sheet.
3.The Mesozoic strata in the footwall of the Gavarnie Thrust were deformed during the emplacement of the thrust sheet. A strong slaty cleavage developed in the Triassic red beds while a mylonitic foliation developed in the overlying Upper Cretaceous limestone. Bedding parallel thrusts also developed in the Triassic strata and localised shortening and layer normal shear strains (wrench strains) in the strata appear to reflect differential

displacements on these thrusts.

4. The thin layer of Upper Cretaceous limestone along the base of the Gavarnie thrust sheet has been extensively duplicated by minor thrusts that branch onto the Gavarnie thrust. The estimated 11.5km displacement on the thrust for a section through the study area may be a significant overestimate when the displacement on the minor thrusts is taken into account.

5. The Gavarnie thrust is folded into a regional-scale culmination by later thrust-related deformation in the Hercynian basement. On the southern limb of the culmination the basement and Mesozoic strata are folded together into a train of symmetrical folds. The northwest curvature of the fold axes across the region suggests the folds are oblique tip-line folds associated with a blind imbricate stack of thrusts within the basement. It seems that in this part of the Central Pyrenees the Lower Thrusts of Munoz et. al. (1986) do not branch onto the Gavarnie Thrust and that the displacement on these thrusts increases towards the east.

7.3. The structure of the Pic de Port Vieux culmination (chapter 4).

The Pic de Port Vieux culmination is a 0.5km across culmination in the Gavarnie thrust produced by a number of thrust structures in the basement and Mesozoic cover. The culmination is located on the east flank of the Cirque de Barroude. The roof of the culmination is formed by the Pic de Port Vieux Thrust which thrusts a layer of Triassic red beds 0.85 Km over the upper Cretaceous limestone.and branches obliquely onto the overlying Gavarnie Thrust.

7.3.1. The deformation sequence in the culmination.

Four local phases of trusting (P1-P4) have been identified in the PPV culmination:

P1. Minor imbrication of the Mesozoic strata.

P2. Emplacement of the Gavarnie and Pic de Port Vieux Thrust sheets.

P3. Development of the culmination.

P4. Oblique reactivation of some of the earlier thrusts.

The sequence P1-P3 is foreland propagating. P4 is an out-of-sequence event related to SE directed distributed shearing along the base of the Gavarnie Thrust sheet. The Gavarnie Thrust breaches the P1 thrusts.

7.3.2. Deformation in the Pic de Port Vieux Thrust sheet.

1. The progressive deformation of the PPVT sheet changed from distributed shearing (cleavage development) to deformation that involved mesoscopic fault arrays .
2. Three different fault arrays are present in the PPVT sheet. The first faults that formed are bedding-parallel slip surfaces surfaces and localised within siltstone and mudstone beds. These were followed first by a set of high angle top-to-north normal faults and then a set of low angle top-to-south normal faults. Both these later fault sets accommodated transport subparallel extension of the thrust sheet.
3. The high angle faults formed while the thrust sheet was being emplaced, the low angle faults record a later extension of the the sheet after the PPVT (*sensu stricto*) had ceased movement.The later extension of the thrust sheet detached along a shear zone within the Cretaceous limestone in the footwall of the thrust.
4. Both the high angle and low angle faults developed as isolated discontinuities within the thrust sheet and branched onto rather than off of the thrust during their propagation.
5. The change in the type of extensional fault appears related to a 30 degree clockwise rotation in the orientation of the σ_1 stress with respect to the fault. σ_1 was approximately perpendicular to the thrust during or after movement on the high angle faults and changed to oblique to the thrust during movement on the low angle faults. This rotation is recorded by successive high angle vein arrays in the thrust sheet. Most of the extension was accommodated on the low angle faults.
6. The intrablock deformation in the fault array is accommodated by the development of extension veins and both reverse (back-shear) and extensional shear zones. The back-shear zone possess similar orientations to, and both cut and are cross cut by, the extensional shear zones. They record localised shortening strains that developed within the fault blocks.
7.The low angle faults appear to have operated in a domino fashion with bedding rotated clockwise in the fault blocks.
8. The 30 degree rotation of the $\sigma 1$ stress relative to the PPVT was not related to movement of the thrust sheet over a ramp. It is interpreted as a result in the change in the dynamics of the overlying thrust wedge as initial loading was superseded by spreading in the Gavarnie Thrust sheet.
9. The spreading in the Gavarnie Thrust sheet is modeled as a response to the changing geometry of the South Pyrenean thrust belt associated with underplating of the lower thrust sheets. In this respect the belt is interpreted as a dynamic orogenic wedge.

7.3.3. Deformation within the Pic de Port Vieux culmination.

1. The culmination formed as a result of two structures: a duplex within the Cretaceous limestone and a leading imbricate stack of thrusts in the Hercynian basement.
2. Cleavage-fault relations suggest that the duplex formed before the basement imbricate stack but was reactivated during movement on the lower structure.
3. The basement imbricate stack is an oblique tip structure and the cleavage, folds axes and fault movement directions are rotated up to 45 degrees clockwise of the regional N-S movement direction. This supports the pole of rotation model for oblique slip at lateral faults tips as proposed by Coward (1984).
4. Distributed shortening in the Triassic strata above the BIS intensified cleavage. The main effect of this deformation was to locally reactivate earlier thrusts within the tip zone. This occurred by the development of localised upper strain detachments.
5. The main upper strain detachment in the culmination occurred along the PPVT. The reactivation was restricted to the back-limbs of folds in the thrust and produced new faults that cut across the fold crests. This type of fault is called a back-limb splay.
6. The upper strain detachment on some of the faults operated intermittently and when they were not moving the faults were folded.
7. The development of an upper strain detachment produced faults that moved diachronously in the fault array. Displacement transfer occurred between the faults by the detachment of the associated distributed strain As a result the sequence of movement of secondary thrusts in the culmination does not agree with simple foreland or hinterland propagation models and many faults appear locally out-of-sequence although on the scale of the whole structure they can be treated as in-sequence.
8. If the assumption is made that all the faults link to a basal decollement, then the shortening estimate in the culmination will be greatly overestimated . In general, it can be envisaged that in areas where faulting competes with distributed strain to produce shortening, restoration of the fault displacements may lead to significant errors if the possibility of strain detachments and discontinuous faults is not taken into account.

7.3.4. Secondary fault arrays in the culmination.

1. Secondary fault arrays developed within the PPVT sheet and within a fault zone along the Triassic unconformity. All the the faults are shear-fibre coated movement planes.
2.The faults slipped by a crack-seal stick-slip mechanism.
3. The complexity of the fault patterns appears to have resulted from the simultaneous propagation and interaction of a large number of faults.
4. The larger faults appear to have developed by the linking together of smaller originally

discontinuous faults and show the greatest displacements. Localisation of displacement did not occur by a change in slip mechanism.
5. The faults tip by splaying, by the development of feather vein arrays or into shear zones (en echelon sigmoidal vein arrays). Where splaying occurs it is often a result of the interaction of the propagating fault with a pre-existing or simultaneously propagating fault.

7.4. Microstructures associated with thrusting in Cirque de Barroude (chapter 5).

Microstructures have been studied in selected rocks using optical microscopy, back-scattered electron microscopy and transmission electron microscopy. Two main localities were studied: the PPV culmination and a 20m wide fault zone within the basement adjacent to the Gavarnie thrust. The former has enabled the study of cleavages in the Triassic and Cretaceous strata, the latter of thrust-related fabrics in the basement. Together they allow a comparison of the deformation mechanisms that operated in the different lithologies and how these influenced the observed mesoscopic deformation.The main conclusions reached are outlined below.

7.4.1 Deformation in the Triassic and Cretaceous strata of Pic de Port Vieux

1. The cleavage in the Triassic strata formed by a combination of kinking and localised pressure solution of phyllosilicate grains, and extensive pressure solution of quartz grains. Recrystallisation of the matrix phyllosilicate grains occurred within the cleavage lamellae and along kink-band boundaries.
2. Pressure solution was a more active deformation mechanism in both the Triassic shales and Cretaceous limestone during the development of the culmination than during the deformation associated with the emplacement of the Gavarnie Thrust sheet and suggests that pressure solution is more important in coaxial rather than noncoaxial strain histories.
3. The shear zone in the Cretaceous limestone in the footwall of the PPVT appears to have developed by a combination of crystal plasticity and grain boundary sliding.in the fine grained calcite. The former process is more readily apparent in coarser grained calcite veins deformed within the shear zone. Similar deformation mechanisms may have operated during the later cleavage development in the limestone in the culmination.and were in addition augmented by pressure solution.
4. Competency switching appears to have occurred between the limestone and the Triassic shales during the deformation with the limestone less competent during shearing associated with emplacement of the Gavarnie and Pic de Port Vieux thrusts and more

competent during shortening associated with the culmination development. This behaviour may have been related to the kinematics of the deformation and the fine grain size of the limestone. In shear the limestone probably geometrically softened relative to the shales, whereas when shortened, a Hall-Petch relationship combined with geometrical hardening is considered to have increased the competency of the limestone relative to the Triassic shales.

7.4.2. Deformation in the Gavarnie Thrust fault zone.

1. The basement strata appear to have suffered advanced argillic alteration prior to thrust related deformation.This alteration may have been a late post-kinematic Hercynian event.
2. A phyllonitic fabric developed in the altered strata adjacent to the Gavarnie Thrust. This fabric appears to have developed by a combination of kinking, migration of kink band boundaries and recrystallisation of phyllosilicate grains within the altered rock. Relict quartz grains in the altered strata deformed by fracturing and grain rotation and did not deform ductiley.
3. The ductile fabric in the fault zone is overprinted by an array of shear fractures that cut through the mica matrix of the altered strata leaving the quartz grains relatively undeformed. The fractures possess a continuum of scales and anastomose to produce a penetrative shear fabric.
4. In three dimensions the slip surfaces define polyhedra that enclose the resistant quartz grains. The dilation associated with movement of these fractures may have been related to the fact that the number of slip surface orientations that formed did not satisfy the Von Mises criterion.
5. The finite strain state within the fault zone appears best approximated by a combination of simple shear and flattening. This agrees with the extensional strains inferred in the Gavarnie Thrust sheet from the mesostructures in the PPV culmination (chapter 4).
6. The shear fracture system in the altered basement was fed by two fluids during the deformation. One fluid appears to have been in equilibrium with the altered basement strata, the other was external in origin. This latter fluid produced Mg metasomatism in the basement adjacent to the thrust and accounts for changes in fracture fill chemistry across the fault zone. This fluid appears to have been sourced from a thin layer of Cretaceous mylonitic limestone that occurs along the thrust plane. The strong host rock control on fluid compositions suggests that fluid:rock ratios were small and that major fluid flow was not channelled along the fault zone during the thrusting.

7.5 Fluids and thrusting (chapter 6).

The role of fluids in faulting has been studied primarily by microthermometric analyses of fluid inclusions hosted in cavity fill quartz and by microprobe analyses of chlorites in the same cavities and in the adjacent wall rocks.The former characterises the bulk fluid compositions, the latter allows some inferences to be made regarding the minor element chemistries in the fluid and regarding he fluid flow and fluid-rock reactions in the thrust sheet.

7.5.1. Fluid inclusion analyses.

1. Two fluids (referred to as fluids A and B) coexisted in the thrust system at the time of the deformation. They appear to have been generated by slight mixing between a highly saline Na-Ca-Cl brine and meteoric water.
2. The inclusions of both fluids contain bitumen solids that suggest they were mature formation brines and not metamorphic fluids. The fluids must have migrated into the basement and Triassic red beds but the timing of this migration is not known. The fact that large-scale fluid migration is not documented from the fault zones and the fluids appear to be locally equilibrated may suggest that the formation brine migrated into the strata before the thrusting.
3. The trapping conditions (conditions of deformation) were in the range 250-300 °C and 1.5- 2Kbars pressure.
4. Primary inclusions in any one sample contain a range of fluid densities. These correspond to a maximum pressure difference of 700 bars. If microhydrofracturing was responsible for the range of fluid densities then the tensile strength of the inclusions may have had an upper bound of approximately 700 bars. Alternatively this figure could represent the maximum fluid pressure fluctuations that occurred during formation of the fault-parallel cavities.

7.5.2. Chlorite analyses.

A combined BSEM-microprobe study of chlorites from fault-related veins and cavities in the PPV culmination and from shear veins in the Hercynian basement within the GT fault zone has been made. The results show:
1. The chlorites in the PPVT sheet are compositionally zoned in terms of Fe and Mg. The zones occur as discrete micron-scale growth bands in the cavity-fill chlorites.and in chlorites in alteration haloes around the cavities.
2. A gradient in Mg/Mg+Fe content of chlorites occurs in the sheared Hercynian

basement adjacent to the GT. The Mg content of the chlorites increases towards the thrust. These chlorites also fall on an enriched Al(vi) (octahedrally coordinated) trend when compared with the zoned chlorites in the Triassic shales and the Cretaceous limestone. This reflects the host-rock composition.

3. Syntectonic fluid-rock reaction with the limestone appears to have stripped Mg from the dolomite (dedolomitisation) and precipitated Al-poor, Mg-rich chlorites. In the Triassic red beds and Hercynian basement the chlorites that formed were Fe-rich. These differences suggest that host rock composition was the major control on the minor element chemistries of fluids A and B.

4. The host-rock control on the fluid chemistry suggests fluid- rock ratios were low .

5. The presence of Fe-Mg zoned chlorites appears to reflect the localised pulsing (advection) of fluid equilibrated with the limestone along high permeability fracture zones in the Triassic and basement strata.

7.5.3. Fluid processes.

1. Fluid flow appears to have been channelled along fault zones while the surrounding rocks remained generally impermeable.

2. The inferred pulsing of fluid within these zones probably occurred by dilatancy pumping associated with hydrofracture episodes.

3. Seismic pumping is unlikely to have operated because the faults slipped by an aseismic crack-seal process. It is more likely that high fluid pressures in the fault system resulted from inelastic porosity reduction (distributed strain) associated with the movement and displacement gradients on the thrusts.

4. Cavities along faults probably remained open between fracture events with the fluids 'sealed in' at lithostatic pressures. This was facilitated by the low permeability of the wall rocks and rapid sealing of the feeding fractures.

5. The presence of a range of fluid salinities in the fault- related veins suggests that the reservoir that fed the fault system was heterogeneous. It may have comprised pockets of different fluids isolated from each other and periodically tapped during fracture episodes.

6. Rapid sealing of the fault zones after fracture episodes is considered to have prevented homogenisation of the fluid compositions in the fault system.

7.Meteoric water is inferred to have entered the system to generate the different fluid salinities. This may have occurred as a result of active extension within the overlying Gavarnie Thrust sheet.during the thrusting.

7.6 Suggestion for future work.

A number of interesting problems have been unearthed during this work that are still in need of further research.

7.6.1 Field structures.

1. Mapping and photogeological interpretation of the Gavarnie thrust sheet indicates that a phase of extension occurred within the thrust sheet. Further mapping is required to place the normal faults that developed in the deformation sequence of the thrust sheet and to see if these are possibly of the same age as the extension observed in the PPVT sheet.
2. Further work is also required to assess the areal extent of the inferred spreading in the Gavarnie thrust sheet and its time relations with the regional culmination. This could be done by studying in more detail the strain associated with and the areal extent of the late-stage shear band arrays in the Silurian graphitic phyllite in the hanging wall of the thrust. The shear bands appear to have operated similar to domino faulting and are possibly related to the extension rather than the emplacement of the GT sheet.
3. A more detailed study is required to asses the origin and nature of the major formation boundaries in the Gavarnie thrust sheet and to see if they can be placed as Alpine or Hercynian features.
4. Apart from the extension that appears syntectonic with the thrusting, a later phase of E-W extension has occurred in the region. This is responsible for the late normal fault that cuts the PPVT on the NE flank of Pic de Port Vieux. A number of other similarly orientated faults cut the GT in the study area and also cut the thrust in the Cirque de Troumouse and around Punta Suelza.further east This extension may be related to the arching of the regional culmination or it may be a later phenomenon. It does not appear in tectonic models of the belt and is in need of further research.

7.6.2 Microstructural work.

1. A petrofabric study of the fine grained Cretaceous limestone is required to properly assess the deformation mechanism that contributed to the observed competancy switching between the limestone and Triassic shales. Because of the fine grain size of the limestone this would probably require X-ray goniometry.
2. A strain gradient occurs across the PPV culmination. The preliminary microstructural work completed here suggests that this gradient is accommodated largely by an increase in pressure solution deformation.within the culmination relative to outside it. A

more detailed TEM study of the cleavages in the Triassic shales and Cretaceous limestone would help to assess the role of pressure solution in generating the fabric intensity gradient and how this relates to the deformation kinematics.

7.6.3 Fluid geochemistry.

1. The fluid inclusion study completed here is based on six samples. To gain a better understanding of the fluid compositions and compositional variations within the culmination it would be desirable to expand the sample population.This could also include studying inclusions in quartz from the different generations of veins to see if the fluid compositions changed during the progressive deformation sequence.
2.The fluid inclusion study could also be expanded to other parts of the Gavarnie thrust sheet and its footwall strata. This would perhaps enable an assessment of any regional variations in fluid composition and of fluid flow pathways. It would also provide a larger database for understanding the fluid mixing observed in the samples already studied.
3. It has been inferred from thrust related vein mineral assemblages that fluid-rock ratios were low and that fluid migration only occurred on a small scale (between neighbouring beds) during faulting. This could be confirmed or refuted by studying the radiogenic (Sr, Pb) and stable isotopes (O and C) of the fluids and of the wall rocks. If the fluid has similar isotopic signatures to the host rocks in the culmination then it would suggest that the fluid had equilibrated isotopically with the host rock and was probably locally derived. The Sr and Pb signatures of the fluid would also characterise whether it came from the basement , the Triassic , or the Cretaceous strata. This would help to map out fluid flow pathways similar to the use of chlorites in this study. Oxygen and carbon isotopes of the vein material would also serve to reveal the importance of the meteoric fluid in the system because it should have a distinct isotopically light signature.
4. The presence of quartz-hematite veins along some of the faults means that it might be possible to use quartz-hematite oxygen isotope thermometry to obtain a more accurate estimate of the trapping temperatures in the veins. This would help constrain the deformation conditions more accurately than present.

REFERENCES

BALLY, A.W., GORDY, P.L. and STEWART, G.A., 166. Structure, seismic data, and orogenic evolution of Southern Canadian Rocky Mountains. Bull. Can Pet. Geo. 14, p. 337-381.

BANDA, E. and WICKHAM, S.M., 1986. The geological evolution of the Pyrenees - an introduction. Tectonophysics 129, p.1-8.

BATES, M.P., 1987. Palaeomagnetic studies of fold and thrust geolmetry in the Southern Pyrenees. Ph. D. Thesis. Leeds University. p.475.

BEACH, A. and JACK, S., 1982. Syntectonic vein development in a thrust sheet from the external French Alps. Tectonophysics 81, p. 67-84.

BERGER, P. and JOHNSON, A.M., 1982. Folding of passive layers and forms of minor structures near terminations of blind thrust faults - application to the central Appalachian blind thrust. J. Struct. Geol. 4, p. 343-353.

BODNAR, R.J., REYNOLDS, T.J. and KUEHN, C.A., 1985. Fluid systematics in epithermal systems. In: B.R.Berger and P.M.Bethke (eds.), Geology and geochemistry of epithermal systems. Revs. in Economic Geology 2, chpt. 5, p. 73-97.

BOILLOT, G., 1984. Some remarks on the continental margins in the Aquitaine and French Pyrenees. Geol. Mag. 121, p.407-412.

BOILLOT, G., 1986. Comparison between the Galacia and Aquitaine margins. In: E. Banda and S.M. Wickham (Editors), The Geological Evolution of the Pyrenees. Tectonophysics 129, p. 243-255.

BORRADAILE, G.J., BAYLY, M.B. and POWELL, C.McA., 1982. Atlas of deformational and metamorphic rock fabrics. Springer-Verlag.

BOTTRELL, S.H., YARDLEY,B. and BUCKLEY, F. 1988. A modified crush-leach method for the analysis of fluid inclusion electrolytes. Bull. Mineral. 111, p. 279-296.

BOYER,S.E. and ELLIOTT, D., 1982. Thrust systems. A.A.P.G. Bull. 66, p.1196-1230.

BRACE, W.F., 1980. Permeability of crystalline and argillaceous rocks. Int. J. Rock Mech. Min. Sci. 17, p. 241-251.

BRADBURY, H.J. and WOODWELL, G.R., 1987. Ancient fluid flow within foreland terrains. In Goff, J.C. and Williams, B.P.J. (eds.) Fluid flow in sedimentary basins and aquifers. Geol. Soc. Spec. Publ. 34, p. 87-102.

BURKHARD, M. and KERRICH,R., 1988. Fluid regimes in the deformation of the Helvetic nappes, Switzerland, as inferred from stable isotope data. Contrib. Mineral. Petrol. 99, p. 416-429.

BURRUS, R.C. and HOLLISTER, L.S., 1979. Evidence from from fluid inclusions for a palaeogeological gradient at the geothermal test site, Los Alamos, New Mexico. J. Volc. Geotherm. Res. 5, p. 163-177.

BUTLER, R.W.H., 1982. Hangingwall strain: a function of duplex shape and footwall topography. Tectonophysics 88, p. 235-246.

BUTLER, R.W.H., 1982. The terminology of structures in thrust belts. J.Struct. Geol. 4, p. 239-245.

BUTLER, R.W.H., 1987. Thrust sequences. J. Geol. Soc. Lond. 144, p. 619-634.

CARPENTER, A.B., TROUT, M.L. and PICKETT, E.E., 1974. Preliminary report on the origin and chemical evolution of lead and zinc rich oil field brines in Central Mississippi. Econ. Geol. 69, p. 1191-1206.

CELLO, G. and NUR, A., 1988. Emplacement of foreland thrust systems. Tectonics 7, p. 261-271.

CHAPPLE, W.M., 1978. The mechanics of thin-skinned fold-and-thrust belts. G. Soc. Am. Bull. 89, p. 1189-1198.

CHOUKROUNE, P. and SEGURET, M., 1973. Tectonics of the Pyrenees: role of compression and gravity. In: Gravity and Tectonics, Ed. K.H. DeJong and R. Schotten, Wiley.

COBBOLD, P.R., 1977. Description and origin of banded deformation structures. I I.Rheology and the growth of banded perturbations. Can. J. E. Sci. 14, p. 2510-2523.

COLLINS, A.G., 1975. Geochemistry of oil field waters. Elsevier, 485p.

COWARD, M.P. 1982. Surge zones in the Moine Thrust zone of North West Scotland. J. Struct. Geol. 4, p. 247-256.

COWARD, M.P., 1984. The strain and textural history of thin-skinned tectonic zones: examples from the Assynt region of the Moine Thrust zone, North West Scotland. J.Struct. Geol. 6, P. 89-99.

COWARD, M.P. and KIM, J.H., 1981. Strain within thrust sheets. In: Thrust and Nappe Tectonics, (eds) , Geol. Soc. Lond. Spec. Publ. 9, p. 275-292.

COWARD, M.P. and POTTS,G.J., 1983. Complex strain patterns developed at the frontal and lateral tips to shear zones and thrust zones. J. Struct. Geol. 5, p.383-399.

COX, S.F. and ETHERIDGE, M.A., 1983. Crack-seal fibre growth mechanisms and their significance in the development of oriented layer silicate microstructures. Tectonophysics 92, p.147-170.

CRAWFORD, M.L., 1981. Phase equilibria in aqueous fluid inclusions. In:Hollister, L.S. and Crawford, M.L. (eds), Short course in fluid inclusions - applications to petrology. Min. Assoc. Canada, Calgary, Alberta. p.75-97.

CRAWFORD, M.L., FILER, J. and WOOD, C., 1979. Saline fluid inclusions associated with retrograde metamorphism. Bull. Mineral. 102, p. 562-569.

CRAWFORD, M.L., KRAUS,D.W. and HOLLISTER, L.S.,1979. Petrologic and fluid inclusion study of calc-silicate rocks, Prince Rupert, British Colombia. Am. J. Sci. 279. 1135-1159.

CURNELLE, R., DUBOIS, P. AND SEGUIN, J.C., 1982. The Mesozoic- Tertiary evolution of the Aquitaine Basin. Phil. Trans R. Soc. Lond. A305, P.63-84.

CURTIS,C.D., HUGHES, C.R., WHITEMAN, J.A. and WHITTLE, C.K., 1985. Compositional variation within some sedimentary chlorites and some comments on their origin. Min. Mag. 49, p. 375-386.

DAHLSTROM, C.D.A., 1969. Balanced cross sections. Can. J. Earth Sci. 6, p. 743-757.

DAHLSTROM, C.D.A, 1970. Structural geology in the eastern margin of the Canadian Rocky Mountains. Bull. Can. Petr. Geol. 18, p.332-406.

DAVIS, D., SUPPE, J. and DAHLEN, F.A., 1983. Mechanics of fold and thrust belts and accretionary wedges. J. Geophys. Res.. 88, p. 1153-1172.

DERAMOND, J., 1979. Deformation et desplacement des nappes: Exemple de la Nappe de Gavarnie (Pyrenees Centrales). These Sc. Toulouse, 409p.

DERAMOND, J., JOSEPH, J., MAJESTE-MENJOULAS, C. and MIROUSE, R., 1980. Géometrie des déformations dans une Nappe Complexe: La Nappe de Gavarnie (Pyrénées centrales, France.) Geol. Rund. 69, p. 659-677.

DERAMOND, J., DEBAT, P. and LAMOUROUX, C., 1981. Desplacement de la Nappe de Gavarnie: Glissement sur les discontinuites et deformations continues. Revue de Geologie Dynamique et de Geographic Physique 23, p. 211-224.

DERAMOND, J., GRAHAM, R.H., HOSSACK, J.R. BABY, P. and CROUZET, G., 1985. Nouveau modèle de la chaine des Pyrenees. C.R. Acad. Sci. Paris, Ser. 2, p.

DURNEY, D.W. and RAMSAY J.G., 1973. Incremental strains measured by syntectonic crystal growths. In: DeJong, K.A. and Scholten, R. (eds.). Gravity and Tectonics. Wiley-Interscience, New York. p. 67-96.

DYER, R. 1988, Using joint interactions to estimate palaeostress ratios. J. Struct. Geol. 10, p. 685-700.

ECORS, 1988. the ECORS deep reflection seismic survey across the Pyrenees. Nature 333, p.508-511.

EISENSTADT, G. and DE POAR, D.G., 1987. Alternative model of thrust- fault propagation. Geology 15, p. 630-633.

ELLIOTT, D., 1976. The motion of thrust sheets. J. Geophys. Res.. 81, p. 949-963.

ELLIOTT, D., 1976.The energy balance and deformation mechanisms of thrust sheets. Phil. Trans. R. Soc. Lond. A283, p. 289-312.

ELLIOTT, D. and JOHNSON, M.W.R., 1980. The structural evolution of the northern part of the Moine Thrust Zone. Trans. R. Soc. Edinb. 71, p. 69-966.

ELLIS, M.A. and DUNLAP, W.J., 1988. Displacement variation along thrust faults: implications for the development of large faults. J. Struct. Geol. 10, p. 183-192.

ENGELDER, T., 1984. The role of pore water circulation during the deformation of foreland fold and thrust belts. J. Geophys. Res.. 89, p.4319-4325.

ENGESER, T. and SCHWENTKE, W., 1986. Towards a new concept of the tectogenesis of the Pyrenees. In: E. Banda and S.M. Wickham (Editors), The Geological Evolution of the Pyrenees. Tectonophysics 129, p. 233-242.

ETHERIDGE, M.A. and HOBBS,B.E.,1974. Chemical and deformational controls on recrystallisation of mica. Contrib. Min. Petrol. 43, p.111-124.

ETHERIDGE, M.A., WALL, V.J. and COX, S.F., 1984. High fluid pressures during regional metamorphism and deformation: implications for mass transport and deformation mechanisms. J.G. R. B6, p.4344-4358.

FARRELL, S.G., WILLIAMS, G.D., and ATKINSON, C.D., 1987. Constraints on the age of movement of the Montsech and Cotiella Thrusts, south central Pyrenees, Spain. J. Geol. Soc. Lond. 144, p.907-914.

FISCHER, M.W., 1984. Thrust tectonics in the North Pyrenees. J. Struct. Geol. 6, p.721-726.

FONTBOTE, J.M., MUNOZ, J.A, and SANTANACH, P., 1986. On the consistency of proposed models for the Pyrenees with the structure of the eastern part of the belt. In: E. Banda and S.M. Wickham (Editors), The Geological Evolution of the Pyrenees. Tectonophysics 129, p. 291-302.

FOSTER, M.D., 1962. Interpretation of the composition and a classification of the chlorites. U.S. Geol. Surv.Prof. Paper 414-A, 33p.

FOURNIER, R.O., 1985. Carbonate transport and deposition in the epithermal environment. In: B.R.Berger and P.M.Bethke (eds.), Geology and geochemistry of epithermal systems. Revs. in Economic Geology 2, chpt. 4, p. 63-72.

FOURNIER, R.O., 1985. The behaviour of silica in hydrothermal systems. In: B.R.Berger and P.M.Bethke (eds.), Geology and geochemistry of epithermal systems. Revs. in Economic Geology 2, chpt. 3, p. 45-61.

FRAPE, S.K., FRITZ, P. and MCNUTT, 1984. Water-rock interaction and chemistry of groundwaters from the Canadian shield. Geochim. Cosmochim. Acta 48, p. 1617-1627.

FYFE, W.S. and KERRICH, R., 1985. Fluids and thrusting. Chemical Geology 49, p. 353-362.

GANDHI, C. and ASHBY, M.F., 1979. Fracture mechanism maps for materials which cleave: F.C.C., B.C.C. and H.C.P. metals and ceramics. Acta. Metallurgica 27, p. 1565-1602.

GAPAIS, D., BALE, P., CHOUKROUNE, P., COBBOLD, P.R., MAHJOUB, Y.and MARQUER, D., 1987. Bulk kinematics from shear zone patterns, some field examples. J. Struct. Geol. 9, p. 635-646.

GARDNER,D.A.C. and SPANG, J.H., 1973. Model studies of the displacement transfer associated with overthrust faulting. Bull. Can. Petrol. Geol. 21, p.534-552.

GAVILGLIO,P., 1986. Crack-seal mechanism in a limestone: a factor of deformation in strike -slip faulting. Tectonophysics 131, p.247-255.

GOLDSTEIN, A.G.,1988. Factors affecting the kinematic interpretation of assymetric boudinage in shear zones. J. Struct Geol. 10, p. 707-716.

GRANIER, T., 1985. Origin, damping and pattern of development of faults in granite. Tectonics 4, p. 721-737.

GRANT, N.T., BANKS, D.A., MCCAIG, A.M. and YARDLEY, B.W.D., 1988 The chemistry, source and behaviour of fluids involved in Alpine thrusting of the Central Pyrenees. Submitted to J. Geophys. Res.

GRETENER, P.E., 1972. Thoughts on overthrust faulting in a layered sequence. Bull. Can Pet. Geol. 20, p. 583-607.

GRETENER, P.E., 1981. Pore pressure, discontinuities, isostacy and overthrusts. In: Thrust and Nappe Tectonics, (eds) , Geol. Soc. Lond. Spec. Publ. 9, p. 33-39.

GRIMAUD, S., BOILLOT, G., COLETTE, B., MANFRET, A., MIKS, P.R. and ROBERTS, D.B., 1982. Western extension of the Iberian- European plate boundary during the Early Cenozoic (Pyrenean) convergence: a new model. Marine Geology 45, p.63-77.

HELGESON, H.C. and LICHTENER, P.C., 1987. Fluid flow and mineral reactions at high temperatures and pressures. J. Geol. Soc. Lond. 144, p. 313-326.

HEMLEY, J.J., MONTOYA, J.W., MARINENKO, J.W. and LUCE, R.W., 1980. Equilibria in the system Al2O3-SiO2-H2O and some general implications for alteration/ mineralization processes. Econ. Geol. 75. p. 210-228.

HOBBS, B.E., MEANS,W.D., and WILLIAMS, P.F., 1982. The relationship between foliation and strain: an experimental investigation. J. Struct. Geol. 4, p. 411-428.

HOLLAND,H.D. and MALININ, S.D., 1979. The solubility and occurrence of ore minerals. In: H. Barnes, (ed.), Geochemistry of hydrothermal ore deposits. Wiley, p.461-508.

HOSSACK, J.R., 1979. The use of balanced cross section in calculation of orogenic contraction : a review. J. Geol. Soc. Lond. 136, p. 705-711.

HUBBERT, M.K. and RUBEY, W.W., 1959. Role of fluid pressure in mechanics of overthrust faulting. Geol. Soc. Am. Bull. 70, p. 115-205.

JOSEPH, J., 1972. Le paleozoique de la Nappe de Gavarnie entre le cirque de Troumouse et le Gave de Pau. These 3° cycle, Toulouse, 143p.

KERRICH, R., 1986. Fluid infiltration into fault zones: chemical, isotopic and mechanical effects. Pageoph. 124, p. 225-268.

KERRICH, R., 1986. Fluid transport in lineaments. Phil. Trans. R.Soc. Lond. A317, p.219-251.

KERRICH, R., LA TOUR, T.E. and WILLMORE, L., 1984. Fluid participation in deep fault zones: evidence from geological, geochemical and $^{18}O/^{16}O$ relations. J. Geophys. Res.. 89, p.4331-4343.

KERRICH, R. and HYNDMAN, D., 1986. Thermal and fluid regimes in the Bitterroot lobe-Sapphire block detachment zone, Montana: Evidence from 18O/16O and geologic relations. Geol. Soc. Am. Bull. 97, p. 147-155.

KILSDONK, B. and WILTSCHKO, D.V, 1988. Deformation mechanisms in the southeastern ramp region of the Pine Mountain block, Tennessee. G.S.A.Bull. 100, p. 653-664.

KNIPE, R.J., 1981. The interaction of deformation and metamorphism in slates. In: G.S. Lister, H.J. Behr, K.Weber and H.J. Zwart (eds.), The effect of deformation on rocks. Tectonophysics 78, p.249-272.

KNIPE, R.J., 1985. Footwall geometry and the rheology of thrust sheets. J. Struct. Geol. 7, p.1-10.

KNIPE, R.J. and WHITE, S.H., 1977. Microstructural variation of an axial plane cleavage around a fold: A H.V.E.M. study. Tectonophysics 39, p. 355-380.

KRANIDIOTIS, P. and MACLEAN, W.H., 1987. Systematics of alteration at the Phelps Dodge massive sulphide deposit, Matagami, Quebec. Econ. Geol. 82, p. 1895-1911.

LABAUME, P., SEGURET, M. and SEYVE, C., 1985. Evolution of a turbiditic foreland basin and analogy with an accretionary prism: example of the Eocene South- Pyrenean Basin. Tectonics 4, p.661-685.

LAW, R.D., 1987. Heterogeneous deformation and quartz crystallographic fabric transitions: natural examples from the Moine Thrust Zone at the Stack of Glencoul, northern Assynt. J. Struct. Geol. 9, p. 819-934.

LAW, R.D., KNIPE, R.J. and DAYAN, H., 1984. Strain path partitioning within thrust sheets: microstructural and petrofabric evidence from the Moine Thrust Zone at Loch Eriboll, North-west Scotland. J. Struct. Geol. 6, p. 477-497.

LEE, J.H., PEACOR, D.R., LEWIS, D.D. and WINTACH, R.P., 1984. chlorite-illite/ muscovite interlayered and interstratified crystals: a TEM/STEM study. Contrib. Min. Petrol. 88, p.372-385.

LEE, J.H., AHN, J.H., and PEACOR, D.R., 1985. Textures in layered silicates: progressive changes through diagenesis and low-temperature metamorphism. J. Sed. Petrology 55, p.532-540.

LISTER, G.S. and SNOKE, A.W., 1984. S-C mylonites. J. Struct. Geol. 6, p.617-638.

LISTER, G.S. and WILLIAMS, P.F., 1983. The partitioning of deformation in flowing rock masses. Tectonophysics 92, 1-33.

LISTER, G.S., BOLAND, J.N. and ZWART, H.J., 1986. Step-wise growth of biotite porphyroblasts in pelitic schists of the western Lys-Coillaouas massif (Pyrenees). J. Struct. Geol. 8, p. 543-562.

LLOYD, G.E., 1987. Atomic number and crystallographic contrast images with the SEM: a review of backscattered electron techniques. Min. Mag. 51, p. 3-19.

LLOYD, G.E., FERGUSON, C.C. and RENDING, K., 1982. A stress-transfer model for the development of extension fracture boudinage. J. Struct. Geol. 4, p. 355-372.

LOGAN, J.M., FRIEDMAN, M., HIGGS, N.G., DENGO, C. and SHIMAMOTO, T., 1979. Experimental studies of simulated gouge and their application to studies of natural fault gouse. In: Analysis of actual fault zones in bedrock. Speed, R.C. and Sharp, R.V. (eds.) U.S. geol. surv. Open-file Report. 79-1239. p. 276-304.

LOSH, S., 1985. Fluid migration and interaction in brittle-ductile shear zones, Central Pyrenees, France. Unpubl. Ph.D. thesis, Yale University.

LUCAS, C., 1985. Le Gres Rouge de versant nord des Pyrenees. Essai sur la geodynamique de depots continentaux du Permian et du Trias. Ph.D. Toulouse, 265p.

MAJESTE-MENJOULAS, C., 1979. Evolution d'un segment de chaine varique: le Palaeozoique de la nappe de Gavarnie et le chevauchement de Cinq-Monts-Gentiane. These Sc. Toulouse, 331 p.

MANDL, G. and SHIPPAM, G.K., 1981. Mechanical model of thrust sheet gliding and imbrication. In: Thrust and Nappe Tectonics, (eds) , Geol. Soc. Lond. Spec. Publ. 9, p. 79-98.

MARTINEZ, A., 1968. Etude structurale de la region de la Cinqueta- substratum de la Nappe de Gavarnie (Pyrenees, Espagne). These 3° cycle, Montpelier, 107p.

MATTAUER, M., 1985. Presentation d'un modele lithospherique de la chaine des Pyrenees. C.R. Acad. Sci. Paris 300, Ser. II, p. 71-74.

MATTAUER, M., and HENRY, J., 1974. The Pyrenees. In: Mesozoic- Cenozoic orogenic belts. (Ed. Spencer, A.M.) Spec. Publ. Geol. Soc. Lond. 4, Scottish Academic Press.

MCCAIG, A.M., 1986. Thick- and Thin-skinned tectonics in the Pyrenees. In: E. Banda and S.M. Wickham (Editors), The Geological Evolution of the Pyrenees. Tectonophysics 129, p. 319-342.

MCCAIG, A.M., 1987. Deformation and fluid-rock interaction in metasomatic dilatant shear bands. Tectonophysics 135, p.121-132.

MCCAIG, A.M., 1988. Deep fluid circulation in fault zones. Geology 16, p.867-870.

MEY, P.H.W., NAGTEGAAL, P.J.C., ROBERTI, K.J. and HARTLEVELT, J.J.A., 1968. Lithostratigraphic subdivision of post-Hercynian deposits in the South Southern Pyrenees, Spain. Leid. Geol. Med. 41, p. 221-228.

MITRA, G., 1979. Ductile deformation zones in Blue Ridge basement rocks and estimation of finite strains. Geol. Soc. Am. Bull. 90, p.935-951.

MORLEY, C.K., 1986. Vertical strain variations in the Osen-Røa thrust sheet, North Western Oslo Fjord, Norway. J. Struct. Geol. 8, p.621-632.

MORLEY, C.K., 1987. Lateral and vertical changes of deformation style in the Osen-Røa thrust sheet, Oslo Region. J. Struct. Geol. 9, p.331-343.

MORLEY, C.K., 1988. Out-of-sequence thrusts. Tectonics 7, p. 539-562.

MULLER, J., DUCASSE, L. and VELASQUE, P.C., 1988. Pyrenee' Alpine structures: Crustal underthrusts controlled by Cretaceous inherited faults. In: Symposium on the geology of the Pyrenees and Betics, Abs. p.63.

MULLIS, V.J., 1987. Fluideinschluss- untersuchungen in den Nagna- Bohrungen der Nordschweis. Eclogae. Geol. Helv. 80, p. 553-568.

MUNOZ, J.A., and MARTINES, A., and VERGES, J., 1986. Thrust sequences in the eastern Spanish Pyrenees. J. Struct. Geol. 8. p.399-406.

NAYLOR, M.A., MANDL,G. and SIJPESTEIJN, C.H., 1986. Fault geometries in basement - induced wrench faulting under different initial stress states. J.G.S. 8, p. 737-752

OLIVER, J., 1986. Fluids expelled tectonically from orogenic belts: Their role in hydrocarbon migration and other geologic phenomena. Geology 14, p. 99-102.

OLSSEN, W.A., 1974. Grain size dependence of yield stress in marble. J. Geophys. Res.. 79, p. 4859-4862.

ONASCH, C.M., 1983. Dynamic analysis of rough cleavage in the Marlinsberg Formation, Maryland. J. Struct. Geol. 5, p. 73-82.

PARISH, M., 1984. A structural interpretation of a section of the Gavarnie Nappe and its implications for Pyrenean geology. J. Struct. Geol. 6, p.247-255.

PARRY, W.T. and BRUHN, R.L., 1986. Pore fluid and seismogenic characteristics of fault rock at depth on the Wasatch Fault, Utah. J. Geophys. Res. 91, p.730-744.

PEYBERNES, B. and SOUQUET, P., 1984. Basement blocks and tectono-sedimentary evolution in the Pyrenees during Mesozoic times. Geol Mag. 121, p.397-405.

PLATT. J.P., 1984. Secondary cleavages in ductile shear zones. J. Struct. Geol. 6, p.439-442.

PLATT. J.P., 1986. Dynamics of orogenic wedges and the uplift of high-pressure metamorphic rocks. G. S. Am. Bull. 97, p. 1037-1053.

PLATT. J.P., 1987. The uplift of high-pressure-low-temperature metamorphic rocks. Phil Trans. R.Soc. Lond. A321, p.87-103.

PLATT, J.P. and LEGETT, J.K., 1986. Stratal extension in thrust footwalls, Makran Accretionary Prism: Implications for thrust tectonics. A.A.P.G. Bull. 70, p. 191-203.

POLLARD, D.D. and SEGALL, P., 1987. Theoretical displacements and stresses near fractures in rock, with applications of faults, joints, veins, dykes and solution surfaces. In: Atkinson, B.K. (ed.) Fracture mechanics of rock. Acad. Press. Lond., England. p.277-349.

POTTER, R.W. II, and BROWN, D.L., 1977. The volumetric properties of aqueous sodium chloride solutions from 0° to 500°C at pressures up to 2000 bars based on a regression of available data in the literature. U. S. Geological Survey, Bulletin 1421-A, 36p.

PRICE, R.A., 1967. The tectonic significance of mesoscopic subfabrics in the southern Rocky Mountains of Alberta and British Columbia. Can. J. E. Sci. 4, p. 39-70.

PRICE, N.J., 1977. Aspects of gravity tectonics and the development of listric faults. J. Geol. Soc. Lond. 133, p. 311-327.

PUIGDEFABREGAS , C. and SOUQUET, R., 1986. Tectono-sedimentary cycles and depositional sequences of the Mesozoic and Tertiary from the Pyrenees. In: E. Banda and S.M. Wickham (Editors), The Geological Evolution of the Pyrenees. Tectonophysics 129, p. 173-204.

PUIGDEFABREGAS, C., MUNOZ, J.A., LOSANTOS, M. and BERASTEGUI, X., 1988. The ECORS Geological cross section. in: Symposium on the geology of the Pyrenees and Betics, Abs. p.87.

RAMSAY, J.G., 1980. The crack-seal mechanism of rock deformation. Nature 284, p. 135-140.

RAMSAY, J.G., 1982. Rock ductility and its influence on the development of tectonic structures in mountain belts. In: Hsu, J. (Ed.) Mountain Building Processes, Academic press. p. 111-127.

RAMSAY J.G. and HUBER, M.I., 1983. The techniques of modern structural geology, Volume 1: Strain analysis. Academic Press.

RAMSAY J.G. and HUBER, M.I., 1987. The techniques of modern structural geology, Volume 2: Folds and Fractures. Academic Press.

RECHES, Z., 1978. Analysis of faulting in 3-D strain field. Tectonophysics 47, p. 109-129.

RECHES, Z., 1988. Evolution of fault patterns in clay experiments. Tectonophysics 145, p. 141-156.

REYNOLDS, S.J. and LISTER, G.S., 1987. Structural aspects of fluid-rock interactions in detachment zones. Geology 15, p. 362-366.

RICE, J.R. and SIMMONS, D.A., 1976. The stabilization of spreading shear faults by coupled deformation-diffusion effects in fluid-infiltrated porous materials. J. Geophys. Res. 81, p. 5322-5334.

RICH, J.L., 1934. Mechanics of low-angle overthrust faulting as illustrated by Cumberland thrust block, Virginia, Kentucky and Tennessee. A.A.P. G. Bull. 18, p. 1584-1596.

RIDLEY, J., 1986. Parallel stretching lineations and fold axes oblique to a shear displacement direction - a model and observations. J. Struct. Geol. 8, p. 647-653.

RODDAZ, B., 1977. Le prolongement oriental de la nappe de Gavarnie et son substratum entre Barroude et le Moudang (Pyrenees Centrales). These 3° cycle, Toulouse, 140p.

ROEDDER, E., 1984. Fluid inclusions: Reviews in Mineralogy 12, Min. Soc. America.

ROSENBERG, P.E. and HOLLAND, H.D., 1964. Calcite - dolomite- magnesite stability relations in solutions at elevated temperatures. Science 145, p. 700-701.

RUTTER, E.H., 1976. The kinetics of rock deformation by pressure solution. Phil. Trans. R. Soc. Lond. A283, p. 203-219.

RUTTER, E.H. and MAINPRICE, D.H., 1978. The effect of stress relaxation on faulted and unfaulted sandstone. Pageoph. 116, p. 634-654.

RUTTER, E.H. and BRODIE, K.H., 1988. The role of tectonic grain size reduction in the rheological stratification of the lithosphere. Geol. Rund. 77, p. 295-308.

RYE, D.M., and BRADBURY, H.J. 1988. Fluid flow in the crust: an example from a Pyrenean thrust ramp. Am. J. Sci. 288. P. 197-235.

SAINT-BLANQUAT, M., BRUNEL, M. and MATTAUER, M., 1986. Les zones de cisaillement du massif Nord-pyrénéen du Saint-Berthélémy témoins de l'extension crustale d'âge crétacé. C. R. Acad. Sci. Paris 303, p. 1339-1344.

SANDERSON, D.J., 1982. Models of strain variation in nappes and thrust sheets: a review. In: G.D. Williams (ed.), Strain within thrust belts. Tectonophysics 88, p. 201-233.

SCHMID, S.M., 1975. The Glarus overthrust: Field evidence and mechanical model. Eclogae. Geol. Helv. 68, p. 247-280.

SCHMID, S.M. 1982. Microfabric studies as indicators of deformation mechanisms and flow laws operative in mountain building. In: Hsu, J. (Ed.) Mountain Building Processes, Academic press. p. 95-110.

SECOR, D.T., 1965. Role of fluid pressures in jointing. Am. J. Sci. 263, p. 633-646.

SEGALL, P. and POLLARD, D.D., 1983. Joint formation in granitic rock of the Sierra Nevada. Geol. Soc. Am. Bull. 94, p. 563-575.

SEGALL, P. and POLLARD, D.D., 1983. Nucleation and growth of strike slip faults in granite. J. G. R. 88, p. 555-568.

SEGURET, M., 1972. Etude tectonique des nappes et series decollees de la partie centrale du versant sud des Pyrenees. Pub. Ustela. Ser. Geol. Struct. Nr. 2, Montpellier.

SEGURET, M., LABAUME, P. and MADARIGA, R., 1984. Eocene seismicity in the Pyrenees from megaturbidites of the South Pyrenean Basin (Spain). Mar. Geol. 55, p. 117-131.

SEGURET, M. and DAIGNERES, M., 1985. Coupes balancées d'échelle crustale des Pyrenees. C.R. Acad. Sci. Paris. Ser. II,30. p. 341-346.

SEGURET, M., and DAIGNIERES, M., 1986. Crustal scale balanced cross section of the Pyrenees; discussion. In: E. Banda and S.M. Wickham (Editors), The Geological Evolution of the Pyrenees. Tectonophysics 129, p. 303-318.

SHEPERD,T., RANKIN, A.H. and ALDERTON, D.H.M., 1985. A practical guide to fluid inclusion studies. Chapt. 6. Practical aspects of thermometric analysis. Blackie, Glasgow. p. 93-142.

SHI, Y. and WANG, C.-Y., 1986. Pore pressure generation in sedimentary basins: overloading versus aquathermal. J. Geophys. Res. 91, p. 2153-2162.

SHI, Y. and WANG, C.-Y., 1988. Generation of high pore pressures in accretionary prisms: Inferences from the Barbados Subduction Complex. J. Geophys. Res. 93, p. 8893-8910.

SIBSON, R.H., 1981. Controls on low-stress hydro-fracture dilatancy in thrust, wrench and normal fault terrains. Nature 289, p. 665-667.

SIBSON, R.H., McM. MOORE, K. and RANKIN, A.H., 1975. Seismic pumping- a hydrothermal fluid transport mechanism. J. Geol. Soc. Lond. 131, p. 653-659.

SIBSON, R.H., FRANCOIS, ROBERT and POULSEN, K., HOWARD., 1988. High- angle reverse faults, fluid-pressure cycling, and mesothermal gold-quartz deposits. Geology 16, p. 551-555.

SIMO, A., 1986. Carbonate platform depositional sequences, Upper Cretaceous, south- central Pyrenees (Spain). In: E. Banda and S.M. Wickham (Editors), The Geological Evolution of the Pyrenees. Tectonophysics 129, p. 205-231.

SINHA, A.K., HEWITT, D.A. and RIMSTIDT, J.D., 1986. Fluid interaction and element mobility in the development of ultramylonites. Geology 14, p. 883-886.

SMITH, D.L. and EVANS, B., 1984. Diffusional crack healing in quartz. J.Geophys. Res. 89, p. 4125-4136.

SOKOUTIS, D., 1987. Finite strain effects in experimental mullions. J. Struct. Geol. 9, p. 233-242.

SOLE-SUGRANES, L.,1978. Gravity and compressive nappes in the South Central Pyrenees (Spain). Am. J. Sci. 278, p. 609-637.

SOULA, J.C., LAMOUROUX, C., VIALLARD, P., BESSIERE, G., DEBAT, P. and FERRET, B., 1986. The mylonite zones in the Pyrenees and their place in the alpine tectonic evolution. Tectonophysics 129, p. 115-147.

STEPHENS, M.B., GLASSON, M.J. and KEAYS, R.R.,1979. Structural and chemical aspects of metamorphic layering development in metasediments from Clunes, Australia. Am. J. Sci. 279, p. 129-160.

TEUFEL, C.W. 1980. Precursive pore pressure changes associated with premonitory slip during stick-slip sliding. Tectonophysics 69, p. 189-199.

TEUFEL, L.W., 1981. Pore volume changes during frictional sliding of simulated faults. A.G.U. Monograph: Mechanical deformation of crustal rocks. p.135-145.

VAN DEN DRIESSCHE, J. and BRUN, J.-P., 1987. Rolling structures at large shear strain. J. Struct. Geol. 9, p. 691-704.

VAN LITH, J.G.J., 1965. Geology of the Spanish part of the Gavarnie Nappe (Pyrenees) and its underlying sediments near Bielsa (Province of Huesca). Geologica Ultraiectina 10, p. 5-64.

VERNON, R.H., 1977. Microfabric of mica aggregates in partly recrystallised biotite. Contrib. Min. Pet. 61, p. 175-185.

VROLIJK, P., MYERS, G. and MOORE, J.C., 1988. Warm fluid migration along tectonic melanges in the Kodiak Accretionary Complex, Alaska. J. Geophys. Res. 93, p. 10313-10324.

WALDER, J. and NUR, A., 1984. Porosity reduction and crustal pore pressure development. J. Geophys. Res. 89, p. 11539-11548.

WELBON, A., 1988. The influence of intrabasinal faults on the development of a linked thrust system. Geol. Rund. 771, p. 11-24.

WHITE, S.H. and KNIPE, R.J., 1978. Transformation- and reaction-enhanced ductility in rocks. J. Geol. Soc. Lond. 135, p. 513-516.

WHITE, S.J. and KNIPE, R.J., 1978. Microstructure and cleavage development in selected slates. Contrib. Mineral. Petrol. 66, p. 165-174.

WHITE, S.H., BURROWS, S.E., CARRERAS, J., SHAW, N.D.and HUMPHREYS, F.J., 1980. On mylonites in ductile shear zones. J. Struct. Geol. 2, p. 175-187.

WILLIAMS, G.D., 1985 Thrust sequences in the South Central Pyrenees. J. Struct. Geol. 7, p. 11-18.

WILLIAMS, G.D., and FISCHER, M.W, 1984. A balanced cross section across the Pyrenean orogenic belt. Tectonics 3, p.773-780.

WILSON, C.J.L. and BELL, I.A., 1979. Deformation of biotite and muscovite: optical microstructure. Tectonophysics 58, p.179-200.

WOJTAL, S. and MITRA, G. 1986. Strain hardening and softening in fault zones from foreland thrust zones. Geol. Soc. Am. Bull. 97, p. 674-687.

WOJTAL, S., 1986. Deformation within foreland thrust sheets by population of minor faults. J. Struct. Geol. 8, p. 341-360.

YARDLEY, B.W.D., 1986. Fluid migration and veining in the Connemara schists. Advances in Physical Geochemistry 5, p. 109-131.

ZWART, H.J., 1979. The Geology of the Central Pyrenees. Lied. Geol. Med. 50, p. 1-74.

APPENDIX 1

Microstructural techniques.

The microstructural study of specimens referred to in the text is based on oriented hand specimens collected during field work. Oriented thin sections were cut from these rocks for optical study. In addition, polished thin sections and uncovered lakeside thin sections were also prepared. The former were used for microprobe work and for back scattered electron microscopy (BSEM). The latter were for preparing the foils for ion beam thinning that were used on the transmission electron microscope (TEM). Resin mounted polished blocks were used in addition to polished thin sections for studying fine grained rocks as these could be prepared with a minimum of surface damage (see Lloyd (1987) for a discussion of the preparation of these blocks).

The oriented sections and blocks were generally cut as near as possible perpendicular to the movement plane and parallel to the movement direction. This plane will be referred to as the xz coordinate plane (figure 1). It does not necessarily coincide with the XZ plane of the strain ellipsoid. In some hand specimens xy and yz sections were also prepared and were used to obtain information on the three dimensional form of the microstructures.

The instruments used in the study were as follows:
1. Microprobe work was performed using a JEOL-JXA-50A electron microprobe in the Earth Sciences department. This was fitted with a Link Systems 860, Series 2 microanalyser. Spot analyses were done using a 100s analysis time.
2. The BSEM work was done on a Cambridge Series 2 electron microscope using a 20kV operating voltage and a working distance of 16mm. SEM work was done with a 24mm working distance.
3. The Tem work used the JEOL-200 CX 220KV scanning transmission electron microscope housed in Electron Optics, Department of Metallurgy. Qualitative microanalyses were carried out on this instrument using a Link System, System 860, Series 2 Energy Dispersive microanalyser.

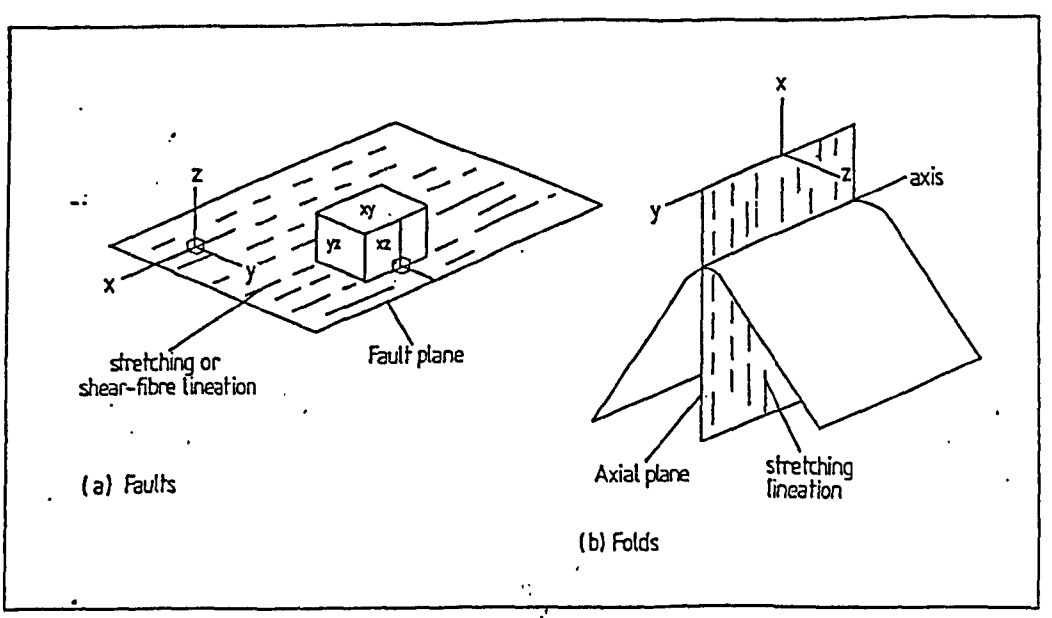

Figure A1. Coordinate framework used to describe the orientation of thin sections. a) Coordinate axes for faults. b) Coordinate axes for folds.

analysis	1	2	3	4	5	6	7	8	9	10
oxide	chlorite	chlorite	chlorite	chlorite	chlorite	chlorite	chlorite	chlorite	chlorite	chlorite
Si	26.27	26.29	26.17	27.18	27	26.29	26.47	26.23	26.22	25.68
Ti	0	0.14	0	0	0	0.07	0	0	0	0.03
Al	23.05	22.3	21.81	22.97	22.95	22.95	23.11	22.44	22.97	23.12
Cr	0	0	0	0	0.03	0	0.18	0.01	0.02	0
Fe	23.46	21.27	19.91	18.84	18.49	18.8	19.07	19.53	21.54	21.43
Mn	0.01	0	0.01	0.12	0	0.08	0	0.14	0	0.16
Mg	15.68	16.47	17.51	18.8	18.75	18.96	18.27	16.74	16.56	16
Ca	0	0.02	0.02	0.06	0.08	0.02	0	0.01	0.06	0
Na	0	0.36	0.05	0.28	0.11	0.25	0	0.03	0.12	0.17
K	0.03	0.09	0.07	0.04	0.07	0	0.05	0	0	0
Ni	0	0	0.15	0	0.01	0	0	0.17	0.01	0.02
O	0	0	0	0						
total	88.50	86.94	85.70	88.29	87.49	87.42	87.15	85.30	87.50	88.61
formula										
Si	5.396	5.453	5.473	5.467	5.468	5.35	5.402	5.492	5.4	5.352
Ti	0	0.022	0	0	0	0.011	0	0	0	0.005
Al	5.585	5.455	5.379	5.448	5.481	5.509	5.561	5.54	5.579	5.68
Cr	0	0	0	0	0.004	0	0.029	0.001	0.003	0
Fe	4.031	3.691	3.482	3.169	3.132	3.2	3.254	3.421	3.711	3.735
Mn	0.001	0	0.002	0.02	0	0.014	0	0.024	0	0.029
Mg	4.8	5.092	5.457	5.636	5.659	5.751	5.555	5.224	5.083	4.969
Ca	0	0.003	0.004	0.013	0.017	0.004	0	0.003	0.012	0
Na	0	0.145	0.022	0.11	0.042	0.099	0	0.013	0.047	0.069
K	0.007	0.024	0.019	0.01	0.017	0	0.014	0	0	0
Ni	0	0	0.025	0.011	0.002	0	0	0.029	0.002	0.003
O	28	28	28	28	28	28	28	28	28	28
total	19.820	19.885	19.863	19.884	19.822	19.938	19.815	19.747	19.837	19.842
ratios										
Al	0.39	0.38	0.38	0.38	0.38	0.38	0.39	0.39	0.39	0.39
Fe	0.28	0.26	0.24	0.22	0.22	0.22	0.23	0.24	0.26	0.26
Mg	0.33	0.36	0.38	0.40	0.40	0.40	0.39	0.37	0.35	0.35
Mg No.	54.354	57.976	61.047	64.009	64.373	64.250	63.061	60.428	57.801	57.089

APPENDIX 2 REPRESENTATIVE ANALYSES OF ZONED CHLORITES IN SAMPLE NFS4.1

analysis	1	2	3	4	5	6	7	8	9	10
oxide	chlorite	chlorite	chlorite	chlorite	chlorite	chlorite	chlorite	chlorite	chlorite	chlorite
Si	25.59	25.917	25.571	26.398	26.372	27.33	26.991	26.885	27.335	25.189
Ti	0	0.053	0	0	0	0.104	0.073	0.009	0.022	0.022
Al	23.172	23.757	23.434	22.996	23.007	22.956	23.196	23.244	22.782	23.625
Cr	0.059	0.076	0	0.036	0	0	0.034	0	0	0.045
Fe	27.318	27.256	25.02	22.396	22.087	21.908	22.006	24.118	23.449	26.797
Mn	0.056	0	0.082	0	0.164	0.053	0.15	0.077	0.156	0
Mg	13.681	13.531	15.505	16.49	17.513	18.604	16.878	16.841	16.491	13.935
Ca	0	0.004	0.047	0	0.042	0.005	0.004	0	0.105	0.012
Na	0.068	0.1	0.182	0	0.054	0.517	0	0.143	0.316	0.099
K	0.123	0	0.001	0.03	0.085	0	0.011	0	0.03	0.023
Ni	0.026	0	0	0.021	0	0.105	0	0	0.026	0.251
O										
total	90.093	90.694	89.842	88.367	89.324	91.582	89.343	91.317	90.712	89.978
formula										
Si	5.281	5.294	5.23	5.401	5.34	5.385	5.443	5.363	5.476	5.193
Ti	0	0.008	0	0	0	0.015	0.011	0.001	0.003	0.003
Al	5.637	5.72	5.649	5.546	5.491	5.332	5.514	5.465	5.379	5.746
Cr	0.01	0.012	0	0.006	0	0	0.005	0	0	0.007
Fe	4.715	4.656	4.279	3.832	3.74	3.61	3.711	4.024	3.929	4.624
Mn	0.01	0	0.014	0	0.028	0.009	0.026	0.013	0.027	0
Mg	4.209	4.12	4.727	5.03	5.286	5.465	5.074	5.008	4.925	4.286
Ca	0	0.001	0.01	0	0.009	0.001	0.001	0	0.023	0.003
Na	0.027	0.039	0.072	0	0.021	0.197	0	0.055	0.123	0.04
K	0.032	0	0	0.008	0.022	0	0.003	0	0.008	0.006
Ni	0.004	0	0	0.003	0	0.017	0	0	0.004	0.042
O	28	28	28	28	28	28	28	28	28	28
total	19.925	19.850	19.981	19.826	19.937	20.031	19.788	19.929	19.897	19.950
ratios										
Al	0.39	0.39	0.39	0.38	0.38	0.37	0.39	0.38	0.38	0.39
Fe	0.32	0.32	0.29	0.27	0.26	0.25	0.26	0.28	0.28	0.32
Mg	0.29	0.28	0.32	0.35	0.36	0.38	0.35	0.35	0.35	0.29
Mg No.	47.165	46.946	52.487	56.759	58.564	10.000	57.758	55.447	55.625	48.103

APPENDIX 2 REPRESENTATIVE ANALYSES OF ZONED CHLORITES IN SAMPLE NFS2.S3

analysis	B8562	B8560	BL9	BL3	BL12	BL19	BL11	BL6	BL6	BL13	BL1	BL20
oxide	*chlorite*	*chlorite*	*chlorite*	*chlorite*	*chlorite*	*chlorite*	*chlorite*	*chlorite*	*chlorite*	*chlorite*	*chlorite*	*chlorite*
Si	27.573	24.933	28.949	30.18	26.644	24.358	26.576	30.733	28.521	25.638	30.24	24.735
Ti	0.01	0.017	0.086	0.079	0.043	0	0.058	0.089	0	0	0.023	0.015
Al	24.751	24.555	24.673	23.435	25.434	24.152	25.362	20.281	20.968	24.826	22.33	24.247
Cr	0.047	0.06	0	0	0.044	0.018	0	0.071	0	0.032	0.017	0.019
Fe	17.626	28.462	16.686	4.488	24.687	29.521	20.298	1.241	9.06	28.779	1.188	30.2
Mn	0.124	0.084	0.073	0	0.042	0.102	0.123	0.024	0	0.08	0.086	0.127
Mg	18.489	8.991	16.926	26.199	14.084	8.622	13.186	29.927	25.406	10.424	28.434	9.375
Ca	0.007	0.171	0.079	0.093	0.016	0.015	0.056	0.096	0.321	0.06	0.059	0
Na	0.415	0.403	0.27	0	0.591	0.225	0.307	0.385	0.237	0.713	0.608	0.045
K	0	0.074	0.076	0	0.097	0.004	0.124	0.059	0.091	0.095	0.022	0.075
Ni	0.011	0.044	0.021	0.072	0	0.144	0.044	0.118	0	0.073	0	0.015
O	0	0	0	0								
total	89.05	87.79	87.84	84.55	91.68	87.16	86.13	83.02	84.60	90.72	83.01	88.85
formula												
Si	5.445	5.317	5.736	5.833	5.302	5.27	5.5	5.983	5.696	5.288	5.874	5.254
Ti	0.002	0.003	0.013	0.011	0.006	0	0.009	0.013	0	0	0.003	0.002
Al	5.76	6.172	5.763	5.339	5.966	6.159	6.187	4.654	4.936	6.035	5.113	6.07
Cr	0.007	0.01	0	0	0.007	0.003	0	0.011	0	0.005	0.003	0.003
Fe	2.911	5.076	2.765	0.725	4.109	5.342	3.513	0.202	1.513	4.964	0.193	5.365
Mn	0.021	0.015	0.012	0	0.007	0.019	0.021	0.004	0	0.014	0.014	0.023
Mg	5.442	2.858	4.999	7.548	4.178	2.781	4.068	8.685	7.564	3.025	8.234	2.968
Ca	0.001	0.039	0.017	0.019	0.003	0.004	0.012	0.02	0.069	0.013	0.012	0
Na	0.159	0.167	0.104	0	0.228	0.094	0.123	0.146	0.092	0.285	0.229	0.018
K	0	0.02	0.019	0	0.025	0.001	0.033	0.015	0.023	0.025	0.006	0.02
Ni	0.002	0.008	0.003	0.011	0	0.025	0.007	0.018	0	0.012	0	0.003
O	28	28	28	28	28	28	28	28	28	28	28	28
total	19.750	19.685	19.43	19.49	19.83	19.70	19.47	19.75	19.89	19.67	19.68	19.73
ratios												
Al	0.41	0.44	0.43	0.39	0.42	0.43	0.45	0.34	0.35	0.43	0.38	0.42
Fe	0.21	0.36	0.20	0.05	0.29	0.37	0.26	0.01	0.11	0.35	0.01	0.37
Mg	0.39	0.20	0.37	0.55	0.29	0.19	0.30	0.64	0.54	0.22	0.61	0.21
Mg No.	65.150	36.022	64.387	91.237	50.416	34.236	53.660	97.727	83.331	37.865	97.710	35.617

APPENDIX 2 REPRESENTATIVE ANALYSES OF BASEMENT LOG CHLORITES

analysis	1	2	3	4	5	6	7	8	9	10
oxide	pyrophyllite	muscovite	pyrophyllite	pyrophyllite	muscovite	muscovite	pyrophyllite	pyrophyllite	pyrophyllite	pyrophyllite
Si	63.415	46.654	63.993	61.107	52.405	50.755	63.969	65.26	66.043	65.746
Ti	0.078	0.032	0.037	0.041	0	0.074	0	0.085	0.054	0
Al	28.525	36.037	27.673	28.55	32.09	32.934	28.125	28.607	27.635	28.345
Cr	0	0	0.051	0.017	0.075	0.002	0.07	0	0.014	0.08
Fe	0.298	0.168	0.483	0.689	0.548	0.261	0.233	0.345	0.149	0.089
Mn	0.036	0.063	0.016	0.042	0.042	0	0	0	0	0.003
Mg	0.011	0.455	0	0.283	0.507	0.537	0.282	0.121	0.106	0.218
Ca	0.027	0.019	0.012	0.08	0.051	0	0	0	0	0.092
Na	0.011	1.039	0.151	0.216	0.985	0.334	0.348	0	0.043	0.216
K	0.558	9.066	0.591	0.711	0.269	7.027	0.382	0.289	0.066	0.18
Ni	0.126	0	0.073	0	6.269	0.072	0.078	0	0.028	0
O										
total	93.085	93.533	93.080	89.736	93.241	91.996	93.487	94.707	94.138	94.969
formula										
Si	7.83	6.23	7.907	7.861	6.867	6.737	7.862	7.894	8.008	7.924
Ti	0.007	0.003	0.003	0.004	0	0.007	0	0.008	0.005	0
Al	4.151	5.672	4.03	4.026	4.956	5.153	4.074	4.079	3.95	4.027
Cr	0	0	0.005	0.002	0.008	0	0.007	0	0.001	0.008
Fe	0.031	0.019	0.05	0.074	0.06	0.029	0.024	0.035	0.015	0.009
Mn	0.004	0.007	0.002	0.005	0.005	0	0	0	0	0
Mg	0.002	0.091	0	0.054	0.099	0.106	0.052	0.022	0.019	0.039
Ca	0.004	0.003	0.002	0.011	0.007	0	0	0	0	0.012
Na	0.003	0.269	0.036	0.054	0.25	0.086	0.083	0	0.01	0.05
K	0.088	1.545	0.093	0.117	1.048	1.19	0.06	0.045	0.01	0.028
Ni	0.012	0	0.007	0	0	0.008	0.008	0	0.003	0
O	22	22	22	22	22	22	22	22	22	22
total	12.132	13.839	12.135	12.208	13.300	13.316	12.170	12.083	12.021	12.097
ratios										
Al/AFM	0.99	0.98	0.99	0.97	0.97	0.97	0.98	0.99	0.99	0.99
Fe/AFM	0.01	0.00	0.01	0.02	0.01	0.01	0.01	0.01	0.00	0.00
Mg/AFM	0.00	0.02	0.00	0.01	0.02	0.02	0.01	0.01	0.00	0.01
muscovite	0.09	0.89	0.05	0.07	0.57	0.63	0.07	0.05	0.00	0.04
celadonite	0.03	0.06	0.03	0.07	0.08	0.07	0.04	0.04	0.02	0.02
pyrophyllite	0.97	0.74	0.97	0.94	0.79	0.80	0.96	0.97	0.99	0.97

APPENDIX 2 REPRESENTATIVE ANALYSES OF SLIP SURFACE MICAS

analysis	1	2	3	4	5	6	7	9	10	11	12
oxide	mica	mica	mica	mica	mica	mica	mica	mica	mica	mica	mica
Si	47.721	49.351	53.942	47.504	47.887	42.417	53.614	47.924	47.659	43.46	48.764
Ti	0.111	0	0	0.234	0	0.102	0.063	0.411	0.217	0.039	0.063
Al	34.38	34.103	30.431	33.089	34.569	24.831	34.642	28.84	29.768	30.82	32.655
Cr	0.073	0.017	0	0	0.061	0.049	0.059	0.012	0	0.067	0.062
Fe	1.002	0.923	0.631	1.772	0.332	0.755	0.866	5.668	4.648	1.057	1.876
Mn	0	0.033	0.004	0.032	0.027	0	0	0.097	0.014	0.066	0
Mg	1.069	1.001	0.375	1.254	1.573	0.523	0.547	3.255	2.486	0.928	0.342
Ca	0	0	0.039	0.033	0	0.109	0.067	0	0.052	0.036	0.017
Na	1.011	0.334	0.598	0.338	0.611	0.508	0.536	0.356	0	0.383	0.096
K	10.239	9.776	6.392	10.608	10.728	5.016	6.768	8.189	7.788	9.229	10.3
Ni	0.044	0.043	0.05	0.066	0.033	0	0.034	0	0.041	0.051	0
O											
total	95.650	95.581	92.462	94.930	95.821	74.310	97.196	94.752	92.673	86.136	94.175
formula											
Si	6.307	6.466	7.084	6.356	6.306	6.955	6.736	6.48	6.515	6.365	6.534
Ti	0.011	0	0	0.024	0	0.013	0.006	0.042	0.022	0.004	0.006
Al	5.356	5.267	4.711	5.218	5.365	4.799	5.13	4.596	4.796	5.32	5.157
Cr	0.008	0.002	0	0	0.006	0.006	0.006	0.001	0	0.008	0.007
Fe	0.111	0.101	0.069	0.198	0.037	0.104	0.091	0.641	0.531	0.13	0.21
Mn	0	0.004	0	0.004	0.003	0	0	0.011	0.002	0.008	0
Mg	0.211	0.195	0.073	0.25	0.309	0.128	0.102	0.656	0.507	0.203	0.068
Ca	0	0	0.006	0.005	0	0.019	0.009	0	0.008	0.006	0.002
Na	0.259	0.085	0.152	0.088	0.156	0.162	0.13	0.093	0	0.109	0.025
K	1.726	1.643	1.071	1.811	1.802	1.049	1.085	1.413	1.358	1.725	1.761
Ni	0.005	0.005	0.005	0.007	0.004	0	0.003	0	0.004	0.006	0
O	22	22	22	22	22	22	22	22	22	22	22
total	13.994	13.768	13.171	13.961	13.988	13.235	13.298	13.933	13.743	13.884	13.770
ratios											
Al/AFM	0.94	0.95	0.97	0.92	0.94	0.95	0.96	0.78	0.82	0.94	0.95
Fe/AFM	0.02	0.02	0.01	0.03	0.01	0.02	0.02	0.11	0.09	0.02	0.04
Mg/AFM	0.04	0.04	0.02	0.04	0.05	0.03	0.02	0.11	0.09	0.04	0.01
muscovite	0.85	0.77	0.46	0.82	0.85	0.52	0.63	0.76	0.74	0.82	0.73
celadonite	0.17	0.15	0.07	0.25	0.17	0.13	0.10	0.70	0.54	0.17	0.15
pyrophyllite	-0.02	0.08	0.47	-0.07	-0.02	0.35	0.27	-0.46	-0.28	0.01	0.12

APPENDIX 2 REPRESENTATIVE ANALYSES OF MATRIX MICAS

CATALOGUE NUMBER	SAMPLE NUMBER	ORIENTATION	CATALOGUE NUMBER	SAMPLE NUMBER	ORIENTATION
7126	B8533	102/60S	47775	B8533	018/90
7127	B8562	106/72S	47782	B8580	040/90
7128	B8530	338/72W	47782	B8580	040/90
7172	B85170	005/90	47783	B8568	022/70NW
7174	B8560	020/90	47788	B8569	020/90
7175	B8567	030/60W	48942	NFS4.2	040/80:119/66
7176	B8563	001/90	48953	BL11	128/70S:120/17N
7177	B8562	015/90	49195	NFS4.1	355/78E
7178	B8533	102/60S	49196	BL1	028/72W
7430	NFS4.2	040/80NW	49197	BL9	015/75W
7433	PPVS.S1.1	360/60E	49198	BL3	328/84E
7434	BL6	012/83W	49199	BL14	011/86E
7435	NFS2.S3	167/84E	49200	BL17	020/60E
7526	NFS4.1	355/78E	49201	BL10	335/90
7527	BL1	028/78W	49202	BL16	005/75W
7528	BL20	360/88W	49203	BL20	360/88W
7529	BL13	020/76W	49204	BL19	044/90
7530	BL19	023/74W	49205	BL13	020/76W
7531	BL21	014/84W	49206	BL21	014/84W
7533	NFS1.19	044/90	49208	BL2	022/65E
47520	B8560	030/90	49209	BL12	017/80W
47522	B8562	010/90	49210	BL25	007/90
47523	B8563	001/90	49211	NFS1.19	044/90
47525	B8533	018/88NW	49213	BL22	040/80SE
47531	B8580	024/76W	49447	BG6	028/74E
47535	B8568	022/70NW	49453	FI1	
47773	B85170	005/90	49454	FI2	
47774	B8567	030/60W			

Line of Section
figure 3.6

420 421 422 423

51 50 49 48 47 46 45

N

PIC DE GERBATS 2904

PETIT PIC BLANC ▲ 2957

PIC HEID ▲ 3022

PIC DE TROUMOUSE ▲ 3085

3133 ▲ PIC DE LA MUNIA

3003 ▲ ROBINERA

Murrailles de Barroude

Refuge de Barroude

CIRQUE DE BARROUDE

Lacs de Barroude

2355

Port de Barroude 2534

Soum de Barroude

PIC DE PORT VIEUX 2723

PIC DE BARROSA 2746

2763

CIRQUE DE BARROSA

SIERRA DE LIENA

2543

2515

Liena Fault

La Coma ▲ 2120

▲ 1960

▲ 1690

figure 3.11

B B' C C'

Sia Thrust Unit
Bouneau Fm
Sugar Marble Fm
Fourche de Sede Fm
Silurian Graphitic Phyllite
Upper Cretaceous Lst
Triassic Red Beds
Migmatite
Granite / Granodiorite

Gavarnie Thrust
Other Thrust
High angle oblique-slip reverse fault
Normal fault
Landslide
Bedding
Cleavage
• 1960 Spot height (metres)
Fold axis

0 1Km

Figure 3.1. 1:10000 geological map of the of the Barroude-Liena area. Stratigraphical boundaries in the Gavarnie thrust sheet are taken from Van Lith (1965), Parish (1984) and from the authors observations.

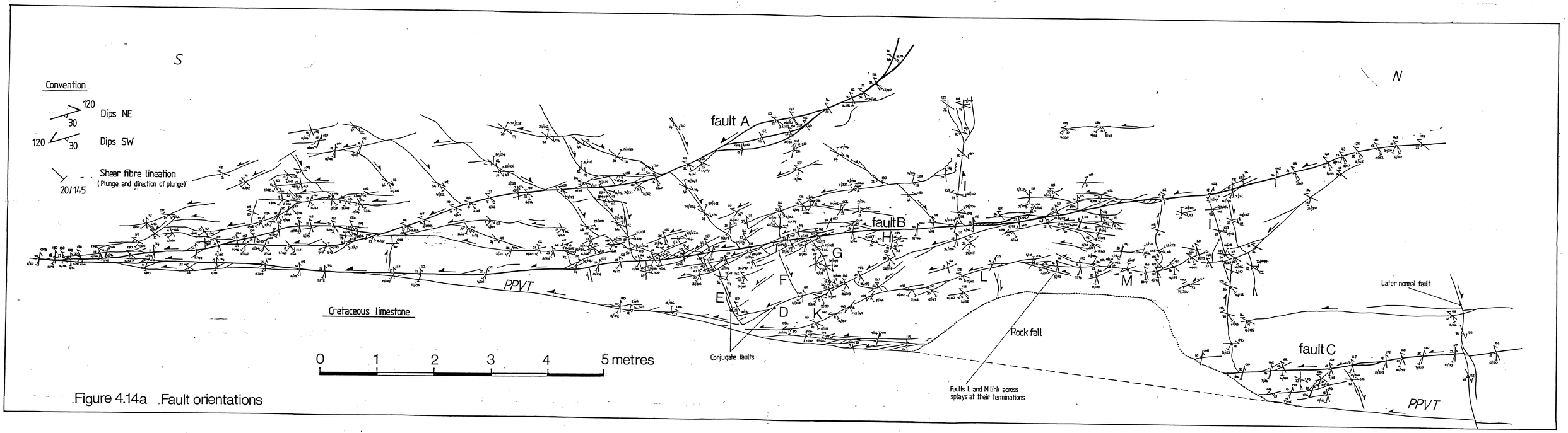

Figure 4.14a Fault orientations

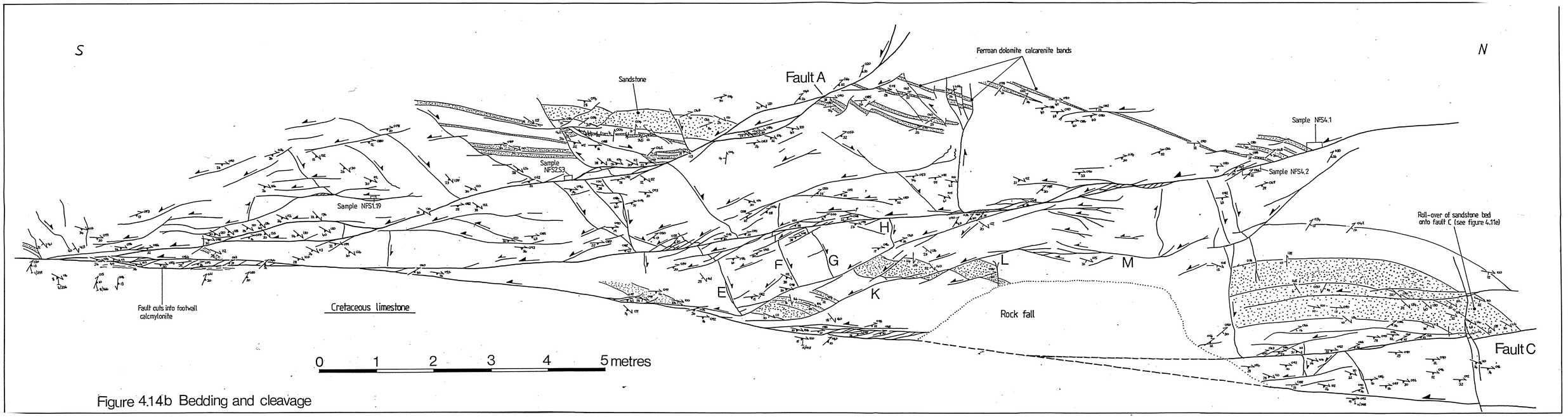

Figure 4.14b Bedding and cleavage

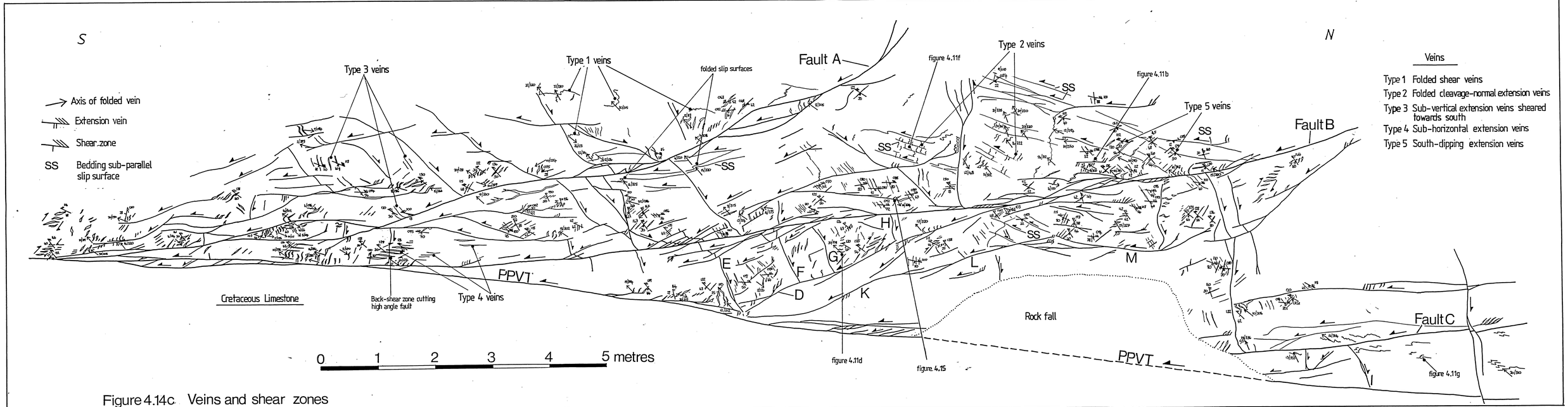

Figure 4.14c Veins and shear zones